3*d* - Transition Metal Chalcogenides for Applications in Photo- and Electrocatalysis

Dissertation

zur Erlangung des akademischen Grades

„doctor rerum naturalium"

(Dr. rer. nat.)

in der Bayreuther Graduiertenschule für Mathematik und Naturwissenschaften (BayNAT) der Universität Bayreuth

vorgelegt von

Judith Zander

geboren in Gifhorn

Bayreuth, Juli 2023

Die vorliegende Arbeit wurde in der Zeit von November 2020 bis Juli 2023 in Bayreuth am Lehrstuhl für Physikalische Chemie III unter Betreuung von Herrn Prof. Dr. Roland Marschall angefertigt.

Vollständiger Abdruck der von der Bayreuther Graduiertenschule für Mathematik und Naturwissenschaften (BayNAT) der Universität Bayreuth genehmigten Dissertation zur Erlangung des akademischen Grades einer Doktorin der Naturwissenschaften (Dr. rer. nat.)

Form der Dissertation: Kumulative Dissertation

Dissertation eingereicht am: 27.07.2023

Zulassung durch die Promotionskommission: 17.08.2023

Wissenschaftliches Kolloquium: 17.11.2023

Amtierender Direktor: Prof. Dr. Jürgen Köhler

Prüfungsausschuss:

Prof. Dr. Roland Marschall   (Gutachter)

Prof. Dr.-Ing. Christina Roth   (Gutachterin)

Prof. Dr. Matthias Breuning   (Vorsitz)

Prof. Dr. Birgit Weber

Acknowledgements

First and foremost, I want to thank Prof. Dr. Roland Marschall. Thank you for providing the opportunity of pursuing my PhD in your group and for supporting me throughout these years. You introduced me into a topic I came to love very much and I am immensely grateful for that! I am sure that it will have a fundamental impact in my future. You also managed to find the exact right balance between providing the guidance I needed, without trying to control me overly much – that is something by no means taken for granted and I count myself lucky to have had you as my PI.

Second, I want to thank Prof. Dr.-Ing. Christina Roth and Prof. Dr. Birgit Weber for being my mentors and offering their assistance. Especially I thank Prof. Dr.-Ing Christina Roth for providing access to her labs and the CO_2-reduction setup and I am grateful to Dr. Tintula Kottakkat and Hendrik Hoffmann for introducing me to the setup and helping me with the measurements.

Very importantly, I would like to thank everyone who is, or who formerly was, a member of the PC III working group. Without you, this work would not have been possible. I am grateful for every discussion we had that provided me with new ideas and insights, about the cooperations in the lab and of course for all the measurements you did for me. In this regard, I especially want to thank Dr. Anja Hofmann and Mirco Ade for REM and EDX analysis, Dr. Jana Timm and Jonas Jungmann for physisorption measurements, Dr. Christopher Simon and Jonas Jungmann for TEM analysis and Dr. Morten Weiss and Lion Schumacher for the XPS measurements. Dr. Morten Weiss, I owe you a lot also in regards to the assistance you provided in XPS and Rietveld analysis. I am quite aware how annoying I could be, questioning everything and always finding a new problem to throw at you. Sometimes I am a bit surprised that you didn't throw me out of a window. Furthermore, I want to apologise to Lion Schumacher who probably can't hear the sentence 'I have some more samples for XPS' anymore and who measured them anyway. I also want to stress the gratitude I feel to everyone who was at a point sharing an office with me, which especially includes Mirco Ade (sorry for the 'Micro' again), Lion Schumacher and Jonas Jungmann. Thank you for enduring my shouting at my computer (on top of occasional unexpected squeaking noises) and for helping me if the desktop turned black again – or similarly annoying and totally unnecessary things happened.

Before I forget it, I also want to thank everyone who read this thesis despite the not-so-very-short theoretical background section. All of you provided valuable advice and suggestions and thus contributed a lot to the thesis being what it is now.

But of course it doesn't end here! I am furthermore grateful for the assistance I got from students who taught me how to supervise someone else in the lab and who didn't complain when I buried them under work – I do feel a bit sorry. Special thanks go to the members of the inofficial 'Workgroup Zander' or 'Team Sulphides', which include Julia Wölfel, Teresa Mauerer, Julian Merlin Kaulbersch, Jan Hetzel and Fabiane Lira. If all of you hadn't been able to work this well and this independently, there have been times when I would have gone crazy.

And this was only the scientific part... Just as important as the fruitful work together, was the overall enjoyable atmosphere in lab and office, every one of you contributed to. I truly appreciate all the non-scientific discussions we engaged in and the fun we had together outside of the lab. Thanks for bearing my squeaking around! I valued the monthly group events – be it a wonderful barbecue, a visit to the Christmas market, or laser tag. I have to say that I am also quite pleased that half of the chair is now diving – although exhausting, it was fun teaching you – and am looking forward to a joint diving holiday!

Last but not least, I want to thank my family and friends for their love, understanding and continuing support. All of you provided a wonderful counterpart to work and were the reason for many relaxing, enjoyable and simply fun times that reminded me that life is not only all about work. Especially, I would like to thank Andreas Schnek Erhardt, who started the journey of studying chemistry together with me and offered me his friendship throughout these years. Thank you for all the practical courses we did together during the Bachelor studies, for all the activities we did in the following years and for your continued friendship although I was spending so much time in the lab. Additionally, I want to thank Dr. Anja Hofmann for the late nights in the lab that alone would have been infinitely more boring, for the many discussions – work related and completely unrelated – and for all the activities, we did outside of work. It is incredibly valuable if the colleagues you spend every day with also become your friends. Special thanks also go to Dr. Morten Weiss again, who was always there to help me with basically everything and made sure that I spend at least some evenings relaxing. I am very grateful that I met you and treasure all the hiking trips we did together – I just can't imagine that otherwise I would never have known how beautiful the landscape around Bayreuth truly is!

Of course there are many others whom I met independent of university, some of which I have known for a long time. I am grateful that I met you all and for every day we spend having fun and talking about everything but work. Additionally, I want to thank my family – I kept staving it off until the end, because I feel unable to find words suitable for expressing my gratitude. No matter what, you were always there, offering love and support in every regard, and at the same time trusted me to go out into the world and find my own way.

And now… let's finally do some science!

Table of Content

Abstract

This work focusses on the development of iron chalcogenide based materials for both photo- and electrocatalytic applications. Both applications are currently receiving global attention, since they represent sustainable alternatives to conventional fossil-fuel reliant industrial processes. However, electrochemical reactions, such as water electrolysis, are still not cost-competitive. Hence, continued research is required in this field, especially focussing on the design of new, earth-abundant catalysts.

The first work in this thesis is therefore focussing on the development of a microwave-assisted solvothermal synthesis of $CuFe_2O_4$ nanoparticles. An optimisation of synthesis parameters, including the solvent mixture and the pH value allows for the preparation of $CuFe_2O_4$ particles with a narrow size distribution over a wide range of different synthesis times and temperatures. Specifically, the synthesis time could be decreased down to 1 min at 175 °C, while the synthesis temperature could be lowered to 120 °C. After a thorough material characterisation, including the degree of inversion, the $CuFe_2O_4$ particles were employed in the electrochemical reduction of CO_2 to CO. The synthesis time was shown to have a significant influence on both CO yield and selectivity. The highest activity was thereby observed for $CuFe_2O_4$ synthesised for 10 min, reaching 0.2 $\mu mol\,h^{-1}\,g^{-1}$ and a Faradaic efficiency of 20%. This could be explained by a combination of a decrease in the degree of inversion during continued heating in the microwave, a larger amount of organics for particles obtained after very short times, and a slightly higher crystallite size observed after medium synthesis times of 10 min. It was thus shown that the electrocatalytic performance can be tuned by the synthesis conditions. Additionally, no carbon containing products except CO were observed and H_2 was the only other product formed, making $CuFe_2O_4$ an interesting, earth-abundant catalyst for the direct production of syngas.

Compared to electrocatalysis, photocatalysis combines light absorption and charge carrier excitation with the subsequent target reactions into one system, without the need for an external driving force. To improve the efficiency, charge separation is commonly promoted by the addition of a cocatalyst. Charges are transferred to these cocatalysts and they provide active sites for the reaction – thus they share many similarities with electrocatalysts. The second work presented in this thesis therefore targets the synthesis and application of Ni_2FeS_4 as an earth-abundant cocatalyst substitute for noble metals in the H_2 evolution from water. Firstly, the microwave-assisted synthesis of Ni_2FeS_4 in organic solvents and benzyl mercaptan as sulphur source was optimised. Thus, it could be shown that phase pure, crystalline Ni_2FeS_4 nanosheets can be prepared in only 1 min. Subsequently, Ni_2FeS_4 was used as a cocatalyst on TiO_2 (P25). The photocatalytic activity of P25 could thus be promoted by a factor of 8 and reached 25-28 $\mu mol\,h^{-1}$ under simulated sunlight. Exceptionally low mass-ratios of 0.5 wt.% of Ni_2FeS_4 could be realised, without a loss of activity. Furthermore, a stable H_2 evolution was observed over the course of 20 h. If UV irradiation was used instead of simulated sunlight, the activity enhancement is even more pronounced, initially reaching 48 times that of bare P25. Ni_2FeS_4 is thus a suitable, non-noble cocatalyst for the HER, which can additionally be prepared under mild conditions.

While H_2 is an ideal green fuel, its storage is complicated and large portions of the produced H_2 are actually required as feedstock for industrial processes. One such process is the Haber-Bosch process for the synthesis of NH_3. Photocatalytic nitrogen reduction offers a sustainable alternative, but it requires the development of efficient N_2 activation catalysts. Carbon nitrides (CN) are among the most widely investigated catalysts for these nitrogen fixation reactions. Therefore, vacancy rich carbon nitride (V_N-CN) was synthesised in the third work of this thesis and combined with biomimetic FeS_2

(pyrite). This combination resulted in an increased ammonia yield by approx. 400% compared to unmodified carbon nitride, even at low loadings of FeS_2. However, a set of material characterisation and control experiments revealed that ammonia is not generated *via* the reduction of N_2 gas, but instead by a decomposition of cyano-groups at the defect sites in V_N-CN. FeS_2 is further promoting this light-induced decomposition reaction by coordinating to the defect sites and activating the cyano-groups *via* π-back-donation. It was thus shown that although comparatively high ammonia yields can be achieved by this system, it is not *via* photocatalytic NRR, for which V_N-CN is therefore unsuitable.

Kurzfassung

Der Fokus dieser Arbeit liegt auf der Entwicklung von Eisen-Chalkogenid-basierten Materialien für Anwendungen in der Photo- sowie in der Elektrokatalyse. Beide Anwendungsfelder werden weltweit mit Interesse verfolgt, da sie nachhaltige Alternativen zu konventionellen, auf fossilen Rohstoffen basierenden industriellen Prozessen bieten. Elektrochemische Prozesse, wie zum Beispiel die Wasserelektrolyse, sind die Kosten betreffend jedoch noch nicht konkurrenzfähig. Daher erfordert es weiterreichende Forschung auf diesem Gebiet, besonders was die Entwicklung von neuen Katalysatoren aus häufig-vorkommenden Elementen angeht.

Die erste Arbeit dieser Thesis befasst sich daher mit der solvothermalen Mikrowellensynthese von $CuFe_2O_4$-Nanopartikeln. Eine Optimierung der Syntheseparameter, inklusive der Lösungsmittelmixtur und des pH-Wertes erlaubt es, $CuFe_2O_4$ Partikel mit einer schmalen Größenverteilung und über einen weiten Bereich an verschiedenen Synthesezeiten und –temperaturen, herzustellen. Genauer konnte die Synthesezeit auf 1 min bei 175 °C reduziert werden, während die Synthesetemperatur auf 120 °C verringert werden konnte. Nach einer sorgfältigen Charakterisierung, inklusive der Bestimmung des Inversionsgrades, wurden die $CuFe_2O_4$-Partikel in der elektrokatalytischen Reduktion von CO_2 zu CO eingesetzt. Dabei zeigte sich, dass die Synthesezeit einen deutlichen Einfluss auf die CO Produktion und auf die Selektivität hat. Die höchste Aktivität wurde dabei für $CuFe_2O_4$ beobachtet, dass in 10 min synthetisiert wurde, wobei eine Aktivität von 0.2 $\mu mol\ h^{-1}\ g^{-1}$ und eine Faraday'sche Effizienz von 20 % erreicht wurden. Diese Beobachtung konnte durch die Kombination eines abnehmenden Inversionsgrades mit anhaltender Zeit in der Mikrowelle, größeren Anteilen an organischen Überresten in Partikeln die für sehr kurze Zeit synthetisiert wurden, sowie einer leicht erhöhten Kristallitgröße bei einer mittleren Synthesezeit von 10 min erklärt werden. Es konnte somit gezeigt werden, dass die elektrokatalytischen Eigenschaften durch die Synthesebedingungen beeinflusst werden können. Zudem wurde kein kohlenstoffhaltiges Produkt außer CO beobachtet und H_2 war das einzige Nebenprodukt. Somit ist $CuFe_2O_4$ ein interessanter Katalysator aus häufig vorkommenden Elementen für die direkte Produktion von Synthesegas.

Im Vergleich zur Elektrokatalyse vereint Photokatalyse Lichtabsorption und Ladungsträgeranregung mit den nachfolgenden Zielreaktionen in einem System, ohne eine externe Triebkraft zu benötigen. Um die Effizienz zu erhöhen, werden Cokatalysatoren aufgebracht, welche die Ladungsseparation verbessern. Ladungsträger migrieren zu diesen Cokatalysatoren, welche zugleich aktive Zentren für die Reaktion bieten. Damit teilen sie viele Gemeinsamkeiten mit Elektrokatalysatoren. Die zweite Arbeit, die in dieser These thematisiert wird, hatte es daher zum Ziel, Ni_2FeS_4 zu synthetisieren, und als Cokatalysator aus häufig-vorkommenden Elementen – alternativ zu Edelmetallen – in der H_2-Entwicklung aus Wasser einzusetzen. Zunächst wurde die Mikrowellensynthese von Ni_2FeS_4 in organischen Lösungsmitteln und mit Benzylmercaptan als Schwefelquelle, optimiert. So konnte gezeigt werden, dass phasenreine, kristalline Ni_2FeS_4-Nanosheets in nur 1 min hergestellt werden können. Anschließend wurde Ni_2FeS_4 als Cokatalysator auf TiO_2 (P25) eingesetzt. Die photokatalytische Aktivität von P25 konnte so um das Achtfache gesteigert werden und erreichte 25-28 $\mu mol\ h^{-1}$ unter simuliertem Sonnenlicht. Außergewöhnlich geringe Massenbeladungen von 0.5 wt.% Ni_2FeS_4 konnten dabei realisiert werden, ohne eine Verringerung der Aktivität herbeizuführen. Des Weiteren wurde eine stabile H_2-Entwicklung über den Verlauf von 20 h beobachtet. Wenn UV-Strahlung anstele von sichtbarem Licht verwendet wurde, war die Aktivitätssteigerung noch ausgeprägter und eine Aktivität von 48-mal der von reinem P25 konnte erreicht werden. Von daher ist Ni_2FeS_4 ein geeigneter, unedler

Cokatalysator für die Wasserstoffentwicklung, der zudem unter milden Bedingungen hergestellt werden kann.

Wasserstoff ist ein idealer, grüner Brennstoff, doch die Lagerung ist kompliziert und große Mengen des produzierten Wasserstoffs werden stattdessen für gewöhnlich als Ausgangsmaterial in industriellen Prozessen eingesetzt. Ein Beispiel für einen solchen Prozess ist der Haber-Bosch-Prozess für die Synthese von Ammoniak. Photokatalytische Stickstoffreduktion stellt eine nachhaltige Alternative dazu dar, setzt allerdings die Entwicklung effizienter Katalysatoren für die Stickstoffaktivierung voraus. Kohlenstoffnitride (engl. Carbon nitrides, CN) gehören dabei zu den meist-erforschten Katalysatoren für Stickstofffixierungsreaktionen. Daher wurde defektreiches Kohlenstoffnitrid (V_N-CN) im Rahmen der dritten vorgestellten Arbeit hergestellt, und mit biomimetischem FeS_2 (Pyrit) kombiniert. Diese Kombination führte zu einer erhöhten Ammoniakproduktion um ca. 400 % verglichen mit unmodifiziertem Kohlenstoffnitrid, selbst bei einer geringen Beladung mi FeS_2. Eine Reihe an Kontrollexperimenten und Materialcharakterisierungen zeigte jedoch, dass der Ammoniak nicht durch eine Reduktion des gasförmigen Stickstoffs gebildet wird, sondern stattdessen durch eine Zersetzungsreaktion von Cyanogruppen an den Defektstellen in V_N-CN. FeS_2 verstärkt diese licht-induzierte Zersetzungsreaktion, indem es an die Defektstellen koordiniert und die Cyanogruppen durch π-Rückbindung aktiviert. Es konnte somit gezeigt werden, dass obgleich relativ hohe Ausbeuten an Ammoniak mit diesem System erreicht werden können, es sich dabei nicht um photokatalytische Stickstoffreduktion handelt, für welche V_N-CN im Umkehrschluss nicht geeignet ist.

1 Introduction

The last decades have shown that climate change is an undeniable fact that is having an increasingly tangible influence on the planet and on human societies. Rising sea levels as a result of melting polar ice shields, extreme weather phenomena like droughts, floods or hurricanes, and an overall rise in temperature are all effects that can be felt even now and are bound to occur increasingly more often in the coming years.[1] Such consequences of global warming not only pose an economic stress by causing billions of dollar damages, but they endanger vulnerable ecosystems and have a negative impact on food supply – an effect especially harmful for people in countries with low income.[2,3] Scientists agree that anthropogenic emissions of carbon dioxide (CO_2) and other greenhouse gases are at the core of the problem. Hence, the reduction of emissions and replacement of carbon fuel-based processes with environmentally benign, carbon neutral alternatives are arguably the key challenges of the current century – more precisely, the next couple of decades. Since greenhouse gasses accumulate in the atmosphere, continuing emissions will only aggravate the problem of rising temperatures. Already the average annual temperature increased by around 1 °C compared to pre-industrial levels, which is mirrored by an increase in the CO_2 concentration in the atmosphere by 100 ppm in the last 50 years alone (**Figure 1a** and **b**).[2] During the same period, a continuous increase in mean sea levels, a decrease in the extent of Arctic ice, and an increase in billion dollar disasters has been recorded, elucidating the correlation with the rising CO_2 concentration (**Figure 1c-e**).[4,5]
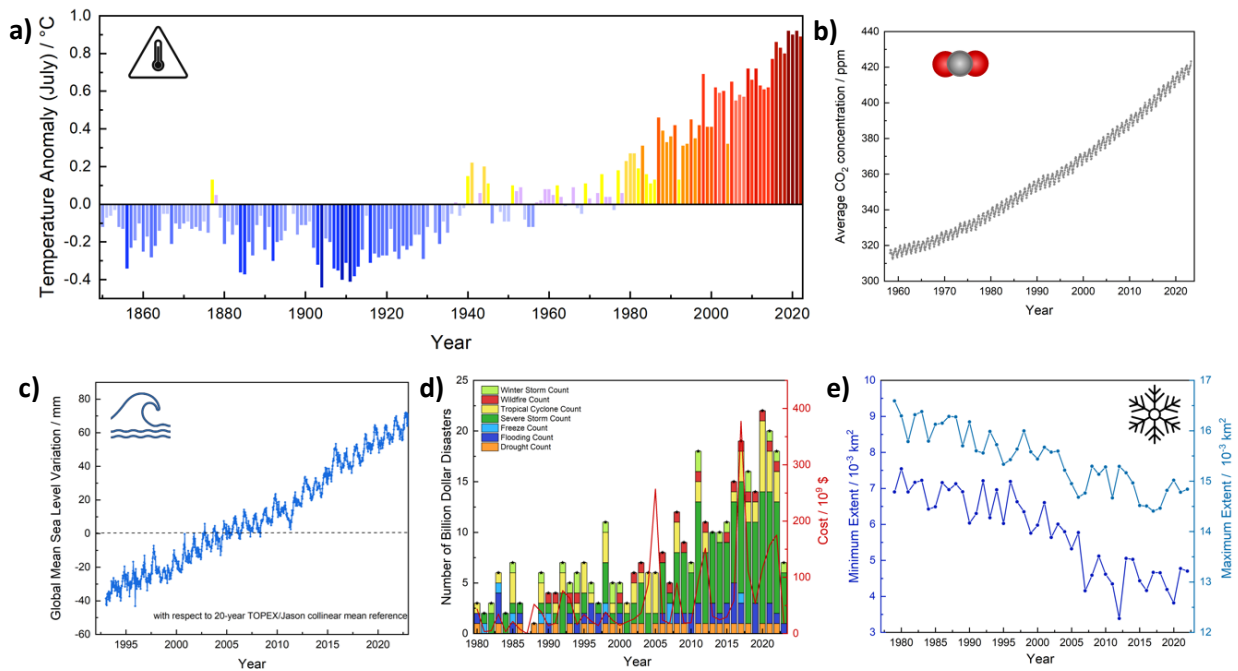
Figure 1 Increase in temperature relative to 1951-1980 (a), along with a rise in atmospheric CO_2 concentration, as monitored by the Mauna-Loa observatory (b). Additionally, an increase in the mean sea levels (c), the number of billion-dollar weather and climate disasters – here as an example for the United States (d), and a decrease in the Arctic ice coverage (e) are depicted over the previous decades. The data for temperature anomalies, CO_2 concentration and U.S. billion-dollar disaster was retrieved from the NOAA National Center for Environmental Informations (NCEI) and the Earth System Research Laboratories.[6–8] The data for sea level variations was retrieved from NASA's Physical Oceanography Distributed Active Archive Center (PODAAC) and that for Arctic sea ice coverage from NASA's National Snow and Ice Data Center (NSIDC).[4,5]

Due to the accumulation of greenhouse gases, an increase in temperature compared to preindustrial levels between 1.5 and 4.5 °C can be expected until the end of the century – the magnitude depending

on how fast emissions can be reduced to virtually zero. This is modelled by the representative concentration pathways (RCPs), which encompass different scenarios for the extent of future CO_2 emissions based on the kind and speed of human mitigation measures, as well as socio-economic developments.[9,10] Since even a temperature increase of only a few degrees has a significant impact on nature and human civilisation alike, most nations agreed to limit the rise in temperature to a maximum of 2 °C compared to pre-industrial levels and take efforts not to exceed 1.5 °C in the Paris agreement.[11] A severe reduction of greenhouse gas emissions already in the next decade is required in order to achieve that goal. Among the most important strategies for such a reduction are the generation of electricity from renewable energy sources – such as wind, water, or solar power – and the replacement of conventional gasoline- and diesel-based vehicles by battery or fuel cell powered ones.[12–16] Apart from greenhouse gas emissions from vehicles, industrial processes significantly contribute to the total emissions.[17,18] Therefore, either the capture of CO_2 in exhaust gas, or the development of new, efficient, and compatible alternatives that do not require fossil fuels is additionally required.[19] Furthermore, the current war in Ukraine has shown additional drawbacks of relying on fossil fuels for countries without noteworthy gas or oil reserves of their own, as this results in an economical dependence on others.[20]

Among all renewable energy sources, the sun is the one with the most potential in terms of annual energy supply, easily surpassing all other renewables and all recoverable fossil reserves combined.[13] As illustrated in **Figure 2a**, the radiative energy reaching the earth is sufficient to cover the global annual demand several times over.
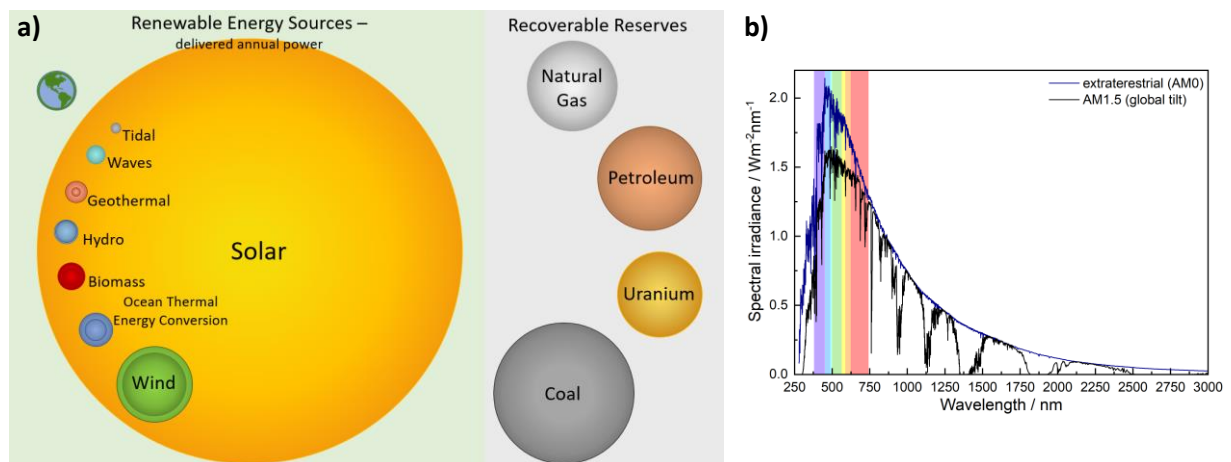
Figure 2 Potential of renewable energy sources in comparison with reasonably recoverable reserves based on the estimations of 2015 (a). The volume of each sphere is proportional to the respective power – adapted with permission from Perez *et al*. (Copyright Elsevier 2022)[13] Solar spectrum at the top of the atmosphere and at median latitudes (AM 1.5G) (b).[21] The data was retrieved from the National Renewable Energy Laboratory (NREL).[22]

There are several ways of exploiting solar power. The first is photovoltaics and thus the conversion of solar to electric energy (**Figure 3**). It is currently the best-known method for solar energy conversion and the most developed, achieving sufficient efficiencies to replace fossil energy carriers.[23,24] However, using solar power for the direct generation of electricity requires an adaptation to the fluctuations in energy supply due to the day and night rhythm and additional seasonal changes thereof, as well as weather conditions.[25,26] Therefore, energy needs to be stored either as electric energy in batteries, or as chemical energy in molecules, which requires a second process of energy conversion from electric

to chemical one. This can be achieved by electrocatalysis, wherein a chemical reaction proceeds in contact with a catalyst under potential application (Figure 3).[27,28]

The second approach for solar energy conversion is *via* photocatalysis, wherein solar energy can directly be converted into chemical energy, thus omitting additional conversion processes and their energetic losses (Figure 3). Photoelectrochemistry is a combination of both strategies, wherein electrocatalysis is performed under light irradiation. The performance of the (photo)-electrocatalyst can thereby be significantly improved compared to the same process in the dark. A prerequisite for the conversion of solar energy in both photovoltaics and photocatalysis is an efficient absorption of solar irradiation by semiconductor materials and subsequent separation of photoexcited charge carriers. This results in substantial requirements for suitable materials, one of the most important ones being a high charge carrier mobility and low recombination rates, in addition to a good stability, suitable band positions and a small enough band gap for visible light absorption, since this is the portion of sun light with the highest intensity (**Figure 2b**).[23,29,30] The multitude and complexity of these demands on a material are the main reasons why the efficiencies in solar energy conversion are still rather low, highlighting the need for continued research for new materials and optimisation of existing ones.
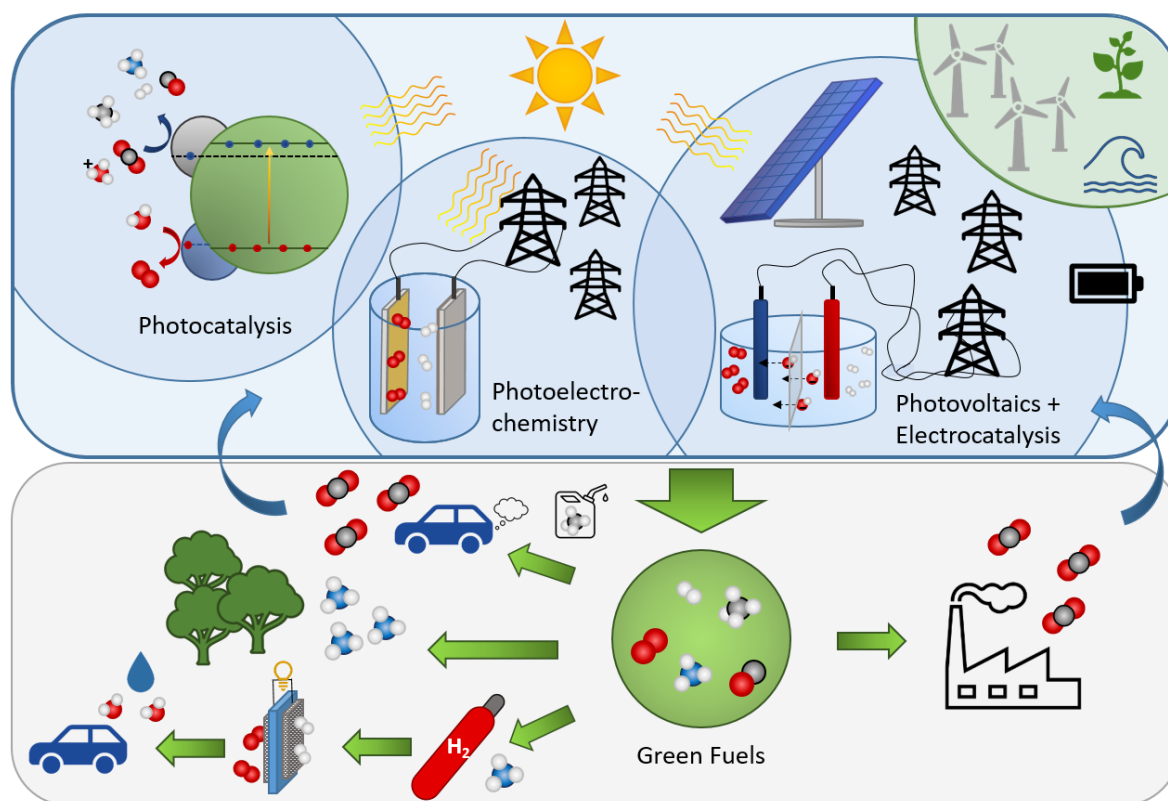
Figure 3 Solar energy harvesting and conversion through photocatalysis, photoelectrochemistry, and photovoltaics coupled to electrocatalysis. The generated products can directly be employed in industry or as green fuels in the transportation sector. The capture and conversion of emitted CO_2 by photo- and electrocatalysis back to valuable chemicals and fuels could in principal close the carbon cycle for a zero-emission economy.

Some of the desired primary products in both photo- and electrocatalysis are hydrogen (H_2), ammonia (NH_3), or methane (CH_4), which are obtained by the splitting of water into H_2 and O_2,[31–34] the reduction of dinitrogen to NH_3,[35–38] or the reduction of CO_2 to CH_4 and other valuable carbon-based products, such as CO or methanol, respectively.[39–42] H_2 is a viable candidate for chemical energy storage. It can

directly be used as a fuel, *e.g.* in fuel cells as an alternative to batteries in vehicles or in stationary applications for power generation. It is a clean fuel with a unsurpassed gravimetric energy density, whose combustion only yields water.[12,43] Apart from the use as fuel, H_2 is an important chemical in many industrial processes.[27] Thus, it is required for oil refining, methanol production, or the synthesis of NH_3 in the Haber-Bosch process. Currently H_2 is mainly generated *via* methane steam reforming. Its production significantly contributes to the carbon footprint, therefore alternative synthesis pathways *via* electro- or photocatalysis are highly desirable.[44,45] So far the efficiency and cost of these sustainable alternatives are not yet satisfactory, though, and most commonly noble metal catalysts such as platinum are employed, resulting in high material and overall process costs that cannot compete with traditional, fossil-fuel reliant H_2 synthesis methods.[31,46] Therefore, the development of new, efficient, earth-abundant and low-cost materials for hydrogen evolution catalysts is of great importance.

A problem in using H_2, however, is the longterm storage, which requires high pressures or cryogenic temperatures and therefore high-power inputs, suffers from low efficiencies, or from safety issues. Alternatively, NH_3 and synthetic fuels can be synthesised *via* either photo- or electrocatalytic N_2 and CO_2 reduction, respectively, using water as the hydrogen source and electricity from renewable energy sources. In both cases the reduction of a gaseous reactant is required, which is hindered by the low solubility of these gasses in aqueous media. Additionally, the formation of multiple high energetic bonds must occur, and numerous side-products may be formed at similar potentials, rendering the entire process significantly more challenging than water electrolysis. This is in turn mirrored by even lower efficiencies and selectivities.[37,41,47] Therefore, much progress is required to make photo- and electrocatalytic N_2 and CO_2 reduction competitive to established fossil-fuel based processes. Such developments are even more crucial, considering the industrial importance of NH_3 as essential component in the fabrication of fertilisers – and thus the feeding of the world's population. Moreover, NH_3 can be used as either a storage medium, or a replacement for H_2. It is easily liquefied at comparatively low pressure, is safe and easy to transport and its combustion does not generate CO_2. Additionally, it can also be directly employed in fuel cells.[48–51] Similarly, methanol, or other potential CO_2-reduction products such as CH_4 and CO, are important fuels either in internal combustion engines or in fuel cells, and essential feedstock for the fabrication of carbon containing high-value chemicals, *e.g. via* the Fischer-Tropsch process.[52]

In both photo- and electrocatalysis, the initial research focussed on noble metal catalysts, that are often very efficient, but result in high production costs due to element scarcities. Nowadays the development of earth-abundant, mainly transition metal based, alternatives has become more important.[53–57] However, continuing research is required in this field, in order to achieve high selectivities and efficiencies necessary for large-scale applications. Amongst earth-abundant photo- and electrocatalysts, the development of materials containing iron is especially desirable. Iron is one of the most common elements in the earth's crust (**Figure 4**). It is cheap, non-toxic and globally available, while still being redox-active – a prerequisite for electrocatalysts.[58] This makes it a very desirable component in new catalyst materials and is likely also the reason for its central role in the active centres of enzymes. Thus, it is a major element in hydrogenases, nitrogenases, and the carbon monoxide dehydrogenase.[59] In nature it most commonly occurs as oxygen or sulphur containing minerals, such as Fe_2O_3 (hematite), spinel-type Fe_3O_4 (magnetite), FeOOH (goethite), or FeS_2 (pyrite), elucidating the availability and stability of such materials.[60]

For the development of new catalyst materials, element abundancy is not the only crucial factor, however. The material synthesis must additionally be taken into account, because high-temperature

requirements, long synthesis times, or cost-intensive refinement of raw materials can significantly increase the cost of the catalyst itself, which will in turn have a negative impact on the overall production cost. Especially transition metal oxides are traditionally obtained *via* high-temperature solid-state synthesis. Thus, new synthesis methods need to be developed to reduce the energy requirement of the material synthesis and thus the overall cost. Additionally, a low synthesis temperature allows for the preparation of nanocrystalline materials with high surface areas.[62]
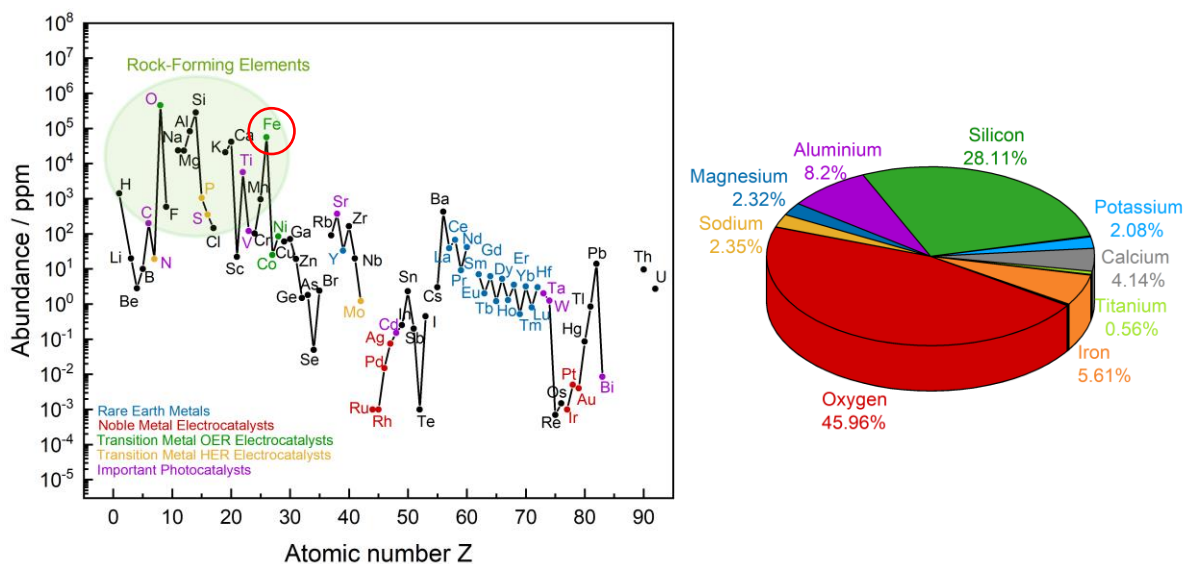
Figure 4 Most common elements in the earth's crust. Some of the most important elements for noble metal electrocatalysts, transition metal electrocatalysts, and prominent constituents of state of the art photocatalysts are highlighted in colour. Data is taken from the CRC Handbook of Chemistry and Physics.[61]

In summary, to achieve a future large-scale production of H_2 and other valuable products, new catalyst systems need to be developed that achieve the necessary efficiencies and selectivities, that are based on earth-abundant materials – especially iron – and that are at the same time obtained *via* fast low-temperature syntheses. Only the parallel fulfilment of all three factors will allow for photo- and electrocatalysis to become economically feasible alternatives to fossil-fuel based processes.

2 Theoretical Background

2.1 Semiconductor Photocatalysis
2.1.1 Fundamentals of Photocatalysis

The term 'photocatalysis' according to IUPAC refers to chemical transformation reactions that are catalysed by a material upon light absorption.[63] Photocatalysts are materials that possess medium to small band gaps that are suitable for the harvesting of sunlight, *i.e.* usually semiconductor solids, or molecular complexes. Electrons can be excited from the valence band/ highest occupied molecular orbital (HOMO) to the conduction band/ lowest unoccupied molecular orbital (LUMO) upon the absorption of photons with an energy exceeding the band gap (HOMO/LUMO gap) energy, thereby generating excitons. Both excited electrons and the holes left in the valence band can subsequently participate in redox-reactions. A prerequisite hereby is a suitable alignment of redox-potential and energy level in the photocatalyst. Electrons can reduce a component, if the conduction band minimum is at a more negative energy than the respective redox-potential of the catalysed reaction, while holes can be used for oxidation reactions, if the maximal valence band energy exceeds the respective redox-potential. Typical reduction processes are the evolution of hydrogen from water, the synthesis of ammonia from dinitrogen, or the conversion of CO_2 into methane, CO or ethylene. Common oxidation reactions on the other hand are the oxidation of water to O_2, the degradation of pollutants, *e.g.* dyes, or the generation of nitrates from N_2.[64–73]
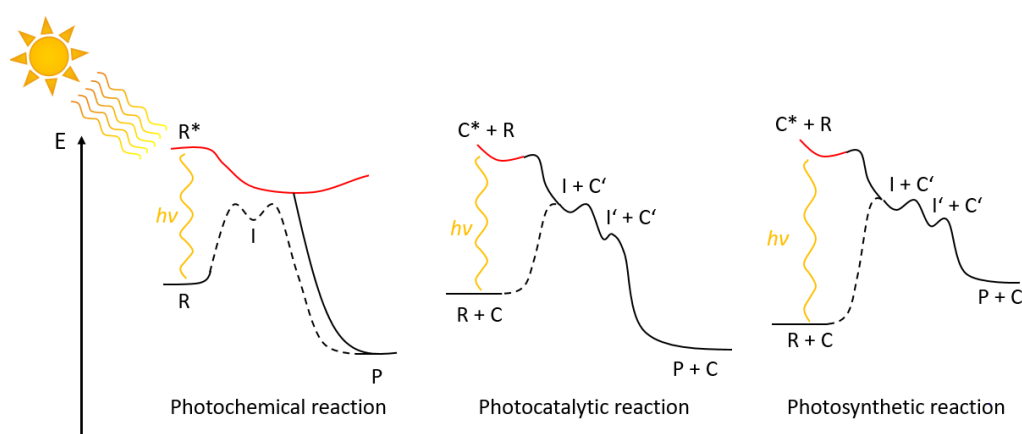
Figure 5 Differences in the course of photochemical (left), photocatalytic (middle), and photosynthetic (right) reactions. Partially adapted with permission from Ravelli *et al.* (Copyright RSC 2009).[29] Relative energies of reactants (R), the catalyst (C), intermediates (I) and products (P) are shown over the course of the reaction. Excited states are marked by an asterisk. Energy barriers in the absence of light activation are depicted in dashed lines.

Nowadays the term 'photocatalysis' is used in relation to both endergonic and exergonic reactions, while originally it was only referring to energetically down-hill reactions, whereas the term 'photosynthesis' was used for reactions with a Gibbs free enthalpy $\Delta G > 0$.[29,30] From the reactions mentioned above, water splitting, N_2 or CO_2 reduction are prominent examples for photosynthetic reactions, whereas the oxidative decomposition of pollutants belongs to the category of photocatalysis. Both require the participation of a catalyst that is returned to its original state after the reaction, in contrast to photochemical reactions, wherein one or more reactants directly absorb light and are thus transferred to an energetically excited state (**Figure 5**). Not only is the change in the Gibbs free enthalpy different for photocatalytic and photosynthetic reactions, but the rate determining steps

might vary significantly. A photosynthetic reaction is thermodynamically not favoured and thus fast charge and product separation are crucial for a high efficiency and the suppression of back-reactions. In contrast, a photocatalytic reaction is often limited by the surface area and number of active surface sites available for activation and conversion of reactants.[29,30,64] For simplicity reasons the term "photocatalysis" is used throughout this work for reactions with both $\Delta G > 0$ and $\Delta G < 0$.

The strategy to utilise light absorption for the driving of photosynthetic reactions mainly started when in 1972 Fujishima and Honda first reported on photoelectrochemical water splitting over TiO_2 and a couple of years later Inoue and Fujishima explored the reduction of CO_2.[74,75] In the following years, research in the field expanded significantly, mostly focussing on abundant metal oxides and sulphides, especially TiO_2, CdS or ZnO.[76,77] Such heterogeneous photocatalysts have the advantage of often good stability and easy separation of the catalyst from the reaction dispersion. On the other hand, molecular photocatalysts in homogeneous systems allow for a more intimate contact between reactants and catalyst and a better tailoring of the HOMO/LUMO positions and gap.[29,78] Often, more than one semiconductor is combined, additional metal electrocatalysts are included in the system, or hybrids of semiconductor and molecular catalyst are formed, in order to improve light harvesting, charge carrier separation and utilisation efficiency.[79–83]
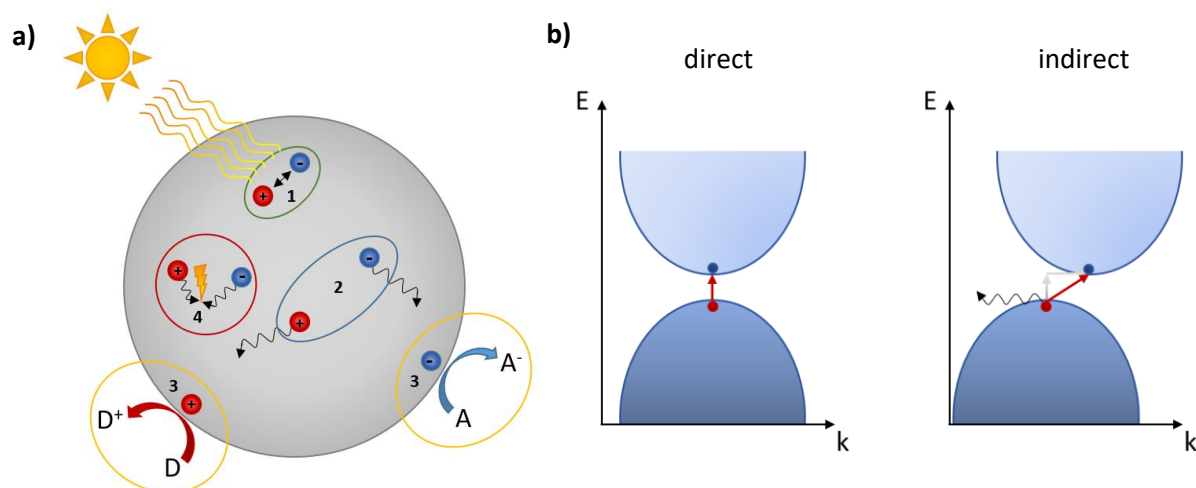
Figure 6 Processes occurring in a semiconductor upon light irradiation: 1: light absorption; 2: charge carrier separation; 3: consumption of charge carriers at the surface in redox reactions; 4: recombination (a). Electronic transitions in a direct and indirect semiconductor are depicted in (b).

Photocatalytic processes in semiconductor materials can be divided into a series of reaction steps: The first and fundamental prerequisite is the absorption of light of sufficient energy for the excitation of valence band electrons. Thus, the incident light must be of higher energy than that of the band gap.[64,66,80] The process of charge excitation is thereby dependent on the band structure of the semiconductor. For direct semiconductors, excitation proceeds directly from the valence band maximum to the conduction band minimum, which are of the same crystal momentum. In indirect semiconductors, on the other hand, valence band maximum and conduction band minimum are located at different wave-vectors, additionally requiring phonon participation for the conservation of momentum (**Figure 6**).[23]

Since sustainable photocatalysis relies on the sun as light source, efficient absorption in the visible light range is necessary. However, good light absorption alone does not make a good photocatalyst, if the excited charges cannot be used to drive reactions. The second crucial step is therefore spatial charge

separation inside the semiconductor and towards the surface, on which the target reaction can take place (Figure 6). Besides sufficient energy of the separated charge carriers, a good adsorption of reactants to active surface sites is required, for the conversion reactions to be efficient. The last step is the desorption of products and regeneration of free surface sites. If charge carriers are not separated and consumed quickly enough in these steps, recombination of electrons and holes may occur, either in the bulk, or on the surface, drastically reducing the number of charge carriers available for redox-reactions and thus also the efficiency. Light harvesting is generally more efficient for direct semi-conductors, but recombination rates are also far higher since no phonon participation is required. In systems of only one bulk semiconductor, the reached efficiencies are commonly very low. Hence, the improvement of charge separation has become a key challenge in the development of new, highly active photocatalytic systems.[64,81,83–85]

When discussing the efficiency of a photocatalytic system, usually characteristics such as the solar-to-hydrogen efficiency (STH), or the quantum efficiency (QE) or apparent quantum yield (AQY) are considered.[65,86,87] The quantum efficiency describes the rate of a reaction divided by the absorbed photon flux. Since the determination of absorbed photons is usually impractical, the photonic efficiency (ζ) is used instead, which considers the entirety of incident photons. The determination of incident photons is not trivial, since it varies between reaction setups and also different locations in the same setup, but is still significantly easier to estimate compared to the absorbed photon flux. The same is true for the quantum yield, *i.e.* the number of events per absorbed photon of specific energy. Here the AQY (also external quantum yield) is commonly used, which again considers the incident photons. For water splitting, the STH is another important measure for the performance of a photocatalytic system, especially for solar irradiation. It is defined as the ratio of the chemical energy of the produced hydrogen to the energy of incident sun light.[65,86,87] The STH vastly depends on the range of adsorbed light – and thus the semiconductor band gap – and cannot exceed 3.3 % under solely UV absorption.[86]

The different definitions for the discussed efficiencies are given by equations 1 to 4.

Quantum efficiency:
$$QE = \frac{R}{q_p} \; ; \; \text{with the photon flux } q_p = \frac{dN_p}{dt} \tag{1}$$

with R the reaction rate (product formed or reactant consumed), q_p the photon flux, N_p the number of photons and t the time.[86]

Photonic efficiency:
$$\zeta(\lambda) = \frac{R}{I} \tag{2}$$

with R the reaction rate in a specific time window and I the rate of incident photons of defined wavelength range.[86]

Apparent quantum yield:
$$AQY(\lambda)(\%) = \frac{n_{e^-}}{I(\lambda)} = \frac{\alpha \cdot R}{I(\lambda)} \tag{3}$$

with n_e the number of reacted electrons, $I(\lambda)$ the number of incident photons, α the stoichiometric coefficient in the reaction (*i.e.* 2 for H_2 and 4 for O_2) and R the reaction rate.[65,85,86]

Solar-to-hydrogen efficiency:
$$STH = \int_{\lambda_i}^{\lambda_f} QE = \frac{R \cdot \Delta G}{P \cdot A} \tag{4}$$

with R the reaction rate, ΔG the Gibbs energy for water splitting, the energy flux P for sun light (AM 1.5G; 100 mWcm^{-2}), and the irradiated area A.[65,86]

Such measures for the efficiency gain more and more importance in the characterisation of new photocatalytic systems. Still, differences in the employed setups, light sources, and environmental conditions in combination with incomplete reports on reaction conditions and errors in the reporting of the photocatalytic activity – such as normalisation to mass – result in issues of comparability and discrepancies between different research groups.[87]

2.1.2 Principles of Charge Separation in Semiconductor Photocatalysts and Strategies for Activity Enhancement

For efficient separation of photo-excited charge carriers, first of all the exciton binding energy needs to be overcome: this is a material property largely dependent on the dielectric constant and the effective masses of electrons and holes. For efficient charge separation it should be lower than the thermal energy.[64] Additionally, the lifetime of charge carriers needs to be sufficiently long for them to migrate to the surface of the semiconductor and thus participate in a reaction. The lifetime further depends on the rate of recombination in the bulk, *e.g.* at defects or grain boundaries, or at the surface. Thus, the lifetime directly influences the diffusion length of minority charge carriers.[64] To increase the probability for charge carriers to reach the surface, **nanostructuring** can be useful to minimise the distance electrons and holes have to travel.[88] Additional positive effects of nanostructuring can be an improved light harvesting due to scattering phenomena, or the adjustment of band gap and potential in very small particles based on quantum confinement effects, or *via* potential determining ions that exert an electric field. Furthermore, the high surface to bulk ratio is beneficial for the adsorption and activation of reactants.[88] At the same time, however, the material properties are changed from those observed in the bulk to surface controlled properties. The surface is commonly rich in defects that can alter the potential of surface states compared to band potentials in the bulk and might act as recombination sites. Additionally, the space charge layer that can significantly promote charge separation in bulk materials cannot be formed in nanoparticles (see following pages).[64,88]

One commonly applied strategy for improved activities is the use of sacrificial agents. These are reagents that are either oxidised easily by excited holes or reduced easily by electrons, thus efficiently scavenging one type of charge carriers, reducing the time for recombination and leaving larger numbers of the other carrier type that can be used for the desired reaction (**Scheme 1**). The sacrificial agent can either be reduced/ oxidised directly by the charge carrier, or the reaction may proceed *via* the trapping of formed radicals, *e.g.* $^{\cdot}$OH for hole scavengers.[89,90] Very common is the addition of a hole scavenger in hydrogen evolution reactions from water, due to slow water oxidation kinetics. Widely used hole scavengers are amines, such as triethanolamine, alcohols – especially methanol and ethanol –, and inorganic sulphur compounds, such as NaS_2, or Na_2SO_3.[89,91,92] Examples for electron scavengers are $AgNO_3$, iodates such as KIO_3 or $NaIO_3$, or other electron acceptors such as peroxidisulphate or Fe^{3+} compounds.[93–95] Those are often used when the oxidation reaction from water is forced. Which potential sacrificial agent results in the best performance thereby depends on the pH, but also on the photocatalyst used. This is due to intermediate oxidation products affecting the photocatalytic processes – *e.g.* by competing with the desired reaction – but also differences in the reaction mechanisms, oxidation potential and permittivity, as well as differences in the interaction between sacrificial agent and the photocatalyst.[89–91,95,96] Especially for sulphide-based photocatalysts, the choice of sacrificial agent might furthermore influence the photocatalyst stability.[91,97]

Sacrificial agents can significantly boost the activity for one half reaction – however, they come in hand with a series of problems and drawbacks that are often ignored. On the one hand they are an additional material that is required in the system – usually at significant amounts – but not directly used for valuable products. They both increase the production costs and have a negative environmental impact on a process that aims at sustainable syntheses – both aspects can be significantly improved, if the sacrificial agent is at the same time turned into valuable products, or if waste is decomposed.[98–101] Additionally, they can have less obvious influences that can lead to the misinterpretation of results. The use of methanol, for example might boost the amount of generated hydrogen from water, due to hydrogen also being a side-product of methanol oxidation, with the extent of contribution from methanol being a topic of debate.[91,95,102–104] Moreover, produced radicals during the oxidation of hole scavengers can inject additional electrons into the conduction band of the photocatalyst and thus increase the amount of electrons available for hydrogen evolution – an effect known as photocurrent-doubling.[87,105,106] Even worse, this oxidation – and thus hydrogen evolution – is not strictly restricted to light conditions, but can also occur in the dark over selected catalysts, such as platinum, thereby falsifying the amount of H_2 actually produced *via* photocatalysis.[107,108]

a)

Methanol Oxidation (in Water)

$H_2O + h^+ \rightarrow \,^{\cdot}OH + H^+$

$CH_3OH + \,^{\cdot}OH \rightarrow \,^{\cdot}CH_2OH + H_2O$

Or: $CH_3OH + \,^{\cdot}OH \rightarrow CH_3O^{\cdot} + H_2O$

$^{\cdot}CH_2OH \rightarrow HCHO + H^+ + e^-$

$2\,H^+ + 2\,e^- \rightarrow H_2$

$HCHO + H_2O \rightarrow HCOOH + H_2$

$HCOOH \rightarrow CO_2 + H_2$

b)

Silver Nitrate Reduction

$Ag^+ + e^- \rightarrow Ag^0$

$n\,Ag^0 \rightarrow Ag^0_n$

c)

Iodate Reduction

$IO_3^- + 6\,e^- + 3\,H_2O \rightarrow I^- + 6\,OH^-$

d)

Peroxodisulphate Reduction

$S_2O_8^{2-} + e^- \rightarrow SO_4^{\cdot-} + SO_4^{2-}$

$SO_4^{\cdot-} + H_2O \rightarrow SO_4^{2-} + \,^{\cdot}OH + H^+$
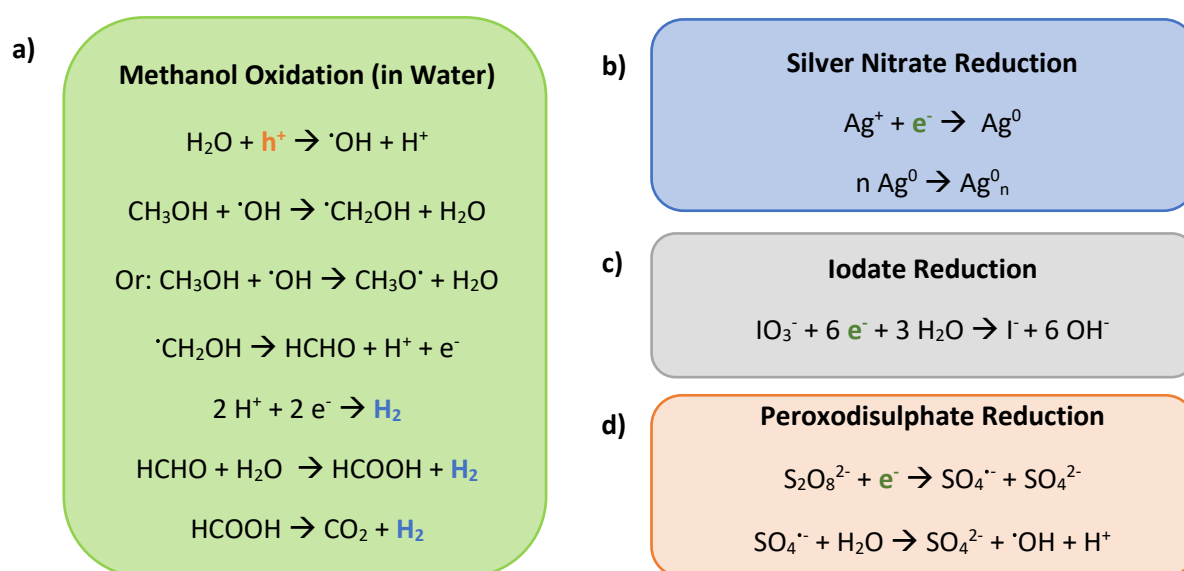
Scheme 1 Schematic reactions of MeOH oxidation (a)[90,95] AgNO$_3$ reduction (b),[95] iodate reduction (c),[109] and peroxodisulphate reduction (d).[95]

Several sacrificial agents, such as methanol, iodates, or even worse AgNO$_3$ suffer from self-decomposition under light irradiation, especially under high-intensity UV light. Thus, significant amounts of oxygen are produced from irradiated aqueous solutions of electron scavengers even in the absence of a photocatalyst.[93]

Additionally, the use of AgNO$_3$ results in the deposition of silver on the photocatalyst, which might alter the charge transfer mechanisms in the system and will also affect light harvesting.[95] If the concentration of a reaction product in solution has to be determined after the photocatalytic experiment, as *e.g.* in the nitrogen reduction reaction (NRR), the sacrificial agent and its decomposition products can additionally interfere with the quantification.[110] The sacrificial agent can also influence the morphology and distribution of photodeposited cocatalysts.[111] Due to the multitude of additional effects a sacrificial agent can have, careful control experiments should be performed to paint a complete picture of occurring processes.

Another efficient strategy for activity enhancement directly targets the charge separation in the semiconductor photocatalyst itself. To better understand such approaches, one first needs to address the question of how excited charge carriers are intrinsically separated and transferred to a semiconductor surface: Electrons and holes follow concentration gradients (diffusion current) and electric field gradients (drift current). The former is usually not very efficient and depends a lot on the charge carrier mobility, whereas the latter is the fundamental driving force for charge separation.[64,112] Both forms of charge separation are not independent of each other, however. Photoelectrochemistry applies an external bias and thus assists in the charge separation in direction of applied potential.[113] Photocatalysis on the other hand does not have such an advantage and thus requires internal electric field gradients in the photocatalytic system itself.[64] The most important electric field for charge separation is build up at interfaces. A semiconductor surface usually differs from the bulk, since surface atoms lack sufficient neighbours. This is well known for oxides, where undercoordinated oxygen atoms form dangling bonds that are often terminated by protons, forming hydroxyl groups. Alternatively, the oxygen atom can be negatively charged, which results in a charging of the surface.[23,84] Which kind of surface termination/ charge is present, depends on the environment, *e.g.* air or water as surrounding medium, and the pH value – or more precisely the difference between the pH and the point of zero charge (PZC).[114] As a consequence of structure disruption at the surface, the electronic structure of surface and bulk almost always differ and electronic surface states are formed at an energy within the band gap of the semiconductor (at least for anionic dangling bonds).[115,116] However, there is no strict cut between the electronic structure of surface and bulk, but a continuous gradient that is build up by an equilibration of Fermi levels and surface states – at least in doped semiconductors. These are semiconductors, that possess either an excess of electrons (n-type), or excess holes (p-types), which are also referred to as majority charge carriers and cause a shift in the Fermi level closer towards the conduction or valence band, respectively. The same situation occurs if a semiconductor is in contact with either a metal, a second semiconductor, or a liquid electrolyte. Such an establishment of electric field gradients represents an effective way to improve charge carrier separation in semiconductor photocatalyst.[64,84,116]

In the simplest case, an interface between a metal and a semiconductor is formed across which charges can be separated. Both have different Fermi levels. When brought into contact, electrons will transfer from the constituent with the higher Fermi level to the one with a lower Fermi level, thus reducing the overall free energy of the system. Often, the density of surface states is higher than the number of bulk dopants, which results in the Fermi level being almost independent of the bulk dopant concentration, but instead determined by surface states. This effect is called Fermi level pinning.[23,84,113,116]

In photocatalysis, especially reduction reactions, usually noble metals with large work functions (ϕ_m) are employed as so-called **cocatalysts**, to which excited electrons are transferred. For n-type semiconductors the work function of the metal is usually higher which leads to electron transfer from the semiconductor to the metal until an equilibrium, *i.e.* alignment of the Fermi levels, is reached. In this state the metal surface is negatively charged, whereas the interfacial region in the semiconductor is positively charged. Since the number of charges in a semiconductor is limited, the loss of electrons at the interface cannot be mitigated and a depletion layer is formed. The reverse case is true if the semiconductor work function is larger than that of the metal, resulting in electron transfer to the semiconductor, where they accumulate at the interface, forming an accumulation zone.[84,113,114,116]
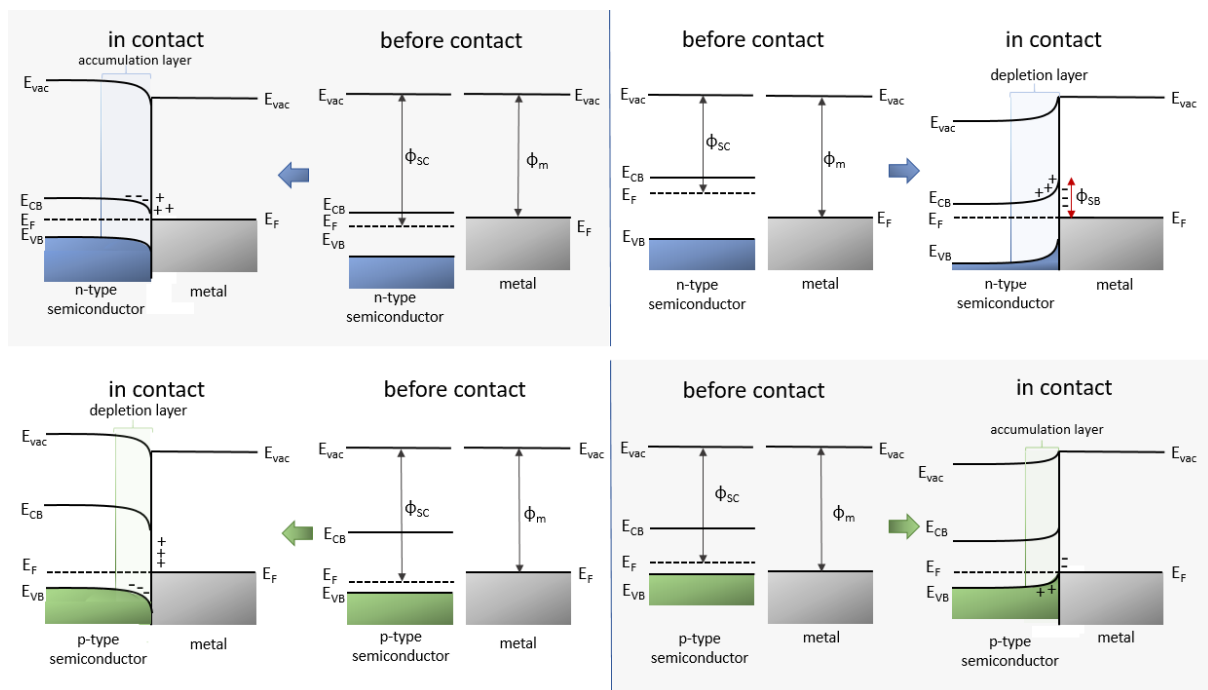
Figure 7 Band bending at the interface of a semiconductor (SC) and metal: For an n-type semiconductor with $E_F(SC) < E_F(m)$ (left), or with $E_F(SC) > E_F(m)$ (right) shown at the top and for a p-type semiconductor with $E_F(SC) < E_F(m)$ (left), or with $E_F(SC) > E_F(m)$ (right). Partially inspired by ref.[116]

Both depletion and accumulation zones are types of space charge regions. The potentials of conduction and valence band in such space charge regions differ from the bulk, since an electric field is formed, due to charged interfaces between metal and semiconductor, which results in band bending. Additionally, the concentration of minority and majority charge carriers is different in proximity to the interface. For $\phi_{SC} < \phi_m$ the bands in n-type semiconductors bend upwards, since electrons are repelled by the metal surface, increasing the energy of electrons in proximity to the interface (**Figure 7**). Such an upward bending results in a barrier being formed between metal and semiconductor, the so called Schottky barrier, which impedes an electron back-transfer to the semiconductor. For $\phi_m < \phi_{SC}$ the bands bend downwards. In p-type semiconductors, similar band bending situations can occur, but with reverse direction of the band bending, *i.e.* downward bending for depletion layer and upward bending for accumulation layer formation, since holes are consumed/ generated in the process of Fermi level equilibration. Since the Fermi level of n-type semiconductors is close to the conduction band energy, whereas that for p-type semiconductors is closer to the valence band, work functions for p-type semiconductors are usually larger. Therefore, when in contact with a metal of relatively large work function, such as noble metals, depletion layers are predominantly formed in n-type semiconductors, whereas accumulation layer formation is common in p-type semiconductors.[84,113,114,116]

Often photocatalysts are nanoparticulate powders. If the particles are small, the normally established bulk space charge region at an interface with a metal can exceed the dimensions of the particle. In this case, the band bending is significantly reduced and does not significantly contribute to charge transfer in the semiconductor. This is further aggravated by a low concentration of bulk charge carriers (**Figure 8**).[113,116–118] Furthermore, the situation is often complicated by defects at the interface.[64]

The system of a semiconductor photocatalyst and a metal cocatalyst serves multiple purposes, the most significant of which is the improved charge separation. The metal thereby often acts as an electron sink and thus as the active site for reduction reactions. Especially for photocatalysts that suffer

from photocorrosion, the improved charge separation can result in an improved stability of the photocatalyst.[119]
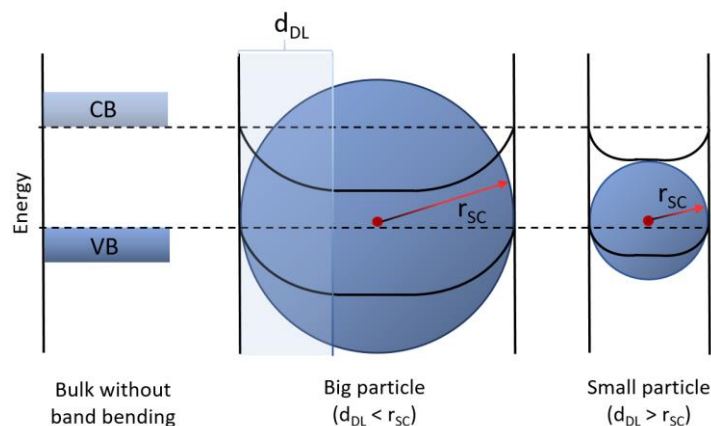
Figure 8 Band bending in a big particle *vs*. a small photocatalyst particle. Adapted with permission from Hagfeldt *et al*.[118] Copyright from the American Chemical Society 2012.

Furthermore, the reduction and oxidation sites are spatially separated, which leads to controlled charge migration, and a suppression of the reverse reaction. Apart from having a large work function for efficient charge separation, the metal also needs to possess active sites for the adsorption and reaction of reactants and a low overpotential. The latter two are characteristics also found in efficient electrocatalysts and determine the efficiency of reactant activation. Since the adsorption of reactants and the conversion mechanism are influenced by the cocatalyst, the selectivity can additionally be influenced.[54,119–123]

A special group of cocatalyts are metal nanoparticles additionally exhibiting localised surface plasmon resonance (LSPR). In this case, the metal nanoparticle not only assists in charge separation, but can additionally serve as a sensitizer, since light is absorbed to induce electron oscillations. Most common metals for plasmonic interactions are Au, Ag, and Cu due to their high concentration of delocalised charges. Resonance frequency and thus the range of light absorption are strongly dependent on particle size and shape. So-called hot charge carriers are created upon the excitation of LSPRs, either directly through absorption, or *via* the decay of plasmons. Such hot electrons possess sufficiently high energies to overcome the Schottky-barrier and transfer to the semiconductor conduction band (**Figure 9**). Additional effects are an improved charge carrier excitation by influencing the electric field in the proximity, improved light absorption in the semiconductor due to scattering effects, or an increased local temperature through plasmon decay.[84,120,124]

Band bending and the generation of intrinsic electric fields is not limited to semiconductor-metal interfaces, but also present at semiconductor-semiconductor interfaces. Hence, combinations of two semiconductors can be designed to improve charge separation. If two semiconductors are brought into contact, charges can be excited in both, depending on the respective band gaps. If the band gaps of both semiconductors differ sufficiently, larger portions of the incident light might be harvested compared to one material alone. Commonly, electrons will transfer from the semiconductor with the more negative conduction band potential to that with the less negative band potential, while holes migrate from the semiconductor with the more positive valence band potential level to the one with a lower valence band potential, following the potential gradient across the contact area. Such a kind of semiconductor combination is called **heterojunction**.[80–82,125–128]

13
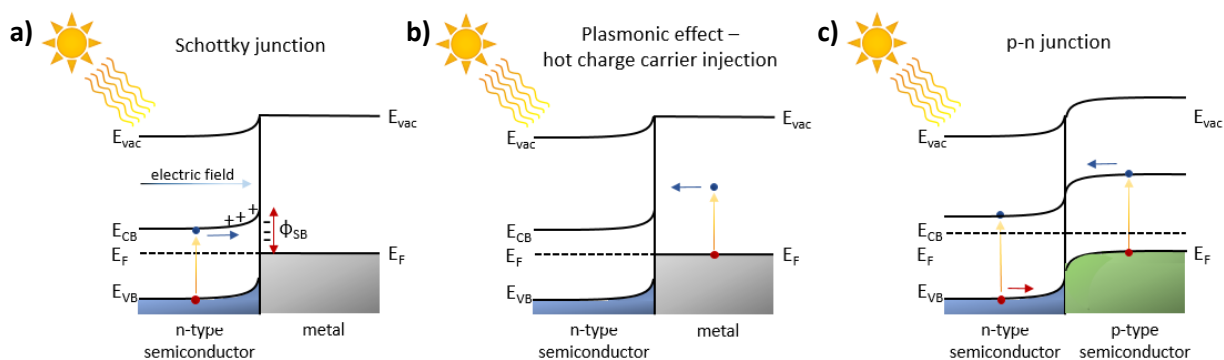
Figure 9 Charge separation with electron transfer from an n-type semiconductor to a metal cocatalyst over a Schottky contact (a), hot electron injection into the conduction band of a n-type semiconductor (b), and charge separation over a p-n-junction (c).

There are three different types of heterojunctions that are divided based on the relative band positions. In type I both the conduction band and the valence band of one semiconductor are of higher (more negative and more positive, respectively) energy than that of the other, hence both types of charge carriers will accumulate on one of the constituents, which might result in recombination, if the charges are not consumed quickly enough in redox reactions. In type II heterojunctions, the conduction and valence band positions are stacked: electrons are transferred to one of the semiconductors, while the holes travel to the other, resulting in optimal charge separation and thus the separation of reduction and oxidation reactions on different semiconductors. Type III heterojunctions are an extreme case of staggered band potentials, only with a larger offset (**Figure 10**).[81,82,126] A type II heterojunction is especially favourable, if bands bend towards another – a band alignment best achieved in p-n-junctions (Figure 9).[84,125,127] A special kind of heterojunction can be formed between two phases or modifications of the same material, *e.g.* rutile and anatase in TiO_2, or differently synthesised g-C_3N_4.[129–131]

Band bending in heterojunctions can either assist in charge separation, or impede it, depending on the work functions of the semiconductors. Charge separation in heterojunction systems relies on the migration of electrons between conduction bands and of holes between valence bands in different semiconductors. A different charge transfer mechanism is realised in direct **Z-schemes**.[132–134] Again, reduction reactions take place on one of the semiconductors, whereas oxidation reactions occur on the other. The leftover charge carriers, however, directly recombine across the interface (Figure 10). Such a transfer mechanism is especially favoured if conduction band potential of one and valence band potential of the other semiconductors are of relatively similar energy and band bending assists in the transfer.[132] Normally, both semiconductors are n-type in such a band alignment. While charge separation in type II heterojunctions comes at the drawback of reducing the energy difference between oxidation and reduction potentials, reduction reactions in direct Z-schemes occur on the semiconductor with the more negative conduction band and oxidation reactions on the one with the more positive valence band. This can significantly increase the potential difference and thus the thermodynamic driving force for redox reactions.[84,135] An advantage of both type II heterojunction and Z-scheme is the separation of reduction and oxidation sites and thus the inhibition of the reverse reaction.

The reports on direct Z-schemes practically have greatly increased during the last decade. In principle, Z-schemes are an imitation of charge transfer mechanisms between different photosystems in natural photosynthesis, wherein both photosystems are excited upon light irradiation and electrons are

transferred from one to the other. Redox mediators are used for the exchange of the residual charge carrier on each system and prevent recombination.[136,137]
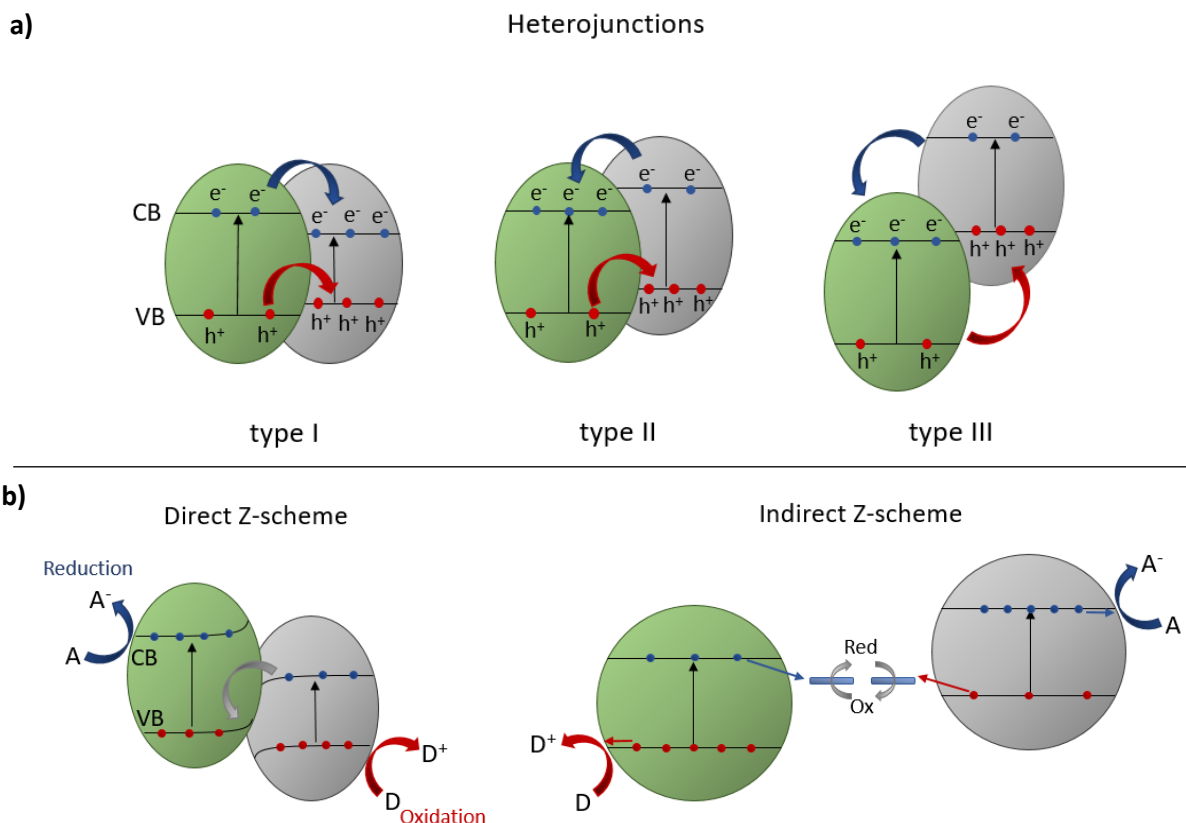
Figure 10 Schematic charge transfer in different types of heterojunctions (a) and in Z-schemes (b).

A similar mechanism has in the past been examined in terms of indirect Z-schemes, using redox shuttles based on Fe^{3+}/Fe^{2+}, VO_2^+/VO^{2+}, or IO_3^-/I^- for charge transfer between two semiconductors that are not in direct contact with each other.[109,134,138,139] No satisfactory efficiencies were achieved by such systems, however, resulting in a continuous decrease in the interest in Z-scheme systems, which only experienced a renaissance with the introduction of first all-solid Z-schemes (here a metal intermediate layer between both photocatalysts is used for electron mediator) and later direct Z-schemes or, more recently, S-schemes.[135] The latter are in principal synonymous to direct Z-schemes, only with – at least theoretically – a better characterisation of charge transfer mechanisms.[132] Unfortunately, the exact band potential situation is oftentimes not characterised and discussed sufficiently and the classification into direct Z-scheme or type II heterojunction is often rather arbitrary.

A special kind of composite material is that between a semiconductor and a photoactive small molecule (dye). Here, the dye acts as photosensitizer, absorbing light – also of wavelengths exceeding the band gap energy of the semiconductor – and transferring the excited charge carrier to the semiconductor, thereby significantly extending visible light harvesting in the system. The dye can be reduced back to its original state by an electron donor.[140,141]

Apart from an improved charge separation, the combination of two or more photocatalysts can have additional advantages. As discussed above, efficient light absorption is a prerequisite for solar energy conversion. For visible light absorption, semiconductors with band gap energies below 3 eV are required. At the same time the conduction and valence band levels need to be at sufficiently negative/ positive energy, respectively, for charge carriers to be used for the desired reactions. Moreover, good

reactant adsorption and low charge carrier recombination rates are required. The combination of these demands is hard to fulfil by one photocatalyst, manifesting the importance of composite systems, wherein the benefits of both are exploited.

In addition to that, material properties can be tuned in order to better meet the requirements. Thus, both band potentials and band gap energy can be adapted to some extent. **Element doping** is a strategy well known in photovoltaics to increase the amount of charge carriers in a system. The incorporation of additional elements into a material alters its electronic structure. Thus, dopant levels above the valence band (donor levels), or below the conduction band (acceptor levels) can narrow the band gap substantially (**Figure 11**). Electrons can be excited from the additional donor levels to the conduction band in the first case, while in the second case excitation can proceed from the valence band into the additional dopant levels. Both approaches result in an extended visible light absorption. For low dopant concentrations, both acceptor and donor levels are localised. If the dopant concentration is sufficiently high to form a delocalised band inside of the band gap, these additional levels are referred to as mid-gap states.[83,84,142–144]

In oxide materials, the valence band is mainly formed by oxygen p-orbitals, whereas empty transition metal d-orbitals often form the conduction bands. If sulphur instead of oxygen p-orbitals constitute the valence band, its energy is at a less positive potential, due to the participation of electrons in $3p$ orbitals in sulphur. This results in lower band gap energies of sulphides compared to oxides.[114] Doping is possible with cations either with a higher valence, often of metals with fully occupied d-orbitals for the introduction of additional donor levels, or with empty orbitals, such as alkali or alkaline-earth metals for the lowering of the CB potential.[142] Doping with anions of lesser electronegativity – *e.g.* nitrogen, sulphur, or phosphor in oxide materials – on the other hand mainly introduces additional occupied donor states.[145–148] If the energy difference to O $2p$ states is small, the dopant orbitals can mix with the oxygen ones.[149] Depending on the energy difference between band potential and dopant level, it can be differentiated between shallow and deep dopants, which not only differ in their potential, but also in the extent of ionisation.[23] Doping might furthermore induce lattice expansion or distortion, which has an additional effect on the electronic structure.[84]
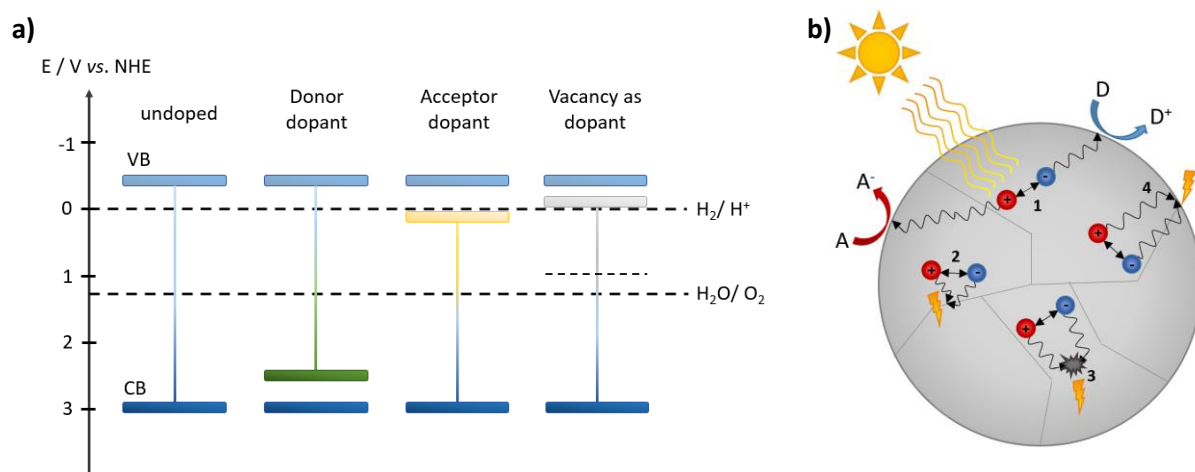
Figure 11 Reduction of the band gap by doping and the introduction of donor levels above the conduction band (green), of acceptor levels beneath the valence band (yellow), or intrinsic narrowing of the band gap by the existence of oxygen vacancies (grey) (a). Additionally, a deep dopant level is indicated by the dashed line. Charge carrier recombination at defect sites is shown in (b). 1: charge carrier generation and separation, 2: recombination at grain boundaries, 3: recombination at point defect in the bulk, 4: surface recombination.

Apart from altering the band gap energy and the potential of conduction and valence band, doping can affect charge separation efficiencies. On the one hand dopants can act as recombination centres, especially for deep-traps in the middle of the band gap (Figure 11).[23,112] On the other, however, dopants can decrease the concentration of defects, which are predominant bulk recombination centres. Hence, the dopant concentration also directly affects the charge carrier mobility.[112] Thus, the presence of oxygen defects in oxide materials commonly results in partial reduction of adjacent cations, *e.g.* of Ti^{4+} to Ti^{3+} in TiO_2. *Via* intentional doping of metal cations with a lower valence, the amount of reduced metal species can be decreased, thereby decreasing charge carrier recombination.[150–152] If excessive amounts of an alivoalent dopant (*i.e.* a dopant of either higher or lower valence) is introduced, however, more defects in the form of vacancies or partially reduced metal species are generated.[153] A strategy to prevent this and keep charge balance can be the co-doping of elements with both higher and lower valence.[84,143,154,155] Additionally, recombination can be suppressed by trapping electrons.[142,145,156] This can be beneficial if the trapped charge carriers can be used for the targeted redox-reactions. At high concentration, excitation can occur from or into mid-gap states, thereby significantly improving overall light harvesting.[83]

A special kind of doping is the introduction of defects, typically in the form of **vacancies**, which are intrinsic dopants. Vacancies reduce the coordination number of adjacent atoms, increasing their reactivity.[157] Generally, it can be distinguished between electronic defects and ionic defects. The first represents additional electrons and holes, whereas the latter encompasses the presence of additional ions, or the lack of a lattice ion. Naturally occurring ionic point defects are divided into interstitial defects (Frenkel defects), *i.e.* the presence of ions in between lattice sites occupied by the constituent elements in the crystal structure, and Schottky defects, *i.e.* the absence of ions from their normal lattice sites (**Figure 12**). Both follow the principle of charge neutrality and are intrinsic defects.[67,158] The absence of a charged ion in principle equals to a defect site carrying the opposite charge. Thus the creation of a positively charged anion vacancy, *e.g.* oxygen vacancy, always requires charge compensation by the creation of a cation vacancy or of excess electrons.[23]
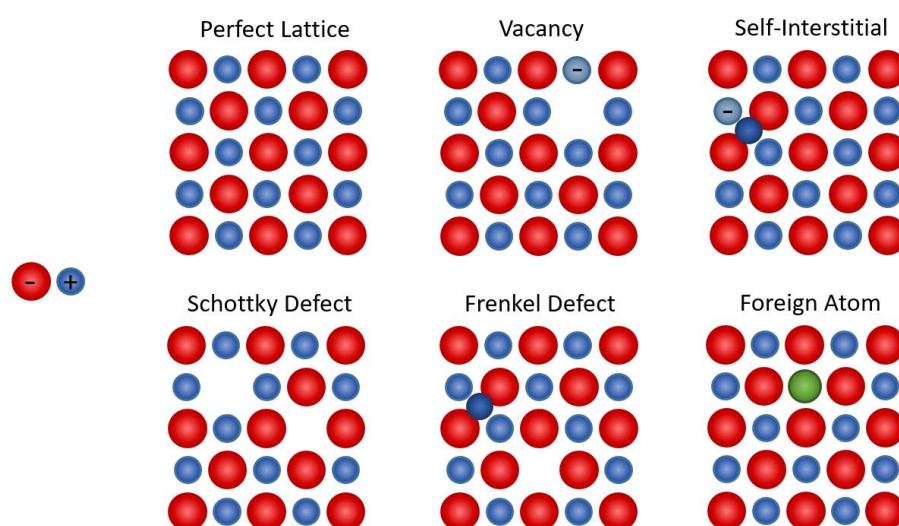
Figure 12 Examples of point-defects in a close-packed lattice of anions and cations with conservation of charge neutrality.

The same principle is true for element doping, in which the introduction of cations with a different valence must be compensated *e.g. via* the creation/ consumption of oxygen defects. Alternatives for the preservation of charge neutrality would be compensation by electrons or holes, or in the case of acceptor dopants (negatively charged, due to the lower valence), with interstitial cations.[23] Anionic

defects are frequently present in metal chalcogenides or nitrides. Thus, oxygen vacancies are common in metal oxides and were shown to improve the photocatalytic activity in several cases.[159] Since they are positively charged, they act as electron acceptors.[84,159,160] In carbon nitrides on the other hand, nitrogen vacancies play an important role.[161–164] Strategies for the creation of anionic vacancies include reduction with $NaBH_4$,[165] reduction with H_2 at elevated temperature,[166] annealing in argon or vacuum,[167,168] or etching.[169,170]

Apart from the so far discussed point defects, additional defects, such as stacking faults, dislocations, distortions, or grain boundaries between crystallites can exist.[171–173] While bulk defects frequently serve as recombination sites and are thus impedimental for high efficiencies (Figure 11), surface defects can assist in charge separation and electron transfer to/from adsorbing reactants. Similar to extrinsic dopants, they can alter the electronic structure, enhance light absorption and extent the lifetime of excited charge carriers.[172,173] The role of defects can exceed that of changing the electronic structure. Thus, surface vacancies can additionally serve as active sites for catalytic reactions. They differ in energy from the surrounding atoms, which is often favourable for the adsorption and subsequent activation of reactants.[174–176]

Apart from the combination of photocatalysts, or intrinsic changes in the semiconductor itself, the promotion of charge separation and suppression of recombination can be achieved by tailoring the morphology of the photocatalyst. One example would be nano-structuring, as discussed above. Another is facet engineering.[177,178] This principle is based on the fact that catalytic reactions normally proceed on the surface of a material and are thus directly influenced by the surface structure. Parameters influenced by the surface composition are *e.g.* adsorption and activation energies. Often, some crystal facets are more active for a reaction than others. Additionally, charge separation might be more favourable in some directions than in others.[177,179,180] Ideally, a directed separation of electrons and holes to different, species-specific sites in the crystal structure would be realised.[178]

2.1.3 Photocatalytic Water Splitting

Photocatalytic water splitting is probably the most extensively investigated photocatalytic reaction. It combines the reduction of protons to hydrogen with the oxidation of water to oxygen (Eq. 5 - 8).[64,65,85,112,144,181] It thus represents a sustainable pathway to directly generate H_2 as a green fuel, using sunlight and water (**Figure 13**). Both reactions are highly pH dependent, as they involve protons. While the hydrogen evolution reaction (HER) is more favourable in acidic and neutral environment, the oxygen evolution reaction (OER) proceeds much faster in an alkaline environment, as can be seen from equations 8 and 10.[65,112] Additionally, both HER and OER result in a change of local pH, since protons are consumed or produced, respectively.[64] It is furthermore evident, that the oxygen evolution is a multi-reactant, multi-electron process, which results in slow reaction kinetics. Hence, the OER is usually the rate and efficiency limiting factor in overall water splitting (OWS).[121,181–183]

In photocatalysis, the reduction and oxidation potential are determined by the band gap and band positions, since they predetermine the potential of photo-excited charges. In theory, 1.23 V *vs.* RHE are required for the splitting of water. Additionally, the valence band maximum has to be located at more positive potentials than 1.23 V *vs.* RHE and the conduction band minimum at more negative

potentials than 0 V for electrons and holes to have sufficient energy for water oxidation/reduction.[65,184,185] However, there is an activation barrier for the electron transfer to species at the catalyst surface that increases the required energy input. Thus, in praxis the band gap needs to be larger than at least approx. 1.6 V.[183]

$$2\,H^+ + 2\,e^- \;\rightarrow\; H_2 \qquad\qquad E^\circ_{RHE} = \; 0 \qquad (5)$$

$$2\,H_2O + 4\,h^+ \rightarrow\; 4\,H^+ + O_2 \qquad E^\circ_{RHE} = \; 1.23\ V \qquad (6)$$

$$4\,OH^- + 4\,h^+ \rightarrow\; O_2 + 2\,H_2O \qquad E^\circ_{RHE} = \; 1.23\ V \qquad (7)$$

$$H_2O \rightarrow H_2 + 0.5\,O_2 \qquad \Delta G = 238\,\frac{kJ}{mol} \qquad (8)$$
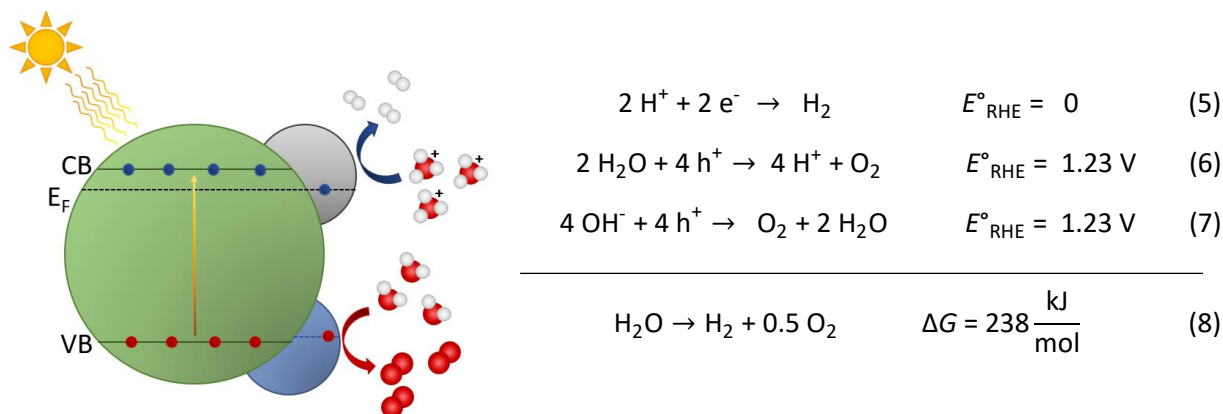
Figure 13 Water splitting on a photocatalyst equipped with both an oxidation and a reduction cocatalyst.

For semiconductor photocatalysis, the potential available for the driving of redox-reactions is usually not equal to the band gap potential, but instead to the photovoltage, *i.e.* the potential difference between quasi-Fermi levels of electrons and holes. Those are the shifted Fermi levels upon illumination and charge excitation.[186] The photovoltage depends amongst others on the flat band potential (*i.e.* the band potential established if an external voltage is applied to flatten band bending), the extent of Fermi level pinning (*i.e.* the control of surface states over the Fermi level and thus independence of bulk dopant concentration), and the surrounding environment. It is thus commonly smaller than the band gap potential.[116,121]

The more negative the conduction band potential and the more positive the valence band potential, the higher the driving force for the respective reaction. At the same time, the band gap must not be too large to allow for efficient solar light harvesting.[65] These requirements are in addition to efficient charge separation and reactant adsorption and activation, as discussed above, which makes overall water splitting with one system highly difficult. Therefore, commonly only one half-reaction is investigated for a material – at least initially. This allows for a systematic optimisation of this side, before the development of systems covering both half reactions is attempted. Instead of performing the other half reaction, a sacrificial agent is employed to increase the number of available charge carriers and thereby the quasi-Fermi levels and thus driving force for a photocatalytic reaction.[187]

Since both HER and OER require (photogenerated) charge carriers, the efficiency moreover depends on the carrier diffusion length – especially that of the minority charge carrier. Many photocatalysts for the OWS are n-type (**Figure 14**), which means that hole diffusion is another limiting factor affecting the OER. The problem is further aggravated by the larger effective mass of holes compared to electrons.[188] The slow hole diffusion is a major problem *e.g.* in hematite, Fe_2O_3, photoelectrodes.[189–191] Furthermore, the greater mass of O_2 compared to H_2 in combination with frequently high oxygen affinity of the materials result in a slower diffusion from the catalyst surface.[188]
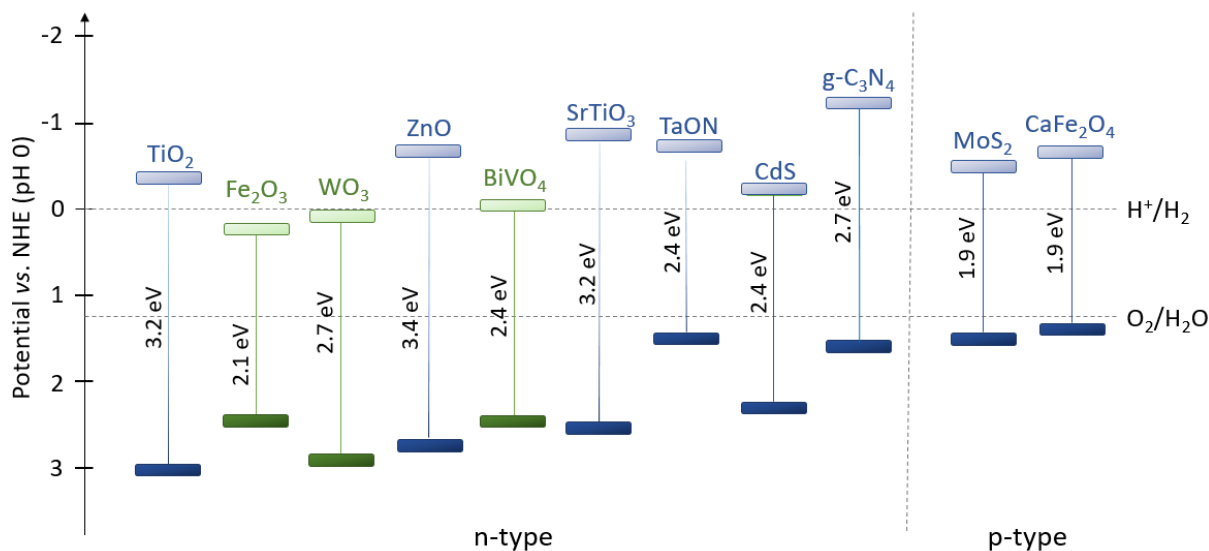
Figure 14 Band positions for important water splitting photocatalysts. Those capable (at least in theory) to perform overall water splitting are depicted in blue, while those with suitable band potentials for only the OER are shown in green. Values for band potentials are taken from listed references: TiO$_2$ (anatase) and SrTiO$_3$,[192] Fe$_2$O$_3$,[193] WO$_3$,[194,195] ZnO,[196] BiVO$_4$,[197] CdS,[198] g-C$_3$N$_4$,[199] MoS$_2$ (monolayer),[200] TaON and CaFe$_2$O$_4$.[201]

As illustrated by the requirements for and issues faced in overall water splitting, efficient OWS over one semiconductor photocatalyst is challenging. Nevertheless, the activities and efficiencies reached increased during the past decades of research, often strongly coupled to strategies of efficiency enhancement. Some important semiconductor photocatalysts for OWS and OER are depicted in Figure 14.

The HER as the easier but in terms of products also the more interesting reaction, is the better researched half reaction of the two. Initially, much focus was put on TiO$_2$, following in the footsteps of Fujishima and Honda.[77,202] Anatase is thereby generally more active compared to rutile or brookite, due to a commonly higher surface area and greater abundance of oxygen vacancies – this is especially obvious in N-doped anatase.[202–204] Even more active are composites of anatase and rutile.[129,130] Another important HER catalyst is CdS, which absorbs visible light and has been extensively studied in the past.[205–210] However, CdS suffers from a poor stability and extensive photo-corrosion, and is additionally problematic due to the toxicity of Cd.[97] Since Wang *et al.* reported on photocatalytic HER with polymeric carbon nitride,[211] a visible light absorbing, carbon-based polymer, many papers featuring carbon nitrides have been published.[212–220] Many reports are based on g-C$_3$N$_4$, although in reality, most structures of obtained carbon nitrides are not graphitic, but instead not fully condensed and of low crystallinity.[221–224] More recently, crystalline carbon nitrides have also been explored.[225–229] Various heterojunctions have been developed for improved photocatalytic performance compared to the single component system. Especially composites with TiO$_2$, CdS, and g-C$_3$N$_4$ as one of the principal constituents have been tested.[230–236]

Noble metal cocatalysts are usually added to improve the HER efficiency.[119] The proton first adsorbs to the metal surface and M-H bonds are formed coupled to an electron transfer. Subsequently, H$_2$ is formed catalytically. The most important noble metal cocatalysts for the HER are Pt and Rh. This is due to a direct dependence of the hydrogen evolution rate on the M-H bond strength, which is optimal for Pt.[119] Sometimes Pd, Ag, or Au are used as well, the latter two often in the context of plasmonic excitation.[237–240] A huge advantage of noble metal cocatalysts besides the large work function is the possibility to directly deposit them out of a salt solution selectively on sites with high electron

concentrations using photodeposition.[241,242] Earth abundant cocatalysts such as Co-phosphides (CoPi),[243,244] MoS_2,[245,246] Ni, or NiS[247–249] have recently emerged to reduced material costs.[54,56,250,251] Some of these can be photodeposited as well.[252]

For the OER the number of reported photocatalysts is lower, as is the observed activity. Still, the development of more sophisticated systems using combinations of semiconductors, doping, or morphology engineering led to a gradual improvement during the past decades.[94] As for the HER, TiO_2 is one of the most widely investigated semiconductors.[93,253,254] $BiVO_4$ has emerged as another promising material for the OER, especially after Mo doping was shown to significantly improve the electron transport and thus the performance.[197,255–257] Other important OER catalysts are WO_3,[258–260] and Fe_2O_3,[190,191,261,262] especially in photoelectrochemistry also owing to their visible light absorption properties.[194,201] Additionally, ferrites have shown potential in photoelectrochemichal water oxidation, e.g. $ZnFe_2O_4$, or $CaFe_2O_4$.[263–270] Cocatalysts are again important for the achievement of good O_2 evolution rates. Conventionally, IrO_2 and RuO_2 were mainly used.[93,260,271–273] This was followed later by Co based cocatalyts, such as Co-phosphate, Co_2O_3 or CoOOH.[256,258,274,275] More recently Co-, Ni- and Fe-oxyhydroxides have emerged as earth abundant, and – at least for Fe-rich oxyhydroxides – non-toxic cocatalysts.[276–282]

Initially, TiO_2 and $SrTiO_3$ were mainly investigated for the OWS. Many of the first reported activities were very low, however, and sometimes ambiguous.[85,283–285] A major problem often encountered is that of the back-reaction of H_2 and O_2 to H_2O, which is catalysed at the same sites as the water splitting reaction.[185] $K_4Nb_6O_{17}$ was discovered in which the separation of both reactions to separate layers is realised (**Figure 15**).[286] A similar strategy is pursued in layered perovskites, especially titanates.[287,288] Some years later, tantalates were discovered as active photocatalysts for OWS.[289–292] Especially NiO-loaded, La:doped $NaTaO_3$ showed a very promising activity, which was attributed to a separation of HER and OER onto different sites in the structure (Figure 15).[293] A relatively high conduction band potential and thus enhanced driving force for reduction reactions contributes to the superior activity compared to titantes or niobates.[85] Another active water splitting catalysts is Zn-doped Ga_2O_3.[294,295] Many active photocatalyst for OWS contain metals with d^0 or d^{10} configuration. For these semiconductor oxides, the valence band level is predominantly determined by that of O $2p$.[65,201]

The water formation reaction cannot only be suppressed by spatial separation of reaction sites, but also by cocatalyst engineering: Core-shell cocatalysts are especially advantageous in this regard. The reduction reaction proceeds at the core and the outer shell is penetrable for the evolved H_2, but prevents access of O_2 to the active catalyst sites. Prominent examples are Ni/NiO or Rh/Cr_2O_3 cocatalysts.[296–300] For the Ni/NiO system, Ni additionally serves as hydrogen evolution cocatalyst, while NiO is an electrocatalyst for the OER.[301] The role of Cr_2O_3 on the other hand is ambiguous, but mainly seems to be the blocking of the Rh surface for oxygen.[300]

Initially it was assumed that water oxidation cocatalysts are not necessary for OWS due to the high valence band potential of many oxides. However, the deposition of both HER and OER cocatalyst could significantly increase the activity of several materials, such as carbon nitrides,[302] or GaN:ZnO.[272] Recently, $SrTiO_3$ has received a lot of attention, after the group of Domen added a CoOOH cocatalyst in addition to conventional Rh/Cr_2O_3 onto Al-doped $SrTiO_3$ and achieved a very high quantum efficiency.[274] In fact, the system was efficient enough for large scale studies in a prototype panel reactor system, to explore the options for future industrial H_2 production via photocatalysis. No economically viable H_2 production could be realised, though.[303] Doping of $SrTiO_3$ with Rh or Al has generally proven an efficient strategy for reducing the band gap and removing Ti^{3+} trap states.[151,284,304]
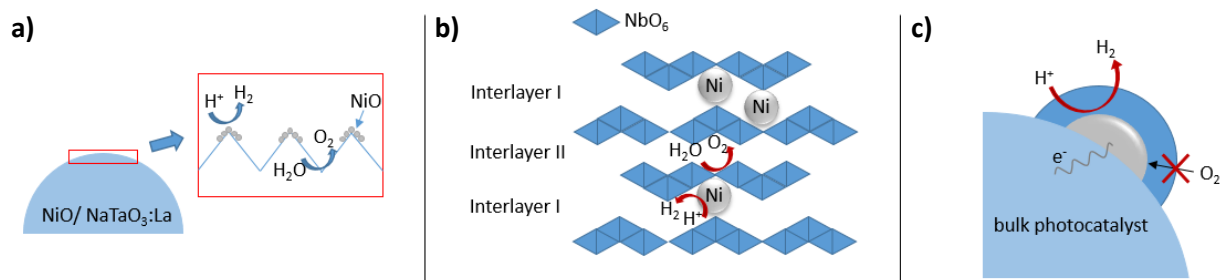
Figure 15 Strategies for activity enhancement for OWS *via* separation of reactions on different sites (a), adapted with permission from Kato *et al.*,[293] or in different layers (b).[286] Alternatively, core-shell cocatalysts, such as Rh/Cr$_2$O$_3$ have proven beneficial for an inhibition of the reverse reaction (c).

Many of the state-of-the-art photocatalysts, such as TiO$_2$, or SrTiO$_3$ are only active under UV light. Therefore, strategies to improve visible light absorption – such as conversion to oxynitrides or oxysulphides – are currently extensively investigated.[155,181,305–308] One of the most important visible-light active photocatalysts of this category is TaON, especially after modification with ZrO$_2$.[309,310] An additional example is (Ga$_{1-x}$Zn$_x$)N$_{1-x}$O$_x$,[311–313] which shows a good water splitting activity under visible light irradiation, or Zn-Ge-oxynitride.[314] A prominent example for an oxysulphide photocatalyst is Y$_2$Ti$_2$O$_5$S$_2$.[315]

A major problem in the design of new photocatalyst materials is a certain lack of knowledge regarding the intermediates of a photocatalytic reaction, the presence or absence of rate determining steps, or correlations of parameters such as light intensity, sacrificial agent concentration, or number of active surface sites, with the activity.[117,187] Additionally, material changes might occur under the conditions employed in a photocatalytic experiment and/ or light irradiation, especially at the surface.[316–318] Continuous mechanistic research and the combination of theoretical calculations and *operando* measurements will be needed for a better understanding of fundamental processes in semiconductor photocatalysis, which is in turn indispensable for the rational design of new photocatalytic systems that may tackle the issue of low efficiency. During the past decade, characterisation studies on electrocatalytic reaction systems *in operando* have been addressed more widely, especially using X-ray absorption (XAS) and near ambient pressure X-ray photoelectron spectroscopy (NAP-XPS).[279,319–324] Valuable insights can also be gained for photocatalysis, since electrocatalysts are frequently used as cocatalysts in combination with semiconductor photocatalysts. Furthermore, *operando* studies are gradually more addressed in photocatalysis, as well.[325–328]

2.1.4 Photocatalytic Nitrogen Reduction

Ammonia, NH$_3$, is one of the most important synthetic chemicals, as it is crucial for the fabrication of fertilisers and thus the nutrition of the world's population that would not otherwise be possible.[330] Over 175 million tons of NH$_3$ are annually produced and a growth in the production is expected, in tandem with a growing world population.[331,332] This makes it the second most produced chemical worldwide;[333] 80 % - 85 % of the synthesised NH$_3$ are further used for the production of fertilisers.[331,334] Additionally, ammonia is becoming more and more important as a chemical storage medium for H$_2$ due to its high content of bound hydrogen of 17.6 wt.% and storage at low pressures in liquefied

form.[48,51,335] It can directly be employed in solid oxide fuel cells.[48,336] Industrially, NH_3 is produced by the Haber-Bosch process from H_2 and N_2 gases at elevated temperatures and pressures in large centralised plants (**Figure 16a**).[331,337–339] The production requires 1 - 2 % of the global energy consumption and contributes to global CO_2 emissions by a share of $1-2$ %, mainly due to the generation of H_2 *via* methane steam reforming prior to the actual Haber-Bosch process, which alone has a share of around 2 % of the annual fossil energy demand.[335,340,341]
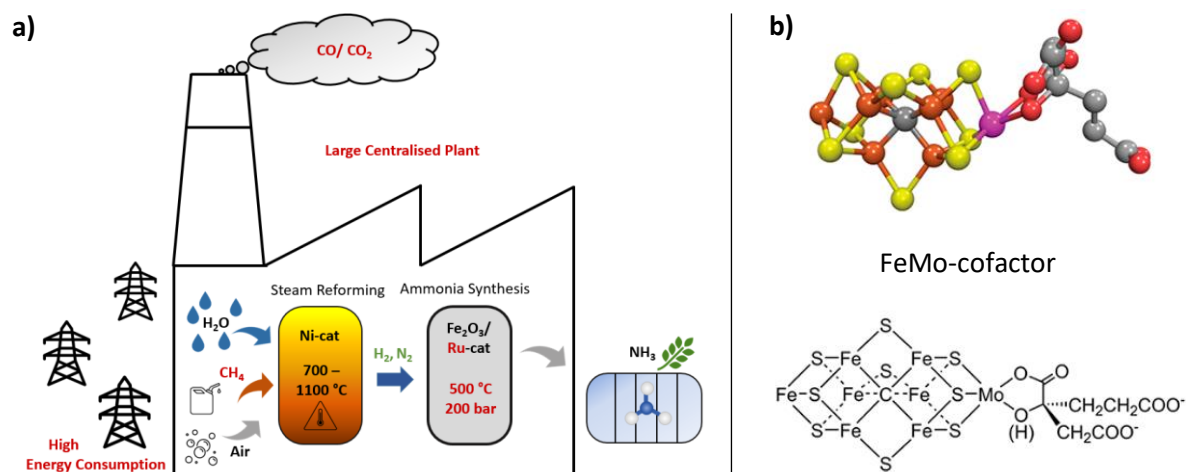
Figure 16 Illustration of the conventional Haber-Bosch process in centralised power plants, with on-site generation of H_2 *via* steam-reforming (a) and structure of the FeMo-cofactor in nitrogenase enzymes (b). The structure is reprinted with permission from reference [329] (Copyright American Chemical Society). Sulphur atoms are depicted in yellow, iron in orange, molybdenum in purple and carbon and oxygen are shown in black and red, respectively.

Photocatalytic nitrogen reduction aims at the direct production of ammonia from gaseous N_2 (or ideally air) and water under ambient conditions.[38,71,72,174,342–346] Ambient nitrogen reduction is already realised by nitrogenase enzymes in microorganisms, in which the cofactor at the active site is mainly composed of iron and sulphur atoms, in addition to molybdenum, vanadium, or more iron (**Figure 16b**). The full mechanism is not completely understood yet. In general, coordination of N_2 to the active centre is followed by activation, which facilitates the reduction and protonation. ATP is used as an energy source, H_2 is produced as a concomitant by-product and the reversible replacement of a sulphur atom was found to play an important role in the process.[329,347–351] Investigations on transition metal catalysts revealed that nitrogen is activated *via* back-donation from the metal centre to nitrogen, increasing the electron density in anti-bonding orbitals.[348,352] The structural composition of the active centre led to many biomimetic approaches focussing on iron, molybdenum and/or sulphur containing compounds.[353–362] Examples include binary sulphides, such as MoS_2,[357,363] or FeS_2,[355,364,365] iron-molybdenum oxides, such as $FeMoO_4$,[356,366] and $Fe_2(MoO_4)_3$,[358] and ternary oxides and sulphides, such as $FeMo_3S_4$,[362] Fe-doped $SrMoO_4$,[367] or Bi_2MoO_4.[157] All of these examples except Bi_2MoO_4 were reported for electrocatalytic nitrogen conversion, however, due to the numerous high demands on a photocatalyst for the NRR. Especially for ternary iron-molybdenum oxides and sulphides, the number of reports is scarce and the achieved activities and selectivities were comparatively low.

Photocatalytic nitrogen reduction suffers from low efficiencies. This is partially due to the very stable N-N triple bond that is highly inert, as well as unfavourable one or two electron transfer steps to the LUMO, which is located at a high energy. The NRR is furthermore a multi-electron, multi-proton process, since the reduction of one molecule of N_2 requires the transfer of six electrons and six protons, as elucidated by equations 9-12.[38,47,368] The high energy requirement for the formation of

intermediates kinetically impedes the reduction, which from a thermodynamic perspective is quite favourable (Eq. 12). Both proton affinity and energy barrier for consecutive steps decrease after the first electron transfer steps.[352]

$$N_2 + 8\,H^+ + 6\,e^- \rightarrow 2\,NH_4^+ \quad E^\circ_{RHE} = 0.274\ V \tag{9}$$

$$N_2 + 6\,H^+ + 6\,e^- \rightarrow 2\,NH_3 \quad E^\circ_{RHE} = -0.148\ V\ (alkaline) \tag{10}$$

$$H_2O\ (l) + 2\,h^+ \rightarrow 0.5\,O_2\ (g) + 2\,H^+(aq) \quad E^\circ_{RHE} = 1.23\ V \tag{11}$$

$$N_2 + 3\,H_2O \rightarrow 2\,NH_3 + 1.5\,O_2 \quad \Delta G = 678\ kJ/mol \tag{12}$$
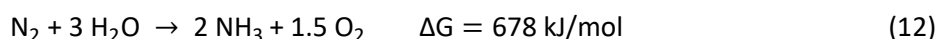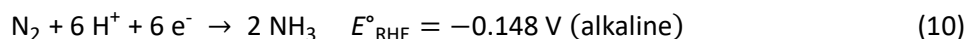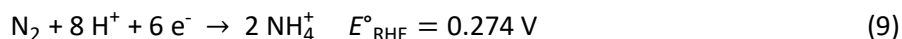
The small potential difference of the N_2/NH_3 and the H^+/H_2 redox couple, together with the kinetic limitations in the NRR, makes hydrogen evolution the most important competitive reaction. Hence, selective NRR is highly challenging in aqueous media and requires catalysts that preferentially bind nitrogen rather than hydrogen atoms at the surface.[369] Additional side-reactions can be the oxidation of N_2 to NO, nitrates, or nitrites, the production of hydrazine N_2H_4, or the oxidation of NH_3.[47,72,370,371] Since N_2 reduction to ammonia requires protons, the reaction in aqueous media is dependent on the pH, with higher activities observed under acidic conditions, in agreement to a higher abundance of protons.[368] Apart from the parasitic HER, NRR in aqueous media is further impeded by the low solubility of gaseous N_2. An emerging strategy for the circumvention of this problematic in electrocatalytic NRR is the use of ionic liquids that can both improve the Faradaic efficiency and the ammonia yields.[369,372,373]
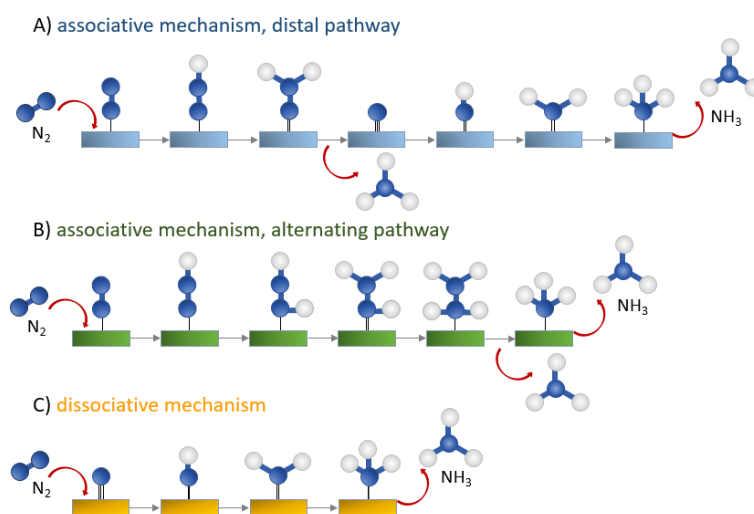
Figure 17 The three main pathways for nitrogen reduction. Adapted from references [342,368,374].

A prerequisite for good activity in NRR is an efficient adsorption and activation of N_2. The first electron or proton coupled electron transfer steps are with -4.16 V *vs.* NHE, or -3.2 V *vs.* RHE strongly endergonic and represent high activation barriers for the reaction.[47] A lowering of these activation energies through interaction with a catalyst surface is thus crucial. Hence, an abundancy of active sites in combination with the presence of metals with an ability for back-donation are targeted material properties in the design of NRR catalysts.[352] The reduction of N_2 to NH_3 involves bond dissociation as well as protonation and reduction steps. The precise order of these steps is, however, not predetermined but depends on the respective catalyst. Mainly three different pathways are postulated (**Figure 17**). One is the dissociative pathway – the route mainly followed in thermal catalysis, such as the Haber-Bosch process. Herein N_2 is cleaved into bound N-adatoms upon adsorption to the catalyst,

which are subsequently hydrogenated to form NH_3. A second pathway is associative in nature: Adsorbed dinitrogen is first protonated and the N-N bond is only cleaved upon dissociation of NH_3. Depending on whether both nitrogen atoms are alternately protonated up until the point when one nitrogen atom is protonated fully and dissociates as NH_3, or whether the proton and electron transfer steps are initially restricted to one nitrogen atom, two pathways are differentiated: the distal and the alternating one.[342,368,369] The associative nitrogen reduction pathways commonly assume end on adsorption of the N_2 molecule onto the catalyst surface. Alternatively, a simultaneous adsorption of both nitrogen atoms side-on in a bridge mode could also be assumed.[369]

Which of the two pathways is followed strongly depends on the material, as the adsorption of N_2 is crucial. Generally, one of the two pathways requires a higher activation barrier than the other and the rate determining step depends on the respective surface and – as for the HER on metal electrocatalysts – on the bonding strength towards N_2.[369,375] It is often difficult to distinguish between possible reduction pathways. Mostly DFT calculations are used to evaluate which pathway is the most likely on a specific surface.[355,366,376] However, they always require a set of assumptions and possible models that are used for the calculations. Additionally, the detection of hydrazine can be an indication for the alternating pathway, since $*N_2H_2$ and $*N_2H_4$ species are formed, that may desorb from the surface.[377–379]

A serious problem for efficient NRR over only one material is the linear scaling relationship between the binding energies of the key intermediates $*N_2H$ and $*NH_2$.[47,375,380] They represent the most important product of the first proton coupled electron transfer step and the educt of the last step, *i.e.* the proton coupled reduction and desorption of NH_3.[47] The better $*N_2H$ is stabilised as an intermediate – and thus the better the first proton-coupled electron transfer step – the more the dissociation of NH_3 in the last step is inhibited. As a consequence the difference in ΔG of these two intermediates is much larger than what would be required for both reaction steps to occur at the same potential – this in turn results in a higher required overpotential.[47,380] These scaling relationships have been established for electrocatalytic nitrogen reduction, but can in principle also be valid for photocatalysis and prevent efficient NRR over a single material. Therefore, strategies need to be developed, that circumvent this limitation by following altogether different mechanism.[380] In electrocatalysis this has been achieved with Li-mediated approaches that exacerbates the ability of Li-metal to spontaneously form nitrides at ambient conditions that can be hydrolysed to NH_3 in the presence of a proton donor, which ideally acts as a proton shuttle.[381,382] Semiconductor nitrides allow for the possibility of nitrogen reduction *via* a Mars-van-Krevelen mechanism, *i.e.* the conversion of lattice nitrogen to ammonia followed by subsequent replenishment of the extracted nitrogen.[37,383,384] This mechanism is altogether different from the adsorption and activation of gaseous N_2 at the surface and can thus avoid the dependencies of convention reduction intermediates. Photocatalytic systems were found to deviate from the linear scaling relationships to some extent, which was attributed to a suppression of the HER. Correlations with the metal-H bonding strength of the cocatalyst and nitrogen binding energies were found to play an important role.[72,385,386]

As in water splitting, the initial research was based on TiO_2, after Dhar observed nitrogen fixation in desert soils.[387] This work was reinitiated years later by Schrauzer and Guth, who established a relationship between the presence of hydroxyl groups in metal oxides and the ability for photocatalytic nitrogen reduction.[388] In the following years, the interest in photocatalytic nitrogen reduction experienced a sharp increase, still focussed mainly on metal oxides. A higher activity of rutile compared to anatase was observed and subsequently, doping strategies with metal ions, especially Fe^{3+}, were

introduced to tune the ratio of both phases in a TiO_2-only composite while at the same time improving the light absorption properties, charge separation and the number of active adsorption sites.[72,388–390] Iron doping might also stabilise oxygen vacancies, that are beneficial for the NRR.[379] Pristine TiO_2 was found to be inactive for the NRR. Therefore TiO_2-based systems always rely on structural modifications of the oxide itself – *e.g.* through the amount of surface –OH groups, or the abundance of defects, especially oxygen vacancies V_O – or on the combination with a second material.[391,392] Nowadays TiO_2 remains one of the most widely investigated photocatalysts for the NRR.[175,379,392–399]

Due to the intrinsically low activity and poor selectivity of most catalyst systems, common strategies such as the addition of a cocatalyst, the formation of heterojunctions, doping, or the tuning of morphology and exposed sites are widely pursued in order to improve both the charge carrier separation and the nitrogen adsorption and activation. In many cases, several strategies are combined to achieve both an efficient separation of charges and activation.[170,174,397,400–403] The choice of noble metal cocatalyst not only affects the activity, but also the selectivity – two characteristics that are highly interdigitated for the NRR. Thus, for TiO_2 the activity decreases in the order of Ru>Rh>Pd>Pt, due to a decrease in the M-H bond strength, which in turn increases the overpotential for the HER.[385] Apart from the introduction of 'classical' cocatalysts, plasmonic sensitisation with noble metal nanoparticles has been used in prominent systems based on TiO_2 nanorods, or $SrTiO_3$.[175,404–406] Apart from TiO_2, common metal oxides such as Fe_2O_3 and $SrTiO_3$ were initially employed and are still frequently investigated up to date.[407–412] More recently, bismuth oxyhalides, such as BiOCl or BiOBr received a lot of attention, due to high reported yields achieved *via* a good control of exposed facets/ active sites and facile introduction of oxygen vacancies that trap electrons and serve as efficient nitrogen adsorption sites.[179,402,413,414] The benefits of vacancies for nitrogen adsorption and activation were also shown for other material classes, such as nitrides, making defect engineering one of the most important strategy for improving NH_3 yields in photocatalytic NRR.[171] Other important photocatalysts for the NRR are *e.g.* V_N-containing GaN nanowires,[415] etched LDHs,[170] or V_O-rich $W_{18}O_{49}$ nanowires/-rods[416,417] – most of which contain high amounts of vacancies.

The exact mechanism is oftentimes not fully understood, even for TiO_2 itself. DFT calculations considering adsorption and bond activation are often employed to gain mechanistic insights, but the complexity of the systems and the number of possible reactions result in divergences between the studies, as simplified models are employed, neglecting one factor or the other. Exemplary factors are the role of surface hydrogenation,[418] oxygen vacancies,[393] adventitious carbon,[419] or the role of additionally present ions.[420]

Another widely investigated material is graphitic carbon nitride (g-C_3N_4), which was reported to be one of the most active photocatalysts for the NRR so far.[169,222,223,383,421,422] C_3N_4 is a polymeric material based on carbon and nitrogen. It is non-toxic, based on abundant elements, easy to synthesise *via* thermal polymerisation of low-molecular weight precursors such as melamine,[423,424] urea,[422,425–427] or dicyandiamide,[162,428,429] and absorbs visible light with a band gap of approx. 2.7 eV.[211,426,430] It has emerged as a famous non-metallic photocatalyst after Wang *et al.* reported its activity for the HER in 2009.[211] Due to its organic framework, the structure and properties can be tuned extensively, *via* synthesis conditions, precursor choice and ratio, or post-synthetic treatment. The layer stacking distance, surface area, C/N ratio, band gap, charge separation efficiency and number/character of defects are all parameters that can be tailored.[143,423,426,427,429,431,432] Carbon nitrides employed in photocatalysis are rarely of high crystallinity, thus containing a lot of defects, that were shown to be

beneficial for the activity.[163,171,421] Especially carbon nitrides obtained *via* thermal polymerisation are often largely amorphous.[223,424,433]

Additionally, residues of low molecular weight intermediates increase the disorder and prevent a defined stacking of layers.[212,430] The polymerisation temperature was shown to have a significant impact on the properties of the obtained carbon nitride, with increased condensation and a red shifted absorption observed after polymerisation at higher temperatures.[424,434] Pyrolysis time and duration additionally have an influence on both the degree of condensation, but also on surface area and layer thickness.[435]
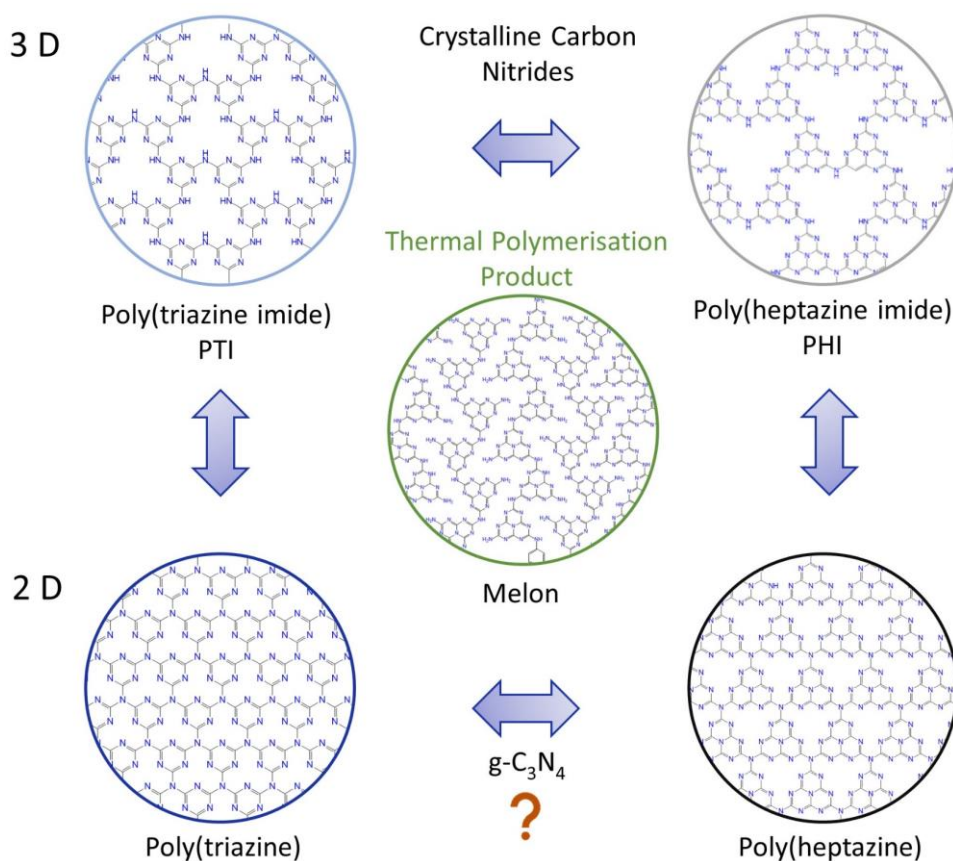
Figure 18 Structures of carbon nitrides: Polytriazine (first structural model for g-C_3N_4), polyheptazine (thermodynamically more stable), melon (the identified thermal polymerisation product), and the crystalline forms PTI (poly(triazine imide) and PHI poly(heptazine imide).[222]

Different structure models were proposed in the search for the structure of ideal g-C_3N_4, of which the two most common ones contain a triazine, or a tris-*s*-triazine (heptazine) unit as primary building block (**Figure 18**). Compared to the triazine-network, structures based on tri-*s*-triazine building blocks were calculated to be more stable, which was further supported by the finding of melem, that already contains the tri-*s*-triazine unit as an intermediate.[430,436] While most of the earlier works assume a fully condensed network that forms a sheet-like structure (hence the prefix 'graphitic'), reports *e.g.* by Lotsch *et al.* refute this picture, postulating a structure-model based on melon-chains for carbon nitride synthesised *via* thermal polymerisation (Figure 18).[221–223,428] More recently, crystalline carbon nitrides have moved into the focus of photocatalytic research, due to their better defined structure and increased stability. Of the crystalline polymeric nitrides, poly(triazine imide) (PTI) and poly(heptazine imide) (PHI) synthesised in alkali chloride salt melts, *e.g.* LiCl, NaCl, or KCl, exist.[225,229,437–439] They consist of 2D crystalline sheets of condensed triazine or heptazine units, respectively, that form stacks with

the metal ions in pores and intercalated chlorido ions.[222] The alkali ions thereby have a dominant structural directing influence, with the composition of the salt melt being the decisive factor for the formation of either triazine or heptazine based frameworks.[437] By varying the ratio of salt to urea, composite materials of disordered polymeric nitride (tris-*s*-triazine based) and PTI can be formed, as shown *e.g.* by Jin *et al.*[227] Additionally, the C/N ratio can be tuned by the choice of the precursor.[228]

Pristine C_3N_4 usually only exhibits rather low photocatalytic activities, due to fast charge-carrier recombination rates.[213,440] Many systems focussing on heterojunctions or Z-schemes of g-C_3N_4 and a secondary photocatalyst have been reported. Examples for the NRR employ oxides, such as TiO_2,[441] Cs_xWO_3,[442] Ga_2O_4,[443] $BiOBr$,[444] or sulphides such as MoS_2,[445] or $ZnMoCdS$.[446] Another feasible strategy for activity enhancement (HER, CO_2RR and NRR alike) is doping with either cations,[447–449] or non-metals, predominantly sulphur and oxygen,[199,450–453] but often also phosphorous and boron.[454–459] Sulphur doping can be done easily by including thiourea in the synthesis.[460] For the introduction of other dopants, additives such as B_2O_3, $NaBH_4$, or oxalic acids can be introduced into the synthesis.[199,454,458] Metal cations, such as Fe^{3+}, K^+, and Cu^+ were shown to act as active adsorption sites,[401,448,449] whereas non-metal doping mainly results in an altered band structure that can improve charge separation and narrows the band gap.[458] The most efficient strategy for improved performance in the photocatalytic NRR is the introduction of nitrogen vacancies (V_N) into the structure.[143,163,169,174,220,440,461,462] These vacancies are of similar size as nitrogen in N_2, thus presumably acting as very efficient adsorption and activation sites (**Figure 19**).[176,463,464] It is generally agreed that the NRR over V_N-rich C_3N_4 proceeds *via* a Mars-van-Krevelen mechanism.[383] There are different strategies to introduce vacancies. Some rely on the post-synthetic treatment of C_3N_4, *e.g.* by KOH,[169] HCl,[462] or either direct, or post-synthetic calcination in an N_2 or H_2 atmosphere.[166,465–467] These approaches etch nitrogen out of the structure. Other synthesis strategies directly employ KOH in the synthesis, yielding a K^+-intercalated, V_N-rich C_3N_4. NH_3 production rates of up to 3632 µmol g^{-1}h^{-1} were reported for such systems.[169] Cyano,[383,463,468] or cyanimide groups at the vacancies were found to play an important role in the enhanced ammonia generation.[469]
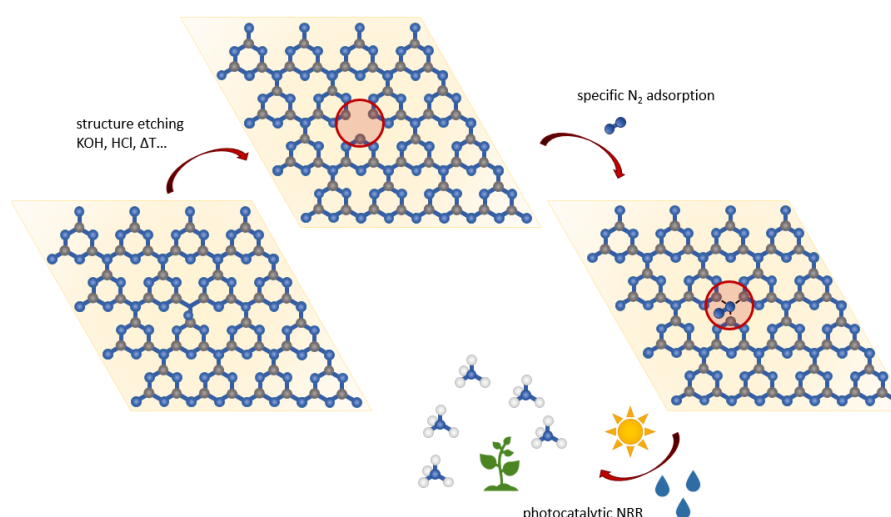
Figure 19 The principle of specific nitrogen adsorption and activation during photocatalytic nitrogen reduction over vacancy-rich g-C_3N_4. The general principle is also working for other carbon nitride structure models, such as melon or poly(heptazine).

A problem connected to NRR over nitrides is the presence of nitrogen in the structure and arising questions about the source of the nitrogen in NH_3. This is even worsened by discontinuities in reported photocatalytic systems – such as light source and reactor geometry[470] - difficulties in accurate ammonia

quantification due to generally low yields and the interference of sacrificial agents or additional ions with the testing methods for NH_4^+.[110,471,472] Additionally, adventitious NH_3 sources may falsify the results.[473] These issues are increasingly topic of debate in electrocatalytic NRR,[474,475] but still frequently ignored in photocatalytic NRR, preventing a comparison between different works and resulting in doubts about the accuracy of published results. This is changing currently, with a series of control experiments being more and more often demanded nowadays.[476]

An alternative to nitrogen fixation *via* reduction of N_2 is the oxidation to nitrates that can subsequently be employed for the synthesis of HNO_3.[396,477,478] Similar systems – often based on TiO_2 – can alternatively be used for the reduction of nitrate – either to NH_3 or to N_2.[479–484] Notably, the systems of metal loaded TiO_2 are essentially the same as commonly applied for the NRR to ammonia,[392,485] and also for the reverse reaction, *i.e.* the oxidation of NH_3,[486,487] elucidating how multiple reactions can occur simultaneously on one photocatalyst, which seriously impedes the product selectivity.

2.2 Sustainable Electrocatalysis
2.2.1 General Aspects

In contrast to photocatalysis, the electrocatalyst is not harvesting the required energy for driving a target reaction by itself, but instead the energy has to be applied externally in form of an electric potential. The external energy supply generally increases the number of materials that can be used as a catalyst. However, the adsorption, activation of reactants, and desorption of products strongly depend on the electrode material. In the case of water electrolysis – probably the most prominent electrocatalytic reaction – the required potential is 1.23 V, as discussed earlier. However, the presence of reaction barriers, slow mass transfer, and slow reaction kinetics lead to the need of applied overpotentials, which is why in practice much higher voltages (typically around $1.6 - 1.8$ V) are needed.[46,488] The interaction between the catalyst material and the educt *via* adsorption and activation at the surface can hereby significantly reduce the overpotential for a reaction and depends on the bonding strength of reaction intermediates.[46] This in turn results in an increase in the efficiency and a decrease in the wasted energy. Thus, both selectivity and activity are influenced by the choice of material.[489]
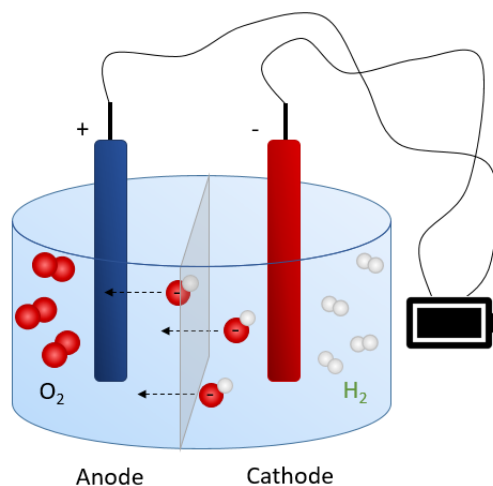
Figure 20 Schematic representation of water electrolysis with two compartments separated by an ion-exchange membrane.

The electrocatalyst comprises the working electrode in an electrochemical cell, *i.e.* the electrode at which the desired reaction is taking place. The reduction reaction proceeds at the cathode, while at the same time oxidation reactions occur at the anode. Commonly, a standard counter electrode is employed and only one reaction is analysed, so both oxidation and reduction reaction can be optimised separately.[46] The surface area of the counter electrode should be larger than that of the working electrode, to avoid kinetic limitations at the side that is not the focus of the experiment. Full cell setups can also be developed, wherein both anode and cathode are comprised of a designed material to effectively catalyse and optimise both half reactions in *e.g.* overall water splitting (**Figure 20**).

Candidates for electrocatalysts are therefore characterised by properties that effect the efficiency of the target reaction. This is on the one hand the charge transfer resistance and thus conductivity of the material, but also the kinetics of activation and conversion processes on the surface. The most important characteristics for the evaluation of the performance of an electrocatalyst are the overpotential η, the onset potential, and the faradaic efficiency (FE). The first two are measures for the activity and energy efficiency, whereas the third describes the selectivity by putting the total current in relation to the product yield.[31,46,488] The overpotential is reported at a certain current density, commonly 10 mA cm^{-2}.[31,46]

The overpotential can be calculated as the difference between the applied potential ($E_{applied}$), the theoretically required potential (E_0), and the current drop over the electrolyte and wires (iR), according to equation 13:[31]

$$\eta = E_{applied} - E_0 - \text{iR} \qquad (13)$$

Since the loading of active mass per surface area can differ significantly, it can make sense to normalise the activity to the mass loading. Additionally, the surface area is an important parameter, as it correlates with the abundancy of adsorption and activation sites. Therefore, normalisation to the Brunauer-Emmett-Teller (BET) or more accurately the electrochemical active surface area (ECSA) can help in the evaluation of the activity and reduce the influence of different mass loadings.[31,46,490] If possible, the turnover frequency (TOF), *i.e.* the amount of product per time and number of surface sites can be calculated for further characterisation of the activity.[31] Electrochemical impedance spectroscopy (EIS) is another powerful tool in the evaluation of electrocatalyst materials, as it can give insights into the charge transfer resistance, but also the ECSA.[46,491]

The simplest electrocatalysts are metals, which can be highly active in some reactions, *e.g.* in hydrogen evolution. Often noble metals are employed, though, which increases the material costs and is the reason for the development of more sophisticated and abundant alternatives. Key requirements for suitable electrocatalysts are thereby good activity and low overpotential, a large number of active sites, good long-term stability, high conductivity, and effective mass transfer properties.[46,492]

2.2.2 Water Electrolysis

In water electrolysis, water or OH^- is oxidised to O_2 at the anode, while at the same time protons are reduced to H_2 at the cathode. If the electric energy can be generated from renewable sources, it is a sustainable alternative way for the industrial production of H_2. Up to date, mostly noble metal catalysts are employed. In combination with non-ideal efficiencies this results in production costs that cannot compete with the price for H_2 generated *via* conventional steam reforming.[492] For the HER, Pt-group metals are the most employed catalysts, whereas Ir- and Ru-oxides are used for the OER.[493] The reason for the high activity of these materials lies in their specific interaction with the educts and/or reaction intermediates. Thus, the metal-H bond strength plays a decisive role in the activity of a metal for the HER. A volcano-type relationship between the logarithm of the exchange current density and the M-H bond strength has been observed, with Pt located close to the top of the volcano plot (**Figure 21**).[494,495] Additionally, noble metals such as Pt have the advantage of chemical inertness and high electronic conductivity.[489]

Hydrogen evolution proceeds on a catalyst surface *via* adsorbed H-species. The first step is therefore the adsorption and reduction of protons (or water, depending on the reaction pH) to form $M\text{-}H_{ad}$ species (Volmer reaction – eq. 14). In a second step, formation of H_2 can either occur *via* electrochemical desorption (Heyrovsky reaction – eq. 15), wherein the $M\text{-}H_{ad}$ species reacts with another proton/ water to H_2 involving electron transfer, or H_2 can be formed upon combination and chemical desorption of two H-adatoms (Tafel reaction – eq. 16).[31,496,497]

$$H^+ + M + e^- \rightarrow MH_{ad} \text{ (acidic)} \quad \text{or} \quad H_2O + M + e^- \rightarrow MH_{ad} + OH^- \text{ (alkaline)} \quad (14)$$

$$MH_{ad} + H^+ + e^- \rightarrow M + H_2 \text{ (acidic)} \quad \text{or} \quad MH_{ad} + H_2O + e^- \rightarrow M + OH^- + H_2 \text{ (alkaline)} \quad (15)$$

$$2\,MH_{ad} \rightarrow 2\,M + H_2 \quad (16)$$
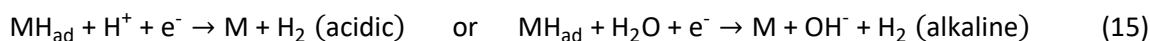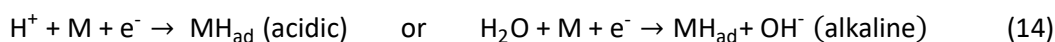
Research on the development of earth-abundant catalysts is often focussed on HER in alkaline media, because these are the reaction conditions commonly required for the OER.[498] Compared to HER in an acidic environment, the formation of H-adatoms is hindered, because it requires the adsorption and dissociation of water molecules. The activity is hence largely dependent on water adsorption and activation, in combination with the $M\text{-}H_{ad}$ binding energy and OH^- adsorption.[31] In neutral electrolytes, the mechanism is even more complicated, due to the low concentration of H_3O^+-ions that leads to pH gradients and diffusion limitations and insufficient Nernst potential to provide the thermodynamic driving force for direct H_2O dissociation.[497]
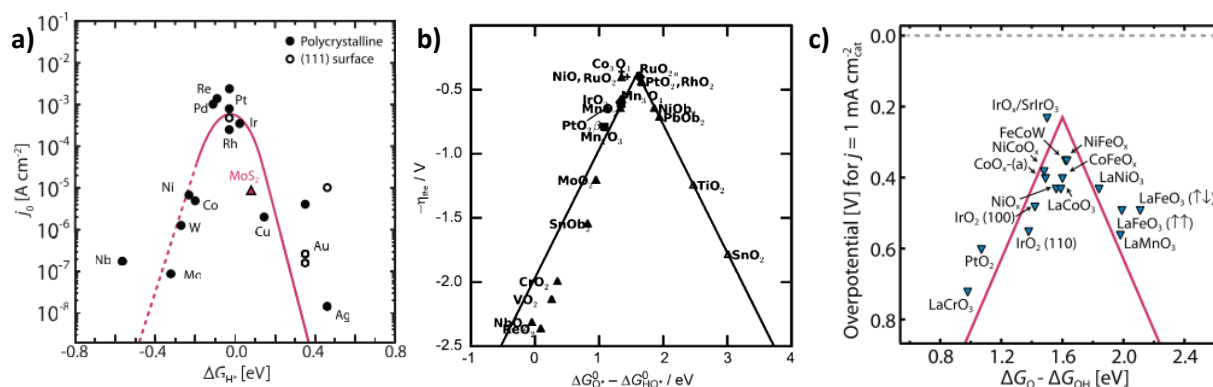
Figure 21 Volcano plots for HER metal catalysts (a), as well as several binary oxides at 10 mA cm^{-2} (b), and ternary oxide catalysts at 1 mA cm^{-2} employed in the OER (c). (a) and (c) reprinted from *She et al.* with permission from AAAS,[28] (b) used with permission from Wiley.[500]

The oxygen evolution reaction is usually the more hindered one due to the required four electron transfer. Furthermore, the mechanism is more complex and differs between material classes and even between catalysts of the same material but with different morphologies.[496] Adsorbed surface M-OH and M-O species are generally important intermediates, though. Desorptive formation of O_2 might again proceed either *via* the coupling of two O_{ad}-species, or *via* reaction of one O_{ad} and OH^-.[488] Depending on the mechanism, peroxide M-OOH species might be formed as additional intermediates.[31] As in the NRR, the bonding strength of the intermediates to the catalyst are correlated – thus there is always an overpotential in practice.[46,121,182,183,499] Based on that, a volcano-relationship between the overpotential and the transition enthalpy of the oxide catalyst (as related measure for oxygen binding energies) can be drawn again.[496] More recently, DFT calculations were used to directly evaluate surface binding energies and their influence on the activity. They revealed a constant energy difference of 3.2 eV for M-OH and M-OOH bond strength, which is why differences between oxide catalysts are based on different O adsorption energies.[499,500] These scaling relationships severely limit the options of reducing the overpotential. A different approach therefore involves lattice-oxygen that can mediate the OER by reacting with adsorbed *O species to O_2. The formed oxygen vacancies can then be refilled by OH^- in the electrolyte.[501]

Tafel analysis can help in the identification of reaction mechanisms and of the intrinsic activity. It relates the overpotential to the logarithmic current density and thus the rate of the reaction. The slope of the obtained plot can be a measure for the reaction kinetics and identification of the rate determining step,[502] and the intercept with the x-axis gives the exchange current density j_0 – *i.e.* the reaction rate at $\eta = 0$. It is an approximation of the Butler-Volmer equation and based on various assumptions, such as no contributions from mass transfer limitations, no interference of adsorbates, and a potential independent reaction mechanism.[488] In praxis, these assumptions are not necessarily fulfilled. Therefore, Tafel analysis should be performed with care and caution must be taken in the interpretation. Still, some insights can be gained from Tafel plots. On the one hand, a Tafel slope of ~120 mV/dec for the OER can be an indication of the Volmer step being the rate determining one, whereas a smaller slope of around 30-40 mV/dec is a suggestion of desorption being the rate determining step.[488,489] Generally, a low Tafel slope signifies a smaller increase in the overpotential and thus faster electron transfer kinetics. The exchange current density should on the other hand be high for fast reaction rates at the electrode.[31]

The Tafel equation is given as:[31,489]
$$|\eta| = a + b \ln j = 2.3 \frac{RT}{\alpha nF} \log(j/j_0) \tag{17}$$

with the Tafel slope *b*, the current density *j*, the universal gas constant *R*, the Faraday constant *F*, the temperature *T*, the anodic charge transfer coefficient α (around 0.5 for the simplest case), and the number of transferred electrons *n*.[31,489]

In order to decrease the production costs, highly active earth-abundant catalysts are desirable.[489,493] For the HER, transition metal sulphides,[503,504] carbides and phosphides have shown promise,[505–507] while oxides are potential OER catalysts.[488,508] More recently, sulphides have emerged as highly efficient electrocatalysts for the OER as well. Under operating conditions they are usually transformed into metal (oxy)-hydroxides, that are, however, often more active than their oxide-derived counterparts.[509,510] For the HER, Ni-based catalysts, such as Ni phosphides,[507] or Ni sulphides have shown promise.[511,512] Additionally, some of the highest activities have been observed for MoS_2, after it was discovered that preferential exposure of active edge sites could dramatically enhance the

activity.[513–516] Other prominent transition metal electrocatalyst are phosphides, such as CoP,[517] or WS$_2$.[518]

For the OER, some of the most active class of transition metal electrocatalysts comprise cobalt oxides, hydroxides and oxyhydroxides,[280,519,520] but also ternary oxides such as CoFe$_2$O$_4$,[521] MCo$_2$O$_4$ (M designating a variety of metal 2+-cations),[522,523] or LiCoO$_2$.[524] A major reason for that is the high redox-activity of cobalt and transition between the oxidation states +II, +III and +IV.[502] The use of cobalt as a replacement for noble metal catalyst is not without problems, though. Several cobalt compounds are hazardous, the natural abundance of Co is locally restricted, the mining of the respective ores often happens under questionable circumstances in politically unstable regions, and the Co price is a consequently comparatively high and liable to severe market fluctuations. This is why battery research aims at a reduction of Co in the active electrode material,[525] and a good reason not to implement Co in industrial water electrolysis. In this regard, manganese oxides, as well as nickel- or iron- based materials are more desirable electrocatalysts.[46,526–530] Apart from materials only containing either of the two metals, Ni-Fe oxides, (oxy)-hydroxides, layered double hydroxides (LDHs) and sulphides have emerged as outstanding OER electrocatalysts.[279,531–536] A synergy has been found between Ni and Fe that promotes the activity.[282]

Some earth-abundant bifunctional materials that can catalyse both HER and OER are also developed. These are predominantly based on Co, Ni, and Fe and have the advantage of simplifying the system and avoiding discrepancies in the operation conditions of HER and OER catalyst (*e.g.* the pH).[496] One of the most important bifunctional electrocatalysts for water splitting is likely based on Co phosphide. The Co-catalysts can be electrodeposited directly from phosphate buffer and consist of metallic Co and Co phosphide or Co oxo/hydroxo-phosphate for the reduction site and amorphous Co oxide on the oxidation site.[537–539] Furthermore, Ni phosphides and sulphides or Ni-Fe LDHs are important earth-abundant, bifunctional electrocatalysts.[540–542]

An alternative strategy for the reduction of material cost is the transition from bulk metal catalysts to nano-sized ones with a high active surface area in contact with the reaction medium. The reduction in size can however have a negative effect on the stability and might exhibit a different activity than the bulk material.[543] Another challenge in the design of systems for industrial water electrolysis is the high throughput required for large scale H$_2$ production and thus the operation at high current densities. Overpotentials scale differently with the current density for different materials and some noble metal catalysts become a lot less efficient at high current densities. This increases the interest in the development of earth-abundant alternatives.[31] For industrial purposes, the separation of evolving H$_2$ and O$_2$ gasses is furthermore an important factor to be considered in the system design.[544]

Up to date, mainly post-catalytic characterisation and an evaluation of the electrochemical data are used to formulate a mechanism of the occurring reactions at the electrodes. In many cases it was found that the as-prepared catalyst changes substantially during the experiment.[545] However, while such *ex-situ* characterisation enables the discovery of material changes, they do not necessarily unveil the actual active species formed under operating conditions, nor do they allow for the tracking of reaction intermediates. In the case of oxides for the OER, it was thus found that most oxides are not thermodynamically stable under the employed potential and the active species is in many cases composed (oxy)hydroxides.[546] Therefore, further *operando* experiments are required to elucidate the real reaction mechanisms and enable the rational design of new catalysts.[547,548]

2.2.3 CO$_2$ Reduction

CO$_2$ is the most important greenhouse gas, not due to the strength of the greenhouse gas effect of one molecule, which is far lower compared to *e.g.* methane, but due to the excessive human-caused emissions, its resulting abundance in the atmosphere, and its long lifetime there.[549] The extraction of CO$_2$ from industrial emission gases and the capture of atmospheric CO$_2$ have been investigated in the past decades in order to decrease the CO$_2$ concentration in the atmosphere and thus mitigate effects of global warming.[19,550,551] The captured CO$_2$ can be stored, however, large scale storage underground or at a substantial depth in the oceans also includes risks and challenges, mainly involving concerns about leakages.[552] An alternative pathway could be the conversion of CO$_2$ to fuels and carbon feedstock for industrial processes in a closed carbon cycle.[550] Approaches towards CO$_2$ utilisation include thermal catalysis to fuels and chemicals, especially formic acid, the synthesis of polymers or urea, as well as the use in the food industry.[553]

Electrochemical CO$_2$ reduction is especially promising, since electricity generated from renewable sources can be used for the synthesis of fuels and carbon-based high-value chemicals under ambient conditions.[39,41,554–556] This process is challenging, though, and the efficiency and selectivity of current electrocatalysts limited.[555] As in nitrogen reduction this is due to the inert nature of the C=O bonds, the competitive HER in aqueous media, the low solubility of CO$_2$ in water, and the necessity for multiple electron and proton transfer steps, all of which severely hamper the reaction kinetics (equations 18 - 25).[39,557–559] The first electron transfer is the most energy intensive step resulting in a high activation barrier. Proton-coupled electron transfer steps on the other hand are much more feasible. Still, overpotentials are usually sufficiently high for the competitive HER to become a significant problem.[554] This is partly due to a conformity change from linear to bend connected to the first reduction step. Adsorption and activation are therefore the most critical steps in CO$_2$-reduction.[557] Several different products can be obtained *via* the reduction of CO$_2$ in aqueous electrolytes, the most common of which include **CO**, **CH$_4$**, **CH$_3$OH**, **formic acid** and **formaldehyde**.[560] For selected catalysts higher carbon products (C$_{2+}$) can also be obtained. Such a wide range of possible products that require a similar energy input severely challenges the selectivity of the reaction.[558]

$$CO_2 + e^- \rightarrow CO_2^{\cdot-} \qquad\qquad E_{RHE} = -1.49 \text{ V} \qquad (18)$$

$$CO_2 + 2\,e^- + 2\,H^+ \rightarrow \textbf{CO}_{(g)} + H_2O \qquad\qquad E_{RHE} = -0.10 \text{ V} \qquad (19)$$

$$CO_2 + 2\,e^- + 2\,H^+ \rightarrow \textbf{HCOOH}_{(aq)} \qquad\qquad E_{RHE} = -0.12 \text{ V} \qquad (20)$$

$$CO_2 + 4\,e^- + 4\,H^+ \rightarrow \textbf{HCHO} + H_2O \qquad\qquad E_{RHE} = -0.07 \text{ V} \qquad (21)$$

$$CO_2 + 6\,e^- + 6\,H^+ \rightarrow \textbf{CH}_3\textbf{OH}_{(aq)} + H_2O \qquad\qquad E_{RHE} = -0.03 \text{ V} \qquad (22)$$

$$CO_2 + 8\,e^- + 8\,H^+ \rightarrow \textbf{CH}_{4(g)} + H_2O \qquad\qquad E_{RHE} = +0.17 \text{ V} \qquad (23)$$

$$CO_2 + 12\,e^- + 12\,H^+ \rightarrow \textbf{C}_2\textbf{H}_{4(g)} + 4\,H_2O \qquad\qquad E_{RHE} = -0.08 \text{ V} \qquad (24)$$

$$2\,H^+ + 2\,e^- \rightarrow \textbf{H}_2 \qquad\qquad E_{RHE} = 0 \text{ V} \qquad (25)$$

Which of the products is favoured not only depends on the applied potential, but also largely on the catalyst itself.[560] Metal electrodes are often employed due to the simplicity of the system and their robustness. Empty *d*-orbitals can assist in the coordination and activation of CO_2.[559] Metals can be divided into four different groups based on the preferentially formed product (**Figure 22**).[39,560] The first group is formed by amongst others Hg, Pb, In, Bi, Tl, and Cd. CO_2 does not coordinate to these metals and formic acid is obtained as the main product. These metals also have a high overpotential for the HER. The second group consists of Ag, Au, and Zn that produce CO as the main product and trace amounts of formic acid.[41] So far, CO and formate are the only products that can be produced selectivity. CO hereby offers the additional advantage of easy separation owing to its gaseous nature. Since overpotentials for HER are lower compared to metals of group one, it can be aimed to directly synthesise a gas mixture of targeted CO/H_2 ratios that can be fed into the Fischer-Tropsch process.[41]
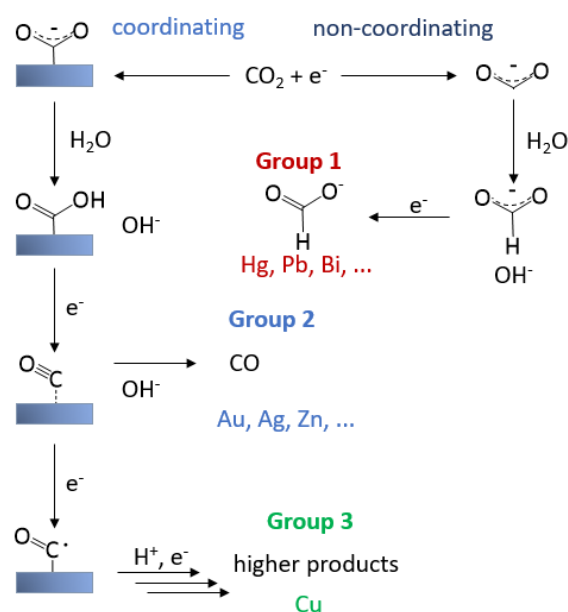
Figure 22 Division of metal electrode material into three groups based on the yielded product. Reproduced with permission from Wiley.[41]

The third group only includes Cu, which is special in that it yields methane but also higher C_{2+}-products, such as C_2H_4, C_2H_2, or alcohols, since surface-bound CO can directly be hydrogenated.[559] This is generally advantageous, as it directly produces valuable products. However, activity and selectivity are usually rather low, since the yield of C_1 products is more favourable. For Ni, Pt, Fe, Al, or Ga, which comprise a fourth group the HER becomes the dominant reduction reaction.[554,559] The differences in the product selectivity between group two metal surfaces and Cu is predominantly determined by the binding energy of the CO-intermediate, which is stronger for Cu compared to Au or Ag.[561] For materials that bind intermediates too strongly, desorption is hindered and the active sites are blocked, resulting in catalyst poisoning and performance degradation.[562] The binding energy thereby not only depends on the bulk metal, but is also influenced by the surface morphology and exposed crystal facets.[558] In addition to CO binding, the binding energy of carbon intermediates, of protons and of oxygen species can all affect the product distribution.[563] These findings are an indication that in principal product selectivity can be steered by engineering the catalyst surface towards an ideal CO binding energy.

Due to the competitive HER, electrode materials are often chosen based on their overpotential for the HER instead of primarily focussing on the CO_2-reduction abilities. Here Sn, Bi, or Pb are promising candidates.[41]

The selectivity can further be influenced by the reaction environment, *e.g.* the electrolyte, the pH, or the supply with CO_2.[39,564] Electrochemical CO_2RR is commonly performed in a two-compartment cell, with water oxidation proceeding in the counter-electrode compartment. Saturation with CO_2 precedes the reaction.[556] The alkali cation in the electrolyte can have a significant impact on the activity and selectivity in CO_2 reduction. The presence of larger cations in the CO_2RR over Cu was found to increase the selectivity towards C_{2+}-product formation.[565,566] The degree of cation adsorption at the surface was suggested to be the cause for such effects.[566] Alternatively, the hydrolysis of cations was argued to be the dominant factor in altering product selectivities.[567] Thus, the actual reason for the cation effect is thus not fully uncovered yet. The anion can additionally have an effect. Frequently $NaHCO_3$[568] or $KHCO_3$[565] electrolytes at neutral or near neutral pH are used. In contrast to most other anions, bicarbonate acts as a buffer, to prevent the formation of pH gradients. Such gradients might be formed due to the consumption of significant numbers of protons at high current densities, especially for a catalyst with a high surface area. Additionally, the buffer anion might act as a proton donor.[39] The pH not only determines the availability of protons, but also affects the supply of CO_2 to the electrode, since it influence the equilibrium between dissolved CO_2 and carbonate species.[41,569] Furthermore, apart from electrolyte ions, additives can influence the selectivity by changing the balance of CO_2 and water at the interface, in addition to influencing the CO binding configuration.[570,571]

To increase the concentration of CO_2 in the aqueous electrolyte, high pressure setups have been examined. That way far higher current densities and efficiencies could be achieved. The pressure can moreover affect the product distribution.[572] The solubility can alternatively be improved by use of non-aqueous solvents, however, water should still be present, to obtain the desired products.[41] Ionic liquids can also be used, offering the advantage of higher CO_2 solubilities and lower overpotentials. However, they come with a higher cost and lower stability in the presence of water.[556]

Extensive research focusses on the use of Cu electrodes, since they pave the way for the synthesis of more valuable C_{2+}-products.[573–575] Compared to CO or HCOOH formation, the reduction mechanism towards C_{2+}-products is highly complex and still under debate.[558] In order to improve the activity and the selectivity, nanostructuring is a prominent approach, since more active surface states can be introduced this way and the binding energy for intermediates – and thus the product selectivity – can be influenced.[558,576–578] Another important factor is the surface coverage with C_1 intermediates available for coupling reactions, which might likewise be tailored through morphological and compositional engineering.[558] Examples for compositional engineering hereby include surface alloying or doping,[579,580] as well as the introduction of defects.[578]

Another strategy employs copper oxides as precursor materials for the electrode formation.[581] A topic of extensive debate is thereby the role of surface oxygen species and defects. There is a general consent that the precursor and thus the history of copper electrodes has a significant impact on the activity. Thus, oxide derived Cu electrodes are more active and more selective towards C_{2+}-products compared to non-oxide derived ones.[565,581,582] Sub-surface oxygen is proposed to be crucial in the activity enhancement[583] – a suggestion that has been refuted by others that elucidate the rapid consumption of oxide-species at the highly reducing potentials required for the CO_2-reduction reaction (CO_2RR).[584–586] Additional factors that might contribute to an increased activity of oxide derived

catalysts are the presence of undercoordinated Cu-species, as well as the presence of Cu in mixed oxidation states.[581,587]

Non-metal electrocatalysts have also been employed in the last decades. Important examples include heteroatomic carbon materials,[588–590] carbon nanotube supported transition metals,[591] ternary oxides,[592] as well as 2D materials such as MoS_2.[593,594] As in water electrolysis or nitrogen reduction, other transition metal sulphides have emerged as earth abundant alternatives to metal catalysts due to their high conductivity. Thus, nickel iron sulphides have shown promise in an efficient, solvent dependent CO_2 reduction.[595,596]

A serious problem that yet needs to be solved is the oftentimes low stability of CO_2 reduction catalysts due to poisoning by strongly bound intermediates, the formation of carbon layers, or morphological changes.[41,597] Additionally, the character of the active sites, as well as the reaction pathways and intermediates – especially for C_{2+}-product formation – are often still not well understood. *Operando* and *in-situ* studies have emerged recently to resolve these problems and shed light on underlying mechanisms.[555,598]

2.3 3*d* Transition Metal Chalcogenides
2.3.1 Spinel Oxides

Spinels are transition metal compounds of the general formula AB_2X_4. A and B represent metal ions, whereas X denotes the anion, which is usually a chalcogenide, but a few spinels with fluorine, nitrogen, or cyanide anions were also reported.[599] The structure is cubic, with the space group $Fd\bar{3}m$, or in selected cases $F\bar{4}3m$. The structure type is derived from the gemstone $MgAl_2O_4$. The A-ions are usually in the oxidation state +II, whereas the B-ions occur in the oxidation state +III.[599,600] A and B-ions can thereby be of the same element, as *e.g.* in magnetite, Fe_3O_4, or of different elements.[599] In selected cases, the A-ion can also occur in the state of +I. Here, charge neutrality is achieved with B-ions in the oxidation state of +IV. A prominent example is $LiMn_2O_4$ (LMO), which is an important candidate as a cathode material for Li-ion batteries.[601,602] The anion is most often oxygen, but natural thiospinels are also known, such as *e.g.* violarite, Ni_2FeS_4.[603,604]

In a normal spinel structure, the anions form a cubic close-packed lattice and the A-ions occupy 1/8th of the tetrahedral sites, whereas the B-ions occupy ½ of the octahedral sites.[605] Neighbouring octahedra are edge sharing, whereas octahedra and tetrahedra are connected at the corners (**Figure 23**).

The cation site distribution can deviate from this configuration and reach full inversion: In that case the A-ions occupy 1/4th of the octahedral sites and the B-ions occupy 1/8th of the tetrahedral site and another 1/4th of the octahedral sites. The degree of inversion is expressed by the inversion parameter λ, with $\lambda = 0$ for a normal spinel structure and $\lambda = 1$ for a completely inverted one. The degree of inversion depends on the metal cations – more specifically on the ionic radius, electrostatic charge compensation, the spin state (high-spin or low-spin), and on the difference in the sum of the crystal field stabilisation energies (CFSE) for cations in a tetrahedral (T_d) and octahedral (O_h) coordination (Figure 23).[600,606,607] Thus, small ions generally favour the smaller tetrahedral sites, whereas larger ions favour octahedral sites.[607] Electrostatic stabilisation on the other hand favours an octahedral

coordination of the M^{3+}-ion for better local charge compensation.[600] The CFSE depends mostly on the number and distribution of *d*-electrons (since oxygen is a weak field ligand, high spin (HS) configuration is assumed) and can be approximated as:[600,608–610]

$$\text{CFSE}_{O_h} = \left[4\,Dq \cdot n_{e_g\text{-electrons}} - 6\,Dq \cdot n_{t_{2g}\text{-electrons}}\right] = x\,Dq = x\,\Delta_O \tag{26}$$

$$\text{CFSE}_{T_d} = \left[6\,Dq \cdot n_{e_g\text{-electrons}} - 4\,Dq \cdot n_{t_{2g}\text{-electrons}}\right] = y\,Dq = y\,\Delta_T = y \cdot \frac{4}{9}\Delta_O \tag{27}$$

The e_g-orbitals hereby represent the *d*-orbitals whose energy is lowered due to the coordination by the anions, while t_{2g}-orbitals comprise those whose energy is increased compared to a non-coordinated ion (Figure 23 b).[609] *Dq* represents the crystal field parameter, a relative unit of energy.[611] These calculations neglect, in a first approximation, electron pairing energies.[612] From the energy difference of an ion in octahedral and in tetrahedral coordination, the octahedral site preference can be calculated.[608,609] Alternatively, the CFSE can be calculated for the A- and B-ion on both tetrahedral and octahedral site, respectively and the sum for normal and inverse spinel structure can be obtained as:

$$\text{Normal:} \quad \text{CSFE} = \text{CSFE}_{T_d}(A) + 2 \cdot \text{CSFE}_{O_h}(B) \tag{28}$$

$$\text{Inverse:} \quad \text{CSFE} = \text{CSFE}_{T_d}(B) + \text{CSFE}_{O_h}(B) + \text{CSFE}_{O_h}(A) \tag{29}$$

The structure with the larger CSFE is the thermodynamically more stable one.[608,612]
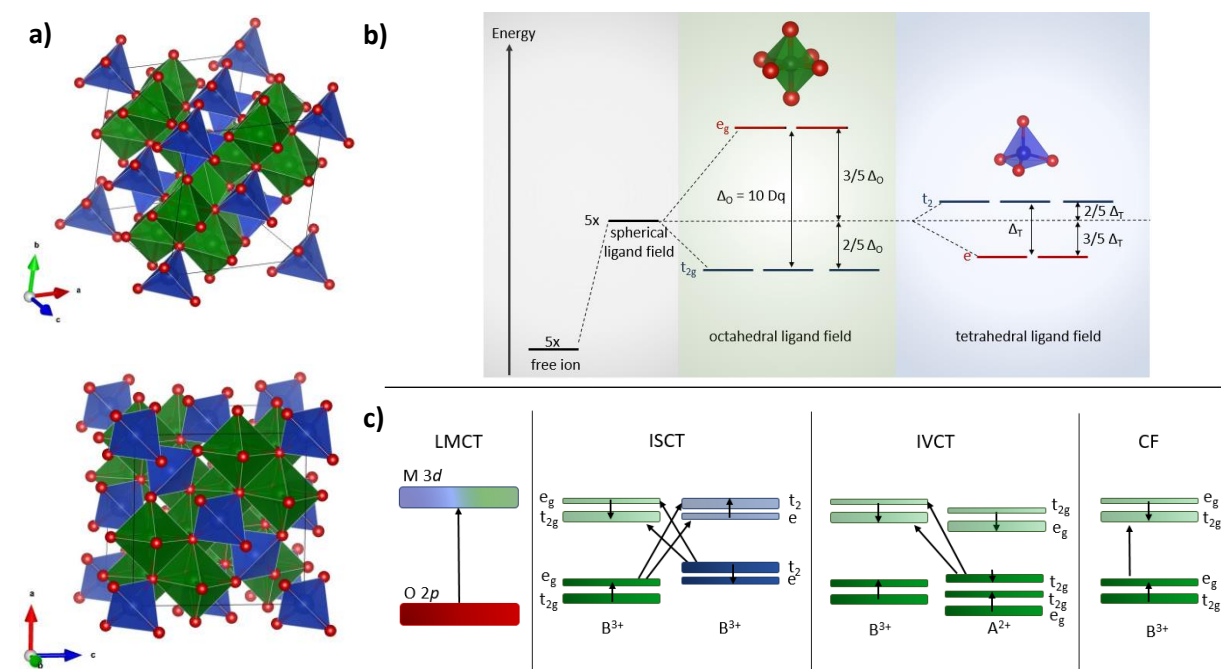
Figure 23 Structure of a normal spinel (a), with the A ion depicted in blue, the B ion in green, and oxygen in red, together with crystal field splitting in octahedral and tetrahedral coordination (b). Optical transition in spinel oxides are depicted in (c) in a permitted adaptation of reference [606]. Transitions in octahedral sites are depicted in green, those involving tetrahedral sites in blue.

Often, different factors (*e.g.* size compared to CSFE) favour a different cation distribution – as is the case for Fe^{3+}.[606] Such considerations only reflect the thermodynamically most stable cation distribution. Often, the structure is, however, predominantly determined by kinetic influences. Thus,

the synthesis conditions can have a huge effect on the degree of inversion obtained.[613] At high synthesis temperatures, entropic contributions that favour a higher degree of inversion and thus more disordered cation distributions, come increasingly into play.[605]

Correlated to their structure, spinels have interesting optical and magnetic properties. Metal cations in tetrahedral and octahedral sites are bridged by oxygen atoms at high angles, resulting in strong antiferromagnetic coupling *via* superexchange dominating the overall magnetic properties. Octahedrally coordinated B-ions are ferromagnetically aligned to each other, albeit at a significantly lower magnitude due to the angle of interaction being close to 90 °. The same holds true for A-ions. Since oxygen is a low-field ligand, transition metals are usually in high-spin configuration, which results in large individual magnetic moments. In total, spinels are most often ferrimagnetic, since the number of occupied octahedral and tetrahedral sites is not equal. Neither are the magnetic moments of the A and B-ions, with the degree of inversion additionally influencing the magnetic properties to a significant extent.[599,606,607] Among spinel oxides, metal ferrites are of special interest due to their magnetic properties based on the high magnetic moment of Fe^{3+} in HS configuration, but also due to the non-toxicity and abundancy of iron, which makes it readily available at low cost.[606]

The degree of inversion additionally influences the optical and the electronic properties of spinel oxides.[606,614] Depending on the coordination environment and thus different crystal-field splitting of *d*-orbital energies, different *d*-sub-bands are formed for the constituent ions.[114] A change in the degree of inversion results in variations in the energy of bands derived from M^{2+} and M^{3+} *d*-orbitals, respectively, and consequently their contributions to the formed valence and conduction band.[606,615] This will in turn alter the band gap and the band potentials alike. Additionally, the optical properties are more complex than simple valence band maximum to conduction band minimum transitions. Ligand to metal charge-transfer transitions (LMCT) from oxygen to *d*-orbitals of either A- or B-ions represent one type of present transition. Others include transitions between 3*d* bands of ions of the same character but located at different sites (inter-sublattice transfer between T_d and O_h - ISCT), between M^{2+} and M^{3+} 3*d* bands (inter-valent charge-transfer - IVCT), or between e_g and t_{2g} orbitals of ions on the same site (crystal field transitions - CF). The latter require only small excitation energies (usually NIR), whereas the former three commonly fall into the visible light and UV range (**Figure 23**). *d-d* transitions are usually of low intensity because they are parity and possibly also spin forbidden.[606,616–618] Generally, only transitions with spin conservation, and, according to the Laporte rule, only transitions with a change in parity, *i.e.* g (gerade) → u (ungerade) or u → g are allowed. For spinels with a completely normal structure, *i.e.* no Fe^{3+} ions at tetrahedral sites, ISCT between 3*d* orbitals of Fe at octahedral and at tetrahedral sites, respectively, is not possible. Neither is IVCT in one sublattice. In addition to that, if no partially filled *d*-orbitals are present in the M^{2+}-ion (as for Mg^{2+} and Zn^{2+}), no ISCT and IVCT between M^{2+} and Fe^{2+} *d*-orbitals can occur. Therefore, the contributions of different optical transitions to the absorption spectrum vary with respect to the employed M^{2+} ion and with the degree of inversion. Since localised *d-d* transitions determine the absorption spectra of spinel ferrites, they do not necessarily correlate with the electronic band gap.[263,619,620]

Spinel oxides are most commonly prepared *via* co-precipitation,[621–624] solvothermal synthesis,[625–629] or solid-state reaction.[630–632] While well established, theses syntheses approaches suffer from fast reaction kinetics in an aqueous environment that are hard to control,[633] residual stabilising agents, as in the case of co-precipitation,[628] or they require long reaction times at elevated temperatures (solid-state).[630,632,634] Even if the initial synthesis temperature is relatively low, often an additional calcination step is required, that significantly increases the total time and energy input required.[607,623,635]

Additionally, a high annealing temperature leads to large crystallite sizes. This often results in low surface areas and thus low number of active sites, which is usually impedimental for catalytic applications that proceed on the particle surface.[593] Microwave-assisted solvothermal synthesis offers a feasible alternative for the preparation of directly crystalline binary and ternary oxides – amongst others spinel oxides.[636,637] In this approach, a very fast, highly homogenous heating of the solution results in the simultaneous formation of many crystallisation nuclei that grow largely independent of each other. The end-results are nanoparticles in often quite narrow size distributions (depending on the exact synthesis conditions, especially the solvent).[636] Aqueous microwave-assisted methods commonly using metal nitrates or chlorides have been reported for the preparation of various spinel oxides such as $CuFe_2O_4$, Co_3O_4, or $ZnAl_2O_4$.[638–640] An advantage of these water-based syntheses are the low cost of water, the lack of environmental issues connected with the solvent, and the comparatively low boiling point. The reaction is often sensitive to the pH value.[638] Reaction times can be very short (in the order of a few minutes) and reaction temperatures are often below 250 °C.[636,638]

Non-aqueous syntheses come with the drawbacks of higher solvent costs and higher boiling points. On the other hand, highly homogeneous solutions can be obtained and homogeneity is even ensured after the condensation to oxide nanoparticles starts due to stabilisation of the dispersion by the solvent.[641] The control over particle size, crystallinity, and morphology is also better, since the reaction rates are slower compared to those in water.[633] Ethylene glycol is a common solvent, often in combinations with water.[642] Similarly, triethylene glycol (TEG) has been used for the preparation of nanocrystalline spinel oxides.[637] Of special interest is the synthesis of metal oxides extensively explored by the group of Niederberger, which is based on the reaction of metal precursors with organic ligands, such as acetates, acetylacetonates, or alcoholates in high boiling solvents such as benzyl alcohol, benzylamine or 1-phenylethanol.[633,636,641,643] Herein, the solvent is actively participating in the reaction. In the case of acetylacetonates, the alcohol undergoes a nucleophilc attack on one carbonyl group of the ligand, which is followed by C-C cleavage in the ligand (**Scheme 2**). The formed ester is replaced by a second solvent molecule. In a subsequent aldol-like condensation, a C-C bond is formed between the second solvent molecule and the coordinating enolate that was left of the acetylacetonate ligand. Liberation of the formed ketone leaves a R_2M-OH species that will undergo subsequent condensation steps to the metal oxide.[633]
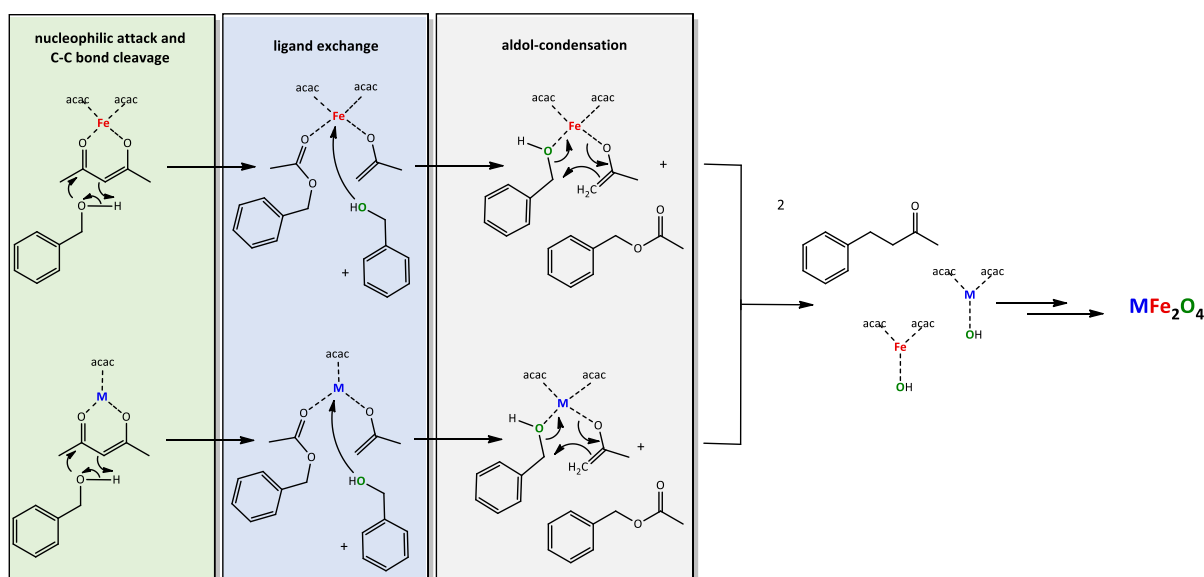
Scheme 2 Reaction of metal acetylacetonate precursors and an alcohol solvent in the microwave, as reported by the group of Niederberger.[633]

Redox reactions occur not only with the ligand and solvent, but to an extent also with the metal centres, which can lead to a partial reduction of the employed metal ions.[633] The formed nanocrystals commonly have organic residues adhering to the surface, even after post-synthetic washing steps. These might influence the material properties.[641] Various different spinel oxides can be synthesised in a non-aqueous microwave assisted approach, such as Fe_3O_4, $MgFe_2O_4$, $MnFe_2O_4$, $NiFe_2O_4$, or $ZnFe_2O_4$.[619,627,636,644,645] With adaptation of the employed solvent, other spinels can be obtained as well.[646]

Spinels find application in electrode materials, with $LiMn_2O_4$ (LMO) being the most important representative of the spinel family.[601,647] Important properties are hereby the stable cubic structure, as well as a good electron conductivity due to Mn^{3+}-Mn^{4+}-interactions, a high Li conductivity in a 3D network and a high operating voltage.[601,648,649] Additionally, their magnetic properties make them interesting for data storage devices.[650] Ferrites are of additional interest because of the combination of low toxicity and magnetic properties that makes them desirable candidates for biomedical applications.[651,652] Nowadays, especially iron, manganese, and cobalt based spinels are widely investigated for electrochemical OER and the oxygen reduction reaction (ORR).[607,653] Co_3O_4 and MCo_2O_4 are efficient catalysts for both ORR and OER.[522,523,654–656] However, more abundant ferrites have also shown a good activity. Thus, $NiFe_2O_4$ and $CoFe_2O_4$ are promising earth-abundant alternatives to IrO_2 or RuO_2.[534,657–661] In addition to the application in electrocatalysis, spinels are also investigated as photocatalysts.[619,662–667] The small band gaps of most spinel oxides between 1 and 3 eV make them suitable for visible light absorption. Additionally, their band positions are favourable for reduction reactions, oxidation reactions, or both.[267,667,668] The valence band is formed predominantly by oxygen $2p$ orbitals, whereas the conduction band is constituted from hybridised O $2p$ and Fe $3d$ orbitals, as shown for $ZnFe_2O_4$.[669] For spinels with partially filled d-orbitals, such as $NiFe_2O_4$, or $CoFe_2O_4$, M^{2+} states contribute to the valence band and can change the band structure depending on the degree of inversion.[670,671] Although the band gap and position are in theory ideal, the photocatalytic activity for spinel oxides is often rather low and restricted to oxidative decomposition. One reason for this observation is the fast charge carrier recombination and often low conductivity (although higher compared to single component oxides).[267,668] Another reason is the significant difference between the electronic and the optical band gap, due to high exciton binding energies.[620] Nevertheless, due to their desirable band gaps and band positions, spinels are especially interesting for photo-electrochemical applications.[263,267,269,668,672]

Most often, spinels with one M^{2+} and one M^{3+}-ion each are investigated, however, recently high-entropy oxides received considerable interest. In this context, spinel oxides containing 5 or more different cations – mainly transition metal ions – were synthesised and characterised mainly in regard of their magnetic properties and the performance in electrochemical OER.[673–676]

2.3.2 Binary and Ternary Iron Sulphides

Compared to oxides, sulphides have a significantly smaller band gap, since the valence band is formed mainly by sulphur $3p$ orbitals, that are located at a higher potential compared to oxygen $2p$ (**Figure 24**).[147] The conduction band is commonly constituted by transition metal s- and empty d-orbitals.[114,677] Depending on the number of d-electrons and occurrence in high-spin or low-spin configuration,

occupied *d*-orbitals contribute to the valence band edge, whereas unoccupied *d*-orbitals predominantly influence the conduction band potential for both oxides and sulphides. A higher density of *d*-states at the band edges results in a narrowing of the band gaps. The small band gap endows sulphides with very high, in some cases almost metallic conductivities – at least if partially filled *d*-orbitals are present.[114] The increased conductivity compared to their oxide counterparts makes them very interesting for electrochemical applications. Furthermore, the active centres of enzymes for nitrogen reduction, CO dehydrogenation and hydrogen evolution often contain sulphur, which makes sulphides ideal candidates for bio-inspired catalyst design.[362,595] As mentioned above, molybdenum and nickel sulphides are efficient hydrogen evolution catalysts.[511–513,678–682] Moreover, especially sulphides containing iron and nickel have shown very high activities in electrochemical CO$_2$RR,[595] as well as in the alkaline OER that surpasses their related oxides.[526,532,683–685] Even though sulphides are intrinsically prone to oxidation, stable performances have been observed.[683] The active surface species is often an oxyhydroxide, oxysulphide, or sulphate.[603,682] For photocatalytic approaches, the small band gap is advantageous in terms of light harvesting – however, the reduced valence band potential limits the suitability for oxidation reactions, and the narrow band gap makes a simultaneous performance of both oxidation and reduction reactions on one semiconductor challenging.[114,686] Photocatalytic applications are therefore often restricted to either reduction reactions, or oxidation reactions – most often decomposition reactions.[687,688] Strategies to overcome these limitations commonly focus on the construction of heterojunction systems and Z-schemes.[446,689,690] Additionally, sulphide photocatalysts are often prone to photo-corrosion.[686,691,692]
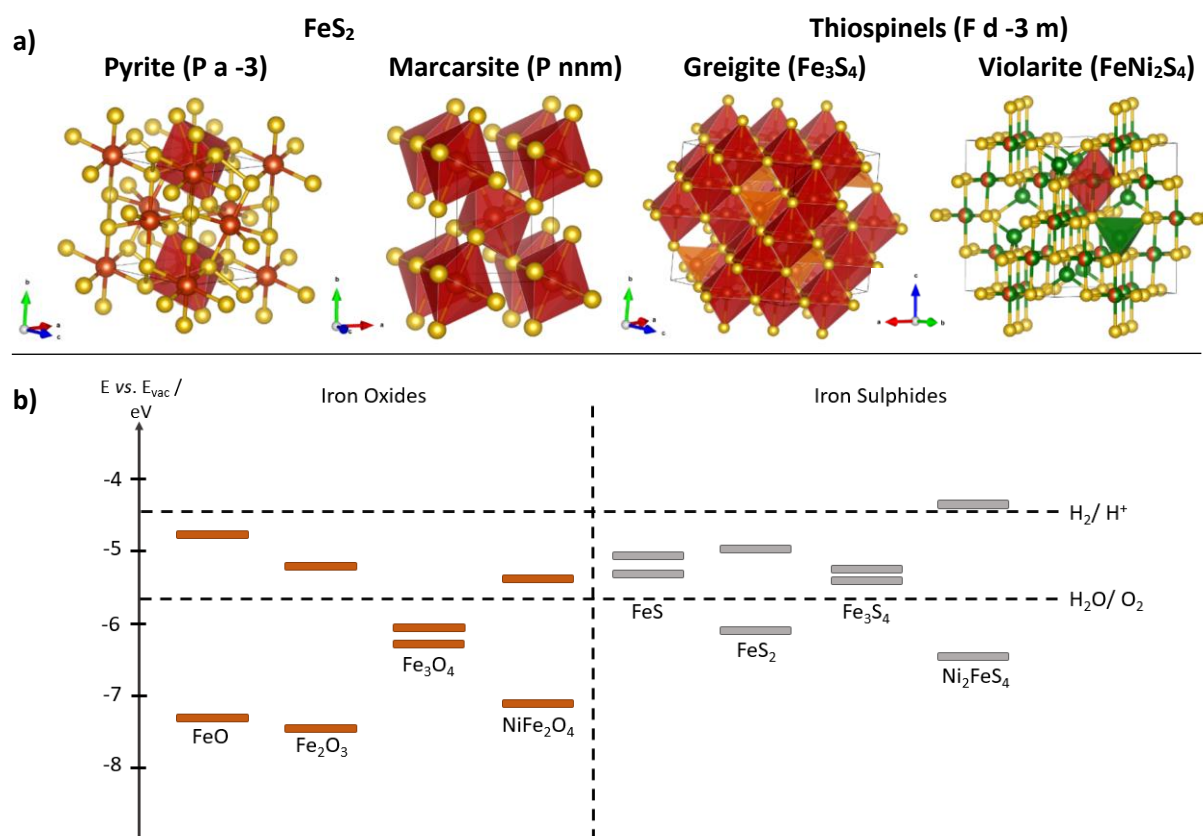
Figure 24 Crystal structures of FeS$_2$,[704,705] Fe$_3$S$_4$,[706] and Ni$_2$FeS$_4$ (a),[707] and comparison of calculated band positions of iron oxides and sulphides (b).[114] Ni is depicted in green, Fe in red, and S in golden yellow. Band positions for NiFe$_2$O$_4$ and Ni$_2$FeS$_4$ were calculated with the electron affinities and ionisation potentials reported by Pearson.[708] A band gap of 1.64 eV was assumed for NiFe$_2$O$_4$ and of 2 eV for Ni$_2$FeS$_4$.[668,709] Since all of these values for band potentials are calculated and thus neglect dopant concentrations and any influences connected to the degree of inversion, real band gap values might deviate, since the Fermi level no longer resides in the middle of the band gap and the orbitals constituting valence and conduction bands

might differ. Additionally, the calculation depends strongly on the assumed – often optical – band gap. Commonly, various band gaps are reported for one and the same material, though. Thus, the band gap of Fe_3S_4 was determined to be around 0.8 eV at low temperatures and thus larger than predicted ones due to spin ordering.[693] Calculations are for pH 0: the point of zero charge for Ni_2FeS_4 was approximated with 2, that of $NiFe_2O_4$ with 7.[114]

Iron sulphides are especially intriguing, due to their high abundance and low toxicity. Naturally occurring iron sulphides are FeS, Fe_3S_4, Fe_9S_8, and FeS_2.[60,693–695] The latter crystallises in two modifications, cubic pyrite and orthorhombic marcarsite. Both polymorphs often coexist, but pyrite is the thermodynamically more stable form.[115,696] Greigite, Fe_3S_4, with a cubic spinel structure is also metastable compared to pyrite and its mineral formation is likely kinetically driven.[60] FeS_2 and Fe_3S_4 have been explored for electrochemical and photocatalytic HER, as well as NRR, due to the fact that iron and sulphur are prominent building units in the active centre of both hydrogenase and nitrogenase enzymes.[365,504,697–699] Additionally, photocatalytic dye degradation was reported for FeS_2.[700] The band gap of FeS_2 is with around 0.95 eV very small, favouring visible light absorption.[701,702] Apart from application in photocatalysis, the good light harvesting properties make pyrite an interesting material for solar cells, although a careful control over the defect concentration is required.[695,696,703]

Another interesting spinel sulphide is violarite, Ni_2FeS_4. It shares compositional similarity to the active centre of nitrogenase enzymes. Additionally, it contains both Ni and Fe in close proximity, thus allowing for synergetic effects. Ni_2FeS_4 can be obtained at low reaction temperatures and very short synthesis times of down to 1 min by employing an adaptation of the non-aqueous microwave assisted synthesis, wherein parts of the alcohol solvent are replaced by benzylmercaptan. This approach makes use of the fact that the solvent plays an integrate part in the synthesis and serves as source for oxygen – or in this case sulphur.[596] Nickel-iron sulphides have shown promise in electrochemical OER and CO_2RR. Thus, the group of Apfel explored the activity of pentlandite ($Fe_{4.5}Ni_{4.5}S_8$) for alkaline OER, acidic HER and CO_2RR in organic solvents.[512,595]

3 Synopsis

The transition from a fossil fuel-based energy economy towards a sustainable future not only requires an expansion of currently available technologies for the conversion of regenerative energy sources – such as photovoltaics, wind turbines, etc. – but also the development of new technologies. More importantly, renewable energy usage has to become cost-competitive in order to allow for a wide-spread access including countries of lower gross domestic product, GDP. This is not only restricted to primary energy harvesting, but also includes the subsequent conversion of the collected energy – mostly in form of electricity – into valuable target products, such as fuels or high-value chemicals. To tackle this issue, two main problems need to be addressed: Firstly, the efficiency of energy conversion needs to be improved and secondly noble and scarce metals have to be replaced by earth-abundant elements.

At the heart of processes converting electricity into valuable products is usually the catalyst, whose task it is to drive the reaction as selectively as possible, with as high yields as possible, and with as little energy losses (mostly in the form of overpotentials) as possible – and moreover for extended time periods under oftentimes harsh conditions. So far, unfortunately, there is a huge gap between catalysts achieving satisfying efficiencies and low material costs, necessitating the development of new, cost-effective and at the same time active and selective materials.

The first part of this work is inspired by this challenge and focusses on $CuFe_2O_4$ as an earth-abundant catalyst for the reduction of carbon dioxide.[642] In order to establish a low-cost catalyst material, it is not only important that solely easily available elements are used, but also that the synthesis does not require a high energy input, long durations, or additional – and often extensive – post-synthetic treatment. The aim of this work was therefore the development of a new synthesis route to yield phase-pure $CuFe_2O_4$ after short synthesis times at low temperatures and without subsequent calcination steps.

Microwave-assisted solvothermal synthesis is well suited to fulfil these demands, as previously demonstrated by the group of Marschall for the synthesis of various spinel oxides.[619,644–646] Compared to these works in 1-phenylethanol, the solvent had to be adapted due to Cu^{2+} being reduced by the organic solvent. Mixtures of water and ethylene glycol were employed instead, which allowed for the preparation of phase-pure $CuFe_2O_4$ nanoparticles. Not only is water an attractive solvent due to its abundance, low cost and non-toxicity, but additionally this solvent mixture allowed for a reduction of the synthesis temperature down to 120 °C. At such a low temperature, the crystallinity was relatively low, however, but a slight increase by only 10-20 °C resulted in the formation of highly crystalline nanoparticles with a narrow size distribution of around 14 nm (**Figure 25**). A further increase of the synthesis temperature only led to a slight increase in particle size, due to the fast kinetics in the microwave and a homogeneous distribution of the precursors in the reaction vial, which is realised by the addition of ethylene glycol. Furthermore, it was possible to realise very short synthesis times of as short as 1 min (here at 175 °C).

In total, the synthesis temperature can be varied between 120 °C and 200 °C and the synthesis time was adjusted between 1 and 30 min. The phase purity was verified by X-ray diffraction (XRD), that also revealed a crystallite size of around 10 – 11 nm independent of the synthesis temperature, with an exception of the particles synthesised at 120 °C, which exhibited a smaller crystallite size. Moreover, the crystallite size showed a dependence on the synthesis time, with the largest size observed for

particles obtained after medium synthesis times. In good agreement to XRD and transmission electron microscopy (TEM) analysis, the Raman spectra and Brunauer-Emmett-Teller (BET) surface areas are highly comparable for $CuFe_2O_4$ obtained after different synthesis times. For the nanoparticles synthesised at varied temperatures, a decrease of the BET surface area with an increasing temperature is observed, which can be explained by the low crystallinity of particles obtained at low temperatures and by the decrease in residual organics with an increasing synthesis temperature, as observed by thermogravimetric analysis coupled to mass spectrometry (TGA-MS).
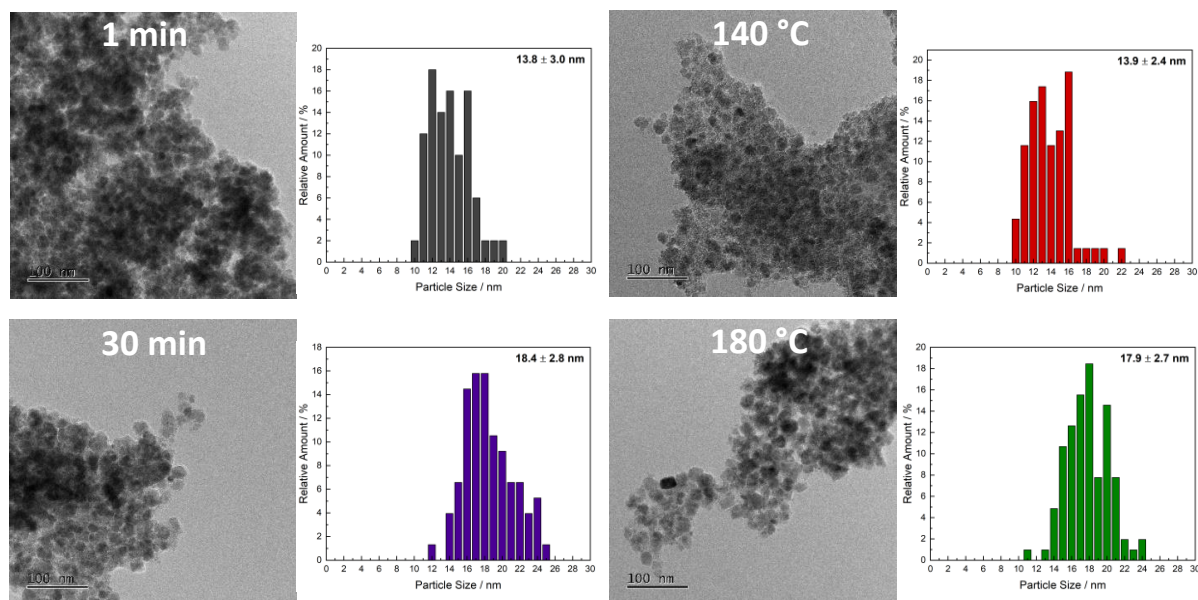
Figure 25 TEM images of $CuFe_2O_4$ nanoparticles obtained *via* the microwave assisted synthesis in water/ ethylene glycol mixtures, using different synthesis times and temperatures.

One of the most important characteristics of a spinel material is its degree of inversion that can influence the material properties. The microwave synthesis is controlled by kinetics, which becomes apparent by the fact that the obtained $CuFe_2O_4$ nanoparticles have a cubic structure, although normally a tetragonal distortion is favoured at room temperatures.[630] Therefore, it is hard to predict the degree of inversion, which can depend significantly on the synthesis conditions. The degree of inversion was determined by X-ray photoelectron spectroscopy (XPS) and Rietveld refinement of the XRD data. Both methods showed a decrease of the degree of inversion with an increasing synthesis time, indicating microwave-induced cation migration during prolonged heating. The synthesis temperature on the other hand did not have an effect on the degree of inversion. However, an increasing amount of Cu^+ (instead of Cu^{2+}) was observed for particles obtained at low temperature.

Having successfully developed a low-temperature, time-efficient synthesis of nanocrystalline $CuFe_2O_4$, the spinel oxide was then employed in the electrochemical CO_2RR using a H-cell setup. CO was observed as the only carbon-containing product starting at a voltage of -0.6 V *vs*. RHE. At increasingly more negative potentials, the HER becomes dominant, and the selectivity drops down. Therefore, a potential of -0.7 V *vs*. RHE was chosen for the evaluation of the influence of the synthesis conditions on the activity and selectivity. Interestingly, the synthesis time in the microwave was found to have a significant impact on the performance of $CuFe_2O_4$ in the reduction of CO_2 to CO (**Figure 26**). Increasing the synthesis time from 1 to 10 min first resulted in an increasing activity and selectivity, while further prolonged durations led to a decrease in both activity and selectivity. Several factors need to be considered in order to explain the observed dependencies. On the one hand, $CuFe_2O_4$ obtained after

very short synthesis times contained a larger fraction of organic residues that decrease the amount of active material on the electrode and impede charge transfer. In an adverse trend, the degree of inversion decreased during the continued heating in the microwave. This can affect the electronic structure of the spinel, as well as the coordination environment of Cu and Fe in the structure – both have an effect on the catalytic performance.
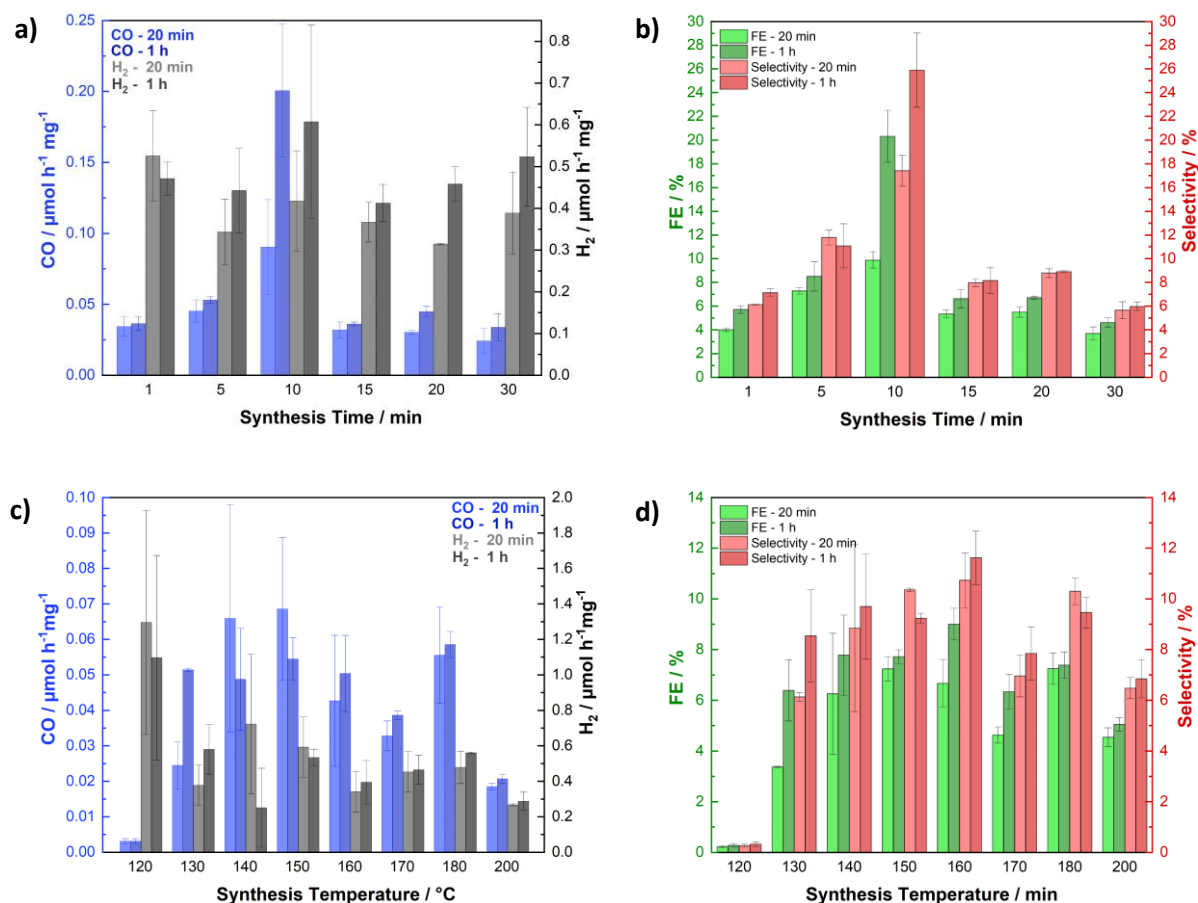
Figure 26 CO and H_2 yield for $CuFe_2O_4$ nanoparticles obtained after different synthesis times (a) and corresponding FE and selectivity (b). Additionally, the CO and H_2 yield for particles synthesised at a range of different temperatures is shown in (c), together with corresponding FE and selectivity (d).

In contrast to the synthesis time, the synthesis temperature did not have a significant effect on either activity or selectivity (Figure 26). This observation is in agreement with the similar degree of inversion, underlining the dominant influence of this parameter on the performance. $CuFe_2O_4$ obtained at very low temperatures (120 °C) exhibited a lower activity, due to the low crystallinity and high amount of organic residues. For particles synthesised at a higher temperature (200 °C) the activity was also lower, which can be attributed to the appearance of trace-amounts of Cu_2O. No CO formation was observed during a comparative experiment in an Ar atmosphere, verifying true CO_2 reduction. Apart from developing an energy efficient synthesis of $CuFe_2O_4$, this work could thus show that $CuFe_2O_4$ is a promising, earth-abundant catalyst for the reduction of CO_2 to syngas, with the catalytic activity being dependent on the degree of inversion and thus the synthesis conditions.

Currently an electrification of industrial processes is targeted in tandem with an extension of the conversion of renewable energy into electricity. For such a strategy to work, a stable, well-distributed electric grid capable of satisfying the electricity demand is required, however. This is problematic especially for developing countries. In addition to that, a cascade of conversion processes – from the renewable energy source into electricity, followed by AC/DC conversion processes and potentially intermediated storage, and lastly from electricity to the actual product – goes in hand with potential losses at each conversion step. Therefore, it is beneficial to explore alternative strategies. One such approach is photocatalysis, which combines light harvesting and product generation in one system. Additionally, it exploits the vast energy supply delivered by the sun that can be globally accessed. Since the solar energy is harvested on site, decentralisation is much easier and no access to mains electricity is required.

When developing a photocatalytic system, much can be learned from parallels to electrochemistry. This is especially valid if cocatalysts are used to increase the charge separation efficiency and overall activity. Such cocatalysts essentially fulfil the same role as conventional electrocatalysts – *i.e.* they have to efficiently use the charges delivered to them for the targeted conversion reactions. Since commonly noble metals are employed, the development of earth-abundant electrocatalysts that work as cocatalysts on conventional photocatalyst is required. Such a necessity was the motivation for the second work, in which Ni_2FeS_4 was used as a cocatalyst on TiO_2.[710]

As for electrocatalysts in the CO_2RR, an energy saving synthesis of both photocatalyst and cocatalyst is a prerequisite for overall low material costs. For sulphides this is even more challenging than for oxides since oxygen is far more abundant in the atmosphere and in water. Additionally, many sulphides are unstable in water or air, which might result in the formation of oxides instead of sulphides and limits the synthesis options. Therefore, oftentimes long reaction times, or the use of toxic H_2S are required for the preparation of – especially ternary – sulphides. We have shown that a much faster and straightforward synthesis of Ni_2FeS_4 can be realised using a microwave-assisted synthesis in organic solvents and benzyl mercaptan as a sulphur source.[596] Starting from these results, the synthesis was further optimised in the second work of this thesis. The synthesis time could thus be lowered from 30 min to 5 min without changes in the crystallinity or morphology, as verified by XRD, XPS, scanning electron microscopy (SEM), and TEM analysis (**Figure 27**). The time could be reduced further down to 1 min, which resulted in a slightly decreased crystallinity and incomplete oxidation of Ni^{2+} to Ni^{3+}. Otherwise, the reaction was mostly completed after only 1 min at the target temperature of 200 °C in the microwave, which could also be directly monitored by the initial appearance of light flashes, that were not observed after the first couple of minutes.

In a next step, composites of Ni_2FeS_4 and TiO_2 (P25) were formed, employing different ratios of the sulphide and TiO_2. The amount of sulphide was thereby varied between 0.1 and 10 wt.%. Due to the strong light absorbing properties of Ni_2FeS_4, the addition of even low amounts to P25 resulted in a colour change from white to grey and an increased absorption of visible and near infrared (NIR) radiation. The homogeneous distribution of Ni_2FeS_4 was additionally verified by energy dispersive X-ray (EDX) mapping (**Figure 28**).

The prepared composites were employed in the photocatalytic HER under 1 sun simulated sunlight, using 10 vol.% of methanol as a hole scavenger. The addition of Ni_2FeS_4 could significantly improve the activity of P25 by a factor of eight, reaching a H_2 evolution rate of 25-28 µmol h^{-1}. Ni_2FeS_4 alone was found to be inactive under the employed conditions, which is a first indication that it is acting as a cocatalyst to improve the activity of P25. Furthermore, very low loadings of the sulphide on TiO_2 could

be realised. Only 0.5 wt.% of Ni_2FeS_4 were sufficient to reach a H_2 evolution rate of 25 µmol h^{-1}, which was comparable to the effect of 1 – 5 wt.% (Figure 28). This finding is another confirmation of the role of Ni_2FeS_4 being that of a cocatalyst.
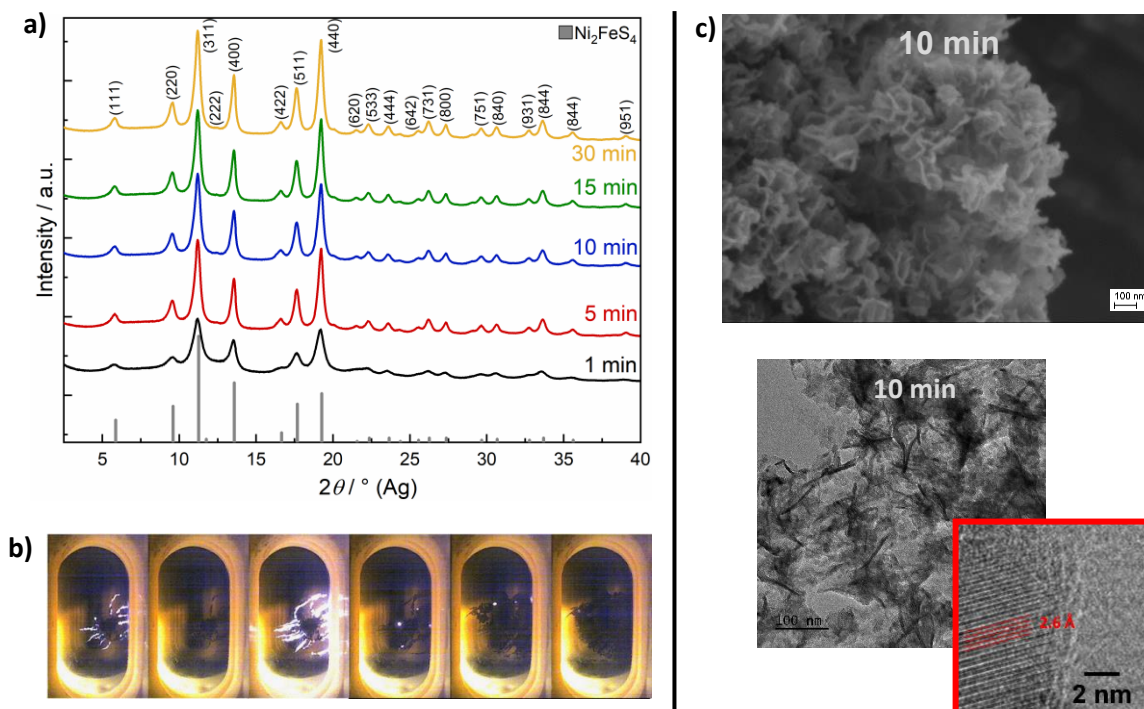
Figure 27 XRD patterns for Ni_2FeS_4 obtained after different synthesis times in the microwave (a), photographs of the microwave vessels during the reaction taken by an integrated camera (b), and nanosheet morphology of Ni_2FeS_4 observed in SEM and TEM images.

In order to evaluate whether the synthesis conditions of Ni_2FeS_4 affect its performance as a cocatalyst, composites of 5 wt.% of Ni_2FeS_4 obtained after different synthesis times and P25 were fabricated. All exhibited a comparable activity, in agreement to the lack of differences observed in the characterisation.

The suitability of Ni_2FeS_4 as a cocatalyst was then further confirmed by performing the photocatalytic HER experiment with ethanol instead of methanol as a scavenger. The relative activity increase was comparable to the results obtained with methanol. Additionally, the cocatalyst effect could be observed in a combination with other materials apart from TiO_2, which was shown for $SrTiO_3$.

Since TiO_2 only absorbs UV light, its photocatalytic performance under solar irradiation is limited. Therefore, the HER activity of pristine P25, of Ni_2FeS_4, and of 5wt.% Ni_2FeS_4@P25 was additionally examined under irradiation by a 500 W Hg lamp. Under these conditions, the activity increase after the addition of Ni_2FeS_4 was even more pronounced. Thus, the H_2 evolution rate could be increased by a factor of up to 48, reaching 2300 µmol h^{-1} in the absence of any noble metal cocatalyst. Notably, Ni_2FeS_4 itself was slightly active for the HER under these conditions, implying charge carrier excitation in the sulphide as well. This might alter the charge carrier separation in the composite and explain the even stronger effect of Ni_2FeS_4 addition compared to the situation under simulated sun-light. The assumption is furthermore supported by the fact that a loading of 5 wt.% of the sulphide led to a higher H_2 evolution rate compared to a loading of 0.5 wt.%, even though both composites showed the same performance under simulated sun light (Figure 28). Lastly, the stable performance of the Ni_2FeS_4 cocatalyst was verified by a 20 h experiment under 1 sun illumination, demonstrating the efficiency

and stability of this earth-abundant cocatalyst, both of which are a prerequisite for any replacements of noble metal cocatalysts.
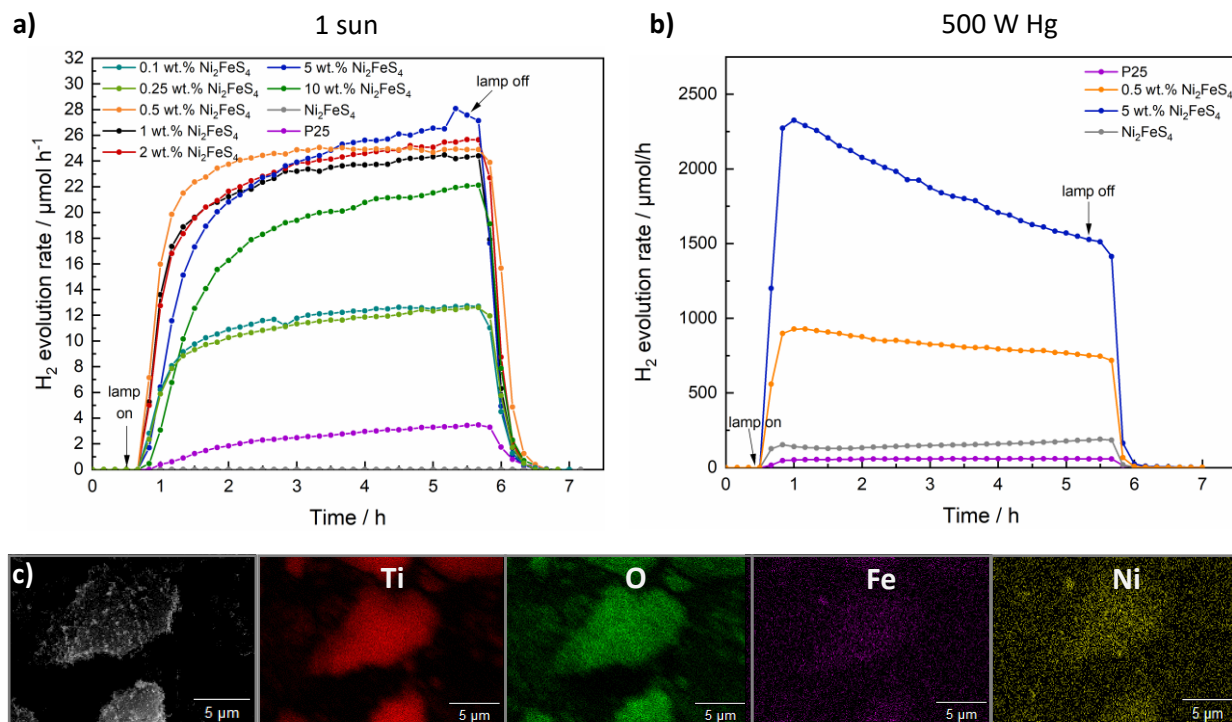
Figure 28 H_2 evolution observed for Ni_2FeS_4 loaded onto P25 under 1 sun simulated sunlight (a), as well as under UV illumination (b) and EDX mapping of such a composite (5 wt.% of Ni_2FeS_4), elucidating the homogeneous distribution of the sulphide over P25 (c).

An efficient, low-cost and sustainable production of H_2 is important in order to allow for a widespread application of fuel cells as an alternative to combustion engines. Additionally, H_2 is of great demand in many industrial processes, and ensuring the availability of low-cost green H_2 is therefore at the core of decreasing the carbon footprint of large-scale industrial processes, such as the Haber-Bosch process for the production of ammonia, NH_3. The synthesis of H_2 and subsequent use in fuel cells or industry generally requires an intermediate storage. This is problematic, however, due to the small size and high volatility, as well as to the flammability of H_2, and the small volumetric energy density. The direct synthesis of higher-value hydrogen containing chemicals by photocatalysis in an aqueous media is therefore preferable. Specifically, the photocatalytic reduction of ambient N_2 and water to NH_3 would not only represent an economic one-step alternative to the Haber-Bosch process, but would also enable the use of green NH_3 as a chemical storage medium for H_2.

Since carbon nitrides belong to the most efficient photocatalysts for the NRR, at least according to literature, the third part of this work combined carbon nitride with FeS_2 (pyrite) in a biomimetic approach to improve the activity in photocatalytic NH_3 generation.[711] First, carbon nitride (CN) was synthesised *via* thermal polymerisation of melamine. In a next step, nitrogen vacancies were introduced by etching with KOH, based on literature reports.[169] Subsequently, composites of the vacancy-rich carbon nitride (V_N-CN) and commercial FeS_2 were fabricated, using varying weight ratios of FeS_2 ranging from 1 to 15 wt.%. XRD patterns of the obtained materials showed reflections for both FeS_2 and CN, indicating successful composite formation (**Figure 29**). This conclusion was supported by

a change in colour and improved visible and NIR light absorption apparent in the UV/vis spectra, as well as by SEM analysis, that showed the contact between both FeS_2 and CN (Figure 29).
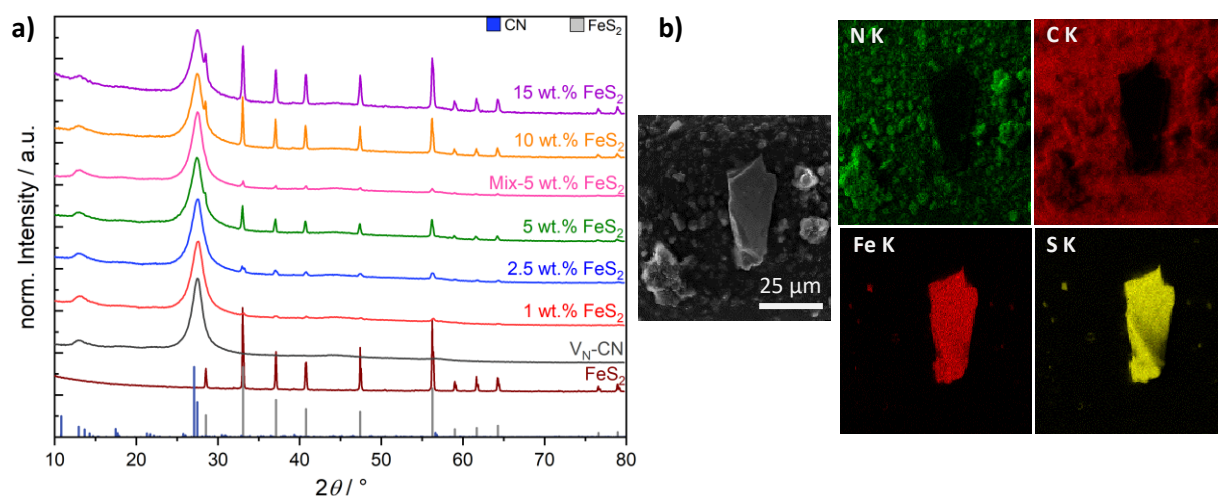
Figure 29 XRD patterns of composites of FeS_2 and V_N-CN are shown in (a), while in (b) the contact between V_N-CN and FeS_2 is depicted.

A more thorough characterisation of the composite materials additionally revealed electronic interactions between both constituents. Thus, the band gap of CN gradually increased with an increasing amount of FeS_2 in the composite. Moreover, both the C 1s and the N 1s XP spectra of the composites shift towards higher binding energies compared to V_N-CN, indicating an electron extraction from the carbon nitride matrix (**Figure 30**) and thus electron transfer to FeS_2. For further confirmation, photoluminescence spectra of the composites were measured, and the results compared to those obtained for bulk V_N-CN. Generally, a markedly lower emission intensity was observed for the composites. In addition to that, a small shift towards a lower emission wavelength was observed, together with a change in the relative emission intensity of two bands. More specifically, the contribution of lone-pair and defect emission in relation to direct band gap emission was decreased in the composites, indicating the inhibition of radiative recombination at defect sites, and thus pointing at a charge transfer with FeS_2 taking place at the defect sites (Figure 30). This finding was further supported by an increased fluorescence lifetime in the composites and a decreased quantum yield, both of which indicate an improved charge separation.
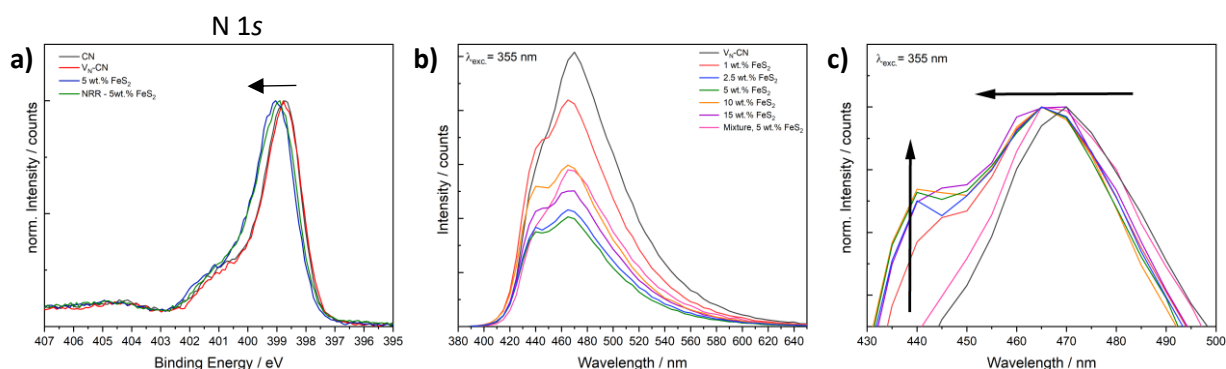
Figure 30 Shift of the N 1s XP spectrum of a composite with 5 wt.% of FeS_2 shown in (a), decrease in the radiative emission intensity of the composites (b) and relative changes observed in normalised emission spectra (c).

The composites were then employed in experiments for photocatalytic nitrogen reduction under 350 W irradiation by a doped Hg-lamp. 20 vol.% of methanol were used as hole scavenger to improve the activity for N_2 reduction. In agreement to literature, the introduction of nitrogen vacancies significantly enhanced the ammonia yield compared to untreated CN. Additionally, the ammonia yield was increased even further upon the addition of FeS_2 to V_N-CN (**Figure 31**).
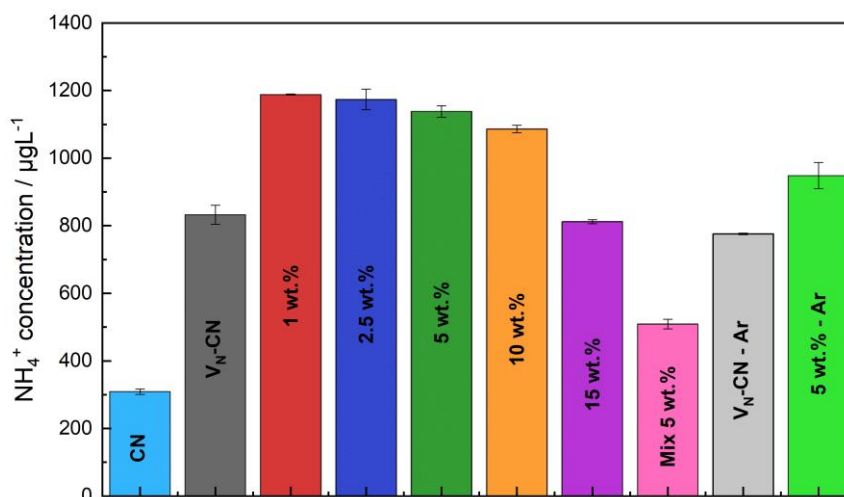
Figure 31 NH_4^+ concentrations measured after an irradiation of aqueous dispersions of V_N-CN and of composites with FeS_2 for 7 h, determined *via* ion chromatography. The reference measurements for V_N-CN and the composite containing 5 wt.% of FeS_2 are shown in pale grey and pale green on the right side.

When the same experiment was performed in an Ar atmosphere instead of N_2, almost the same ammonia yield was obtained, though, which is a strong indication that not gaseous N_2 is reduced, but that the nitrogen is instead extracted from the CN-framework. This finding was further confirmed by post-catalytic characterisation, that revealed a decrease in the amount of cyano groups that are introduced at defect sites by the KOH treatment. Moreover, the C/N ratio was increased after the photocatalytic experiment for both V_N-CN and the composites with FeS_2. Combined with the changes of the electronic structure, this observation points towards an activation of cyano groups at the defect sites by coordination to FeS_2, most probably *via* π-backdonation. In total, the results of this work strongly emphasise that carbon nitrides (at least if synthesised *via* thermal polymerisation) are unstable under light irradiation and thus unsuitable for the photocatalytic NRR. The introduction of vacancies aggravates the situation and promotes nitrogen extraction at the defect sites.

All of the herein discussed catalysts are constituted from earth-abundant elements. Specifically, they contain iron as the major element, which is highly abundant, non-toxic and can be obtained at low cost. Due to its abundance, nature is using iron in many catalytic systems ranging from hydrogenase enzymes, over CO dehydrogenases, to nitrogenases, all of which contain iron as major element in their active centres. The works in this thesis elucidate how it is possible to design artificial earth-abundant solid-state catalysts for a variety of catalytic reactions, as well. The targeted conversion reactions thereby span both fields of electro- and photocatalysis, as well as multiple kinds of reactions, including CO_2 reduction, HER and NRR. All of these sustainable energy conversion processes can be expected to become increasingly important in the near future, in the context of mitigating climate change. Until

electrocatalysis can compete with established fossil-fuel-based processes in terms of cost and efficiency, however, much research is still required. For photocatalysis, the situation is even worse although the expected technology costs are much lower, highlighting the importance of continued research in this field, especially focussing on the design of new, earth-abundant materials, and on improving existing systems towards a higher efficiency and selectivity.

The following chapters will provide full-text manuscripts of the herein discussed works.

4 Individual Contributions to Joint Publications

The publications that are part of this thesis are the result of cooperation with others. The following chapter will delineate the individual contributions of each author to the published manuscripts. The corresponding author of all publications is Prof. Dr. Roland Marschall, marked by an asterisk.

4.1 Publication 1: "Fast and Facile Microwave Synthesis of Cubic CuFe$_2$O$_4$ Nanoparticles for Electrochemical CO$_2$ Reduction"

Judith Zander, Morten Weiss, Roland Marschall*

The concept of the manuscript was developed by Prof. Dr. Roland Marschall and myself. I optimised and performed the synthesis of CuFe$_2$O$_4$. Additionally, I characterised the obtained nanoparticles by UV/vis, diffuse reflectance infrared Fourier transform (DRIFT) spectroscopy, and XRD, including Rietveld refinement. I also performed and evaluated the electrochemical CO$_2$ reduction experiments, and wrote the first draft of the manuscript. Dr. Morten Weiss did the XPS measurements and evaluated the data together with me. He also provided assistance in the Rietveld refinement. Prof. Dr. Roland Marschall supervised the work and provided scientific advice. All authors read and contributed to the final version of the manuscript.

Additionally, Dr. Holger Schmalz, Lena Geiling, and Dr. Christopher Simon performed the Raman, TG-MS and TEM analysis, respectively. Mirco Ade and Dr. Anja Hofmann did the SEM and EDX analysis, Dr. Jana Timm and Jonas Jungmann performed the N$_2$-physisorption measurements, and Julia Wölfel and Teresa Maurer provided assistance in the synthesis under my supervision. All of these contributions are acknowledged in the manuscript. I was responsible for evaluating the data resulting from the listed measurements.

4.2 Publication 2: "Ni$_2$FeS$_4$ as highly efficient earth-abundant co-catalyst in photocatalytic hydrogen evolution"

Judith Zander, Roland Marschall*

The concept of the manuscript was developed by Prof. Dr. Roland Marschall and me. I performed the synthesis of Ni$_2$FeS$_4$ and most of the characterisation, including UV/vis, DRIFT, Raman, and XRD. I also did the photocatalytic experiments and wrote the first draft of the manuscript. Prof. Dr. Roland Marschall supervised the work, was involved in scientific discussions, and contributed to the final draft of the manuscript.

Mirco Ade and Jonas Jungmann performed SEM/EDX and TEM analysis, respectively. Lena Geiling was responsible for the TG-MS measurements and Dr. Morten Weiss and Lion Schumacher measured the XP spectra. Additionally, Jonas Jungmann and Dr. Jana Timm did the N$_2$ physisorption measurements. All those contributions are acknowledged in the manuscript. The resulting data was evaluated by me.

4.3 Publication 3: "Light-Induced Ammonia Generation over Defective Carbon Nitride Modified with Pyrite"

Judith Zander, Jana Timm, Morten Weiss, Roland Marschall*

The concept of the manuscript was developed by Prof. Dr. Roland Marschall and me. I synthesised the materials, performed most of the characterisation, conducted the photocatalytic experiments and wrote the first draft of the manuscript. The characterisation measurements performed by me include XRD, UV/vis, DRIFT, elemental analysis (EA), photoluminescence, as well as ammonia quantification. Dr. Jana Timm did the transient absorption spectroscopy (TAS), including the corresponding data evaluation. She additionally performed the physisorption measurements and provided assistance in the photoluminescence measurements. Dr. Morten Weiss performed the XPS analysis and evaluated the data together with me. Prof. Dr. Roland Marschall supervised the work, provided scientific advice, and corrected the manuscript. All authors read and contributed to the final version of the manuscript.

In addition to the authors, Mirco Ade and Lena Geiling contributed to the work by performing SEM/EDX and TG-MS analysis, respectively. They are acknowledged in the publication.

5 References

(1) Clarke, B.; Otto, F.; Stuart-Smith, R.; Harrington, L. *Environ. Res. Clim.* **2022**, *1*, 012001.

(2) Allen, M. R.; Dube, O. P.; Solecki, W.; Aragón-Durand, F.; Cramer, W.; Humphreys, S.; Kainuma, M.; Kala, J.; Mahowald, N.; Mulugetta, Y.; Perez, R.; Wairiu, M.; Zickfeld, K. *Global Warming of 1.5 °C. An IPCC Special Report on the Impacts of Global Warming of 1.5 °C above Pre-Industrial Levels and Related Global Greenhouse Gas Emission Pathways, in the Context of Strengthening the Global Response to the Threat of Climate Chang*; Ismail Elgizouli Idris, Andreas Fischlin, X. G., Ed.; Cambridge University Press: Cambridge, 2018; Vol. Chapter 1.

(3) Smith, A. B.; Katz, R. W. *Nat. Hazards* **2013**, *67*, 387–410.

(4) Beckley, B.; Yang, X.; Zelensky, N. P.; Holmes, S. A.; Lemoine, F. G.; Ray, R. D.; Mitchum, G. T.; Desai, S.; Brown, S. T. *Global Mean Sea Level Trend from Integrated Multi-Mission Ocean Altimeters TOPEX/Poseidon, Jason-1, OSTM/Jason-2, and Jason-3 Version 5.1 Ver 5.1 PO.DAAC, CA, USA*. https://podaac.jpl.nasa.gov/dataset/MERGED_TP_J1_OSTM_OST_GMSL_ASCII_V51 (accessed 2023-05-27).

(5) *NASA National Snow and Ice Data Center - Arcitc Sea Ice News and Analysis*. https://nsidc.org/arcticseaicenews/sea-ice-tools/ (accessed 2023-05-27).

(6) *NOAA National Centers for Environmental Information - "Billion-Dollar Weather and Climate Disasters."* https://www.ncei.noaa.gov/access/billions/ (accessed 2023-06-03).

(7) *NOAA National Centers for Environmental Information - "Climate at a Clance National Time Series."* https://www.ncei.noaa.gov/access/monitoring/climate-at-a-glance/national/time-series (accessed 2023-05-26).

(8) Trans, P. (NOAA/GML); Keeling, R. (Scripps I. of O. *NOAA Earth System Research Laboratories - "Trends in Atmospheric Carbon Dioxide."* https://gml.noaa.gov/ccgg/trends/data.html (accessed 2023-05-26).

(9) van Vuuren, D. P.; Edmonds, J.; Kainuma, M.; Riahi, K.; Thomson, A.; Hibbard, K.; Hurtt, G. C.; Kram, T.; Krey, V.; Lamarque, J. F.; Masui, T.; Meinshausen, M.; Nakicenovic, N.; Smith, S. J.; Rose, S. K. *Clim. Change* **2011**, *109*, 5–31.

(10) Meinshausen, M.; Smith, S. J.; Calvin, K.; Daniel, J. S.; Kainuma, M. L. T.; Lamarque, J.; Matsumoto, K.; Montzka, S. A.; Raper, S. C. B.; Riahi, K.; Thomson, A.; Velders, G. J. M.; van Vuuren, D. P. P. *Clim. Change* **2011**, *109*, 213–241.

(11) United Nations FCCC/CP. *Adoption of the Paris Agreement, 21. Conference of the Parties*; Paris, 2015.

(12) Ehteshami, S. M. M.; Chan, S. H. *Energy Policy* **2014**, *73*, 103–109.

(13) Perez, M.; Perez, R. *Sol. Energy Adv.* **2022**, *2*, 100014.

(14) Chalk, S. G.; Miller, J. F. *J. Power Sources* **2006**, *159*, 73–80.

(15) Ajanovic, A.; Haas, R. *Fuel Cells* **2019**, *19*, 515–529.

(16) Bauen, A. *J. Power Sources* **2006**, *157*, 893–901.

(17) Pardo, N.; Moya, J. A. *Energy* **2013**, *54*, 113–128.

(18) Akashi, O.; Hanaoka, T.; Matsuoka, Y.; Kainuma, M. *Energy* **2011**, *36*, 1855–1867.

(19) Kuramochi, T.; Ramírez, A.; Turkenburg, W.; Faaij, A. *Prog. Energy Combust. Sci.* **2012**, *38*, 87–112.

(20) Lo, G.-D.; Marcelin, I.; Bassène, T.; Sène, B. *Financ. Res. Lett.* **2022**, *50*, 103194.

(21) Gueymard, C. A. *Sol. Energy* **2004**, *76*, 423–453.

(22) NREL. *Reference Air Mass 1.5 Spectra*. https://www.nrel.gov/grid/solar-resource/spectra-am1.5.html (accessed 2020-08-01).

(23) Van De Krol, R.; Grätzel, M. *Photoelectrochemical Hydrogen Production*; Van De Krol, R., Grätzel, M., Eds.; Springer: New York, Dordrecht, Heidelberg, London, 2012.

(24) Polman, A.; Knight, M.; Garnett, E. C.; Ehrler, B.; Sinke, W. C. *Science* **2016**, *352*, aad4424.

(25) Mulder, F. M. *J. Renew. Sustain. Energy* **2014**, *6*, 033105.

(26) Anvari, M.; Lohmann, G.; Wächter, M.; Milan, P.; Lorenz, E.; Heinemann, D.; Tabar, M. R. R.;

Peinke, J. *New J. Phys.* **2016**, *18*, 063027.

(27) Daiyan, R.; Macgill, I.; Amal, R. *ACS Energy Lett.* **2020**, *5*, 3843–3847.

(28) She, Z. W.; Kibsgaard, J.; Dickens, C. F.; Chorkendorff, I.; Nørskov, J. K.; Jaramillo, T. F. *Science* **2017**, *355*, eaad4998.

(29) Ravelli, D.; Dondi, D.; Fagnoni, M.; Albini, A. *Chem. Soc. Rev.* **2009**, *38*, 1999–2011.

(30) Osterloh, F. E. *ACS Energy Lett.* **2017**, *2*, 445–453.

(31) Li, S.; Li, E.; An, X.; Hao, X.; Jiang, Z.; Guan, G. *Nanoscale* **2021**, *13*, 12788–12817.

(32) Khan, M. A.; Zhao, H.; Zou, W.; Chen, Z.; Cao, W.; Fang, J.; Xu, J.; Zhang, L.; Zhang, J. *Electrochem. Energy Rev.* **2018**, *1*, 483–530.

(33) You, B.; Sun, Y. *Acc. Chem. Res.* **2018**, *51*, 1571–1580.

(34) Chen, Z.; Dinh, H. N.; Miller, E. *Photoelectrochemical Water Splitting - Standards, Experimental Methods, and Protocols*; Chen, Z., Dinh, H. N., Miller, E., Eds.; Springer: New York Heidelberg, 2013.

(35) Deng, J.; Iñiguez, J. A.; Liu, C. *Joule* **2018**, *2*, 846–856.

(36) Guo, X.; Du, H.; Qu, F.; Li, J. *J. Mater. Chem. A* **2019**, *7*, 3531–3543.

(37) Suryanto, B. H. R.; Du, H. L.; Wang, D.; Chen, J.; Simonov, A. N.; MacFarlane, D. R. *Nat. Catal.* **2019**, *2*, 290–296.

(38) Ziegenbalg, D.; Zander, J.; Marschall, R. *ChemPhotoChem* **2021**, *5*, 792–807.

(39) Nitopi, S.; Bertheussen, E.; Scott, S. B.; Liu, X.; Engstfeld, A. K.; Horch, S.; Seger, B.; Stephens, I. E. L.; Chan, K.; Hahn, C.; Nørskov, J. K.; Jaramillo, T. F.; Chorkendorff, I. *Chem. Rev.* **2019**, *119*, 7610–7672.

(40) Nahar, S.; Zain, M. F. M.; Kadhum, A. A. H.; Hasan, H. A.; Hasan, M. R. *Materials* **2017**, *10*, 629.

(41) Jones, J. P.; Prakash, G. K. S.; Olah, G. A. *Isr. J. Chem.* **2014**, *54*, 1451–1466.

(42) Sato, S.; Arai, T.; Morikawa, T. *Inorg. Chem.* **2015**, *54*, 5105–5113.

(43) De Bruijn, F. *Green Chem.* **2005**, *7*, 132–150.

(44) Takise, K.; Sekine, Y. *Accounts Mater. Surf. Res.* **2019**, *4*, 115–134.

(45) Van de Voorde, M. *Hydrogen Production and Energy Transition*; Van de Voorde, M., Ed.; De Gruyter: Berlin/Boston, 2021; Vol. 1.

(46) Yu, M.; Budiyanto, E.; Tüysüz, H. *Angew. Chemie Int. Ed.* **2022**, *61*, e202103824.

(47) Van Der Ham, C. J. M.; Koper, M. T. M.; Hetterscheid, D. G. H. *Chem. Soc. Rev.* **2014**, *43*, 5183–5191.

(48) Klerke, A.; Christensen, C. H.; Nørskov, J. K.; Vegge, T. *J. Mater. Chem.* **2008**, *18*, 2304–2310.

(49) Al-Aboosi, F. Y.; El-Halwagi, M. M.; Moore, M.; Nielsen, R. B. *Curr. Opin. Chem. Eng.* **2021**, *31*, 100670.

(50) Kobayashi, H.; Hayakawa, A.; Somarathne, K. D. K. A.; Okafor, E. C. *Proc. Combust. Inst.* **2019**, *37*, 109–133.

(51) Lan, R.; Irvine, J. T. S.; Tao, S. *Int. J. Hydrogen Energy* **2012**, *37*, 1482–1494.

(52) Dry, M. E. *Catal. Today* **2002**, *71*, 227–241.

(53) Fukuzumi, S.; Lee, Y. M.; Nam, W. *Coord. Chem. Rev.* **2018**, *355*, 54–73.

(54) Ran, J.; Zhang, J.; Yu, J.; Jaroniec, M.; Qiao, S. Z. *Chem. Soc. Rev.* **2014**, *43*, 7787–7812.

(55) Hunter, B. M.; Gray, H. B.; Müller, A. M. *Chem. Rev.* **2016**, *116*, 14120–14136.

(56) Kahng, S.; Yoo, H.; Kim, J. H. *Adv. Powder Technol.* **2020**, *31*, 11–28.

(57) Han, L.; Dong, S.; Wang, E. *Adv. Mater.* **2016**, *28*, 9266–9291.

(58) Du, P.; Eisenberg, R. *Energy Environ. Sci.* **2012**, *5*, 6012–6021.

(59) Rees, D. C. *Annu. Rev. Biochem.* **2002**, *71*, 221–246.

(60) Schwertmann, U.; Fitzpatrick, R. W. *Catena Suppl.* **1992**, *21*, 7–30.

(61) *CRC Handbook of Chemistry and Physics*, 97th ed.; Haynes, W. M., Lide, D. R., Bruno, T. J., Eds.; CRC Press, 2017.

(62) Mabate, T. P.; Maqunga, N. P.; Ntshibongo, S.; Maumela, M.; Bingwa, N. *SN Appl. Sci.* **2023**, *5*, 196.

(63) McNaught, A.D.; Wilkinson, A. *IUPAC. Compendium of Chemical Terminology*, 2nd ed.; Blackwell Scientific Publications: Oxford, 1997.

(64) Takanabe, K. *ACS Catal.* **2017**, *7*, 8006–8022.

(65) Wang, Z.; Li, C.; Domen, K. *Chem. Soc. Rev.* **2019**, *48*, 2109–2125.

(66) Fan, W.; Zhang, Q.; Wang, Y. *Phys. Chem. Chem. Phys.* **2013**, *15*, 2632–2649.

(67) Gaya, U. I. *Heterogeneous Photocatalysis Using Inorganic Semiconductor Solids*; Springer Science+Business Media: Dordrecht, 2014.

(68) Cieśla, P.; Kocot, P.; Mytych, P.; Stasicka, Z. *J. Mol. Catal. A Chem.* **2004**, *224*, 17–33.

(69) Kisch, H. *Angew. Chemie - Int. Ed.* **2013**, *52*, 812–847.

(70) Asai, Y.; Katsuragi, H.; Kita, K.; Tsubomura, T.; Yamazaki, Y. *Dalt. Trans.* **2020**, *49*, 4277–4292.

(71) Chen, X.; Li, N.; Kong, Z.; Ong, W. J.; Zhao, X. *Mater. Horizons* **2018**, *5*, 9–27.

(72) Medford, A. J.; Hatzell, M. C. *ACS Catal.* **2017**, *7*, 2624–2643.

(73) Shi, R.; Waterhouse, G. I. N.; Zhang, T. *Sol. RRL* **2017**, *1*, 1700126.

(74) Fujishima, A.; Honda, K. *Nature* **1972**, *238*, 37–38.

(75) Inoue, T.; Fujishima, A.; Konishi, S.; Honda, K. *Nature* **1979**, *277*, 637–638.

(76) Serpone, N.; Emeline, A. V.; Horikoshi, S.; Kuznetsov, V. N.; Ryabchuk, V. K. *Photochem. Photobiol. Sci.* **2012**, *11*, 1121–1150.

(77) Hashimoto, K.; Irie, H.; Fujishima, A. *Japanese J. Appl. Physics, Part 1 Regul. Pap. Short Notes Rev. Pap.* **2005**, *44*, 8269–8285.

(78) Kosco, J.; Moruzzi, F.; Willner, B.; McCulloch, I. *Adv. Energy Mater.* **2020**, *10*, 2001935.

(79) Djurišić, A. B.; Leung, Y. H.; Ching Ng, A. M. *Mater. Horizons* **2014**, *1*, 400–410.

(80) Wang, H.; Zhang, L.; Chen, Z.; Hu, J.; Li, S.; Wang, Z.; Liu, J.; Wang, X. *Chem. Soc. Rev.* **2014**, *43*, 5234–5244.

(81) Marschall, R. *Adv. Funct. Mater.* **2014**, *24*, 2421–2440.

(82) Low, J.; Yu, J.; Jaroniec, M.; Wageh, S.; Al-Ghamdi, A. A. *Adv. Mater.* **2017**, *29*, 1601694.

(83) Li, X.; Yu, J.; Low, J.; Fang, Y.; Xiao, J.; Chen, X. *J. Mater. Chem. A* **2015**, *3*, 2485–2534.

(84) Bai, S.; Jiang, J.; Zhang, Q.; Xiong, Y. *Chem. Soc. Rev.* **2015**, *44*, 2893–2939.

(85) Maeda, K. *J. Photochem. Photobiol. C Photochem. Rev.* **2011**, *12*, 237–268.

(86) Qureshi, M.; Takanabe, K. *Chem. Mater.* **2017**, *29*, 158–167.

(87) Wang, Z.; Hisatomi, T.; Li, R.; Sayama, K.; Liu, G.; Domen, K.; Li, C.; Wang, L. *Joule* **2021**, *5*, 344–359.

(88) Osterloh, F. E. *Chem. Soc. Rev.* **2013**, *42*, 2294–2320.

(89) Sathiyan, K.; Bar-Ziv, R.; Marks, V.; Meyerstein, D.; Zidki, T. *Chem. - A Eur. J.* **2021**, *27*, 15936–15943.

(90) Kumaravel, V.; Imam, M. D.; Badreldin, A.; Chava, R. K.; Do, J. Y.; Kang, M.; Abdel-Wahab, A. *Catalysts* **2019**, *9*, 276.

(91) Wang, M.; Shen, S.; Li, L.; Tang, Z.; Yang, J. *J. Mater. Sci.* **2017**, *52*, 5155–5164.

(92) López, C. R.; Melián, E. P.; Ortega Méndez, J. A.; Santiago, D. E.; Doña Rodríguez, J. M.; González Díaz, O. *J. Photochem. Photobiol. A Chem.* **2015**, *312*, 45–54.

(93) Vignolo-González, H. A.; Laha, S.; Jiménez-Solano, A.; Oshima, T.; Duppel, V.; Schützendübe, P.; Lotsch, B. V. *Matter* **2020**, *3*, 464–486.

(94) Lin, S.; Huang, H.; Ma, T.; Zhang, Y. *Adv. Sci.* **2021**, *8*, 23–25.

(95) Schneider, J.; Bahnemann, D. W. *J. Phys. Chem. Lett.* **2013**, *4*, 3479–3483.

(96) Chen, J.; Ollis, D. F.; Rulkens, W. H.; Bruning, H. *Water Res.* **1999**, *33*, 661–668.

(97) Hessel, C.; Perini, N.; Sitta, E. *J. Solid State Electrochem.* **2023**, *27*, 705–714.

(98) Cruz, P. L.; Dufour, J.; Iribarren, D. *Renew. Energy* **2023**, *210*, 424–430.

(99) Zhang, T.; Lu, S. *Chem Catal.* **2022**, *2*, 1502–1505.

(100) Chu, S.; Zhang, B.; Zhao, X.; Soo, H. Sen; Wang, F.; Xiao, R.; Zhang, H. *Adv. Energy Mater.* **2022**, *12*, 2200435.

(101) Cargnello, M.; Gasparotto, A.; Gombac, V.; Montini, T.; Barreca, D.; Fornasiero, P. *Eur. J. Inorg. Chem.* **2011**, *2011*, 4309–4323.

(102) Kandiel, T. A.; Dillert, R.; Robben, L.; Bahnemann, D. W. *Catal. Today* **2011**, *161*, 196–201.

(103) Wang, X. L.; Liu, W.; Yu, Y. Y.; Song, Y.; Fang, W. Q.; Wei, D.; Gong, X. Q.; Yao, Y. F.; Yang, H. G. *Nat. Commun.* **2016**, *7*, 11918.

(104) Zhao, J.; Shi, R.; Li, Z.; Zhou, C.; Zhang, T. *Nano Sel.* **2020**, *1*, 12–29.

(105) Schoenmakers, G. H.; Vanmaekelbergh, D.; Kelly, J. J. *J. Chem. Soc. - Faraday Trans.* **1997**, *93*,

1127–1132.

(106) Kalamaras, E.; Lianos, P. *J. Electroanal. Chem.* **2015**, *751*, 37–42.

(107) Antolini, E. *Appl. Catal. B Environ.* **2018**, *237*, 491–503.

(108) Zabidi, N. A. M.; Tapp, D.; Thomas, T. F. *J. Phys. Chem.* **1995**, *99*, 14733–14737.

(109) Sayama, K.; Mukasa, K.; Abe, R.; Abe, Y.; Arakawa, H. *Chem. Commun.* **2001**, *1*, 2416–2417.

(110) Zhao, Y.; Shi, R.; Bian, X.; Zhou, C.; Zhao, Y.; Zhang, S.; Wu, F.; Waterhouse, G. I. N.; Wu, L. Z.; Tung, C. H.; Zhang, T. *Adv. Sci.* **2019**, *6*, 1802109.

(111) Cao, S.; Shen, B.; Huang, Q.; Chen, Z. *Appl. Surf. Sci.* **2018**, *442*, 361–367.

(112) Takanabe, K. Solar Water Splitting Using Semiconductor Photocatalyst Powders. In *Solar Energy for Fuels*; Tüysüz, H., Chan, C. K., Eds.; Springer Cham: Heidelberg, New York, Dordrecht, London, 2015; Vol. 310, pp 73–103.

(113) Schleuning, M.; Ahmet, I. Y.; van de Krol, R.; May, M. M. *Sustain. Energy Fuels* **2022**, *6*, 3701–3716.

(114) Xu, Y.; Schoonen, M. A. A. *Am. Mineral.* **2000**, *85*, 543–556.

(115) Rosso, K. M.; Vaughan, D. J. *Rev. Mineral. Geochemistry* **2006**, *61*, 505–556.

(116) Zhang, Z.; Yates, J. T. *Chem. Rev.* **2012**, *112*, 5520–5551.

(117) Ohtani, B. *Phys. Chem. Chem. Phys.* **2014**, *16*, 1788–1797.

(118) Hagfeldt, A.; Grätzel, M. *Chem. Rev.* **1995**, *95*, 49–68.

(119) Yang, J.; Wang, D.; Han, H.; Li, C. A. N. *Accounts Chem. Reasearch* **2013**, *46*, 1900–1909.

(120) Linic, S.; Christopher, P.; Ingram, D. B. *Nat. Mater.* **2011**, *10*, 911–921.

(121) Ding, C.; Shi, J.; Wang, Z.; Li, C. *ACS Catal.* **2017**, *7*, 675–688.

(122) Xia, C.; Hong, T.; Nguyen, C.; Cuong, X.; Young, S. *Fuel* **2022**, *307*, 121745.

(123) Ran, J.; Jaroniec, M.; Qiao, S. Z. *Adv. Mater.* **2018**, *30*, 1704649.

(124) Jiang, R.; Li, B.; Fang, C.; Wang, J. *Adv. Mater.* **2014**, *26*, 5274–5309.

(125) Jang, J. S.; Kim, H. G.; Lee, J. S. *Catal. Today* **2012**, *185*, 270–277.

(126) Moniz, S. J. A.; Shevlin, S. A.; Martin, D. J.; Guo, Z. X.; Tang, J. *Energy Environ. Sci.* **2015**, *8*, 731–759.

(127) Yang, H. *Mater. Res. Bull.* **2021**, *142*, 111406.

(128) Schumacher, L.; Marschall, R. *Top. Curr. Chem.* **2022**, *380*, 53.

(129) Ruan, X.; Cui, X.; Cui, Y.; Fan, X.; Li, Z.; Xie, T.; Ba, K.; Jia, G.; Zhang, H.; Zhang, L.; Zhang, W.; Zhao, X.; Leng, J.; Jin, S.; Singh, D. J.; Zheng, W. *Adv. Energy Mater.* **2022**, *12*, 2200298.

(130) Scanlon, D. O.; Dunnill, C. W.; Buckeridge, J.; Shevlin, S. A.; Logsdail, A. J.; Woodley, S. M.; Catlow, C. R. A.; Powell, M. J.; Palgrave, R. G.; Parkin, I. P.; Watson, G. W.; Keal, T. W.; Sherwood, P.; Walsh, A.; Sokol, A. A. *Nat. Mater.* **2013**, *12*, 798–801.

(131) Yang, X.; Qian, F.; Zou, G.; Li, M.; Lu, J.; Li, Y.; Bao, M. *Appl. Catal. B Environ.* **2016**, *193*, 22–35.

(132) Xu, Q.; Zhang, L.; Cheng, B.; Fan, J.; Yu, J. *Chem* **2020**, *6*, 1543–1559.

(133) Yuan, Y.; Guo, R.; Hong, L.; Ji, X.; Lin, Z.; Li, Z.; Pan, W. *Mater. Today Energy* **2021**, *21*, 100829.

(134) Ng, B.; Putri, L. K.; Kong, X. Y.; Teh, Y. W.; Pasbakhsh, P.; Chai, S. *Adv. Sci.* **2020**, *7*, 1903171.

(135) Zhou, P.; Yu, J.; Jaroniec, M. *Adv. Mater.* **2014**, *26*, 4920–4935.

(136) Govindjee; Shevela, D.; Björn, L. O. *Photosynth. Res.* **2017**, *133*, 5–15.

(137) Li, H.; Tu, W.; Zhou, Y.; Zou, Z. *Adv. Sci.* **2016**, *3*, 1500389.

(138) Sasaki, Y.; Iwase, A.; Kato, H.; Kudo, A. *J. Catal.* **2008**, *259*, 133–137.

(139) Miseki, Y.; Fujiyoshi, S.; Gunji, T.; Sayama, K. *J. Phys. Chem. C* **2017**, *121*, 9691–9697.

(140) Zhang, X.; Peng, T.; Song, S. *J. Mater. Chem. A* **2016**, *4*, 2365–2402.

(141) Watanabe, M. *Sci. Technol. Adv. Mater.* **2017**, *18*, 705–723.

(142) Shao, W.; Wang, H.; Zhang, X. *Dalt. Trans.* **2018**, *47*, 12642–12646.

(143) Yu, X.; Ng, S. F.; Putri, L. K.; Tan, L. L.; Mohamed, A. R.; Ong, W. J. *Small* **2021**, *17*, 2006851.

(144) Kudo, A.; Kato, H.; Tsuji, I. *Chem. Lett.* **2004**, *33*, 1534–1539.

(145) Basavarajappa, P. S.; Patil, S. B.; Ganganagappa, N.; Reddy, K. R.; Raghu, A. V.; Reddy, C. V. *Int. J. Hydrogen Energy* **2020**, *45*, 7764–7778.

(146) Shwetharani, R.; Sakar, M.; Fernando, C. A. N.; Binas, V.; Balakrishna, R. G. *Catal. Sci. Technol.* **2019**, *9*, 12–46.

(147) Guo, R.; Tian, R.; Shi, D.; Li, H.; Liu, H. *ACS Appl. Nano Mater.* **2019**, *2*, 7755–7765.

(148) Ksibi, M.; Rossignol, S.; Tatibouët, J. M.; Trapalis, C. *Mater. Lett.* **2008**, *62*, 4204–4206.

(149) Lu, J.; Jin, H.; Dai, Y.; Yang, K.; Huang, B. *Int. J. Photoenergy* **2012**, *2012*, 928503.

(150) Takata, T.; Domen, K. *J. Phys. Chem. C* **2009**, *113*, 19386–19388.

(151) Zhao, Z.; Goncalves, R. V.; Barman, S. K.; Willard, E. J.; Byle, E.; Perry, R.; Wu, Z.; Huda, M. N.; Moulé, A. J.; Osterloh, F. E. *Energy Environ. Sci.* **2019**, *12*, 1385–1395.

(152) Xiao, J.; Hisatomi, T.; Domen, K. *Acc. Chem. Res.* **2023**, *56*, 878–888.

(153) Zhou, W.; Fu, H. *Inorg. Chem. Front.* **2018**, *5*, 1240–1254.

(154) Kato, H.; Kudo, A. *J. Phys. Chem. B* **2002**, *106*, 5029–5034.

(155) Hojamberdiev, M.; Vargas, R.; Kadirova, Z. C.; Kato, K.; Sena, H.; Krasnov, A. G.; Yamakata, A.; Teshima, K.; Lerch, M. *ACS Catal.* **2022**, *12*, 1403–1414.

(156) Pradhan, N.; Das Adhikari, S.; Nag, A.; Sarma, D. D. *Angew. Chemie - Int. Ed.* **2017**, *56*, 7038–7054.

(157) Hao, Y.; Dong, X.; Zhai, S.; Ma, H.; Wang, X.; Zhang, X. *Chem. - A Eur. J.* **2016**, *22*, 18722–18728.

(158) Feng, Y.; Wu, J.; Chi, Q.; Li, W.; Yu, Y.; Fei, W. *Chem. Rev.* **2020**, *120*, 1710–1787.

(159) Hao, L.; Huang, H.; Zhang, Y.; Ma, T. *Adv. Funct. Mater.* **2021**, *31*, 2100919.

(160) Bi, X.; Du, G.; Kalam, A.; Sun, D.; Yu, Y.; Su, Q.; Xu, B.; Al-Sehemi, A. G. *Chem. Eng. Sci.* **2021**, *234*, 116440.

(161) Peng, G.; Wu, J.; Wang, M.; Niklas, J.; Zhou, H.; Liu, C. *Nano Lett.* **2020**, *20*, 2879–2885.

(162) Niu, P.; Liu, G.; Cheng, H. M. *J. Phys. Chem. C* **2012**, *116*, 11013–11018.

(163) Meng, A.; Teng, Z.; Zhang, Q.; Su, C. *Chem. - An Asian J.* **2020**, *15*, 3405–3415.

(164) Jiang, L.; Yang, J.; Yuan, X.; Guo, J.; Liang, J.; Tang, W.; Chen, Y.; Li, X.; Wang, H.; Chu, W. *Adv. Colloid Interface Sci.* **2021**, *296*, 102523.

(165) Zhang, X.; Wang, C.; Chen, J.; Zhu, W.; Liao, A.; Li, Y.; Wang, J.; Ma, L. *ACS Appl. Mater. Interfaces* **2014**, *6*, 20625–20633.

(166) Liao, J.; Cui, W.; Li, J.; Sheng, J.; Wang, H.; Dong, X.; Chen, P.; Jiang, G.; Wang, Z.; Dong, F. *Chem. Eng. J.* **2020**, *379*, 122282.

(167) Gao, J.; Xue, J.; Jia, S.; Shen, Q.; Zhang, X.; Jia, H.; Liu, X.; Li, Q.; Wu, Y. *ACS Appl. Mater. Interfaces* **2021**, *13*, 18758–18771.

(168) Hou, L.; Zhang, M.; Guan, Z.; Li, Q.; Yang, J. *Appl. Surf. Sci.* **2018**, *428*, 640–647.

(169) Li, X.; Sun, X.; Zhang, L.; Sun, S.; Wang, W. *J. Mater. Chem. A* **2018**, *6*, 3005–3011.

(170) Zhao, Y.; Zheng, L.; Shi, R.; Zhang, S.; Bian, X.; Wu, F.; Cao, X.; Waterhouse, G. I. N.; Zhang, T. *Adv. Energy Mater.* **2020**, *10*, 2002199.

(171) Shi, R.; Zhao, Y.; Waterhouse, G. I. N.; Zhang, S.; Zhang, T. *ACS Catal.* **2019**, *9*, 9739–9750.

(172) Liu, J.; Wei, Z.; Shangguan, W. *ChemCatChem* **2019**, *11*, 6177–6189.

(173) Bai, S.; Zhang, N.; Gao, C.; Xiong, Y. *Nano Energy* **2018**, *53*, 296–336.

(174) Yan, D.; Li, H.; Chen, C.; Zou, Y.; Wang, S. *Small Methods* **2019**, *3*, 1800331.

(175) Li, C.; Wang, T.; Zhao, Z. J.; Yang, W.; Li, J. F.; Li, A.; Yang, Z.; Ozin, G. A.; Gong, J. *Angew. Chemie - Int. Ed.* **2018**, *57*, 5278–5282.

(176) Lv, C.; Qian, Y.; Yan, C.; Ding, Y.; Liu, Y.; Chen, G.; Yu, G. *Angew. Chemie - Int. Ed.* **2018**, *57*, 10246–10250.

(177) Liu, G.; Yu, J. C.; Lu, G. Q.; Cheng, H. M. *Chem. Commun.* **2011**, *47*, 6763–6783.

(178) Bai, S.; Wang, L.; Li, Z.; Xiong, Y. *Adv. Sci.* **2017**, *4*, 1600216.

(179) Bai, Y.; Ye, L.; Chen, T.; Wang, L.; Shi, X.; Zhang, X.; Chen, D. *ACS Appl. Mater. Interfaces* **2016**, *8*, 27661–27668.

(180) Li, J.; Yu, Y.; Zhang, L. *Nanoscale* **2014**, *6*, 8473–8488.

(181) Lin, L.; Hisatomi, T.; Chen, S.; Takata, T.; Domen, K. *Trends Chem.* **2020**, *2*, 813–824.

(182) Zuo, S.; Wu, Z. P.; Zhang, H.; Lou, X. W. *Adv. Energy Mater.* **2022**, *12*, 2103383.

(183) Song, J.; Wei, C.; Huang, Z. F.; Liu, C.; Zeng, L.; Wang, X.; Xu, Z. J. *Chem. Soc. Rev.* **2020**, *49*, 2196–2214.

(184) Kudo, A.; Miseki, Y. *Chem. Soc. Rev.* **2009**, *38*, 253–278.

(185) Hisatomi, T.; Takanabe, K.; Domen, K. *Catal. Letters* **2015**, *145*, 95–108.

(186) Tan, M. X.; Kenyon, C. N.; Lewis, N. S. *J. Phys. Chem.* **1994**, *98*, 4959–4962.

(187) Liu, B.; Zhao, X.; Terashima, C.; Fujishima, A.; Nakata, K. *Phys. Chem. Chem. Phys.* **2014**, *16*,

8751–8760.

(188) Bie, C.; Wang, L.; Yu, J. *Chem* **2022**, *8*, 1567–1574.

(189) Peter, L. M.; Upul Wijayantha, K. G. *ChemPhysChem* **2014**, *15*, 1983–1995.

(190) Ahn, H. J.; Kwak, M. J.; Lee, J. S.; Yoon, K. Y.; Jang, J. H. *J. Mater. Chem. A* **2014**, *2*, 19999–20003.

(191) Morrish, R.; Rahman, M.; MacElroy, J. M. D.; Wolden, C. A. *ChemSusChem* **2011**, *4*, 474–479.

(192) Fujisawa, J. ichi; Eda, T.; Hanaya, M. *Chem. Phys. Lett.* **2017**, *685*, 23–26.

(193) Xu, Q.; Zhu, B.; Jiang, C.; Cheng, B.; Yu, J. *Sol. RRL* **2018**, *2*, 1800006.

(194) Sivula, K.; Formal, F. Le; Grätzel, M. *Chem. Mater.* **2009**, *21*, 2862–2867.

(195) Kalanur, S. S.; Noh, Y. G.; Seo, H. *Appl. Surf. Sci.* **2020**, *509*, 145253.

(196) Miyazawa, N.; Usami, N.; Wang, H.; Kubo, T.; Segawa, H.; Takeda, T.; Kobayashi, M.; Mita, Y.; Higo, A. *IEEE Trans. Semicond. Manuf.* **2021**, *34*, 256–261.

(197) Martinez Suarez, C.; Hernández, S.; Russo, N. *Appl. Catal. A Gen.* **2015**, *504*, 158–170.

(198) Oladeji, I. O.; Chow, L.; Ferekides, C. S.; Viswanathan, V.; Zhao, Z. *Sol. Energy Mater. Sol. Cells* **2000**, *61*, 203–211.

(199) Katsumata, H.; Higashi, F.; Kobayashi, Y.; Tateishi, I.; Furukawa, M.; Kaneco, S. *Sci. Rep.* **2019**, *9*, 14873.

(200) Choudhury, P.; Ravavarapu, L.; Dekle, R.; Chowdhury, S. *J. Phys. Chem. C* **2017**, *121*, 2959–2967.

(201) Sivula, K.; Van De Krol, R. *Nat. Rev. Mater.* **2016**, *1*, 15010.

(202) Guo, Q.; Zhou, C.; Ma, Z.; Yang, X. *Adv. Mater.* **2019**, *31*, 1901997.

(203) Sekiya, T.; Yagisawa, T.; Kamiya, N.; Mulmi, D. Das; Kurita, S.; Murakami, Y.; Kodaira, T. *J. Phys. Soc. Japan* **2004**, *73*, 703–710.

(204) Foo, C.; Li, Y.; Lebedev, K.; Chen, T.; Day, S.; Tang, C.; Tsang, S. C. E. *Nat. Commun.* **2021**, *12*, 661.

(205) Wang, H.; Chen, W.; Zhang, J.; Huang, C.; Mao, L. *Int. J. Hydrogen Energy* **2015**, *40*, 340–345.

(206) Shen, R.; Ren, D.; Ding, Y.; Guan, Y.; Ng, Y. H.; Zhang, P.; Li, X. *Sci. China Mater.* **2020**, *63*, 2153–2188.

(207) Jang, J. S.; Joshi, U. A.; Lee, J. S. *J. Phys. Chem. C* **2007**, *111*, 13280–13287.

(208) Wang, X.; Liu, G.; Wang, L.; Chen, Z. G.; Lu, G. Q.; Cheng, H. M. *Adv. Energy Mater.* **2012**, *2*, 42–46.

(209) Chen, J.; Wu, X.-J.; Yin, L.; Li, B.; Hong, X.; Fan, Z.; Chen, B.; Xue, C.; Zhang, H. *Angew. Chemie* **2015**, *127*, 1226–1230.

(210) Wang, X.; Liu, G.; Chen, Z. G.; Li, F.; Wang, L.; Lu, G. Q.; Cheng, H. M. *Chem. Commun.* **2009**, 3452–3454.

(211) Wang, X.; Maeda, K.; Thomas, A.; Takanabe, K.; Xin, G.; Carlsson, J. M.; Domen, K.; Antonietti, M. *Nat. Mater.* **2009**, *8*, 76–80.

(212) Ye, S.; Wang, R.; Wu, M. Z.; Yuan, Y. P. *Appl. Surf. Sci.* **2015**, *358*, 15–27.

(213) Ong, W. J.; Tan, L. L.; Ng, Y. H.; Yong, S. T.; Chai, S. P. *Chem. Rev.* **2016**, *116*, 7159–7329.

(214) Da Silva, E. S.; Moura, N. M. M.; Coutinho, A.; Dražić, G.; Teixeira, B. M. S.; Sobolev, N. A.; Silva, C. G.; Neves, M. G. P. M. S.; Prieto, M.; Faria, J. L. *ChemSusChem* **2018**, *11*, 2681–2694.

(215) Cao, S.; Yu, J. *J. Phys. Chem. Lett.* **2014**, *5*, 2101–2107.

(216) Shen, R.; Xie, J.; Zhang, H.; Zhang, A.; Chen, X.; Li, X. *ACS Sustain. Chem. Eng.* **2018**, *6*, 816–826.

(217) Zhang, H.; Yu, A. *J. Phys. Chem. C* **2014**, *118*, 11628–11635.

(218) Zhou, L.; Zhang, H.; Sun, H.; Liu, S.; Tade, M. O.; Wang, S.; Jin, W. *Catal. Sci. Technol.* **2016**, *6*, 7002–7023.

(219) Shu, Z.; Xie, C.; Zhou, J.; Li, T.; Chen, Y.; Wang, W.; Tan, Y.; Zhao, Z. *J. Alloys Compd.* **2018**, *747*, 140–148.

(220) Tay, Q.; Kanhere, P.; Ng, C. F.; Chen, S.; Chakraborty, S.; Huan, A. C. H.; Sum, T. C.; Ahuja, R.; Chen, Z. *Chem. Mater.* **2015**, *27*, 4930–4933.

(221) Lotsch, B. V.; Döblinger, M.; Sehnert, J.; Seyfarth, L.; Senker, J.; Oeckler, O.; Schnick, W. *Chem. - A Eur. J.* **2007**, *13*, 4969–4980.

(222) Lau, V. W.; Lotsch, B. V. *Adv. Energy Mater.* **2022**, *12*, 2101078.

(223) Tyborski, T.; Merschjann, C.; Orthmann, S.; Yang, F.; Lux-Steiner, M. C.; Schedel-Niedrig, T. *J. Phys. Condens. Matter* **2013**, *25*, 395402.

(224) Fina, F.; Callear, S. K.; Carins, G. M.; Irvine, J. T. S. *Chem. Mater.* **2015**, *27*, 2612–2618.

(225) Schlomberg, H.; Kröger, J.; Savasci, G.; Terban, M. W.; Bette, S.; Moudrakovski, I.; Duppel, V.; Podjaski, F.; Siegel, R.; Senker, J.; Dinnebier, R. E.; Ochsenfeld, C.; Lotsch, B. V. *Chem. Mater.* **2019**, *31*, 7478–7486.

(226) Bhunia, M. K.; Yamauchi, K.; Takanabe, K. *Angew. Chemie* **2014**, *126*, 11181–11185.

(227) Jin, A.; Jia, Y.; Chen, C.; Liu, X.; Jiang, J.; Chen, X.; Zhang, F. *J. Phys. Chem. C* **2017**, *121*, 21497–21509.

(228) Bhunia, M. K.; Melissen, S.; Parida, M. R.; Sarawade, P.; Basset, J. M.; Anjum, D. H.; Mohammed, O. F.; Sautet, P.; Le Bahers, T.; Takanabe, K. *Chem. Mater.* **2015**, *27*, 8237–8247.

(229) Schwinghammer, K.; Tuffy, B.; Mesch, M. B.; Wirnhier, E.; Martineau, C.; Taulelle, F.; Schnick, W.; Senker, J.; Lotsch, B. V. *Angew. Chemie Int. Ed.* **2013**, *52*, 2435–2439.

(230) Shi, X.; Fujitsuka, M.; Kim, S.; Majima, T. *Small* **2018**, *14*, 1703277.

(231) Fu, J.; Yu, J.; Jiang, C.; Cheng, B. *Adv. Energy Mater.* **2018**, *8*, 1701503.

(232) Liu, X.; Wang, B.; Liu, M.; Liu, S.; Chen, W.; Gao, L.; Li, X. *Appl. Surf. Sci.* **2021**, *554*, 149617.

(233) Elbanna, O.; Fujitsuka, M.; Majima, T. *ACS Appl. Mater. Interfaces* **2017**, *9*, 34844–34854.

(234) Zhang, K.; Jin, L.; Yang, Y.; Guo, K.; Hu, F. *J. Photochem. Photobiol. A Chem.* **2019**, *380*, 111859.

(235) Liu, Y.; Zheng, X.; Yang, Y.; Li, J.; Liu, W.; Shen, Y.; Tian, X. Photocatalytic Hydrogen Evolution Using Ternary-Metal-Sulfide/TiO2 Heterojunction Photocatalysts. *ChemCatChem*. March 8, 2022, p e202101439.

(236) He, H.; Lin, J.; Fu, W.; Wang, X.; Wang, H.; Zeng, Q.; Gu, Q.; Li, Y.; Yan, C.; Tay, B. K.; Xue, C.; Hu, X.; Pantelides, S. T.; Zhou, W.; Liu, Z. *Adv. Energy Mater.* **2016**, *6*, 1600464.

(237) Low, J.; Qiu, S.; Xu, D.; Jiang, C.; Cheng, B. *Appl. Surf. Sci.* **2018**, *434*, 423–432.

(238) An, X.; Kays, J. C.; Lightcap, I. V.; Ouyang, T.; Dennis, A. M.; Reinhard, B. M. *ACS Nano* **2022**, *16*, 6813–6824.

(239) Borgwardt, M.; Mahl, J.; Roth, F.; Wenthaus, L.; Brauße, F.; Blum, M.; Schwarzburg, K.; Liu, G.; Toma, F. M.; Gessner, O. *J. Phys. Chem. Lett.* **2020**, *11*, 5476–5481.

(240) Iwase, A.; Kato, H.; Kudo, A. *Catal. Letters* **2006**, *108*, 7–10.

(241) Kraeutler, B.; Bard, A. J. *J. Am. Chem. Soc.* **1978**, *100*, 4317–4318.

(242) Wenderich, K.; Mul, G. *Chem. Rev.* **2016**, *116*, 14587–14619.

(243) Zhao, D.; Sun, B.; Li, X.; Qin, L.; Kang, S.; Wang, D. *RSC Adv.* **2016**, *6*, 33120–33125.

(244) Cao, S.; Chen, Y.; Hou, C. C.; Lv, X. J.; Fu, W. F. *J. Mater. Chem. A* **2015**, *3*, 6096–6101.

(245) Lu, K. Q.; Qi, M. Y.; Tang, Z. R.; Xu, Y. J. *Langmuir* **2019**, *35*, 11056–11065.

(246) Liang, Z.; Xue, Y.; Wang, X.; Zhou, Y.; Zhang, X.; Cui, H.; Cheng, G.; Tian, J. *Chem. Eng. J.* **2021**, *421*, 130016.

(247) Zhang, L.; Tian, B.; Chen, F.; Zhang, J. *Int. J. Hydrogen Energy* **2012**, *37*, 17060–17067.

(248) Wang, Z.; Fan, J.; Cheng, B.; Yu, J.; Xu, J. *Mater. Today Phys.* **2020**, *15*, 100279.

(249) Luo, B.; Song, R.; Zeng, Z.; Jing, D. *Appl. Surf. Sci.* **2020**, *511*, 145646.

(250) Chang, K.; Hai, X.; Ye, J. *Adv. Energy Mater.* **2016**, *6*, 1502555.

(251) Zhu, Q.; Xu, Z.; Qiu, B.; Xing, M.; Zhang, J. *Small* **2021**, *2101070*, 2101070.

(252) Zhao, H.; Mao, Q.; Jian, L.; Dong, Y.; Zhu, Y. *Chinese J. Catal.* **2022**, *43*, 1774–1804.

(253) Ohno, T.; Tanigawa, F.; Fujihara, K.; Izumi, S.; Matsumura, M. *J. Photochem. Photobiol. A Chem.* **1999**, *127*, 107–110.

(254) Niishiro, R.; Konta, R.; Kato, H.; Chun, W. J.; Asakura, K.; Kudo, A. *J. Phys. Chem. C* **2007**, *111*, 17420–17426.

(255) Yao, W.; Iwai, H.; Ye, J. *J. Chem. Soc. Dalt. Trans.* **2008**, 1426–1430.

(256) Pilli, S. K.; Furtak, T. E.; Brown, L. D.; Deutsch, T. G.; Turner, J. A.; Herring, A. M. *Energy Environ. Sci.* **2011**, *4*, 5028–5034.

(257) Kim, T. W.; Choi, K.-S. *Science* **2014**, *343*, 990–995.

(258) Seabold, J. A.; Choi, K. S. *Chem. Mater.* **2011**, *23*, 1105–1112.

(259) Reinhard, S.; Rechberger, F.; Niederberger, M. *Chempluschem* **2016**, *81*, 935–940.

(260) Ma, S. S. K.; Maeda, K.; Abe, R.; Domen, K. *Energy Environ. Sci.* **2012**, *5*, 8390–8397.

(261) Bassi, P. S.; Xianglin, L.; Fang, Y.; Loo, J. S. C.; Barber, J.; Wong, L. H. *Phys. Chem. Chem. Phys.* **2016**, *18*, 30370–30378.

(262) Young, K. M. H.; Klahr, B. M.; Zandi, O.; Hamann, T. W. *Catal. Sci. Technol.* **2013**, *3*, 1660–1671.

(263) Ulpe, A. C.; Bauerfeind, K. C. L.; Granone, L. I.; Arimi, A.; Megatif, L.; Dillert, R.; Warfsmann, S.; Taffa, D. H.; Wark, M.; Bahnemann, D. W.; Bredow, T. *Zeitschrift fur Phys. Chemie* **2020**, *234*, 719–776.

(264) Ahmed, M. G.; Kandiel, T. A.; Ahmed, A. Y.; Kretschmer, I.; Rashwan, F.; Bahnemann, D. *J. Phys. Chem. C* **2015**, *119*, 5864–5871.

(265) Cai, J.; Li, S.; Qin, G. *Appl. Surf. Sci.* **2019**, *466*, 92–98.

(266) Zhu, X.; Guijarro, N.; Liu, Y.; Schouwink, P.; Wells, R. A.; Le Formal, F.; Sun, S.; Gao, C.; Sivula, K. *Adv. Mater.* **2018**, *30*, 1801612.

(267) Guijarro, N.; Bornoz, P.; Prévot, M.; Yu, X.; Zhu, X.; Johnson, M.; Jeanbourquin, X.; Le Formal, F.; Sivula, K. *Sustain. Energy Fuels* **2018**, *2*, 103–117.

(268) Cao, J.; Xing, J.; Zhang, Y.; Tong, H.; Bi, Y.; Kako, T.; Takeguchi, M.; Ye, J. *Langmuir* **2013**, *29*, 3116–3124.

(269) McDonald, K. J.; Choi, K. S. *Chem. Mater.* **2011**, *23*, 4863–4869.

(270) Tahir, A. A.; Wijayantha, K. G. U. *J. Photochem. Photobiol. A Chem.* **2010**, *216*, 119–125.

(271) Xu, X. T.; Pan, L.; Zhang, X.; Wang, L.; Zou, J. J. *Adv. Sci.* **2019**, *6*, 1801505.

(272) Xiong, A.; Yoshinaga, T.; Ikeda, T.; Takashima, M.; Hisatomi, T.; Maeda, K.; Setoyama, T.; Teranishi, T.; Domen, K. *Eur. J. Inorg. Chem.* **2014**, *2014*, 767–772.

(273) Iwase, A.; Kato, H.; Kudo, A. *Chem. Lett.* **2005**, *34*, 946–947.

(274) Takata, T.; Jiang, J.; Sakata, Y.; Nakabayashi, M.; Shibata, N.; Nandal, V.; Seki, K.; Hisatomi, T.; Domen, K. *Nature* **2020**, *581*, 411–414.

(275) Kanan, M. W.; Surendranath, Y.; Nocera, D. G. *Chem. Soc. Rev.* **2009**, *38*, 109–114.

(276) Liu, C.; Zhang, C.; Yin, G.; Zhang, T.; Wang, W.; Ou, G.; Jin, H.; Chen, Z. *ACS Appl. Mater. Interfaces* **2021**, *13*, 13301–13310.

(277) Deng, J.; Lv, X.; Zhang, H.; Zhao, B.; Sun, X.; Zhong, J. *Phys. Chem. Chem. Phys.* **2016**, *18*, 10453–10458.

(278) Ge, G.; Liu, M.; Liu, C.; Zhou, W.; Wang, D.; Liu, L.; Ye, J. *J. Mater. Chem. A* **2019**, *7*, 9222–9229.

(279) Friebel, D.; Louie, M. W.; Bajdich, M.; Sanwald, K. E.; Cai, Y.; Wise, A. M.; Cheng, M. J.; Sokaras, D.; Weng, T. C.; Alonso-Mori, R.; Davis, R. C.; Bargar, J. R.; Nørskov, J. K.; Nilsson, A.; Bell, A. T. *J. Am. Chem. Soc.* **2015**, *137*, 1305–1313.

(280) Kim, C.; Lee, S.; Kim, S. H.; Kwon, I.; Park, J.; Kim, S.; Lee, J. H.; Park, Y. S.; Kim, Y. *Nanoscale Adv.* **2021**, *3*, 6386–6394.

(281) Laskowski, F. A. L.; Nellist, M. R.; Qiu, J.; Boettcher, S. W. *J. Am. Chem. Soc.* **2019**, *141*, 1394–1405.

(282) González-Flores, D.; Klingan, K.; Chernev, P.; Loos, S.; Mohammadi, M. R.; Pasquini, C.; Kubella, P.; Zaharieva, I.; Smith, R. D. L.; Dau, H. *Sustain. Energy Fuels* **2018**, *2*, 1986–1994.

(283) Deák, P.; Kullgren, J.; Aradi, B.; Frauenheim, T.; Kavan, L. *Electrochim. Acta* **2016**, *199*, 27–34.

(284) Avcıoğlu, C.; Avcıoğlu, S.; Bekheet, M. F.; Gurlo, A. *ACS Appl. Energy Mater.* **2023**, *6*, 1134–1154.

(285) Domen, K.; Kudo, A.; Onishi, T. *J. Catal.* **1986**, *102*, 92–98.

(286) Kudo, A.; Sayama, K.; Tanaka, A.; Asakura, K.; Domen, K.; Maruya, K.; Onishi, T. *J. Catal.* **1989**, *120*, 337–352.

(287) Hu, Y.; Mao, L.; Guan, X.; Tucker, K. A.; Xie, H.; Wu, X.; Shi, J. *Renew. Sustain. Energy Rev.* **2020**, *119*, 109527.

(288) Kim, J.; Hwang, D. W.; Kim, H. G.; Bae, S. W.; Lee, J. S.; Li, W.; Oh, S. H. *Top. Catal.* **2005**, *35*, 295–303.

(289) Kato, H.; Kudo, A. *Catal. Today* **2003**, *78*, 561–569.

(290) Shimizu, K.; Itoh, S.; Hatamachi, T.; Kodama, T.; Sato, M.; Toda, K. *Chem. Mater.* **2005**, *17*, 5161–5166.

(291) Marschall, R.; Soldat, J.; Wark, M. *Photochem. Photobiol. Sci.* **2013**, *12*, 671–677.

(292) Soldat, J.; Marschall, R.; Wark, M. *Chem. Sci.* **2014**, *5*, 3746–3752.

(293) Kato, H.; Asakura, K.; Kudo, A. *J. Am. Chem. Soc.* **2003**, *125*, 3082–3089.

(294) Yamakata, A.; Vequizo, J. J. M.; Ogawa, T.; Kato, K.; Tsuboi, S.; Furutani, N.; Ohtsuka, M.; Muto, S.; Kuwabara, A.; Sakata, Y. *ACS Catal.* **2021**, *11*, 1911–1919.

(295) Sakata, Y.; Matsuda, Y.; Nakagawa, T.; Yasunaga, R.; Imamura, H.; Teramura, K. *ChemSusChem* **2011**, *4*, 181–184.

(296) Maeda, K.; Teramura, K.; Lu, D.; Saito, N.; Inoue, Y.; Domen, K. *Angew. Chemie* **2006**, *118*, 7970–7973.

(297) Domen, K.; Kudo, A.; Onishi, T.; Kosugi, N.; Kuroda, H. *J. Phys. Chem.* **1986**, *90*, 292–295.

(298) Domen, K.; Naito, S.; Onishi, T.; Tamaru, K. *Chem. Phys. Lett.* **1982**, *92*, 433–434.

(299) Maeda, K.; Sakamoto, N.; Ikeda, T.; Ohtsuka, H.; Xiong, A.; Lu, D.; Kanehara, M.; Teranishi, T.; Domen, K. *Chem. - A Eur. J.* **2010**, *16*, 7750–7759.

(300) Maeda, K.; Teramura, K.; Lu, D.; Saito, N.; Inoue, Y.; Domen, K. *J. Phys. Chem. C* **2007**, *111*, 7554–7560.

(301) Townsend, T. K.; Browning, N. D.; Osterloh, F. E. *Energy Environ. Sci.* **2012**, *5*, 9543–9550.

(302) Liu, M.; Zhang, G.; Liang, X.; Pan, Z.; Zheng, D.; Wang, S.; Yu, Z.; Hou, Y.; Wang, X. *Angew. Chemie - Int. Ed.* **2023**, e202304694.

(303) Nishiyama, H.; Yamada, T.; Nakabayashi, M.; Maehara, Y.; Yamaguchi, M.; Kuromiya, Y.; Nagatsuma, Y.; Tokudome, H.; Akiyama, S.; Watanabe, T.; Narushima, R.; Okunaka, S.; Shibata, N.; Takata, T.; Hisatomi, T.; Domen, K. *Nature* **2021**, *598*, 304–307.

(304) Kato, H.; Sasaki, Y.; Shirakura, N.; Kudo, A. *J. Mater. Chem. A* **2013**, *1*, 12327–12333.

(305) Vonrüti, N.; Aschauer, U. *J. Mater. Chem. A* **2019**, *7*, 15741–15748.

(306) Ahmed, M.; Xinxin, G. *Inorg. Chem. Front.* **2016**, *3*, 578–590.

(307) Wang, Q.; Nakabayashi, M.; Hisatomi, T.; Sun, S.; Akiyama, S.; Wang, Z.; Pan, Z.; Xiao, X.; Watanabe, T.; Yamada, T.; Shibata, N.; Takata, T.; Domen, K. *Nat. Mater.* **2019**, *18*, 827–832.

(308) Maeda, K.; Domen, K. *MRS Bull.* **2011**, *36*, 25–31.

(309) Maeda, K.; Terashima, H.; Kase, K.; Higashi, M.; Tabata, M.; Domen, K. *Bull. Chem. Soc. Jpn.* **2008**, *81*, 927–937.

(310) Ma, S. S. K.; Maeda, K.; Domen, K. *Catal. Sci. Technol.* **2012**, *2*, 818–823.

(311) Kamata, K.; Maeda, K.; Lu, D.; Kako, Y.; Domen, K. *Chem. Phys. Lett.* **2009**, *470*, 90–94.

(312) Lukic, S.; Busser, G. W.; Zhang, S.; Menze, J.; Muhler, M.; Scheu, C.; Winterer, M. *Zeitschrift fur Phys. Chemie* **2020**, *234*, 1133–1153.

(313) Yashima, M.; Yamada, H.; Maeda, K.; Domen, K. *Chem. Commun.* **2010**, *46*, 2379–2381.

(314) Ma, B.; Yang, J.; Han, H.; Wang, J.; Zhang, X.; Li, C. *J. Phys. Chem. C* **2010**, *114*, 12818–12822.

(315) Nandal, V.; Shoji, R.; Matsuzaki, H.; Furube, A.; Lin, L.; Hisatomi, T.; Kaneko, M.; Yamashita, K.; Domen, K.; Seki, K. *Nat. Commun.* **2021**, *12*, 7055.

(316) Tao, X.; Shi, W.; Zeng, B.; Zhao, Y.; Ta, N.; Wang, S.; Adenle, A. A.; Li, R.; Li, C. *ACS Catal.* **2020**, *10*, 5941–5948.

(317) Mei, B.; Han, K.; Mul, G. *ACS Catal.* **2018**, *8*, 9154–9164.

(318) Liu, L.; Corma, A. *Nat. Rev. Chem.* **2021**, *5*, 256–276.

(319) Chen, S.; Ma, L.; Huang, Z.; Liang, G.; Zhi, C. *Cell Reports Phys. Sci.* **2022**, *3*, 100729.

(320) Ogasawara, H.; Kaya, S.; Nilsson, A. *Top. Catal.* **2016**, *59*, 439–447.

(321) Lian, X.; Gao, J.; Ding, Y.; Liu, Y.; Chen, W. *J. Phys. Chem. Lett.* **2022**, *13*, 8264–8277.

(322) Stoerzinger, K. A.; Hong, W. T.; Crumlin, E. J.; Bluhm, H.; Shao-Horn, Y. *Acc. Chem. Res.* **2015**, *48*, 2976–2983.

(323) Tesch, M. F.; Simonov, A. N. *Curr. Opin. Electrochem.* **2022**, *35*, 101038.

(324) Fabbri, E.; Nachtegaal, M.; Binninger, T.; Cheng, X.; Kim, B. J.; Durst, J.; Bozza, F.; Graule, T.; Schäublin, R.; Wiles, L.; Pertoso, M.; Danilovic, N.; Ayers, K. E.; Schmidt, T. J. *Nat. Mater.* **2017**, *16*, 925–931.

(325) Caudillo-Flores, U.; Muñoz-Batista, M. J.; Kubacka, A.; Fernández-García, M. *ChemPhotoChem* **2018**, *2*, 777–785.

(326) Guo, S.; Li, Y.; Tang, S.; Zhang, Y.; Li, X.; Sobrido, A. J.; Titirici, M. M.; Wei, B. *Adv. Funct. Mater.* **2020**, *30*, 2003035.

(327) Spanu, D.; Minguzzi, A.; Recchia, S.; Shahvardanfard, F.; Tomanec, O.; Zboril, R.; Schmuki, P.; Ghigna, P.; Altomare, M. *ACS Catal.* **2020**, *10*, 8293–8302.

(328) Lawley, C.; Nachtegaal, M.; Stahn, J.; Roddatis, V.; Döbeli, M.; Schmidt, T. J.; Pergolesi, D.; Lippert, T. *Nat. Commun.* **2020**, *11*, 1728.

(329) Hoffman, B. M.; Lukoyanov, D.; Yang, Z. Y.; Dean, D. R.; Seefeldt, L. C. *Chem. Rev.* **2014**, *114*, 4041–4062.

(330) Erisman, J. W.; Sutton, M. A.; Galloway, J.; Klimont, Z.; Winiwarter, W. *Nat. Geosci.* **2008**, *1*, 636–639.

(331) Wang, M.; Khan, M. A.; Mohsin, I.; Wicks, J.; Ip, A. H.; Sumon, K. Z.; Dinh, C. T.; Sargent, E. H.; Gates, I. D.; Kibria, M. G. *Energy Environ. Sci.* **2021**, *14*, 2535–2548.

(332) *Food and Agriculture Organization of United Nations, World Fertilizer Trends and Outlook to 2020*; 2017.

(333) Ghavam, S.; Vahdati, M.; Wilson, I. A. G.; Styring, P. *Front. Energy Res.* **2021**, *9*, 580808.

(334) Kandemir, T.; Schuster, M. E.; Senyshyn, A.; Behrens, M.; Schlögl, R. *Angew. Chemie - Int. Ed.* **2013**, *52*, 12723–12726.

(335) MacFarlane, D. R.; Cherepanov, P. V.; Choi, J.; Suryanto, B. H. R.; Hodgetts, R. Y.; Bakker, J. M.; Ferrero Vallana, F. M.; Simonov, A. N. *Joule* **2020**, *4*, 1186–1205.

(336) Quach, T. Q.; Giap, V. T.; Keun Lee, D.; Pineda Israel, T.; Young Ahn, K. *Appl. Energy* **2022**, *324*, 119718.

(337) Haber, F.; Le Rossignol, R. *Zeitschrift für Elektrochemie und Angew. Phys. Chemie* **1913**, *19*, 53–108.

(338) Schlögl, R. *Angew. Chemie - Int. Ed.* **2003**, *42*, 2004–2008.

(339) Smith, C.; Hill, A. K.; Torrente-Murciano, L. *Energy Environ. Sci.* **2020**, *13*, 331–344.

(340) Bicer, Y.; Dincer, I.; Zamfirescu, C.; Vezina, G.; Raso, F. *J. Clean. Prod.* **2016**, *135*, 1379–1395.

(341) Liu, X.; Elgowainy, A.; Wang, M. *Green Chem.* **2020**, *22*, 5751–5761.

(342) Chen, S.; Liu, D.; Peng, T. *Sol. RRL* **2021**, *5*, 2000487.

(343) Li, M.; Huang, H.; Low, J.; Gao, C.; Long, R.; Xiong, Y. *Small Methods* **2019**, *3*, 1800388.

(344) Cheng, M.; Xiao, C.; Xie, Y. *J. Mater. Chem. A* **2019**, *7*, 19616–19633.

(345) Shen, H.; Yang, M.; Hao, L.; Wang, J.; Strunk, J.; Sun, Z. *Nano Res.* **2022**, *15*, 2773–2809.

(346) Wei, Y.; Jiang, W.; Liu, Y.; Bai, X.; Hao, D.; Ni, B. J. *Nanoscale* **2022**, *14*, 2990–2997.

(347) Pérez-González, A.; Jimenez-Vicente, E.; Gies-Elterlein, J.; Salinero-Lanzarot, A.; Yang, Z. Y.; Einsle, O.; Seefeld, L. C.; Dean, D. R. *MBio* **2021**, *12*, e01568-21.

(348) Buscagan, T. M.; Rees, D. C. *Joule* **2019**, *3*, 2662–2678.

(349) Lee, C. C.; Kang, W.; Jasniewski, A. J.; Stiebritz, M. T.; Tanifuji, K.; Ribbe, M. W.; Hu, Y. *Nat. Catal.* **2022**, *5*, 443–454.

(350) Sippel, D.; Rohde, M.; Netzer, J.; Trncik, C.; Gies, J.; Grunau, K.; Djurdjevic, I.; Decamps, L.; Andrade, S. L. A.; Einsle, O. *Science* **2018**, *359*, 1484–1489.

(351) Einsle, O.; Rees, D. C. *Chem. Rev.* **2020**, *120*, 4969–5004.

(352) Jia, H. P.; Quadrelli, E. A. *Chem. Soc. Rev.* **2014**, *43*, 547–564.

(353) Liu, J.; Kelley, M. S.; Wu, W.; Banerjee, A.; Douvalis, A. P.; Wu, J.; Zhang, Y.; Schatz, G. C.; Kanatzidis, M. G. *Proc. Natl. Acad. Sci. U. S. A.* **2016**, *113*, 5530–5535.

(354) Tanifuji, K.; Ohki, Y. *Chem. Rev.* **2020**, *120*, 5194–5251.

(355) Wang, H. Bin; Wang, J. Q.; Zhang, R.; Cheng, C. Q.; Qiu, K. W.; Yang, Y. J.; Mao, J.; Liu, H.; Du, M.; Dong, C. K.; Du, X. W. *ACS Catal.* **2020**, *10*, 4914–4921.

(356) Chu, K.; Li, Q. Q.; Cheng, Y. H.; Liu, Y. P. *ACS Appl. Mater. Interfaces* **2020**, *12*, 11789–11796.

(357) Tian, L.; Zhao, J.; Ren, X.; Sun, X.; Wei, Q.; Wu, D. *ChemistryOpen* **2021**, *10*, 1041–1054.

(358) Chen, C.; Liu, Y.; Yao, Y. *Eur. J. Inorg. Chem.* **2020**, *2020*, 3236–3241.

(359) Brown, K. A.; Harris, D. F.; Wilker, M. B.; Rasmussen, A.; Khadka, N.; Hamby, H.; Keable, S.; Dukovic, G.; Peters, J. W.; Seefeldt, L. C.; King, P. W. *Science* **2016**, *352*, 448–450.

(360) Li, G.; Li, F.; Liu, J.; Fan, C. *J. Solid State Chem.* **2020**, *285*, 121245.

(361) Coucouvanis, D. *Acc. Chem. Res.* **1991**, *24*.

(362) Wang, J.; Nan, H.; Tian, Y.; Chu, K. *ACS Sustain. Chem. Eng.* **2020**, *8*, 12733–12740.

(363) Chu, K.; Liu, Y. P.; Li, Y. B.; Guo, Y. L.; Tian, Y. *ACS Appl. Mater. Interfaces* **2020**, *12*, 7081–7090.

(364) Feng, D.; Zhang, X.; Sun, Y.; Ma, T. *Nano Mater. Sci.* **2020**, *2*, 132–139.

(365) Gao, L.; Guo, C.; Zhao, M.; Yang, H.; Ma, X.; Liu, C.; Liu, X.; Sun, X.; Wei, Q. *ACS Appl. Mater. Interfaces* **2021**, *13*, 50027–50036.

(366) Wu, J.; Wang, Z. X.; Li, S.; Niu, S.; Zhang, Y.; Hu, J.; Zhao, J.; Xu, P.; Xu, P. *Chem. Commun.* **2020**,

56, 6834–6837.

(367) Luo, J.; Bai, X.; Li, Q.; Yu, X.; Li, C.; Wang, Z.; Wu, W.; Liang, Y.; Zhao, Z.; Liu, H. *Nano Energy* **2019**, *66*, 104187.

(368) Xue, X.; Chen, R.; Yan, C.; Zhao, P.; Hu, Y.; Zhang, W.; Yang, S.; Jin, Z. *Nano Res.* **2019**, *12*, 1229–1249.

(369) Hou, J.; Yang, M.; Zhang, J. *Nanoscale* **2020**, *12*, 6900–6920.

(370) Qing, G.; Ghazfar, R.; Jackowski, S. T.; Habibzadeh, F.; Ashtiani, M. M.; Chen, C. P.; Smith, M. R.; Hamann, T. W. *Chem. Rev.* **2020**, *120*, 5437–5516.

(371) Ithisuphalap, K.; Zhang, H.; Guo, L.; Yang, Q.; Yang, H.; Wu, G. *Small Methods* **2019**, *3*, 1800352.

(372) Tian, Y.; Liu, Y.; Wang, H.; Liu, L.; Hu, W. *ACS Sustain. Chem. Eng.* **2022**, *10*, 4345–4358.

(373) Zhou, F.; Azofra, L. M.; Ali, M.; Kar, M.; Simonov, A. N.; McDonnell-Worth, C.; Sun, C.; Zhang, X.; MacFarlane, D. R. *Energy Environ. Sci.* **2017**, *10*, 2516–2520.

(374) Shipman, M. A.; Symes, M. D. *Catal. Today* **2017**, *286*, 57–68.

(375) Skúlason, E.; Bligaard, T.; Gudmundsdóttir, S.; Studt, F.; Rossmeisl, J.; Abild-Pedersen, F.; Vegge, T.; Jónsson, H.; Nørskov, J. K. *Phys. Chem. Chem. Phys.* **2012**, *14*, 1235–1245.

(376) Liu, H.; Fang, Z.; Su, Y.; Suo, Y.; Huang, S.; Zhang, Y.; Ding, K. *Chem. - An Asian J.* **2018**, *13*, 799–808.

(377) Chen, G. F.; Ren, S.; Zhang, L.; Cheng, H.; Luo, Y.; Zhu, K.; Ding, L. X.; Wang, H. *Small Methods* **2019**, *3*, 1800337.

(378) Hu, C.; Chen, X.; Jin, J.; Han, Y.; Chen, S.; Ju, H.; Cai, J.; Qiu, Y.; Gao, C.; Wang, C.; Qi, Z.; Long, R.; Song, L.; Liu, Z.; Xiong, Y. *J. Am. Chem. Soc.* **2019**, *141*, 7807–7814.

(379) Bo, Y.; Wang, H.; Lin, Y.; Yang, T.; Ye, R.; Li, Y.; Hu, C.; Du, P.; Hu, Y.; Liu, Z.; Long, R.; Gao, C.; Ye, B.; Song, L.; Wu, X.; Xiong, Y. *Angew. Chemie - Int. Ed.* **2021**, *60*, 16085–16092.

(380) Montoya, J. H.; Tsai, C.; Vojvodic, A.; Nørskov, J. K. *ChemSusChem* **2015**, *8*, 2180–2186.

(381) Cherepanov, P. V.; Krebsz, M.; Hodgetts, R. Y.; Simonov, A. N.; Macfarlane, D. R. *J. Phys. Chem. C* **2021**, *125*, 11402–11410.

(382) Andersen, S. Z.; Statt, M. J.; Bukas, V. J.; Shapel, S. G.; Pedersen, J. B.; Krempl, K.; Saccoccio, M.; Chakraborty, D.; Kibsgaard, J.; Vesborg, P. C. K.; Nørskov, J.; Chorkendorff, I. *Energy Environ. Sci.* **2020**, *13*, 4291–4300.

(383) Wang, W.; Zhang, H.; Zhang, S.; Liu, Y.; Wang, G.; Sun, C.; Zhao, H. *Angew. Chemie - Int. Ed.* **2019**, *58*, 16644–16650.

(384) Abghoui, Y.; Skúlason, E. *Catal. Today* **2017**, *286*, 69–77.

(385) Ranjit, K. T.; Varadarajan, T. K.; Viswanathan, B. *J. Photochem. Photobiol. A Chem.* **1996**, *96*, 181–185.

(386) Vojvodic, A.; Medford, A. J.; Studt, F.; Abild-Pedersen, F.; Khan, T. S.; Bligaard, T.; Nørskov, J. K. *Chem. Phys. Lett.* **2014**, *598*, 108–112.

(387) Dhar, N. R.; Pant, N. N. *Nature* **1944**, *153*, 115–116.

(388) Schrauzer, G. N.; Guth, T. D. *J. Am. Chem. Soc.* **1977**, *99*, 7189–7193.

(389) Schrauzer, G. N.; Strampach, N.; Hui, L. N.; Palmer, M. R.; Salehi, J. *Proc. Natl. Acad. Sci.* **1983**, *80*, 3873–3876.

(390) Soria, J.; Conesa, J. C.; Augugliaro, V.; Palmisano, L.; Schiavello, M.; Sclafani, A. *J. Phys. Chem.* **1991**, *95*, 274–282.

(391) Bourgeois, S.; Diakite, D.; Perdereau, M. *React. Solids* **1988**, *6*, 95–104.

(392) Hirakawa, H.; Hashimoto, M.; Shiraishi, Y.; Hirai, T. *J. Am. Chem. Soc.* **2017**, *139*, 10929–10936.

(393) Xie, X. Y.; Xiao, P.; Fang, W. H.; Cui, G.; Thiel, W. *ACS Catal.* **2019**, *9*, 9178–9187.

(394) Li, C.; Gu, M. Z.; Gao, M. M.; Liu, K. N.; Zhao, X. Y.; Cao, N. W.; Feng, J.; Ren, Y. M.; Wei, T.; Zhang, M. Y. *J. Colloid Interface Sci.* **2022**, *609*, 341–352.

(395) Xue, X.; Chen, H.; Xiong, Y.; Chen, R.; Jiang, M.; Fu, G.; Xi, Z.; Zhang, X. L.; Ma, J.; Fang, W.; Jin, Z. *ACS Appl. Mater. Interfaces* **2021**, *13*, 4975–4983.

(396) Comer, B. M.; Medford, A. J. *ACS Sustain. Chem. Eng.* **2018**, *6*, 4648–4660.

(397) Zhao, Y. Y.; Zhao, Y. Y.; Shi, R.; Wang, B.; Waterhouse, G. I. N.; Wu, L. Z.; Tung, C. H.; Zhang, T. *Adv. Mater.* **2019**, *31*, 1806482.

(398) Guan, R.; Wang, D.; Zhang, Y.; Liu, C.; Xu, W.; Wang, J.; Zhao, Z.; Feng, M.; Shang, Q.; Sun, Z.

Appl. Catal. B Environ. **2021**, *282*, 119580.

(399) Liu, S.; Wang, Y.; Wang, S.; You, M.; Hong, S.; Wu, T. S.; Soo, Y. L.; Zhao, Z.; Jiang, G.; Qiu, J.; Wang, B.; Sun, Z. *ACS Sustain. Chem. Eng.* **2019**, *7*, 6813–6820.

(400) Rong, X.; Chen, H.; Rong, J.; Zhang, X.; Wei, J.; Liu, S.; Zhou, X.; Xu, J.; Qiu, F.; Wu, Z. *Chem. Eng. J.* **2019**, *371*, 286–293.

(401) Liu, G.; Tang, Z.; Gu, X.; Li, N.; Lv, H.; Huang, Y.; Zeng, Y.; Yuan, M.; Meng, Q.; Zhou, Y.; Wang, C. *Appl. Catal. B Environ.* **2022**, *317*, 121752.

(402) Li, H.; Shang, J.; Ai, Z.; Zhang, L. *J. Am. Chem. Soc.* **2015**, *137*, 6393–6399.

(403) Chu, K.; Li, Q. qing; Liu, Y. ping; Wang, J.; Cheng, Y. hua. *Appl. Catal. B Environ.* **2020**, *267*, 118693.

(404) Xiao, C.; Hu, H.; Zhang, X.; MacFarlane, D. R. *ACS Sustain. Chem. Eng.* **2017**, *5*, 10858–10863.

(405) Oshikiri, T.; Ueno, K.; Misawa, H. *Angew. Chemie - Int. Ed.* **2014**, *53*, 9802–9805.

(406) Oshikiri, T.; Ueno, K.; Misawa, H. *Angew. Chemie - Int. Ed.* **2016**, *55*, 3942–3946.

(407) Khader, M. M.; Lichtin, N. N.; Vurens, G. H.; Salmeron, M.; Somorjai, G. A. *Langmuir* **1987**, *3*, 303–304.

(408) Tennakone, K.; Ileperuma, O. A.; Thaminimulla, C. T. K.; Bandara, J. M. S. *J. Photochem. Photobiol. A Chem.* **1992**, *66*, 375–378.

(409) Miyama, H.; Fujii, N.; Nagae, Y. *Chem. Phys. Lett.* **1980**, *74*, 523–524.

(410) Tennakone, K.; Wickramanayake, S.; Fernando, C. A. N.; Ileperuma, O. A.; Punchihewa, S. *J. Chem. Soc. Chem. Commun.* **1987**, 1078–1080.

(411) Tennakone, K.; Fernando, C. A. N.; Wickramanayake, S.; Damayanthi, M. W. P.; Silva, L. H. K.; Wijeratne, W.; Illeperuma, O. A.; Punchihewa, S. *Sol. Energy Mater.* **1988**, *17*, 47–53.

(412) Huang, B.; Liu, Y.; Pang, Q.; Zhang, X.; Wang, H.; Shen, P. K. *J. Mater. Chem. A* **2020**, *8*, 22251–22256.

(413) Li, H.; Shang, J.; Shi, J.; Zhao, K.; Zhang, L. *Nanoscale* **2016**, *8*, 1986–1993.

(414) Li, H.; Li, J.; Ai, Z.; Jia, F.; Zhang, L. *Angew. Chemie - Int. Ed.* **2018**, *57*, 122–138.

(415) Liu, M.; Wang, Y.; Kong, X.; Tan, L.; Li, L.; Cheng, S.; Botton, G.; Guo, H.; Mi, Z.; Li, C. J. *iScience* **2019**, *17*, 208–216.

(416) Zhang, N.; Jalil, A.; Wu, D.; Chen, S.; Liu, Y.; Gao, C.; Ye, W.; Qi, Z.; Ju, H.; Wang, C.; Wu, X.; Song, L.; Zhu, J.; Xiong, Y. *J. Am. Chem. Soc.* **2018**, *140*, 9434–9443.

(417) Vu, M. H.; Nguyen, C. C.; Do, T. O. *ACS Sustain. Chem. Eng.* **2020**, *8*, 12321–12330.

(418) Ling, C.; Zhang, Y.; Li, Q.; Bai, X.; Shi, L.; Wang, J. *J. Am. Chem. Soc.* **2019**, *141*, 18264–18270.

(419) Comer, B. M.; Liu, Y. H.; Dixit, M. B.; Hatzell, K. B.; Ye, Y.; Crumlin, E. J.; Hatzell, M. C.; Medford, A. J. *J. Am. Chem. Soc.* **2018**, *140*, 15157–15160.

(420) Bu, T. A.; Hao, Y. C.; Gao, W. Y.; Su, X.; Chen, L. W.; Zhang, N.; Yin, A. X. *Nanoscale* **2019**, *11*, 10072–10079.

(421) Raciti, E.; Gali, S. M.; Melchionna, M.; Filippini, G.; Actis, A.; Chiesa, M.; Bevilacqua, M.; Fornasiero, P.; Prato, M.; Beljonne, D.; Lazzaroni, R. *Chem. Sci.* **2022**, *13*, 9927–9939.

(422) Cao, S.; Chen, H.; Jiang, F.; Wang, X. *Appl. Catal. B Environ.* **2018**, *224*, 222–229.

(423) Meng, Y.; Xin, G.; Chen, D. *Optoelectron. Adv. Mater. Rapid Commun.* **2011**, *5*, 648–650.

(424) Yan, S. C.; Li, Z. S.; Zou, Z. G. *Langmuir* **2009**, *25*, 10397–10401.

(425) Liu, J.; Zhang, T.; Wang, Z.; Dawson, G.; Chen, W. *J. Mater. Chem.* **2011**, *21*, 14398–14401.

(426) Dong, F.; Wu, L.; Sun, Y.; Fu, M.; Wu, Z.; Lee, S. C. *J. Mater. Chem.* **2011**, *21*, 15171–15174.

(427) Martin, D. J.; Qiu, K.; Shevlin, S. A.; Handoko, A. D.; Chen, X.; Guo, Z.; Tang, J. *Angew. Chemie - Int. Ed.* **2014**, *53*, 9240–9245.

(428) Alwin, E.; Nowicki, W.; Wojcieszak, R.; Zieliński, M.; Pietrowski, M. *Dalt. Trans.* **2020**, *49*, 12805–12813.

(429) Shi, H.; Long, S.; Hou, J.; Ye, L.; Sun, Y.; Ni, W.; Song, C.; Li, K.; Gurzadyan, G. G.; Guo, X. *Chem. - A Eur. J.* **2019**, *25*, 5028–5035.

(430) Jürgens, B.; Irran, E.; Senker, J.; Kroll, P.; Müller, H.; Schnick, W. *J. Am. Chem. Soc.* **2003**, *125*, 10288–10300.

(431) Wang, H.; Li, M.; Li, H.; Lu, Q.; Zhang, Y.; Yao, S. *Mater. Des.* **2019**, *162*, 210–218.

(432) Jiao, Y.; Hu, R.; Wang, Q.; Fu, F.; Chen, L.; Dong, Y.; Lin, Z. *Chem. - A Eur. J.* **2021**, *27*, 10925–

10931.

(433) Thomas, A.; Fischer, A.; Goettmann, F.; Antonietti, M.; Müller, J. O.; Schlögl, R.; Carlsson, J. M. *J. Mater. Chem.* **2008**, *18*, 4893–4908.

(434) Mo, Z.; She, X.; Li, Y.; Liu, L.; Huang, L.; Chen, Z.; Zhang, Q.; Xu, H.; Li, H. *RSC Adv.* **2015**, *5*, 101552–101562.

(435) Dong, F.; Wang, Z.; Sun, Y.; Ho, W. K.; Zhang, H. *J. Colloid Interface Sci.* **2013**, *401*, 70–79.

(436) Kroke, E.; Schwarz, M.; Horath-Bordon, E.; Kroll, P.; Noll, B.; Norman, A. D. *New J. Chem.* **2002**, *26*, 508–512.

(437) Chen, Z.; Savateev, A.; Pronkin, S.; Papaefthimiou, V.; Wolff, C.; Willinger, M. G.; Willinger, E.; Neher, D.; Antonietti, M.; Dontsova, D. *Adv. Mater.* **2017**, *29*, 1700555.

(438) Bojdys, M. J.; Müller, J. O.; Antonietti, M.; Thomas, A. *Chem. - A Eur. J.* **2008**, *14*, 8177–8182.

(439) Lin, L.; Yu, Z.; Wang, X. *Angew. Chemie* **2019**, *131*, 6225–6236.

(440) Kumar, A.; Raizada, P.; Hosseini-Bandegharaei, A.; Thakur, V. K.; Nguyen, V. H.; Singh, P. *J. Mater. Chem. A* **2021**, *9*, 111–153.

(441) Liu, Q.; Ai, L.; Jiang, J. *J. Mater. Chem. A* **2018**, *6*, 4102–4110.

(442) Liang, H.; Zou, H.; Hu, S. *New J. Chem.* **2017**, *41*, 8920–8926.

(443) Cao, S.; Zhou, N.; Gao, F.; Chen, H.; Jiang, F. *Appl. Catal. B Environ.* **2017**, *218*, 600–610.

(444) Gao, K.; Zhang, C.; Zhu, H.; Xia, J.; Chen, J.; Xie, F.; Zhao, X.; Tang, Z.; Wang, X. *Chem. - A Eur. J.* **2023**, *29*, e202300616.

(445) Chu, K.; Liu, Y. P.; Li, Y. B.; Guo, Y. L.; Tian, Y. *ACS Appl. Mater. Interfaces* **2020**, *12*, 7081–7090.

(446) Zhang, Q.; Hu, S.; Fan, Z.; Liu, D.; Zhao, Y.; Ma, H.; Li, F. *Dalt. Trans.* **2016**, *45*, 3497–3505.

(447) Wang, S.; Zhan, J.; Chen, K.; Ali, A.; Zeng, L.; Zhao, H.; Hu, W.; Zhu, L.; Xu, X. *ACS Sustain. Chem. Eng.* **2020**, *8*, 8214–8222.

(448) Hu, S.; Chen, X.; Li, Q.; Li, F.; Fan, Z.; Wang, H.; Wang, Y.; Zheng, B.; Wu, G. *Appl. Catal. B Environ.* **2017**, *201*, 58–69.

(449) Hu, S.; Qu, X.; Bai, J.; Li, P.; Li, Q.; Wang, F.; Song, L. *ACS Sustain. Chem. Eng.* **2017**, *5*, 6863–6872.

(450) Fu, J.; Zhu, B.; Jiang, C.; Cheng, B.; You, W.; Yu, J. *Small* **2017**, *13*, 1603938.

(451) Wang, K.; Li, Q.; Liu, B.; Cheng, B.; Ho, W.; Yu, J. *Appl. Catal. B Environ.* **2015**, *176–177*, 44–52.

(452) Chen, Y.; Su, F.; Xie, H.; Wang, R.; Ding, C.; Huang, J.; Xu, Y.; Ye, L. *Chem. Eng. J.* **2021**, *404*, 126498.

(453) Guo, H.; Shu, Z.; Chen, D.; Tan, Y.; Zhou, J.; Meng, F.; Li, T. *Chem. Phys.* **2020**, *533*, 110714.

(454) Wang, W.; Zhou, H.; Liu, Y.; Zhang, S.; Zhang, Y.; Wang, G.; Zhang, H.; Zhao, H. *Small* **2020**, *16*, 1906880.

(455) Sagara, N.; Kamimura, S.; Tsubota, T.; Ohno, T. *Appl. Catal. B Environ.* **2016**, *192*, 193–198.

(456) Zhu, Y. P.; Ren, T. Z.; Yuan, Z. Y. *ACS Appl. Mater. Interfaces* **2015**, *7*, 16850–16856.

(457) Liu, B.; Ye, L.; Wang, R.; Yang, J.; Zhang, Y.; Guan, R.; Tian, L.; Chen, X. *ACS Appl. Mater. Interfaces* **2018**, *10*, 4001–4009.

(458) Zhao, D.; Dong, C. L.; Wang, B.; Chen, C.; Huang, Y. C.; Diao, Z.; Li, S.; Guo, L.; Shen, S. *Adv. Mater.* **2019**, *31*, 1903545.

(459) Liang, C.; Niu, H. Y.; Guo, H.; Niu, C. G.; Huang, D. W.; Yang, Y. Y.; Liu, H. Y.; Shao, B. Bin; Feng, H. P. *Chem. Eng. J.* **2020**, *396*, 125395.

(460) Ye, L.; Chen, S. *Appl. Surf. Sci.* **2016**, *389*, 1076–1083.

(461) Yu, H.; Shi, R.; Zhao, Y.; Bian, T.; Zhao, Y.; Zhou, C.; Waterhouse, G. I. N.; Wu, L. Z.; Tung, C. H.; Zhang, T. *Adv. Mater.* **2017**, *29*, 1605148.

(462) Ma, H.; Shi, Z.; Li, Q.; Li, S. *J. Phys. Chem. Solids* **2016**, *99*, 51–58.

(463) Zhou, N.; Qiu, P.; Chen, H.; Jiang, F. *J. Taiwan Inst. Chem. Eng.* **2018**, *83*, 99–106.

(464) Dong, G.; Ho, W.; Wang, C. *J. Mater. Chem. A* **2015**, *3*, 23435–23441.

(465) Lin, Y.; Yang, Y.; Guo, W.; Wang, L.; Zhang, R.; Liu, Y.; Zhai, Y. *Appl. Surf. Sci.* **2021**, *560*, 150029.

(466) Praus, P.; Řeháčková, L.; Čížek, J.; Smýkalová, A.; Koštejn, M.; Pavlovský, J.; Filip Edelmannová, M.; Kočí, K. *Sci. Rep.* **2022**, *12*, 13622.

(467) Zhu, Y.; Liu, X.; Liu, H.; He, G.; Xiao, J.; Xie, H.; Sun, Y.; Han, L. *SusMat* **2022**, *2*, 617–629.

(468) Xue, Y.; Guo, Y.; Liang, Z.; Cui, H.; Tian, J. *J. Colloid Interface Sci.* **2019**, *556*, 206–213.

(469) Lau, V. W. H.; Moudrakovski, I.; Botari, T.; Weinberger, S.; Mesch, M. B.; Duppel, V.; Senker, J.; Blum, V.; Lotsch, B. V. *Nat. Commun.* **2016**, *7*, 12165.

(470) Kisch, H.; Bahnemann, D. *J. Phys. Chem. Lett.* **2015**, *6*, 1907–1910.

(471) Duan, G. Y.; Ren, Y.; Tang, Y.; Sun, Y. Z.; Chen, Y. M.; Wan, P. Y.; Yang, X. J. *ChemSusChem* **2020**, *13*, 88–96.

(472) Ngo, T. T.; Phan, A. P. H.; Yam, C. F.; Lenhoff, H. M. *Anal. Chem.* **1982**, *54*, 46–49.

(473) Andersen, S. Z.; Čolić, V.; Yang, S.; Schwalbe, J. A.; Nielander, A. C.; McEnaney, J. M.; Enemark-Rasmussen, K.; Baker, J. G.; Singh, A. R.; Rohr, B. A.; Statt, M. J.; Blair, S. J.; Mezzavilla, S.; Kibsgaard, J.; Vesborg, P. C. K.; Cargnello, M.; Bent, S. F.; Jaramillo, T. F.; Stephens, I. E. L.; Nørskov, J. K.; Chorkendorff, I. *Nature* **2019**, *570*, 504–508.

(474) Choi, J.; Suryanto, B. H. R.; Wang, D.; Du, H. L.; Hodgetts, R. Y.; Ferrero Vallana, F. M.; MacFarlane, D. R.; Simonov, A. N. *Nat. Commun.* **2020**, *11*, 5546.

(475) Tang, C.; Qiao, S. Z. *Chem. Soc. Rev.* **2019**, *48*, 3166–3180.

(476) Huang, P. W.; Hatzell, M. C. *Nat. Commun.* **2022**, *13*, 7908.

(477) Yuan, S. J.; Chen, J. J.; Lin, Z. Q.; Li, W. W.; Sheng, G. P.; Yu, H. Q. *Nat. Commun.* **2013**, *4*, 2249.

(478) Kuang, M.; Wang, Y.; Fang, W.; Tan, H.; Chen, M.; Yao, J.; Liu, C.; Xu, J.; Zhou, K.; Yan, Q. *Adv. Mater.* **2020**, *32*, 2002189.

(479) Doudrick, K.; Yang, T.; Hristovski, K.; Westerhoff, P. *Appl. Catal. B Environ.* **2013**, *136–137*, 40–47.

(480) Ren, H. T.; Jia, S. Y.; Zou, J. J.; Wu, S. H.; Han, X. *Appl. Catal. B Environ.* **2015**, *176–177*, 53–61.

(481) Ranjit, K. T.; Varadarajan, T. K.; Viswanathan, B. *J. Photochem. Photobiol. A Chem.* **1995**, *89*, 67–68.

(482) Sá, J.; Agüera, C. A.; Gross, S.; Anderson, J. A. *Appl. Catal. B Environ.* **2009**, *85*, 192–200.

(483) Geng, Z.; Chen, Z.; Li, Z.; Qi, X.; Yang, X.; Fan, W.; Guo, Y.; Zhang, L.; Huo, M. *Dalt. Trans.* **2018**, *47*, 11104–11112.

(484) Anderson, J. A. *Catal. Today* **2011**, *175*, 316–321.

(485) Rao, N. N.; Dube, S.; Manjubala; Natarajan, P. *Appl. Catal. B, Environ.* **1994**, *5*, 33–42.

(486) Altomare, M.; Selli, E. *Catal. Today* **2013**, *209*, 127–133.

(487) Lee, J.; Park, H.; Choi, W. *Environ. Sci. Technol.* **2002**, *36*, 5462–5468.

(488) Li, X.; Hao, X.; Abudula, A.; Guan, G. *J. Mater. Chem. A* **2016**, *4*, 11973–12000.

(489) Faber, M. S.; Jin, S. *Energy Environ. Sci.* **2014**, *7*, 3519–3542.

(490) Watzele, S.; Hauenstein, P.; Liang, Y.; Xue, S.; Fichtner, J.; Garlyyev, B.; Scieszka, D.; Claudel, F.; Maillard, F.; Bandarenka, A. S. *ACS Catal.* **2019**, *9*, 9222–9230.

(491) McCrory, C. C. L.; Jung, S.; Peters, J. C.; Jaramillo, T. F. *J. Am. Chem. Soc.* **2013**, *135*, 16977–16987.

(492) Jiang, W. J.; Tang, T.; Tang, T.; Zhang, Y.; Hu, J. S.; Hu, J. S. *Acc. Chem. Res.* **2020**, *53*, 1111–1123.

(493) Zhu, Y. P.; Guo, C.; Zheng, Y.; Qiao, S. Z. *Acc. Chem. Res.* **2017**, *50*, 915–923.

(494) Trasatti, S. *J. Electroanal. Chem.* **1972**, *39*, 163–184.

(495) Skúlason, E.; Tripkovic, V.; Björketun, M. E.; Gudmundsdóttir, S.; Karlberg, G.; Rossmeisl, J.; Bligaard, T.; Jónsson, H.; Nørskov, J. K. *J. Phys. Chem. C* **2010**, *114*, 18182–18197.

(496) Yan, Y.; Xia, B. Y.; Zhao, B.; Wang, X. *J. Mater. Chem. A* **2016**, *4*, 17587–17603.

(497) Zhou, Z.; Pei, Z.; Wei, L.; Zhao, S.; Jian, X.; Chen, Y. *Energy Environ. Sci.* **2020**, *13*, 3185–3206.

(498) Mohammed-Ibrahim, J.; Xiaoming, S. *J. Energy Chem.* **2019**, *34*, 111–160.

(499) Man, I. C.; Su, H. Y.; Calle-Vallejo, F.; Hansen, H. A.; Martínez, J. I.; Inoglu, N. G.; Kitchin, J.; Jaramillo, T. F.; Nørskov, J. K.; Rossmeisl, J. *ChemCatChem* **2011**, *3*, 1159–1165.

(500) Rossmeisl, J.; Qu, Z. W.; Zhu, H.; Kroes, G. J.; Nørskov, J. K. *J. Electroanal. Chem.* **2007**, *607*, 83–89.

(501) Zhang, K.; Zou, R. *Small* **2021**, *17*, 2100129.

(502) Tahir, M.; Pan, L.; Idrees, F.; Zhang, X.; Wang, L.; Zou, J. J.; Wang, Z. L. *Nano Energy* **2017**, *37*, 136–157.

(503) Kong, D.; Cha, J. J.; Wang, H.; Lee, H. R.; Cui, Y. *Energy Environ. Sci.* **2013**, *6*, 3553–3558.

(504) Faber, M. S.; Lukowski, M. A.; Ding, Q.; Kaiser, N. S.; Jin, S. *J. Phys. Chem. C* **2014**, *118*, 21347–21356.

(505) Xiao, P.; Ge, X.; Wang, H.; Liu, Z.; Fisher, A.; Wang, X. *Adv. Funct. Mater.* **2015**, *25*, 1520–1526.

(506) Alhajri, N. S.; Anjum, D. H.; Takanabe, K. *J. Mater. Chem. A* **2014**, *2*, 10548–10556.

(507) Laursen, A. B.; Patraju, K. R.; Whitaker, M. J.; Retuerto, M.; Sarkar, T.; Yao, N.; Ramanujachary, K. V.; Greenblatt, M.; Dismukes, G. C. *Energy Environ. Sci.* **2015**, *8*, 1027–1034.

(508) Wang, T.-W.; Wang, T.; Chou, W.; Wu, L.; Lin, S. *Phys. Chem. Chem. Phys.* **2021**, *23*, 2305–2312.

(509) Fu, G.; Lee, J. M. *J. Mater. Chem. A* **2019**, *7*, 9386–9405.

(510) Wang, M.; Zhang, L.; He, Y.; Zhu, H. *J. Mater. Chem. A* **2021**, *9*, 5320–5363.

(511) Bentley, C. L.; Andronescu, C.; Smialkowski, M.; Kang, M.; Tarnev, T.; Marler, B.; Unwin, P. R.; Apfel, U. P.; Schuhmann, W. *Angew. Chemie - Int. Ed.* **2018**, *57*, 4093–4097.

(512) Konkena, B.; Puring, K. J.; Sinev, I.; Piontek, S.; Khavryuchenko, O.; Dürholt, J. P.; Schmid, R.; Tüysüz, H.; Muhler, M.; Schuhmann, W.; Apfel, U. P. *Nat. Commun.* **2016**, *7*, 12269.

(513) Li, H.; Tsai, C.; Koh, A. L.; Cai, L.; Contryman, A. W.; Fragapane, A. H.; Zhao, J.; Han, H. S.; Manoharan, H. C.; Abild-Pedersen, F.; Nørskov, J. K.; Zheng, X. *Nat. Mater.* **2016**, *15*, 364–364.

(514) Voiry, D.; Salehi, M.; Silva, R.; Fujita, T.; Chen, M.; Asefa, T.; Shenoy, V. B.; Eda, G.; Chhowalla, M. *Nano Lett.* **2013**, *13*, 6222–6227.

(515) Lukowski, M. A.; Daniel, A. S.; Meng, F.; Forticaux, A.; Li, L.; Jin, S. *J. Am. Chem. Soc.* **2013**, *135*, 10274–10277.

(516) Jaramillo, T. F.; Jørgensen, K. P.; Bonde, J.; Nielsen, J. H.; Horch, S.; Chorkendorff, I. *Science* **2007**, *317*, 100–102.

(517) Hellstern, T. R.; Benck, J. D.; Kibsgaard, J.; Hahn, C.; Jaramillo, T. F. *Adv. Energy Mater.* **2016**, *6*, 1501758.

(518) Bajpai, R.; Roy, S.; Verma, S. *ACS Appl. Nano Mater.* **2022**, *5*, 8511–8525.

(519) Xiong, M.; Ivey, D. G. *Electrochim. Acta* **2018**, *260*, 872–881.

(520) Bajdich, M.; García-Mota, M.; Vojvodic, A.; Nørskov, J. K.; Bell, A. T. *J. Am. Chem. Soc.* **2013**, *135*, 13521–13530.

(521) Zhu, S.; Lei, J.; Qin, Y.; Zhang, L.; Lu, L. *RSC Adv.* **2019**, *9*, 13269–13274.

(522) Serov, A.; Andersen, N. I.; Roy, A. J.; Matanovic, I.; Artyushkova, K.; Atanassov, P. *J. Electrochem. Soc.* **2015**, *162*, F449–F454.

(523) Harada, M.; Kotegawa, F.; Kuwa, M. *ACS Appl. Energy Mater.* **2022**, *5*, 278–294.

(524) Maiyalagan, T.; Jarvis, K. A.; Therese, S.; Ferreira, P. J.; Manthiram, A. *Nat. Commun.* **2014**, *5*, 3949.

(525) Lee, S.; Manthiram, A. *ACS Energy Lett.* **2022**, *7*, 3058–3063.

(526) Wan, K.; Luo, J.; Zhou, C.; Zhang, T.; Arbiol, J.; Lu, X.; Mao, B. W.; Zhang, X.; Fransaer, J. *Adv. Funct. Mater.* **2019**, *29*, 1900315.

(527) Stern, L. A.; Hu, X. *Faraday Discuss.* **2014**, *176*, 363–379.

(528) Fink, M. F.; Weiss, M.; Marschall, R.; Roth, C. *J. Mater. Chem. A* **2022**, *10*, 15811–15838.

(529) Tesch, M. F.; Bonke, S. A.; Jones, T. E.; Shaker, M. N.; Xiao, J.; Skorupska, K.; Mom, R.; Melder, J.; Kurz, P.; Knop-Gericke, A.; Schlögl, R.; Hocking, R. K.; Simonov, A. N. *Angew. Chemie* **2019**, *131*, 3464–3470.

(530) Chen, R.; Zhang, Z.; Wang, Z.; Wu, W.; Du, S.; Zhu, W.; Lv, H.; Cheng, N. *ACS Catal.* **2022**, *12*, 13234–13246.

(531) Gong, M.; Dai, H. *Nano Res.* **2015**, *8*, 23–39.

(532) Yu, J.; Cheng, G.; Luo, W. *J. Mater. Chem. A* **2017**, *5*, 15838–15844.

(533) Zhang, G.; Zeng, J.; Yin, J.; Zuo, C.; Wen, P.; Chen, H.; Qiu, Y. *Appl. Catal. B Environ.* **2021**, *286*, 119902.

(534) Simon, C.; Timm, J.; Tetzlaff, D.; Jungmann, J.; Apfel, U. P.; Marschall, R. *ChemElectroChem* **2021**, *8*, 227–239.

(535) Lee, S.; Bai, L.; Hu, X. *Angew. Chemie* **2020**, *132*, 8149–8154.

(536) Wang, J.; Cao, F.; Shen, C.; Li, G.; Li, X.; Yang, X.; Li, S.; Qin, G. *Catal. Sci. Technol.* **2020**, *10*, 4458–4466.

(537) Cobo, S.; Heidkamp, J.; Jacques, P. A.; Fize, J.; Fourmond, V.; Guetaz, L.; Jousselme, B.; Ivanova, V.; Dau, H.; Palacin, S.; Fontecave, M.; Artero, V. *Nat. Mater.* **2012**, *11*, 802–807.

(538) Liu, M.; Li, J. *ACS Appl. Mater. Interfaces* **2016**, *8*, 2158–2165.

(539) Zhu, Y.-P.; Liu, Y.-P.; Ren, T.-Z.; Yuan, Z.-Y. *Adv. Funct. Mater.* **2015**, *25*, 7337–7347.

(540) Gultom, N. S.; Abdullah, H.; Hsu, C. N.; Kuo, D. H. *Chem. Eng. J.* **2021**, *419*, 129608.

(541) Feng, L. L.; Yu, G.; Wu, Y.; Li, G. D.; Li, H.; Sun, Y.; Asefa, T.; Chen, W.; Zou, X. *J. Am. Chem. Soc.* **2015**, *137*, 14023–14026.

(542) Wang, X.; Li, W.; Xiong, D.; Petrovykh, D. Y.; Liu, L. *Adv. Funct. Mater.* **2016**, *26*, 4067–4077.

(543) Reier, T.; Oezaslan, M.; Strasser, P. *ACS Catal.* **2012**, *2*, 1765–1772.

(544) McHugh, P. J.; Stergiou, A. D.; Symes, M. D. *Adv. Energy Mater.* **2020**, *10*, 2002453.

(545) Ding, H.; Liu, H.; Chu, W.; Wu, C.; Xie, Y. *Chem. Rev.* **2021**, *121*, 13174–13212.

(546) Burke, M. S.; Enman, L. J.; Batchellor, A. S.; Zou, S.; Boettcher, S. W. *Chem. Mater.* **2015**, *27*, 7549–7558.

(547) Zhu, Y.; Wang, J.; Chu, H.; Chu, Y. C.; Chen, H. M. *ACS Energy Lett.* **2020**, *5*, 1281–1291.

(548) Zhu, Y.; Kuo, T. R.; Li, Y. H.; Qi, M. Y.; Chen, G.; Wang, J.; Xu, Y. J.; Chen, H. M. *Energy Environ. Sci.* **2021**, *14*, 1928–1958.

(549) Montzka, S. A.; Dlugokencky, E. J.; Butler, J. H. *Nature* **2011**, *476*, 43–50.

(550) Lackner, K. S.; Brennan, S.; Matter, J. M.; Park, A. H. A.; Wright, A.; Van Der Zwaan, B. *Proc. Natl. Acad. Sci. U. S. A.* **2012**, *109*, 13156–13162.

(551) Keith, D. W.; Holmes, G.; St. Angelo, D.; Heidel, K. *Joule* **2018**, *2*, 1573–1594.

(552) Ajayi, T.; Gomes, J. S.; Bera, A. *Pet. Sci.* **2019**, *16*, 1028–1063.

(553) Zhang, Z.; Pan, S. Y.; Li, H.; Cai, J.; Olabi, A. G.; Anthony, E. J.; Manovic, V. *Renew. Sustain. Energy Rev.* **2020**, *125*, 109799.

(554) Kumar, B.; Brian, J. P.; Atla, V.; Kumari, S.; Bertram, K. A.; White, R. T.; Spurgeon, J. M. *Catal. Today* **2016**, *270*, 19–30.

(555) Zou, Y.; Wang, S. *Adv. Sci.* **2021**, *8*, 2003579.

(556) Lu, Q.; Jiao, F. *Nano Energy* **2016**, *29*, 439–456.

(557) Schneider, J.; Jia, H.; Muckerman, J. T.; Fujita, E. *Chem. Soc. Rev.* **2012**, *41*, 2036–2051.

(558) Xiao, C.; Zhang, J. *ACS Nano* **2021**, *15*, 7975–8000.

(559) Chang, F.; Xiao, M.; Miao, R.; Liu, Y.; Ren, M.; Jia, Z.; Han, D.; Yuan, Y.; Bai, Z.; Yang, L. *Electrochem. Energy Rev.* **2022**, *5*, 4.

(560) Hori, Y.; Wakebe, H. H. I.; Tsukamoto, T.; Koga, O. *Electrochim. Acta* **1994**, *39*, 1833–1839.

(561) Hussain, J.; Jónsson, H.; Skúlason, E. *ACS Catal.* **2018**, *8*, 5240–5249.

(562) Hansen, H. A.; Varley, J. B.; Peterson, A. A.; Nørskov, J. K. *J. Phys. Chem. Lett.* **2013**, *4*, 388–392.

(563) Bagger, A.; Ju, W.; Varela, A. S.; Strasser, P.; Rossmeisl, J. *ChemPhysChem* **2017**, *18*, 3266–3273.

(564) Clark, E. L.; Resasco, J.; Landers, A.; Lin, J.; Chung, L. T.; Walton, A.; Hahn, C.; Jaramillo, T. F.; Bell, A. T. *ACS Catal.* **2018**, *8*, 6560–6570.

(565) Lum, Y.; Yue, B.; Lobaccaro, P.; Bell, A. T.; Ager, J. W. *J. Phys. Chem. C* **2017**, *121*, 14191–14203.

(566) Murata, A.; Hori, Y. *Bull. Chem. Soc. Jpn.* **1991**, *64*, 123–127.

(567) Singh, M. R.; Kwon, Y.; Lum, Y.; Ager, J. W.; Bell, A. T. *J. Am. Chem. Soc.* **2016**, *138*, 13006–13012.

(568) Chen, Y.; Li, C. W.; Kanan, M. W. *J. Am. Chem. Soc.* **2012**, *134*, 19969–19972.

(569) Dunwell, M.; Yang, X.; Setzler, B. P.; Anibal, J.; Yan, Y.; Xu, B. *ACS Catal.* **2018**, *8*, 3999–4008.

(570) Buckley, A. K.; Cheng, T.; Oh, M. H.; Su, G. M.; Garrison, J.; Utan, S. W.; Zhu, C.; Toste, F. D.; Goddard, W. A.; Toma, F. M. *ACS Catal.* **2021**, *11*, 9034–9042.

(571) Zhang, Z. Q.; Banerjee, S.; Thoi, V. S.; Shoji Hall, A. *J. Phys. Chem. Lett.* **2020**, *11*, 5457–5463.

(572) Hara, K. *J. Electrochem. Soc.* **1995**, *142*, L57–L59.

(573) Karapinar, D.; Creissen, C. E.; Rivera De La Cruz, J. G.; Schreiber, M. W.; Fontecave, M. *ACS Energy Lett.* **2021**, *6*, 694–706.

(574) Ni, Z.; Liang, H.; Yi, Z.; Guo, R.; Liu, C.; Liu, Y.; Sun, H.; Liu, X. *Coord. Chem. Rev.* **2021**, *441*, 213983.

(575) Kuhl, K. P.; Cave, E. R.; Abram, D. N.; Jaramillo, T. F. *Energy Environ. Sci.* **2012**, *5*, 7050–7059.

(576) Durand, W. J.; Peterson, A. A.; Studt, F.; Abild-Pedersen, F.; Nørskov, J. K. *Surf. Sci.* **2011**, *605*, 1354–1359.

(577) Jeon, H. S.; Kunze, S.; Scholten, F.; Roldan Cuenya, B. *ACS Catal.* **2018**, *8*, 531–535.

(578) Scholten, F.; Nguyen, K. L. C.; Bruce, J. P.; Heyde, M.; Roldan Cuenya, B. *Angew. Chemie - Int. Ed.* **2021**, *60*, 19169–19175.

(579) Ding, M.; Chen, Z.; Liu, C.; Wang, Y.; Li, C.; Li, X.; Zheng, T.; Jiang, Q.; Xia, C. *Mater. Reports Energy* **2023**, *3*, 100175.

(580) Vasileff, A.; Zhi, X.; Xu, C.; Ge, L.; Jiao, Y.; Zheng, Y.; Qiao, S. Z. *ACS Catal.* **2019**, *9*, 9411–9417.

(581) Wang, S.; Kou, T.; Baker, S. E.; Duoss, E. B.; Li, Y. *Mater. Today Nano* **2020**, *12*, 100096.

(582) Kas, R.; Kortlever, R.; Milbrat, A.; Koper, M. T. M.; Mul, G.; Baltrusaitis, J. *Phys. Chem. Chem. Phys.* **2014**, *16*, 12194–12201.

(583) Dattila, F.; Garclá-Muelas, R.; López, N. *ACS Energy Lett.* **2020**, *5*, 3176–3184.

(584) Lum, Y.; Ager, J. W. *Angew. Chemie - Int. Ed.* **2018**, *57*, 551–554.

(585) Mandal, L.; Yang, K. R.; Motapothula, M. R.; Ren, D.; Lobaccaro, P.; Patra, A.; Sherburne, M.; Batista, V. S.; Yeo, B. S.; Ager, J. W.; Martin, J.; Venkatesan, T. *ACS Appl. Mater. Interfaces* **2018**, *10*, 8574–8584.

(586) Lee, S. H.; Lin, J. C.; Farmand, M.; Landers, A. T.; Feaster, J. T.; Avilés Acosta, J. E.; Beeman, J. W.; Ye, Y.; Yano, J.; Mehta, A.; Davis, R. C.; Jaramillo, T. F.; Hahn, C.; Drisdell, W. S. *J. Am. Chem. Soc.* **2021**, *143*, 588–592.

(587) Chou, T. C.; Chang, C. C.; Yu, H. L.; Yu, W. Y.; Dong, C. L.; Velasco-Vélez, J. J.; Chuang, C. H.; Chen, L. C.; Lee, J. F.; Chen, J. M.; Wu, H. L. *J. Am. Chem. Soc.* **2020**, *142*, 2857–2867.

(588) Asset, T.; Garcia, S. T.; Herrera, S.; Andersen, N.; Chen, Y.; Peterson, E. J.; Matanovic, I.; Artyushkova, K.; Lee, J.; Minteer, S. D.; Dai, S.; Pan, X.; Chavan, K.; Calabrese Barton, S.; Atanassov, P. *ACS Catal.* **2019**, *9*, 7668–7678.

(589) Jia, C.; Dastafkan, K.; Ren, W.; Yang, W.; Zhao, C. *Sustain. Energy Fuels* **2019**, *3*, 2890–2906.

(590) Cui, X.; Pan, Z.; Zhang, L.; Peng, H.; Zheng, G. *Adv. Energy Mater.* **2017**, *7*, 1701456.

(591) Zhang, T.; Han, X.; Yang, H.; Han, A.; Hu, E.; Li, Y.; Yang, X.; Wang, L.; Liu, J.; Liu, B. *Angew. Chemie Int. Ed.* **2020**, *59*, 12055–12061.

(592) Wen, G.; Ren, B.; Park, M. G.; Yang, J.; Dou, H.; Zhang, Z.; Deng, Y.; Bai, Z.; Yang, L.; Gostick, J.; Botton, G. A.; Hu, Y.; Chen, Z. *Angew. Chemie Int. Ed.* **2020**, *59*, 12860–12867.

(593) Liu, J.; Guo, C.; Vasileff, A.; Qiao, S. *Small Methods* **2017**, *1*, 1600006.

(594) Li, F.; Zhao, S. F.; Chen, L.; Khan, A.; MacFarlane, D. R.; Zhang, J. *Energy Environ. Sci.* **2016**, *9*, 216–223.

(595) Piontek, S.; Junge Puring, K.; Siegmund, D.; Smialkowski, M.; Sinev, I.; Tetzlaff, D.; Roldan Cuenya, B.; Apfel, U. P. *Chem. Sci.* **2019**, *10*, 1075–1081.

(596) Simon, C.; Zander, J.; Kottakkat, T.; Weiss, M.; Timm, J.; Roth, C.; Marschall, R. *ACS Appl. Energy Mater.* **2021**, *4*, 8702–8708.

(597) Popović, S.; Smiljanić, M.; Jovanovič, P.; Vavra, J.; Buonsanti, R.; Hodnik, N. *Angew. Chemie* **2020**, *132*, 14844–14854.

(598) Zhang, Y.; Guo, S. X.; Zhang, X.; Bond, A. M.; Zhang, J. *Nano Today* **2020**, *31*, 100835.

(599) Tsurkan, V.; Krug von Nidda, H. A.; Deisenhofer, J.; Lunkenheimer, P.; Loidl, A. *Phys. Rep.* **2021**, *926*, 1–86.

(600) Sickafus, K. E.; Wills, J. M.; Grimes, N. W. *J. Am. Ceram. Soc.* **1999**, *82*, 3279–3292.

(601) Huang, Y.; Dong, Y.; Li, S.; Lee, J.; Wang, C.; Zhu, Z.; Xue, W.; Li, Y.; Li, J. *Adv. Energy Mater.* **2021**, *11*, 2000997.

(602) Thackeray, M. M. *Adv. Energy Mater.* **2021**, *11*, 2001117.

(603) Jiang, J.; Zhang, Y. J.; Zhu, X. J.; Lu, S.; Long, L. L.; Chen, J. J. *Nano Energy* **2021**, *81*, 105619.

(604) Townsend, M. G.; Gosselin, J. R.; Horwood, J. L.; Ripley, L. G.; Tremblay, R. J. *Phys. Status Solidi* **1977**, *40*, K25–K29.

(605) Navrotsky, A.; Kleppa, O. J. *J. Inorg. Nucl. Chem.* **1967**, *29*, 2701–2714.

(606) Sanchez-Lievanos, K. R.; Stair, J. L.; Knowles, K. E. *Inorg. Chem.* **2021**, *60*, 4291–4305.

(607) Zhao, Q.; Yan, Z.; Chen, C.; Chen, J. *Chem. Rev.* **2017**, *117*, 10121–10211.

(608) McClure, D. S. *J. Phys. Chem. Solids* **1957**, *3*, 311–317.

(609) Dunitz, J. D.; Orgel, L. E. *J. Phys. Chem. Solids* **1957**, *3*, 318–323.

(610) Weber, B. *Koordinationschemie*; Springer Spektrum: Berlin, Heidelberg, 2014.

(611) Crystal, T.; Splitting, F.; Dq, P. **1967**, 430–451.

(612) Suchow, L. *J. Chem. Educ.* **1976**, *53*, 560.

(613) Santos-Carballal, D.; Roldan, A.; Grau-Crespo, R.; De Leeuw, N. H. *Phys. Rev. B - Condens. Matter*

Mater. Phys. **2015**, *91*, 195106.

(614)   Zhang, R.; Yuan, Q.; Ma, R.; Liu, X.; Gao, C.; Liu, M.; Jia, C. L.; Wang, H. *RSC Adv.* **2017**, *7*, 21926–21932.

(615)   Fritsch, D.; Ederer, C. *Appl. Phys. Lett.* **2011**, *99*, 26–29.

(616)   Fontijn, W. F. J.; Van Der Zaag, P. J.; Feiner, L. F.; Metselaar, R.; Devillers, M. A. C. *J. Appl. Phys.* **1999**, *85*, 5100–5105.

(617)   Kim, K. J.; Lee, H. S.; Lee, M. H.; Lee, S. H. *J. Appl. Phys.* **2002**, *91*, 9974–9977.

(618)   Kim, K. J.; Lee, J. H.; Lee, S. H. *J. Magn. Magn. Mater.* **2004**, *279*, 173–177.

(619)   Bloesser, A.; Kurz, H.; Timm, J.; Wittkamp, F.; Simon, C.; Hayama, S.; Weber, B.; Apfel, U.; Marschall, R. *ACS Appl. Nano Mater.* **2020**, *3*, 11587–11599.

(620)   Chen, J.; Hsu, H. S.; Huang, Y. H.; Huang, D. J. *Phys. Rev. B* **2018**, *98*, 085141.

(621)   Ferreira, T. A. S.; Waerenborgh, J. C.; Mendonça, M. H. R. M.; Nunes, M. R.; Costa, F. M. *Solid State Sci.* **2003**, *5*, 383–392.

(622)   Gonzalez-Sandoval, M. P.; Beesley, A. M.; Miki-Yoshida, M.; Fuentes-Cobas, L.; Matutes-Aquino, J. A. *J. Alloys Compd.* **2004**, *369*, 190–194.

(623)   Wang, L.; Bock, D. C.; Li, J.; Stach, E. A.; Marschilok, A. C.; Takeuchi, K. J.; Takeuchi, E. S. *ACS Appl. Mater. Interfaces* **2018**, *10*, 8770–8785.

(624)   Roy, S.; Ghose, J. *J. Appl. Phys.* **2000**, *87*, 6226–6228.

(625)   Jovanović, S.; Spreitzer, M.; Tramšek, M.; Trontelj, Z.; Suvorov, D. *J. Phys. Chem. C* **2014**, *118*, 13844–13856.

(626)   Jiang, M.; Gao, Y.; Wang, Z.; Ding, Z. *Appl. Catal. B Environ.* **2016**, *198*, 180–188.

(627)   Dolcet, P.; Kirchberg, K.; Antonello, A.; Suchomski, C.; Marschall, R.; Diodati, S.; Muñoz-Espí, R.; Landfester, K.; Gross, S. *Inorg. Chem. Front.* **2019**, *6*, 1527–1534.

(628)   Rafienia, M.; Bigham, A.; Ali Hassanzadeh-Tabrizi, S. *J Med Sign Sens* **2018**, *8*, 108–126.

(629)   Gyergyek, S.; Drofenik, M.; Makovec, D. *Mater. Chem. Phys.* **2012**, *133*, 515–522.

(630)   Balagurov, A. M.; Bobrikov, I. A.; Maschenko, M. S.; Sangaa, D.; Simkin, V. G. *Crystallogr. Reports* **2013**, *58*, 710–717.

(631)   Godinho, M. I.; Catarino, M. A.; Da Silva Pereira, M. I.; Mendonça, M. H.; Costa, F. M. *Electrochim. Acta* **2002**, *47*, 4307–4314.

(632)   Wan, C.; Nuli, Y.; Zhuang, J.; Jiang, Z. *Mater. Lett.* **2002**, *56*, 357–363.

(633)   Niederberger, M.; Garnweitner, G. *Chem. - A Eur. J.* **2006**, *12*, 7282–7302.

(634)   Qin, H.; He, Y.; Xu, P.; Huang, D.; Wang, Z.; Wang, H.; Wang, Z.; Zhao, Y.; Tian, Q.; Wang, C. *Adv. Colloid Interface Sci.* **2021**, *294*, 102486.

(635)   Belhadj, H.; Messaoudi, Y.; Khelladi, M. R.; Azizi, A. *Int. J. Hydrogen Energy* **2022**, *47*, 20129–20137.

(636)   Bilecka, I.; Djerdj, I.; Niederberger, M. *Chem. Commun.* **2008**, 886–888.

(637)   Solano, E.; Perez-Mirabet, L.; Martinez-Julian, F.; Guzmán, R.; Arbiol, J.; Puig, T.; Obradors, X.; Yañez, R.; Pomar, A.; Ricart, S.; Ros, J. *J. Nanoparticle Res.* **2012**, *14*, 1034.

(638)   Phuruangrat, A.; Kuntalue, B.; Thongtem, S.; Thongtem, T. *Mater. Lett.* **2016**, *167*, 65–68.

(639)   Li, L.; Ren, J. *Mater. Res. Bull.* **2006**, *41*, 2286–2290.

(640)   Zawadzki, M. *Solid State Sci.* **2006**, *8*, 14–18.

(641)   Deshmukh, R.; Niederberger, M. *Chem. - A Eur. J.* **2017**, *23*, 8542–8570.

(642)   Zander, J.; Weiss, M.; Marschall, R. *Adv. Energy Sustain. Res.* **2023**, *4*, 2200184.

(643)   Pinna, N.; Garnweitner, G.; Antonietti, M.; Niederberger, M. *J. Am. Chem. Soc.* **2005**, *127*, 5608–5612.

(644)   Simon, C.; Blösser, A.; Eckardt, M.; Kurz, H.; Weber, B.; Zobel, M.; Marschall, R. *Zeitschrift fur Anorg. und Allg. Chemie* **2021**, *647*, 2061–2072.

(645)   Simon, C.; Zakaria, M. B.; Kurz, H.; Tetzlaff, D.; Blösser, A.; Weiss, M.; Timm, J.; Weber, B.; Apfel, U. P.; Marschall, R. *Chem. - A Eur. J.* **2021**, *27*, 16990–17001.

(646)   Bloesser, A.; Timm, J.; Kurz, H.; Milius, W.; Hayama, S.; Breu, J.; Weber, B.; Marschall, R. *Sol. RRL* **2020**, *4*, 1900570.

(647)   Thackeray, M. M.; Amine, K. *Nat. Energy* **2021**, *6*, 566.

(648)   Yonemura, M.; Yamada, A.; Kobayashi, H.; Tabuchi, M.; Kamiyama, T.; Kawamoto, Y.; Kanno, R.

J. Mater. Chem. **2004**, *14*, 1948–1958.

(649) Thackeray, M. M. *J. Electrochem. Soc.* **1995**, *142*, 2558–2563.

(650) Hu, W.; Qin, N.; Wu, G.; Lin, Y.; Li, S.; Bao, D. *J. Am. Chem. Soc.* **2012**, *134*, 14658–14661.

(651) Sanpo, N.; Berndt, C. C.; Wen, C.; Wang, J. *Acta Biomater.* **2013**, *9*, 5830–5837.

(652) Kefeni, K. K.; Msagati, T. A. M.; Nkambule, T. T.; Mamba, B. B. *Mater. Sci. Eng. C* **2020**, *107*, 110314.

(653) Liu, X. M.; Cui, X.; Dastafkan, K.; Wang, H. F.; Tang, C.; Zhao, C.; Chen, A.; He, C.; Han, M.; Zhang, Q. *J. Energy Chem.* **2020**, *53*, 290–302.

(654) Wang, X.; Ouyang, T.; Wang, L.; Zhong, J.; Liu, Z. *Angew. Chemie* **2020**, *132*, 6554–6561.

(655) Bikkarolla, S. K.; Papakonstantinou, P. *J. Power Sources* **2015**, *281*, 243–251.

(656) Kim, J.; Gwon, O.; Kwon, O.; Mahmood, J.; Kim, C.; Yang, Y.; Lee, H.; Lee, J. H.; Jeong, H. Y.; Baek, J. B.; Kim, G. *ACS Nano* **2019**, *13*, 5502–5512.

(657) Li, M.; Xiong, Y.; Liu, X.; Bo, X.; Zhang, Y.; Han, C.; Guo, L. *Nanoscale* **2015**, *7*, 8920–8930.

(658) Lu, X.; Li, M.; Peng, Y.; Xi, X.; Li, M.; Chen, Q.; Dong, A. *J. Am. Chem. Soc.* **2021**, *143*, 16925–16929.

(659) Silva, V. D.; Ferreira, L. S.; Simões, T. A.; Medeiros, E. S.; Macedo, D. A. *J. Colloid Interface Sci.* **2019**, *540*, 59–65.

(660) Zhang, Y.; Lu, T.; Ye, Y.; Dai, W.; Zhu, Y.; Pan, Y. *ACS Appl. Mater. Interfaces* **2020**, *12*, 32548–32555.

(661) Maruthapandian, V.; Mathankumar, M.; Saraswathy, V.; Subramanian, B.; Muralidharan, S. *ACS Appl. Mater. Interfaces* **2017**, *9*, 13132–13141.

(662) Chandrasekaran, S.; Bowen, C.; Zhang, P.; Li, Z.; Yuan, Q.; Ren, X.; Deng, L. *J. Mater. Chem. A* **2018**, *6*, 11078–11104.

(663) Wang, S.; Hou, Y.; Wang, X. *ACS Appl. Mater. Interfaces* **2015**, *7*, 4327–4335.

(664) Becker, A.; Kirchberg, K.; Marschall, R. *Zeitschrift fur Phys. Chemie* **2020**, *234*, 645–654.

(665) Sarkar, J.; Bhattacharyya, S. *Arch. Thermodyn.* **2012**, *33*, 23–40.

(666) Battiston, S.; Rigo, C.; Da Cruz Severo, E.; Mazutti, M. A.; Kuhn, R. C.; Gündel, A.; Foletto, E. L. *Mater. Res.* **2014**, *17*, 734–738.

(667) Kefeni, K. K.; Mamba, B. B. *Sustain. Mater. Technol.* **2020**, *23*, e00140.

(668) Taffa, D. H.; Dillert, R.; Ulpe, A. C.; Bauerfeind, K. C. L.; Bredow, T.; Bahnemann, D. W.; Wark, M. *J. Photonics Energy* **2016**, *7*, 012009–1.

(669) Ziaei, V.; Bredow, T. *Eur. Phys. J. B* **2017**, *90*, 29.

(670) Holinsworth, B. S.; Mazumdar, D.; Sims, H.; Sun, Q. C.; Yurtisigi, M. K.; Sarker, S. K.; Gupta, A.; Butler, W. H.; Musfeldt, J. L. *Appl. Phys. Lett.* **2013**, *103*, 082406.

(671) Dileep, K.; Loukya, B.; Pachauri, N.; Gupta, A.; Datta, R. *J. Appl. Phys.* **2014**, *116*, 103505.

(672) Park, S.; Baek, J. H.; Zhang, L.; Lee, J. M.; Stone, K. H.; Cho, I. S.; Guo, J.; Jung, H. S.; Zheng, X. *ACS Sustain. Chem. Eng.* **2019**, *7*, 5867–5874.

(673) Mao, A.; Xiang, H. Z.; Zhang, Z. G.; Kuramoto, K.; Zhang, H.; Jia, Y. *J. Magn. Magn. Mater.* **2020**, *497*, 165884.

(674) Sun, Z.; Zhao, Y.; Sun, C.; Ni, Q.; Wang, C.; Jin, H. *Chem. Eng. J.* **2022**, *431*, 133448.

(675) Johnstone, G. H. J.; González-Rivas, M. U.; Taddei, K. M.; Sutarto, R.; Sawatzky, G. A.; Green, R. J.; Oudah, M.; Hallas, A. M. *J. Am. Chem. Soc.* **2022**, *144*, 20590–20600.

(676) Dąbrowa, J.; Stygar, M.; Mikuła, A.; Knapik, A.; Mroczka, K.; Tejchman, W.; Danielewski, M.; Martin, M. *Mater. Lett.* **2018**, *216*, 32–36.

(677) Shan, B. F.; Deng, J.; Zhao, Z. Y. *Phys. Status Solidi Basic Res.* **2021**, *258*, 2100268.

(678) Benck, J. D.; Chen, Z.; Kuritzky, L. Y.; Forman, A. J.; Jaramillo, T. F. *ACS Catal.* **2012**, *2*, 1916–1923.

(679) Tran, P. D.; Nguyen, M.; Pramana, S. S.; Bhattacharjee, A.; Chiam, S. Y.; Fize, J.; Field, M. J.; Artero, V.; Wong, L. H.; Loo, J.; Barber, J. *Energy Environ. Sci.* **2012**, *5*, 8912–8916.

(680) Li, Y.; Nakamura, R. *Chinese J. Catal.* **2018**, *39*, 401–406.

(681) Ren, G.; Hao, Q.; Mao, J.; Liang, L.; Liu, H.; Liu, C.; Zhang, J. *Nanoscale* **2018**, *10*, 17347–17353.

(682) Guo, M.; Li, P.; Wang, A.; Wang, J.; Chen, J.; Lei, F.; Hao, P.; Sun, X.; Xie, J.; Tang, B. *Chem. Commun.* **2023**, *59*, 5098–5101.

(683) Jin, Y.; Yue, X.; Du, H.; Wang, K.; Huang, S.; Shen, P. K. *J. Mater. Chem. A* **2018**, *6*, 5592–5597.

(684) Cui, M.; Yang, C.; Li, B.; Dong, Q.; Wu, M.; Hwang, S.; Xie, H.; Wang, X.; Wang, G.; Hu, L. *Adv. Energy Mater.* **2021**, *11*, 2002887.

(685) Wu, L.; Shen, X.; Ji, Z.; Yuan, J.; Yang, S.; Zhu, G.; Chen, L.; Kong, L.; Zhou, H. *Adv. Funct. Mater.* **2022**, *33*, 2208170.

(686) Mamiyev, Z.; Balayeva, N. O. *Catalysts* **2022**, *12*, 1316.

(687) Huerta-Flores, A. M.; Torres-Martínez, L. M.; Moctezuma, E.; Singh, A. P.; Wickman, B. *J. Mater. Sci. Mater. Electron.* **2018**, *29*, 11613–11626.

(688) Zhang, K.; Guo, L. *Catal. Sci. Technol.* **2013**, *3*, 1672–1690.

(689) Zhong, W.; Gao, D.; Yu, H.; Fan, J.; Yu, J. *Chem. Eng. J.* **2021**, *419*, 129652.

(690) Di, T.; Xu, Q.; Ho, W.; Tang, H.; Xiang, Q.; Yu, J. *ChemCatChem* **2019**, *11*, 1394–1411.

(691) Yepsen, O.; Yáñez, J.; Mansilla, H. D. *Sol. Energy* **2018**, *171*, 106–111.

(692) Yaseen, S.; Tahir, M. B.; Wattoo, A. G. *Int. J. Energy Res.* **2022**, *46*, 634–666.

(693) Wu, M.; Tse, J. S.; Pan, Y. *Sci. Rep.* **2016**, *6*, 21637.

(694) Bourdoiseau, J.-A.; Jeannin, M.; Rémazeilles, C.; Sabot, R.; Refait, P. *J. Raman Spectrosc.* **2011**, *42*, 496–504.

(695) Sorenson, S. A.; Patrow, J. G.; Dawlaty, J. M. *J. Phys. Chem. C* **2016**, *120*, 7736–7747.

(696) Wu, L.; Dzade, N. Y.; Gao, L.; Scanlon, D. O.; Öztürk, Z.; Hollingsworth, N.; Weckhuysen, B. M.; Hensen, E. J. M.; de Leeuw, N. H.; Hofmann, J. P. *Adv. Mater.* **2016**, *28*, 9602–9607.

(697) Chang, C. C.; Li, S. R.; Chou, H. L.; Lee, Y. C.; Patil, S.; Lin, Y. S.; Chang, C. C.; Chang, Y. J.; Wang, D. Y. *Small* **2019**, *15*, 1904723.

(698) Chen, X.; Yin, H.; Yang, X.; Zhang, W.; Xiao, D.; Lu, Z.; Zhang, Y.; Zhang, P. *Inorg. Chem.* **2022**, *61*, 20123–20132.

(699) Zhang, M.; Chen, X.; Jiang, X.; Wang, J.; Xu, L.; Qiu, J.; Lu, W.; Chen, D.; Li, Z. *ACS Appl. Mater. Interfaces* **2021**, *13*, 14198–14206.

(700) Morales-Gallardo, M. V.; Ayala, A. M.; Pal, M.; Cortes Jacome, M. A.; Toledo Antonio, J. A.; Mathews, N. R. *Chem. Phys. Lett.* **2016**, *660*, 93–98.

(701) Liang, Y.; Bai, P.; Zhou, J.; Wang, T.; Luo, B.; Zheng, S. *CrystEngComm* **2016**, *18*, 6262–6271.

(702) Eschrig, H. *Phys. Rev. B - Condens. Matter Mater. Phys.* **1999**, *60*, 14035–14041.

(703) Shukla, S.; Xing, G.; Ge, H.; Prabhakar, R. R.; Mathew, S.; Su, Z.; Nalla, V.; Venkatesan, T.; Mathews, N.; Sritharan, T.; Sum, T. C.; Xiong, Q. *ACS Nano* **2016**, *10*, 4431–4440.

(704) Brostigen, G.; Kjekshus, A. *Acta Chem. Scand.* **1969**, *23*, 2186–2188.

(705) Buerger, M. J. *Zeitschrift für Krist. - Cryst. Mater.* **1937**, *97*, 504–513.

(706) Skinner, B. J.; Erd, R. C.; Grimaldi, F. S. *J. Mineral. Soc. Am.* **1964**, *49*, 543–555.

(707) Tenailleau, C. *Am. Mineral.* **2006**, *91*, 1442–1447.

(708) Pearson, R. G. *Inorg. Chem.* **1988**, *27*, 734–740.

(709) Sun, Q. C.; Sims, H.; Mazumdar, D.; Ma, J. X.; Holinsworth, B. S.; O'Neal, K. R.; Kim, G.; Butler, W. H.; Gupta, A.; Musfeldt, J. L. *Phys. Rev. B - Condens. Matter Mater. Phys.* **2012**, *86*, 205106.

(710) Zander, J.; Marschall, R. *J. Mater. Chem. A* **2023**.

(711) Zander, J.; Timm, J.; Weiss, M.; Marschall, R. *Adv. Energy Mater.* **2022**, *12*, 2202403.

6 Publication 1: "Fast and Facile Microwave Synthesis of Cubic CuFe₂O₄ Nanoparticles for Electrochemical CO₂ Reduction"

J. Zander[a,b], M. Weiss[a], R. Marschall[a,b]*

[a] Department of Chemistry
University of Bayreuth
Universitätsstraße 30, Bayreuth 95447, Germany
*E-mail: roland.marschall@uni-bayreuth.de , ORCID: 0000-0002-1057-0459

[b] Bavarian Center for Battery Technology (BayBatt), University of Bayreuth,
Universitätsstrasse 30, 95447 Bayreuth, Germany

6.1 Main Manuscript

Nanoparticles of cubic CuFe₂O₄ were obtained in a fast microwave-assisted hydrothermal synthesis. By adjusting the pH value and solvent ratio (ethylene glycol to water), phase-purity and high crystallinity is achieved at very short reaction times of 1 min, or low temperatures of 120 °C, without the need for subsequent heat treatment steps. The influence of the synthesis time or temperature on material properties and performance in electrochemical CO₂ reduction to CO are investigated. While particle size and crystallinity are not changed significantly with longer synthesis times at 175 °C, prolonged heating results in a decrease of the degree of inversion, which leads to a decrease in the CO₂ reduction ability. The best performance is observed for CuFe₂O₄ with an intermediate degree of inversion of approx. 0.75, together with the largest crystallite size and micro-strain, as revealed by Rietveld refinement. For CuFe₂O₄ synthesised under these conditions, a CO evolution rate of 0.2 μmol h⁻¹ g⁻¹ is obtained at a Faradaic efficiency of 20%. The CO to H₂ ratio is 1:3, which makes it a promising candidate for a sustainable production of syngas.

6.1.1 Introduction

The combination of rising CO_2 concentrations in the atmosphere and the necessity for alternative production pathways of valuable carbon containing chemicals have provoked an increasing interest in the capture and conversion of CO_2. Electrochemical CO_2 reduction is hereby especially promising, since it enables the direct conversion of electricity from renewable sources into chemical fuels, that can on the one hand serve as storage media to mitigate fluctuations in the power supply by renewables and on the other hand can be used as feedstock for industrial processes, such as Fischer-Tropsch, or the syntheses of valuable chemicals.[1-4] CO_2 reduction is a multi-electron and frequently also a multi-proton transfer reaction. This, together with the inert nature and the possibility of various reduction products,

usually results in high required overpotentials and the occurrence of multiple reaction products.[5] The selectivity hereby strongly depends on the catalyst. Until recently, copper was the only metal electrocatalyst yielding CH_4 and higher carbon products, such as C_2H_4 or ethanol,[4] with Zhou *et al.* reporting in 2022 the production of linear and branched C_3 to C_6 hydrocarbons also over polarized $Ni^{\delta+}$ associated with Ni–O bonds.[6] Copper containing materials, especially oxides, are likewise of interest due to their comparatively high activity and broad substrate scope. Copper oxides, such as CuO or Cu_2O, are reduced to metallic copper at the surface under operating conditions.[7-10]

Another interesting copper oxide is $CuFe_2O_4$ that only contains abundant iron as an additional element. $CuFe_2O_4$ belongs to the class of spinel-type materials that are normally of cubic crystal structure with the space group $Fd\bar{3}m$. However, due to the strong Jahn-Teller distortions induced by Cu^{2+}, lowering of the symmetry to tetragonal is favoured at lower temperatures.[11] A cubic structure is stable above around 400 °C.[11-12] Spinels are of high interest also due to their magnetic and electronic properties, which can be adjusted by the degree of inversion, *i. e.* the cation distribution between tetrahedral and octahedral sites, and in the special case of $CuFe_2O_4$ also by the structure.[13-16] The degree of inversion influences the structure, due to the strong Jahn-Teller distortion caused by Cu^{2+} at octahedral sites.[17] The exact relationship between structure and inversion parameter is, however, debated. A completely inverted structure was reported for cubic $CuFe_2O_4$ based on neutron diffraction results, with a slight reduction of the inversion parameter by a few percent upon phase transition to tetragonal.[18] On the other hand, a strong correlation between phase transition and cation migration is commonly believed to be present.[13-15,19] Thus, Ohnishi *et al.* observed a normal cation distribution for $CuFe_2O_4$ in the high-temperature cubic form. Copper migration to octahedral sites proceeds during cooling between approx. 700 and 360 °C, where the stronger Jahn-Teller distortion causes the transition to tetragonal and results in a strong correlation between inversion parameter and structure.[11-14,19-21] Cubic $CuFe_2O_4$ was reported as a normal spinel[19-20] as well as inverted.[11] The critical inversion parameter for phase transition is believed to be 0.75.[19] The cation distribution is largely dependent on the synthesis conditions, such as particle size and calcination temperature,[11,21-23] that appear to have the most significant impact on both structure and degree of inversion. Calculations have shown that the cation distribution significantly affects the electronic properties, with a change from a completely inverted structure to a normal one resulting in a change from semi-conducting to half-metallic properties.[19,24] This has experimentally been observed by a reduced grain resistance and improved conductivity for partially inverse tetragonal $CuFe_2O_4$ compared to normal cubic $CuFe_2O_4$.[19]

$CuFe_2O_4$ has been used for several catalytic processes, such as methanol steam reforming,[22] photocatalytic degradation,[23] photocatalytic water-splitting,[25] photo-electrochemical hydrogen evolution,[26] photo-electrochemical water oxidation,[27,28] as well as gas sensor material[29] or for protein separation.[30] A huge advantage is the easy recovery of the material due to its magnetic properties. Additionally, $CuFe_2O_4$ is an effective electrocatalyst for oxygen evolution, for which it showed a very low overpotential, even surpassing the performance of $CoFe_2O_4$ and $NiFe_2O_4$.[31] $CuFe_2O_4$ has also been used for the photo-electrochemical (PEC) CO_2 reduction reaction (CO_2RR).[32,33] Thus, the group of Khan first employed pure $CuFe_2O_4$ for PEC CO_2RR to methanol and then switched to a composite with graphene oxide, thereby increasing the Faradaic efficiency to 87 %, reportedly due to better charge separation.[32,33] Improved activity – also for the conversion to methanol – could also be observed for a composite with TiO_2, as reported by Hafeez *et al.*[34]

Common synthesis methods include co-precipitation,[29] solid state reaction,[11,19] sol-gel synthesis,[31] combustion synthesis,[35] or solvothermal synthesis.[30,36] Methods requiring calcination temperatures of

more than 300 °C yield tetragonal $CuFe_2O_4$, if cooled slowly, and cubic, if quenched rapidly from high temperatures. Additionally, most of these techniques yield large particle sizes, with inhomogeneous size distributions and low surface areas, because of the high temperature requirements, which is often impedimental for catalytic performance.[22] To obtain nano-sized or nano-structured particles, different strategies, such as hard-templating, soft-templating, or combustion synthesis can be employed.[22,23,35] In contrast to solid state synthesis, hydrothermal synthesis allows for the direct preparation of the cubic form.[36] As an alternative, microwave-assisted syntheses allow for the preparation of spinel ferrite nanoparticles.[37-39] Due to fast homogeneous heating, reaction times can often be significantly reduced compared to conventional hydrothermal synthesis and the size distribution can be narrowed.[37,38,40-42] Phuruangrat *et al.* have shown in first experiments that microwave-assisted hydrothermal synthesis is feasible for the direct synthesis of crystalline $CuFe_2O_4$ in its cubic form.[43] Jalajerdi *et al.* obtained tetragonal $CuFe_2O_4$ after an aqueous microwave synthesis followed by calcination.[44] The size distribution is relatively broad, however. To improve the size distribution of nanoparticles, triethylene glycol (TEG) has been used as a solvent in a solvothermal synthesis of $CuFe_2O_4$ nanorods, serving as reducing agent, high boiling solvent and stabiliser.[45] Similar approaches with the solvent acting as a stabilising agent, have been shown for other ferrites in our group as well.[37-39] For copper ferrite, a microwave synthesis in organic solvents, however, results in a reduction of Cu^{2+} and the formation of Cu^0 by-phases.[41]

We herein present a fast, reproducible microwave-assisted synthesis of cubic $CuFe_2O_4$ nanoparticles in water, with additional ethylene glycol acting as stabilising agent in the reaction solution, improving phase purity and homogeneity by preventing the precipitation of hydroxides. We further examine the influence of synthesis parameters on the material properties, the degree of inversion, and on the activity in electrochemical CO_2 reduction. The best performance is observed for $CuFe_2O_4$ with an intermediate degree of inversion of approx. 0.75, for which a CO evolution rate of 0.2 µmol h^{-1} g^{-1} was obtained at a Faradaic efficiency of 20%. The CO to H_2 ratio was 1:3.

6.1.2 Results and Discussion

The synthesis of $CuFe_2O_4$ in water is strongly pH-dependent, which was also observed for a hydrothermal synthesis approach.[36] Fe_2O_3 was the only reaction product observed in the XRD patterns under acidic conditions, CuO was the main product at near neutral conditions, and $CuFe_2O_4$ was only observed at pH > 10 (Figure S1, Supporting Information). In contrast to Phuruangrat *et al.*, we observed CuO occurring as by-phases in varying amounts when the synthesis was conducted in pure water, especially at a pH below 12 (Figure S1, Supporting Information). This is likely due to the precipitation of hydroxides upon pH adjustment before transfer to the microwave, which results in visibly inhomogeneous mixing. Upon addition of ethylene glycol as a complexing agent, which optically improved the dispersion, the synthesis reproducibly yielded phase-pure cubic $CuFe_2O_4$ at medium amounts of ethylene glycol (EG). If the amount of EG exceeded 40%, a reduction of copper was observed (Figure S2, Supporting Information), in good agreement to the results reported by Solano *et al.*[41] The best results were obtained using a EG:water ratio of 5:10 (1:2).

After having established the general reaction parameters, we varied the reaction time and temperature for the microwave synthesis. The corresponding XRD patterns are depicted in **Figure 1** and S3, Supporting Information. A reduction of the synthesis time to only 1 min was possible, without the appearance of any by-phases and without apparent loss of crystallinity. A similar reduction of the synthesis time to 1 min could additionally be shown at 150 °C (Figure S4, Supporting Information). The employed synthesis temperature has a stronger influence on crystallinity and phase purity. While the distinct reflections for cubic $CuFe_2O_4$ are apparent even after reaction at only 120 °C for 15 min, the crystallinity was low and a shoulder to the left of the (311) reflection indicated the presence of a possible tetragonal phase. When the temperature was raised to 200 °C, Cu_2O by-phases were observed in high-resolution Ag-XRD patterns (Figure 1 and S3, Supporting Information), likely due to the strong reducing ability of EG at this temperature.
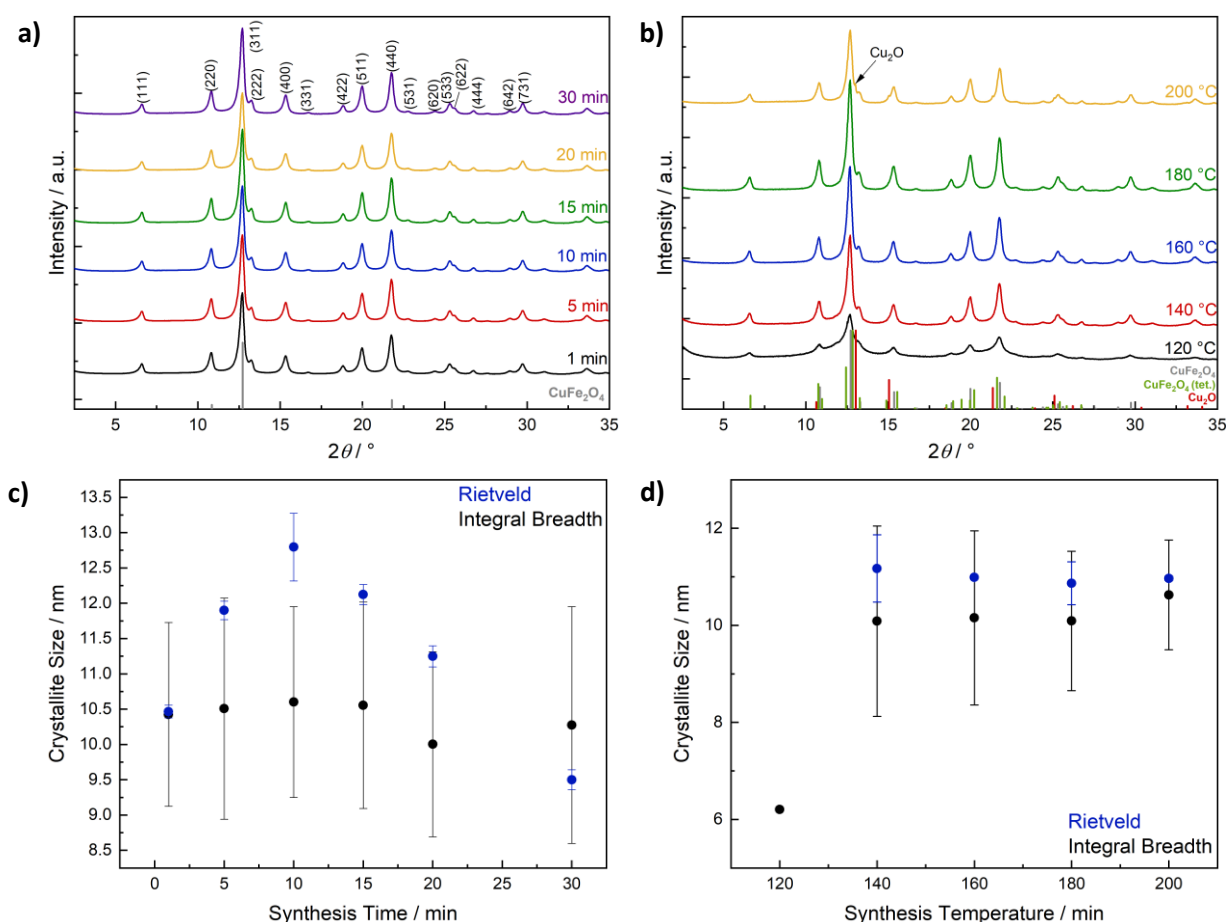
Figure 1 Ag-XRD patterns for $CuFe_2O_4$ obtained after different reaction temperatures at 175 °C a) and after 15 min at different reaction times b). Following ICDD reference patterns were used: $CuFe_2O_4$ (*c*): 01-077-0010; $CuFe_2O_4$ (*t*): 00-034-0425, Cu_2O: 00-005-0667. Crystallite sizes obtained *via* the integral breadth method and Rietveld refinement are depicted in c) and d). Error bars for the integral breadth method are estimated by averaging over different reflections in the cubic structure; error bars for sizes derived from Rietveld analysis indicate averaging of at least two independent fits.

The crystallite sizes for $CuFe_2O_4$ obtained after different reaction times, as well as at different temperatures, were first calculated by the integral breadth method and additionally by Rietveld refinement, due to the high background (Figure 1c,d). The prominent background could be an indication of an amorphous phase that probably corresponds to organic residues. Both methods yield a crystallite size of 10 - 13 nm, depending on the reaction time. A correlation with the degree of inversion was noted and is discussed in the following sections. A significantly smaller crystallite size of

only approx. 6.5 nm was estimated after the reaction proceeded at 120 °C, whereas the crystallite size remains unchanged for increasing reaction temperatures. The determination of crystallite size by the integral breadth method for the 120 °C sample was only possible for the (400) reflection, due to low crystallinity and peak overlap. For the same reasons, Rietveld refinement did not result in a good fit.

SEM images show the agglomeration of very small nanoparticles (Figure S5, Supporting Information), that have an almost perfect Cu:Fe ratio of 0.5 determined by EDXS. For further evaluation of the synthesis parameters on the crystal morphology, the obtained particles were analysed with TEM (**Figure 2** and S6, Supporting Information). Slightly increasing particle sizes with increasing synthesis time were estimated, with the particles growing from approx. 13.5 to 18.5 nm. Similar sizes were obtained after reaction at temperatures between 140 and 180 °C as well (Figure S6, Supporting Information), with the size increasing from 14 to 18 nm. The average particle size is only slightly larger than the determined crystallite size, indicating that the nanoparticles are mostly single-crystalline. The crystallinity and cubic structure were further confirmed by measuring lattice spacing in high-resolution images (Figure S5, Supporting Information). The spacing corresponding to the (311)-plane in the cubic structure was the most prominent one.
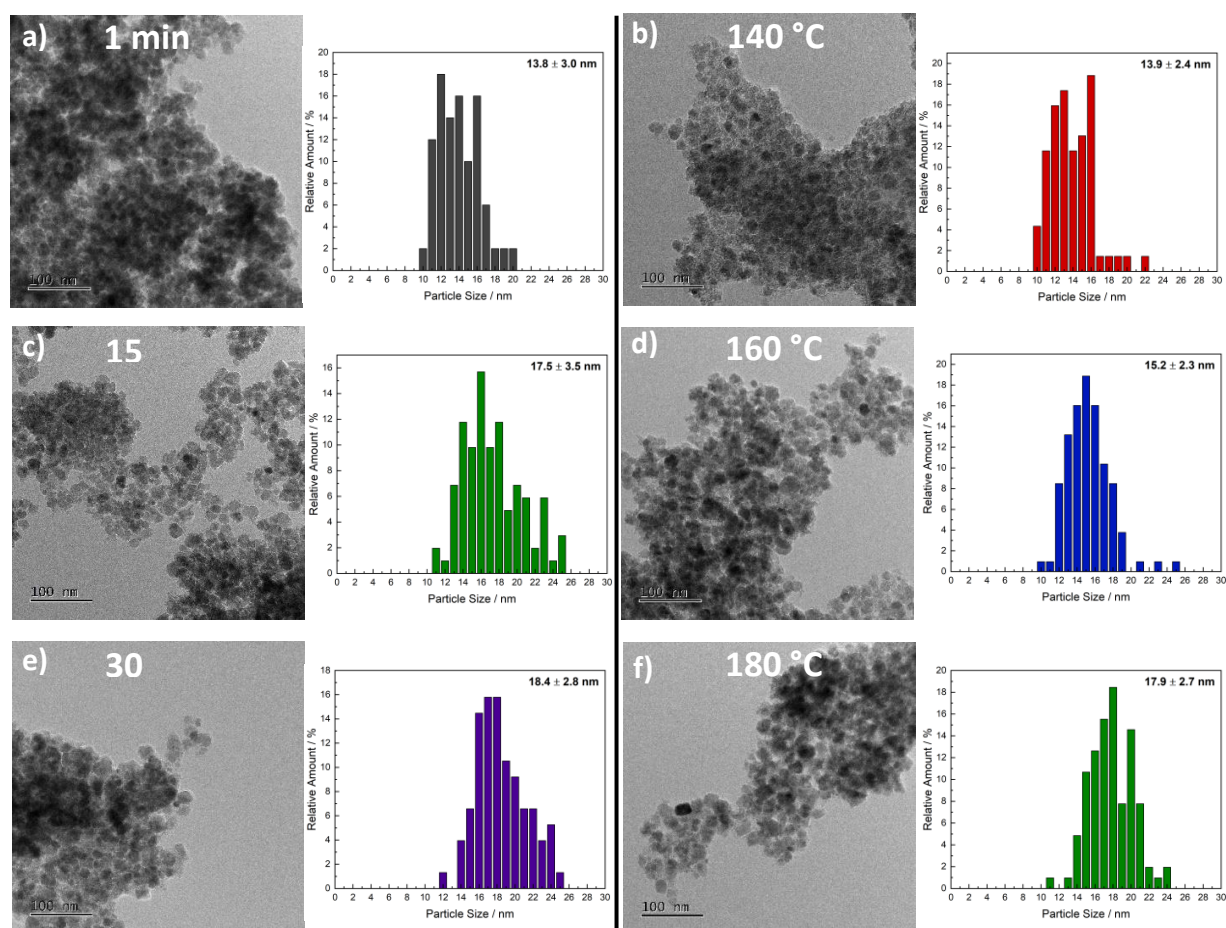
Figure 2 TEM images of $CuFe_2O_4$ particles obtained after different reaction times at 175 °C a,c,e) and after 15 min at different reaction temperatures b,d,f), as well as corresponding particle size distribution. For the determination of size distributions, at least 50 particles were measured.

The surface area was evaluated by the BET model. The surface area of $CuFe_2O_4$ particles synthesised at a fixed temperature of 175 °C is around 120 $m^2 g^{-1}$, independent of the synthesis time (Figure S7,

Supporting Information). The corresponding isotherms have the typical shape for nanoparticle agglomerates, revealing that the high surface area is a result of the small size of the obtained nanoparticles. Correspondingly, no defined pore size is observed and the void size between nanoparticles peaks around the particle diameter. The particles obtained after shorter reaction times exhibit a tendency to form agglomerates with smaller voids, possibly due to organic residues and very small amorphous compounds. The similar surface area independent of the size is in good agreement to the similar sizes observed in the TEM images. The surface area for particles obtained after reaction at different temperatures decreases with increasing reaction temperature from 250 to 100 $m^2\,g^{-1}$, although the particle size was very similar. This might be an indication of different agglomeration behaviour that is also apparent in different shapes of the isotherms and might either depend on the amount of organic residues, or on different magnetic properties. The packing of nanoparticles is much denser for samples synthesised at low temperature (*i.e.* 120 or 140 °C), which show a narrow pore size distribution that peaks around 5 nm (Figure S7, Supporting Information). The dense packing is furthermore hinted at in the TEM images. Larger amounts of organic residues or amorphous matter might contribute to void filling between particles. The BET surface area for $CuFe_2O_4$ obtained after different reaction times at 150 °C are around 150 $m^2\,g^{-1}$, thus larger than for the particles prepared at 175 °C, which is in good agreement to the increased surface area at lower temperatures mentioned above.

To evaluate whether the differences in the agglomeration behaviour are due to organic residues on the surface, TG-MS measurements were conducted for $CuFe_2O_4$ obtained after different reaction times or at different temperatures (**Figure 3**). As expected, the mass loss during annealing in air increases with decreasing reaction times. An initial increase of the mass below 100 °C can probably be attributed to oxidation of organic matter, likely followed by a loss of adsorbed H_2O at approx. 125 °C and decomposition of organic matter mainly into CO_2 at 150 to 350 °C (Figure S9, Supporting Information). A similar effect is observed for samples obtained after different reaction times, with the mass loss being even more pronounced for $CuFe_2O_4$ synthesised at lower temperatures, with the sample synthesised at 120 °C showing a mass loss of 15%.

The higher amounts of organic residues might explain the increased surface area for samples obtained at low temperatures. Corresponding to the decomposition of organic residues, exothermic peaks can be observed in the DSC measurements (Figure S9, Supporting Information). Additionally, two steps with increasing heat flow are visible, one between 300 and 400 °C and one between 620 and 700 °C. Those features might correspond to phase-transitions, first from cubic to tetragonal and later from tetragonal to cubic. The onset temperature for the first phase transition shifts towards higher temperatures with increasing synthesis duration and the increase in the heat flow decreases. Both might be an indication of different initial cation distributions.

The organic residues are also apparent in the DRIFT spectra for all samples (Figure 3c,d, S9, Supporting Information). Additionally, differences between samples obtained after different reaction times, or at varied temperatures, are apparent, indicating structural changes that are not visible in the XRD patterns and thus do not significantly influence the crystallinity. All samples exhibit the characteristic absorbance at 400 – 550 cm^{-1} corresponding to metal-oxygen vibrations at octahedral sites, v_2, and the absorbance between 620 and 750 cm^{-1}, v_1, corresponding to metal-oxygen vibrations at tetrahedral sites.[46-49] The vibrations show only negligible changes in dependence of the synthesis time or temperature, indicating a complete condensation of metal-oxygen bonds even at short times and low temperatures, in good agreement to highly similar XRD patterns. An exception is $CuFe_2O_4$ synthesised

at only 120 °C, for which the M-O vibrations are less intense, likely due to incomplete condensation to the oxide.
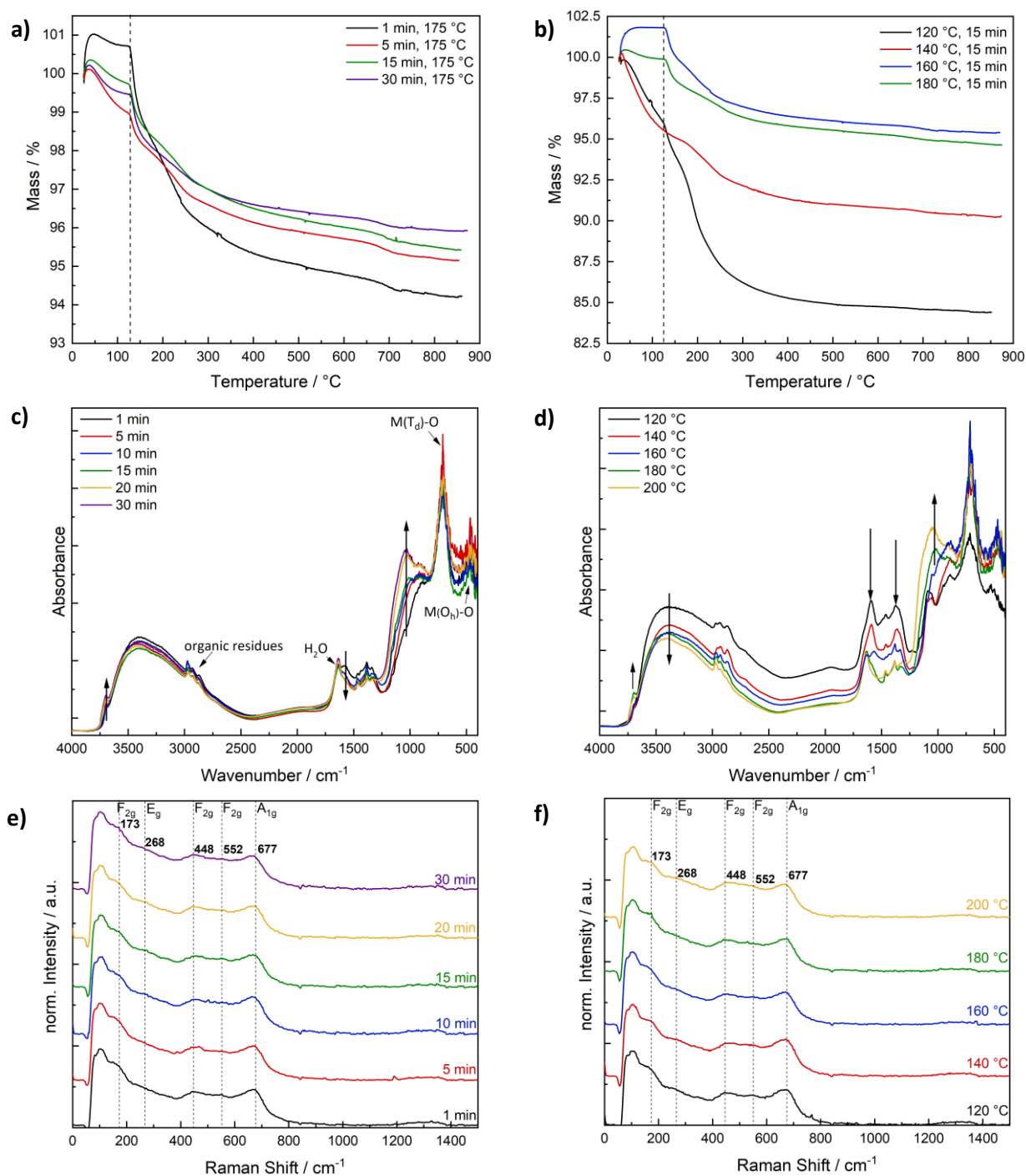
Figure 3 Observed mass loss during annealing of $CuFe_2O_4$ particles obtained after reaction for different duration at 175 °C a), or for 15 min at different temperatures b), DRIFT spectra for $CuFe_2O_4$ synthesised under varied conditions c,d), as well as corresponding Raman spectra e,f).

Correspondingly, a larger amount of hydroxyl-groups is observed between 3000 and 3500 cm^{-1} in addition to organic residues from ethylene glycol and its decomposition products.[45] Noticeably, the intensities of the vibrational bands at 1030 cm^{-1}, corresponding to COH-bonds in poly-ethylene glycol, and at 3690 cm^{-1}, corresponding to non-hydrogen bonded OH, increase with the synthesis time, while those at 1380 and 1330 cm^{-1}, that fall into the range of C-O bonds, decrease slightly.[50] An observed

decrease of the vibration at 1585 cm^{-1} and increase of the vibration at 1030 cm^{-1} are similar to evolutions observed during the polymerisation of ethylene glycol, that might occur as a side reaction.[51] Additional weak absorption bands between 1050 and 1160 cm^{-1}, that are especially visible at short reaction times or low temperatures, might also be attributed to C-O in ethylene glycol residues.[45] A similar trend is visible with increasing reaction temperature, if more pronounced

Raman spectra were recorded for CuFe$_2$O$_4$ obtained under varying synthesis conditions to corroborate the cubic structure and phase purity deduced from the XRD patterns (Figure 3e,f). The visible bands for all samples can be assigned to the 5 expected Raman active modes for cubic CuFe$_2$O$_4$ and are in good agreement to literature values.[47,52] No characteristic bands for common by-phases, such as Fe$_2$O$_3$, are visible. The band at a shift of 173 cm^{-1} is assigned to the F$_{2g}$ mode, that at 268 cm^{-1} to E$_g$, that at 448 cm^{-1} and 553 cm^{-1} to F$_{2g}$ as well and that at 677 cm^{-1} to the A$_{1g}$ mode.[47] Additional humps at 350 cm^{-1} and a shoulder at 620 cm^{-1} might be an indication of locally lowered symmetry due to Jahn-Teller distortions caused by Cu^{2+} ions in an octahedral environment, although a universal distortion of the crystal lattice is not apparent in the XRD patterns. A similar observation has been stated by Silva *et al.* for Co-substituted CuFe$_2$O$_4$.[47] However, additional bands might also be formed due to partial inversion, that also lowers the symmetry.[16] Due to the weak intensity of those bands, no clear conclusion about the local environment of Cu and Fe ions, in terms of phase transformation and degree of inversion, can be drawn from the DRIFT and Raman spectra, however.

For further characterisation of the as-synthesised nanoparticles, UV/vis/NIR measurements were conducted in order to estimate the band gaps. Irrespective of the synthesis conditions, a band gap of approx. 1.9-2.0 eV was obtained from the Kubelka-Munk plots, in good agreement to literature values (Figure S10, Supporting Information).[27,28,53] Since the band gap is highly dependent on the degree of inversion, similar cation distribution independent of the synthesis conditions can be assumed.[19] A feature at 485 nm is apparent in the spectra, corresponding to ligand to metal charge-transfer from oxygen to copper 3*d* orbitals. If this region is ignored in the fit, slightly lower values were obtained, compared to a fit only above the *d-d* band (Figure S10, Supporting Information). A second, weak feature at approx. 800 nm can be attributed to *d-d* transitions in Cu^{2+} at distorted octahedral sites. A third, very weak feature centred around 1500 nm arises due to *d-d* transitions in Cu^{2+} at tetrahedral sites.[54-56] Band gap values were also determined from the Tauc plots, that yield a band gap of 1.7-1.8 eV for an indirect transition that includes a fit over the *d-d* band and thus leads to a slight underestimation of the band gap, and of 2.5 eV for a direct transition, that allows for an exclusion of the *d-d* band for the fit. From the shape of the plots and the estimated band gap values, an indirect band gap is more probable, although this is in discrepancy to the result of the group of Sivula.[27] However, they used n-type, tetragonal thin-film CuFe$_2$O$_4$, which might exhibit considerably alternate properties. The results of Díez-García *et al.* for cubic CuFe$_2$O$_4$ are rather more similar to ours.[53] Notably, the *d-d* band is hardly visible in both reported spectra.

Determination of the Degree of Inversion

Generally, three main methods are employed to determine the degree of inversion for spinel-type materials: Rietveld refinement of XRD data, Mössbauer spectroscopy, and XPS.[16,31] Since all three rely on mathematical fitting of experimental results and thus depend on the quality of the measurement data and the fitting parameters, a complementary determination with several methods is recommendable. We performed Rietveld refinement on the Cu and Ag-XRD patterns for CuFe$_2$O$_4$

obtained under different conditions. The high background due to organic residues, low intensity and broad, asymmetric peak shape make an unambiguous fitting difficult, due to strong correlations between occupation, background, asymmetry, micro-strain and anisotropic size parameters. A degree of inversion between 0.72 and 0.87 was estimated for all samples based on the Cu-XRD data, depending on the fitting conditions (Figure S12, Supporting Information). This is in good agreement to the usually observed value of 0.85 at room temperature, although a tetragonal distortion would normally be expected.[15,21,23,24,57] The degree of inversion decreases with increasing reaction time, signifying that although crystallisation mainly occurs during the first minute of the synthesis, continued microwave irradiation induces a Cu^{2+} migration to tetrahedral sites. The very fast heating and crystallisation, together with an abrupt stop in the microwave irradiation – *i.e.* the apparent driving force for cation redistribution - lead to the thermodynamically unfavourable structure and prevent the distortion that is usually observed during the cooling from high temperatures.

Interestingly, a closer look at the crystallite sizes determined with the integral breadth method and Rietveld refinement reveals that the size is highest after medium synthesis times of 10 min, suggesting that crystallinity is decreasing again after that time (Figure 1). This goes in hand with a pronounced decrease in the inversion parameter, as discussed in the following, indicating that microwave-induced cation redistribution results in an increasing structural disorder. A closer analysis of the crystallite size derived from different reflection peaks reveals that the observed relationship is at least partially an effect of averaging for different (hkl) reflections. All samples show an average crystallite size of approx. 11 nm when analysed with the integral breadth method, but the differences between the determined sizes are largest for very short or very long reaction times, with the smallest deviations observed for $CuFe_2O_4$ obtained after a reaction time of 10 min (Figure S11, Supporting Information). The same trend as for the crystallite size can be observed for micro-strain, while the lattice parameter is slightly smaller for $CuFe_2O_4$ obtained after moderate reaction times, indicating lattice contraction (Figure S11, Supporting Information). Both effects can be a result of Jahn-Teller distortions that would, if in equilibrium, likely result in a tetragonal structure. On the one hand, the strain induced by Jahn-Teller active Cu^{2+} ions on octahedral sites depends on the degree of inversion and would be expected to decrease with a decreasing degree of inversion. This effect is most probably the reason for the decrease in micro-strain and crystallite size for samples obtained at reaction times longer than 10 min, in correlation to a decreasing inversion parameter. Notably, the degree of inversion is around 0.75, or less, after this time. This value represents the critical fraction of Cu^{2+} on octahedral sites above which a distortion was observed in literature.[19] The increasing differences in peak width for different hkl at increasing temperature might be an effect of anisotropic disorder induced by cation migration. For the sample obtained after 30 min, no accurate determination of the degree of inversion was possible. An increase in micro-strain was obtained for different fitting procedures. Possibly, cation migration results not only in the induction of disorder, but also causes additional strain effects due to inhomogeneous ion distribution in different unit cells, and to the creation of defects. Since micro-strain and crystallite size are low for the samples obtained after short reaction times, the presence of defects – due to partially incomplete condensation of the metal-oxide framework – might mitigate strain induced by Jahn-Teller distortions. Additionally, at a degree of inversion of 0.75 the Jahn-Teller distortion at tetrahedral sites (that would result in a decrease of c/a <1) and at octahedral sites (that would lead to c/a>1) might compensate each other best, resulting in overall minimal distortion, but high strain.

The asymmetry of the reflections is even higher for the Ag-XRD data, hence we focussed on measurements with a copper source for the fittings. The strong asymmetry of the reflections might in part be caused by internal stresses caused by the Jahn-Teller active Cu^{2+} ions.[11] A comparable, but

slightly decreasing degree of inversion of around 0.8 was obtained for $CuFe_2O_4$ synthesised for 15 min at different temperatures. Summarised results for the cation distribution with an optimised fitting procedure are listed in **Table 1**.

XP spectra were recorded for $CuFe_2O_4$ synthesised at different temperatures or for different reaction times (**Figure 4**, S13, Supporting Information). The survey scans show the expected ratios for Cu and Fe, with additional small amounts of Si and K (Table S2, Supporting Information). The latter likely result from leaching of the microwave vial and the employed KOH, respectively. The concentration of K and Si increase with the synthesis time and temperature, indicating increasing amounts of doping with these ions. Additionally, the Cu content at the surface is decreased in the sample obtained after 30 min at 175 °C, further strengthening the assumption of defect induction due to increased cation migration with time. In contrast to that, a Cu excess at the surface was observed at high reaction temperatures.

Table 1 Degree of inversion (λ) determined with Rietveld refinement and XPS analysis.

Synthesis Time	λ Rietveld	λ XPS	Cu^+/Cu^{2+}	Synthesis Temperature	λ Rietveld	λ XPS	Cu^+/Cu^{2+}
1 min	0.82	0.84	0.02	120 °C		0.86	1.42
5 min	0.82	0.82	0	140 °C	0.87	0.87	0.08
10 min	0.80	0.78	0.02	160 °C	0.86	0.75	0.05
15 min	0.75	0.80	0.02	180 °C	0.79	0.81	0.03
20 min	0.72	0.78	0	200 °C	0.77	0.80	0.03
30 min	0.87	0.67	0.08				

The Cu $L_3M_{4,5}M_{4,5}$ peak was used for charge correction, since non-negligible amounts of carbonaceous residues from the synthesis, that include significant contributions from alcoholic species to varying extents (Figure S13, Supporting Information), render a correction *via* adventitious carbon unsuitable and would result in vastly fluctuating binding energies. Typical binding energies for Fe^{3+} and Cu^{2+} of 933.1 eV for Cu $2p_{3/2}$ and 710.8 and 724.5 eV for Fe $2p_{3/2}$ and Fe $2p_{1/2}$ were observed, respectively. The high resolution $2p$-spectra for Cu can be fitted with two signals for the metal ion in octahedral and tetrahedral sites, respectively.[23,31,32,58,59] This fitting approach is based on an influence of the coordination environment on the ratios of multiplet splitting,[58-60] but neglects additional effects on multiplet splitting and is further complicated by the possible presence of Cu^+ and/or Cu^0. To some extent the expected influence of Cu^+/Cu^0 can be derived from the Auger signal, which is highly similar for all $CuFe_2O_4$ samples obtained at 175 °C for different reaction times, and supports the predominant oxidation state of +II for copper, which is further apparent in the high shake-up intensity.[61] No indication of Cu^0 species is observed in the Cu $L_3M_{4,5}M_{4,5}$ spectra. Samples obtained at different temperatures, on the other hand, show a strong contribution of Cu^+, with the Cu^+/Cu^{2+} ratio depending on the synthesis temperature (Figure 4, Figure S13, Supporting Information). Interestingly, although Cu^+ by-phases were only observed at very high temperatures, the Cu^+ content increases with decreasing reaction temperature, indicating partially reduced and likely also coordinative unsaturated copper species at the surface. The amount of Cu_2O in the sample obtained at 200 °C is estimated to be 1.2% based on the results from Rietveld refinement. The degree of inversion is clearly changing with prolong reaction times. While an initial 16% of Cu^{2+} on tetrahedral sites is observed after a very short reaction time of 1 min, an increasing amount of 33% of Cu^{2+} is located at tetrahedral sites after 30 min,

in good agreement to the results obtained from Rietveld refinement. Interestingly, the degree of inversion as determined *via* Rietveld refinement shows an almost linear decrease after 10 min of reaction time. An extrapolation of that trend would yield a degree of inversion of approx. 0.66 for the sample obtained after 30 min, which is in very good agreement to the degree of inversion determined with XPS. A similar degree of inversion of λ = 15-20% is obtained independent of the synthesis temperature, with a slight decrease of the inversion parameter with increasing reaction temperature. The degree of inversion and the Cu^+/Cu^{2+} ratio are summarised in Table 1. Evolution of the degree of inversion and the Cu^+/Cu^{2+} ratio in relation to the synthesis time and temperature, respectively, are furthermore clearly demonstrated in the normalised spectra (Figure 4).

A similar fitting procedure should in theory also be possible for the Fe $2p$ spectra, but due to the more complicated multiplet structure, an overlap with a Cu Auger signal and low intensity of the peaks, an unambiguous fitting with only two species for Fe at tetrahedral and at octahedral voids is often neither possible nor meaningful and was therefore not attempted here.[58,59] The Fe $2p$ spectra were instead fitted with typical peak ratios and positions for ferrites, keeping the positions fixed for all samples.[62] When regarding the normalised Fe $2p$ spectra, interestingly a peak broadening towards higher binding energies is observed for samples obtained after 1 min and after 30 min, which would at first glance indicate a larger amount of Fe^{3+} in tetrahedral voids. For $CuFe_2O_4$ obtained after 30 min this is additionally accompanied by a shift of the entire spectrum towards higher binding energies. This is contrary to the effects expected based on analysis of the Cu-spectra and on Rietveld refinement, and could be an indication of independent cation migration of Cu and Fe, which would in turn favour the creation of defects for prolonged reaction times. Fe^{2+} species might also be present. This would induce a shift of the spectra towards lower binding energies, however, which would signify a presence of Fe^{2+} mainly at medium reaction times, which seems unlikely. The shift towards higher binding energy after 30 min could in part also be caused by the extraction of copper, shifting the peaks towards those of Fe_3O_4.[60] Cu defects might likewise lead to a shift in the iron spectra towards higher binding energies.
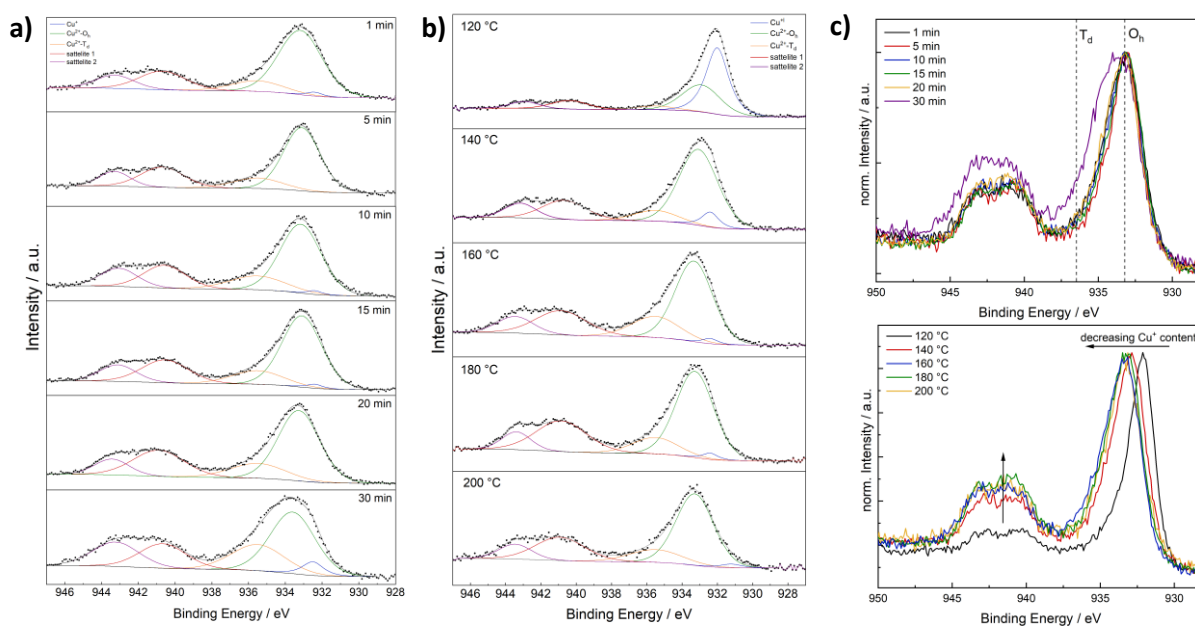
Figure 4 XPS spectra for $CuFe_2O_4$ obtained under different reaction conditions. Cu $2p_{3/2}$ spectra for $CuFe_2O_4$ synthesised at 175 °C for different reaction times a), or at different temperature b), as well as normalised $2p_{3/2}$ spectra c).

The change in the degree of inversion is expected to correlate with changes in the conductivity and the magnetic properties.[19] A similar effect would result from the presence of defects. The agglomeration behaviour of the nanoparticulate powder was visibly altered by the synthesis time: the agglomeration was especially pronounced for $CuFe_2O_4$ obtained at relatively short reaction times (5 and 10 min) and decreased with increasing reaction durations, in relation to a decrease in the degree of inversion, as also observable in DLS and ultracentrifugation measurements (Figure S14, Supporting Information). For $CuFe_2O_4$ with a synthesis time of 1 and 30 min – which are agglomerating least according to DLS measurements – particle diameters of 13 and 16 nm were obtained with the ultracentrifugation experiments, in good agreement to the sizes measured from TEM images. For more strongly agglomerating particles, a shoulder can be observed around 13 nm, but no accurate size determination is possible, due to the pronounced agglomeration tendency.

Electrocatalytic CO₂ Reduction

We evaluated the influence of the synthesis parameters on the electrochemical CO_2RR of $CuFe_2O_4$ electrodes in 0.1 M $KHCO_3$ solutions, using an H-cell setup (Figure S15, Supporting Information). In order to determine the optimal potential, chronoamperometric measurements were performed at different potentials for exemplary electrodes of the sample synthesised for 15 min at 175 °C (Figure S16, Supporting Information). The evolved gases were examined after 20 and 60 min, respectively, to differentiate between the initial activation phase, during which high negative currents occur due to the decomposition of organic residues and possible activation of $CuFe_2O_4$, and the steady state phase, for which the current response is stable. CO was the main C-product at all potentials, with the highest production rate at -0.8 V *vs.* RHE (**Figure 5**). The Faradaic efficiency and selectivity were best at lower potentials of -0.6 V, due to hydrogen evolution taking over at highly reducing potentials. The Faradaic efficiency was lower than the selectivity, which is calculated from only the gaseous products, at all potentials, indicating the formation of other C-products, albeit to a rather low extent. The difference was especially high at low potentials, which is in good agreement to the lower required potentials for methane or methanol formation.[66] A potential of -0.7 V *vs.* RHE was chosen in the following, to evaluate differences in the catalytic performance of $CuFe_2O_4$ prepared under varying synthesis conditions. The measurements were performed at least twice with freshly prepared electrodes, to account for possible variations between measurements.

A maximum CO yield of 0.2 µmol h^{-1} mg^{-1} was observed for $CuFe_2O_4$ synthesised for 10 min in the microwave, with the CO production rate sharply decreasing for samples obtained after longer synthesis times. The hydrogen evolution rate was highly similar for all samples independent of the synthesis time of the catalyst, with three to ten times more hydrogen being produced compared to CO. The CO yield was higher after one hour of potential application, probably due to the initial decomposition of organic residues. The Faradaic efficiency was also better after one hour and highest for the sample obtained after 10 min of reaction time (Figure 5).

Again, the Faradaic efficiency was slightly lower than the calculated selectivity based on gas product analysis, indicating the generation of low amounts of additional, liquid products. The difference in the observed activity and selectivity in dependence of time is probably based on two adverse effects. On the one hand, the relative mass of organic residues increases with decreasing reaction duration, as observed in TG-MS. Correspondingly, both activity and selectivity are lower for $CuFe_2O_4$ obtained after short synthesis times. In an adverse effect, the degree of inversion is decreasing with increasing

reaction time. On the one hand a decrease in the inversion parameter will result in an increased conductivity.[19]
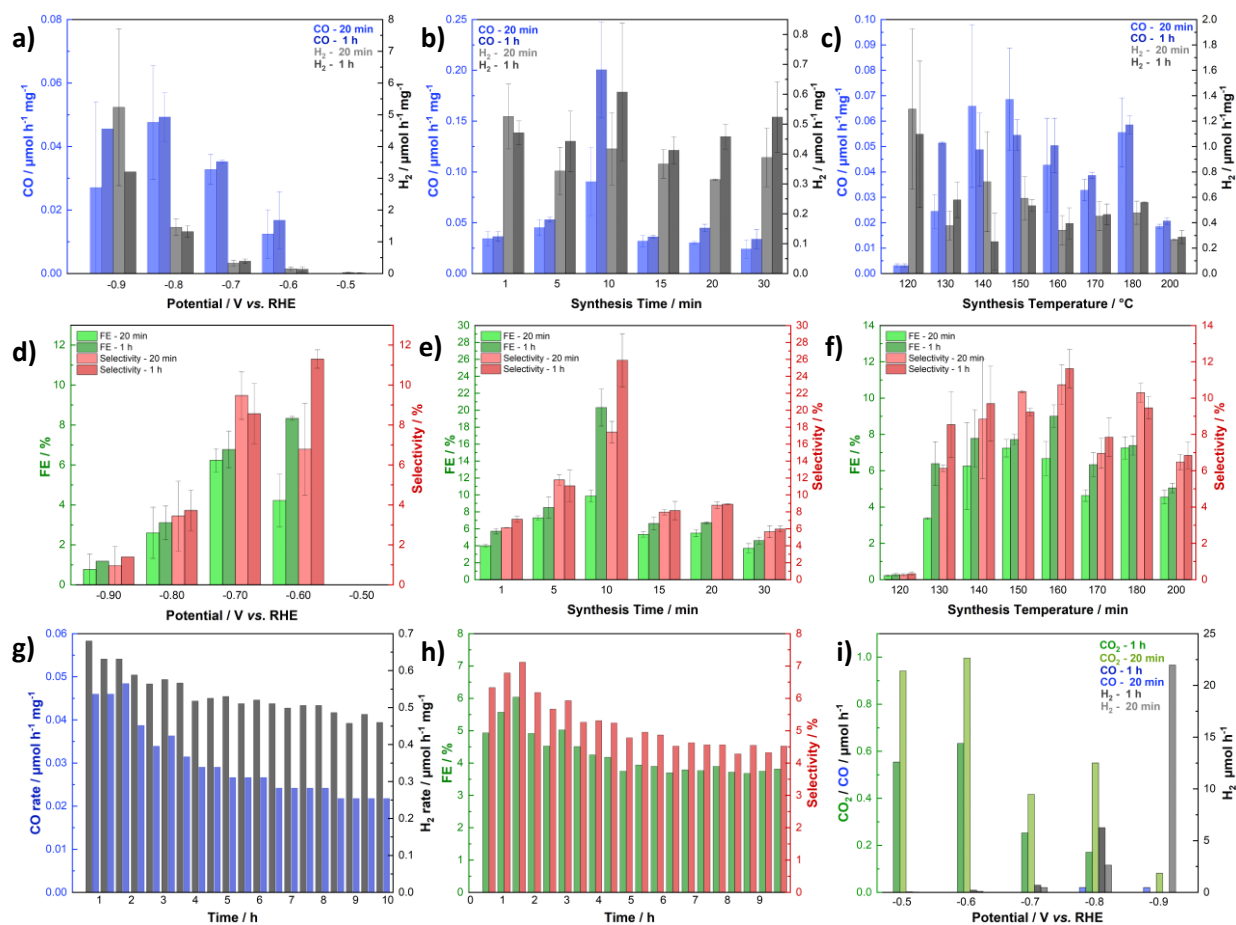
Figure 5 CO and H_2 production rates at a) different potentials for $CuFe_2O_4$ synthesised at 175 °C for 15 min, b) for $CuFe_2O_4$ synthesised at 175 °C obtained after different reaction times, and c) for $CuFe_2O_4$ synthesised at different temperatures. Corresponding Faradaic efficiencies and selectivities for CO are shown in d) for different potentials with $CuFe_2O_4$ synthesised at 175 °C for 15 min, in e) with $CuFe_2O_4$ synthesised at 175 °C obtained after different reaction times and in f) with $CuFe_2O_4$ synthesised for 15 min at different temperatures. The results for the long-time testing are shown in g,h). Comparative measurements in an Ar atmosphere solely yielded CO_2 and H_2 i). The performance evaluation at -0.9 V *versus* RHE was interrupted after 20 min, due to high currents.

Additionally, the local environment of copper – again determined by the degree of inversion – can have an influence on the catalytic performance. At the highly negative potentials employed for the CO_2RR, $CuFe_2O_4$ is likely at least partially reduced similar to what has been reported for binary copper oxide materials. In the case of copper oxide, the morphology and composition of the initial CuO_x have been shown to have a significant influence on the activity and selectivity.[8,9,67-69] While some suggest that sub-surface oxygen or residual Cu^{x+} species play a crucial role in the CO_2 reduction, others argue that copper is completely reduced under the employed conditions.[8,69] Therefore, the initial cation distribution and primary coordination of copper by four or six oxygen atoms, respectively, can also be expected to affect the performance of the catalyst, since it may influence the stability against reduction and the local environment (*e.g.* coordination number) of active copper species. For example Acharya *et al*. observed a dependence of the performance of a $FeNiO(H)_x$ catalyst in electrochemical oxygen evolution on the coordination environment of Fe^{3+},[70] elucidating that the cation coordination environment and change thereof can have a significant influence on the activity in electrocatalysis.

Indeed, Cu^{2+} in the spinel can partially be reduced to Cu^0 as shown by CV measurements in Ar saturated Na_2SO_4 solution.[71,72] The reduction was, however, clearly not completed after one scan, since an evolution with time was observed, indicating, that the process is taking several minutes. If the CV scans were performed on electrophoretic deposited $CuFe_2O_4$ on FTO, a colour change to black was observed, that was changing back to normal after storage under air, or application of a positive potential (Figure S17, Supporting Information). XRD after the experiment shows the spinel structure, proving that the reduction is reversible, or restricted to the surface (Figure S17, Supporting Information). The same redox peaks are apparent in the CV scans performed before the CO_2RR experiments in CO_2 saturated $KHCO_3$, although the reduction peaks overlap with the highly negative current response for CO_2 reduction (Figure S18, Supporting Information). The CV after the CO_2RR still shows the same redox features, supporting the reversibility of the redox processes.

A correlation of the crystallite size and micro-strain of $CuFe_2O_4$ electrocatalysts prepared with different synthesis times with their activity and selectivity in the CO_2RR was also noted and might partially contribute to the observed trend, as both could affect conductivity. Si and K doping, as well as Cu extraction at prolonged reaction times furthermore represents an increasing concentration of defects, that might alter the electronic and surface properties of $CuFe_2O_4$, resulting in a decreased activity.

Additionally, the CO_2RR experiment was performed on $CuFe_2O_4$ obtained at different temperatures. A highly similar activity was observed for samples obtained at temperatures between 130 and 180 °C, even though the amount of organic residues and of Cu^+ species varied between samples. Both differences are small, however, for $CuFe_2O_4$ synthesised in this temperature range. The determined degree of inversion was additionally similar for all samples, supporting the dominant influence of this parameter on the activity. Only for $CuFe_2O_4$ prepared at very low synthesis temperature, *i.e.* 120 °C, the high amounts of organic residues, significant presence of surface Cu^+ species, and low crystallinity resulted in a markedly decreased CO production rate and FE. The CO production rate – and to a lesser extent also the FE – was additionally decreased for the sample obtained at 200 °C. This is likely due to the observed Cu_2O by-phase. Deviations in the amounts of Cu^+ observed in the XPS for samples obtained at different temperatures, apparently only had a negligible influence on the performance, likely because the coordination environment was similar and some reduction of copper proceeds anyway during the electrochemical measurement.

Gas evolution rates are also shown non-normalised in Figure S19, Supporting Information, exhibiting smaller deviations between measurements and a comparable activity between both studies. This is at least partially due to some of the catalyst ink diffusing underneath the Kapton tape, thus contributing to the apparent mass loading while not being in contact with the electrolyte.

Due to the presence of organic residues as observed in the DRIFT and TG-MS measurements and their apparent decomposition in the initial phase of the potential application, we performed a comparative experiment in argon atmosphere, to verify that the observed CO does not stem from organic adsorbates at the catalyst surface. Depending on the applied potential, CO_2 and H_2 were detected with the CO_2 to H_2 ratio highest at low overpotentials (Figure 5). The measured currents were significantly lower than in a CO_2 atmosphere, supporting the CO_2 conversion to CO. Blank carbon paper electrodes only yielded low amounts of hydrogen and no CO (Figure S20, Supporting Information). The duration of the CO_2RR could be extended to several hours at -0.7 V *vs.* RHE, although the activity started to slightly decrease after two hours (Figure 5), as did the current response. Slow material changes might occur with time, such as a more prominent reduction of metal ions or possibly also cation redistribution. However, since no flow setup was used, a portion of the decrease might also simply be

due to electrolyte decomposition and detachment of the catalyst from the carbon paper caused by gas bubble formation. These effects might be mitigated by an optimisation of the electrode preparation that was not in the focus of this research. Still, the preliminary results exhibit the potential of $CuFe_2O_4$ as an electrocatalyst for the CO_2RR. Even after the measurement for 10 h no alcoholic products were found (Figure S21, Supporting Information). Thus, the CO_2 to CO reduction is highly selective, and while large amounts of hydrogen are produced alongside CO, this product composition can be beneficial for the subsequent use as syngas, *e.g.* in the Fischer-Tropsch process. XRD patterns were measured for $CuFe_2O_4$ on carbon paper before and after the electrocatalysis (Figure S22, Supporting Information). Mostly reflections corresponding to $CuFe_2O_4$ are visible after the electrocatalysis, proving the good stability/ reversibility of occurring redox reactions in the material even at highly reducing potentials. After the CO_2RR was conducted for 1 h at -0.9 V vs. RHE, additional reflections for Cu_2O were observed, indicating partial reduction of the material under operating conditions, in agreement to the observed colour change during CV on FTO (Figure S17, Supporting Information) and to what is known for copper oxide-derived electrocatalysts.[8]

6.1.3 Conclusion

We successfully prepared $CuFe_2O_4$ nanoparticles with a cubic, partially inverted spinel structure *via* a fast, low-temperature aqueous approach. A crystalline product was obtained after only 1 min at 175 °C in a microwave-assisted synthesis. A prolonged reaction time resulted in a decrease of the inversion parameter, and only a slight increase in the particle size was observed. The application in electrochemical CO_2 to CO reduction was very selective for CO and hydrogen, and an optimum performance was observed for $CuFe_2O_4$ obtained after medium synthesis duration (10 min), in correlation to the highest crystallite size and a medium degree of inversion. Samples obtained after shorter synthesis times contained large amounts of organic residues adsorbed to the particle surface that likely impede the activity of the $CuFe_2O_4$ catalyst, while those obtained after 30 min exhibited a decreased copper content, likely due to defect induction during cation migration, that likewise diminish the catalytic performance. Moreover, the synthesis temperature could be tuned between 120 and 200 °C. Both the material properties (degree of inversion, crystallite and particle size) and the electrochemical performance were largely independent of the temperature, although high amounts of surface Cu^+ and organic residues impeded the performance of the sample synthesised at only 120 °C, and very low amounts of a Cu_2O by-phase were observed for the one obtained at 200 °C. The mild reaction conditions and very good availability of the material constituents make $CuFe_2O_4$ a promising electrocatalyst for the sustainable production of syngas.

6.1.4 Experimental Section

Microwave assisted synthesis of $CuFe_2O_4$: Chemicals were purchased from commercial providers and used without further purification. In a typical approach 1 mmol of $Fe(NO_3)_3 \cdot 9 H_2O$ (404 mg, Acros Organics +99%) and 0.5 mmol of $Cu(NO_3)_2 \cdot 3 H_2O$ (120.8 mg, Acros Organics +99 %) were dissolved in a mixture of ethylene glycol (Acros Organics, 99.5 %) and water. The pH was adjusted to 12 with 3M KOH solution under rigorous stirring in a borosilicate microwave vial. The vial was sealed and placed in the microwave reactor (Monowave 400, Anton Paar), where it was heated to the desired temperature

as fast as possible under stirring at 800 rpm. After the specified time, the solution was cooled with compressed air to 55 °C. The $CuFe_2O_4$ particles were collected *via* centrifugation, washed thrice with water and once with ethanol and dried over night at 80 °C.

Characterisation: As-synthesised $CuFe_2O_4$ samples were characterised with *powder X-ray diffraction* (XRD), using either a Malvern PANalytical Empyrean device with Cu K_α irradiation (λ_1 = 1.5406 Å; λ_2 = 1.54443 Å) with an acceleration voltage of 40 kV and an emission current of 40 mA, or a STOE STADI P Mythen2 4K diffractometer with Ag $K_{\alpha1}$ irradiation (λ = 0.5594 Å), a Ge(111) monochromator and equipped with four Dectris MYTHEN2 R 1K strip detectors.[73] For Cu-XRD measurements, a spinning sample holder and Bragg-Brentano geometry were used, while the Ag-XRD measurements were performed in transmission geometry with Hilgenberg capillaries (0.5mm). For improved data quality, measurements with Ag irradiation were performed repeatedly and automatically accumulated. *X'Pert Highscore plus* was used for phase analysis. Rietveld refinement was performed using *FullProf*.[74] The instrumental resolution was determined with LaB_6 (NIST SRM 660c). A Thompson-Cox-Hastings pseudo-Voigt function was used for peak shape modelling and the background was approximated by linear interpolation between manually added points.[75] Refined parameters are zero, scale, cell parameters, FWHM with focus on the Lorentz contribution and including asymmetry parameters and size anisotropy, isotropic B values and occupation (using a half inverted structure as starting point). The crystallographic information published by Mahmood *et al*. was used for the refinement of $CuFe_2O_4$,[76] and the information provided by Kirfel *et al.* was employed for a Cu_2O by-phase if required.[77] The fitting procedure was repeated at least twice and depicted error bars represent the standard deviation between fits.

Transmission electron microscopy (TEM) was employed for the determination of sample morphology, size and crystallinity, using a 200 kV JEOL JEM-2200FS EFTEM, equipped with a Schottky FEG and an omega in-column energy filter. Particle sizes were evaluated with ImageJ 1.53e. The morphology was additionally examined by scanning electron microscopy (SEM), that was performed on a Zeiss Leo 1530 device at an acceleration voltage of 3 kV after sputter-coating with platinum (Cressington Sputter Coater 208 HR). The same instrument was used for energy dispersive X-ray diffraction spectroscopy (EDX) using an acceleration voltage of 20 kV and an ultra-dry EDX detector by Thermo Fisher Scientific NS7.

X-ray photoelectron spectroscopy (XPS) was performed on a Physical Electronics PHI VersaProbe III Scanning XPS Microprobe instrument, using monochromatic Al K_α irradiation with a beam diameter of 100 µm. The beam voltage was set to 15 kV, the X-ray power to 25 W. Survey scans were recorded with a step size of 0.4 eV and step time of 50 ms at a pass energy of 224 eV. For high-resolution spectra, step size and time were set to 0.1 eV and 50 ms, respectively, using a pass energy of 26 eV. To avoid charging effects, samples were continuously flooded with electrons and Ar^+ ions at low energy. Data was evaluated with CASA XPS 2.3.17, using Shirley backgrounds and Gaussian-Lorentzian line shapes (GL30, except for Cu_2O (GL80), based on the work of Biesinger).[61] For charge correction, the maximum of the Cu-$L_3M_{4,5}M_{4,5}$ Auger peak was fitted with the minimum required number of peaks and set to a kinetic energy of 917.7 eV.[61] For samples containing large amounts of surface Cu^+, the peak maximum was instead set to a kinetic energy of 916.8 eV. Fe $2p$ spectra were fitted with a doublet separation of 13.8 eV,[78] and restricted area ratios of 2:1 for $2p_{3/2}$ to $2p_{1/2}$ in order to compensate for the overlap between Fe $2p_{3/2}$ and a minor Cu Auger $L_2M_{2,3}M_{2,3}$ signal. Furthermore, FWHM were set to identical for

all Fe peak components within the $2p_{3/2}$ to $2p_{1/2}$ signals, respectively, but not identical for $2p_{3/2}$ and $2p_{1/2}$.[79]

For diffuse reflectance infrared Fourier transformed (DRIFT) spectroscopy, a Bruker Alpha II spectrometer and the software OPUS were used. For Raman measurements, a WITec alpha RA+ imaging system was employed, equipped with a UHTS 300 spectrometer and a Andor Newton 970 EMCCD camera. Diffuse-reflectance UV/vis measurements were performed on a Perkin Elmer Lambda 750 spectrometer, using a Praying Mantis (Harrick) and spectralon as white standard.

Dynamic light scattering measurements were performed on a Litesizer 500 instrument from Anton Paar, at a wavelength of 568 nm and 25 °C. Angle and focus were set to automatic. 5 mg of $CuFe_2O_4$ were dispersed in 20 mL of ultra-pure water for 2 h using ultrasonication. For the calculation of the number weighed intensity distribution, an absorption coefficient of 0.1 m^{-1} and a refractive index of 2.5 were used, respectively. For particle size determination a disc centrifuge DC24000 (CPS Instruments Inc.) was additionally used. Dispersions of 10 mg of sample in 1 mL of ultra-pure H_2O were prepared *via* ultrasonification and 0.1 mL were injected at 24k rpm. A density gradient was prepared using sucrose solutions. The same optical parameters as for DLS measurements were employed and a PVC solution was used as a standard. For both DLS and ultracentrifugal experiments, measurements were repeated at least thrice.

For the characterisation of specific surface area and gas adsorption properties, N_2 physisorption was performed on an Autosorb iQ-MP-MP-AG instrument (Anton Paar QuantaTec) at 77 K. Samples were degassed for 12 h at 120 °C prior to the measurements. For surface area calculation, the Brunauer-Emmet-Teller (BET) model was used and the data was evaluated with ASiQwin. For pore size distributions, the DFT model was used, treating the absorbent as silica.

Thermogravimetric Analysis (TGA) with gas evolution detected via mass spectrometry (MS) was conducted with a Netzsch Jupiter STA 449C thermobalance and a Netzsch Aeolos QMS 402C quadrupole MS. The sample was heated to 850 °C in air, using a heating ramp of 5 K/min.

Electrochemical Experiments: The electrochemical CO_2 reduction (CO2RR) was performed in a two compartment cell, using CO_2 saturated 0.1 M aqueous $KHCO_3$ solution as the electrolyte and a three electrode setup. Anolyte and catholyte compartment were separated by a Selemion AMV-N anion-exchange membrane (AGC group) and both were continuously purged with CO_2 gas from the bottom, with the flow rate for the working electrode compartment set to 20 mL/min (mass flow controller from Bronkhorst). A platinum counter electrode and a Ag/AgCl reference electrode were employed for the measurement. For the preparation of the working electrode, 10 mg of $CuFe_2O_4$ were dispersed in 300 µL of *i*-propanol (p.a) and 20 µL of a 5 wt.% Nafion solution (Alfa Aesar), using ultrasonication for minimum 1 h. Subsequently, 50 µL of the obtained catalyst ink were drop-cast onto carbon paper (Freudenberg H2315-C2) electrodes that were cut into 1 cm wide stripes. The exposed area was restricted to 1 cm^2 using Kapton tape. The electrodes were left to dry for at least one day in air. The electrolyte was purged with CO_2 (99.995 volume%, Air Liquide) for at least 10 min, prior to potential application. The internal resistance was checked and automatically corrected for prior to the actual experiment. A Gamry Reference 3000 potentiostat together with the software Gamry Framework were employed for all electrochemical measurements. The evolved gases were analysed *via* gas chromatography (Shimadzu GC-2014, equipped with a HayeSep Q and a HayeSep R column in series, a thermal conductivity detector and a methaniser in series with a flame ionisation detector (FID)) after

20 and 60 min. The potential was corrected to RHE with $V_{RHE} = V_{Ag/AgCl} + 0.209 + 0.059*pH$. For the reference measurement in Ar, the CO_2 gas was replaced by Ar at a flow rate of 20 mL/min. The pH change from 6.8 to 9.7 was taken into account for the conversion of the applied potential to RHE. Electrolyte from the working electrode compartment was sampled after the end of the experiment and analysed with a liquid chromatograph (Shimadzu, GC-2030), equipped with a SH-Stabilwax column and FID, for the presence of alcohols and aldehydes. Faradaic efficiencies were calculated from the partial current for CO, or H_2, respectively, whereas selectivity calculations are based on the relative fraction of CO in gaseous products, *i.e.* H_2 and CO together. Cyclic voltammetry (CV) measurements in a CO_2 atmosphere were conducted with the same setup at a scan rate of 20 mV/s. For comparative measurements in 0.1 M Na_2SO_4, $CuFe_2O_4$ was deposited electrophoretically on a fluorine doped tin oxide (FTO) substrate. The CV scans were performed with a three electrode setup in a PECC-2 cell (Zahner Elektrik), using platinum as a counter, Ag/AgCl as a reference and the deposited sample on FTO as a working electrode, respectively, with the exposed area of the latter being restricted to 1 cm^2. A Zennium potentiostat (Zahner Elektrik) was used and the scan rate was 20 mV/s.

Supporting Information

Supporting Information is available from the Wiley Online Library or from the author.

Conflict of interest

The authors declare no conflict of interest.

Data Availability Statement

The data that support the findings of this study are available from the corresponding author upon reasonable request. Open Access funding enabled and organized by Projekt DEAL.

6.1.5 References

(1)   Lu, Q.; Jiao, F. *Nano Energy* **2016**, *29*, 439–456.

(2)   Kumar, B.; Brian, J. P.; Atla, V.; Kumari, S.; Bertram, K. A.; White, R. T.; Spurgeon, J. M. *Catal. Today* **2016**, *270*, 19–30.

(3)   Jones, J. P.; Prakash, G. K. S.; Olah, G. A. *Isr. J. Chem.* **2014**, *54*, 1451–1466.

(4)   Nitopi, S.; Bertheussen, E.; Scott, S. B.; Liu, X.; Engstfeld, A. K.; Horch, S.; Seger, B.; Stephens, I. E. L.; Chan, K.; Hahn, C.; Nørskov, J. K.; Jaramillo, T. F.; Chorkendorff, I. *Chem. Rev.* **2019**, *119*, 7610–7672.

(5)   Zou, Y.; Wang, S. *Adv. Sci.* **2021**, *8*, 2003579.

(6)   Zhou, Y.; Martín, A. J.; Dattila, F.; Xi, S.; López, N.; Pérez-Ramírez, J.; Yeo, B. S. *Nat. Catal.* **2022**, *5*, 545–554.

(7)   Fu, W.; Liu, Z.; Wang, T.; Liang, J.; Duan, S.; Xie, L.; Han, J.; Li, Q. *ACS Sustain. Chem. Eng.* **2020**, *8*, 15223–15229.

(8)   Lum, Y.; Ager, J. W. *Angew. Chemie - Int. Ed.* **2018**, *57*, 551–554.

(9)   Mandal, L.; Yang, K. R.; Motapothula, M. R.; Ren, D.; Lobaccaro, P.; Patra, A.; Sherburne, M.; Batista, V. S.; Yeo, B. S.; Ager, J. W.; Martin, J.; Venkatesan, T. *ACS Appl. Mater. Interfaces* **2018**, *10*, 8574–8584.

(10)   Lee, S. H.; Lin, J. C.; Farmand, M.; Landers, A. T.; Feaster, J. T.; Avilés Acosta, J. E.; Beeman, J. W.; Ye, Y.; Yano, J.; Mehta, A.; Davis, R. C.; Jaramillo, T. F.; Hahn, C.; Drisdell, W. S. *J. Am. Chem. Soc.* **2021**, *143*, 588–592.

(11)   Balagurov, A. M.; Bobrikov, I. A.; Pomjakushin, V. Y.; Sheptyakov, D. V.; Yushankhai, V. Y. *J. Magn. Magn. Mater.* **2015**, *374*, 591–599.

(12)   Desai, M.; Prasad, S.; Venkataramani, N.; Samajdar, I.; Nigam, A. K.; Krishnan, R. *J. Appl. Phys.* **2002**, *91*, 2220–2227.

(13)   Yadav, R. S.; Havlica, J.; Masilko, J.; Kalina, L.; Wasserbauer, J.; Hajdúchová, M.; Enev, V.; Kuřitka, I.; Kožáková, Z. *J. Supercond. Nov. Magn.* **2016**, *29*, 759–769.

(14)   Ohnishi, H.; Teranishi, T. *J. Phys. Soc. Japan* **1961**, *16*, 35–43.

(15)   Yang, A.; Zuo, X.; Chen, L.; Chen, Z.; Vittoria, C.; Harris, V. G. *J. Appl. Phys.* **2005**, *97*, 10G107-1.

(16)   Sanchez-Lievanos, K. R.; Stair, J. L.; Knowles, K. E. *Inorg. Chem.* **2021**, *60*, 4291–4305.

(17)   Zuo, X.; Yang, A.; Vittoria, C.; Harris, V. G. *J. Appl. Phys.* **2006**, *99*, 08M909.

(18)   Balagurov, A. M.; Bobrikov, I. A.; Maschenko, M. S.; Sangaa, D.; Simkin, V. G. *Crystallogr. Reports* **2013**, *58*, 710–717.

(19)   Zhang, R.; Yuan, Q.; Ma, R.; Liu, X.; Gao, C.; Liu, M.; Jia, C. L.; Wang, H. *RSC Adv.* **2017**, *7*, 21926–21932.

(20)   Yokoyama, M.; Nakamura, A.; Sato, T.; Haneda, K. *J. Magn. Soc. Japan* **1998**, *22*, 243–245.

(21)   Roy, S.; Ghose, J. *J. Appl. Phys.* **2000**, *87*, 6226–6228.

(22)   Khunphonoi, R.; Khemthong, P.; Luadthong, C.; Kuboon, S.; Kongmark, C.; Viriya-empikul, N.; Kidkhunthod, P.; Pinitsoontorn, S.; Faungnawakij, K. *RSC Adv.* **2022**, *12*, 15526–15533.

(23)   Reitz, C.; Suchomski, C.; Haetge, J.; Leichtweiss, T.; Jagličić, Z.; Djerdj, I.; Brezesinski, T. *Chem. Commun.* **2012**, *48*, 4471–4473.

(24)   Feng, M.; Yang, A.; Zuo, X.; Vittoria, C.; Harris, V. G. *J. Appl. Phys.* **2010**, *107*, 09A521.

(25)   Bera, S.; Ghosh, S.; Maiyalagan, T.; Basu, R. N. *ACS Appl. Energy Mater.* **2022**, *5*, 3821–3833.

(26)   Park, S.; Baek, J. H.; Zhang, L.; Lee, J. M.; Stone, K. H.; Cho, I. S.; Guo, J.; Jung, H. S.; Zheng, X. *ACS Sustain. Chem. Eng.* **2019**, *7*, 5867–5874.

(27) Guijarro, N.; Bornoz, P.; Prévot, M.; Yu, X.; Zhu, X.; Johnson, M.; Jeanbourquin, X.; Le Formal, F.; Sivula, K. *Sustain. Energy Fuels* **2018**, *2*, 103–117.

(28) Liu, Y.; Le Formal, F.; Boudoire, F.; Yao, L.; Sivula, K.; Guijarro, N. *J. Mater. Chem. A* **2019**, *7*, 1669–1677.

(29) Tao, S.; Gao, F.; Liu, X.; Sørensen, O. T. *Mater. Sci. Eng. B Solid-State Mater. Adv. Technol.* **2000**, *77*, 172–176.

(30) Zheng, J.; Lin, Z.; Liu, W.; Wang, L.; Zhao, S.; Yang, H.; Zhang, L. *J. Mater. Chem. B* **2014**, *2*, 6207–6214.

(31) Ferreira, L. S.; Silva, T. R.; Silva, V. D.; Raimundo, R. A.; Simões, T. A.; Loureiro, F. J. A.; Fagg, D. P.; Morales, M. A.; Macedo, D. A. *Adv. Powder Technol.* **2022**, *33*, 103391.

(32) Rezaul Karim, K. M.; Tarek, M.; Ong, H. R.; Abdullah, H.; Yousuf, A.; Cheng, C. K.; Khan, M. M. R. *Ind. Eng. Chem. Res.* **2019**, *58*, 563–572.

(33) Rezaul Karim, K. M.; Ong, H. R.; Abdullah, H.; Yousuf, A.; Cheng, C. K.; Rahman Khan, M. M. *Int. J. Hydrogen Energy* **2018**, *43*, 18185–18193.

(34) Khan, M. R.; Uddin, M. R.; Abdullah, H.; Karim, K. R.; Yousuf, A. *Int. J. Chem. Mol. Nucl. Mater. Metall. Eng.* **2016**, *10*, 1273–1280.

(35) Köferstein, R.; Walther, T.; Hesse, D.; Ebbinghaus, S. G. *J. Solid State Chem.* **2014**, *213*, 57–64.

(36) Ramaprasad, T.; Kumar, R. J.; Naresh, U.; Prakash, M.; Kothandan, D.; Naidu, K. C. B. *Mater. Res. Express* **2018**, *5*, 095025.

(37) Simon, C.; Zakaria, M. B.; Kurz, H.; Tetzlaff, D.; Blösser, A.; Weiss, M.; Timm, J.; Weber, B.; Apfel, U. P.; Marschall, R. *Chem. - A Eur. J.* **2021**, *27*, 16990–17001.

(38) Bloesser, A.; Kurz, H.; Timm, J.; Wittkamp, F.; Simon, C.; Hayama, S.; Weber, B.; Apfel, U.; Marschall, R. *ACS Appl. Nano Mater.* **2020**, *3*, 11587–11599.

(39) Simon, C.; Blösser, A.; Eckardt, M.; Kurz, H.; Weber, B.; Zobel, M.; Marschall, R. *Zeitschrift fur Anorg. und Allg. Chemie* **2021**, *647*, 2061–2072.

(40) Komarneni, S.; D'Arrigo, M. C.; Leonelli, C.; Pellacani, G. C.; Katsuki, H. *J. Am. Ceram. Soc.* **1998**, *81*, 3041–3043.

(41) Solano, E.; Perez-Mirabet, L.; Martinez-Julian, F.; Guzmán, R.; Arbiol, J.; Puig, T.; Obradors, X.; Yañez, R.; Pomar, A.; Ricart, S.; Ros, J. *J. Nanoparticle Res.* **2012**, *14*, 1034.

(42) Bilecka, I.; Djerdj, I.; Niederberger, M. *Chem. Commun.* **2008**, 886–888.

(43) Phuruangrat, A.; Kuntalue, B.; Thongtem, S.; Thongtem, T. *Mater. Lett.* **2016**, *167*, 65–68.

(44) Jalajerdi, R.; Ghanbari, D. *J. Nanostructures* **2016**, *6*, 278–284.

(45) Altincekic, T. G.; Boz, I.; Baykal, A.; Kazan, S.; Topkaya, R.; Toprak, M. S. *J. Alloys Compd.* **2010**, *493*, 493–498.

(46) Chatterjee, B. K.; Bhattacharjee, K.; Dey, A.; Ghosh, C. K.; Chattopadhyay, K. K. *Dalt. Trans.* **2014**, *43*, 7930–7944.

(47) Silva, M. D. P.; Silva, F. C.; Sinfrônio, F. S. M.; Paschoal, A. R.; Silva, E. N.; Paschoal, C. W. A. *J. Alloys Compd.* **2014**, *584*, 573–580.

(48) Waldron, R. D. *Phys. Rev. B* **1955**, *99*, 1727–1735.

(49) Selvan, R. K.; Augustin, C. O.; Berchmans, L. J.; Saraswathi, R. *Mater. Res. Bull.* **2003**, *38*, 41–54.

(50) Shameli, K.; Ahmad, M. Bin; Jazayeri, S. D.; Sedaghat, S.; Shabanzadeh, P.; Jahangirian, H.; Mahdavi, M.; Abdollahi, Y. *Int. J. Mol. Sci.* **2012**, *13*, 6639–6650.

(51) Caccamo, M. T.; Magazù, S. *Appl. Spectrosc.* **2017**, *71*, 401–409.

(52) Zhang, R.; Liu, M.; Lu, L.; Mi, S. B.; Jia, C. L.; Wang, H. *RSC Adv.* **2016**, *6*, 100108–100114.

(53) Díez-García, M. I.; Lana-Villarreal, T.; Gómez, R. *ChemSusChem* **2016**, *9*, 1504–1512.

(54) Le Nestour, A.; Gaudon, M.; Villeneuve, G.; Andriessen, R.; Demourgues, A. *Inorg. Chem.* **2007**,

46, 2645–2658.

(55) Biramally, K.; Pujari, N.; Karidas, S.; Shareefuddin, M. D.; Sreenivasu, D.; Vardhani, C. P. *AIP Conf. Proc.* **2019**, *2104*, 030016.

(56) Rodríguez, F.; Hernández, D.; Garcia-Jaca, J. *Phys. Rev. B - Condens. Matter Mater. Phys.* **2000**, *61*, 16497–16501.

(57) Kulkarni, R. G.; Patil, V. U. *J. Mater. Sci.* **1980**, *15*, 2221–2223.

(58) Fantauzzi, M.; Secci, F.; Sanna Angotzi, M.; Passiu, C.; Cannas, C.; Rossi, A. *RSC Adv.* **2019**, *9*, 19171–19179.

(59) Aghavnian, T.; Moussy, J. B.; Stanescu, D.; Belkhou, R.; Jedrecy, N.; Magnan, H.; Ohresser, P.; Arrio, M. A.; Sainctavit, P.; Barbier, A. *J. Electron Spectros. Relat. Phenomena* **2015**, *202*, 16–21.

(60) Grosvenor, A. P.; Kobe, B. A.; Biesinger, M. C.; McIntyre, N. S. *Surf. Interface Anal.* **2004**, *36*, 1564–1574.

(61) Biesinger, M. C. *Surf. Interface Anal.* **2017**, *49*, 1325–1334.

(62) Biesinger, M. C.; Payne, B. P.; Grosvenor, A. P.; Lau, L. W. M.; Gerson, A. R.; Smart, R. S. C. *Appl. Surf. Sci.* **2011**, *257*, 2717–2730.

(63) Zhou, Y.; Du, Y.; Xi, S.; Xu, Z. J. *Electrocatalysis* **2018**, *9*, 287–292.

(64) Zhou, Y.; Sun, S.; Wei, C.; Sun, Y.; Xi, P.; Feng, Z.; Xu, Z. J. *Adv. Mater.* **2019**, *31*, 1902509.

(65) Harada, M.; Kotegawa, F.; Kuwa, M. *ACS Appl. Energy Mater.* **2022**, *5*, 278–294.

(66) Chandrasekaran, S.; Bowen, C.; Zhang, P.; Li, Z.; Yuan, Q.; Ren, X.; Deng, L. *J. Mater. Chem. A* **2018**, *6*, 11078–11104.

(67) Xie, J.; Huang, Y.; Yu, H. *Front. Environ. Sci. Eng.* **2015**, *9*, 861–866.

(68) Velasco-Vélez, J. J.; Chuang, C. H.; Gao, D.; Zhu, Q.; Ivanov, D.; Jeon, H. S.; Arrigo, R.; Mom, R. V.; Stotz, E.; Wu, H. L.; Jones, T. E.; Roldan Cuenya, B.; Knop-Gericke, A.; Schlögl, R. *ACS Catal.* **2020**, *10*, 11510–11518.

(69) Chou, T. C.; Chang, C. C.; Yu, H. L.; Yu, W. Y.; Dong, C. L.; Velasco-Vélez, J. J.; Chuang, C. H.; Chen, L. C.; Lee, J. F.; Chen, J. M.; Wu, H. L. *J. Am. Chem. Soc.* **2020**, *142*, 2857–2867.

(70) Acharya, P.; Manso, R. H.; Hoffman, A. S.; Bakovic, S. I. P.; Kekedy-Nagy, L.; Bare, S. R.; Chen, J.; Greenlee, L. F. *ACS Catal.* **2022**, *12*, 1992–2008.

(71) Giri, S. D.; Sarkar, A. *J. Electrochem. Soc.* **2016**, *163*, H252–H259.

(72) Caballero-Briones, F.; Artés, J. M.; Díez-Pérez, I.; Gorostiza, P.; Sanz, F. *J. Phys. Chem. C* **2009**, *113*, 1028–1036.

(73) Thomae, S. L. J.; Prinz, N.; Hartmann, T.; Teck, M.; Correll, S.; Zobel, M. *Rev. Sci. Instrum.* **2019**, *90*.

(74) Rodrígues-Carvajal, J. *Comm. Powder Diffr. Int. Union Crystallogr. Newsl.* **2001**, *December 2*, 12–19.

(75) Thompson, P.; Cox, D. E.; Hastings, J. B. *J. Appl. Cryst.* **1987**, *20*, 79–83.

(76) Briceño, S.; Castillo, H. Del; Sagredo, V.; Bramer-Escamilla, W.; Silva, P. *Appl. Surf. Sci.* **2012**, *263*, 100–103.

(77) Kirfel, A.; Eichhorn, K. *Acta Crystallogr.* **1990**, *A46*, 271–284.

(78) Mills, P.; Sullivan, J. L. *J. Phys. D. Appl. Phys.* **1983**, *16*, 723–732.

(79) Moulder, J. F.; Stickle, W. F.; Sobol, P. E.; Bomben, K. D. *Handbook of X-Ray Photoelectron Spectroscopy*; Chastain, J., Ed.; Perkin-Elmer Corporation: Eden Prairie, 1993.

6.2 Supporting Information

Fast and facile microwave synthesis of cubic CuFe$_2$O$_4$ nanoparticles for electrochemical CO$_2$ reduction

J. Zander[a,b], M. Weiss[a], R. Marschall[a,b]*

[a] Department of Chemistry, University of Bayreuth, Universitätsstraße 30, Bayreuth 95447, Germany
[b] Bavarian Center for Battery Technology (BayBatt), University of Bayreuth, Universitätsstrasse 30, 95447 Bayreuth, Germany
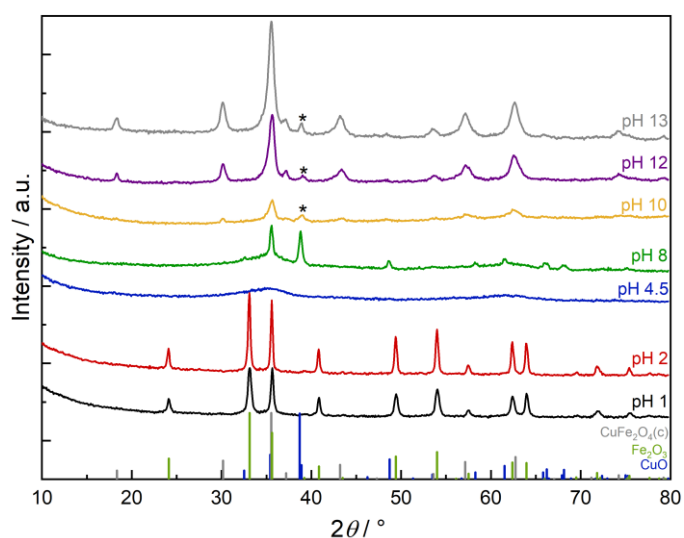
Figure S1 Cu-XRD patterns for CuFe$_2$O$_4$ obtained in water at varied pH, after reaction for 15 min at 150 °C. The main reflection of CuO is marked with a star. Following ICDD reference patterns were used: CuFe$_2$O$_4$: 01-077-0010; Fe$_2$O$_3$: 01-072-0469, CuO: 00-048-1548.
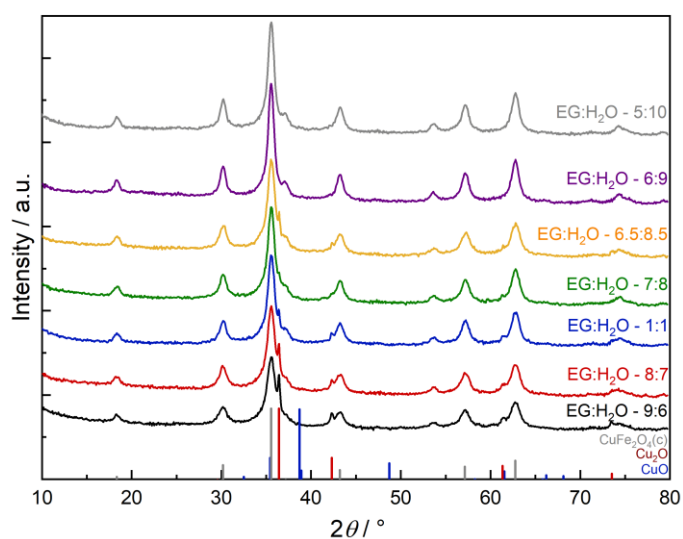
Figure S2 Cu-XRD patterns for CuFe$_2$O$_4$ obtained with different ratios of water and ethylene glycol, after reaction for 30 min at 175 °C. Following ICDD reference patterns were used: CuFe$_2$O$_4$: 01-077-0010; Cu$_2$O: 00-005-0667, CuO: 00-048-1548.
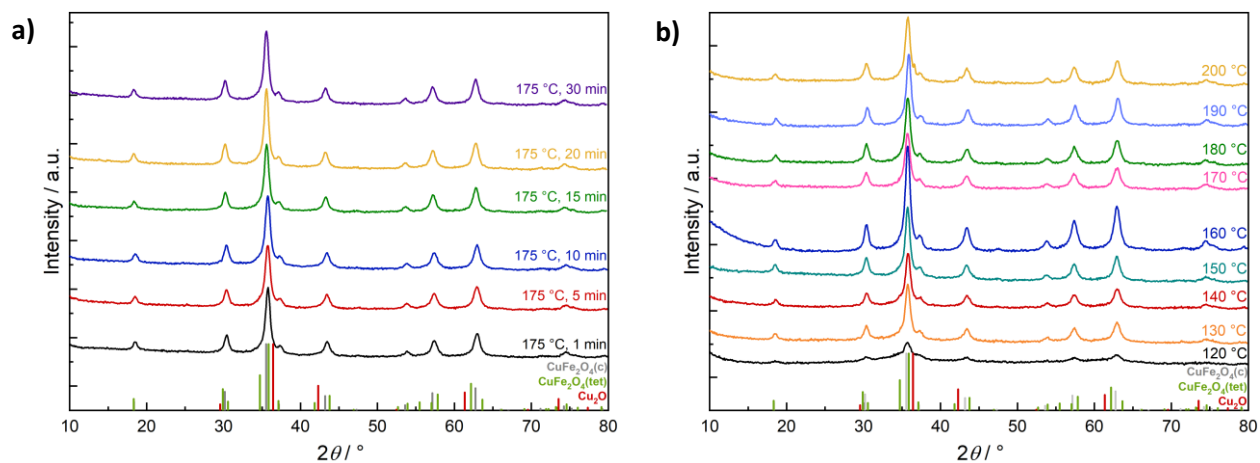
Figure S3 Cu-XRD patterns for CuFe$_2$O$_4$ obtained after different reaction temperatures at 175 °C (a) and after 15 min at different reaction times (b). Following ICDD reference patterns were used: CuFe$_2$O$_4$ (c): 01-077-0010; CuFe$_2$O$_4$ (t): 00-034-0425, Cu$_2$O: 00-005-0667.
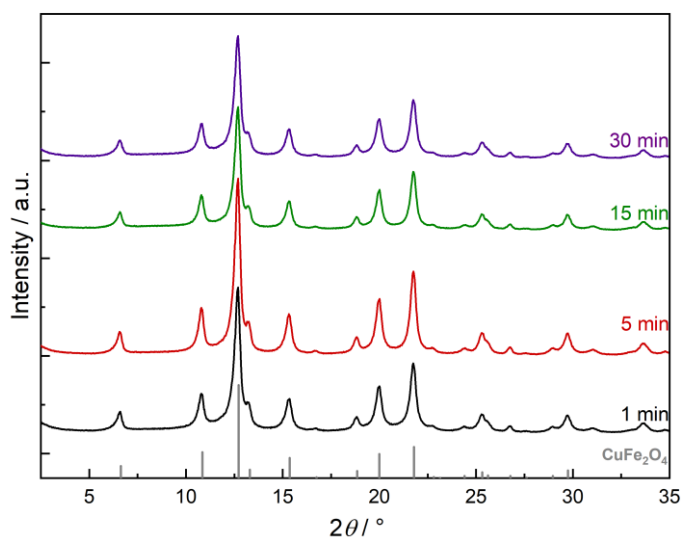
Figure S4 Ag-XRD patterns for CuFe$_2$O$_4$ obtained at 175 °C.
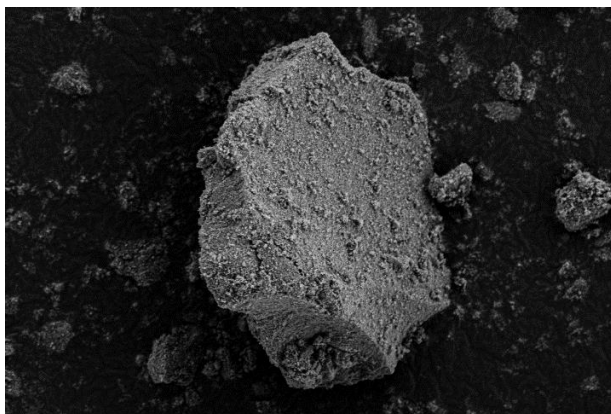
Table S1 EDX results for CuFe$_2$O$_4$.

	Fe At%	Cu At%	O %	Cu:Fe
Spot 1	18.5	9.2	59.3	0.498
Spot 2	27.2	13.8	49.1	0.507

Figure S5 SEM image of agglomerated CuFe$_2$O$_4$ nanoparticles synthesised for 15 min at 175 °C and EDX results of two different sampling areas.
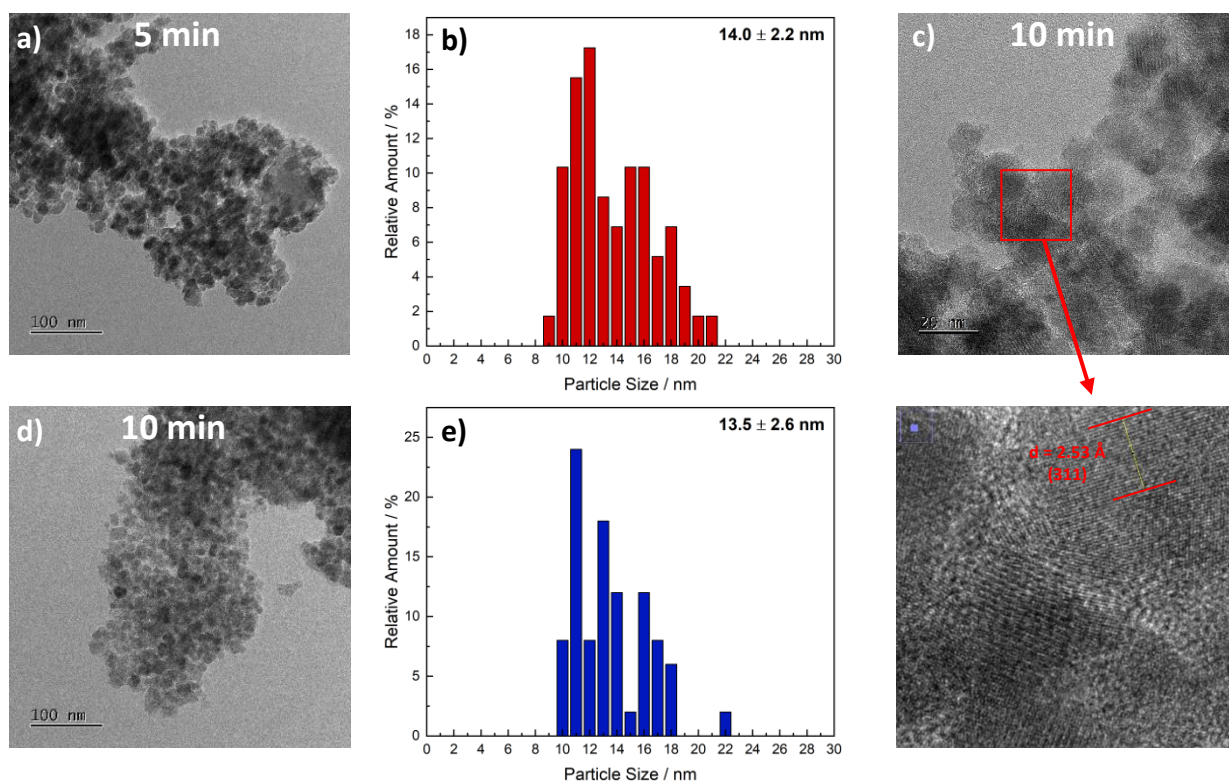
Figure S6 TEM images of CuFe$_2$O$_4$ obtained after reaction for 5 and 10 min, respectively, at 175 °C (a and d) and corresponding particle size distributions (b and e). High-resolution TEM image and lattice spacing is depicted in (c).

Synthesis Time at 175 °C	BET surface area / m²g⁻¹
1 min	119 ± 13
5 min	119 ± 10
10 min	117 ± 5
15 min	123 ± 9
20 min	118 ± 2
30 min	127 ± 9

Synthesis Temperature (15 min)	BET surface area / m²g⁻¹
120 °C	257 ± 48
140 °C	182 ± 15
160 °C	124 ± 4
180 °C	113 ± 9
200 °C	109 ± 5

Synthesis Time at 150 °C	BET surface area / m²g⁻¹
1 min	164 ± 0.6
5 min	153 ± 15
15 min	150 ± 6
30 min	146 ± 4
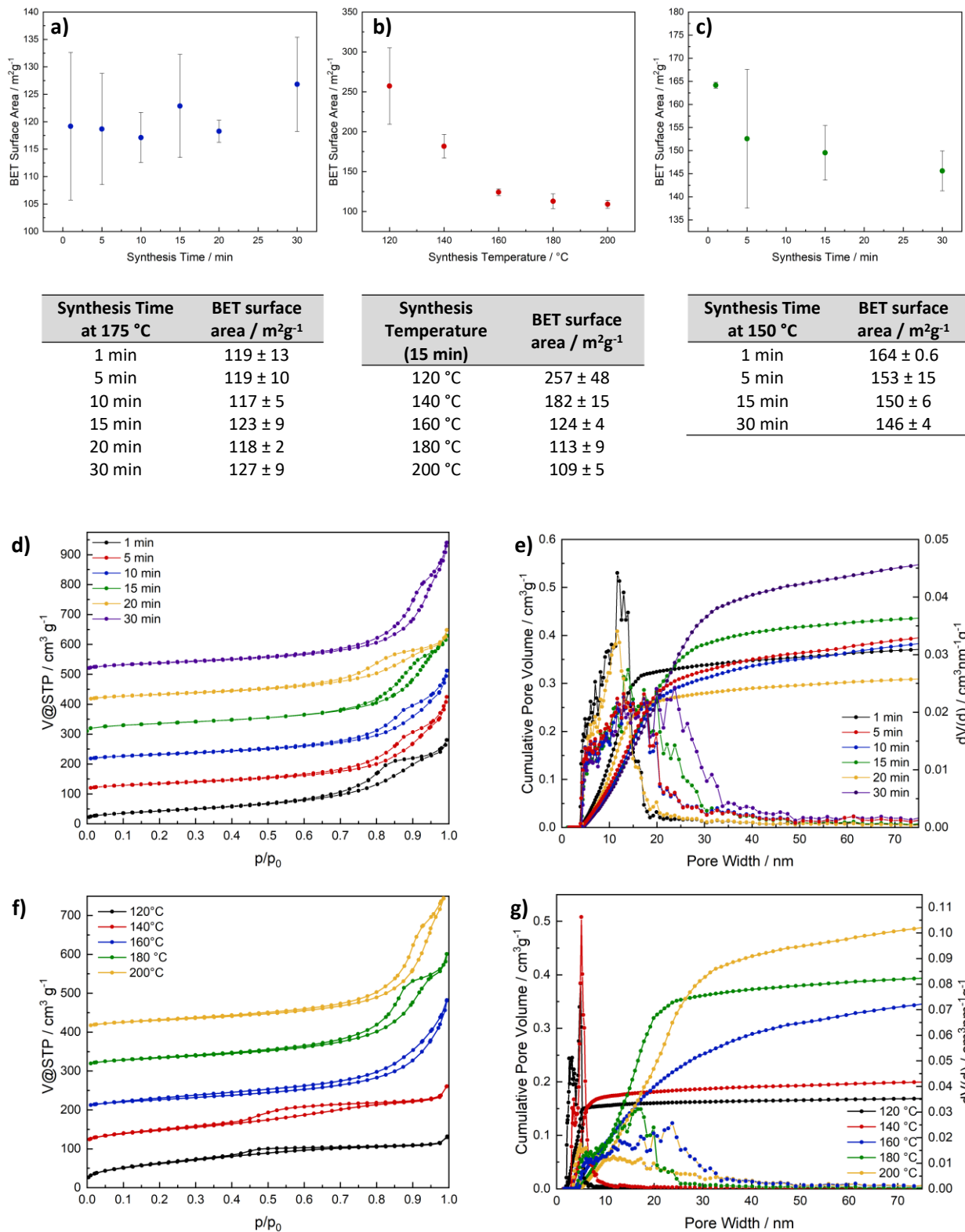
Figure S7 BET surface area in relation to the synthesis time (a), the synthesis temperature (b) and the synthesis time at 150 °C (c). Error bars represent the deviation between measurements of identically synthesised samples. N_2-isotherms for $CuFe_2O_4$ obtained after different reaction times in the microwave are depicted in (d), together with the corresponding pore size distribution (e), underlining the formation of nanoparticle agglomerates. Isotherms are stacked by 100 cm^3g^{-1} for clarity. N_2-isotherms and corresponding pore size distribution for samples obtained at different temperatures are shown in (f) and (g), respectively.
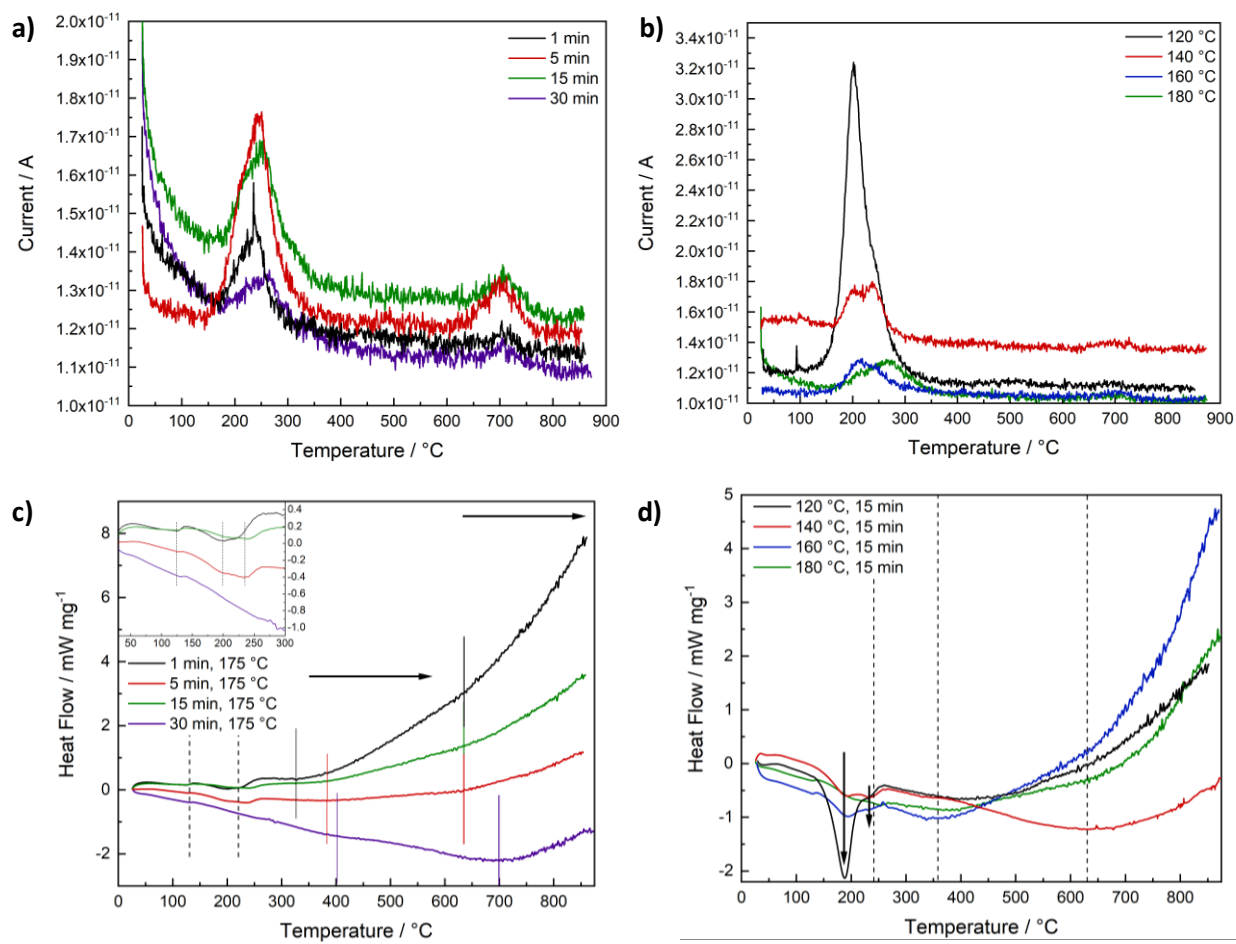
Figure S8 Corresponding MS response for CO_2 observed during the annealing of $CuFe_2O_4$ obtained after microwave synthesis for different durations at 175 °C (a) or for 15 min at different temperatures (b) in air. DSC curves (c) and (d) show the exothermic decomposition and additional features at 300-400 °C and at 620-700 °C that might indicate phase transitions.
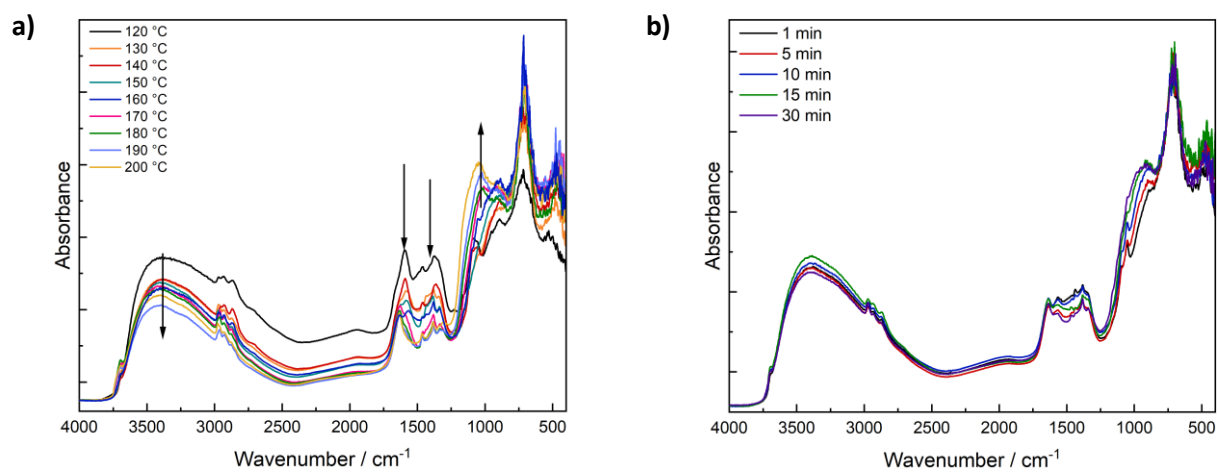
Figure S9 DRIFT spectra for $CuFe_2O_4$ obtained after reaction at different temperatures (a) and synthesised for different times at 150 °C (b).
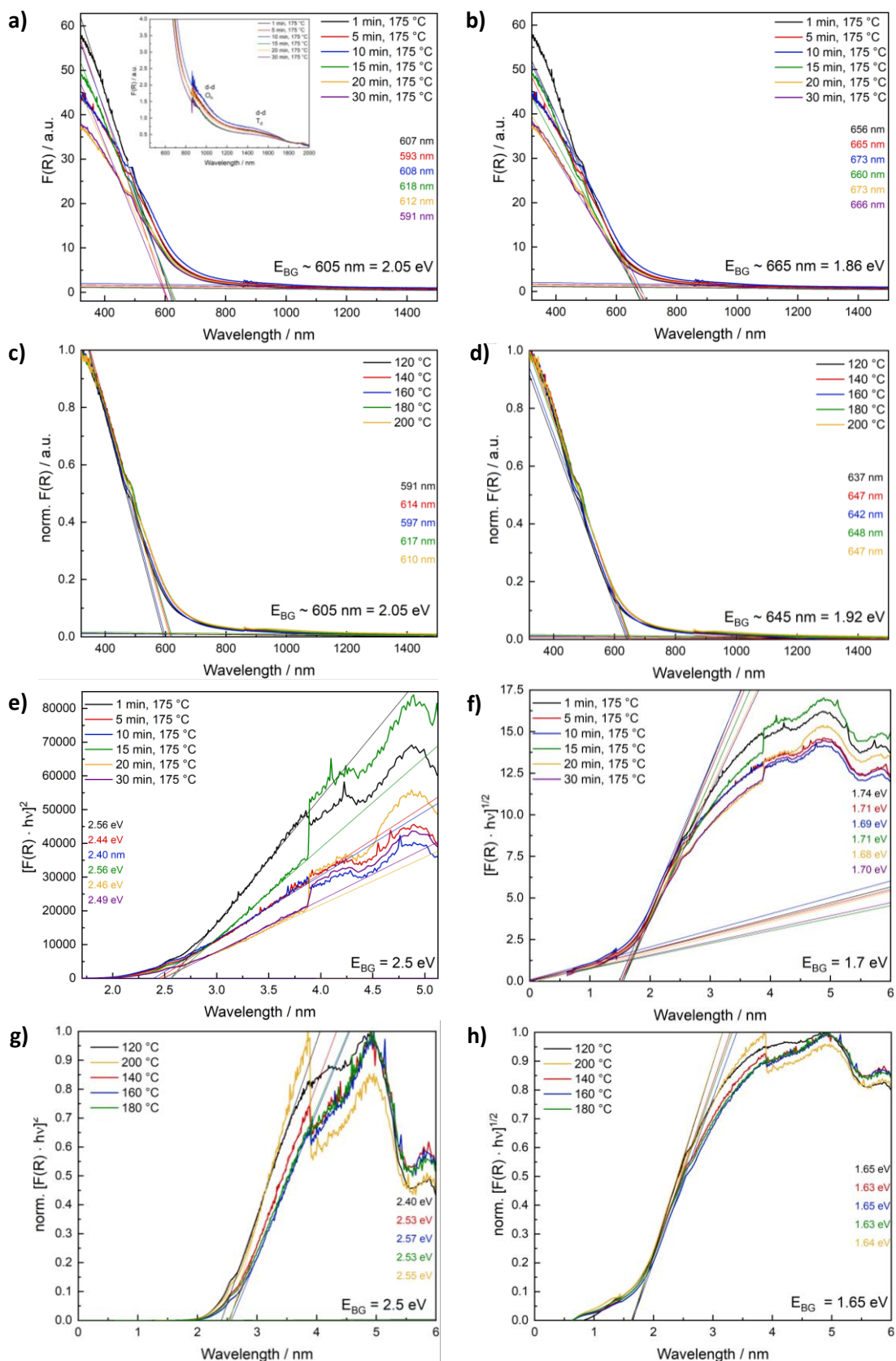
Figure S10 Kubelka-Munk plots of CuFe$_2$O$_4$ obtained after different reaction times at 175 °C with and without a fit over the charge transfer band (a) and (b), of CuFe$_2$O$_4$ synthesised at different temperatures (c) and (d) and corresponding direct and indirect Tauc plots (e)-(h). The inset in (a) elucidates *d-d* transitions in Cu^{2+} contributing to the absorption characteristics. The step at approx. 3.9 eV results from a measurement artefact.
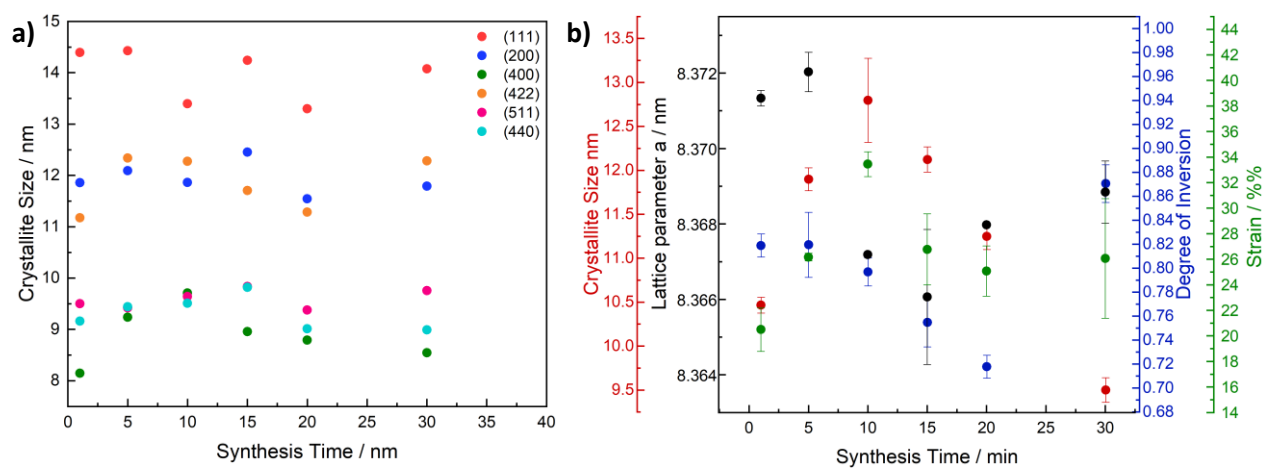
Figure S11 Crystallite sizes for $CuFe_2O_4$ obtained after different reaction times, determined with the integral breadth method for different lattice planes (a) and developments of crystallite size, lattice parameter, upper limit micro-strain and degree of inversion with the reaction time derived from Rietveld refinement (b).
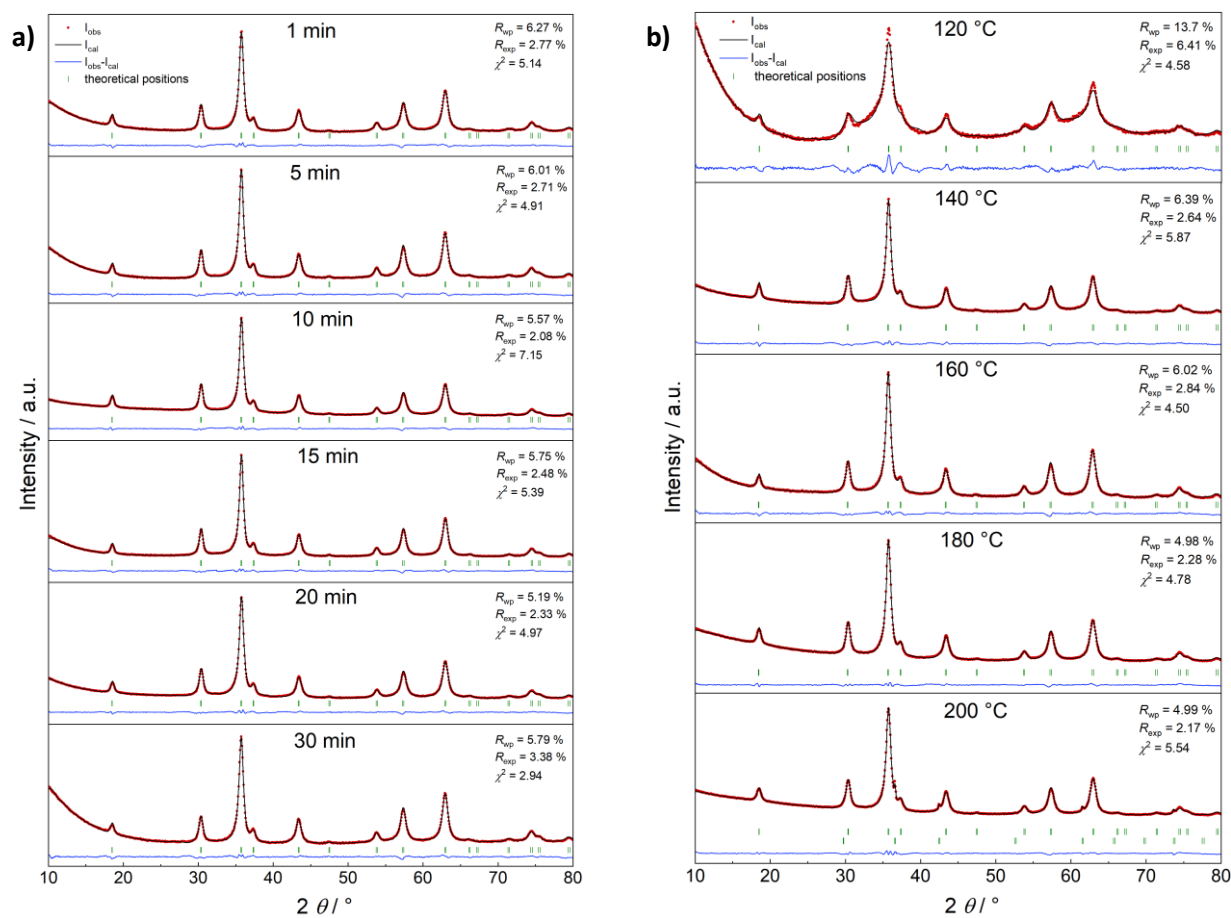
Figure S12 Exemplary Rietveld refinements of $CuFe_2O_4$ obtained after different reaction durations at 175 °C (a) and of $CuFe_2O_4$ synthesised at different temperatures (b).
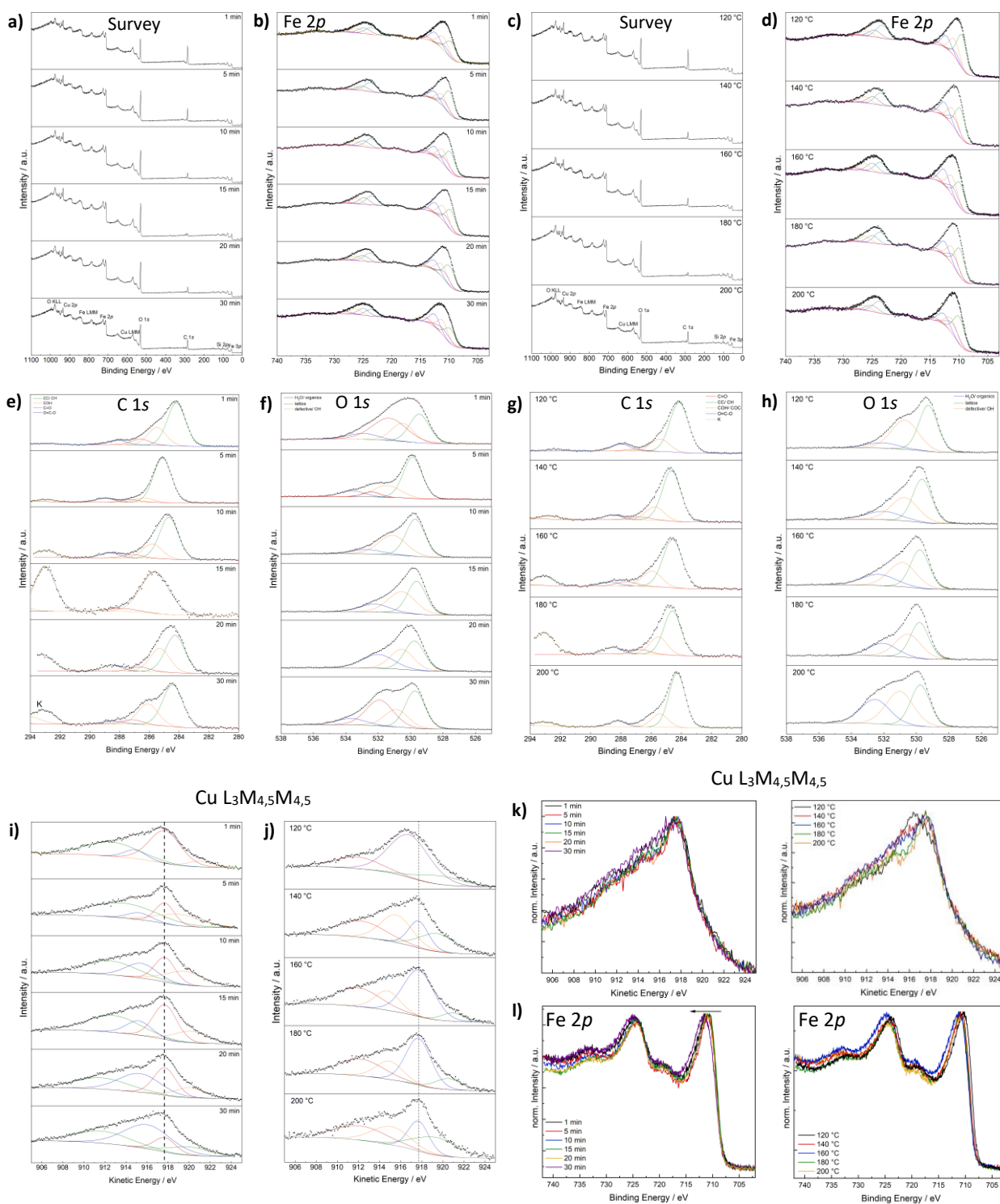
Figure S13 XP spectra for CuFe$_2$O$_4$ obtained under different reaction conditions: survey scans for CuFe$_2$O$_4$ synthesised at 175 °C for different reaction times (a), or at different temperature (c), corresponding Fe 2p spectra (b) and (d), C 1s spectra (e) and (g), O 1s spectra (f) and (h), as well as normalised Auger signals (i) and (j). For samples obtained at either very short (1 min), or long reaction times (30 min) a second organic oxygen species had to be included in the fit of the O 1s spectra. Since the intensity of the carbon C 1s peaks was very low for the sample obtained after 15 min, the fit was performed with only one species for CC/CH and COH. Exemplary fits of the Auger signals are shown in (i) an (j). The spectra were fitted with the minimum required number of peaks instead of the typical signals for Cu$_2$O and CuO, since the intensities and shifts observed in the spectra deviate significantly from literature values for Cu$_2$O and CuO. The high number of peaks of unknown peak maxima results in too many degrees of freedom that prevent an accurate fitting procedure. Instead, only the overall peak maximum was estimated for charge correction. Normalised Fe 2p and Cu L$_3$M$_{4,5}$M$_{4,5}$ peaks are shown in (k) and (l).

106

Table S2 Element ratios derived from survey scans.

Synthesis Conditions	At.% Fe	At.% Cu	At.% O	At.% C	At.% K	At.% Si	Fe/Cu
1 min, 175 °C	9.7	4.9	35.2	47.3	- -	2.9	1.98
5 min, 175 °C	12.8	6.5	43.8	35.6	- -	1.3	1.97
10 min, 175 °C	16.5	8.3	51.3	20.6	- -	3.3	1.99
15 min, 175 °C	20.0	10.3	56.1	8.0	1.5	4.1	1.94
20 min, 175 °C	14.6	7.7	52.2	20.3	0.9	4.2	1.90
30 min, 175 °C	12.0	6.7	45.2	30.7	0.5	4.9	1.79
120 °C, 15 min	11.9	6.1	38.5	42.8	- -	0.7	1.95
140 °C, 15 min	17.1	8.9	48.6	23.7	0.2	1.6	1.92
160 °C, 15 min	15.5	7.8	42.5	32.6	0.5	1.1	1.99
180 °C, 15 min	19.3	9.5	55.1	10.2	1.1	4.9	2.03
200 °C, 15 min	11.9	5.1	46.3	30.3	1.2	5.2	2.33
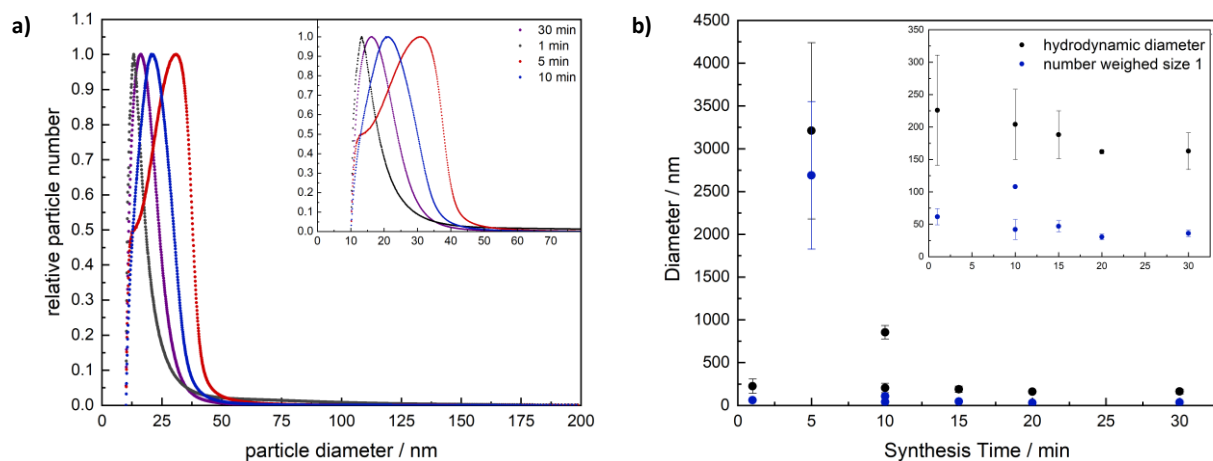
Figure S14 Particle size distributions obtained *via* ultracentrifugation measurements (a) and hydrodynamic radius and size distribution obtained with DLS (b). For the sample obtained after 10 min, four DLS measurements were performed, of which two and two agglomerated similarly. At relatively short reaction times of about 5 min, the agglomeration was most severe. The strong decline towards small diameter visible in ultracentrifugation measurements result from the measurement itself and do not indicate the absence of smaller particles.
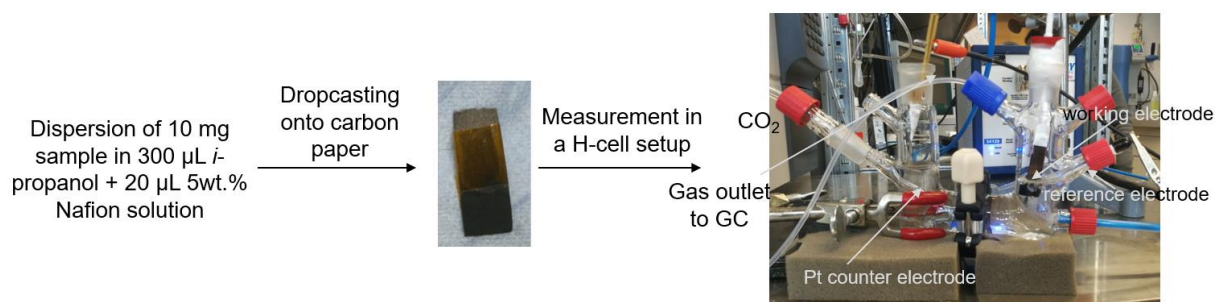
Figure S15 Scheme of electrode preparation and measurement setup in a two compartment H-type cell.
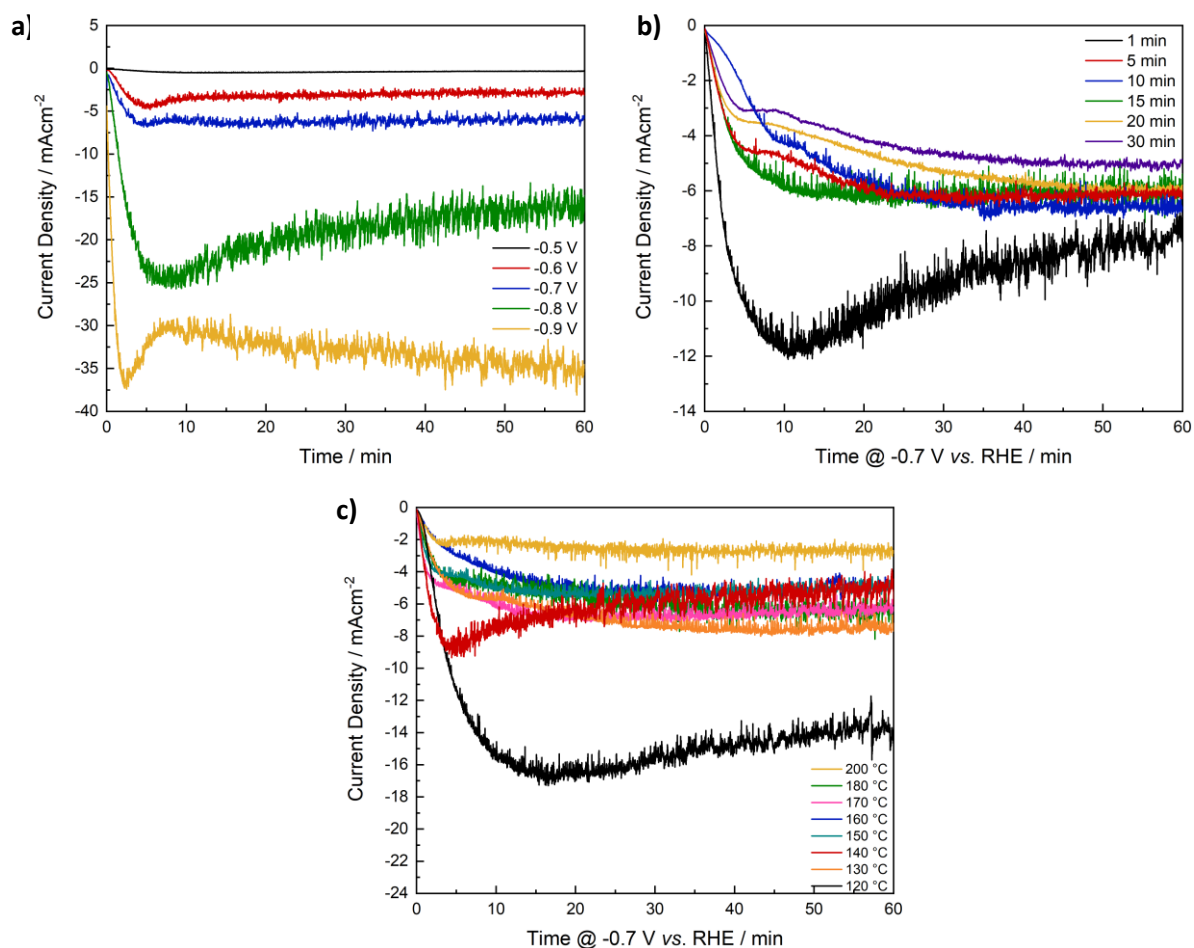
Figure S16 Current response for $CuFe_2O_4$ synthesised for 15 min at 175 °C at different potentials over time (a), at -0.7 V *vs.* RHE for samples obtained after different reaction times (b) and for samples obtained at different temperatures (c).
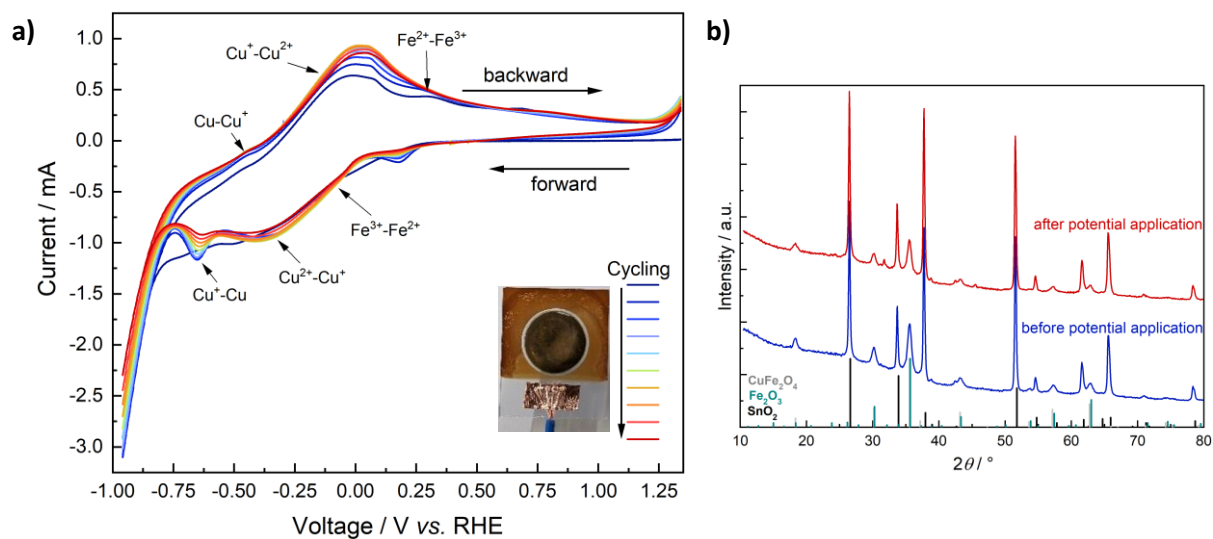
Figure S17 Reversible reduction of CuFe$_2$O$_4$ at the reducing potentials employed for the electrochemical CO$_2$-reduction (a). The black circle shows the reduced species - with the black colouration possibly corresponding to Fe$_3$O$_4$ – that are transforming back to their original brownish colouring. A weak additional reflection in the XRD patterns (b) at approx. 32° 2θ is observed, that might correspond to a Fe$_2$O$_3$ by-phase, but is too weak to allow for unambiguous identification. Following ICDD reference cards were used: SnO$_2$: 00-041-1445; CuFe$_2$O$_4$: 01-077-0010; Fe$_2$O$_3$: 00-025-1402.
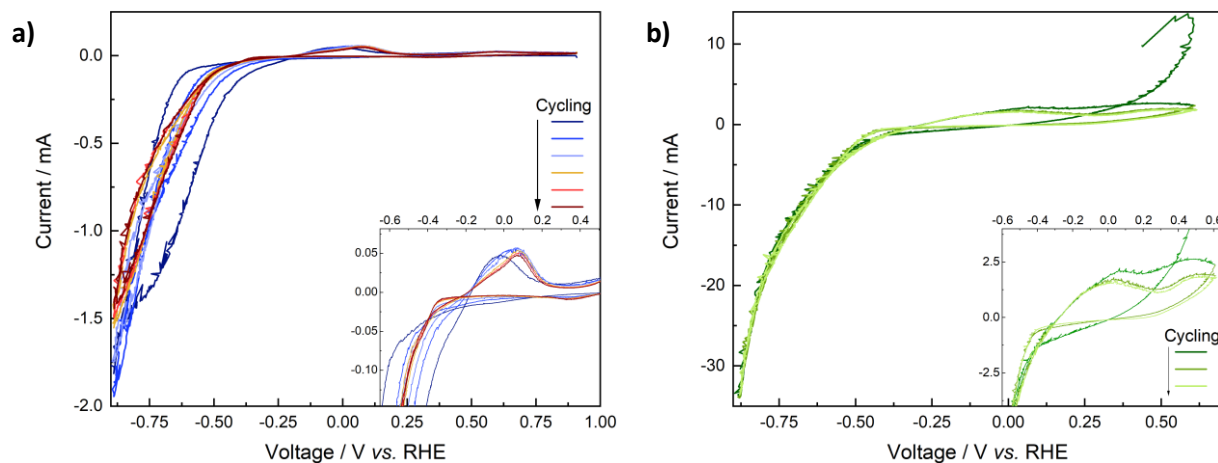
Figure S18 CV scans for electrodes on carbon paper, measured in KHCO$_3$ in an H-cell setup before and after the CO$_2$-reduction (a) and (b).
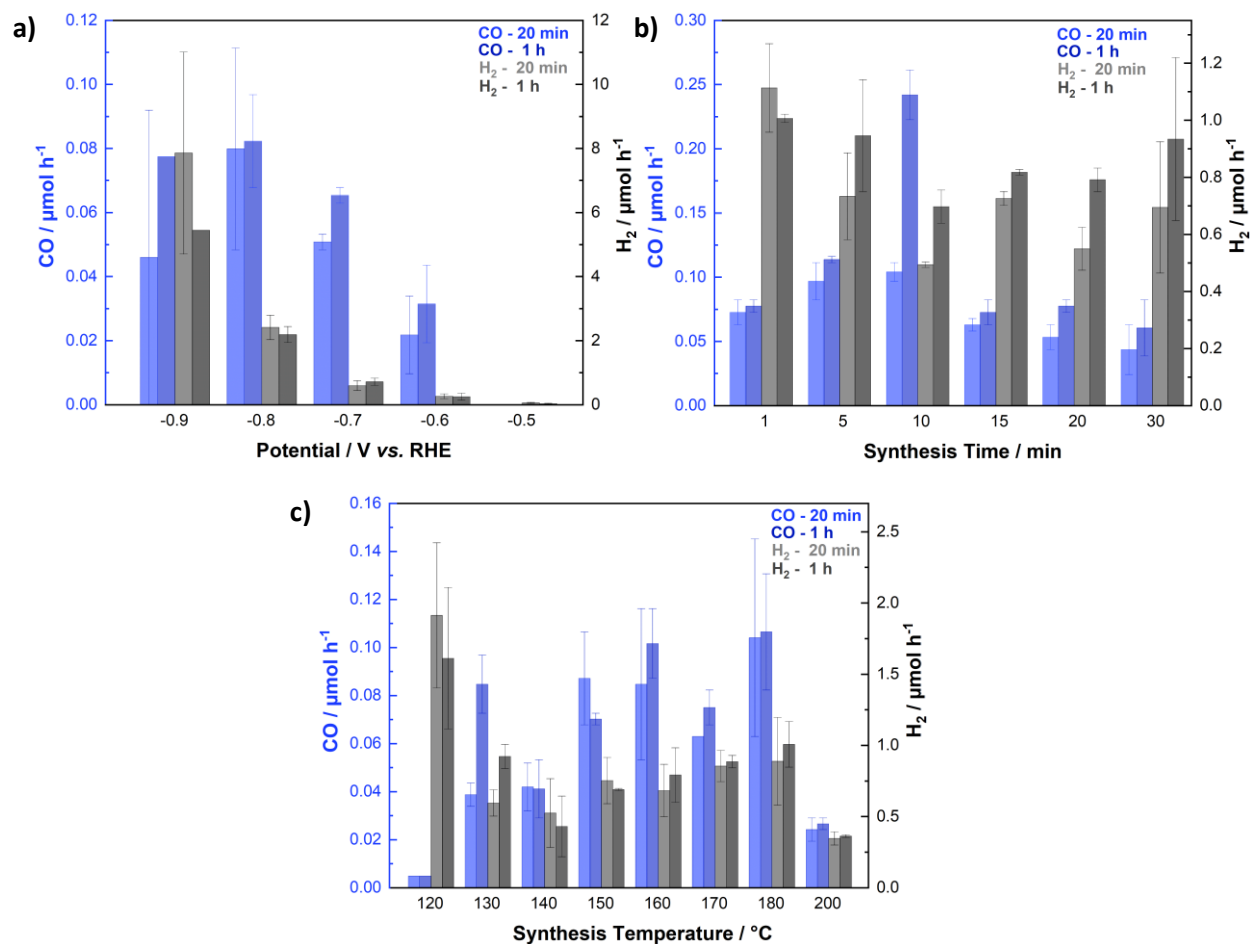
Figure S19 Non-normalised gas rates observed at different potentials (a), for samples obtained after different reaction times (b), or at different temperatures (c).
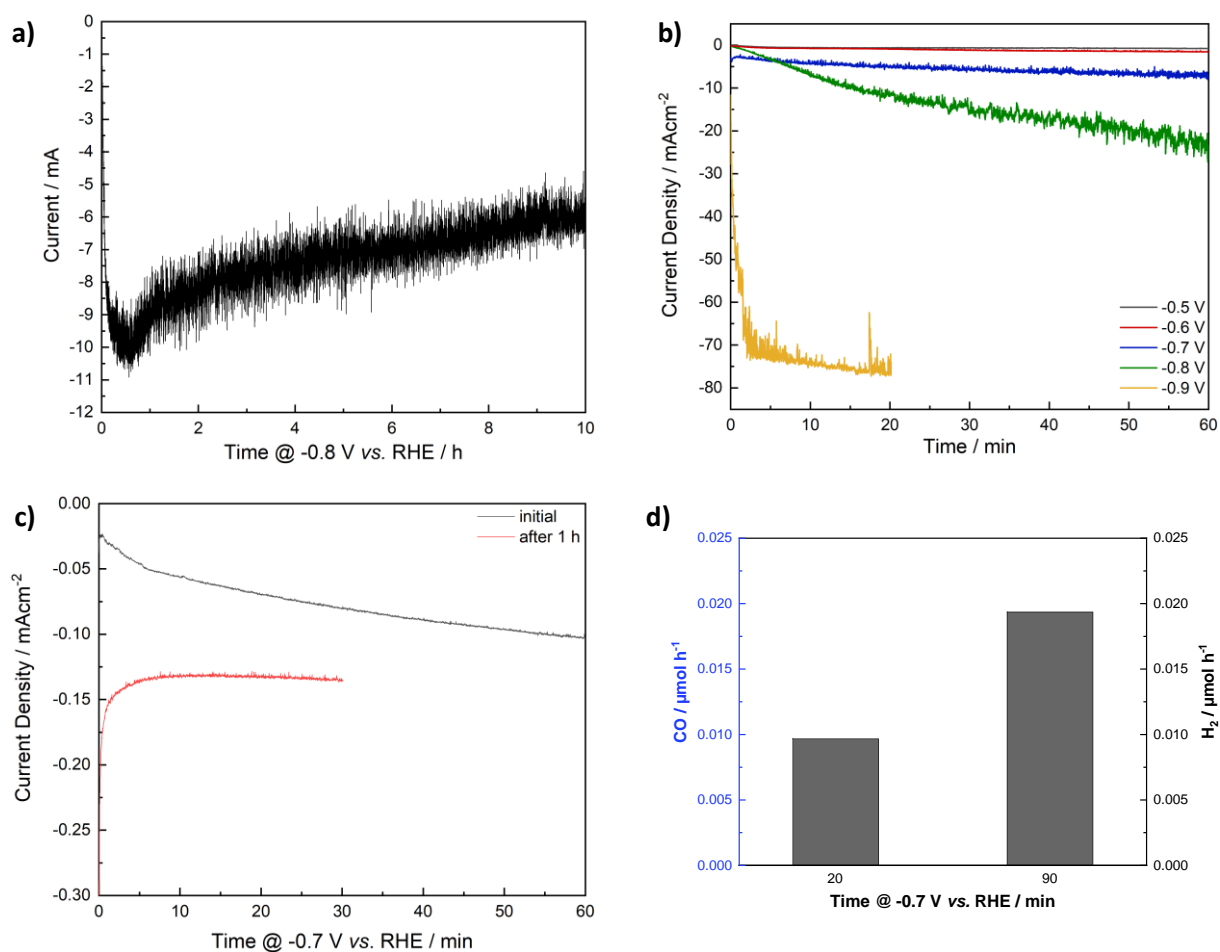
Figure S20 Chronoamperometry at -0.7 V vs. RHE for 10 h (a), at different potentials in an Ar atmosphere (b) and of an uncoated carbon paper electrode (c). The same carbon paper electrode was tested for additional 30 min (shown in red), directly after the 1 h testing. Corresponding gas evolution rates for the carbon paper electrode are shown in (d).
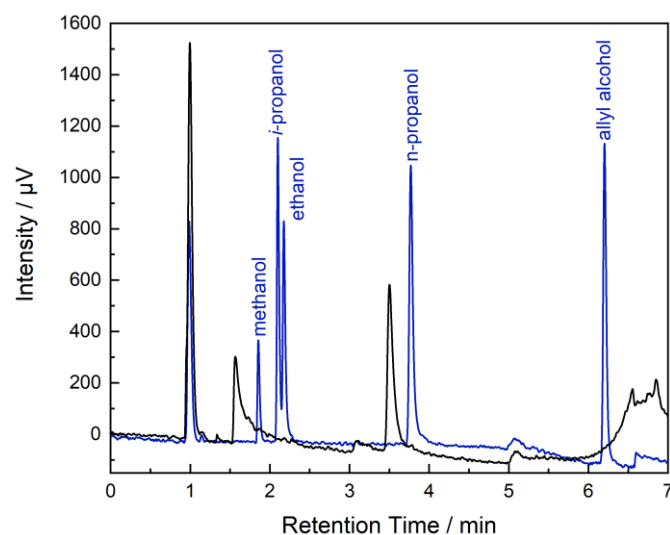
Figure S21 Chromatographic traces for liquid gas chromatography (LGC) measurements of the electrolyte after potential application for 10 h. The Traces for calibration standards are depicted in blue as reference.
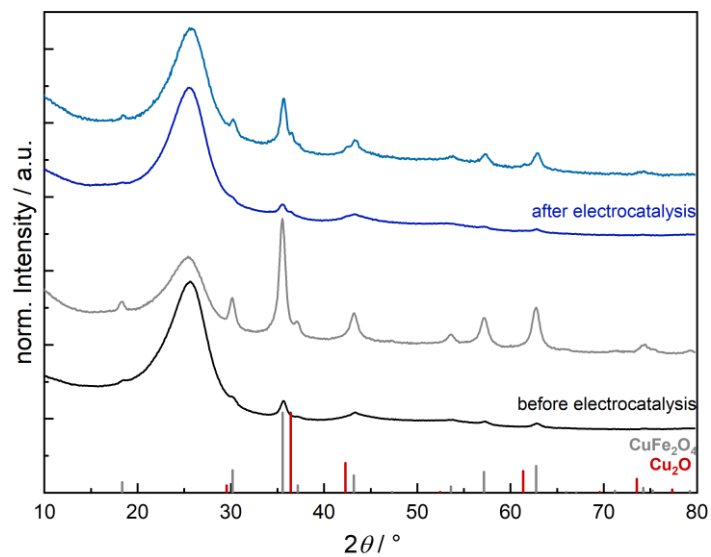
Figure S22 Normalised XRD patterns of electrodes before and after the CO_2-reduction. Depending on the analysed spot, more or less $CuFe_2O_4$ in relation to the carbon paper is visible. The CO_2-reduction was performed for 1 h at -0.8 V (dark blue) and at -0.9 V (pale blue) respectively.

7 Publication 2: "Ni₂FeS₄ as highly efficient earth-abundant co-catalyst in photocatalytic hydrogen evolution"

Judith Zander[a] and Roland Marschall *,[a]

[a] Department of Chemistry
University of Bayreuth
Universitätsstraße 30, Bayreuth 95447, Germany
*E-mail: roland.marschall@uni-bayreuth.de

7.1 Main Manuscript

The earth abundant sulphide Ni_2FeS_4 was used as a highly efficient co-catalyst for the hydrogen evolution reaction (HER) over TiO_2, boosting the activity of pure TiO_2 (P25) by a factor of more than 8 under AM 1.5G simulated sunlight, thus presenting a promising alternative to platinum or rhodium co-catalysts. Low metal-sulphide loadings of only 0.5 wt.% (0.29 wt.% of metals) could be realised, thereby rivalling common loadings of noble metal co-catalysts at significantly lower material costs. The performance was stable under 1 sun irradiation and no decrease in the activity was observed over 20 h hours of irradiation. The synthesis of Ni_2FeS_4 is based on low-cost precursors and can be completed after only 1 min at 200 °C in the microwave, without need for toxic H_2S, presenting an energy efficient and cost-effective possibility to obtain large amounts of such co-catalysts in a short time. This combination of a fast and cheap synthesis together with a high efficiency and stability make Ni_2FeS_4 an outstanding candidate for the use as co-catalyst for the HER with sunlight.

7.1.1 Introduction

The development of a sustainable energy economy has increasingly come into the focus of current research. Apart from the generation of electric power from renewable sources, the synthesis of carbon-free fuels, such as H_2 is required. Currently, H_2 is to a large extent obtained *via* steam-reforming, however and thus still contributing to the carbon footprint.[1] Alternative approaches, such as water electrolysis (using electricity from sustainable energy sources) or photocatalysis, suffer from high costs and low efficiencies.[2-5]

To improve the efficiency of photocatalysts, co-catalysts are added, that improve charge separation, reduce recombination rates, lower the overpotential and provide active sites.[6] For the hydrogen evolution half-reaction (HER), the most efficient co-catalysts are platinum, gold, or rhodium-based, hence an increased activity usually goes in hand with a higher system cost. Earth abundant co-catalysts are therefore desirable. Molecular co-catalysts have been designed and a good performance has been

observed for transition metal complexes.[7,8] However, many suffer from low long-term stabilities, hence, efforts have been made to design new heterogeneous transition metal co-catalysts.

While transition metal oxides, hydroxides and oxyhydroxides of Co, Fe and Ni have shown promise as electrocatalysts for the oxygen evolution reaction (OER), mainly alloys with molybdenum, metal phosphides and sulphides have been used to replace noble metals for the hydrogen evolution.[9-13] Compared to oxides they exhibit a far higher conductivity. The active centres of major hydrogenase enzymes, contain either solely Fe or Fe and Ni atoms together. Therefore, biomimetic approaches exploit compositional similarities.[14,15]

Especially sulphides of the earth abundant metals nickel and iron have emerged as highly efficient electrocatalysts for the HER.[16,17] Thus, Faber *et al.* investigated FeS_2, CoS_2 and NiS_2 for their activity in electrochemical HER, with CoS_2 performing best.[18] Even better activities were observed for ternary Fe-Co sulphides and ternary Fe-Ni sulphides and selenides.[19-21] The activity of Ni and iron hydroxides, as well as sulphides in electrochemical water splitting could further be improved by a combination with MXene nanosheets, elucidating the advantages of composite formations.[22,23]

Good catalysts in the electrochemical HER are oftentimes also good co-catalysts in photocatalysis, since they fulfil a similar role. Thus, MoS_2 and CoP are among both the most important earth-abundant electrocatalysts and co-catalysts.[24-32] Additionally, nickel-based materials have shown promise as co-catalysts.[33] Nickel nanoparticles themselves can already serve as co-catalysts, which has e.g. been shown on CdS.[34-36] Ran *et al.* tested different Ni co-catalysts on $Zn_xCd_{1-x}S$, observing an enhancement effect for metallic Ni, as well as for NiS and $Ni(OH)_2$.[37] Similarly, Pareek *et al.* employed Ni and Co oxide and hydroxide co-catalysts on CdS.[38] Other examples include Ni nitrides, phosphides, or Ni-Fe layered double hydroxides (LDH).[39-42] NiS_x can also be used as a co-catalyst, which has been shown again mainly on $g-C_3N_4$ and CdS.[43-46] Interestingly, NiS can also be photochemically deposited on $g-C_3N_4$, as demonstrated by Zhao *et al*.[47]

Apart from CdS and $g-C_3N_4$ as photocatalyst materials, metallic Ni, as well as binary Ni and Fe sulphides could also improve the HER activity of TiO_2. For example, Tran *et al.* employed Co and Ni nanoclusters on TiO_2 to improve the HER activity under UV irradiation.[48] Xiao *et al.* prepared atomically dispersed Ni on TiO_2 *via* a molten salt synthesis route.[49] Moreover, Ni-Fe alloys were used as a co-catalyst on P25.[50] When binary Ni or Fe sulphides were employed as co-catalysts, usually rather high sulphide loadings were required. Thus, Wang *et al.* synthesised composites of NiS and CuS on TiO_2, with 5 wt.% of each resulting in the highest activity enhancement.[51] This is in agreement to an optimum loading of 7 at.% of NiS on TiO_2 found by Zhang *et al*.[52] FeS_2 was also used as a co-catalyst on TiO_2, exploiting the good light harvesting abilities of the sulphide.[53] The co-catalyst performance of NiS_x could be further increased by the incorporation of Cu, which resulted in a decreased adsorption energy for $S-H_{ads}$ bonds, indicating, that additional metal centres can be beneficial.[54]

Compared to NiS_x and FeS_x, ternary nickel iron sulphides allow for more parameters to adjust the properties and in turn the catalytic activity. They possess an almost metallic conductivity and have already shown promise as electrocatalysts in multiple fields.[55] Our group used Ni_2FeS_4 nanosheets for the electrochemical production of syn-gas.[56] Additionally, the nickel- and iron-based thiospinel shows a low overpotential for the OER in alkaline electrolytes.[55,57,58] The group of Apfel has successfully employed pentlandites, $Fe_{4.5}Ni_{4.5}S_8$, for efficient electrocatalytic hydrogen evolution, with the partial replacement of sulphur by selenium further increasing the activity.[59-61]

Since co-catalysts are essentially electrocatalysts that additionally undergo efficient charge carrier exchange with the photocatalyst, we herein employed Ni_2FeS_4 as a co-catalyst for the first time to boost the hydrogen evolution activity of TiO_2 under sunlight irradiation. Upon decoration with only 0.5 wt.% (0.29 wt.% of metals) of Ni_2FeS_4, the activity of pure P25 could be increased by a factor of more than 8 under AM 1.5G simulated sunlight, thus showing promise as an alternative to platinum or rhodium co-catalysts. This loading rivals common loadings of noble metal co-catalysts at significantly lower material costs. The performance was stable under 1 sun irradiation and no decrease in the activity was observed over 20 h hours of irradiation. The combination of a fast and low-cost synthesis together with a high efficiency and stability makes Ni_2FeS_4 an outstanding candidate for the use as co-catalyst for the HER with sunlight.

7.1.2 Experimental

Synthesis of Ni_2FeS_4

In a typical synthesis procedure 128.5 mg (2 eq., 0.5 mmol) of $Ni(acac)_2$ (SigmaAldrich) and 88.3 mg (1 eq. 0.25 mmol) of $Fe(acac)_3$ (Acros Organics) were dissolved in 5 mL of 1-phenylethanol (SigmaAldrich). 5 mL of benzyl mercaptan (SigmaAldrich) were added directly before the synthesis under stirring in a 30 mL borosilicate microwave vial. The solution was slowly heated under stirring in a microwave reactor (Anton Paar Monowave 400) up to 200 °C. The temperature was held for 1 to 30 min and subsequently the solution was cooled by compressed air. The product was precipitated with *n*-pentane, washed thrice with aceton/water mixtures and once with diethyl ether and then dried at 80 °C overnight in air. For storage, Ni_2FeS_4 was transferred to a glovebox.

Decoration of P25 with Ni_2FeS_4

The respective wt.%-ratios of Ni_2FeS_4 and P25 were ground together in a mortar for 10 min under addition of low volumes of *i*-propanol, followed by annealing either in air in a muffle furnace for 2 h at 200 °C or in a tube furnace under argon.

Photocatalysis

50 mg of the photocatalyst were ultrasonicated in approx. 20 mL of ultrapure water for 10 min. The dispersion was transferred to a home-made glass reactor. Water and methanol were added to a total volume of 150 mL containing 10 vol.% of methanol. The dispersion was stirred and degassed with argon (25 mL/min) prior to the measurement. The gas composition was analysed by gas chromatography (Shimadzu GC-2014) continuously throughout the experiment starting 30 min before switching on the lamp. After 30 min of gas monitoring, the irradiation by a solar simulator (150 W, Xe) equipped with an AM 1.5G filter (Newport) was started. After 5 hours of continued illumination, the lamp was turned off and the gas monitoring continued until the hydrogen concentration reached approx. 0. For measurements under UV irradiation, 150 mg were dispersed in 600 mL of a 10 vol.% aqueous methanol solution. The dispersion was degassed with argon (100 mL/min) prior to the experiment and subsequently irradiated for 5 h by a 700 W Hg lamp operated at 500 W (Peschl Ultraviolet). The gas composition was analysed by gas chromatography before, during and after the irradiation period.

Material Characterisation

Ni_2FeS_4 and P25 decorated with Ni_2FeS_4 were characterised with powder X-ray diffraction using either Cu K_α irradiation, or Ag K_α irradiation. For measurements with a Cu anode, a Malvern PANalytical Empyrean device was used, with an acceleration voltage of 40 kV, an emission current of 40 mA and Bragg-Brentano geometry. Measurements with an Ag anode were performed on a STOE STADI P Mythen2 4 K diffractometer, equipped with a Ge(111) monochromator and four Dectris MYTHEN2 R 1 K strip detectors.[52] Hilgenberg capillaries (0.5 mm) were used and measurements were repeated and accumulated. X'Pert Highscore plus was used for the identification of crystal phases. Crystallite sizes were determined using the integral breadth method, which is the reciprocal crystallite size and calculated as the area of a reflection divided by its height, if the diffraction intensity is plotted versus the scattering vector.[63] Raman measurements were performed on a Horiba Yvon Raman microscope, using a He-Ne-laser with a wavelength of 633 nm and a power of 11.5 W. The laser intensity was reduced down to 10 %, or 25 %. To observe oxidative changes, the power was increased to 50 or 100 % for short periods. Spectra were despiked manually. For diffuse reflectance infrared Fourier transformed (DRIFT) spectroscopy, a Bruker Alpha II spectrometer was used. UV/vis/NIR measurements were conducted on a Perkin Elmer Lambda 750 spectrometer, using a Praying Mantis (Harrick) and spectralon as white standard. The Kubelka–Munk function was used for the calculation of pseudo-absorption, F(R), according to:[64]

$$F(R) = \frac{(1-R)^2}{2R}$$

The band gap was calculate from a fit of the corresponding Tauc plots.[65] $(F(R) \cdot h\nu)^{1/n}$

with n = 0.5 for direct band gaps and n = 2 for indirect ones. Physisorption measurements were performed on a Quadrasorb Evo device from Anton Paar QuantaTec at 77 K. Surface areas were determined using the Brunauer–Emmet–Teller (BET) model, using the software ASiQwin for data evaluation. Samples were degassed for 12 h at 120 °C prior to measurements. X-ray photoelectron spectroscopy (XPS) was performed on a Physical Electronics PHI VersaProbe III Scanning XPS Microprobe instrument. Al K_α irradiation, a beam voltage of 15 kV, a power of 50 W and a beam diameter of 200 μm were used. Step size was 0.8 eV with a time per step of 50 ms and a pass energy of 224 eV for survey spectra and 0.1 eV, 50/ 20 ms and 26 eV for high resolution spectra. Samples were continuously flooded with electrons and Ar^+ at low energy. Data evaluation was done with CASA XPS,[66] using a Shirley Background and Gaussian-Lorentzian profile functions (GL30). For charge correction C 1s was set to 248.8 eV. Morphology imaging by scanning electron microscopy (SEM) was performed on a Zeiss Leo 1530 device at an acceleration voltage of 3 kV, using Pt sputtering (Cressington Sputter Coater 208 HR). The same instrument was employed for energy-dispersive X-ray spectroscopy (EDX) at an acceleration voltage of 20 kV and using an ultra-dry EDX detector by Thermo Fisher Scientific NS7. For thermogravimetric analysis (TGA) coupled with mass spectrometry (MS) a Netzsch Jupiter STA 449C thermobalance and a Netzsch Aeolos QMS 402C quadrupole MS were used. A heating ramp of 2 K/min in synthetic air was employed. Selected solutions were examined after the photocatalytic experiments with ion chromatography. The solution was filtered through a 0.2 μm syringe filter and subsequently analysed by a Dionex Aquion system from Thermo Fisher, equipped with a Dionex IonPac AS9-HC column and IonPac AG9-HC guard column and a UV detector (λ_{det} = 207 nm). 1 mM $NaHCO_3$/ 80 mM Na_2CO_3 was used as eluent. For the electrochemical impedance spectroscopy (EIS), 10 mg of

Ni_2FeS_4 were dispersed in 300 μL of *i*-propanol (p.a.) and 20 μL of a 5 wt.% Nafion solution (Alfa Aesar) and dropcast onto carbon paper (Freudenberg H2315-C2) with the coated area restricted to 1 cm^2 with Kapton tape. A three electrode H-cell setup was used, with 1 M KOH as the electrolyte, a platinum counter electrode and a RHE reference electrode (Gaskatel). A Parstat 3000A-DX potentiostat (Princeton Applied Research) and VersaStudios were employed.

7.1.3 Results and Discussion

We have previously shown that a fast one-pot microwave assisted synthesis of Ni_2FeS_4 is possible, using the metal acetlyacetonates and benzyl mercaptan as a sulphur source.[56] The benzyl mercaptan is therein partially replacing the solvent 1-phenylethanol, that is known to directly take part in the reaction and condensation of organic metal precursors to oxides.[67,68] Redox reactions have to occur during the reaction, as a change in the oxidation state of both nickel and iron from an initial Ni^{2+} and Fe^{3+} in the acetylacetonates to Ni^{3+} and Fe^{2+} in the sulphide is required.[69] A possible reaction sequence based on the mechanism for oxide formation is depicted in **Figure 1**.[70]
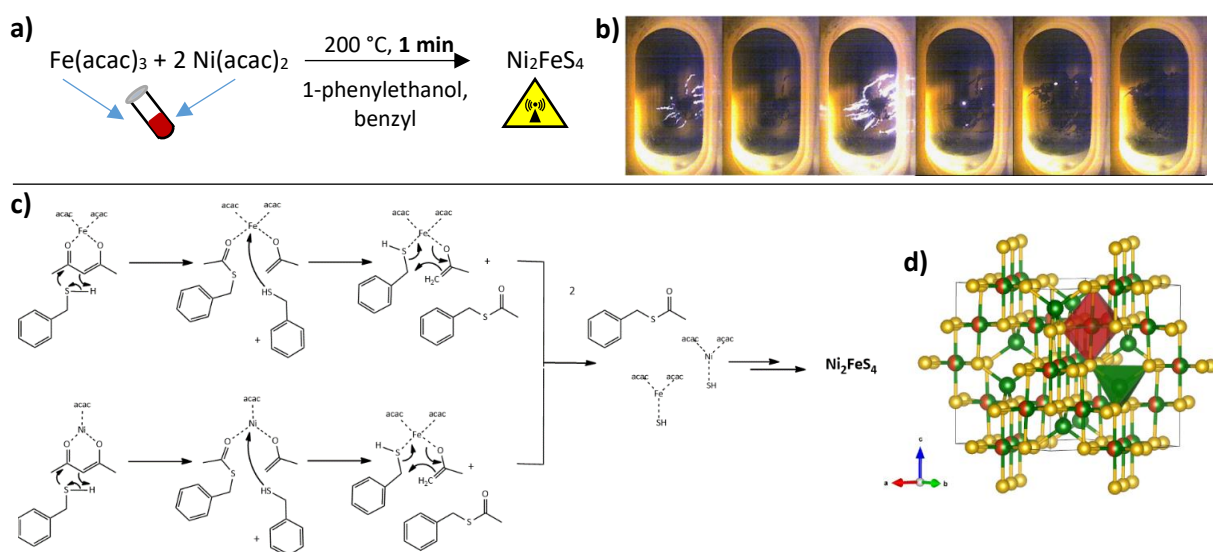
Figure 1 General reaction equation for the formation of Ni_2FeS_4 (a), photographs of observed light flashes and nanosheet formation (b), reaction sequence based on a nucleophilic attack of benzyl mercaptan similar to what was reported for alcohols (c) and crystal structure (d).

The benzyl mercaptan to 1-phenylethanol ratio was 1:1. A preferential/ faster reaction with the sulphur precursor is assumed, hence a dilution with the alcohol is possible. The very fast reaction can be observed directly with an integrated camera (**Figure 1**). Light flashes are visible during the first minutes of the synthesis, possibly either as a result of occurring redox processes, or as a consequence of strong microwave absorption by Ni-SH species, since the nanosheets can be observed to directly grow out of these spots along the wall of the microwave vessel, underlining that condensation and hotspots are directly connected.
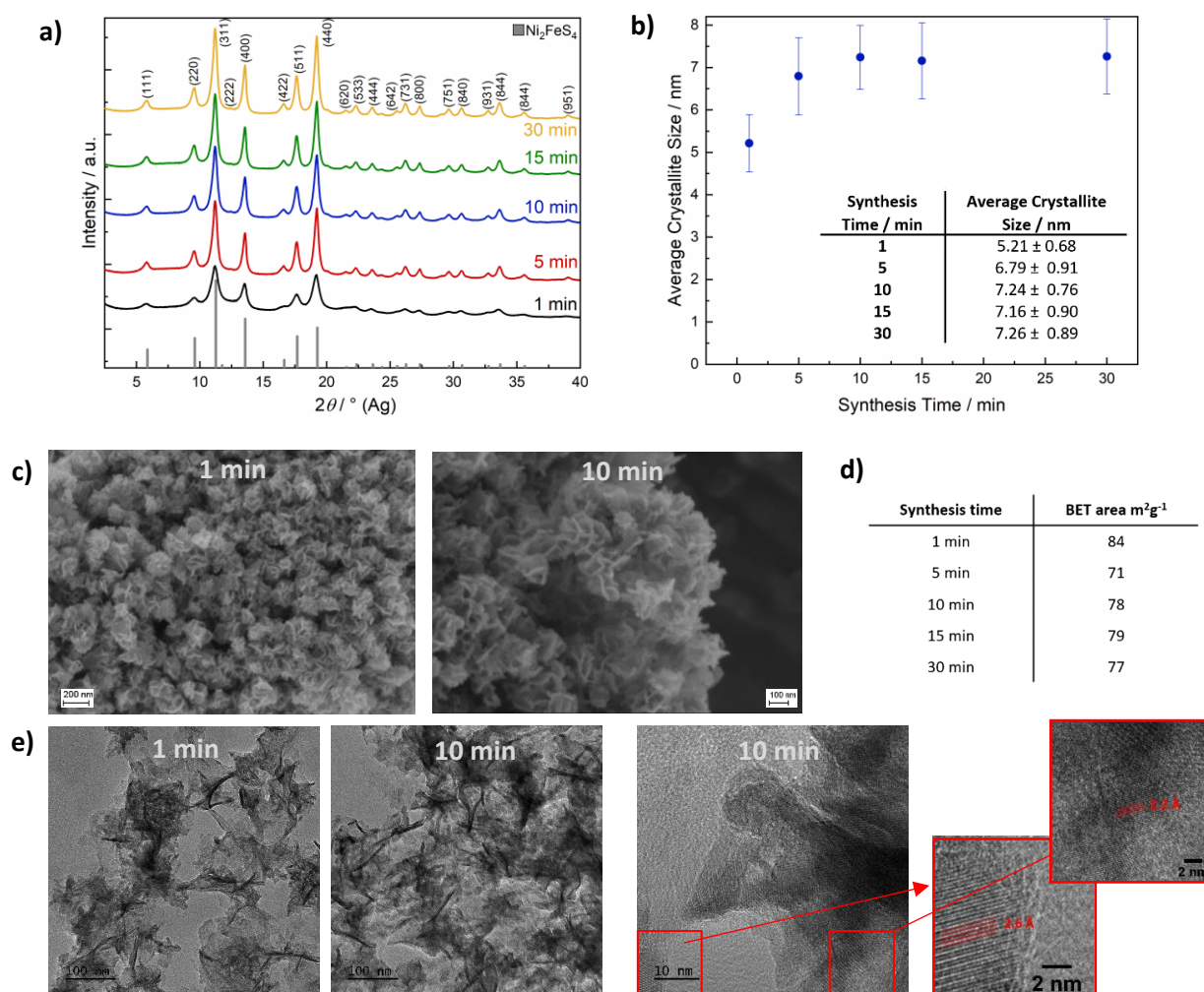
Figure 2 XRD patterns for Ni_2FeS_4 obtained after different synthesis times (a), corresponding crystallite sizes as determined by the integral breadth method (b), SEM images of Ni_2FeS_4 nanosheets obtained after 1 and 10 min (c) and BET surface areas (d). For the identification of reflections, the ICDD reference card 00-047-1740. Additionally, TEM images of Ni_2FeS_4 nanosheets obtained after 1 and 10 min are shown in (e).

The appearance of light flashes is most pronounced during the first minute of the synthesis. Going in hand with this observation, we found that the reaction time can likewise be decreased down to one minute, without significant differences in the crystallinity of the obtained nanosheets and a complete retention of phase-purity, as confirmed by SEM and TEM images (**Figure 2**, **Figure S1** and **Figure S2**) and high-resolution Ag XRD (Figure 2). The measured separation of lattice planes in the sections are 2.2 and 2.6 Å, which corresponds to the (400) and (222) planes of a cubic thiospinel (compare ICDD reference 00-047-1740). The crystallite size is around 7 nm after a reaction time of 5 min, without observed growth upon prolonged heating, which is in good agreement to the visual monitoring of sheet growth. The same trend is reflected in the BET area that is approx. 80 $m^2 g^{-1}$ independent of the synthesis time (Figure 2). EDX confirms an almost ideal nickel to iron ratio of 2, with possibly a slight decrease in the relative nickel ratio after prolonged heating (**Table S1**). The metal to sulphur ratio (M:S) is with 0.8 to 0.9 slightly higher than the expected 0.75, likely due to partial surface oxidation and possibly lower sensitivity for sulphur in the EDX.

X-ray photoelectron spectroscopy (XPS) was conducted on Ni_2FeS_4 synthesised after short (1 min), medium (15 min) and long (30 min) reaction times in the microwave, to gain insights into

the surface composition and to elucidate changes occurring during prolonged heating (**Figure 3** and **Figure S3**). Survey scans reveal a significantly lower M/S ratio of approx. 0.5 compared to EDX results, indicating an excess of sulphur on the surface (**Table S1**). This could be an effect of organic residues from the synthesis, as also evidenced by the high carbon content. Partial surface oxidation is also confirmed by the presence of oxygen. The Ni to Fe ratio decreases from 2.35 to 1.88 upon an increase of the synthesis time from 1 to 30 min. A similar effect is also observed with EDX. This indicates a loss of Ni upon prolonged heating, which is mirrored in a decreasing M/S ratio. A similar loss of the more redox active and better microwave absorbing cation at the surface was observed in the synthesis of $CuFe_2O_4$, alongside cation migration of Cu^{2+}.[71] Possibly, an extended irradiation with microwaves results in changes in the Ni coordination as well. Santos-Carballal *et al.* suggested a normal spinel structure to be the thermodynamically more stable one, that is not formed in synthetic approaches due to kinetic reasons.[72] Prolonged heating might thus lead to cation migration towards a thermodynamically more stable structure. The O $1s$ spectra additionally show a significant decrease in the amount of metal oxygen bonds with increasing synthesis duration, and an increase in the relative ratio of sulphates to hydroxides. To differentiate between sulphates and hydroxides/ organics, the O $1s$ spectra was constrained to FWHM and binding energies reported by Legrand *et al*. for pentlandite.[73] There is still some uncertainty in the relative ratio, as the constraints rely on accurate binding energy reference and the carbon species might change during continued heating as well – although no significant differences in the C $1s$ spectra were observed (**Figure S3**). The evidence for oxidic species would in turn suggest portions of Ni to exist in the oxidation state II+ instead of the further oxidised III+, indicating that oxidation is not yet fully completed after 1 min, but requires further microwave radiation.

The sulphur S $2p$ spectra mainly show the signals for S^{2-} and SO_4^{2-}, revealing a partial surface oxidation – something that is commonly recognised for sulphides that were handled in air, even if only shortly (**Figure 3**).[69] Moreover, disulphides and polysulphides are present in addition to at least one more species at slightly higher binding energies than those expected for polysulphides. These can probably be attributed to thiols together with sulphite species, that are especially pronounced after 1 min.[74] The presence of SO_3^{2-} species together with Ni^{2+} might be an indication that the oxidation of nickel is coupled to an oxidation of sulphur. Both sulphate and sulphide signal are shifted towards higher binding energies for Ni_2FeS_4 synthesised for 30 min (Figure S3), which might be attributed to a higher average oxidation states of the metal ions the sulphide ions are coordinating to. However, an effect of differences in the charge correction cannot be completely excluded. Fe $2p$ spectra are dominated by Ni $L_3M_{23}M_{45}$ Auger peaks at 712 and 706 eV that prevent an accurate fit (**Figure 3**). Still, an increase in the relative intensity of an iron sulphide species at approx. 707.5 eV and a decrease in the amount of oxidic species with time is observed in the normalised spectra, in good agreement to the O $1s$ spectra. Since the most intensive signal is the Ni Auger, spectra normalisation proceeds on this peak. Thus, a relative increase in the Fe-S peak can also be related to an actual decrease in the Ni LMM peak, which is in agreement to the loss of Ni with extended synthesis durations. An accurate fitting of the Ni $2p$ spectra is difficult, since at least three species (a sulphidic one, an oxidic one and a sulphate) are expected, all of which exhibit multiplet splitting.[73,75] Additionally, the nickel sulphide peak might exhibit an asymmetric peak shape.[76] Therefore, the spectra were approximated with one main peak for NiS_x, $Ni(OH)_2$ and $NiSO_4$, respectively, and a satellite for each at 5.5 eV above the main signal. A decrease in the relative amount of oxidic nickel species, *e.g*. $Ni(OH)_2$, with prolonged synthesis time is observed, in good agreement to the observations stated above.
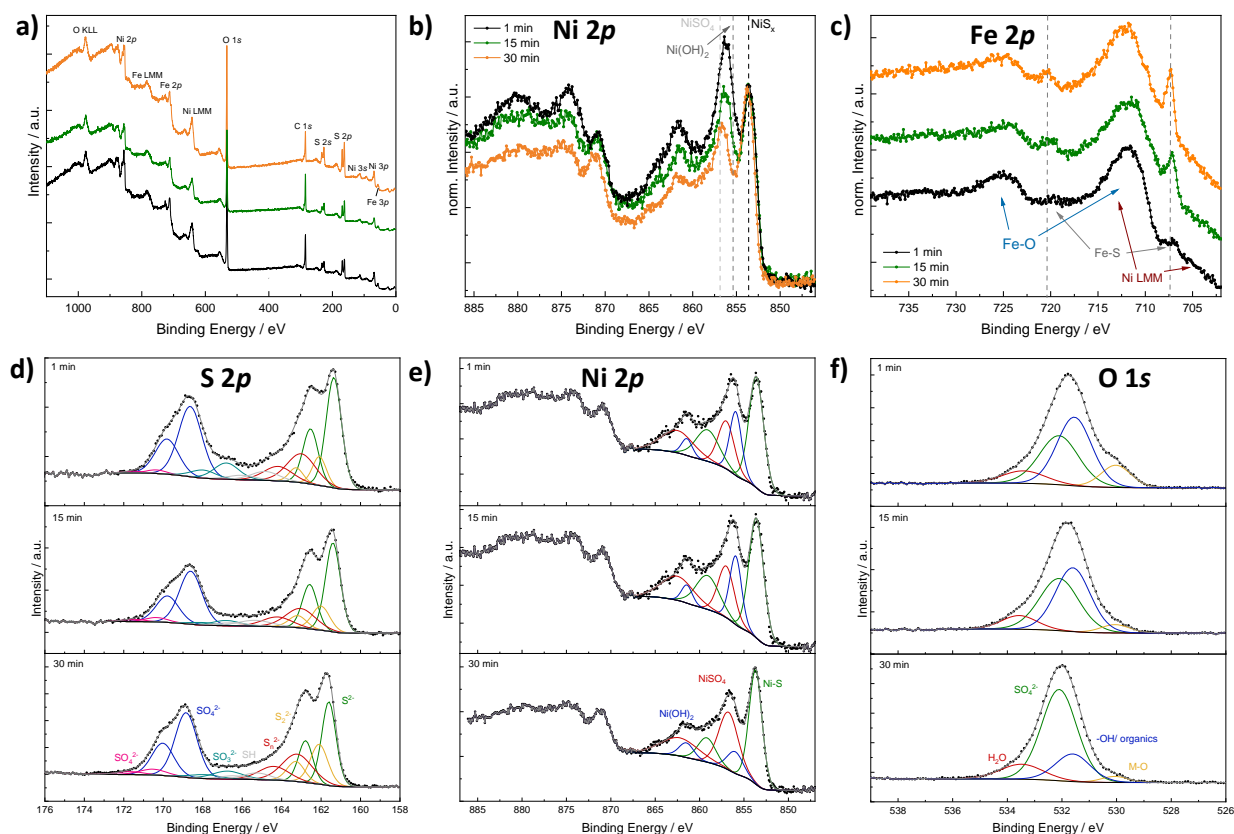
Figure 3 XP spectra for Ni₂FeS₄ obtained after different synthesis durations. Survey scan (a), Ni 2*p* spectra normalised to the Ni-S peak for qualitative comparison (b), normalised Fe 2*p* spectra (c), as well as fitted S 2*p* (d), Ni 2*p* (e) and O 1*s* spectra (d).

The binding energy for the main Ni sulphide peak is with 853.7 eV more in the range for what was observed for Ni-S in octahedral coordination,[73] although half of the nickel species are expected to be in tetrahedral environment assuming a completely inverted structure.[69,77,78] The binding energy for Fe(II) sulphide is with 707.4 eV in good agreement to what has been reported for an octahedral coordination.[73,74] Hence, an inverted spinel structure is likely present, in agreement to literature.[69]

For practical application of a material for catalysis, stability is of crucial importance. Since sulphides are especially prone to oxidation under air, we performed TG-MS measurements to evaluate the stability of Ni₂FeS₄ at elevated temperatures in air (**Figure 4** and **Figure S4**). For all samples, an initial weight loss of 5 to 8 % was observed, that corresponds to the desorption of water, but otherwise the sulphide is stable up to approx. 200 °C. A further temperature increase to 400 °C initially leads to an increase in the mass that can be attributed to surface oxidation and the formation of sulphates/ oxides followed by a mass loss between 350 and 430 °C.[69] The mass loss correlates with a peak for SO_2 at ~420 °C, together with an exothermic peak in the DSC, which can thus be attributed to a decomposition of Ni₂FeS₄ under formation of $NiSO_4$. XRD patterns for Ni₂FeS₄ calcined for 2 h at 400 °C, *i.e.* after the mass loss, mainly show the reflections for $NiSO_4$ (**Figure S5**). Additionally, CO_2 is observed in low amounts, due to the decomposition of organic residues. A second major mass loss at temperatures above 600 °C is similar for all samples and corresponds to about 35%. It is due to the decomposition of $NiSO_4$, which goes in hand with a second evolution of SO_2 above 700 °C.[79] Above 800 °C the mass is decreased to approx. 60%, in correlation to complete loss of sulphur and the formation of oxides (NiO and NiFe₂O₄) as observed in previous studies.[56]
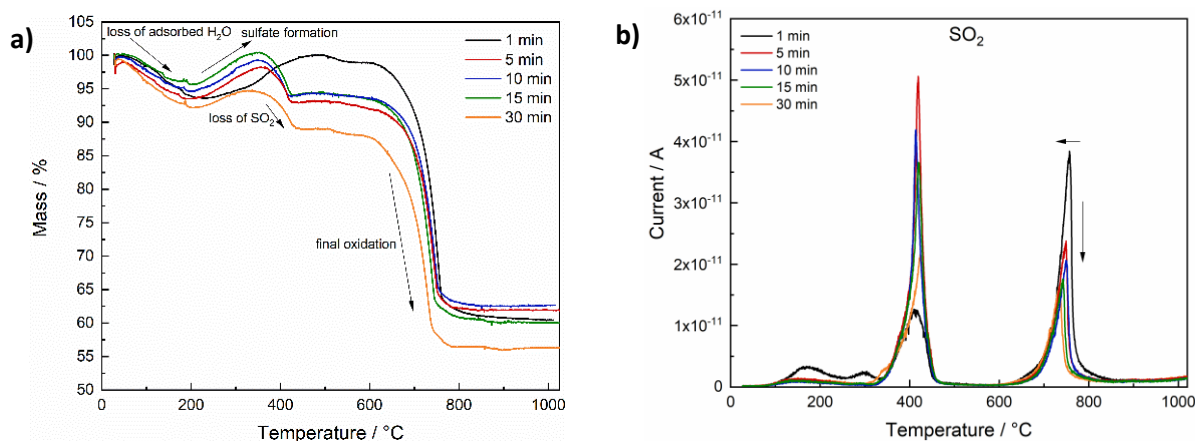
Figure 4 Relative mass loss during TG-MS measurements in air for Ni_2FeS_4 obtained after different synthesis durations (a) and SO_2 evolution detected by MS depending on the temperature (b).

The most striking difference between samples synthesised at different temperatures is the ratio of SO_2 evolved at 400 °C (sulphate formation) and at 740 to 750 °C (decomposition of the metal sulphates). In the case of solely complete conversion of Ni_2FeS_4 to $NiSO_4$ the first and the second peak for SO_2 would be equal, which is roughly the case for the sample obtained after 30 min (Figure S3). Slightly more SO_2 is evolved in the first step, possibly due to the presence of surface SO_4-groups and incomplete conversion to $NiSO_4$. The formation of $NiSO_4$ at approx. 400 °C additionally requires the reduction of Ni^{3+}. For samples obtained after synthesis times between 5 and 15 min, the peak in the DSC curves and the relation of both SO_2 peaks is essentially the same. For the Ni_2FeS_4 synthesised for one minute, the first SO_2 peak is significantly less intense, than the second, and both are significantly smaller and larger, respectively, compared to all other samples. Notably, the initial oxidation of the sample obtained after 1 min also proceeds over a longer time range and the subsequent mass loss above 400 °C is lower. This might indicate, that $NiSO_4$ formation is favoured. Since the evolution of hot spots was not yet finished after 1 min, it can be assumed that the changes in the Ni and Fe valence were not yet complete/ had not yet reached equilibrium conditions and more Ni^{2+} is still present in the structure after 1 min, partly bonded to oxygen as observed in the XP spectra. For Ni_2FeS_4 synthesised for 30 min, the initial SO_2 evolution and the peak in the DSC are smaller again. The relative ratios of both peaks are listed in Table S2. These changes in a sample that had experienced prolonged heating times might be due to changes in the relative ratio of nickel, possibly together with changes in the degree of inversion, as was observed in other microwave assisted synthesis routes of spinel oxides.[71]

Ni_2FeS_4 is absorbing light strongly over the entire visible light range and into the near infrared (NIR) region, as also apparent by its black colour (**Figure S6** and **S7**). A band gap of around 2 eV is tentatively estimated based on the direct Tauc plot. By itself it is inactive in photocatalytic HER (see below), but the good light absorption characteristics together with high conductivity, as evidenced by a small charge transfer resistance in Nyquist plots (**Figure S8**), make it a suitable candidate for a co-catalyst in combination with an active photocatalyst. In this study we chose TiO_2 (P25) as a model photocatalyst system, onto which we loaded Ni_2FeS_4 in different amounts between 0.1 and 10 wt.% by grinding both constituents, followed by subsequent calcination for 2 h at 200 °C in argon, to improve the interparticular contact.

To evaluate the optimal amount of Ni_2FeS_4, we used a synthesis time of 30 min, *i.e.* the conditions employed in previous electrocatalytic experiments.[56] XRD patterns (Cu anode) of the composites mainly show the reflections of TiO_2 – only for higher loadings with Ni_2FeS_4 (5 and 10 wt.%) the main

reflection of the sulphide is visible (**Figure 5**). Other bulk characterisation methods, like Raman (Figure 5) or IR spectra (**Figure S7**) also mainly show the characteristic bands for TiO_2 – which is metal-oxygen bonding vibrations at 920 cm^{-1} and additional bands for -OH vibrations of dangling bonds and adsorbed water – although the good light absorption properties become visible in an increased background noise in both techniques.[80] Very weak bands for adsorbed organics, likely residues from the synthesis of Ni_2FeS_4, are also present. Small differences are observed in the Raman spectra of P25 decorated with Ni_2FeS_4, especially for higher loadings. Bands for Ni_2FeS_4 at 290 and 350 cm^{-1} are apparent even under relatively high laser intensity. When pure Ni_2FeS_4 was measured under the same conditions, a transformation to a pure inverse spinel, possibly $NiFe_2O_4$, was observed, likely due to the strong light absorption and thus sample heating under laser irradiation (**Figure S9**).[81,82] Very weak bands were observed under reduced laser power. SEM images of a composite containing 5 wt.% of Ni_2FeS_4 show homogeneous agglomeration of nanoparticles – mostly TiO_2. EDX analysis over such an agglomerate mainly shows the expected signals for oxygen and titanium, evenly distributed over the entire agglomerate (Figure 5). Signals for Ni and Fe appear in the same areas as those for TiO_2 indicating homogeneous distribution of the sulphide. The changes during the annealing of ground Ni_2FeS_4 and P25 were also followed directly with TG-MS (**Figure S10**). A small signal for SO_2 is observed during the initial heating. However, since only an m/z of 64 was monitored, this signal might also arise from adsorbed organic that was removed during heating. No SO_2 signal is observed during the 2 h at 200 °C, proving the stability of the Ni_2FeS_4 during loading onto P25. Two peaks for SO_2 are observed at 290 °C and at 433 °C, as a consequence of sulphate formation.
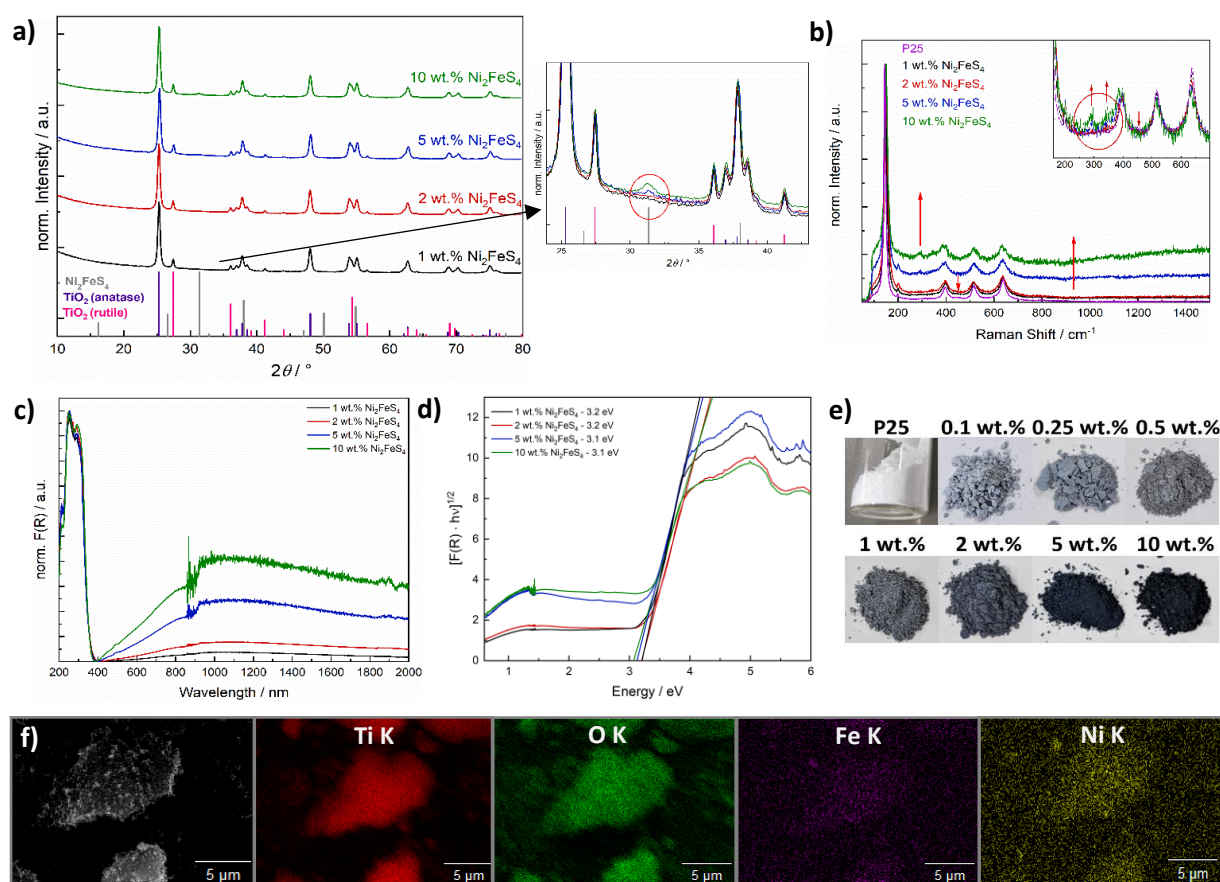
Figure 5 Cu-XRD patterns of P25 loaded with Ni_2FeS_4 with corresponding excerpt showing the main reflection of Ni_2FeS_4 (a), Raman spectra (b), UV/vis/NIR spectra (c and d) and photographs of P25 loaded with Ni_2FeS_4 (f), as well as EDX mapping of a P25 loaded with 5 wt.% of Ni_2FeS_4 (f). (Due to all bulk methods being dominated by characteristics of TiO_2, the characterisation after co-catalyst loadings of 0.1, 0.25 and 0.5 wt.% is omitted here and shown in **Figure S11**)

TiO$_2$ loaded with Ni$_2$FeS$_4$ gains a greyish colouring, even at low loadings, which is also apparent in the UV/vis/NIR spectra (**Figure 5**). For all composites a band gap of 3.1 – 3.2 eV is obtained from the indirect Tauc plots, in agreement to the expected band gap of 3.2 eV for anatase and that measured for P25 before and after Pt photo-deposition (**Figure S11**).[83,84] The slightly higher value is due to the NIR absorption of Ni$_2$FeS$_4$ and especially problematic at higher co-catalyst loadings. The influence of absorption in the sulphide is well visible in an increased pseudo-absorption starting from 400 nm and reaching into the NIR region (Figure 5d). As expected, the portion of absorbed visible and NIR light increases with an increasing content of Ni$_2$FeS$_4$.

The decorated TiO$_2$ was then tested for photocatalytic hydrogen evolution under 1 sun simulated sunlight, using 10 vol.% of methanol as hole scavenger (**Figure 6**). While pure Ni$_2$FeS$_4$ is inactive under the employed conditions, calcined P25 (200 °C, 2 h) shows a hydrogen evolution rate of 3.4 µmol/h by itself. The activity of as received P25 is slightly lower, likely due to the desorption of water and organics during the annealing at 200 °C (**Figure S15**). The loading with Ni$_2$FeS$_4$ can boost the H$_2$ production rate to 24 – 28 µmol h^{-1}, largely independent of the loading over a wide range, demonstrating the effect of Ni$_2$FeS$_4$ as a co-catalyst as opposed to the function as a component in a heterojunction. Only at high loadings of 10 wt.% of the sulphide, a diminished mass of active photocatalyst material and shadowing effects due to strong light absorption of Ni$_2$FeS$_4$ lead to a decrease in the observed activity. The amount of Ni$_2$FeS$_4$ can be decreased, without a loss of activity suggesting efficient charge transfer between Ni$_2$FeS$_4$ and TiO$_2$. Even at low amounts of Ni$_2$FeS$_4$ of 0.5 wt.%, which equals to 0.287 wt.% of metals, an activity of 25 µmol h^{-1} is reached. Such a high activity enhancement at low loading makes Ni$_2$FeS$_4$ a very interesting non-noble metal co-catalyst.
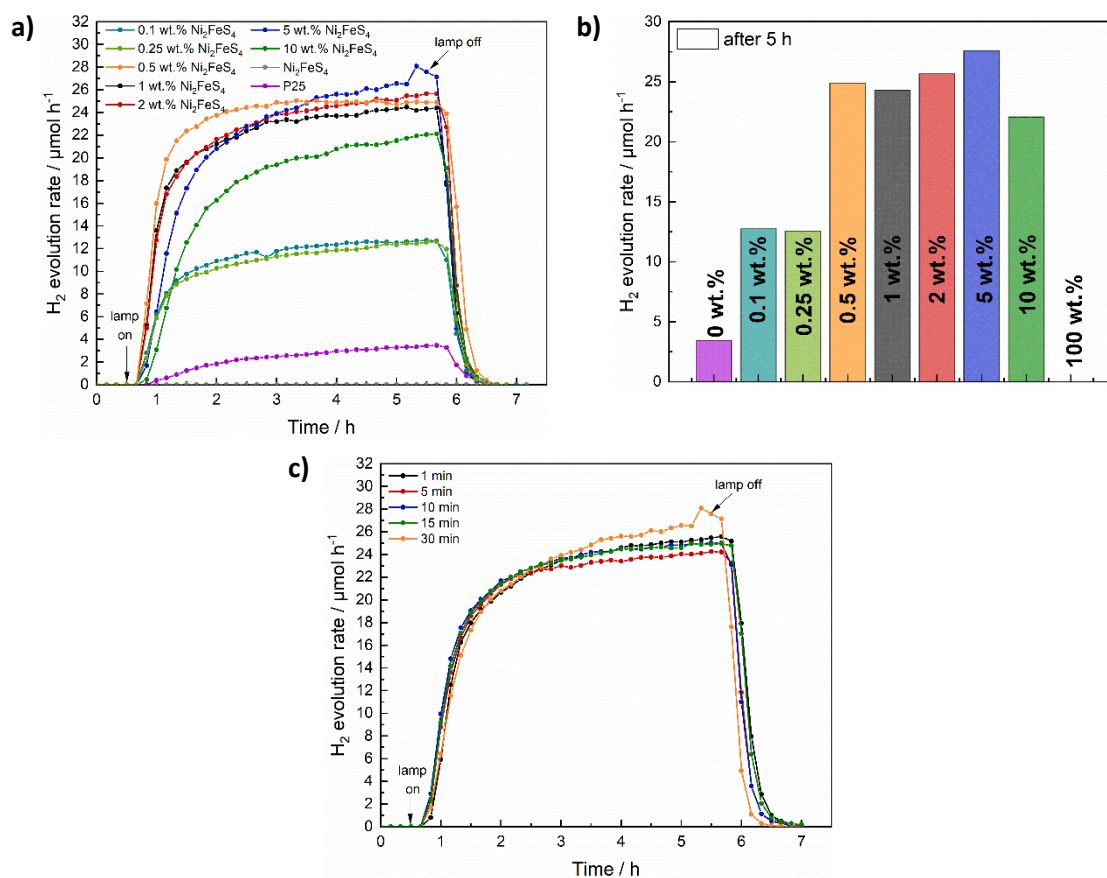
Figure 6 H$_2$ evolution over P25 loaded with different amounts of Ni$_2$FeS$_4$ under 1 sun simulated sunlight (a and b). Additionally, the H$_2$ evolution for 5 wt.% Ni$_2$FeS$_4$@P25, with Ni$_2$FeS$_4$ obtained after different synthesis durations in the microwave is shown (c). The lamp was switched on after 30 min and turned off after 5 h of irradiation.

The steady state activity for P25 with Ni_2FeS_4 is reached faster for lower co-catalyst loadings, possibly due to an initial activation phase. Compared to 0.5 wt.% platinum on either as-obtained P25 or annealed P25, still more than 11 % of the activity with Pt is reached (Figure S15) even at a lower metal loading. The relative activity compared to 0.1 wt.% of Pt is with 16 % even higher.

In a next step the influence of the synthesis conditions of Ni_2FeS_4 on the performance as a co-catalyst on TiO_2 was evaluated. A loading of 5 wt.% was chosen, since the observed HER activity was highest (although similar to lower loadings) and the modification of TiO_2 can be done more accurately for higher mass loadings/ relative ratios of the sulphide. A similar relative loading is apparent in almost identical XRD patterns, Raman, DRIFT and UV/vis/NIR characteristics (**Figure S13**). Essentially the same activity is observed for all measured samples, independent of the synthesis time of Ni_2FeS_4, which is in very good agreement to the lack of differences observed in the characterisation, further confirming the complete reaction after only a couple of minutes (Figure 6c). Interestingly, the differences in the amount of metal oxygen bonds observed by XPS and the loss of Ni upon extended time in the microwave did not appear to have an influence. Since the photocatalysis is performed in an aqueous environment, surface oxidation and formation of oxidic species, especially FeOOH and $Ni(OH)_2$ that were observed for pentlandite likely occur anyway.[73]

To improve the sustainability, a calcination in an argon atmosphere is impedimental. Bulk Ni_2FeS_4 was therefore calcined for 2 h at 200 °C in air and the obtained XRD pattern only showed the expected reflections for the sulphide, without any additional by-phases (**Figure S14**). This is in good agreement to previous observations.[56] Some surface oxidation likely occurs and has been observed for iron in Ni_2FeS_4,[69] but since the M-O ratio did not influence the photocatalytic performance before, it might not have an impedimental effect here either. To validate the thermal stability even in a dilution with TiO_2 and the influence of air calcination on the photocatalytic activity, 1 to 10 wt.% of Ni_2FeS_4 (synthesised for 30 min) were loaded onto P25, followed by calcination in air. XRD measurements show a slightly lower, but still comparable intensity of the main reflection for Ni_2FeS_4 and no oxidation products thereof (**Figure S12**). A highly similar hydrogen evolution activity of around 25 µmol h^{-1} was observed for higher sulphide loadings, when compared to the calcination in argon (**Figure S15**). This is in good agreement to the observed bulk stability. When the concentration of Ni_2FeS_4 was decreased below 5 wt.%, however, a decrease in the hydrogen evolution activity down to 14.5 µmol h^{-1} for 1 wt.% of Ni_2FeS_4 was observed, indicating, that for higher dilutions of the sulphide in the oxide matrix, oxidation and thus partial decomposition might become problematic. A loss in the actual sulphide loading is also apparent in the UV/vis/NIR spectra of the air-calcined samples, which show a less intense absorption in the NIR region compared to the samples calcined in Ar (Figure S14) – thus suggesting partial oxidation. These experiments elucidate that a more expensive calcination in Ar can be avoided at the trade-off of higher required co-catalyst loadings.

To see, if samples obtained after short reaction times are more prone to oxidation, the co-catalyst loading procedure in air was repeated for a 5 wt.% loading with Ni_2FeS_4 synthesised for varied reaction times. All show a similar activity, with a synthesis time of only 1 min yielding the best result (Figure S15). At first glance this finding might seem counter-intuitive, but it is in good agreement to the slightly improved thermal stability for the 1 min sample observed in TG-MS-measurements (Figure 4 and Figure S4).

The successful application of Ni_2FeS_4 as a co-catalyst on TiO_2 requires a suitable band alignment, a large work function and a suitable conduction band potential for proton reduction. To get a rough idea about

the respective band positions, they were calculated from the ionisation energies (E_i) and electron affinities (E_{EA}) of the constituting atoms according to:[85,86]

$$E_{VB} = X - 4.44\ eV + 0.5 \cdot E_{BG}$$

$$with\ X = \sqrt[7]{(X_{Fe}) \cdot (X_{Ni})^2 \cdot (X_S)^4} = 5.299\ eV$$

$$and\ X_{xy} = \frac{E_i + E_{EA}}{2}$$

With an estimated band gap energy (E_{BG}) of 2 eV, a valence band energy of 1.86 V and correspondingly a conduction band energy of -0.14 V *vs*. NHE is obtained. To estimate the Fermi level and thus the work function, Mott-Schottky analysis was performed, that yields a flat band potential of 0.49 V *vs.* RHE (**Figure 7**). If a band diagram is drawn based on these values, and electron transfer in P25 to the conduction band of anatase is assumed[83,87] excited electrons in TiO$_2$ would be transferred to the lower energetic conduction band of Ni$_2$FeS$_4$ (Figure 7). With the taken values, a small Schottky barrier would have to be overcome, however there exist multiple – partially contradicting – reports of work function and band positions in TiO$_2$, depending on the conditions[84,87-89]

The formed barrier would furthermore impede back-transfer and charge recombination. We decided on using the work function for TiO$_2$ with surface adsorbed H$_2$O/ in water, since the flat band potential of Ni$_2$FeS$_4$ was likewise determined in aqueous electrolytes. In spite of uncertainties of exact band positions and of the direction of band bending the relative band positions of TiO$_2$ and Ni$_2$FeS$_4$ should still be valid. If the conduction and valence band for TiO$_2$ are calculated following the same approach as stated above, potentials of E_{VB} = 2.97 eV and E_{CB} = -0.23 eV are obtained. The deviations from experimentally observed values are due to the neglecting of crystal phase, interatomic interactions or environmental conditions, but the relative band positions to Ni$_2$FeS$_4$ and thus direction of charge carrier diffusion remain the same.
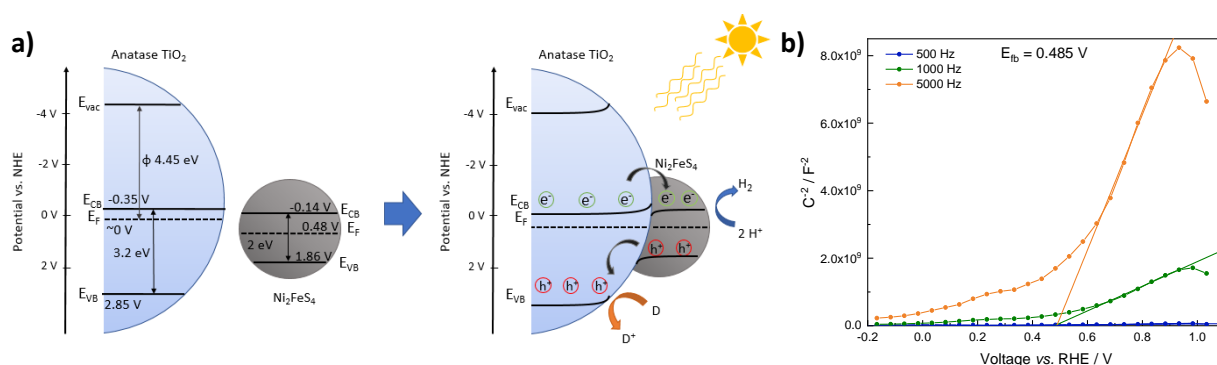
Figure 7 Band positions of TiO$_2$ and Ni$_2$FeS$_4$ before and after contact (a) and Mott-Schottky plots for Ni$_2$FeS$_4$ in 0.5 M Na$_2$SO$_4$ (values are already converted to pH 0) (b).

To verify the role of P25 as the photocatalyst and that of Ni$_2$FeS$_4$ as a co-catalyst, the photocatalytic experiment was repeated for a loading of 5 wt.%, using 420 nm cut-off filter. No activity was observed, although light absorption and excitation in Ni$_2$FeS$_4$ should still occur. Additionally, we wanted to make sure that the observed activity increase is not in parts due to the use of methanol as a scavenger and thus the possibility of hydrogen generated *via* methanol oxidation in the dark, as observed for platinum.[80] Therefore, the photocatalytic experiment was repeated for P25 and P25 decorated with 5 wt.% of Ni$_2$FeS$_4$ using ethanol as a hole scavenger. The observed activity is about half that obtained

in methanol, with a slower activation, due to the kinetically more impeded oxidation of ethanol and different oxidation mechanisms and products.[91,92] The relative activity increase with and without co-catalyst loading is however essentially the same, proving that Ni_2FeS_4 is indeed acting as a co-catalyst (**Figure 8**). Another question that arises when sulphides are used, is the stability under operating conditions. No decline in the hydrogen evolution rate was observed even when the measurement time was extended to 20 h (Figure 8), demonstrating the extraordinary stable activity. XRD patterns of P25 loaded with 5 and 10 wt.% of Ni_2FeS_4 reveal a slight decrease in the relative intensity of the sulphide reflection after photocatalysis (**Figure S16**). Some amorphisation is also observed for the photocatalytic experiment with pure Ni_2FeS_4, although no crystalline oxidation products were formed, highlighting the generally extraordinary photostability of the sulphide. At the same time the light absorption in the visible and NIR range is decreased (**Figure S17**), as is the additional band at 290 cm^{-1} in the Raman spectra. All these observations indicate, that Ni_2FeS_4 is partially oxidised/ dissolved at the surface and thus perhaps not exclusively the active species under operating conditions, similar to what is known for sulphides, especially iron sulphides, in electrocatalysis.[16,22] This finding is further underlined by the observation of SO_3^{2-} and SO_4^{2-} species with ion chromatography (**Figure S18**). Interestingly, SO_4^{2-} was also found in the solution after the irradiation of pure Ni_2FeS_4 with 1 sun simulated sunlight, even though no hydrogen evolution was observed. Some dissolution of surface metal sulphate species is always expected in an aqueous environment, though.[93]
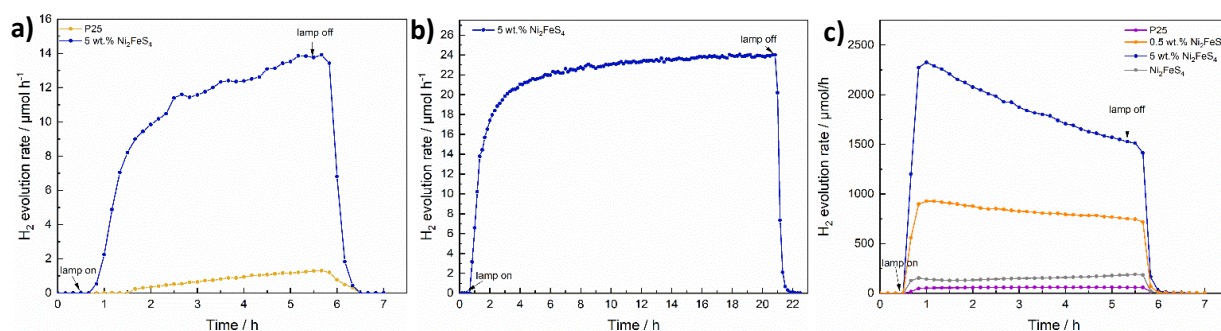
Figure 8 Photocatalytic HER over P25 and 5 wt.% Ni_2FeS_4@P25 using ethanol as a scavenger (a), for longtime irradiation (1 sun) of 5 wt.% Ni_2FeS_4@P25 in aqueous methanol solutions (b), as well as HER rates under UV irradiation (c).

Thus, either the sulphide itself might undergo oxidation during the photocatalysis, or the SO_4^{2-} stems from the sulphate species observed in XPS measurements. In any case, the evolving active species exhibits extraordinary stability and activity, as observed by the longtime photocatalytic testing. Ni_2FeS_4 also undergoes amorphisation to some extent in the absence of light. When it is dispersed for 24 hours in H_2O or 10 % aqueous methanol solutions an amorphisation is observed, although notably no reflections of hydroxides or oxyhydroxides are present (Figure S5). This would again support a partial dissolution of surface species. As a further verification of stability, we performed EDX-mapping, XPS and Ag-XRD on P25 loaded with 5 wt.% of Ni_2FeS_4 after the photocatalytic experiment for 20 h (**Figure S19**). The EDX-mapping shows that Ni and Fe are still distributed homogeneously over the TiO_2 surface. The Ag-XRD results elucidate partial amorphisation as observed for the HER experiments run for 5 h (Figure S16). The XPS survey spectra of 5 wt.% of Ni_2FeS_4@P25 mainly show signals for Ti and O, even before the HER. However, after the 20 h experiment, Ni, Fe and S are still present. Sulphur mainly occurs in the form of sulphates. The intensity for Ni and Fe does not allow for a meaningful fit. Therefore, we additionally performed XPS analysis of Ni_2FeS_4 stirred for 48 h in water. Although the XRD results showed an amorphisation already after 24 h in water (Figure S5), the spectra are highly

comparable to the as-synthesised material. The Ni 2*p* spectra still show signals for nickel sulphide, sulphate and hydroxide and the S 2*p* spectra show contributions from sulphide and sulphate species.

As a final test we wanted to examine the co-catalyst effect of the sulphide also under UV irradiation, *i.e.* the kind of irradiation still commonly employed for large band gap semiconductors such as TiO_2, since these harsh conditions might put more stress on the sulphide co-catalyst. We therefore tested P25 and P25 loaded with 5 wt.% of Ni_2FeS_4 under irradiation from a 500 W Hg lamp (Figure 8). The factor of the activity enhancement is highly similar, but the performance is decreasing over the course of the experiment. Initially, the HER rate is boosted by a factor of 48 to over 2300 µmol h^{-1} for 150 mg of photocatalyst, while towards the end, the activity enhancement goes down to 1520 µmol h^{-1}, which is approx. 26 times the HER rate over pure P25.

Interestingly, pure Ni_2FeS_4 is also active for the HER under UV light (Figure 8). The curve for the HER rate shows a small hump in the first half hour after turning on the lamp. After that, the activity is continuously increasing. This might be explained by an *in-situ* activation, that has been suggested for other transition metal chalcogenides and involves the formation of metal (in this case probably Ni) nanoparticles, that act as a co-catalyst.[94] Such a process under high UV light irradiation might be the reason for the decrease in the activity as observed for Ni_2FeS_4 on P25, since it would change the electronic and chemical structure of the sulphide co-catalyst. Additionally, the UV light activity of Ni_2FeS_4 itself might influence the entire charge separation mechanism, since electrons are also excited in the sulphide. This could result in a heterojunction system and explain the larger factor of activity enhancement compared to the comparison under simulated sunlight. This assumption is supported by the far lower activity now observed for a loading of 0.5 wt.% of Ni_2FeS_4, compared to the 5 wt.% loading. Here, the activity is increased by a factor of only approx. 13, which is closer to the observations under simulated sunlight and can be attributed to the lower ratio of Ni_2FeS_4 and thus the lower number of photoexcited charges in the sulphide, preventing the formation of an efficient heterojunction. After the photocatalysis under intense UV light, some amorphisation is again observed in the XRD patterns, albeit without additional indications of by-phases. Still only the reflections for Ni_2FeS_4 are present, underlining the good stability against photocorrosion even under these harsh irradiation conditions (Figure S16).

The role of Ni_2FeS_4 as a co-catalyst was then finally underlined by testing it on Al-doped $SrTiO_3$ (3 %) for HER under 1 sun illumination (**Figure S20**). By itself, $SrTiO_3$ is basically inactive for the HER under these conditions. The addition of 5 wt.% of Ni_2FeS_4 could significantly boost the activity, although the observed H_2 evolution rates were still far lower than those obtained for P25 in agreement to the generally lower HER activity reported in literature.[95]

7.1.4 Conclusions

Ni_2FeS_4 containing only earth-abundant elements can be synthesised *via* an energy efficient, high throughput microwave-assisted approach at 200 °C, requiring only 1 min of reaction time. Bulk characterisation methods support a complete reaction after such a short time. Ni_2FeS_4 was successfully used as a co-catalyst to improve the sunlight activity of large band gap semiconductors, such as TiO_2 and $SrTiO_3$, achieving an increase in the hydrogen evolution rate by a factor of 8 under 1 sun and by a factor of up to 48 under UV light. Very low co-catalyst loadings of 0.5 wt.% can be used to achieve this outstanding HER rate enhancement. Additionally, an extraordinary stability was observed with no

decrease in the hydrogen evolution being observed during 20 hours of photocatalysis, and no oxidation products of the sulphide co-catalyst were found afterwards. These findings underline the promise of Ni_2FeS_4 as a low-cost, earth abundant co-catalyst for photocatalysis.

Conflicts of interest

There are no conflicts to declare.

7.1.5 References

(1)   Pareek, A.; Dom, R.; Gupta, J.; Chandran, J.; Adepu, V.; Borse, P. H. *Mater. Sci. Energy Technol.* **2020**, *3*, 319–327.

(2)   Lin, L.; Hisatomi, T.; Chen, S.; Takata, T.; Domen, K. *Trends Chem.* **2020**, *2*, 813–824.

(3)   Takanabe, K. *ACS Catal.* **2017**, *7*, 8006–8022.

(4)   Grigoriev, S. A.; Fateev, V. N.; Bessarabov, D. G.; Millet, P. *Int. J. Hydrogen Energy* **2020**, *45*, 26036–26058.

(5)   Yu, M.; Budiyanto, E.; Tüysüz, H. *Angew. Chemie Int. Ed*. **2022**, *61*, e202103824.

(6)   Yang, J.; Wang, D.; Han, H.; Li, C. A. N. *Accounts Chem. Research* **2013**, *46*, 1900–1909.

(7)   Chen, H.; Sun, Z.; Ye, S.; Lu, D.; Du, P. *J. Mater. Chem. A* **2015**, *3*, 15729–15737.

(8)   Peng, Y.; Shang, L.; Cao, Y.; Waterhouse, G. I. N.; Zhou, C.; Bian, T.; Wu, L. Z.; Tung, C. H.; Zhang, T. *Chem. Commun*. **2015**, *51*, 12556–12559.

(9)   Li, D.; Shi, J.; Li, C. *Small* **2018**, *14*, 1704179.

(10)   Li, S.; Li, E.; An, X.; Hao, X.; Jiang, Z.; Guan, G. *Nanoscale* **2021**, *13*, 12788–12817.

(11)   Faber, M. S.; Jin, S. *Energy Environ. Sci.* **2014**, *7*, 3519–3542.

(12)   Li, A.; Sun, Y.; Yao, T.; Han, H. *Chem. - A Eur. J*. **2018**, *24*, 18334–18355.

(13)   Yang, Y.; Zhou, C.; Wang, W.; Xiong, W.; Zeng, G.; Huang, D.; Zhang, C.; Song, B.; Xue, W.; Li, X.; Wang, Z.; He, D.; Luo, H.; Ouyang, Z. *Chem. Eng. J*. **2021**, *405*, 126547.

(14)   Isegawa, M.; Matsumoto, T.; Ogo, S. *Dalt. Trans.* **2022**, *51*, 312–323.

(15)   Simmons, T. R.; Berggren, G.; Bacchi, M.; Fontecave, M.; Artero, V. *Coord. Chem. Rev*. **2014**, *270–271*, 127–150.

(16)   Anantharaj, S.; Sugime, H.; Noda, S. *Chem. Eng. J.* **2021**, *408*, 127275.

(17)   Zou, X.; Zhang, Y. *Chem. Soc. Rev.* **2015**, *44*, 5148–5180.

(18)   Faber, M. S.; Lukowski, M. A.; Ding, Q.; Kaiser, N. S.; Jin, S. *J. Phys. Chem. C* **2014**, *118*, 21347–21356.

(19)   Kong, D.; Cha, J. J.; Wang, H.; Lee, H. R.; Cui, Y. *Energy Environ. Sci.* **2013**, *6*, 3553–3558.

(20)   Yu, J.; Cheng, G.; Luo, W. *J. Mater. Chem. A* **2017**, *5*, 15838–15844.

(21)   Yu, H.; Xie, Y.; Deng, L.; Huang, H.; Song, J.; Yu, D.; Li, L.; Peng, S. *Inorg. Chem. Front*. **2022**, *9*, 146–154.

(22)   Xie, Y.; Yu, H.; Deng, L.; Amin, R. S.; Yu, D.; Fetohi, A. E.; Maximov, M. Y.; Li, L.; El-Khatib, K. M.; Peng, S. *Inorg. Chem. Front.* **2022**, *9*, 662–669.

(23)   Li, L.; Yu, D.; Li, P.; Huang, H.; Xie, D.; Lin, C. C.; Hu, F.; Chen, H. Y.; Peng, S. *Energy Environ. Sci*. **2021**, *14*, 6419–6427.

(24)   Hong, S.; Kumar, D. P.; Kim, E. H.; Park, H.; Gopannagari, M.; Reddy, D. A.; Kim, T. K. *J. Mater. Chem. A* **2017**, *5*, 20851–20859.

(25)   Lu, K. Q.; Qi, M. Y.; Tang, Z. R.; Xu, Y. J. *Langmuir* **2019**, *35*, 11056–11065.

(26)   Shi, X.; Fujitsuka, M.; Kim, S.; Majima, T. *Small* **2018**, *14*, 1703277.

(27)   Zhang, Z.; Liu, G.; Cui, X.; Gong, Y.; Yi, D.; Zhang, Q.; Zhu, C.; Saleem, F.; Chen, B.; Lai, Z.; Yun, Q.; Cheng, H.; Huang, Z.; Peng, Y.; Fan, Z.; Li, B.; Dai, W.; Chen, W.; Du, Y.; Ma, L.; Sun, C. J.; Hwang, I.; Chen, S.; Song, L.; Ding, F.; Gu, L.; Zhu, Y.; Zhang, H. *Sci. Adv*. **2021**, *7*, eabd6647.

(28)   Xu, H.; Yi, J.; She, X.; Liu, Q.; Song, L.; Chen, S.; Yang, Y.; Song, Y.; Vajtai, R.; Lou, J.; Li, H.; Yuan, S.; Wu, J.; Ajayan, P. M. *Appl. Catal. B Environ*. **2018**, *220*, 379–385.

(29)   Liang, Z.; Xue, Y.; Wang, X.; Zhou, Y.; Zhang, X.; Cui, H.; Cheng, G.; Tian, *J. Chem. Eng. J.* **2021**, *421*, 130016.

(30)   Zhao, D.; Sun, B.; Li, X.; Qin, L.; Kang, S.; Wang, D. *RSC Adv.* **2016**, *6*, 33120–33125.

(31)   Cao, S.; Chen, Y.; Wang, C. J.; Lv, X. J.; Fu, W. F. *Chem. Commun*. **2015**, *51*, 8708–8711.

(32)   Jaramillo, T. F.; Jørgensen, K. P.; Bonde, J.; Nielsen, J. H.; Horch, S.; Chorkendorff, I. *Science* **2007**, *317*, 100–102.

(33)   Wang, Z.; Fan, J.; Cheng, B.; Yu, J.; Xu, *J. Mater. Today Phys*. **2020**, *15*, 100279.

(34)   Wang, H.; Chen, W.; Zhang, J.; Huang, C.; Mao, L. *Int. J. Hydrogen Energy* **2015**, *40*, 340–345.

(35)   Simon, T.; Bouchonville, N.; Berr, M. J.; Vaneski, A.; Adrović, A.; Volbers, D.; Wyrwich, R.; Döblinger, M.; Susha, A. S.; Rogach, A. L.; Jäckel, F.; Stolarczyk, J. K.; Feldmann, *J. Nat. Mater*. **2014**, *13*, 1013–1018.

(36)   Zhao, Q.; Sun, J.; Li, S.; Huang, C.; Yao, W.; Chen, W.; Zeng, T.; Wu, Q.; Xu, Q. *ACS Catal*. **2018**, *8*, 11863–11874.

(37)   Ran, J.; Zhang, J.; Yu, J.; Qiao, S. Z. *ChemSusChem* **2014**, *7*, 3426–3434.

(38)   Pareek, A.; Paik, P.; Borse, P. H. *Dalt. Trans*. **2016**, *45*, 11120–11128.

(39)   Qi, H.; Wolfe, J.; Fichou, D.; Chen, Z. *Sci. Rep*. **2016**, *6*, 30882.

(40)   Li, L.; Yi, J.; Zhu, X.; Zhou, M.; Zhang, S.; She, X.; Chen, Z.; Li, H. M.; Xu, H. *ACS Sustain. Chem. Eng*. **2020**, *8*, 884–892.

(41)   Cao, S.; Chen, Y.; Wang, C.; He, P.; Fu, W. *Chem. Commun*. **2014**, *50*, 10427.

(42)   Sun, Z.; Chen, H.; Zhang, L.; Lu, D.; Du, P. *J. Mater. Chem. A* **2016**, *4*, 13289–13295.

(43)   Zhong, Y.; Yuan, J.; Wen, J.; Li, X.; Xu, Y.; Liu, W.; Zhang, S.; Fang, Y. *Dalt. Trans*. **2015**, *44*, 18260–18269.

(44)   Luo, B.; Song, R.; Zeng, Z.; Jing, D. *Appl. Surf. Sci*. **2020**, *511*, 145646.

(45)   Sakizadeh, J.; Cline, J. P.; Wolfe, E.; Thorpe, R.; Snyder, M. A.; Kiely, C. J.; McIntosh, S. *Green Chem.* **2023**, *25*, 566–578.

(46)   Peng, Y.; Zheng, Y.; Yang, Y.; Jiang, R.; Wang, G.; Zhang, Y.; Zhang, E.; Zhao, L.; Duan, C. *J. Colloid Interface Sci.* **2018**, *514*, 634–641.

(47)   Zhao, H.; Zhang, H.; Cui, G.; Dong, Y.; Wang, G.; Jiang, P.; Wu, X.; Zhao, N. *Appl. Catal. B Environ*. **2018**, *225*, 284–290.

(48)   Tran, P. D.; Xi, L.; Batabyal, S. K.; Wong, L. H.; Barber, J.; Chye Loo, J. S. *Phys. Chem. Chem. Phys*. **2012**, *14*, 11596–11599.

(49)   Xiao, M.; Zhang, L.; Luo, B.; Lyu, M.; Wang, Z.; Huang, H.; Wang, S.; Du, A.; Wang, L. *Angew. Chemie* **2020**, *132*, 7297–7301.

(50)   Tudu, B.; Nalajala, N.; Prabhakar Reddy, K.; Saikia, P.; Gopinath, C. S. *ACS Sustain. Chem. Eng*. **2021**, *9*, 13915–13925.

(51)   Wang, Q.; Yun, G.; Bai, Y.; An, N.; Chen, Y.; Wang, R.; Lei, Z.; Shangguan, W. *Int. J. Hydrogen Energy* **2014**, *39*, 13421–13428.

(52)   Zhang, L.; Tian, B.; Chen, F.; Zhang, J. *Int. J. Hydrogen Energy* **2012**, *37*, 17060–17067.

(53)   Kuo, T. R.; Liao, H. J.; Chen, Y. T.; Wei, C. Y.; Chang, C. C.; Chen, Y. C.; Chang, Y. H.; Lin, J. C.; Lee, Y. C.; Wen, C. Y.; Li, S. S.; Lin, K. H.; Wang, D. Y. *Green Chem.* **2018**, *20*, 1640–1647.

(54)   Zhong, W.; Gao, D.; Yu, H.; Fan, J.; Yu, J. *Chem. Eng. J.* **2021**, *419*, 129652.

(55)   Jiang, J.; Zhang, Y. J.; Zhu, X. J.; Lu, S.; Long, L. L.; Chen, J. *J. Nano Energy* **2021**, *81*, 105619.

(56)   Simon, C.; Zander, J.; Kottakkat, T.; Weiss, M.; Timm, J.; Roth, C.; Marschall, R. *ACS Appl. Energy Mater.* **2021**, *4*, 8702–8708.

(57)   Wu, L.; Shen, X.; Ji, Z.; Yuan, J.; Yang, S.; Zhu, G.; Chen, L.; Kong, L.; Zhou, H. *Adv. Funct. Mater.* **2022**, *33*, 2208170.

(58)   Zhou, M.; Weng, Q.; Zhang, X.; Wang, X.; Xue, Y.; Zeng, X.; Bando, Y.; Golberg, D. J. *Mater. Chem. A* **2017**, *5*, 4335–4342.

(59)   Konkena, B.; Puring, K. J.; Sinev, I.; Piontek, S.; Khavryuchenko, O.; Dürholt, J. P.; Schmid, R.; Tüysüz, H.; Muhler, M.; Schuhmann, W.; Apfel, U. P. *Nat. Commun.* **2016**, *7*, 12269.

(60)   Hegazy, M. B. Z.; Harrath, K.; Tetzlaff, D.; Smialkowski, M.; Siegmund, D.; Li, J.; Cao, R.; Apfel, U.-P. *iScience* **2022**, *25*, 105148.

(61)   Smialkowski, M.; Siegmund, D.; Pellumbi, K.; Hensgen, L.; Antoni, H.; Muhler, M.; Apfel, U. P. *Chem. Commun*. **2019**, *55*, 8792–8795.

(62)   Thomae, S. L. J.; Prinz, N.; Hartmann, T.; Teck, M.; Correll, S.; Zobel, M. *Rev. Sci. Instrum*. **2019**, *90,* 043905.

(63)   Langford, J. I.; Wilson, A. J. C. *J. Appl. Cryst.* **1978**, *11*, 102–113.

(64)   Kubelka, P.; Munk, F. *Z. Tech. Phys.* **1931**, *265*, 593–601.

(65)   Tauc, *J. Mat. Res. Bull*. **1968**, *3*, 37–46.

(66)   Fairley, N.; Fernandez, V.; Richard-Plouet, M.; Guillot-Deudon, C.; Walton, J.; Smith, E.; Flahaut, D.; Greiner, M.; Biesinger, M.; Tougaard, S.; Morgan, D.; Baltrusaitis, J. *Appl. Surf. Sci. Adv*. **2021**, *5*, 100112.

(67)   Bilecka, I.; Djerdj, I.; Niederberger, M. *Chem. Commun.* **2008**, 886–888.

(68)   Deshmukh, R.; Niederberger, M. *Chem. - A Eur. J.* **2017**, *23*, 8542–8570.

(69)   Mitchell, C. E.; Santos-Carballal, D.; Beale, A. M.; Jones, W.; Morgan, D. J.; Sankar, M.; De Leeuw, N. H. *Faraday Discuss*. **2021**, *230*, 30–51.

(70)   Niederberger, M.; Garnweitner, G. *Chem. - A Eur. J.* **2006**, *12*, 7282–7302.

(71)   Zander, J.; Weiss, M.; Marschall, R. *Adv. Energy Sustain. Res*. **2023**, *4*, 2200184.

(72)   Santos-Carballal, D.; Roldan, A.; Grau-Crespo, R.; De Leeuw, N. H. *Phys. Rev. B - Condens. Matter Mater. Phys.* **2015**, *91*, 195106.

(73)   Legrand, D. L.; Bancroft, G. M.; Nesbitt, H. W. *Am. Mineral*. **2005**, *90*, 1042–1054.

(74) Pratt, A. R.; Muir, I. J.; Nesbitt, H. W. *Geochim. Cosmochim. Acta* **1994**, *58*, 827–841.

(75) Biesinger, M. C.; Payne, B. P.; Grosvenor, A. P.; Lau, L. W. M.; Gerson, A. R.; Smart, R. S. C. *Appl. Surf. Sci.* **2011**, *257*, 2717–2730.

(76) Nesbitt, H. W.; Legrand, D.; Bancroft, G. M. *Phys. Chem. Miner*. **2000**, *27*, 357–366.

(77) Tenailleau, C. *Am. Mineral.* **2006**, *91*, 1442–1447.

(78) Townsend, M. G.; Gosselin, J. R.; Horwood, J. L.; Ripley, L. G.; Tremblay, R. J. *Phys. Status Solidi* **1977**, *40*, K25–K29.

(79) Ostroff, A. G.; Sanderson, R. T. J. *Inorg. Nucl. Chem*. **1959**, *9*, 45–50.

(80) Jeantelot, G.; Ould-Chikh, S.; Sofack-Kreutzer, J.; Abou-Hamad, E.; Anjum, D. H.; Lopatin, S.; Harb, M.; Cavallo, L.; Basset, J. M. *Phys. Chem. Chem. Phys*. **2018**, *20*, 14362–14373.

(81) Sanchez-Lievanos, K. R.; Stair, J. L.; Knowles, K. E. *Inorg. Chem*. **2021**, *60*, 4291–4305.

(82) Simon, C.; Zakaria, M. B.; Kurz, H.; Tetzlaff, D.; Blösser, A.; Weiss, M.; Timm, J.; Weber, B.; Apfel, U. P.; Marschall, R. *Chem. - A Eur. J.* **2021**, *27*, 16990–17001.

(83) Ruan, X.; Cui, X.; Cui, Y.; Fan, X.; Li, Z.; Xie, T.; Ba, K.; Jia, G.; Zhang, H.; Zhang, L.; Zhang, W.; Zhao, X.; Leng, J.; Jin, S.; Singh, D. J.; Zheng, W. *Adv. Energy Mater*. **2022**, *12*, 2200298.

(84) Scanlon, D. O.; Dunnill, C. W.; Buckeridge, J.; Shevlin, S. A.; Logsdail, A. J.; Woodley, S. M.; Catlow, C. R. A.; Powell, M. J.; Palgrave, R. G.; Parkin, I. P.; Watson, G. W.; Keal, T. W.; Sherwood, P.; Walsh, A.; Sokol, A. A. *Nat. Mater.* **2013**, *12*, 798–801.

(85) Pearson, R. G. *Inorg. Chem*. **1988**, *27*, 734–740.

(86) Butler, M. A. J. *Electrochem. Soc*. **1978**, *125*, 228.

(87) Deák, P.; Kullgren, J.; Aradi, B.; Frauenheim, T.; Kavan, L. *Electrochim. Acta* **2016**, *199*, 27–34.

(88) Kashiwaya, S.; Morasch, J.; Streibel, V.; Toupance, T.; Jaegermann, W.; Klein, A. *Surfaces* **2018**, *1*, 73–89.

(89) Mansfeldova, V.; Zlamalova, M.; Tarabkova, H.; Janda, P.; Vorokhta, M.; Piliai, L.; Kavan, L. J. *Phys. Chem. C* **2021**, *125*, 1902–1912.

(90) Antolini, E. *Appl. Catal. B Environ*. **2018**, *237*, 491–503.

(91) Sathiyan, K.; Bar-Ziv, R.; Marks, V.; Meyerstein, D.; Zidki, T. *Chem. - A Eur. J.* **2021**, *27*, 15936–15943.

(92) López, C. R.; Melián, E. P.; Ortega Méndez, J. A.; Santiago, D. E.; Doña Rodríguez, J. M.; González Díaz, O. *J. Photochem. Photobiol. A Chem.* **2015**, *312*, 45–54.

(93) Richardson, S.; Vaughan, D. *J. Mineral. Mag*. **1989**, *53*, 213–222.

(94) Pilarski, M.; Marschall, R.; Gross, S.; Wark, M. *Appl. Catal. B Environ*. **2018**, *227*, 349–355.

(95) Alammar, T.; Smetana, V.; Pei, H.; Hamm, I.; Wark, M.; Mudring, A. V. *Adv. Sustain. Syst*. **2021**, *5*, 2000180.

7.2 Supporting Information

Ni₂FeS₄ as highly efficient earth-abundant co-catalyst in photocatalytic hydrogen evolution

J. Zander, R. Marschall
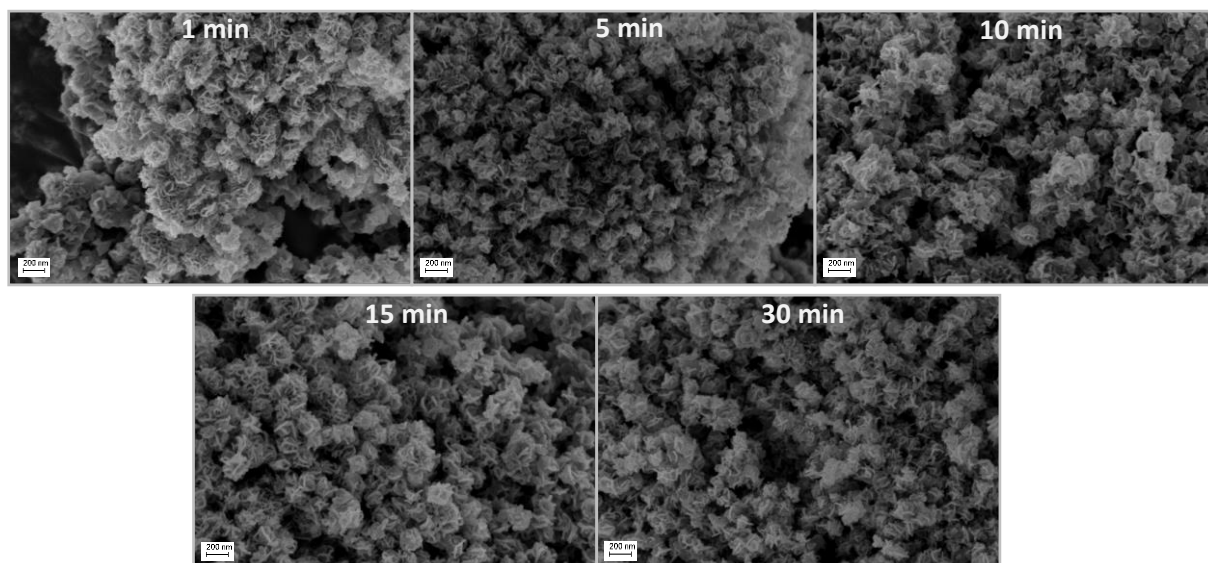
Figure S1 SEM images of Ni₂FeS₄ obtained after different synthesis durations.

Table S1 Element composition as determined *via* EDX (green) and XPS (blue). Values are average for several point areas for EDX.

EDX; XPS	1 min	5 min	10 min	15 min	30 min
At.% O	41.73 ± 5.42 40.69	21.00 ± 2.11	35.25 ± 5.59	34.53 ± 0.51 35.54	32.05 ± 2.21 38.40
At.% Ni	14.80 ± 2.51 7.10	5.80 ± 1.57	12.10 ± 5.80	17.08 ± 0.05 5.92	16.83 ± 0.46 7.15
At.% Fe	7.50 ± 1.85 2.99	2.63 ± 0.72	6.05 ± 3.18	8.83 ± 0.17 3.0	8.70 ± 0.52 3.83
At.% S	27.27 ± 10.89 17.80	12.20 ± 8.00	20.15 ± 10.11	29.65 ± 0.21 18.16	30.53 ± 1.35 24.70
At.% C	16.30 ± 7.62 31.41	61.90 ± 6.42	26.40 ± 24.75	9.88 ± 0.38 37.37	11.78 ± 0.26 25.92
Ni:Fe	2.04 ± 0.49 2.37	2.21 ± 0.16	2.03 ± 0.11	1.92 ± 0.03 1.97	1.94 ± 0.10 1.87
M:S	0.92 ± 0.39 0.567	0.81 ± 0.29	0.90 ± 0.01	0.87 ± 0.002 0.491	0.84 ± 0.02 0.444
SO₄²⁻/S²⁻	1.07			0.96	1.13
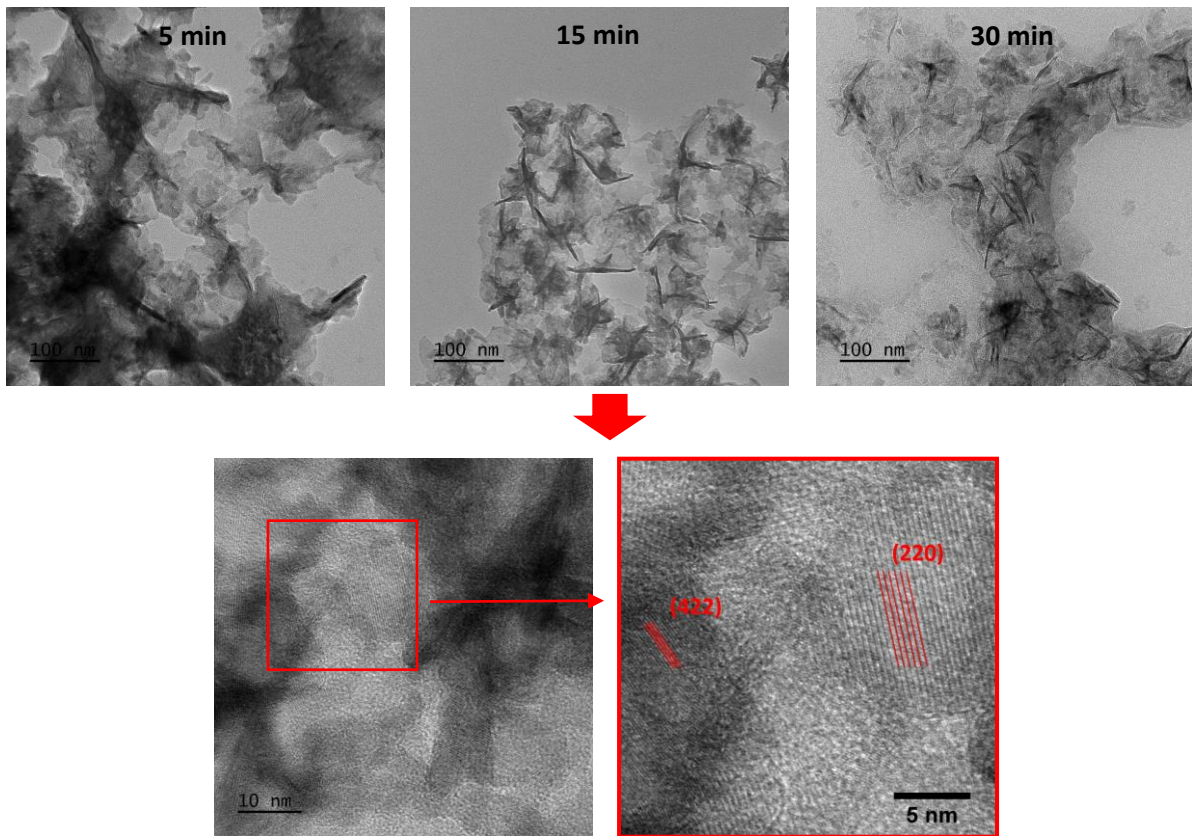
Figure S2 TEM images of Ni_2FeS_4 synthesised for different times in the microwave, including lattice planes corresponding to the (422) and (220) planes in the samples synthesised for 15 min.
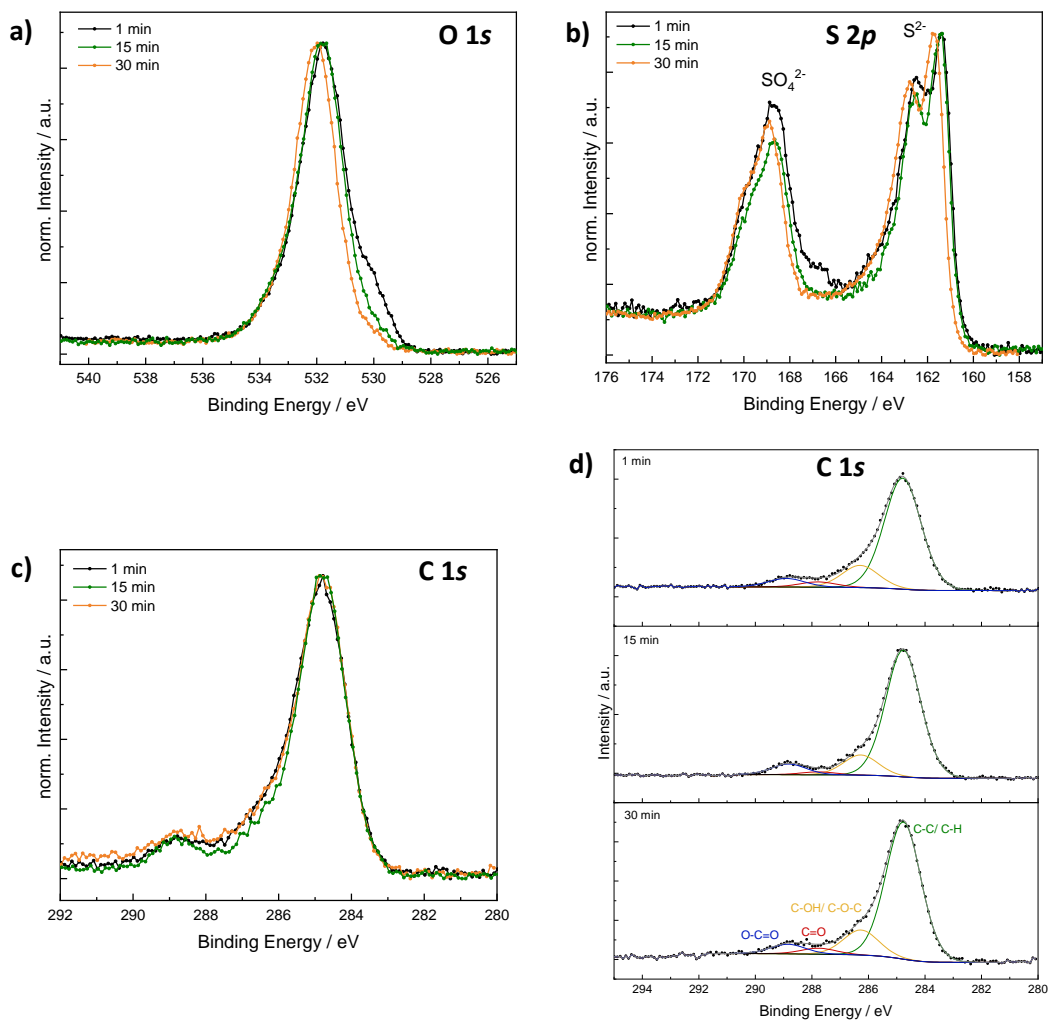
Figure S3 Normalised O 1s spectra (a), S 2p spectra (b) and C 1s spectra (c), as well as fitted C 1s spectra (d) for Ni$_2$FeS$_4$ synthesised for 1, 15 and 30 min.
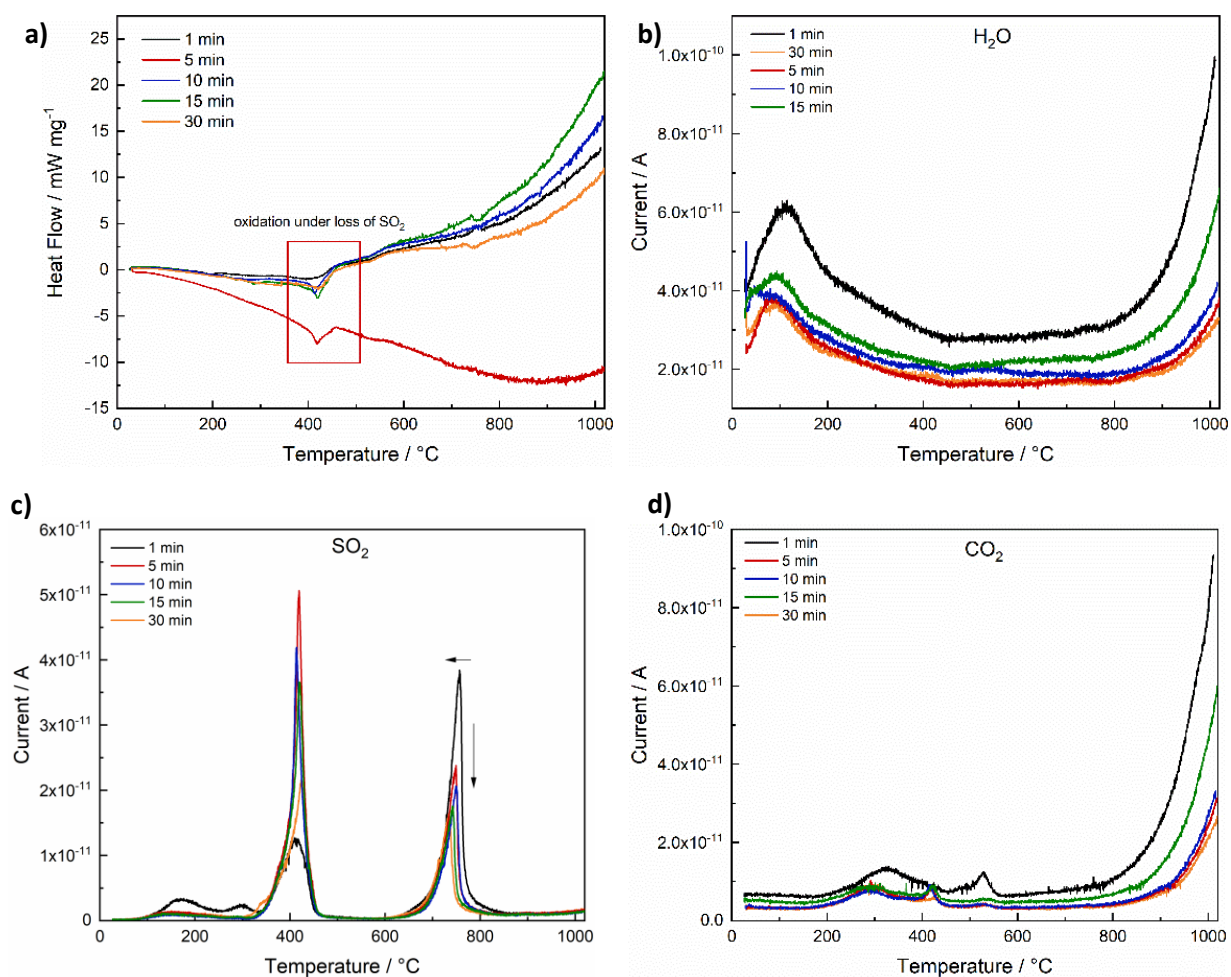
Figure S4 TG-MS measurements for Ni_2FeS_4 with different synthesis durations. DSC curves during a heating with 2 K/min (a) and corresponding gas evolutions monitored with MS: H_2O evolution (b), SO_2 evolution (c), and CO_2 evolution (d).

Table S2 SO_2 peak areas and relative ratios.

Synthesis Time	Area SO_2-1 [A/°C/mg]	Area SO_2-2 [A/°C/mg]	Sum [A/°C/mg]	SO_2-1/ SO_2-2
1 min	$3.04 \cdot 10^{-10}$	$6.00 \cdot 10^{-10}$	$9.03 \cdot 10^{-10}$	0.51
5 min	$5.77 \cdot 10^{-10}$	$3.61 \cdot 10^{-10}$	$9.38 \cdot 10^{-10}$	1.60
10 min	$5.66 \cdot 10^{-10}$	$3.74 \cdot 10^{-10}$	$9.40 \cdot 10^{-10}$	1.51
15 min	$7.99 \cdot 10^{-10}$	$4.66 \cdot 10^{-10}$	$1.26 \cdot 10^{-10}$	1.71
30 min	$4.48 \cdot 10^{-10}$	$3.33 \cdot 10^{-10}$	$7.81 \cdot 10^{-10}$	1.34
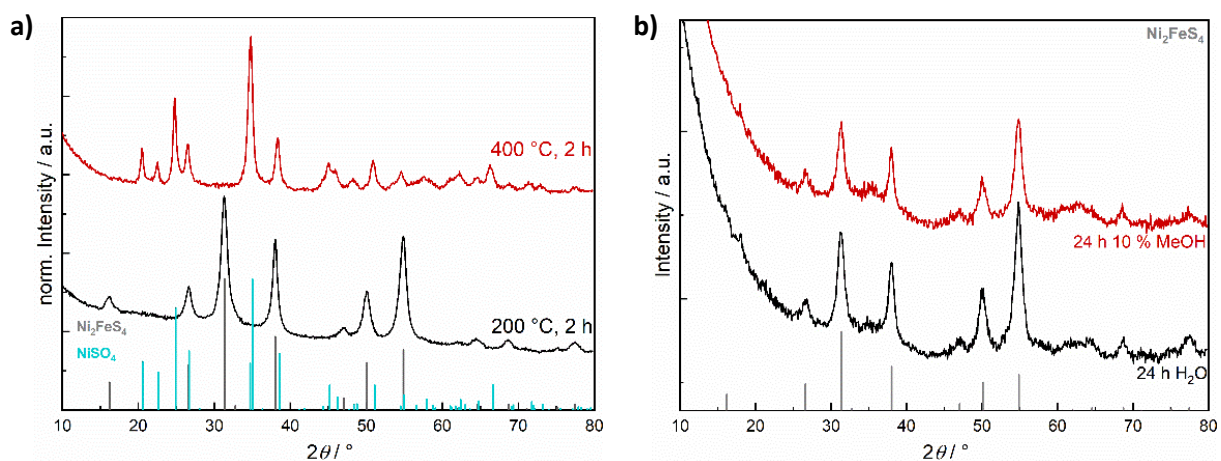
Figure S5 XRD patterns after post-synthetic heat treatment of Ni_2FeS_4 (30 min synthesis time) for 2 h at 200 and 400 °C (a) and after dispersion in H_2O/ 10 vol.% aqueous methanol (b).
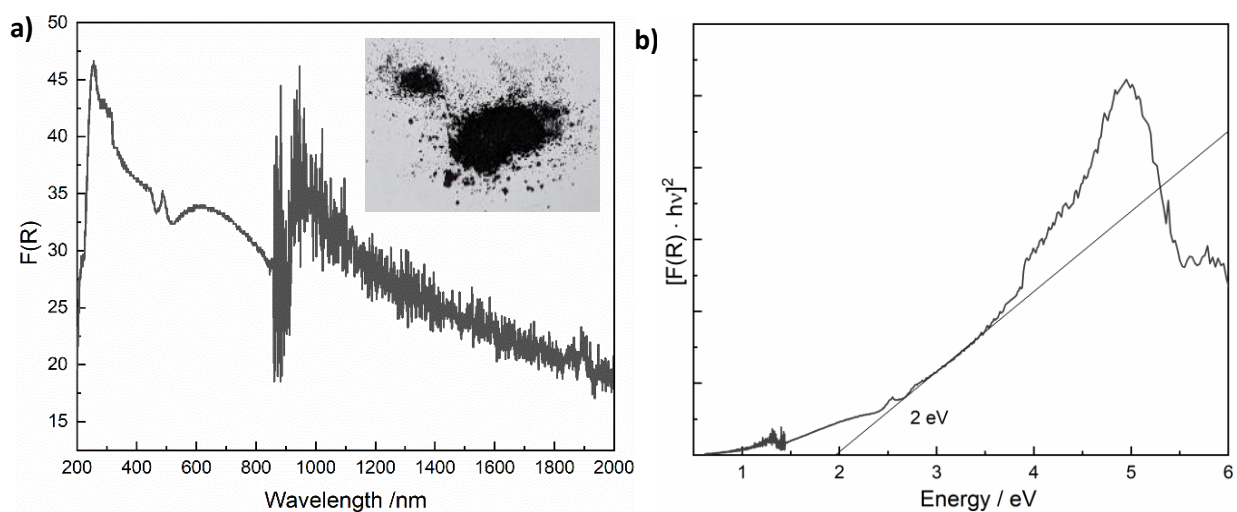
Figure S6 Kubelka-Munk (a) and direct Tauc plot (b) for Ni_2FeS_4 obtained after 30 min at 200 °C, elucidating the strong light absorption properties of the sulphide well into the NIR region.
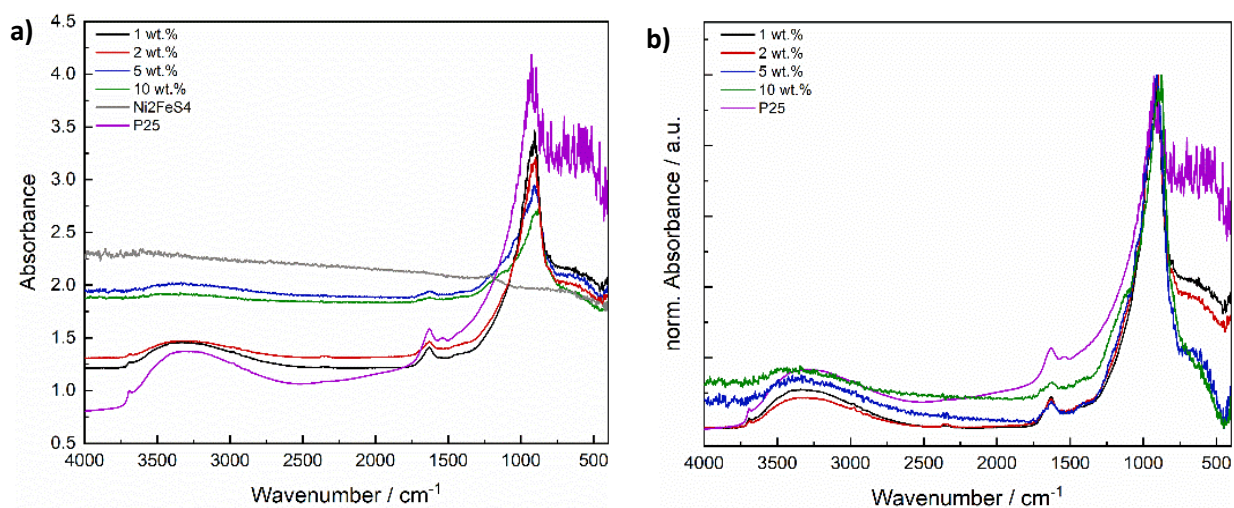
Figure S7 DRIFT spectra for P25 after loading with different amounts of Ni_2FeS_4 without normalisation (a) and normalised (b), to better show the offset caused by the absorption of Ni_2FeS_4.
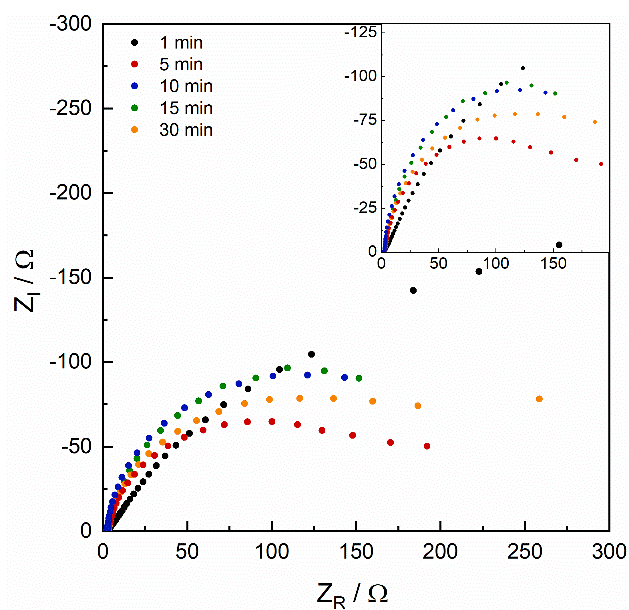
Figure S8 Nyquist plots for Ni_2FeS_4 obtained after different synthesis durations. The impedance measurements were conducted on carbon fibre electrodes in 1 M KOH at open circuit potential.

137
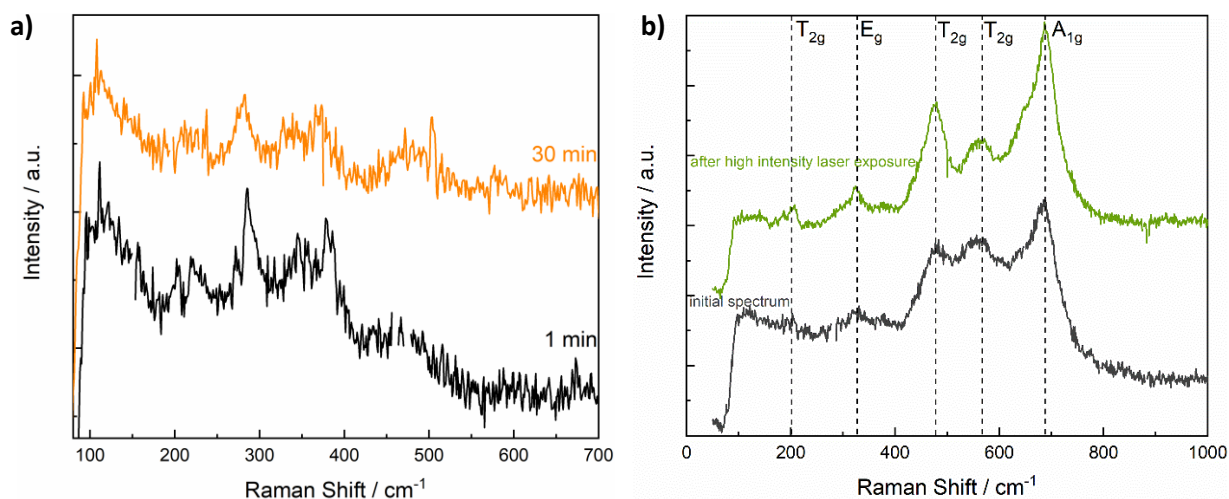
Figure S9 Raman spectra for Ni_2FeS_4 obtained after 1 and after 30 min at low laser intensity are shown in (a) and the transformation to a typical inverse spinel structure, most probably $NiFe_2O_4$, is shown in (b) first at lower laser power but already enough for oxidation (black) and then at a higher laser power (green).
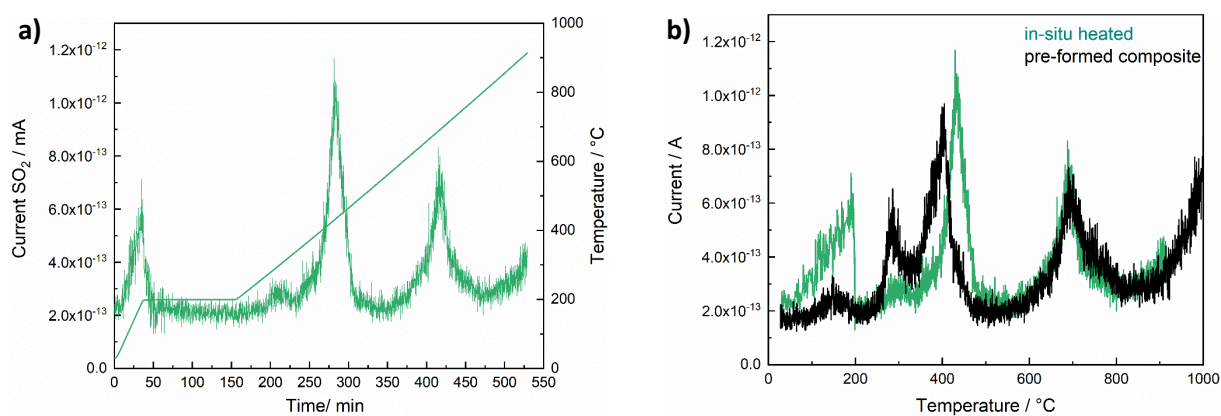
Figure S10 SO_2 gas evolution and temperature profile over time for TiO_2 and Ni_2FeS_4 ground together, but not annealed prior to the TG-MS measurement (a) and MS response for m/z=64 (SO_2) depending on the temperature for a pre-formed and an in-situ formed composite of TiO_2 and 5 wt.% of Ni_2FeS_4 (b).
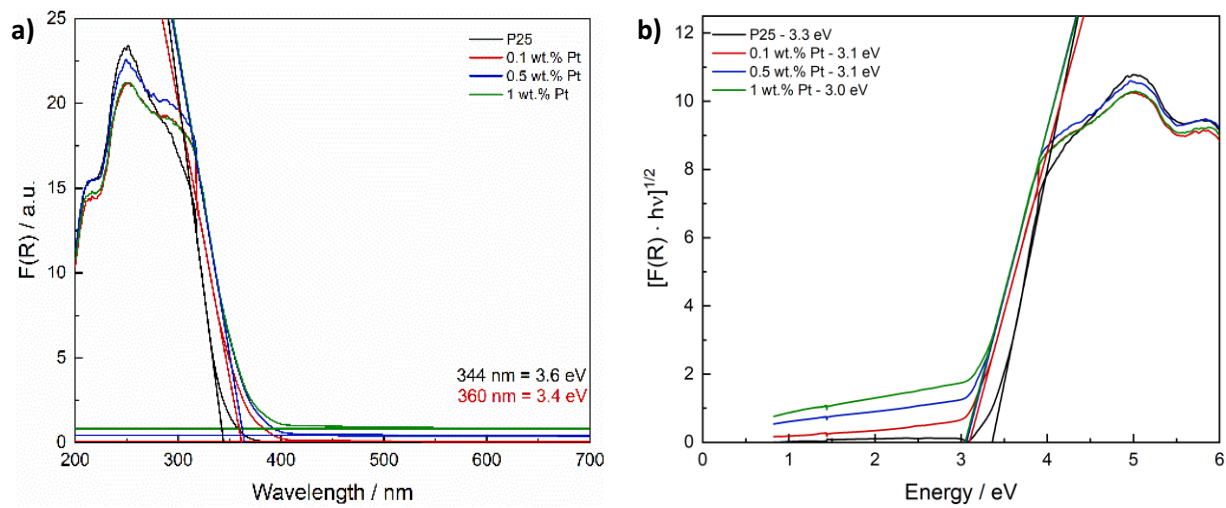
Figure S11 Kubelka-Munk (a) and indirect Tauc plot (b) of P25 before and after photo-deposition of Pt.
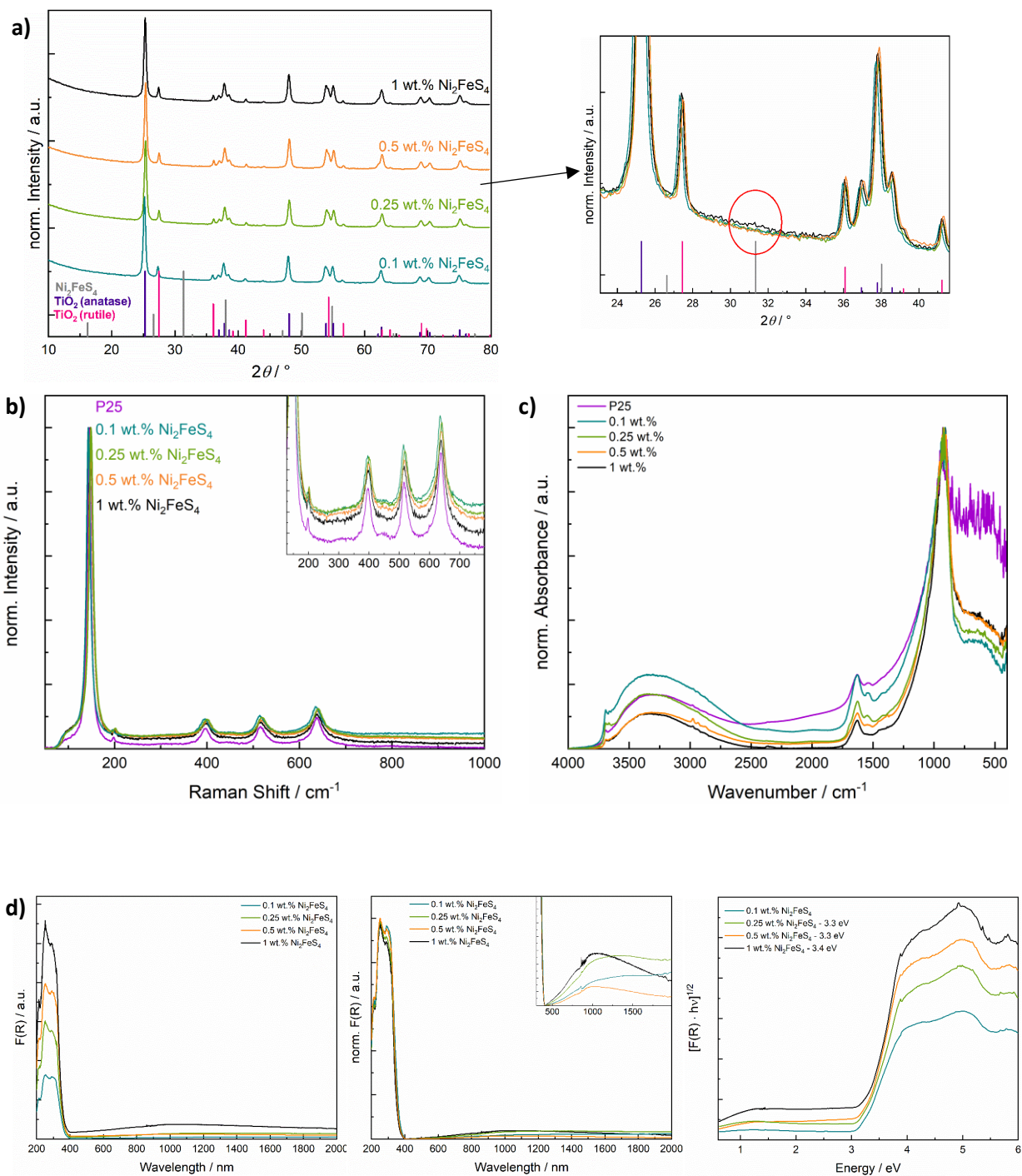
Figure S12 Cu-XRD patterns for TiO$_2$ loaded with Ni$_2$FeS$_4$ including 0.1 wt.% and 0.5 wt.% (a), corresponding Raman spectra (b), DRIFT spectra (c) and UV/vis/NIR spectra (d). At low loadings with Ni$_2$FeS$_4$, an increased pseudo-absorption in the UV region is additionally visible.
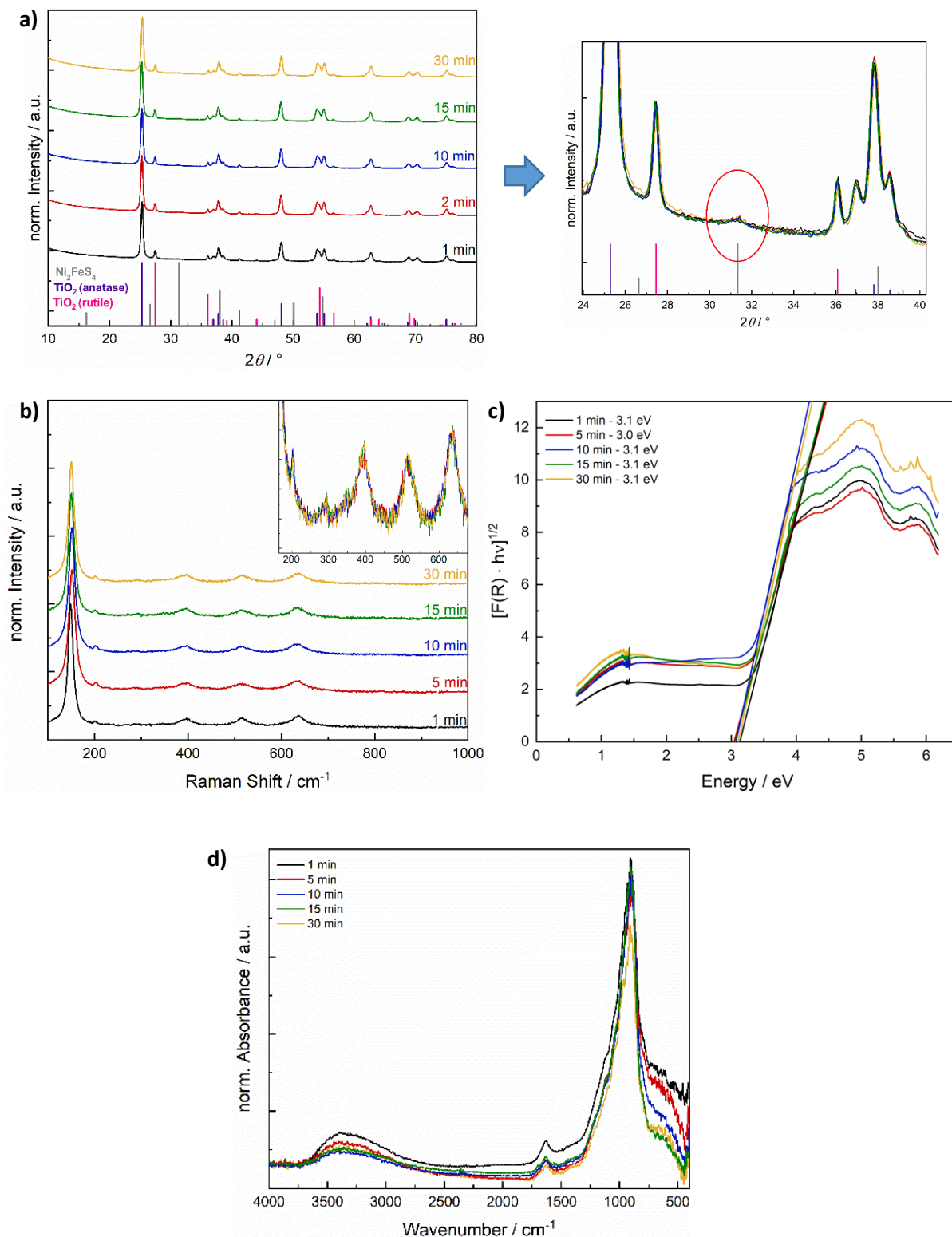
Figure S13 XRD patterns of Ni$_2$FeS$_4$ obtained after different synthesis times and loaded on TiO$_2$ in 5 wt.% (a), corresponding Raman spectra (b), UV/vis/NIR spectra (c) and DRIFT spectra (d).
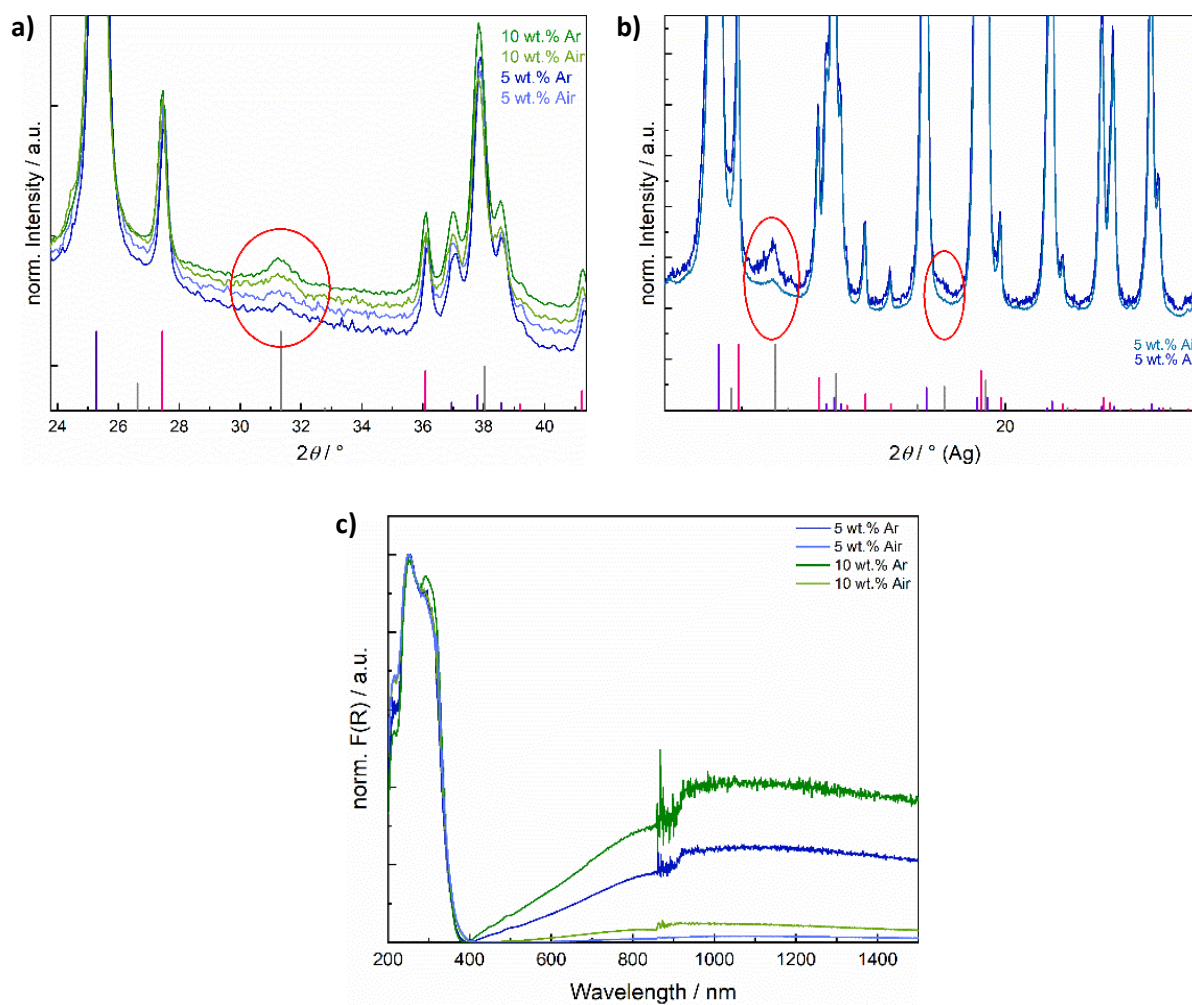
Figure S14 Comparative XRD patterns for a loading of 5 and 10 wt.% at TiO$_2$ and calcination in Ar *vs.* in air – Cu radiation (a), Ag radiation (b) and corresponding UV/vis/NIR spectra (c).
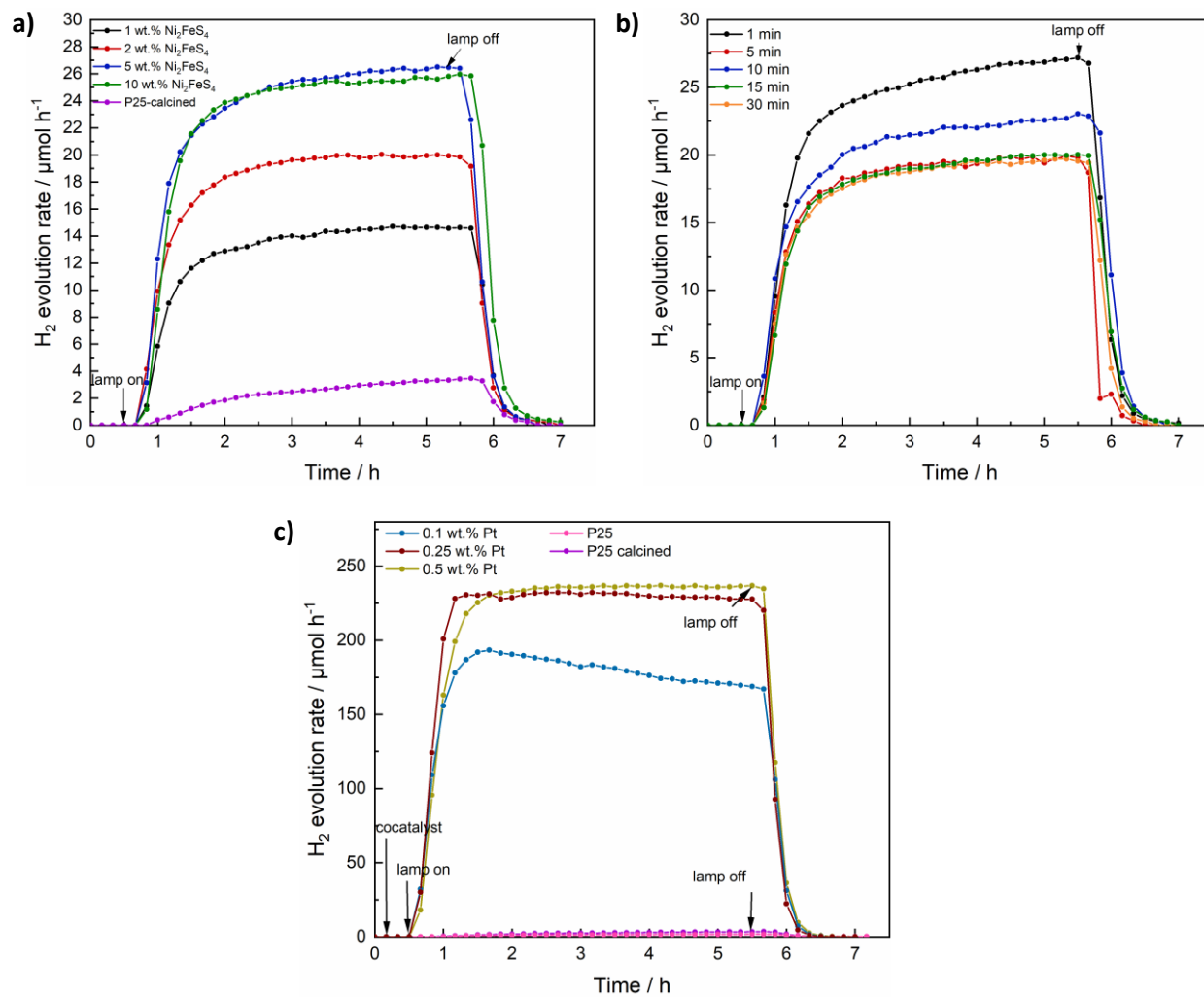
Figure S15 Hydrogen evolution for Ni_2FeS_4 on TiO_2 with different loadings and annealing in air (a) and for 5 wt.% of Ni_2FeS_4 (annealed in air) synthesised for different durations (b). Comparative measurements using photodeposited Pt as cocatalyst (c).
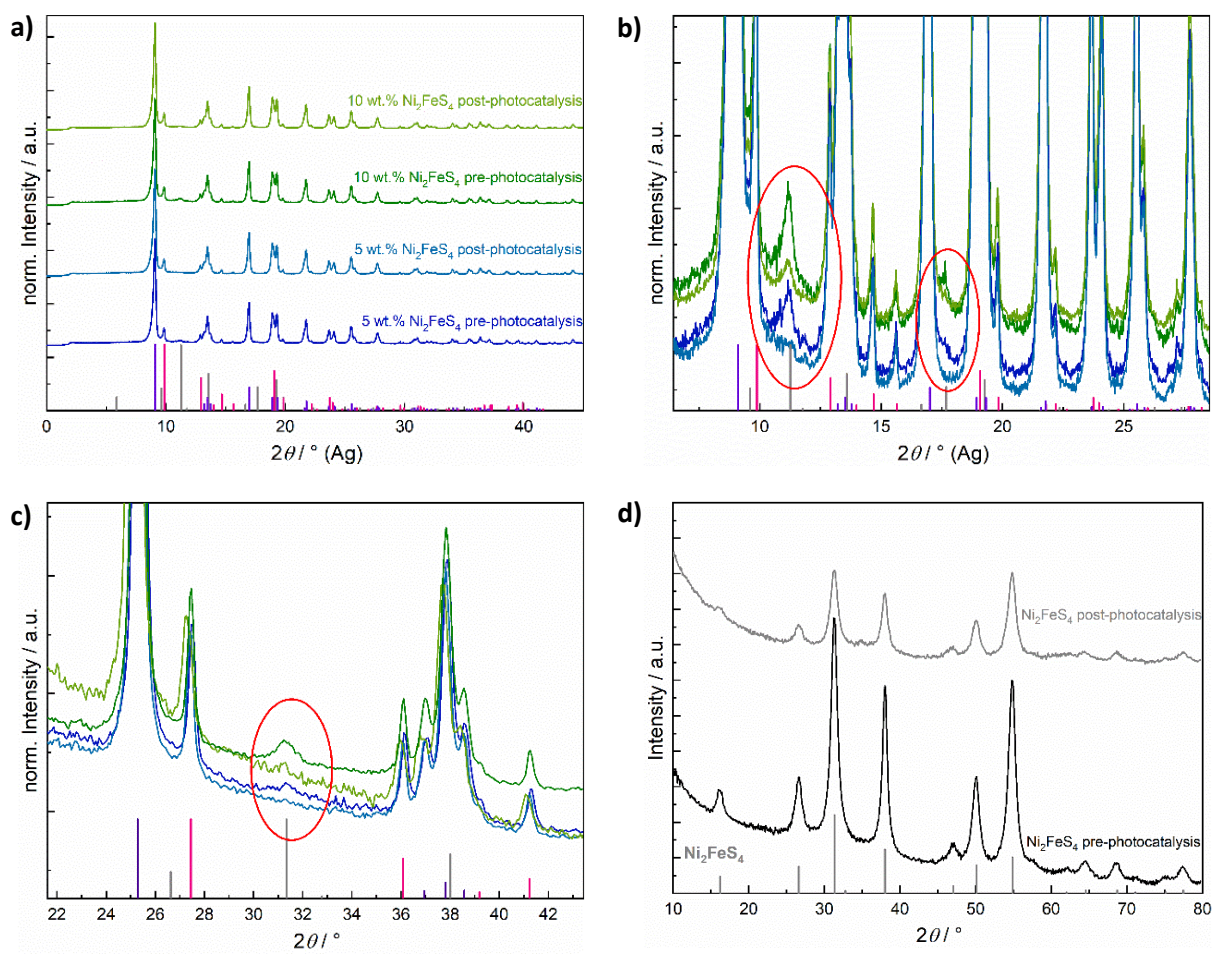
Figure S16 Ag-XRD patterns for 5 and 10 wt.% loading at TiO_2 before and after photocatalysis (a and b), Cu-XRD patterns of the same samples (c) and of Ni_2FeS_4 before and after photocatalysis with a Hg lamp (d).
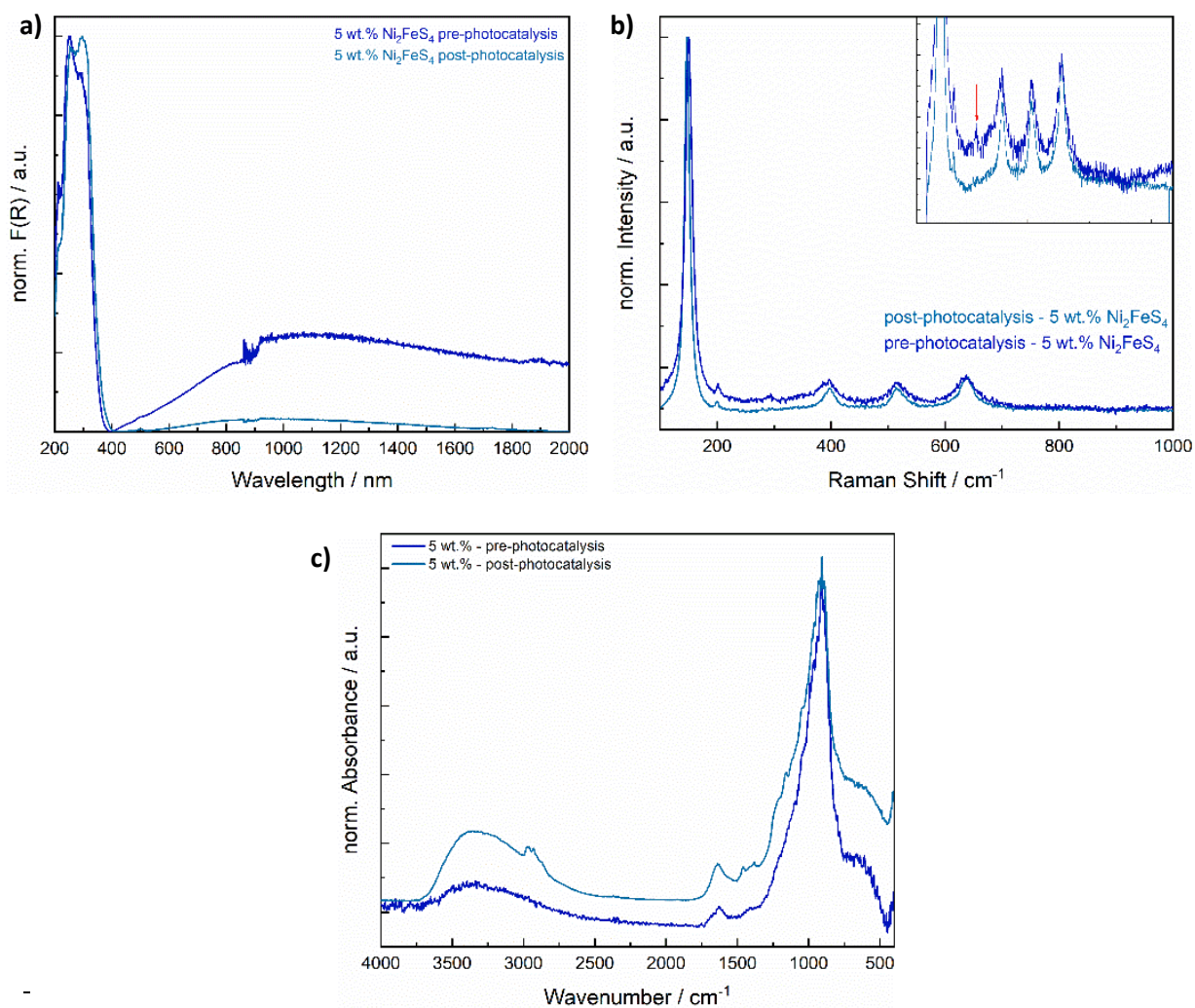
Figure S17 Comparison of TiO$_2$ loaded with 5 wt.% of Ni$_2$FeS$_4$ before and after photocatalysis: UV/vis/NIR spectra (a), Raman spectra (b) and DRIFT spectra (c).
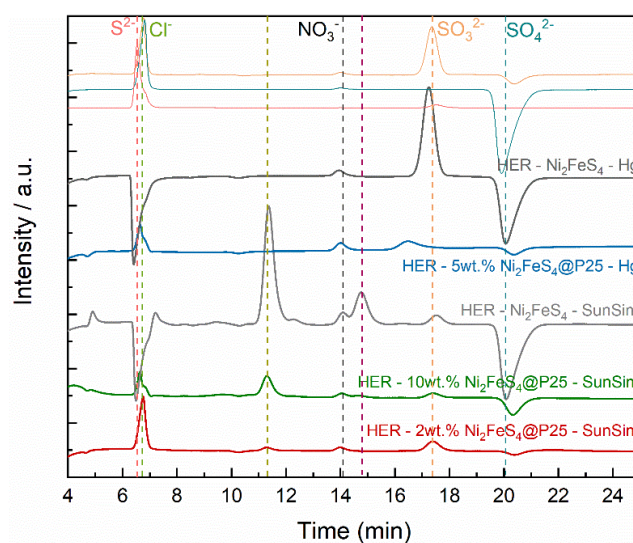
Figure S18 Ion-Chromatography for selected samples after the photocatalysis, showing the evolution of SO$_3^{2-}$ and SO$_4^{2-}$.
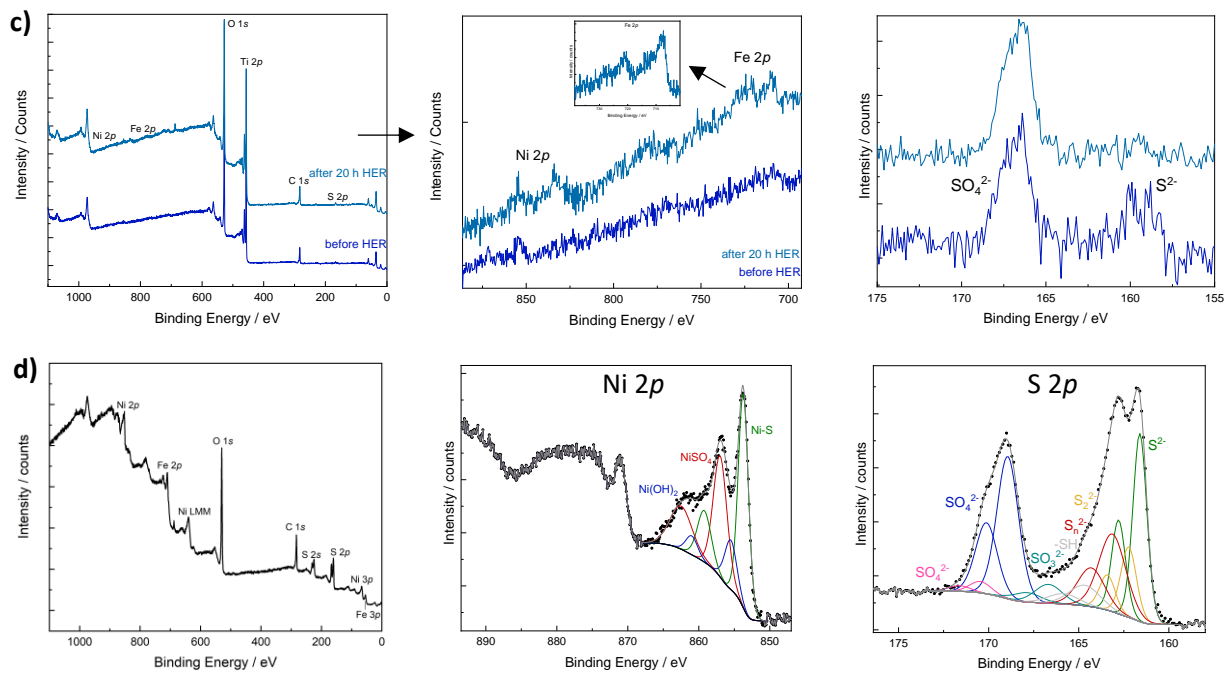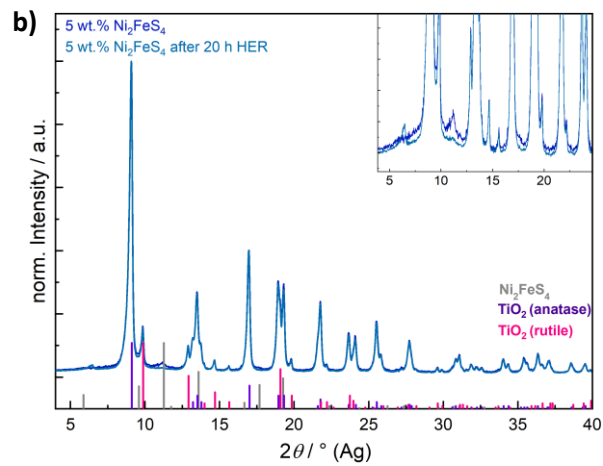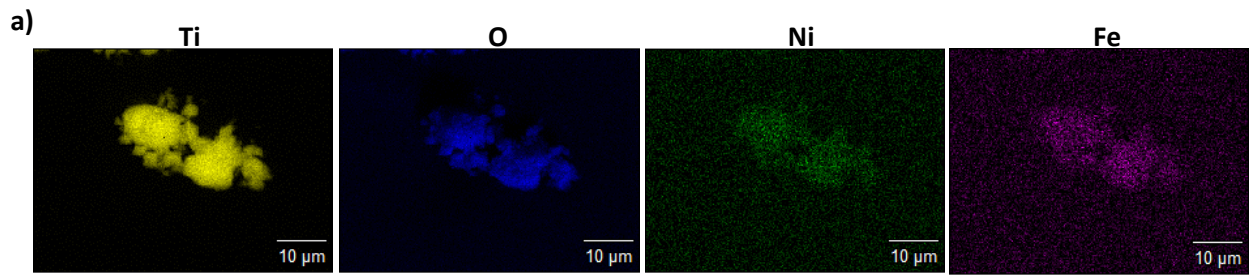
Figure S19 EDX mapping of 5 wt.% Ni$_2$FeS$_4$@P25 after irradiation for 20 h (a), Ag-XRD pattern for the same sample (b) and XPS results for 5 wt.% Ni$_2$FeS$_4$@P25 before and after the 20 h experiment(c), as well as for Ni$_2$FeS$_4$ stirred for 48 h in water.
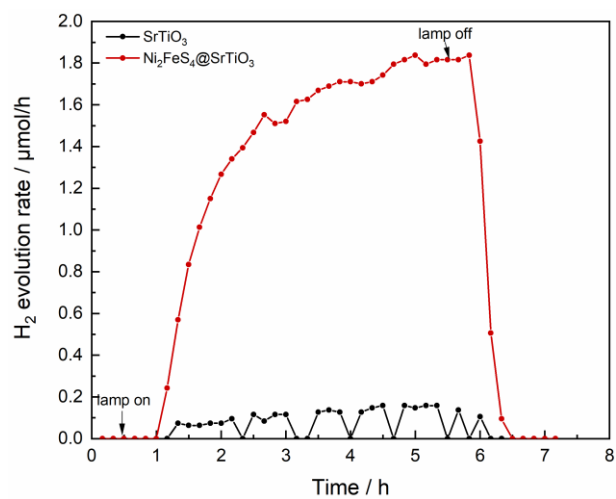
Figure S20 Hydrogen evolution over 5 wt.% of Ni_2FeS_4 on Al-doped $SrTiO_3$ under 1 sun simulated sunlight.

8 Publication 3: "Light-Induced Ammonia Generation over Defective Carbon Nitride Modified with Pyrite"

Judith Zander, Jana Timm, Morten Weiss, Roland Marschall*

Department of Chemistry, University of Bayreuth, 95440 Bayreuth, Germany

*Email: roland.marschall@uni-bayreuth.de ORCID: 0000-0002-1057-0459

8.1 Main Manuscript

Photocatalytic nitrogen fixation under ambient conditions is currently widely explored in an attempt to develop a sustainable alternative for the Haber-Bosch process. In this work we combine defect-rich carbon nitride, one of the most investigated photocatalysts reported in literature for ammonia generation, with earth-abundant and bioinspired FeS_2 to improve the activity for ammonia production. By this combination, an activity enhancement of approx. 400 % compared to unmodified carbon nitride was achieved. The optimal FeS_2 loading was established to be 1 wt.%, with ammonia yields of up to 800 µg L^{-1} after irradiation for 7 hours. By detailed material characterization of the electronic and material properties of the composites before and after the photocatalytic reaction, we reveal that NH_3 generation occurs not photocatalytically from N_2, but *via* a light-induced reduction of =N-CN groups adjacent to nitrogen vacancies in the structure of defect-rich carbon nitride. FeS_2 acts similar to a co-catalyst, enhancing the ammonia yield by π-back-donation from Fe-centers to the imine nitrogen of the defect-rich carbon nitride, thereby activating the structure and boosting the ammonia generation from cyano groups.

8.1.1 Introduction

The Haber-Bosch process is a large-scale industrial process for the production of ammonia (NH_3) from hydrogen (H_2) and nitrogen (N_2) gas at elevated pressures and temperatures. It is a well-established and optimized process, that is crucial for the production of fertilizers. Nevertheless, it still suffers from sustainability issues due to high energy requirements and the utilization of natural gas for the supply of H_2 in large, centralized power plants.[1] The photocatalytic nitrogen reduction reaction (NRR), that directly converts N_2 into NH_3 under (sun)-light irradiation at ambient conditions, presents a feasible alternative.[2,3] However, the NRR is a thermodynamically and kinetically unfavorable process due to the stable and inert nature of the N_2 molecule. Furthermore, the similar potentials for N_2 reduction and H_2

evolution impede a high selectivity in aqueous media so far. This imposes strident demands on an efficient and selective photocatalyst, that are not even close to be met even by the state-of-the art materials, thus highlighting the importance of continued research on the topic.[2,4,5] The low NH_3 yields further pose additional difficulties when it comes to accurate quantification, necessitating careful experiment control to avoid impurities and erroneous results. Discrepancies in the experimental conditions and a lack of standardized procedures further limit the comparability and reproducibility of photocatalytic NRR.[6-9]

Carbon nitrides (CN) like polyheptazine imide, C_3N_4, are low cost, non-toxic polymeric materials with good light absorption characteristics, due to a band gap of approx. 2.7 eV, which have received a lot of attention as an n-type photocatalyst during the past decade.[10,11] CN is commonly synthesized by thermal polymerization of organic precursor molecules, such as urea, melamine or cyanamide. The polymerization conditions, as well as the choice of the precursors have a strong effect on its structure and properties, by influencing the defect concentration, degree of polymerization, optical band gap, and surface area.[12] As-synthesized CN suffers from high recombination rates of photogenerated charge carriers. Therefore, alteration of the structure by doping or defect engineering and the formation of heterojunctions have been widely explored to improve the photocatalytic performance of CN.[13-24]

Some of the highest NH_3 yields in photocatalytic NRR have been reported using defective CN.[15-29] Owing to the polymeric structure of CN, the number of possible defects is vast and versatile.[18,20,21,30,31] A frequently exploited strategy for activity enhancement in CN is the introduction of nitrogen vacancies, which are of the same size as the nitrogen atoms in molecular N_2, and can thus act as efficient adsorption and activation centers.[30]

Another important class of defects are cyano or cyanamide groups, that act as electron-withdrawing groups, assisting in charge separation and suppressing recombination.[14,27,32] The NRR is supposed to proceed *via* a Mars-van-Krevelen mechanism for both defect types, making a distinction between the influence of cyano groups and nitrogen vacancies difficult. Intercalation of potassium was reported to assist in the replenishment of nitrogen in the structure, more specifically of the cyano groups, resulting in an NH_3 production rate of 3.42 mmol g^{-1} h^{-1}.[28] Treatment of bulk CN with KOH, or direct incorporation of KOH into the synthesis recently emerged as a promising strategy for both the introduction of vacancies and of cyano groups. Zhou *et al.* treated bulk CN with KOH in ethanol, followed by solvent evaporation and annealing. They observed an abundance of cyano groups that assisted in charge separation and N_2 adsorption.[27] KOH has also directly been involved in the thermal polymerization of urea, likewise promoting the formation of cyano groups.[14] A similar result was obtained by Wang *et al.*, using KOH in the thermal polymerization of dicyandiamide.[28] Etching with KOH was reported to mostly lead to the formation of vacancies. Still high NH_3 yields of 3.632 mmol g^{-1} h^{-1} were reported, together with a quantum efficiency of over 20 %.[25]

Apart from defect engineering, research on semiconductor materials for artificial photosynthesis is still in its infancy compared to the process optimization in nature. The reduction of molecular N_2 has been realized under ambient conditions at the active centers of selected enzymes, termed nitrogenases. Three different classes of nitrogenases are distinguished, based on the composition of the active centers: all contain sulfur and iron atoms, but differ in the nature of additional constituents, one containing vanadium, one molybdenum and one solely iron.[33] This composition led to the exploration of several iron or molybdenum based compounds for the NRR.[34-42] One of the simplest iron and sulfur containing compounds is FeS_2, which is a non-toxic, stable, and earth-abundant mineral. It shows very high optical absorption and high charge carrier mobility, but its use in photoelectrochemical

applications suffers from charge trapping and recombination.[43] Still, FeS_2 has been explored for photocatalytic dye degradation.[44-46] By itself it is reported to be inactive in photocatalytic NRR, due to unsuitable band positions, but it might still offer beneficial contribution in combination with other materials.[47,48] Thus, composites with FeS_2 have been employed for photocatalytic dye degradation, H_2 evolution, CO_2 reduction and NRR.[49-54] Apart from improving the light absorption properties in composites, FeS_2 can act as an efficient electrocatalyst, which has been shown separately for the H_2 evolution, as well as for the NRR.[55-59] There have been also recent reports on the formation of heterojunctions of FeS_2 with carbon nitride and their photocatalytic application in organic dye and antibiotics removal.[60,61] The reported mechanism and band positions on which the proposed electron transfers are based, are notably different between the reports, requiring further investigation of the interaction between both materials.

In a bioinspired approach, we herein report the combination of the two earth-abundant semiconducting materials FeS_2 and defective CN for light-induced NH_3 generation. Exploiting the good light absorption and N_2 activation characteristics of the Fe-S system together with the reported high activity of defective CN, NH_3 yields of up to 800 µg L^{-1} can be achieved in the course of the reaction (7 h), which equals to an activity enhancement by around 400 % compared to bulk CN. By detailed characterization of the electronic and material properties of the composites before and after reaction, we show that FeS_2 decoration weakens the bonds of CN-terminating imine groups in the vicinity of nitrogen defects by back donation. This facilitates the reduction of terminal cyano groups under light irradiation towards NH_3, with H_2 being the only by-product.

8.1.2 Results and Discussion

8.1.2.1 Material Synthesis and Characterization

The X-ray diffraction (XRD) patterns of the KOH-treated CN (V_N-CN) show the typical two broad reflections at 13° 2θ and at 27.4° 2θ, corresponding to in-plane order and interplanar stacking, respectively, with a d-spacing of approx. 0.326 nm (Figure S2, Supporting Information).[62] The structure of CN obtained *via* thermal polymerization is best described by a model of parallel melon chains connected *via* hydrogen bonds, as found by Lotsch *et al*. and confirmed in later studies. The unit cell is orthorhombic with the space group $P2_12_12_1$.[63-65] This structure model will be assumed in the following, instead of a graphitic sheet-structure with a defined C/N ratio of ¾, as implied by the stoichiometry in C_3N_4. Powder XRD patterns of the composites show the reflections for FeS_2 and for V_N-CN (KOH-etched, vacancy-rich). The intensity of the reflections of FeS_2 increases with increasing FeS_2 amounts in the composites (**Figure 1**). No additional phases could be observed. Enlarged and normalized PXRD patterns of V_N-CN and the composites (Figure S2, Supporting Information) show a shift of the (002) reflection at around 27 °2θ towards higher °2θ values compared to untreated CN. The shift and a decrease in the intensity upon KOH treatment can be assigned to a decrease in interplanar stacking distance and a general loss of order, which has been ascribed to either introduced cyano groups or nitrogen vacancies.[13,66,67]
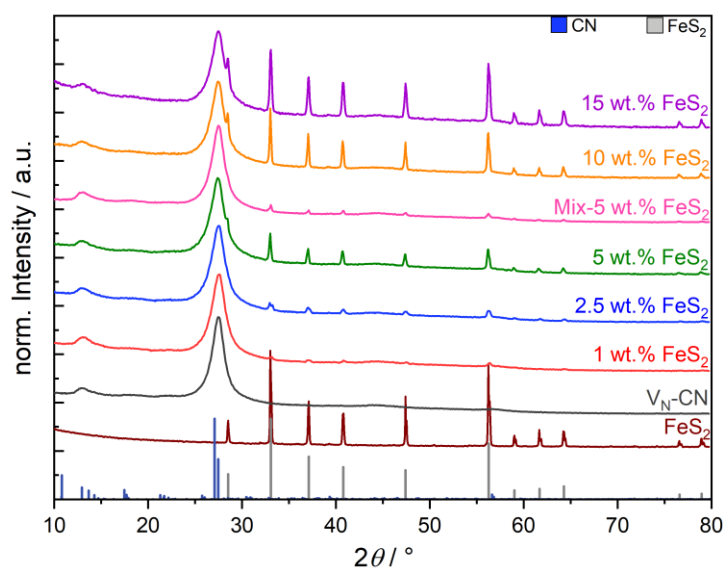
Figure 1 Powder XRD patterns for composites of FeS_2 and V_N-CN and a physical mixture of both constituents (Mix-5wt.%).

For further characterization of the morphology, SEM images and EDX maps were recorded. They show FeS_2 particles in the µm range, distributed all over the V_N-CN matrix (**Figure 2** and Figure S3, Supporting Information). EDX analysis confirmed the particles to be FeS_2 with a ratio close to the ideal value of Fe:S 1:2 (Table S1, Supporting Information) and the surrounding matrix to consist of CN with a C/N ratio of ≈0.52. This is lower than the ideal value of 0.75 and could be an indication of free amino groups in the sample, although it is also effected by the low sensitivity of EDX for light-weight atoms.

Physisorption measurements were conducted to evaluate the surface area of the composites with the BET model (Table S2, Supporting Information). Pristine CN exhibits the highest surface area of 10.6 m^2 g^{-1}, which slightly decreases upon KOH treatment. This is in good agreement with the decreased interlayer stacking distance observed in the XRD patterns and otherwise retention of the morphology. The apparent further decrease of the specific surface area upon composite formation can be explained by a difference in material density and particle size between CN and FeS_2.

The optical properties of a photocatalyst are of utmost importance, since they vastly determine the efficiency in light harvesting. The color of the composites gradually gained a tinge of grey with increased FeS_2 content, compared to the previously pale yellow coloring of both untreated CN and V_N-CN (Figure S1, Supporting Information). Diffuse reflectance UV/vis measurements were conducted to elucidate the effect of FeS_2 addition on the absorption behavior (**Figure 3**). CN is an indirect n-type semiconductor.[68,69] Therefore, an indirect Tauc plot was used for a more accurate determination of the band gap and compared to the values apparent in the Kubelka-Munk plots. KOH treatment results in a slight decrease of the band gap of CN from 2.73 to 2.70 eV, and marginally improved absorption in the UV region. The band gap reduction – and thus red-shifted absorption – could be caused by the introduction of cyano groups, whose electron-withdrawing properties were reported to lower the conduction band edge and lead to a narrowing of the band gap.[20,70] The increased UV absorption might be caused by improved charge separation due to the decreased layer distance and the introduction of

cyano groups, since transitions in the UV region are commonly ascribed to π-π^* transitions in sp^2 hybridized centers of the aromatic system.[28,71]
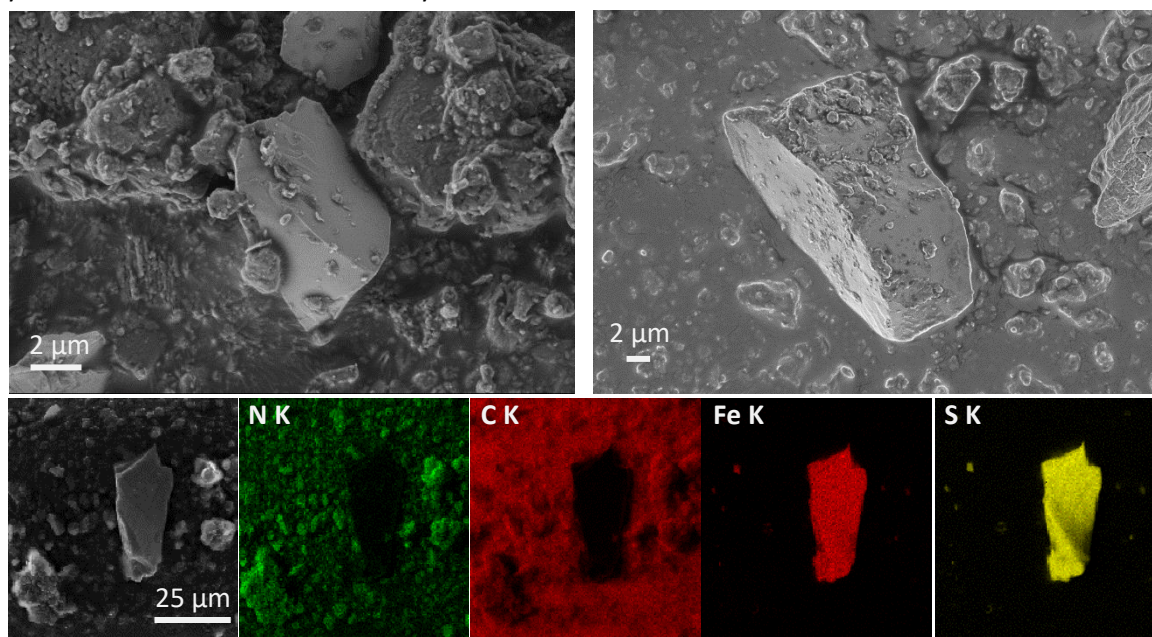
Figure 2 SEM images of a composite of CN and pyrite (5 wt.%), clearly showing the distribution of singular FeS$_2$ particles over CN (top) and EDX maps of a section containing a pyrite particle (bottom).

The composites exhibit essentially all the same band gap, which is an indication that the major contribution to the light absorption is given by CN. This is expected, since its concentration is much higher than that of FeS$_2$. Therefore, only changes in the absorption behavior of CN are evaluated from the spectra. The band gap of the composites is slightly increased but very comparable to V$_N$-CN with a change from 2.70 eV to 2.78 eV (Figure 3b). The UV absorption of the composites is increased compared to V$_N$-CN. Both effects hint at a change in the electronic structure and availability of electrons in the π-system. The color change and increased absorption of visible light upon addition of FeS$_2$ is reflected by diffuse absorption at higher wavelengths, visible in an offset of the baseline (Figure S5, Supporting Information). The effect of band gap widening is especially pronounced for the composites with a FeS$_2$ ratio of 2.5 to 10 wt.% which might indicate optimal charge separation at medium FeS$_2$ loading. All band gaps derived from the Kubelka-Munk and Tauc plots are summarized in Table S3 (Supporting Information).

DRIFT spectra were recorded to further elucidate possible structure changes upon composite formation (Figure 3c,d). Comparable DRIFT spectra of CN and V$_N$-CN were recorded, where the broad signal between 3000 and 3600 cm^{-1} can be assigned to O-H and N-H stretching vibrations, underlining the presence of free amino groups that in turn indicate only partial polymerization. The sharp peaks between 1700 and 1200 cm^{-1} belong to stretching modes of C=N and C–N in the heterocycles, as well as bridging units, and the band at ≈808 cm^{-1} can be assigned to the breathing mode of the *s*-triazine units.[27,72,73] Additionally, a band at 2150 cm^{-1} could be observed, that is ascribed to the presence of cyano groups, that appear to be present in CN and V$_N$-CN as well as in the composites to varying extent.[20,27,73] KOH treatment increases the amount of cyano groups, as well as -OH and/ or -NH$_x$ groups. Additionally, the signals arising from stretching vibrations in the heptazine units are of slightly lower intensity for the defective CN, (relative to the signal at 1720 cm^{-1}), as is the one for deformation

vibrations at 808 cm^{-1} (Figure S6, Supporting Information). This is an indication of structural damage inflicted on the heptazine framework, as would be expected by the formation of defects.
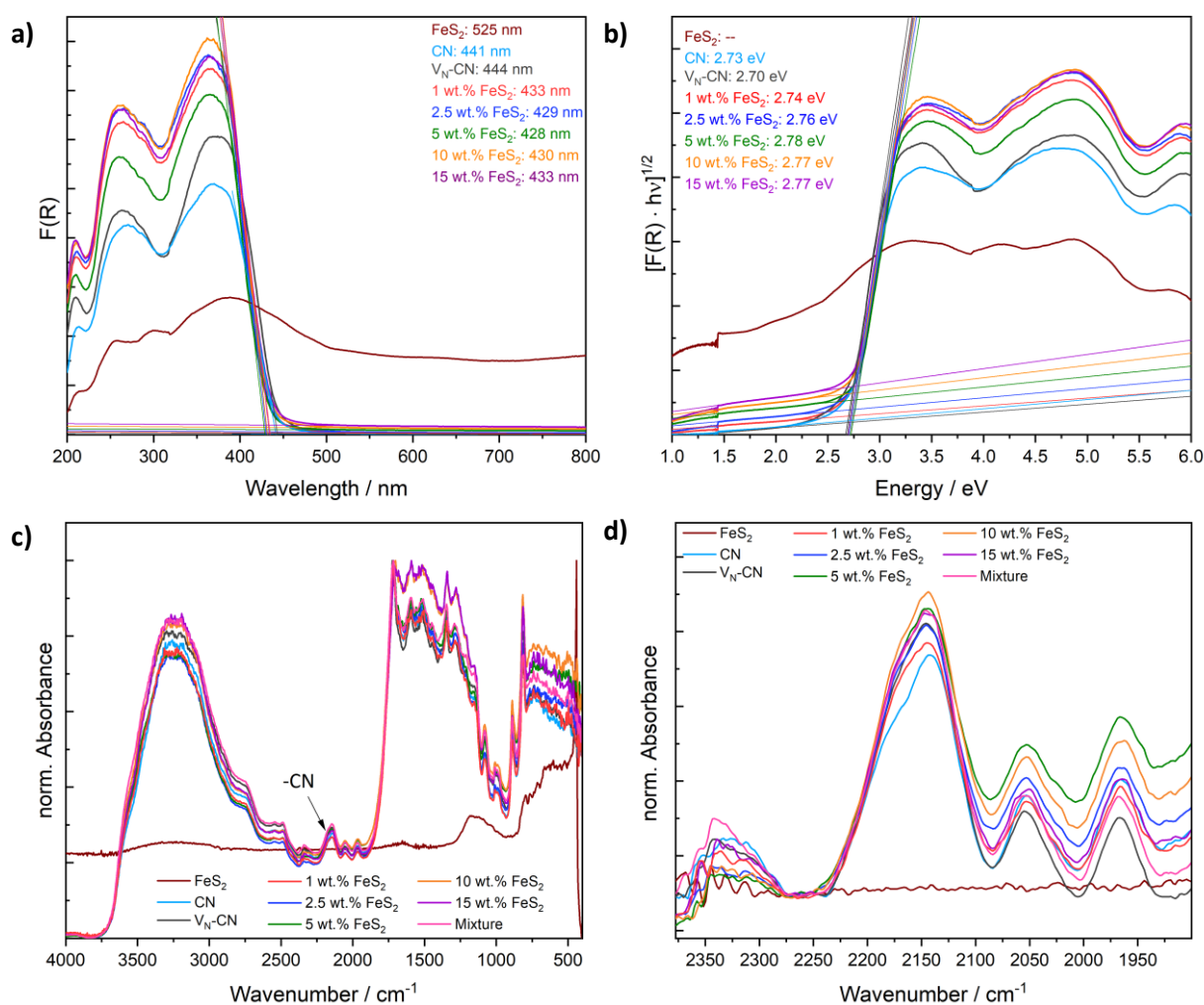
Figure 3 Kubelka-Munk (a) and corresponding indirect Tauc plot (b) for the composites. DRIFT spectra of the composites of FeS$_2$ and V$_N$-CN (c) and a magnified excerpt for the cyano group vibration (d).

The spectra of the composites are fairly similar to that of V$_N$-CN, indicating retention of the structure. An increased absorbance of the vibration of the heptazine units relative to that at 1720 cm^{-1} was observed for the composites with 10 and 15% FeS$_2$ in the normalized spectra – an opposite effect to that caused by the KOH treatment. The signals for heterocycle-vibrations at higher wavenumbers (closer to 1700 cm^{-1}) stem from C=N vibrations, while those at lower wavenumbers (closer to 1100 cm^{-1}) arise from C-N vibrations.[74] Therefore, mainly C=N vibrations appear to be affected by the addition of FeS$_2$. We additionally observe a slight shift of the vibrations for the heptazine unit towards lower wavenumbers, that hints at minor changes in the vibration energy of the entire heptazine framework (Figure S6, Supporting Information).

To further investigate the structural evolutions upon KOH etching and composite formation, XPS measurements were conducted on bulk CN, V$_N$-CN and a composite containing 5 wt.% of FeS$_2$. Survey scans show the expected signals for carbon, nitrogen and low amounts of oxygen in several spots (Figure S7, Supporting Information). The latter is mainly due to adventitious carbon at the surface and not OH-groups in the defective CN, since oxygen was also observed in several spots on bulk CN. C/N ratios for bulk CN, and V$_N$-CN, are 0.62 and 0.71, respectively, after correction for adventitious carbon,

with slight deviations depending on the measured spot (Table S4, Supporting Information). This is in good agreement to the C/N ratio derived from XPS analysis in literature and with the expected ratio for melon.[75,73] The increased carbon ratio in V_N-CN might indicate the introduction of nitrogen vacancies. The C/N ratio in the composite is with 0.71 identical to that of V_N-CN, underlining that the structure remains intact during composite formation.

Generally, KOH treatment on bulk CN is expected to lead to partial hydrolysis of the structure. Yu *et al.* proposed a deprotonation of an apex amine group, during thermal polymerization in the presence of KOH which led to a breaking of the topmost cycle of the heptazine unit and cyano group formation. The overall amount of amino groups is retained here.[73] The reaction conditions notably differ from those employed in this work, but similar structural changes, specifically the introduction of cyano groups in addition to possible vacancy formation, are expected. Nitrogen vacancies are generally believed to be introduced at C-N=C sites.[28] These kinds of possible defects are mainly considered in the following.

Two main peaks are observed in the C 1*s* spectra of CN, corresponding to adventitious carbon at 284.8 eV and N-C=N species in the aromatic system at 288.2 eV (**Figure 4**). The other peak at 281.6 eV can be assigned to carbon adjacent to amino groups.[27,72] Carbon atoms bound to cyano groups are expected to have a similar – though slightly higher – binding energy, that will overlap with this peak.[64,73] A minor shift from 286.1 eV to 286.2 eV is visible in the spectrum for V_N-CN, hinting at an increase in the amount of cyano groups, as observed in the DRIFT spectra. This is further supported by changes in the ratios of the respective signal to that of C-C and N-C=N. Another effect is the observation of a new π-π* satellite at 295.3 eV in case of V_N-CN and a growth in the intensity of the π-π* satellite at ≈293 eV, indicating the presence of larger numbers of free electrons in the vacancy rich system, or more favorable excitation of these. This is in good agreement to the observations from UV spectroscopy and to literature.[28,76] Furthermore, a reduction of the asymmetry of the peak at 288.2 eV upon KOH-treatment indicates damage inflicted on the aromatic system, which is in good agreement with the assumed breaking of some heptazine units. The formation of a composite of V_N-CN and FeS$_2$ results in a comparable C 1*s* XP spectrum only that the signals of carbon in both the -N-C=N and in the cyano group shift towards higher binding energy (Figure 4 and **Table 1**). This might indicate electron extraction from the entire heptazine framework, resulting in partial oxidation.

Four peaks are identified in the N 1*s* spectra for bulk CN at approx. 398.6 eV, 399.2 eV, 401.4 eV and ≈404 eV, in good agreement to the literature (Figure 4).[27,28,72,73] Correlation of the signals with corresponding nitrogen species is challenging, since peak assignment in the literature is ambiguous.[64] The most prominent peak at 398.6 eV in the spectra for bulk CN, and V_N-CN both can be assigned to -C-N=C species in the heptazine units (marked as N-(C)$_2$ in the following), and a small peak at 404.9 eV corresponds to a π-π* satellite. The signals between 401 eV and 399 eV can be attributed to amino groups and to the nitrogen atom in the middle of a heptazine unit (N-(C)$_3$), although the exact assignment of the signals to the two nitrogen species is discussed controversially.[28,64,72,75] Additionally, the signal for amino nitrogen should further be fitted by two, since the structure is not ideally graphitic, but closer to that of parallel melon chains, which results in the presence of both -NH and –NH$_2$ groups, of which the primary amino group is expected at lower binding energy (Figure 4).[62,64] Cyano groups give rise to a signal at ≈400.1 eV, which is indistinguishable from either the signal for the amino groups, or that of N-(C)$_3$.[64]
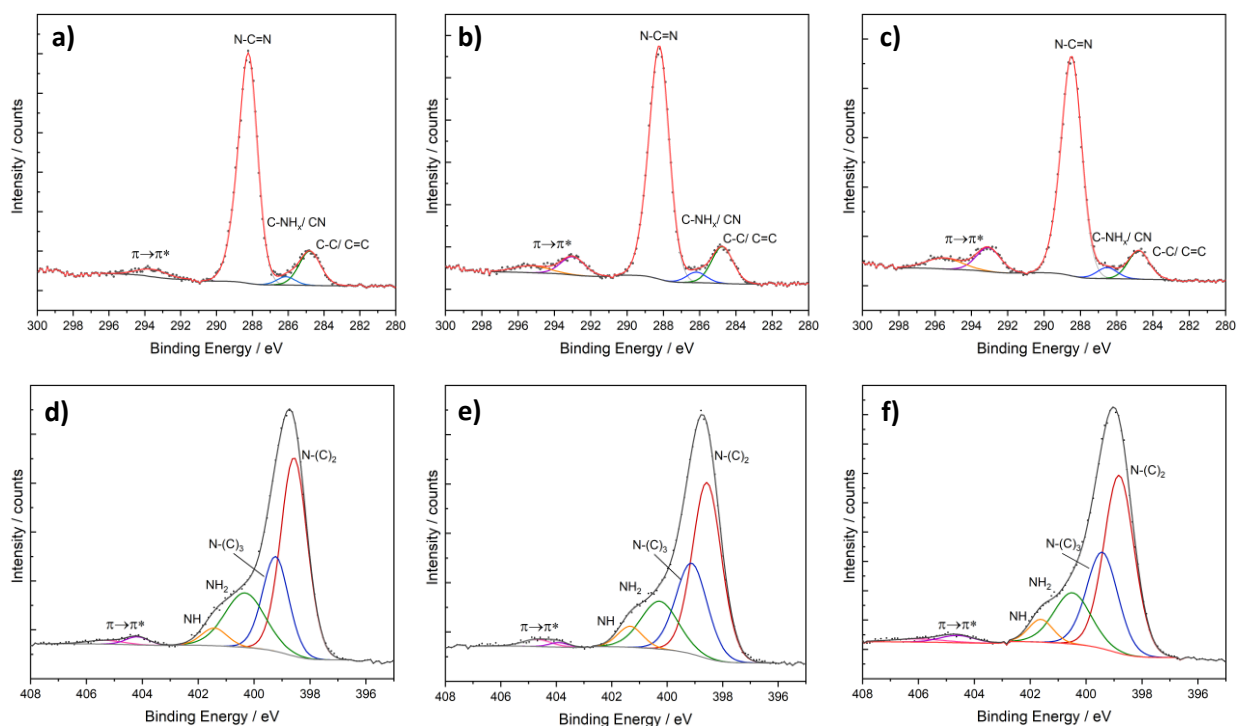
Figure 4 C 1s spectra for a) bulk CN, b) V_N-CN, and c) the composite with 5 wt.% FeS$_2$. Possible fitting of the N 1s spectra for d) bulk CN, e) V_N-CN, and f) the composite containing 5 wt.% of FeS$_2$.

Generally, the nature of the N 1s spectra allows for the possibility of various fits that give good results mathematically but are meaningless in a chemical and physical sense, due to a large number of independent fitting parameters. This is demonstrated in Figure S8, Supporting Information. If we assume that the structure of CN obtained *via* thermal polymerization of melamine lies in between the model of parallel melon chains and of fully condensed sheets, the amount of NH should be smallest, compared to the other nitrogen species.[64] This expectation supports an assignment of the signal at 401.5 eV to NH instead of N-(C)$_3$. Considering, that the signals for primary and secondary amines are likely to be adjacent, we follow assignment of the nitrogen species as: N-(C)$_2$ at 398.7 eV, N-(C)$_3$ at 399.5 eV, NH$_2$ at 400.5 and NH at 401.5 eV, although we stress that a reverse assignment, as suggested in some XPS studies on pristine CN also has its merits.[64,75] To allow for comparison of the spectra for V_N-CN and the composites with that for bulk CN, we therefore fitted the spectra using several constraints based on structural relationships (Figure S9 and Figure S10, Supporting Information). Further information about the fitting process is given in the Supporting Information.

The binding energies and atomic ratios for both the C 1s and the N 1s spectra with the most reasonable fitting result are summarized in Table 1.

In order to still derive meaningful insights into structural changes from the N 1s spectra, despite the variable fitting, we decided on normalization of the spectra (Figure S11, Supporting Information). Two things become immediately obvious. One is a shift of the main peak in the N 1s spectra from 398.7 to 399.0 eV upon composite formation, indicating an increase in the binding energy of N-(C)$_2$ in the heptazine units, as discussed above. Additionally, the 'shoulder' at ≈401 eV is pronounced less sharply, indicating larger amounts of nitrogen species at medium binding energy. The same shift towards higher binding energy is observed in the C 1s spectra, together with an increased intensity of the $\pi \rightarrow \pi^*$-satellite. The lower amount of cyano groups in the untreated CN is also shown by the lower intensity

at 286 eV compared to both V_N-CN and the composite. These observations confirm the main conclusions drawn from the N 1*s* spectra above, without relying on arbitrary fitting results.

Table 1 Binding energy and atomic ratios for different species in the N 1*s* and C 1*s* spectra.

		-NH	-NH$_2$	N-(C)$_3$	N-(C)$_2$	$\pi \rightarrow \pi^*$	N-(C)$_2$/N-(C)$_3$	N-(C)$_2$/NH
CN	Binding energy [eV]	401.4	400.3	399.2	398.6	404.1, 405.3		
	Amount [at.%]	4.4	21.1	23.8	50.8		2.13	11.55
V$_N$-CN	Binding energy [eV]	401.3	400.3	399.1	398.6	404.4		
	Amount [at.%]	5.1	17.5	27.8	49.7		1.79	9.75
5 wt.% FeS$_2$	Binding energy [eV]	401.6	400.5	399.4	398.8	404.7		
	Amount [at.%]	5.1	17.5	27.8	49.7		1.79	9.75

		C-C	N-C=N	C-NH$_x$; CN	$\pi \rightarrow \pi^*$	$\pi \rightarrow \pi^*$	CN/N-C=N	CN/C-C
CN	Binding energy [eV]	284.8	288.2	286.1				
	Amount [at.%]	14.3	82.7	3.0	293.6			0.21
V$_N$-CN	Binding energy [eV]	284.8	288.2	286.2	293.0	295.2		
	Amount [at.%]	14.0	82.3	3.7			0.045	0.26
5 wt.% FeS$_2$	Binding energy [eV]	284.8	288.5	286.5	293.1	295.6		
	Amount [at.%]	11.3	84.4	4.3			0.051	0.38

Concluding these considerations, XPS analysis supports the introduction of both cyano groups and vacancies upon KOH treatment. Furthermore, it elucidates the changes in the electronic structure upon addition of FeS$_2$ to the system, indicating partial electron extraction from the V$_N$-CN matrix. Hydrolysis and introduction of OH-groups similar to what has been observed for hydrothermal treatment with NaOH, involving the breaking of NH-bridging bonds and introduction of OH-groups cannot be totally excluded, but is not likely to have a major influence, since oxygen contents are similar in both CN and V$_N$-CN.[65]

TGA-MS measurements were conducted on the composite containing 5 wt.% of FeS$_2$ and on both of the constituents, FeS$_2$ and V$_N$-CN, to confirm that no structural changes occur during synthesis while thermal treatment for 2 h at 200 °C (Figure S12, Supporting Information). FeS$_2$ was stable up until about 400 °C, above which a gradual extraction of sulfur in the form of SO$_2$ was observed. Notably, the lack of an increase in the mass indicates an absence of significant oxidation during the initial heating phase. For V$_N$-CN, a major mass loss is observed starting at 570 °C, which is completed at around 720 °C. During the heating in synthetic air, NO, H$_2$O and CO$_2$ were found to be the main combustion products up until around 650 °C, after which an increase in the evolution of CO and NO$_2$ was observed (Figure S13, Supporting Information). The two steps of the combustion process are also apparent in the DSC curves (Figure S12, Supporting Information). The TGA curves for the composite show many similarities compared to that of CN. However, both the mass loss curves and the ion currents for the evolving gasses are shifted by almost 100 °C to lower temperatures, signifying that the presence of FeS$_2$ boosts the decomposition, likely acting as a catalyst and activating the heptazine units. Nevertheless, the observed thermal decomposition only occurs at temperatures far above the 200 °C, thus precluding decomposition during the composite formation.

The interaction with FeS_2 mainly involves the nitrogen in V_N-CN, as shown in the much decreased ion current for NO_2 during the second step of the combustion process, indicating, that more nitrogen is extracted from the structure in the beginning. This is confirmed by the DSC curves, where the sharp peak at the end of the combustion process is much less pronounced (at 586 and 712 °C, respectively). While the ion currents for all gaseous combustion products in V_N-CN show one signal with a sharp peak current, those of the composites appear as double peaks. Perhaps they correspond to the combustion of areas in close proximity to FeS_2 and to areas for which the influence of FeS_2 is less. Since the ion currents for both NO and NO_2 are significantly lowered compared to that in CN (also in relation to the ion current for CO_2, so this observation is not only due to the lower content of CN), new nitrogen containing reaction products might be formed, that were not detected.

8.1.2.2 Photocatalytic NH_3 Generation

Photocatalysis was performed in a semi-batch setup using 20 vol.% of methanol as a hole scavenger. The reaction was investigated for V_N-CN and composites therewith containing different amounts of FeS_2. After the irradiation period of 7 h, the solution was directly filtered and analyzed for NH_3 by the salicylate test. Additionally, the concentration of NH_3 in an acid trap located behind the reactor was evaluated. The calibration curves can be found in Figure S14 (Supporting Information). The quantification of NH_3 was performed after stable color development, which was only obtained after several hours in the dark (Figure S15, Supporting Information).

The decoration of V_N-CN with FeS_2 can significantly enhance the NH_3 yield by a factor of 1.63 from 494 µg L^{-1} to 801 µg L^{-1}, which equals to 3.9 and 6.4 µmol h^{-1} for 200 mg photocatalyst, respectively. Compared to the untreated CN the activity is enhanced by ≈400 %, clearly showing that a combination of defect introduction and interaction with FeS_2 is necessary for efficient ammonia generation. The ammonia yield is comparable for a FeS_2 content between 1 and 5 wt.% (**Figure 5** and Figure S17, Supporting Information), although decreasing and dropping significantly for FeS_2 ratios above 10 wt.%. Already low amounts of FeS_2 are sufficient for the activation and further loadings decrease the activity due to shadowing effects and a reduced ratio of the active photocatalyst, because FeS_2 itself is inactive in the N_2 reduction, solely yielding H_2 under illumination (Figure S17 and S21, Supporting Information).

Several control measurements were conducted, to elucidate the source of nitrogen and the selectivity of the reaction (Figure 5 and Figure S18, Supporting Information). First, a dispersion of a composite photocatalyst in water/ methanol was tested for NH_3 after stirring in the dark. No NH_3 was detected in this case. Secondly, a dispersion of V_N-CN was filtered and tested for NH_3 to exclude amino groups in the photocatalyst interfering with the test. No NH_3 was observed in both control measurements. We also tested a physical mixture of FeS_2 (5 wt.%) and V_N-CN for photocatalytic NRR ("Mix 5 wt.%"), without performing the grinding and subsequent calcination steps that establish an interfacial contact between the two constituents. The activity was significantly lower than that of V_N-CN itself, due to the lower amount of active photocatalyst and lack of interaction between FeS_2 and V_N-CN (Figure 5). This clearly indicates an enhancement effect in ammonia generation based on a direct contact between FeS_2 and V_N-CN.

Additionally, the photocatalytic reaction for the composite containing 5 wt.% of FeS_2 was repeated in an argon atmosphere ("5 wt.% - Ar"). A similar activity compared to the reaction in N_2 atmosphere was observed, strongly suggesting that the ammonia generation is not based on N_2 feed gas reduction, but stems from the V_N-CN framework instead (Figure 5).

Literature for NRR over vacancy-rich and cyano-rich CN likewise propose a N_2 conversion pathway following a Mars-van-Krevelen mechanism, therefore this observation is not surprising,[28] however significant NH_3 yields for CN in an argon atmosphere, like we show, were not reported. Therefore, the performance of careful blind experiments in combination with detailed material characterization before and after photocatalysis is of high necessity.
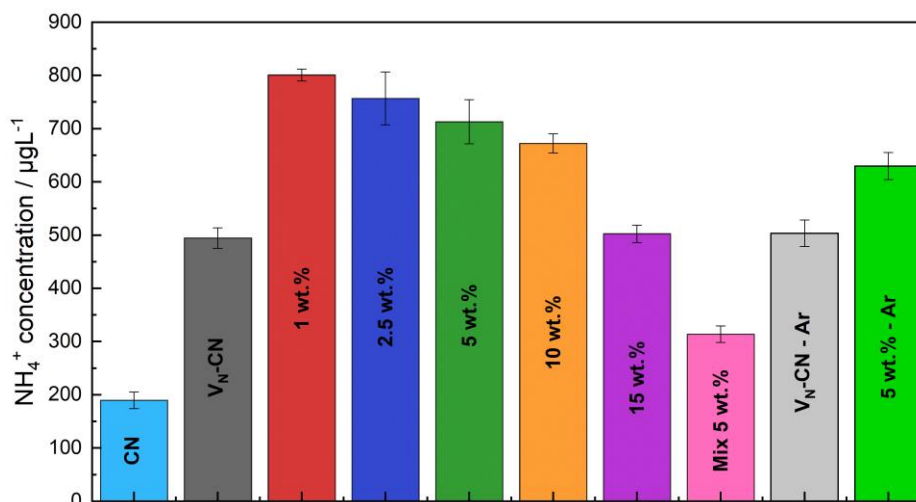
Figure 5. Ammonia concentration after 7 h obtained for composites with a different FeS_2 ratio. The reaction solution was analyzed multiple times for NH_3 and the results were averaged. Additionally, determined concentrations for reference measurement in Ar atmosphere and a physical mixture of FeS_2 and V_N-CN (Mix 5 wt.%) are shown.

The reaction solutions were additionally tested for nitrogen-containing by-products such as hydrazine and NO_3^-. No hydrazine and only trace amounts of NO_3^- around the lower detection limit were found for both V_N-CN, and the composites (Figure S19 and S20, Supporting Information), when the photocatalytic experiment was performed in N_2, but not in an Ar atmosphere. The main side product was H_2, with a production rate of around 200 µmol h^{-1}. The rate was similar for all composites, with a slightly increased H_2 formation rate for higher amounts of FeS_2 in the sample (Figure S21, Supporting Information). FeS_2 itself showed a remarkably high H_2 production rate of 370 µmol h^{-1}. Thus, both the activity improvement for NH_3 generation and the selectivity are highest for lower FeS_2 loadings in the composites.

A gradual decrease in the H_2 evolution rate over time is in good agreement with a possible Mars-van-Krevelen-type of structural changes during the illumination. When the photocatalytic experiment was performed in an argon atmosphere, similar H_2 evolution rates were observed as compared to the results in a N_2 atmosphere (Figure S21, Supporting Information).

In order to elucidate the formation of methanol oxidation products, UV absorption spectra of the reaction solutions were recorded after the photocatalytic experiments. Critical evaluation of the conditions and evolving organic oxidation products is crucial, since the accuracy of the salicylate test can be influenced by a variety of parameters that are too often not considered. There is a correlation between the amount of NH_3 produced and the amount of UV light absorbance by the filtered reaction solutions at 205 to 220 nm (**Figure 6**). This absorbance can mainly be attributed to formic acid that is formed alongside NH_3 (Figure S22, Supporting Information). This could have an effect on the salicylate test, resulting in a significant underestimation of the actual NH_3 concentration.[77] For this reason a 12 % hypochlorite solution was used, which negates the effect of varying acid generation. Additionally, a reference sample of known ammonia concentration was always measured together with the reaction

solution to avoid errors based on the testing solutions. All concentrations given in the paper are averaged between several quantification measurements with the salicylate test.
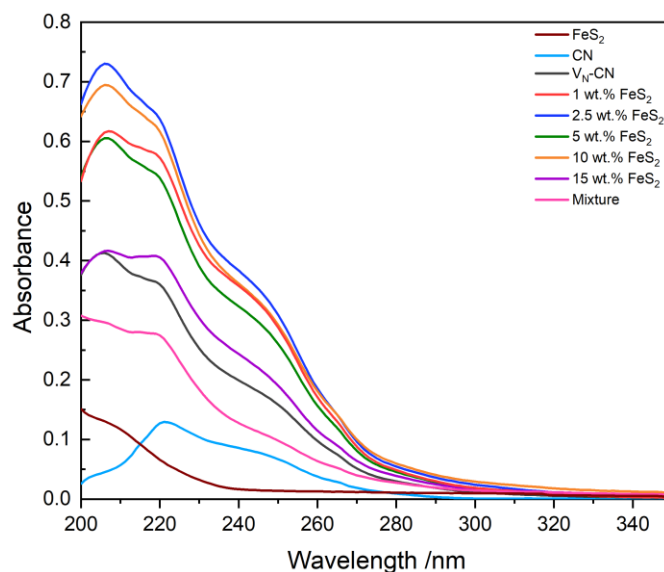
Figure 6 UV spectroscopy for the filtered reaction solutions after the NRR experiments.

Additionally, the spectra clearly show the presence of other ions that absorb UV-light, which is even more obvious in the derivation spectra (Figure S23, Supporting Information). The overlap of multiple features renders an accurate identification nearly impossible, however. Nitrate and nitrite absorb UV light at 203 and at 210 nm, respectively.[78] No clear absorption feature could be identified for nitrite, while a very small contribution of nitrate might be discernible for V_N-CN and composites thereof, which is in good agreement to the results from ion chromatography. The absorption peak at 220 nm probably stems from π-π* transitions, possibly in carbonyl groups of amides or very short conjugated systems.[79] The broad absorbance from 230 nm towards higher wavelengths could in part be caused by very fine FeS$_2$ particles, since a filtered FeS$_2$ dispersion gives rise to a noticeable absorbance signal up to 450 nm (Figure S22, Supporting Information).

To exclude significant errors in the determined ammonia concentration due to the large amounts of organic byproducts, the solutions were measured with ion chromatography and the values compared to those from the colorimetric determination (**Table 2**). The general trend is the same as observed with the salicylate tests, but the determined ammonia concentrations are slightly higher. This is to be expected, since the significant amounts of methanol and formed formic acid largely affect the colorimetric test, resulting in an underestimation of the actual ammonia concentration, and even with careful optimization of the testing procedure, some influence of the organic substances cannot be avoided. A graphic depiction of the concentrations determined with ion chromatography, as well as an exemplary chromatographic trace can be found in Figure S24 (Supporting Information).

Since hardly any difference in the NH$_3$ yield in argon and N$_2$ atmosphere was observed after 7 h for the most active sample, we devised a longtime measurement. A dispersion of the composite containing 5 wt.% FeS$_2$ was first illuminated for 14 h in either N$_2$ or argon atmosphere. Every two hours, a sample was taken and analyzed for NH$_3$. After 14 h, the lamp was switched off and the solution was stirred in the dark for 6 h under continuous gas flow of the respective gas, before illumination was continued for another 6 h (Figure S25, Supporting Information). During the first irradiation period, the generated

amount of NH$_3$ increased almost linearly with a rate of ≈82 µg h^{-1} in N$_2$ and 90 µg h^{-1} in argon atmosphere, respectively.

Table 2 Ammonia concentrations determined with the salicylate test and with ion chromatography.

Sample	Ammonia concentration determined with the salicylate test [µg L^{-1}]	Ammonia concentration determined with ion chromatography [µg L^{-1}]
FeS$_2$	-	6.8 ± 5.7
CN	189.4 ± 15.5	308.7 ± 8.0
V$_N$-CN	494.2 ± 19.1	832.5 ± 28.4
1 wt.% FeS$_2$	800.7 ± 11.3	1188.3 ± 1.4
2.5 wt.% FeS$_2$	756.7 ± 49.6	1173.6 ± 30.5
5 wt.% FeS$_2$	712.7 ± 41.4	1138.1 ± 17.4
10 wt.% FeS$_2$	672.2 ± 18.0	1086.5 ± 11.3
15 wt.% FeS$_2$	502.3 ± 16.5	812.0 ± 6.2
Mix	313.5 ± 15.5	508.7 ± 14.3
V$_N$-CN -Ar	503.4 ± 24.8	775.5 ± 2.4
5 wt.% FeS$_2$-Ar	629.6 ± 25.5	948.3 ± 39.0

Once the lamp was switched off, the measured concentration slightly decreased in both atmospheres, likely due to NH$_3$ carried out of the reactor by the gas flow. After continuing the light irradiation, the NH$_3$ generation was increased again with about the same rate, as before the period in the dark. Afterwards, the determined concentrations seem to level out. This effect is likely caused by a combination of slow degradation of the structure and accumulation of oxidation products. A similar effect was observed for the H$_2$ evolution rate, indicating that the observed effect is not solely caused by the accumulation of formic acid (Figure S25b, Supporting Information).

In addition to the NH$_3$ concentration reported in the reaction solution, NH$_3$ was detected in the acid trap but not included in the concentrations given here. The amounts of NH$_3$ were maximum around 6.5 µg and 3.5 µg total for the experiments in an argon and a nitrogen atmosphere, respectively (Table S8, Supporting Information). Still, the use of an acid trap is sensible. The pH of a dispersion of 20 mg of V$_N$-CN in 20 mL of H$_2$O was ≈9.5. Thus, both NH$_4^+$ and NH$_3$ species can occur in significant amounts. For CN the pH is with ≈8 closer to neutral, perhaps due to higher amount of imine or amine groups in V$_N$-CN. A slightly alkaline pH for CN is expected, due to the large number of amino groups.

8.1.2.3 Post-photocatalytic characterization

Both V$_N$-CN and the composites with FeS$_2$ were thoroughly characterized after the photocatalytic experiments, in order to evaluate the stability and to gain further insights into the ammonia generation pathway. Post-photocatalytic XRD patterns still show the same reflections for phase-pure CN and FeS$_2$ (Figure S26, Supporting Information). The intensity for the FeS$_2$ reflections is significantly decreased after the NRR. This effect could be a result of a loss of interfacial contact between FeS$_2$ and CN as verified by dispersing a composite in water/methanol mixtures and subsequently regaining the material *via* centrifugation (Figure S27, Supporting Information). FeS$_2$ is known for its flotation tendency in mineral separation, due to its relative hydrophobicity.[80] Additionally, we tested the

stability of FeS_2 during both the formation of the composite (with annealing at 200°C) and storage of the sample in air. No changes in the crystal structure of FeS_2 were observed (Figure S27, Supporting Information).

UV/vis spectra show a significantly increased absorbance of UV light and a decrease of the band gap (Figure S28, Supporting Information). Both V_N- CN and the composites showed a pronounced darkening after the NRR that decreased again after storage in air (Figure S29, Supporting Information). The effect of increased UV light absorption is less obvious for the composite containing 15 wt.% compared to the other composites, for which the activity was also lowest. All other composites that exhibited a similar activity, show a similar increase in UV absorption, which likely correlates to higher degrees of structural change. The increased UV absorption is less pronounced for V_N-CN in agreement with the lower activity. The band gap decreases very slightly by 0.03 eV for V_N-CN. For the composite containing 5 wt.%, the decrease is most drastic and the band gap is experiencing a change by 0.07 eV from 2.78 to 2.71 eV. The red shift of the absorption might be caused by defect formation and distortion of the structure.[81]

DRIFT spectra of the composites after the NRR experiments show a marked decrease in the vibrations for the heptazine units (Figure S30 and S31, Supporting Information), especially in relation to the vibration at 1720 cm^{-1}, that falls into the range for C=N vibrations. This vibration is further shifted back to slightly higher wavenumbers. A decrease in the relative intensity of the 808 cm^{-1} vibration agrees with this observation, indicating structural damage to the heptazine framework. Both effects were also observed to a lesser extent upon introduction of vacancies and cyano groups upon KOH treatment and thus confirm further breakdown of the heptazine units during photocatalysis. Additionally, a closer look at the vibration at 2147 cm^{-1} reveals a decrease in the intensity, supporting the assumption that cyano groups are consumed during the photocatalytic experiment (Figure S32, Supporting Information). The effect is even more increased for long-term experiments, highlighting the further degradation of cyano groups with prolonged illumination times (Figure S32, Supporting Information).

XP spectra of the composite containing 5 wt.% of FeS_2 after the photocatalytic reaction show a slight shift for the carbon species adjacent to cyano-/ amino-nitrogen and the N-C=N peak towards lower binding energies (Figure S33, Supporting Information). The intensity for both peaks in the C 1s spectra corresponding to the V_N-CN structure decreases markedly in relation to that of C-C, further indicating structural changes, that do not only extend to nitrogen, but are further inflicted on carbon in the structure. The ratio might also partly be influenced by adsorbed organic residues from the sacrificial agent. Additionally, the intensity for the satellite peaks is decreased, supporting damage to the aromatic system. The calculated C/N ratio from the survey scan was 0.88, without correction for adventitious carbon, because the amount of C-C or C=C bonds possibly present in the structure after partial extraction of nitrogen is unknown. Thus the C/N ratio is increased compared to 0.80 for the same composite before the photocatalytic experiment. This is a strong indication of nitrogen extraction from the V_N-CN matrix.

Sample composition was additionally evaluated by elemental analysis before and after photocatalytic experiments (Figure S34, Supporting Information). The amount of sulfur and thus probably also FeS_2 was noticeably decreased after the photocatalytic experiment for all composites. This is likely an effect of the imperfect interfacial contact and washing of the sample, as has already been observed in the XRD patterns.

For a more detailed comparison, the C/N ratio was calculated for the composite samples before and after the photocatalytic reaction. For all composites, the C/N ratio was about 0.555, which significantly differs from the compositional value of 0.75 and indicates incomplete polymerization and the existence of many free amino groups. The value is in good agreement to the EDX measurements, though. No significant differences of the C/N ratio were observed for different FeS_2 loadings. For all composites, the C/N ratio was visibly increased after the photocatalytic reaction, supporting the extraction of nitrogen from the structure (Figure S34, Supporting Information). Compared to the C/N ratios obtained from XPS measurements, the nitrogen content in the bulk is significantly higher, due to adsorbed carbon impurities and possibly nitrogen deficiency at the surface. Elemental analysis additionally shows an increase in the C/N ratio after the KOH treatment, supporting the generation of nitrogen vacancies (Figure S34c, Supporting Information). Based on the difference in the C/N ratio of 0.005 for V_N-CN, an extracted nitrogen fraction of 0.94% can be estimated. For further information about the calculations see the Supporting Information.

8.1.2.4 Charge Carrier Dynamics

Due to the large variety of defects that can potentially be present in V_N-CN, the electronic structure is rather complex and should be studied in detail, in order to get explanations for the different results in photocatalytic experiments. To investigate the charge carrier dynamics, transient absorption spectroscopy (TAS) in diffuse reflectance geometry was employed. In **Figure 7** the ns-TAS measurements of a composite of V_N-CN and 5 wt.% of FeS_2 in an argon atmosphere are presented. The positive absorption feature between 650 nm and 900 nm can be assigned to photogenerated electrons in V_N-CN.[81-84] The same signal is generally apparent in the measurement of the composite, but an increase of the relative absorption intensity in the range between 650 nm and 750 nm is noticeable, in comparison to the main signal between 750 and 900 nm. This might indicate a change in the electronic structure upon composite formation with FeS_2 and an increased relative amount of photogenerated electrons in an additional excited state, which possibly corresponds to an intraband gap state caused by defects. For a better comparison the main signal of the photogenerated electrons in both materials was analyzed regarding the lifetime of these electrons. The lifetimes monitored at 800 nm for both V_N-CN and the composite are comparable and in the order of ns (Figure S35, Supporting Information). The signal is best fitted with two different lifetimes, that are 3.4 ns and 59.0 ns for V_N-CN and 4.3 ns and 31.7 ns for the composite, respectively.

The shorter lifetime of the electrons is comparable for both materials and could be explained with the fast recombination of charge carriers in the materials. Electrons with fast recombination rates, such as those corresponding to lifetimes of 3-4 ns, can generally not participate in photocatalytic reactions, as they do not reach the surface.[85] The main pathway for exciton separation is between sheets along the stacking direction, for which a hopping rate in the order of 10^9 s^{-1} is assumed, preventing efficient transport to the surface in the short lifetime of only a few nanoseconds.[86] The other lifetime for the composite indicates that the introduction of FeS_2 to the V_N-CN matrix results in the prevention of electron accumulation in deep traps.[81,87]

We additionally used photoluminescence (PL) spectroscopy to gain insights into the radiative energy relaxation levels of the excited photocatalyst. The most dominant PL emission in semiconductors is the band gap emission, where the excited states (charge carriers) recombine and relax to the ground state by emitting radiation. Thus, low PL emission is often an indicator for efficient charge carrier separation

and low recombination rates. CN as a polymeric material with a structure in between that of molecules and solid crystals, generally exhibits a prominent blue fluorescence, that has been shown to be significantly influenced by the introduction of defects.[88,89]
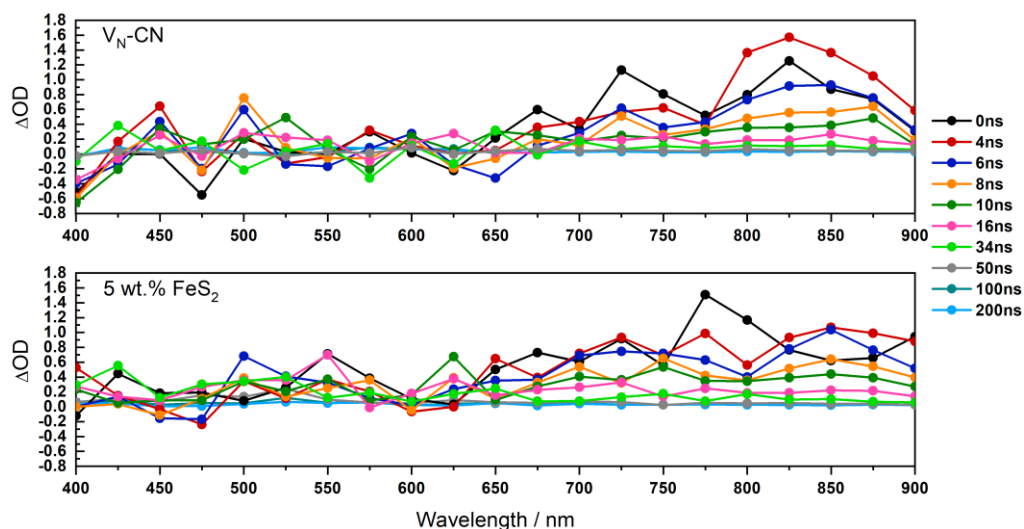
Figure 7 ns-TAS measurements of V_N-CN (top) and the composite containing 5 wt.% of FeS_2 (bottom) in argon. Excitation: 355nm. Connecting lines are only for guiding the eye.

Upon irradiation at wavelengths with a higher energy than that of the band gap, a broad fluorescence signal between 410 and 640 nm is observed for V_N-CN and the composites, with a maximum emission at 470 nm and a slightly less intense emission at 445 nm, as shown in **Figure 8**. Generally, the fluorescence emission of the composites is decreased compared to V_N-CN, indicating better charge separation and thereby reduced recombination. The photoluminescence is shifted to lower wavelengths for the composites, which is in good agreement to the slightly increased band gaps and indicates a decrease in interlayer electronic coupling.[82,90] FeS_2 itself does not show any fluorescence emission.
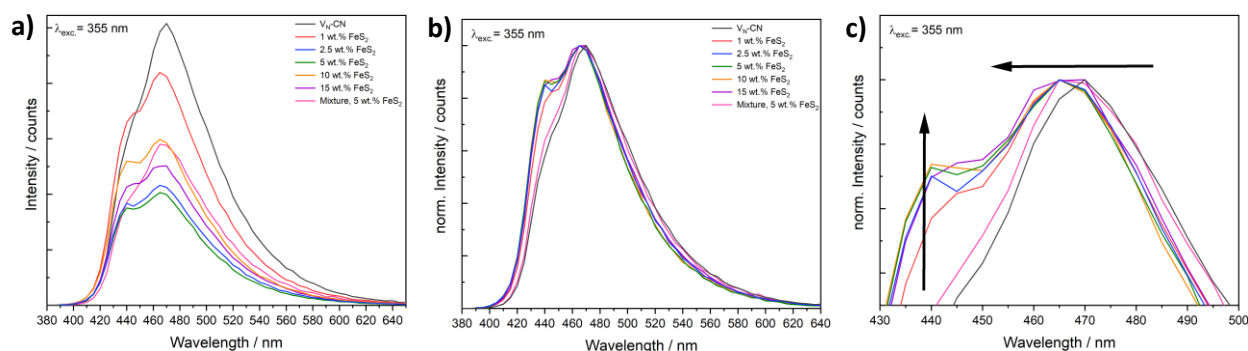
Figure 8 Fluorescence emission spectra for the composites for $\lambda_{exc.}$ = 355 nm (a), normalized emission spectra for $\lambda_{exc.}$ =355 nm (b) and excerpt of the normalized spectra (c).

The intensity for the emission at 445 nm in relation to that at 470 nm is clearly increased for the composites (Figure 8). The emission at 445 nm can be attributed to direct band gap emission, which is in good agreement to the band gap energy determined *via* absorption spectroscopy.[81,91] Emission at 470 nm corresponds to transitions from intra band gap states, likely involving lone electron pairs at N-

(C)$_3$ sites.[92] An additional tail towards higher wavelengths includes contributions from defect emissions, such as transitions from lone pair states of nitrogen atoms in the s-triazine unit, from amino groups, NH-bridging units, or possibly graphitized areas at even higher wavelengths above 500 nm.[88,89] The significantly decreased intensity of lone pair and defect emission in relation to direct band gap emission in the composites, coupled to fluorescence quenching might indicate the inhibition of radiative recombination at defect sites, likely due to interaction of V$_N$-CN with FeS$_2$ involving free electron pairs. Since N-(C)$_3$-sites are also effected, the interaction with iron influences the entire electronic structure of V$_N$-CN, as also observed in DRIFT and XPS measurements. Charge transfer might assist in exciton separation and retard recombination.

The excitation maximum for V$_N$-CN is located at ≈320 nm which corresponds to band gap transitions (Figure S36 and S37, Supporting Information).[92] The ratio of emission intensity at 320 nm excitation to emission intensity at 380 nm excitation in the normalized excitation spectra is significantly decreased for the composites compared to V$_N$-CN, along with a slight red-shift of the entire emission signal. The group of Gan *et al*. ascribes excitation at around 380 nm to transitions from the valence band to lone pairs of –N-(C)$_3$ species, that appears to be more favored for the composites.[92] The absolute emission intensity is decreased at higher wavelengths, since the light absorption is diminished (Figure S37, Supporting Information).

The lifetime of an emission is regarded as a more reliable parameter for judging charge recombination rates. The lifetime was measured for both detection at 445 and 470 nm (Figure S38, Supporting Information). The decay can be fitted with three exponential functions, as is usually done in literature, as well.[14,88] The fluorescence lifetimes are increased again, for the composites, compared to V$_N$-CN (Table S10, Supporting Information).

The shortest lifetime (τ_3 for emission at 445 nm/τ_3' for emission at 470 nm) for both the composites and V$_N$-CN, respectively, can be attributed to recombination in the aromatic system.[66] An increase in the second lifetime, τ_2, for the composites compared to defective CN implies improved intraplanar and intrachain charge separation (Figure S39, Supporting Information).[66] This might be due to polarization of the heptazine framework and electron transfer. The greatest difference is observed in the time constants for τ_1, which can be attributed to charge separation between layers (along the π-stacking direction). This is the main pathway for charge separation in carbon nitride.[86] Hence, charge separation in the π system is significantly improved again by FeS$_2$, affecting both the direct band gap emission at 445 nm and the emission of lone pairs of ternary nitrogen species at 470 nm. The lifetimes are fairly similar for all composites. Fluorescence decay is longer at 470 nm compared to at 445 nm for all samples, supporting the assumption of the main emission at 470 nm mainly being caused by recombination at defect sides (involving free electron pairs of nitrogen species).

Table 3 Quantum Yield at 355 nm for the composites containing different amounts of FeS$_2$.

	V$_N$-CN	1 wt.% FeS$_2$	2.5 wt.% FeS$_2$	5 wt.% FeS$_2$	10 wt.% FeS$_2$	15 wt.% FeS$_2$
355 nm	12.0 %	6.6 %	6.7 %	6.1 %	6.2 %	4.3 %

The quantum yield (QY) was determined at an excitation energy of 355 nm, to ensure that the increased fluorescent lifetimes truly correlate with improved charge carrier separation. The QY is

decreased in the composites with increasing FeS$_2$, implying that radiative recombination is indeed reduced in the composites (**Table 3**).

8.1.2.5 Discussion of the Interaction of FeS$_2$ and V$_N$-CN Resulting in Enhancement of Ammonia Generation

Based on the observations for structural changes in V$_N$-CN induced by the presence of FeS$_2$, we propose an activation of the structure of V$_N$-CN by FeS$_2$.
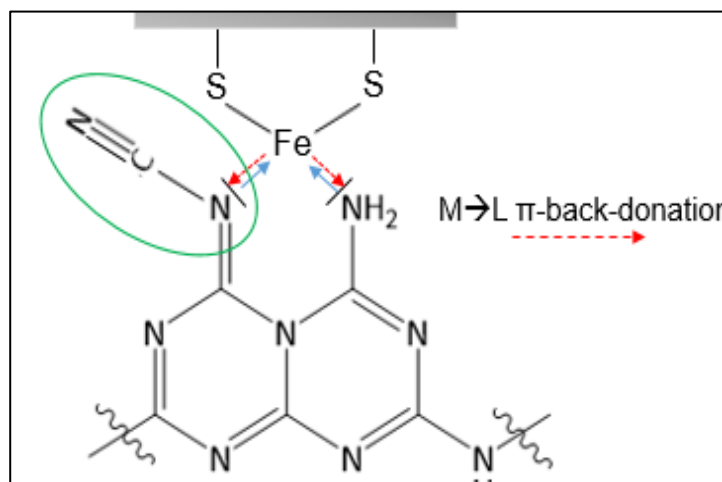
Figure 9 Proposed coordination of nitrogen lone pairs to Fe^{2+} at defect sites and π-back-donation from iron to the nitrogen species, thereby increasing the electron density in the π* orbitals of the aromatic system and activating the =N-CN group.

Since KOH treatment is supposed to introduce defect sites that have two nitrogen species with free electron pairs in the vicinity (imine-type nitrogen in =N-CN units and amino groups),[73] an interaction similar to ligand to metal coordination to Fe^{2+} appears to be feasible, that results in an activation of the CN structure *via* π-back-donation and possibly light induced metal to ligand charge transfer (**Figure 9**).

This model is based on following observations:

1) Increased UV absorbance observed for the composites (more π-π*-transitions) (Figure 3).

2) Band gap widening upon FeS$_2$ addition (Figure 3): possibly due to deformation/ polarization of the structure upon coordination of defects in V$_N$-CN to iron centers due to partial electron transfer (σ-Donor) to FeS$_2$.

3) The shift of both nitrogen and carbon binding energies towards higher values suggests partial oxidation of the structure, thus supporting the σ-donor effect (Figure 4).

4) The increased satellite peaks in the XP spectra suggest higher number of electrons in the π-system, which might be due to π-back-bonding, (Figure 4). Possibly, coordination of the cyano groups and/ or amino groups to Fe^{2+} centers induces a marked electron withdrawing effect and partial charge transfer to iron, reducing the electron delocalization.

5) Fluorescence quenching and decreased QY indicate improved charge transfer (Figure 8 and Table 2).

6) Decreased ratio of emission from lone electron pair states in fluorescence measurements (Figure 8) indicates electronic interaction of defects in V_N-CN with FeS_2.

7) Increased fluorescence lifetime, τ_1, for the composite (Table S10, Supporting Information): electrons in the π-system might be influenced and stabilized by the interaction with iron.

8) An additional signal for photo-generated electrons in the TAS measurements upon composite formation with FeS_2 might arise due to complex interactions of defect states with iron centers, such as light-induced M $\rightarrow$ L-charge transfer (Figure 7).

9) TGA curves show a shift in the decomposition of V_N-CN promoted by FeS_2, indicating structure activation by FeS_2 (Figure S12, Supporting Information).

10) Shift of the vibration energy to lower values for the heptazine units additionally indicate structure activation: signals for C=N vibrations are apparently more influenced by the FeS_2 addition than C-N vibrations, with the relative intensity decreasing (Figure S6, Supporting Information).

11) π-back-donation from Fe-centers to imine bonds are known, as is back-donation and charge transfer with cyano group.[93,94]

12) The oxidation products in the photocatalytic reaction are the same for both, composites and V_N-CN, (Figure 6), suggesting oxidation on V_N-CN.

13) The HER activity is decreased for the composites (Figure S21, Supporting Information), even though FeS_2 is present, indicating that electrons in FeS_2 are used for other redox reactions, such as π-back-bonding and/or re-oxidation of Fe^{3+} to Fe^{2+}.

14) Slightly enhanced ammonia generation was also observed for untreated CN decorated with FeS_2 (Figure S40, Supporting Information) and was expected due to minor defects in CN (cf. DRIFT results). This further underlines the boosting effect in ammonia generation, when FeS_2 and highly defective, KOH-treated CN are present.

15) Interaction of the composite with N_2 is indicated in the TGA-MS measurements, due to coordination to Fe^{2+}. Such an effect could be advantageous for re-incorporation of nitrogen into the structure.

A control experiment in 100 % of methanol yielded comparable ammonia yields in both nitrogen and argon atmosphere, underlining again, that the nitrogen is extracted from the carbon nitride framework and not – at least not completely – replenished. It also highlights, that the degradation is no of an oxidative nature but inherent in the reduction mechanism (Figure S41, Supporting Information)

8.1.3 Conclusion

We have shown that a combination of defect introduction into CN and subsequent composite formation with FeS_2 can significantly improve the amount of ammonia generated in photocatalytic NRR experiments, resulting in four times higher ammonia yields under illumination compared to unmodified CN. The optimal FeS_2 loading was established to be 1 to 5 wt.%. The system only employs inexpensive, earth-abundant and non-toxic materials. However, knowledge about the exact structure of CN and the presence and character of defects proved to be crucial, as they significantly influence the interactions between the two constituents. Charge transfer between FeS_2 and V_N-CN was

established to proceed at the defect sites, resulting in an electronic activation of the structure. Therefore, NH_3 generation was found to occur not photocatalytically from N_2, but rather via a novel activation route of V_N-CN, involving reduction of the =N-CN group adjacent to nitrogen vacancies. A replenishment of nitrogen in the structure could, however, not yet be verified. FeS_2 acts similar to a co-catalyst, enhancing the ammonia generation, although the process is different to that of (metal) electrocatalysts typically employed for photocatalytic HER or OER. Here, π-back-donation from Fe-centers to imine nitrogen and amino groups of the defect-rich CN reduces the activation barrier for the reduction of terminal cyano groups upon illumination.

Although there are numerous reports on CN for the photocatalytic NRR, the complexity of the system, with a broad variety of defects that can theoretically be present, necessitates a strict control of the synthesis parameters and thorough characterization experiments. We deduce that photocatalytic ammonia generation with defective CN is most likely always a product of self-degradation, which can be enhanced by back-donation with suitable coordinating materials.

8.1.4 Experimental Section

Material Synthesis and Characterization

CN was prepared via thermal polymerization of melamine.[95] 1 g of melamine (Sigma Aldrich, 99%) was calcined at 550 °C for 4 h in a closed crucible in air, using a heating ramp of 5 K min^{-1}. The synthesis was repeated several times and the obtained CN powder was ground and thoroughly mixed, before it was used for further modifications and composite formation.

Vacancy-rich CN (V_N- CN) was obtained by dispersing 2 g of the as-synthesized CN in 36 mL of 1 M KOH for 3 h under stirring. Subsequently, the material was collected via centrifugation and washed until neutral with ultrapure water.[25]

For the composite formation, respective amounts of commercial FeS_2 (Sigma Aldrich, 99.8%, 325 mesh) and V_N-CN were ground for 10 min in a mortar, under addition of low amounts of i-propanol (p.a.). Subsequently, the mixture was subjected to heat treatment for 2 h at 200 °C in air, to improve interfacial contact.

The composites were analyzed before and after the photocatalytic experiments. *Powder X-ray diffraction* (XRD) was measured on a Malvern PANalytical Empyrean device with Cu K$_\alpha$ irradiation (λ_1 = 1.5406 Å; λ_2 = 1.54443 Å). Acceleration voltage and emission current were set to 40 kV and 40 mA, respectively. Peak assignment was performed with X'Pert Highscore plus. Following reference cards were used for the reflection assignment in FeS_2 and FeS, respectively: 00-042-1340, 00-023-1123. The diffraction pattern for CN was calculated with Vesta, using crystallographic data from the group of Irvine.[62]

Diffuse-reflectance UV/vis spectra were obtained using a Perkin Elmer Lambda 750 spectrometer with a Praying Mantis (Harrick) and spectralon as white standard. The Kubelka-Munk function was used for the calculation of pseudo-absorption, f(R).[96] $f(R) = \frac{(1-R)^2}{2 \cdot R}$

For band gap determination, a Tauc plot was used.[97] $[f(R) \cdot (h\nu)]^{\frac{1}{n}}$ with n = 0.5 for direct band gaps and n = 2 for indirect ones.

For *diffuse reflectance infrared Fourier transformed spectroscopy* (DRIFT) a Bruker Alpha II spectrometer and the software OPUS were used. Sample scans were taken from 400 to 4000 cm^{-1}, with a resolution of 4 cm^{-1}.

Fluorescence measurements were conducted on a FluoTime 300 spectrometer from PicoQuant, with the software EasyTau2. Emission spectra were recorded at different excitation wavelengths from a 300 W Xe lamp at room temperature in air. Time correlated single photon counting (TCSPC) spectra were measured using 355 nm laser excitation. The software EasyTau2 was employed for fitting of the decay curves, using a tailfit with three exponentials, according to:

$$\text{Dec(t)} = \sum_{i=1}^{n_{Exp}} A_i e^{-\frac{t}{\tau_i}} + Bkgr_{Dec}$$

For steady state measurements, the sample was placed in a holder for solid powder samples. For quantum yield (QY) measurements a thin film on the inside of a cuvette was prepared. The cuvette was placed in an integrating sphere. Measurements were conducted for "out" geometry – meaning that the film was positioned outside of the direct excitation path. For the calculation of the quantum yield, the intensity of the fluorescence emission was integrated, and the area A_S was divided by the total integral excitation intensity as measured in an empty reference cuvette (A_{BE}) minus the excitation intensity that is not absorbed by the sample, A_{SE}.

$$QY = \frac{A_S}{A_{BE} - A_{SE}}$$

X-ray photoelectron spectroscopy (XPS) was performed with a Physical Electronics PHI VersaProbe III Scanning XPS Microprobe device. Monochromatic Al Kα X-ray irradiation with a beam diameter of 100 μm was used, with the beam voltage being set to 15 kV and X-ray power to 25 W. The sample surface was pre-cleaned by argon cluster sputtering with a gas cluster ion-beam. To avoid surface charging, samples were continuously flooded with slow-moving electrons and Ar$^+$. For survey scans, pass energy and step size were set to 224 eV and 0.4 eV, respectively. High-resolution spectra were measured with a pass energy of 26 eV, a step size of 0.1 eV and a step time of 50 ms. For data analysis a CASA XPS 2.3.17 software was used. The background was corrected using Shirley subtraction. Peak fitting was done with Gaussian-Lorentzian line shapes, with 30% Lorentz ratio. For charge correction C 1s was set to 284.8 eV.

Transient absorption spectroscopy data was collected in diffuse reflectance geometry with an LP980 spectrometer (Edinburgh instruments). Pump laser pulse excitation was set at 355 nm (third harmonic of an Nd:YAG laser produced by Ekspla, NT340), while for the probe pulse a 150 W xenon arc lamp was used. Prior to the measurements the powder sample was filled in a cuvette, stored under Argon and sealed directly before the measurement. TAS data was normalized and decays were fitted with exponential decay functions.

N$_2$ *physisorption measurements* were conducted on a Quadrasorb Evo device from Anton Paar QuantaTec at 77 K to determine Brunauer-Emmet-Teller (BET) surface areas, using the software ASiQwin for data evaluation. Samples were degassed for 12 h at 120 °C prior to measurements. Due to the small surface area, Kr at 77 K was used for FeS$_2$, in an AS-iQ-MP-MP-AG instrument from Anton Paar QuantaTec.

CHNS *elemental analysis* was performed with an Unicube instrument from Elementar, using sulfanilamide as standard. Approximately 2 mg of the respective sample were weighed into a tin boat, sealed and combusted at temperatures up to 1143 °C in an oxygen/ argon atmosphere.

Thermogravimetric Analysis (TGA) with gas evolution detection *via* mass spectrometry (MS) was conducted with a Netzsch Jupiter STA 449C thermobalance together with a Netzsch Aeolos QMS 403C quadrupole MS, heating the sample at a rate of 5 K min^{-1} up to 900 °C in synthetic air.

Scanning electron microscopy (SEM) images were recorded on a Zeiss Leo 1530 device with an acceleration voltage of 3 kV after sputter-coating with platinum (Cressington Sputter Coater 208 HR). *Energy dispersive X-ray diffraction spectroscopy* (EDX) measurements were conducted on the same instrument, using and an acceleration voltage of 20 kV. An ultra-dry EDX detector by Thermo Fisher Scientific NS7 was employed.

Photocatalysis: Light-induced ammonia generation was performed in a semi-batch setup using a doped Hg immersion lamp (Z4, 700 W Peschl Ultraviolet) placed in a water-cooled quartz-glass inlay and operated at 350 W. 200 mg of the photocatalyst were dispersed in ≈30 mL of water by ultrasonic treatment for 10 min. The dispersion was transferred to the glass reactor and diluted to 600 mL by the addition of water and methanol. The total amount of methanol was 20 vol.%. Nitrogen was bubbled through the stirred dispersion at a flow rate of 50 mL min^{-1} overnight to flush out residual air. For pre-purification of the inlet gas stream, it was first passed through a 0.1 M $KMnO_4$ solution, followed by a 0.1 M KOH.[8] The dispersion was illuminated for 7 h, during which a constant temperature of 10 °C was ensured by cooling the reactor with the help of a cryostat (Lauda Proline RP845). Evolving gasses were passed through an acid trap containing 10 mL of 1 mM H_2SO_4,[98] dried and subsequently analysed by a quadrupole mass spectrometer (HPR-20 Q/C, Hiden Analytical). After the reaction, the dispersion was immediately filtered and tested for NH_3 using the salicylate test method, a modification of the indophenol blue method.[99,100] For the control experiment in an inert gas atmosphere, an Ar flow of 100 mL min^{-1} was used.

For the salicylate test, a stock solution of sodium hypochlorite and a stock solution containing the catalyst, sodium nitroprusside (Carl Roth, >99%), and sodium salicylate (Carl Roth, >99%), were prepared. The solutions were prepared fresh weekly and stored at 4 °C in the dark. For the preparation of the salicylate/ catalyst solution, 2 g of sodium salicylate and 8 mg of sodium nitroprusside were dissolved in 15 mL of ultrapure deionized water, to which 5 mL of a 2 M sodium hydroxide solution was added. For the preparation of the hypochlorite solution, 200 µL of sodium hypochlorite solution (12% Cl, Carl Roth) and 1 mL of 2 M NaOH were given to 18.8 mL of water. In a typical testing procedure, 500 µL of the hypochlorite solution were given to 2 mL of the reaction solution, which was filtered through a 0.2 µm syringe filter beforehand. Then, 500 µL of the sodium salicylate solution were added. The mixture was stored in the dark at room temperature overnight for color development, before being analyzed by UV/vis spectroscopy (Perkin Elmer Lambda 750 spectrometer), using a mixture of the two testing solutions and 20% aqueous methanol as reference. For the calibration, ammonium chloride (Carl Roth, >99.7%) stock solutions were prepared in a concentration range from 0.1 µg L^{-1} to 10 mg L^{-1} of NH_4^+. Since the experiment was performed in the presence of methanol as a scavenger, 20% of methanol were present in the calibration as well.

To verify the results from the salicylate test, the filtered reaction solutions were additionally analyzed with *ion chromatography* (IC). A Dionex Aquion System from Thermo Fisher, equipped with a Dionex

IonPac CS16 column with a CG16 guard column, CERS suppressor, and electric conductivity detector. 30×10^{-3} M methanesulfonic acid was used as eluent.

Ion chromatography was also used to analyze the reaction solution for nitrate by-products. The reaction solution was filtered with a 0.2 μm syringe filter. A Dionex Aquion system from Thermo Fisher, equipped with a Dionex IonPac AS9-HC column and IonPac AG9-HC guard column was used for the analysis. 1×10^{-3} M $NaHCO_3$/ 8×10^{-3} M Na_2CO_3 was used as eluent, a UV detector was employed for quantification at a wavelength of 207 nm.

For the quantification of hydrazine, the colorimetric method first reported by Watt and Chrisp was employed.[101] For the testing solution, 0.4 g of *p*-dimethylaminobenzaldehyde (Sigma Aldrich, 99%) were dissolved in 20 mL of ethanol (p.a.), to which 2 mL of concentrated HCl were added. For the calibration curve, standard solutions of hydrazine sulfate (Sigma Aldrich, >99%) in water/ methanol mixtures were prepared. For the measurement, 1.5 mL of the filtered reaction solutions were mixed with 1.5 mL of the testing solution and stored in the dark for 20 min for color development, before analysis of the absorbance with UV/vis spectroscopy against a reference containing only the testing solution and a water/ methanol mixture.

Supporting Information

Supporting Information is available from the Wiley Online Library or from the author.

Conflict of Interest

The authors have a financial/commercial Conflict of Interest.

Data Availability Statement

The data that support the findings of this study are available from the corresponding.

8.1.5 References

(1)   Schlögl, R. *Angew. Chemie - Int. Ed.* **2003**, *42*, 2004–2008.

(2)   Medford, A. J.; Hatzell, M. C. *ACS Catal.* **2017**, *7*, 2624–2643.

(3)   Chen, J. G.; Crooks, R. M.; Seefeldt, L. C.; Bren, K. L.; Morris Bullock, R.; Darensbourg, M. Y.; Holland, P. L.; Hoffman, B.; Janik, M. J.; Jones, A. K.; Kanatzidis, M. G.; King, P.; Lancaster, K. M.; Lymar, S. V.; Pfromm, P.; Schneider, W. F.; Schrock, R. R. *Science* **2018**, *360*, eaar6611.

(4)   Jia, H. P.; Quadrelli, E. A. *Chem. Soc. Rev.* **2014**, *43*, 547–564.

(5)   Singh, A. R.; Rohr, B. A.; Schwalbe, J. A.; Cargnello, M.; Chan, K.; Jaramillo, T. F.; Chorkendorff, I.; Nørskov, J. K. *ACS Catal.* **2017**, *7*, 706–709.

(6)   Tang, C.; Qiao, S. Z. *Chem. Soc. Rev.* **2019**, *48*, 3166–3180.

(7)   Andersen, S. Z.; Čolić, V.; Yang, S.; Schwalbe, J. A.; Nielander, A. C.; McEnaney, J. M.; Enemark-Rasmussen, K.; Baker, J. G.; Singh, A. R.; Rohr, B. A.; Statt, M. J.; Blair, S. J.; Mezzavilla, S.; Kibsgaard, J.; Vesborg, P. C. K.; Cargnello, M.; Bent, S. F.; Jaramillo, T. F.; Stephens, I. E. L.; Nørskov, J. K.; Chorkendorff, I. *Nature* **2019**, *570*, 504–508.

(8)   Choi, J.; Suryanto, B. H. R.; Wang, D.; Du, H. L.; Hodgetts, R. Y.; Ferrero Vallana, F. M.; MacFarlane, D. R.; Simonov, A. N. *Nat. Commun.* **2020**, *11*, 5546.

(9)   Ziegenbalg, D.; Zander, J.; Marschall, R. *ChemPhotoChem* **2021**, *5*, 792–807.

(10)   Wang, X.; Maeda, K.; Thomas, A.; Takanabe, K.; Xin, G.; Carlsson, J. M.; Domen, K.; Antonietti, M. *Nat. Mater.* **2009**, *8*, 76–80.

(11)   Ong, W. J.; Tan, L. L.; Ng, Y. H.; Yong, S. T.; Chai, S. P. *Chem. Rev.* **2016**, *116*, 7159–7329.

(12)   Fu, J.; Yu, J.; Jiang, C.; Cheng, B. *Adv. Energy Mater.* **2018**, *8*, 1701503.

(13)   Shi, H.; Long, S.; Hou, J.; Ye, L.; Sun, Y.; Ni, W.; Song, C.; Li, K.; Gurzadyan, G. G.; Guo, X. *Chem. - A Eur. J.* **2019**, *25*, 5028–5035.

(14)   Katsumata, H.; Higashi, F.; Kobayashi, Y.; Tateishi, I.; Furukawa, M.; Kaneco, S. *Sci. Rep.* **2019**, *9*, 14873.

(15)   Liu, B.; Ye, L.; Wang, R.; Yang, J.; Zhang, Y.; Guan, R.; Tian, L.; Chen, X. *ACS Appl. Mater. Interfaces* **2018**, *10*, 4001–4009.

(16)   Elbanna, O.; Fujitsuka, M.; Majima, T. *ACS Appl. Mater. Interfaces* **2017**, *9*, 34844–34854.

(17)   Feng, X.; Chen, H.; Jiang, F.; Wang, X. *J. Colloid Interface Sci.* **2018**, *509*, 298–306.

(18)   Kumar, A.; Raizada, P.; Hosseini-Bandegharaei, A.; Thakur, V. K.; Nguyen, V. H.; Singh, P. *J. Mater. Chem. A* **2021**, *9*, 111–153.

(19)   Zhao, D.; Dong, C. L.; Wang, B.; Chen, C.; Huang, Y. C.; Diao, Z.; Li, S.; Guo, L.; Shen, S. *Adv. Mater.* **2019**, *31*, 1903545.

(20)   Niu, P.; Qiao, M.; Li, Y.; Huang, L.; Zhai, T. *Nano Energy* **2018**, *44*, 73–81.

(21)   Jiang, L.; Yang, J.; Yuan, X.; Guo, J.; Liang, J.; Tang, W.; Chen, Y.; Li, X.; Wang, H.; Chu, W. *Adv. Colloid Interface Sci.* **2021**, *296*, 102523.

(22)   Chen, X.; Li, N.; Kong, Z.; Ong, W. J.; Zhao, X. *Mater. Horizons* **2018**, *5*, 9–27.

(23)   Shi, R.; Zhao, Y.; Waterhouse, G. I. N.; Zhang, S.; Zhang, T. *ACS Catal.* **2019**, *9*, 9739–9750.

(24)   Zhang, G.; Li, Y.; He, C.; Ren, X.; Zhang, P.; Mi, H. *Adv. Energy Mater.* **2021**, *11*, 2003294.

(25)   Li, X.; Sun, X.; Zhang, L.; Sun, S.; Wang, W. *J. Mater. Chem. A* **2018**, *6*, 3005–3011.

(26)   Ma, H.; Shi, Z.; Li, Q.; Li, S. *J. Phys. Chem. Solids* **2016**, *99*, 51–58.

(27)   Zhou, N.; Qiu, P.; Chen, H.; Jiang, F. *J. Taiwan Inst. Chem. Eng.* **2018**, *83*, 99–106.

(28)   Wang, W.; Zhang, H.; Zhang, S.; Liu, Y.; Wang, G.; Sun, C.; Zhao, H. *Angew. Chemie - Int. Ed.* **2019**, *58*, 16644–16650.

(29)   Liang, C.; Niu, H. Y.; Guo, H.; Niu, C. G.; Huang, D. W.; Yang, Y. Y.; Liu, H. Y.; Shao, B. Bin; Feng,

H. P. *Chem. Eng. J.* **2020**, *396*, 125395.

(30)   Cheng, M.; Xiao, C.; Xie, Y. *J. Mater. Chem. A* **2019**, *7*, 19616–19633.

(31)   Meng, A.; Teng, Z.; Zhang, Q.; Su, C. *Chem. - An Asian J.* **2020**, *15*, 3405–3415.

(32)   Lau, V. W. H.; Moudrakovski, I.; Botari, T.; Weinberger, S.; Mesch, M. B.; Duppel, V.; Senker, J.; Blum, V.; Lotsch, B. V. *Nat. Commun.* **2016**, *7*, 12165.

(33)   *Activation of Small Molecules*; Tolman, W. B., Ed.; Wiley-VCH: Weinheim, 2006.

(34)   Liu, J.; Kelley, M. S.; Wu, W.; Banerjee, A.; Douvalis, A. P.; Wu, J.; Zhang, Y.; Schatz, G. C.; Kanatzidis, M. G. *Proc. Natl. Acad. Sci. U. S. A.* **2016**, *113*, 5530–5535.

(35)   Chu, K.; Li, Q. Q.; Cheng, Y. H.; Liu, Y. P. *ACS Appl. Mater. Interfaces* **2020**, *12*, 11789–11796.

(36)   Chen, C.; Liu, Y.; Yao, Y. *Eur. J. Inorg. Chem.* **2020**, *2020*, 3236–3241.

(37)   Lowndes, N. F.; Johnson, A. L.; Johnston, L. H.; Mcintosh, E. M.; Atkinson, T.; Storms, R. K.; Smith, M.; Lee, T. I. *Science* **2003**, *301*, 76–79.

(38)   Howalt, J. G.; Vegge, T. *Phys. Chem. Chem. Phys.* **2013**, *15*, 20957–20965.

(39)   Wu, J.; Wang, Z. X.; Li, S.; Niu, S.; Zhang, Y.; Hu, J.; Zhao, J.; Xu, P.; Xu, P. *Chem. Commun.* **2020**, *56*, 6834–6837.

(40)   Wang, J.; Nan, H.; Tian, Y.; Chu, K. *ACS Sustain. Chem. Eng.* **2020**, *8*, 12733–12740.

(41)   Chu, K.; Liu, Y. P.; Li, Y. B.; Guo, Y. L.; Tian, Y. *ACS Appl. Mater. Interfaces* **2020**, *12*, 7081–7090.

(42)   Tian, L.; Zhao, J.; Ren, X.; Sun, X.; Wei, Q.; Wu, D. *ChemistryOpen* **2021**, *10*, 1041–1054.

(43)   Shukla, S.; Xing, G.; Ge, H.; Prabhakar, R. R.; Mathew, S.; Su, Z.; Nalla, V.; Venkatesan, T.; Mathews, N.; Sritharan, T.; Sum, T. C.; Xiong, Q. *ACS Nano* **2016**, *10*, 4431–4440.

(44)   Liu, S.; Li, M.; Li, S.; Li, H.; Yan, L. *Appl. Surf. Sci.* **2013**, *268*, 213–217.

(45)   Sun, H.; Tang, P. *Adv. Mater. Res.* **2012**, *486*, 55–59.

(46)   Morales-Gallardo, M. V.; Ayala, A. M.; Pal, M.; Cortes Jacome, M. A.; Toledo Antonio, J. A.; Mathews, N. R. *Chem. Phys. Lett.* **2016**, *660*, 93–98.

(47)   Wu, L.; Dzade, N. Y.; Gao, L.; Scanlon, D. O.; Öztürk, Z.; Hollingsworth, N.; Weckhuysen, B. M.; Hensen, E. J. M.; de Leeuw, N. H.; Hofmann, J. P. *Adv. Mater.* **2016**, *28*, 9602–9607.

(48)   Qin, H.; Jia, J.; Lin, L.; Ni, H.; Wang, M.; Meng, L. *Mater. Sci. Eng. B Solid-State Mater. Adv. Technol.* **2018**, *236–237*, 104–124.

(49)   Kokilavani, S.; Syed, A.; Raju, L. L.; Al-Rashed, S.; Elgorban, A. M.; Thomas, A. M.; Khan, S. S. *Surfaces and Interfaces* **2021**, *23*, 101003.

(50)   Ye, X.; Li, X.; Chu, X.; Wang, Z.; Zuo, S.; Wang, T.; Yao, C. *J. Alloys Compd.* **2021**, *871*, 159542.

(51)   Lee, G.; Kang, M. *Curr. Appl. Phys.* **2013**, *13*, 1482–1489.

(52)   Han, E.; Hu, F.; Zhang, S.; Luan, B.; Li, P.; Sun, H.; Wang, S. *Energy and Fuels* **2018**, *32*, 4357–4363.

(53)   Kuo, T. R.; Liao, H. J.; Chen, Y. T.; Wei, C. Y.; Chang, C. C.; Chen, Y. C.; Chang, Y. H.; Lin, J. C.; Lee, Y. C.; Wen, C. Y.; Li, S. S.; Lin, K. H.; Wang, D. Y. *Green Chem.* **2018**, *20*, 1640–1647.

(54)   Wang, D. Y.; Gong, M.; Chou, H. L.; Pan, C. J.; Chen, H. A.; Wu, Y.; Lin, M. C.; Guan, M.; Yang, J.; Chen, C. W.; Wang, Y. L.; Hwang, B. J.; Chen, C. C.; Dai, H. *J. Am. Chem. Soc.* **2015**, *137*, 1587–1592.

(55)   Barawi, M.; Ferrer, I. J.; Flores, E.; Yoda, S.; Ares, J. R.; Sánchez, C. *J. Phys. Chem. C* **2016**, *120*, 9547–9552.

(56)   Wang, H. Bin; Wang, J. Q.; Zhang, R.; Cheng, C. Q.; Qiu, K. W.; Yang, Y. J.; Mao, J.; Liu, H.; Du, M.; Dong, C. K.; Du, X. W. *ACS Catal.* **2020**, *10*, 4914–4921.

(57)   Feng, D.; Zhang, X.; Sun, Y.; Ma, T. *Nano Mater. Sci.* **2020**, *2*, 132–139.

(58)   Chang, C. C.; Li, S. R.; Chou, H. L.; Lee, Y. C.; Patil, S.; Lin, Y. S.; Chang, C. C.; Chang, Y. J.; Wang, D. Y. *Small* **2019**, *15*, 1904723.

(59)   Lashgari, M.; Zeinalkhani, P. *Nano Energy* **2018**, *48*, 361–368.

(60)   Wei, B.; Wang, C.; He, Y.; Ran, G.; Song, Q. *Compos. Commun.* **2021**, *24*, 100652.

(61)   Li, L.; Gao, J.; Yuan, Y.; Zhang, S.; Liang, M.; Liu, Y. *J. Taiwan Inst. Chem. Eng.* **2021**, *126*, 134–144.

(62)   Fina, F.; Callear, S. K.; Carins, G. M.; Irvine, J. T. S. *Chem. Mater.* **2015**, *27*, 2612–2618.

(63)   Lotsch, B. V.; Döblinger, M.; Sehnert, J.; Seyfarth, L.; Senker, J.; Oeckler, O.; Schnick, W. *Chem. - A Eur. J.* **2007**, *13*, 4969–4980.

(64)   Alwin, E.; Nowicki, W.; Wojcieszak, R.; Zieliński, M.; Pietrowski, M. *Dalt. Trans.* **2020**, *49*, 12805–12813.

(65)   Sano, T.; Tsutsui, S.; Koike, K.; Hirakawa, T.; Teramoto, Y.; Negishi, N.; Takeuchi, K. *J. Mater. Chem. A* **2013**, *1*, 6489–6496.

(66)   Choudhury, B.; Paul, K. K.; Sanyal, D.; Hazarika, A.; Giri, P. K. *J. Phys. Chem. C* **2018**, *122*, 9209–9219.

(67)   Dong, G.; Ho, W.; Wang, C. *J. Mater. Chem. A* **2015**, *3*, 23435–23441.

(68)   Wang, S.; Zhan, J.; Chen, K.; Ali, A.; Zeng, L.; Zhao, H.; Hu, W.; Zhu, L.; Xu, X. *ACS Sustain. Chem. Eng.* **2020**, *8*, 8214–8222.

(69)   Wang, H.; Li, M.; Li, H.; Lu, Q.; Zhang, Y.; Yao, S. *Mater. Des.* **2019**, *162*, 210–218.

(70)   Li, H.; Zhang, Z.; Liu, Y.; Cen, W.; Luo, X. *Nanomaterials* **2018**, *8*, 589.

(71)   Zhang, G.; Li, G.; Lan, Z. A.; Lin, L.; Savateev, A.; Heil, T.; Zafeiratos, S.; Wang, X.; Antonietti, M. *Angew. Chemie - Int. Ed.* **2017**, *56*, 13445–13449.

(72)   Sun, Z.; Wang, S.; Li, Q.; Lyu, M.; Butburee, T.; Luo, B.; Wang, H.; Fischer, J. M. T. A.; Zhang, C.; Wu, Z.; Wang, L. *Adv. Sustain. Syst.* **2017**, *1*, 1700003.

(73)   Yu, H.; Shi, R.; Zhao, Y.; Bian, T.; Zhao, Y.; Zhou, C.; Waterhouse, G. I. N.; Wu, L. Z.; Tung, C. H.; Zhang, T. *Adv. Mater.* **2017**, *29*, 1605148.

(74)   Kim, M.; Hwang, S.; Yu, J. S. *J. Mater. Chem.* **2007**, *17*, 1656–1659.

(75)   Akaike, K.; Aoyama, K.; Dekubo, S.; Onishi, A.; Kanai, K. *Chem. Mater.* **2018**, *30*, 2341–2352.

(76)   Lv, C.; Qian, Y.; Yan, C.; Ding, Y.; Liu, Y.; Chen, G.; Yu, G. *Angew. Chemie - Int. Ed.* **2018**, *57*, 10246–10250.

(77)   Zhao, Y.; Shi, R.; Bian, X.; Zhou, C.; Zhao, Y.; Zhang, S.; Wu, F.; Waterhouse, G. I. N.; Wu, L. Z.; Tung, C. H.; Zhang, T. *Adv. Sci.* **2019**, *6*, 1802109.

(78)   Suzuki, N.; Kuroda, R. *Analyst* **1987**, *112*, 1077–1079.

(79)   Ozaki, Y.; Saito, Y.; Kawata, S. Introduction to FUV and DUV Spectroscopy. In *Far-and Deep-Ultraviolet Spectroscopy*; Ozaki, Y., Kawata, S., Eds.; Springer Japan: Tokyo, Heidelberg, New York, Dordrecht, London, 2015; pp 1–16.

(80)   Mu, Y.; Peng, Y.; Lauten, R. A. *Miner. Eng.* **2016**, *96–97*, 143–156.

(81)   Godin, R.; Wang, Y.; Zwijnenburg, M. A.; Tang, J.; Durrant, J. R. *J. Am. Chem. Soc.* **2017**, *139*, 5216–5224.

(82)   Corp, K. L.; Schlenker, C. W. *J. Am. Chem. Soc.* **2017**, *139*, 7904–7912.

(83)   Wang, Y.; Liu, X.; Han, X.; Godin, R.; Chen, J.; Zhou, W.; Jiang, C.; Thompson, J. F.; Mustafa, K. B.; Shevlin, S. A.; Durrant, J. R.; Guo, Z.; Tang, J. *Nat. Commun.* **2020**, *11*, 2531.

(84)   Peng, G.; Albero, J.; Garcia, H.; Shalom, M. *Angew. Chemie - Int. Ed.* **2018**, *57*, 15807–15811.

(85)   Kisch, H. *Angew. Chemie - Int. Ed.* **2013**, *52*, 812–847.

(86)   Merschjann, C.; Tschierlei, S.; Tyborski, T.; Kailasam, K.; Orthmann, S.; Hollmann, D.; Schedel-Niedrig, T.; Thomas, A.; Lochbrunner, S. *Adv. Mater.* **2015**, *27*, 7993–7999.

(87)   Wang, W.; Bai, X.; Ci, Q.; Du, L.; Ren, X.; Phillips, D. L. *Adv. Funct. Mater.* **2021**, *31*, 2103978.

(88)   Jiao, Y.; Hu, R.; Wang, Q.; Fu, F.; Chen, L.; Dong, Y.; Lin, Z. *Chem. - A Eur. J.* **2021**, *27*, 10925–

10931.

(89)   Wu, P.; Wang, J.; Zhao, J.; Guo, L.; Osterloh, F. E. *J. Mater. Chem. A* **2014**, *2*, 20338–20344.

(90)   Zhang, H.; Yu, A. *J. Phys. Chem. C* **2014**, *118*, 11628–11635.

(91)   Jorge, A. B.; Martin, D. J.; Dhanoa, M. T. S.; Rahman, A. S.; Makwana, N.; Tang, J.; Sella, A.; Corà, F.; Firth, S.; Darr, J. A.; McMillan, P. F. *J. Phys. Chem. C* **2013**, *117*, 7178–7185.

(92)   Gan, Z.; Shan, Y.; Chen, J.; Gui, Q.; Zhang, Q.; Nie, S.; Wu, X. *Nano Res.* **2016**, *9*, 1801–1812.

(93)   Jay, R. M.; Norell, J.; Eckert, S.; Hantschmann, M.; Beye, M.; Kennedy, B.; Quevedo, W.; Schlotter, W. F.; Dakovski, G. L.; Minitti, M. P.; Hoffmann, M. C.; Mitra, A.; Moeller, S. P.; Nordlund, D.; Zhang, W.; Liang, H. W.; Kunnus, K.; Kubiček, K.; Techert, S. A.; Lundberg, M.; Wernet, P.; Gaffney, K.; Odelius, M.; Föhlisch, A. *J. Phys. Chem. Lett.* **2018**, *9*, 3538–3543.

(94)   Kostovic, M.; Vucinic, D. *Physicochem. Probl. Miner. Process.* **2016**, *52*, 609–619.

(95)   Yan, S. C.; Li, Z. S.; Zou, Z. G. *Langmuir* **2009**, *25*, 10397–10401.

(96)   Kubelka, P.; Munk, F. *Z. Tech. Phys* **1931**, *265*, 593–601.

(97)   Tauc, J. *Mat. Res. Bull.* **1968**, *3*, 37–46.

(98)   Zhou, F.; Azofra, L. M.; Ali, M.; Kar, M.; Simonov, A. N.; McDonnell-Worth, C.; Sun, C.; Zhang, X.; MacFarlane, D. R. *Energy Environ. Sci.* **2017**, *10*, 2516–2520.

(99)   Bower, C. E.; Holm-Hansen, T. *Can. J. Fish. Aquat. Sci.* **1980**, *37*, 794–798.

(100)   Krom, M. *Analyst* **1980**, *105*, 305–316.

(101)   Watt, G. W.; Chrisp, J. D. *Anal. Chem.* **1952**, *24*, 2006–2008.

8.2 Supporting Information

Light-induced Ammonia Generation over Defective Carbon Nitride Modified with Pyrite

Judith Zander, Jana Timm, Morten Weiss, Roland Marschall*

| V_N-C_3N_4 | 1 wt.% FeS$_2$ | 2.5 wt.% FeS$_2$ | 5 wt.% FeS$_2$ | 10 wt.% FeS$_2$ | 15 wt.% FeS$_2$ |
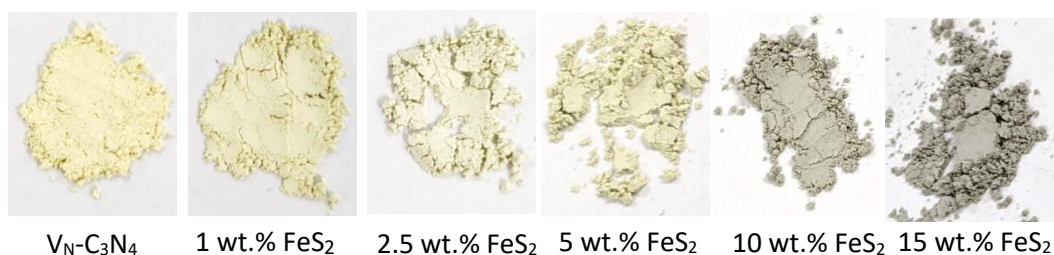
Figure S1 Photographs of composites of V_N-C_3N_4 with and FeS$_2$, demonstrating the color change upon addition of FeS$_2$.
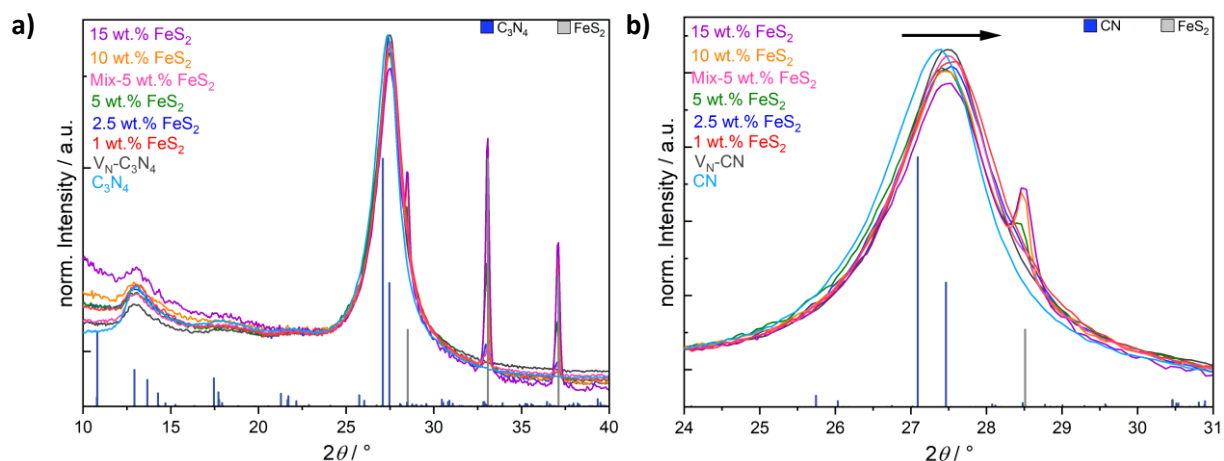
Figure S2 Normalized PXRD patterns for V_N-C_3N_4 and the composites with indices for C_3N_4 (a) and enlarged section of the (002) reflection (b), elucidating the shift towards higher diffraction angles upon KOH-etching, that is retained in the composites.
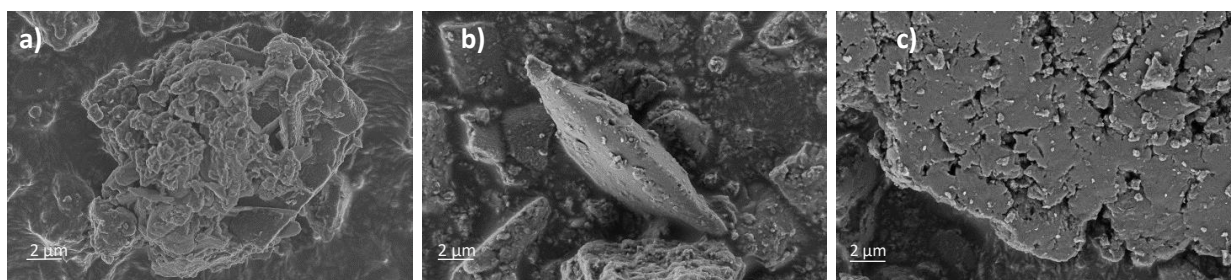
Figure S3 Additional SEM images of FeS$_2$-V$_N$-C$_3$N$_4$-Composites. An image of the composite containing 10 wt.% of FeS$_2$ (a) elucidates the partial wrapping of C$_3$N$_4$ around a pyrite particle. Another one of a composite containing 5 wt.% of FeS$_2$, shows the surface decoration of carbon nitride with a pyrite particle (b). Another image shows an exemplified area of only carbon nitride (c).
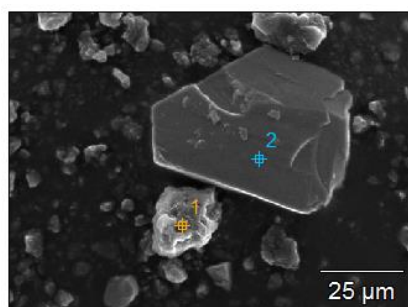
Table S1 Elemental composition of pyrite and C$_3$N$_4$ in the composites.

Location	Atom% C	Atom% N	C/N	Atom% Fe	Atom% S	Fe/S
Point 1	33.9	65.4	0.52			
Point 2	11.3			31.0	57.6	0.54

Figure S4 EDX of a composite sample (10 wt.% FeS$_2$) with two respective points for C$_3$N$_4$ and FeS$_2$.

Table S2 BET surface area of the composites of FeS$_2$ and V$_N$-C$_3$N$_4$.

Sample	BET Surface Area [m^2/g]
C$_3$N$_4$	10.7
V$_N$-C$_3$N$_4$	9.8
1 wt.% FeS$_2$	7.9
2.5 wt.% FeS$_2$	7.8
5 wt.% FeS$_2$	8.9
10 wt.% FeS$_2$	5.6
15 wt.% FeS$_2$	4.0
FeS$_2$ (Kr)	0.24
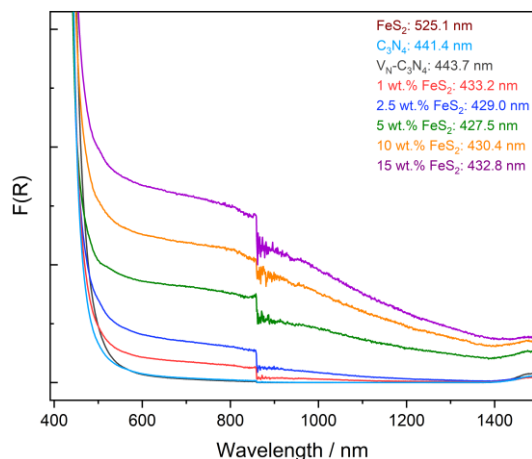
Figure S5 Diffuse absorption due to FeS_2 causing an offset of the baseline in the Kubelka-Munk plots of the composites. The sharp offset at 860 nm results from a detector and monochromator change of the instrument.

Table S3 Band gaps for the composites derived from the Kubelka Munk and the indirect Tauc plots, respectively.

Sample	Band gap derived from the Kubelka-Munk plots [nm/ eV]	Band gap derived from the indirect Tauc plots [eV]
Bulk C_3N_4	442 / 2.81	2.73
V_N- C_3N_4	444 / 2.79	2.70
1 wt.% FeS_2	433 / 2.86	2.74
2.5 wt.% FeS_2	429 / 2.89	2.76
5 wt.% FeS_2	428 / 2.90	2.78
10 wt.% FeS_2	430 / 2.88	2.77
15 wt.% FeS_2	433 / 2.86	2.77
FeS_2	525 / 2.36	--
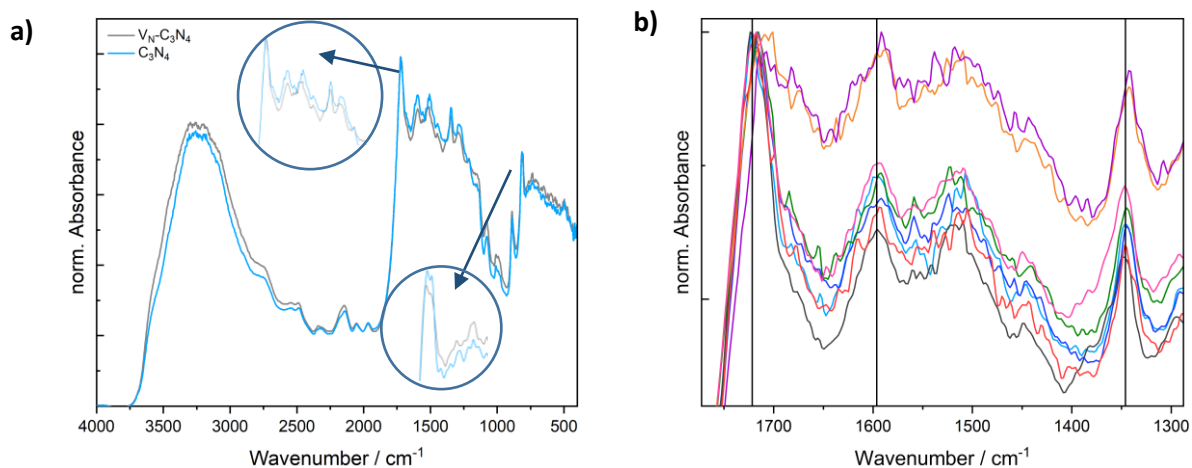
Figure S6 C_3N_4 before and after KOH-treatment (a) and excerpt of the DRIFT spectra of the composites, elucidating a shift of the vibration energies in the heptazine framework towards lower wavenumbers with increasing FeS_2 content (b). The different colors represent the spectra for the different composites, identical to the color code in *e.g.* Figure S5.
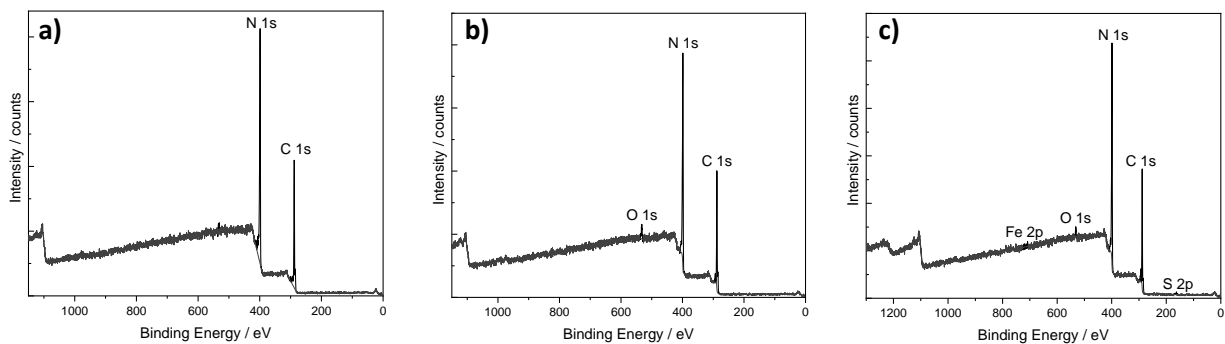
Figure S7 Survey scans for bulk C_3N_4 (a), V_N-C_3N_4 (b) and the composite with 5 wt.% of FeS_2 (c).

Table S4 Atomic ratios derived from XPS survey scans. Different rows for the same material indicate different measurement spots

	N At%	C At%	Fe At%	S At %	O At.%	C/N	C/N (corrected adv. C)
C_3N_4	56.1	43.2			0.7	0.770	0.66
	59.7	40.3				0.675	
average						**0.72**	
V_N-C_3N_4	53.2	44.1			2.7	0.829	0.71
	56.4	43.6				0.773	
	54.3	43.2			2.5	0.7968	
average						**0.80**	
	54.8	43.6	0.1	0.3	1.1	0.796	0.71
5 wt.% FeS_2	53.2	44.0			2.8	0.827	
	55.2	43.3			1.5	0.784	
average						**0.80**	
NRR 5 wt.% FeS_2-	52.1	45.2	0.6	0.3	1.8	0.868	0.63
	51.3	45.9			2.8	0.895	
	52.3	45.4			2.3	0.868	
average						**0.88**	
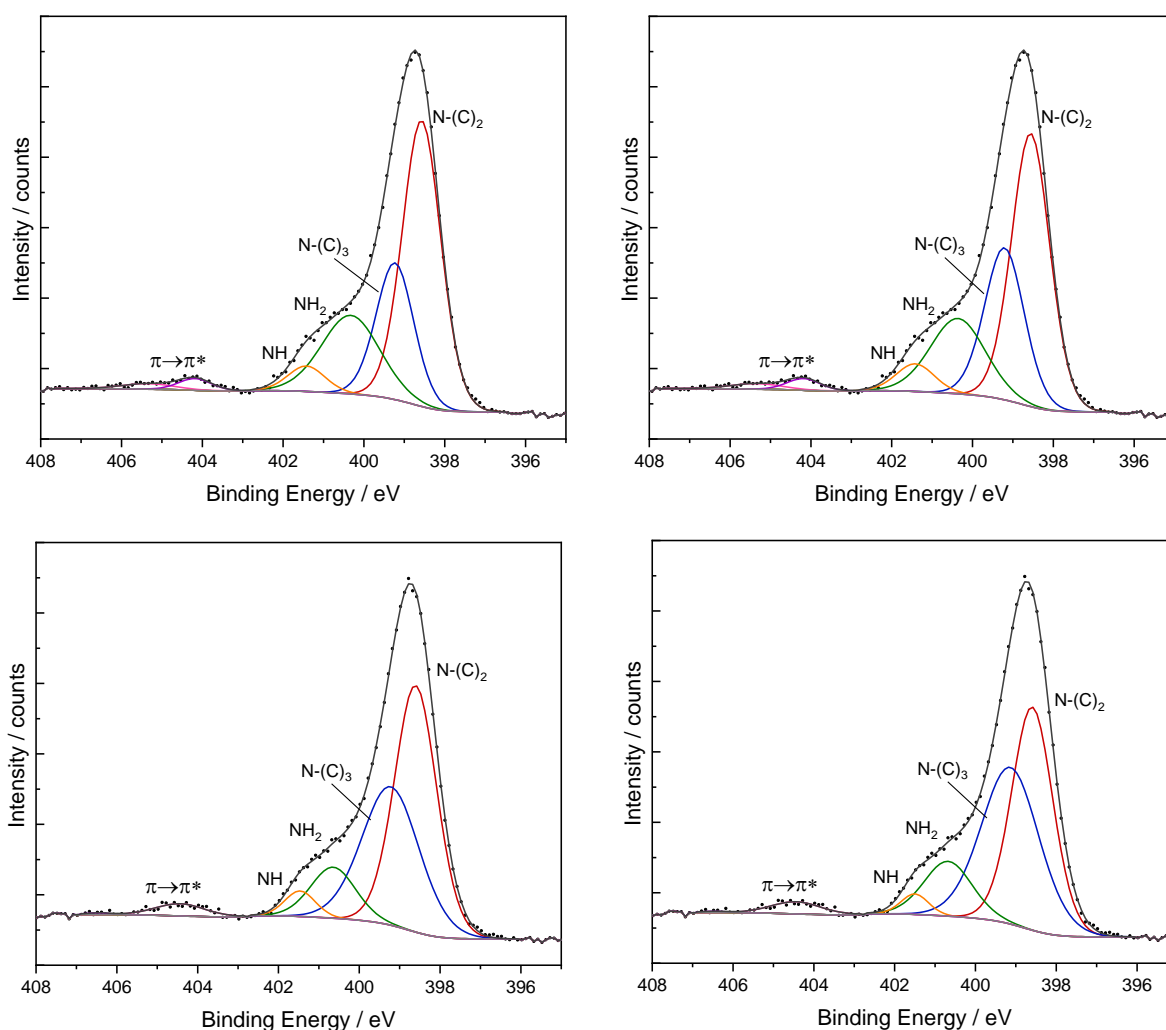
Figure S8 Two possible fits for the N $1s$ spectrum of C_3N_4 obtained for slightly different starting conditions giving both reasonable, but not identical results (top) and for V_N-C_3N_4 (bottom).

Table S5 Binding energies and ratios for the different nitrogen species in the N $1s$ spectra of C_3N_4 and V_N-C_3N_4. Fit employed for the further evaluation of spectra for V_N-C_3N_4 shown in green.

		-NH	-NH₂	N-(C)₃	N-(C)₂
C₃N₄-Fit1	Binding energy / eV	401.4	400.3	399.2	398.6
	Amount / at.%	4.4	21.1	23.8	50.8
C₃N₄-Fit2	Binding energy / eV	401.4	400.4	399.2	398.6
	Amount / at.%	4.9	19.1	27.8	48.2
V_N-C₃N₄-Fit1	Binding energy / eV	401.5	400.7	399.2	398.6
	Amount / at.%	3.7	10.7	37.2	48.5
V_N-C₃N₄-Fit2	Binding energy / eV	401.5	400.7	399.1	398.6
	Amount / at.%	2.6	12.3	42.2	42.9

Further information on fitting the N 1*s* spectra for V$_N$-C$_3$N$_4$ and that of a composite with 5 wt.% of FeS$_2$

First, we kept the area ratio of the peaks at 401.5 and 400.4 eV fixed when fitting the spectrum for V$_N$-C$_3$N$_4$ based on that of bulk C$_3$N$_4$, allowing for only slight shifts (0.2 eV) in both binding energy and FWHM. This constraint is based on the assumption that the signals can be attributed to NH$_2$ and NH species, which should remain unaffected by KOH treatment and that the cyano group is encompassed by the signal for N-(C)$_3$.

As noted, the nitrogen of cyano groups at ~400 eV might also fall under the signal at 400.4 eV. Therefore, we repeated the fit, keeping the ratio of the signals for NH (at 401.5 eV) and N-(C)$_3$ at 399.7 eV fixed. Both fits give good results, but entirely different ratios and peak shifts (***Figure S9***, ***Table S6***). It cannot be determined, which is the more reliable fit, but the one for which the cyano group is assumed to fall under the signal at 400.4 eV gives the more logical changes in the ratios of the respective nitrogen species (***Table S6***). Still, the fitting results are rather arbitrary. Furthermore, it is always possible to introduce more fitting peaks, thus further complicating analysis; for that reason, we have always used the minimum amount of peaks necessary to achieve a good fit. For all fits, the binding energy of the N-(C)$_2$ signal remains the same, but its ratio compared to the N-(C)$_3$ and NH signal is decreased. This is in good agreement to the introduction of cyano groups under simultaneous ring breakage. No prediction can be made for nitrogen vacancies, since the arbitrary fitting does not allow for accurate evaluation of changes for the NH to NH$_2$ and N-(C)$_3$ ratio and the content of N-(C)$_2$ is already expected to decrease upon cyano group formation.

For the fits of the N 1*s* spectrum of the composite, first the parameters for the fit for V$_N$-C$_3$N$_4$ with constant ratio of the two amino peaks were used as starting conditions, assuming that the structure is mostly unchanged upon composite formation. The structure – and hence also the peak fit – of the composite will depend on that of V$_N$-C$_3$N$_4$, which is in turn derived from the bulk C$_3$N$_4$. All area ratios were kept constant, allowing for minor changes of the FWHM and shifts in the peak positions of ± 0.4 eV. The spectrum was additionally fitted by setting the fit parameters for V$_N$-C$_3$N$_4$ with constant NH/N-(C)$_3$ ratio as starting conditions, once with fixed area ratios and once allowing for changes in peak area ratios and FWHM (***Figure S10***). Fitting the spectrum of the composite based on the parameters for V$_N$-C$_3$N$_4$ and removing the constraints did not give realistic results.

Moreover, the fit was repeated with only two signals for NH, NH$_x$, CN and N-(C)$_3$, but the results are just as variable and the sensibility in approximating four chemical species with two signals is questionable (***Figure S9***, ***Table S7***).
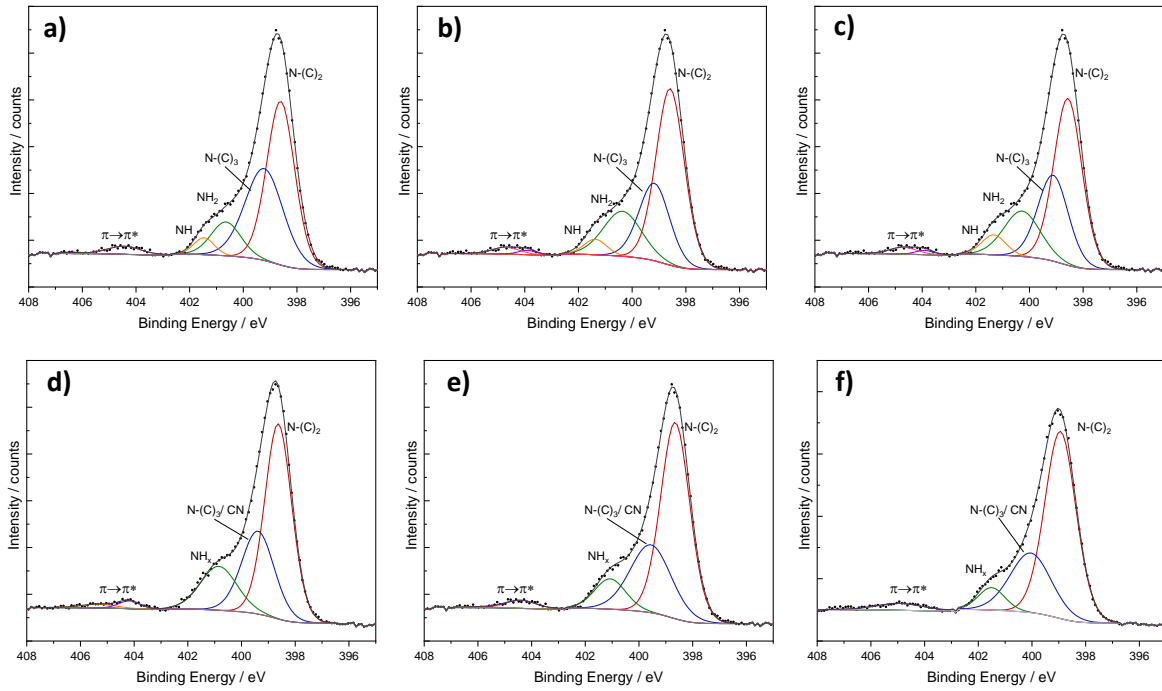
Figure S9 Fitted N 1s spectra for KOH treated C_3N_4, using following fitting constraints: (a) no constraints, starting parameters from the untreated C_3N_4 (fit 1 in Table S5), (b) fit under the prerequisite of retained NH/NH_2 ratio, (c) fit with retained NH/N-$(C)_3$ ratio. The bottom row delineates the possible fitting of the N 1s spectra, with only one signal for the amino groups, (d) for bulk C_3N_4, (e) for V_N-C_3N_4 and (f) for the composite containing 5 wt.% of FeS_2 .
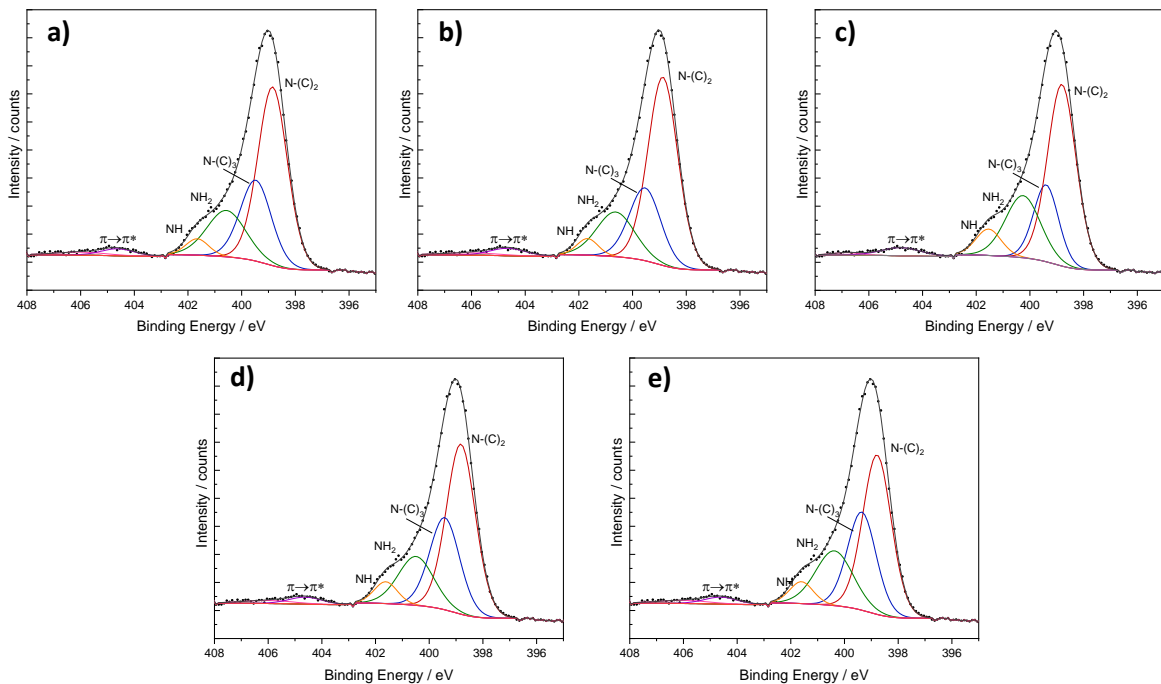
Figure S10 Fit for the N 1s spectrum of the composite with (a): FWHM and area ratios kept the same as for V_N-C_3N_4 (with a fixed NH/NH_2 ratio), (b) allowing for changes in both FWHM and area ratio and (c) fit for the spectrum without any constraints from the parameters of the fit for V_N-C_3N_4. Additionally: (d) fits for the N 1s spectrum of the composite using the parameters of the fit for V_N-C_3N_4 with a fixed NH/N-$(C)_3$ ratio as starting conditions and keeping FWHM and area ratio mostly fixed, or (e) removing constraints for FWHM and area ratio.

Table S6 Binding energies and ratios for the different nitrogen species in the N 1*s* spectra of V_N-C_3N_4 and the composite with 5 wt.% of FeS_2, fitted with different constraints. The best fitting results are shown in green.

	Fit from		-NH	-NH$_2$	N-(C)$_3$	N-(C)$_2$
V_N-C_3N_4	Fig. S9 a	Binding energy / eV	401.5	400.7	399.2	398.6
		Amount / at.%	3.7	10.7	37.2	48.5
	Fig. S9 b	Binding energy / eV	401.4	400.4	399.2	398.6
		Amount / at.%	3.8	18.2	25.2	52.9
	Fig. S9 c	Binding energy / eV	401.3	400.3	399.1	398.6
		Amount / at.%	5.1	17.5	27.8	49.7
5 wt.% FeS$_2$	Fig. S10 a	Binding energy / eV	401.7	400.6	399.5	398.8
		Amount / at.%	3.8	18.2	25.2	52.9
	Fig. S10 b	Binding energy / eV	401.7	400.6	399.5	398.9
		Amount / at.%	3.5	17.0	23.0	56.5
	Fig. S10 c	Binding energy / eV	401.5	400.3	399.4	398.8
		Amount / at.%	6.7	21.9	19.3	52.1
	Fig. S10 d	Binding energy / eV	401.6	400.5	399.4	398.8
		Amount / at.%	5.1	17.5	27.8	49.7
	Fig. S10 e	Binding energy / eV	401.6	400.4	399.4	398.8
		Amount / at.%	5.2	20.7	28.3	45.8

Table S7 Binding energies and ratios for the different nitrogen species in the N 1*s* spectra of C_3N_4, V_N-C_3N_4 and the composite with 5 wt.% of FeS_2, with both amino groups fitted together with only one signal.

		-NH$_x$	N-(C)$_3$	N-(C)$_2$
C_3N_4	Binding energy / eV	400.9	399.4	398.6
	Amount / at.%	16.8	28.2	55.0
V_N-C_3N_4	Binding energy / eV	401.1	399.6	398.7
	Amount / at.%	10.0	29.5	60.5
5 wt.% FeS$_2$	Binding energy / eV	401.5	400.0	398.9
	Amount / at.%	7.0	28.4	64.6
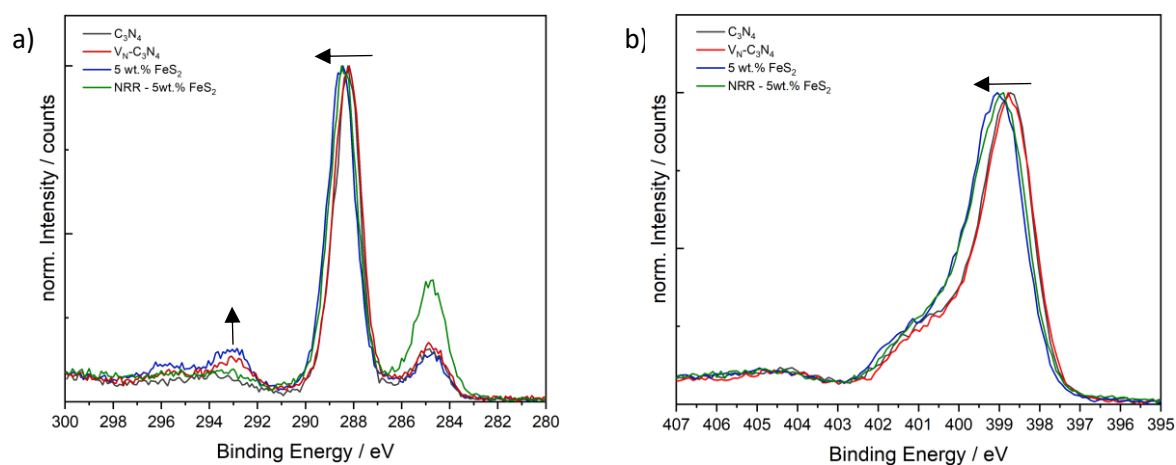
Figure S11 Normalized C 1*s* spectra (a) and N 1*s* spectra (b) for C_3N_4, V_N-C_3N_4, and the composite with FeS_2.
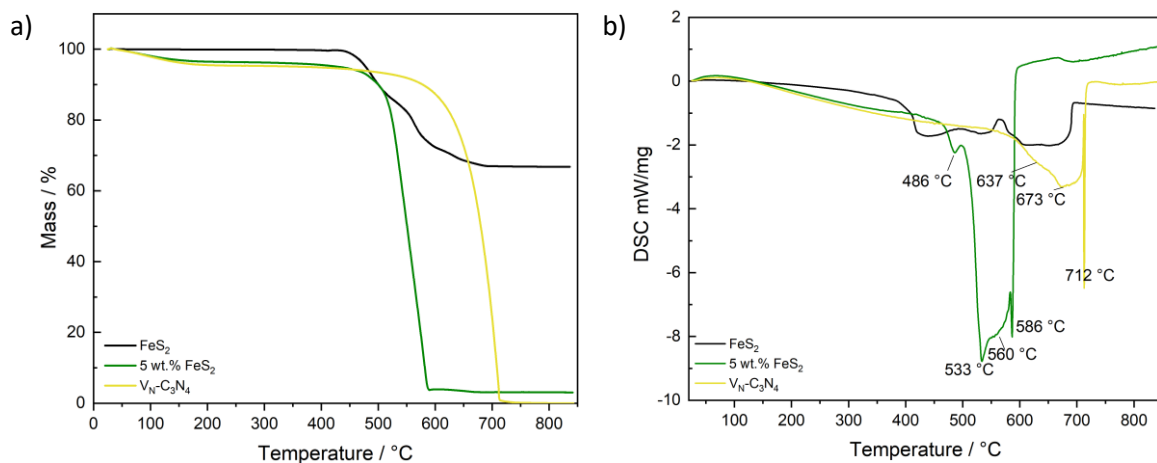
Figure S12 TGA-MS measurements for FeS_2, V_N-C_3N_4 and the composite with 5 wt.% FeS_2. The mass loss is depicted on the left (a) and the corresponding DSC curves are shown on the right (b). A shift in the decomposition temperature of the composite by almost 100 °C is clearly apparent.
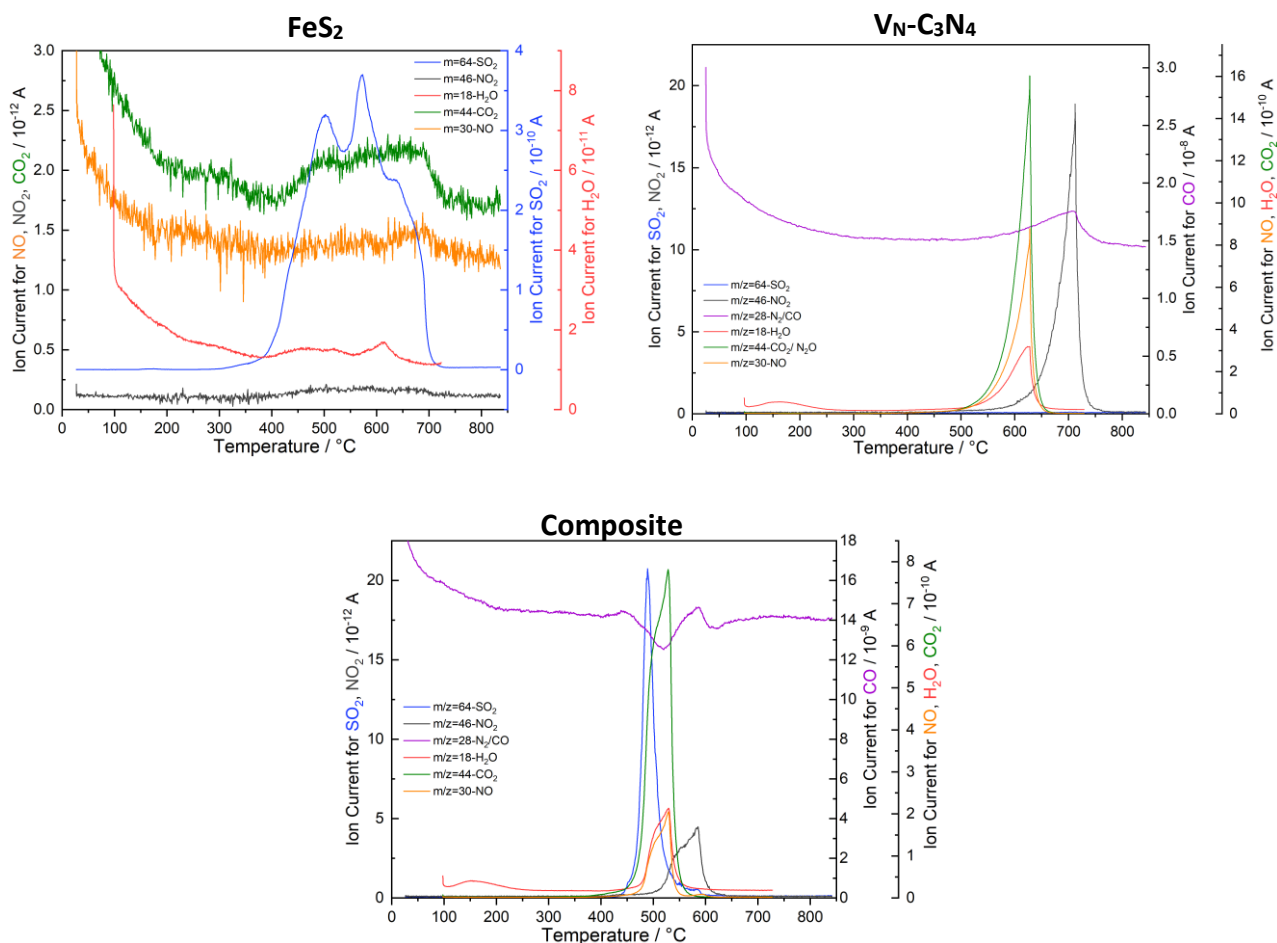
Figure S13 Corresponding ion currents for the TGA-MS measurements.
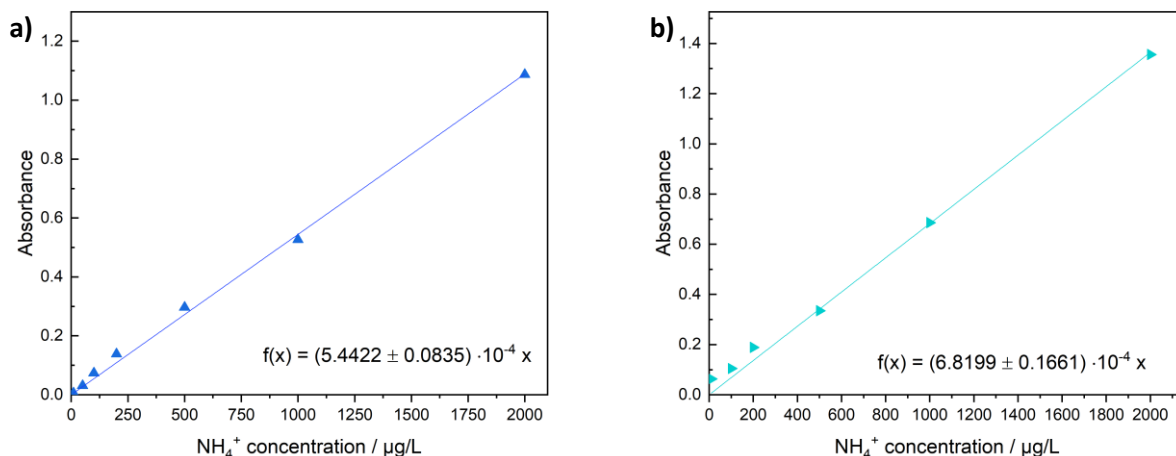
Figure S14 Calibration curve for the salicylate test in methanol/ water (a) and in 1 mM H_2SO_4 (b), using a 12% hypochlorite solution. Considerable deviations in the low concentration area for the calibration in H_2SO_4 indicate either trace amounts of ammonia impurities in the acid, or an interference of SO_4^{2-} with the test (the same effect was observed for Na_2SO_4 solutions). Maximal absorbance at around 660 nm was measured.
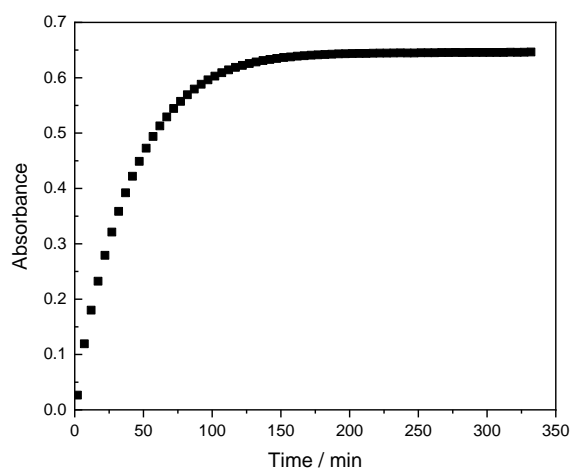
Figure S15 Color development for the salicylate test of a 1 mg/L NH_4^+ solution depending on the time. Absorbance was measured at 667 nm.
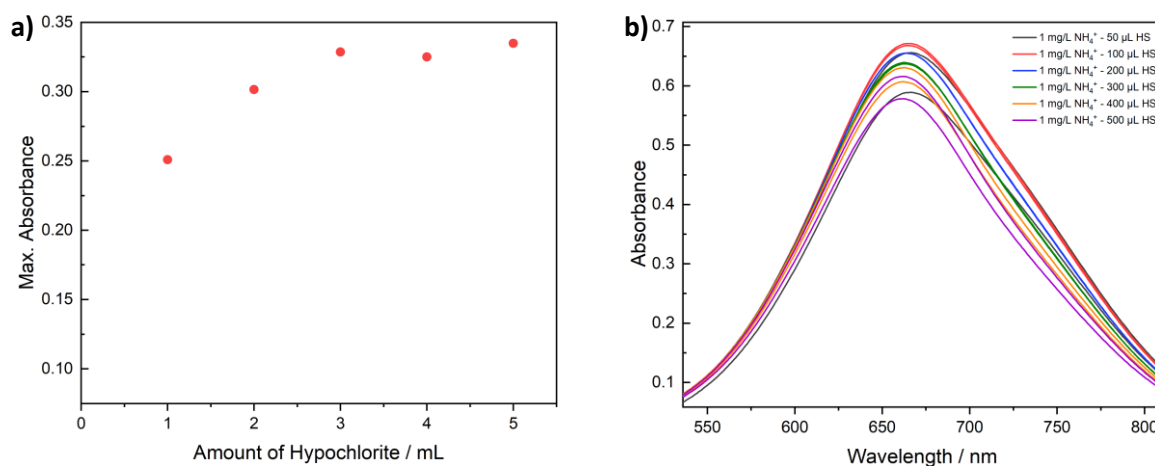
Figure S16 Influence of the amount of hypochlorite solution (12 % Cl_2) added to the stock solution (20 mL) for the test. HS: Hypochlorite solution.
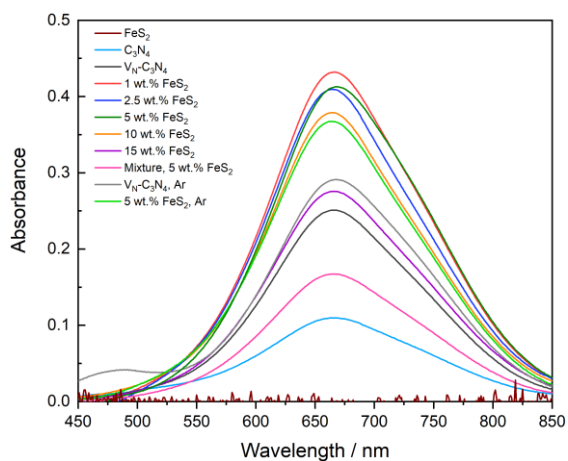
Figure S17 Ammonia quantification for the composite samples after photocatalytic NRR, using a 12 % hypochlorite solution.
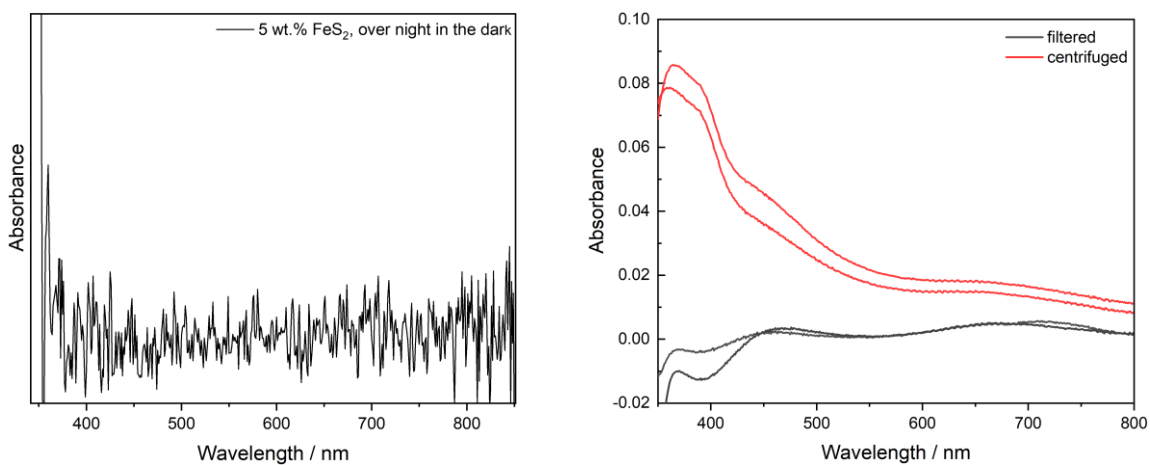
Figure S18 Reference measurements: Ammonia concentration after stirring overnight in the dark (left) and control of the influence of carbon nitride on the salicylate test by dispersing C_3N_4 in water/methanol and subsequently removing the powder *via* filtration or centrifugation and analyzing the solution for ammonia.
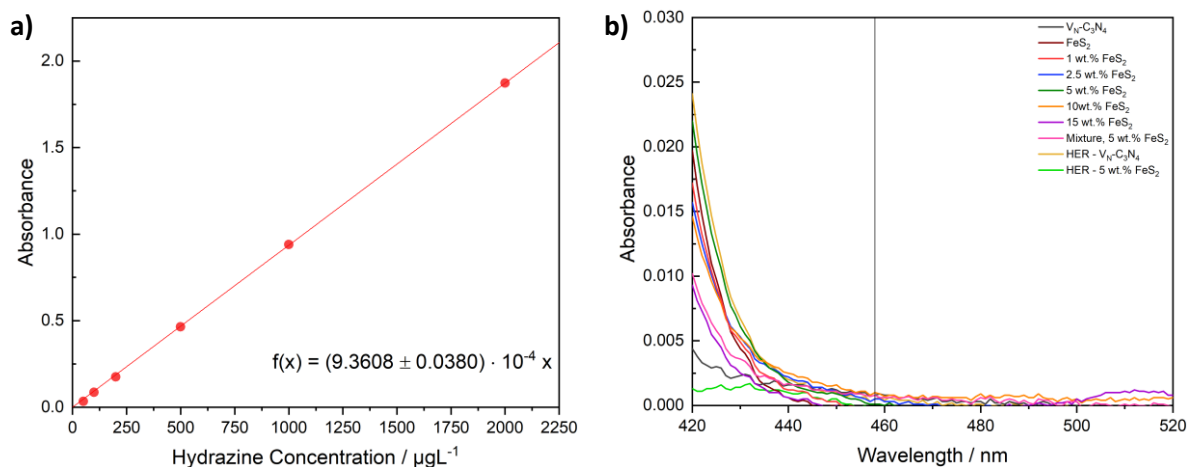
Figure S19 Calibration curve for the test for hydrazine (a) and testing of the reaction solution after photocatalytic NRR (b).
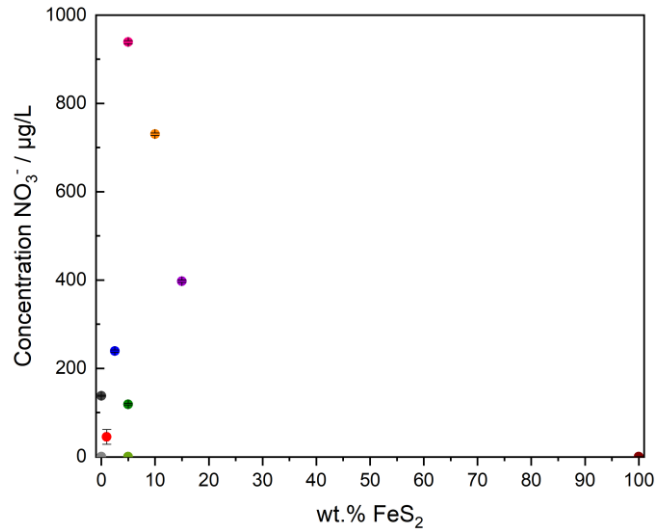
Figure S20 Nitrate concentrations determined by ion chromatography.
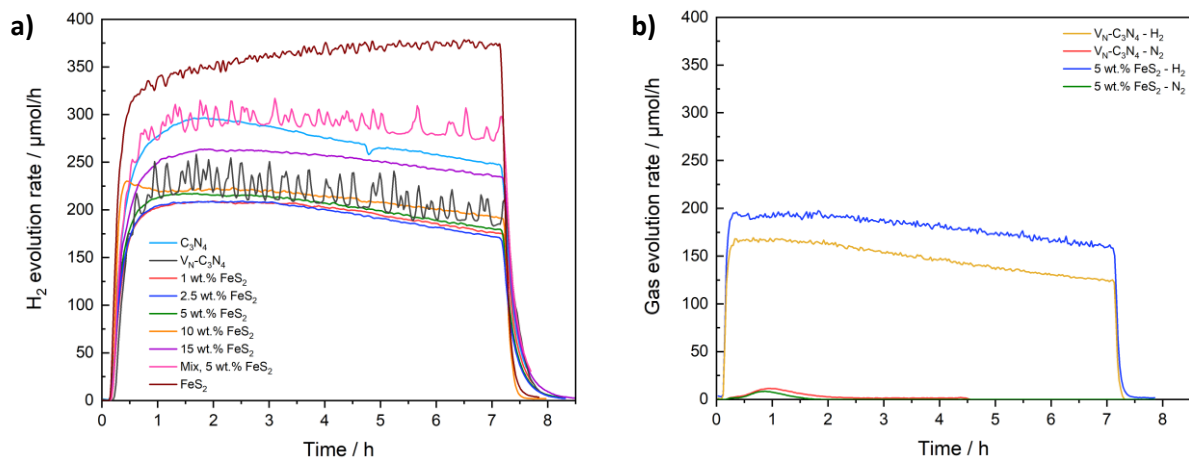
Figure S21 Gas evolution rates for the photocatalytic experiments in N_2 atmosphere (a) and in Ar atmosphere (b).
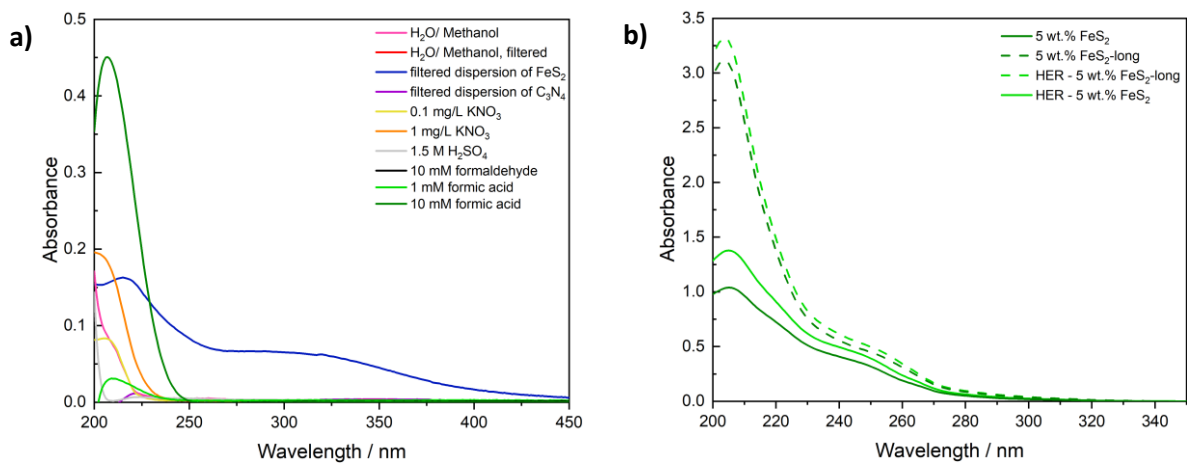
Figure S22 Reference measurements for UV-spectra (a) and UV spectra for the longtime photocatalytic measurements (b).
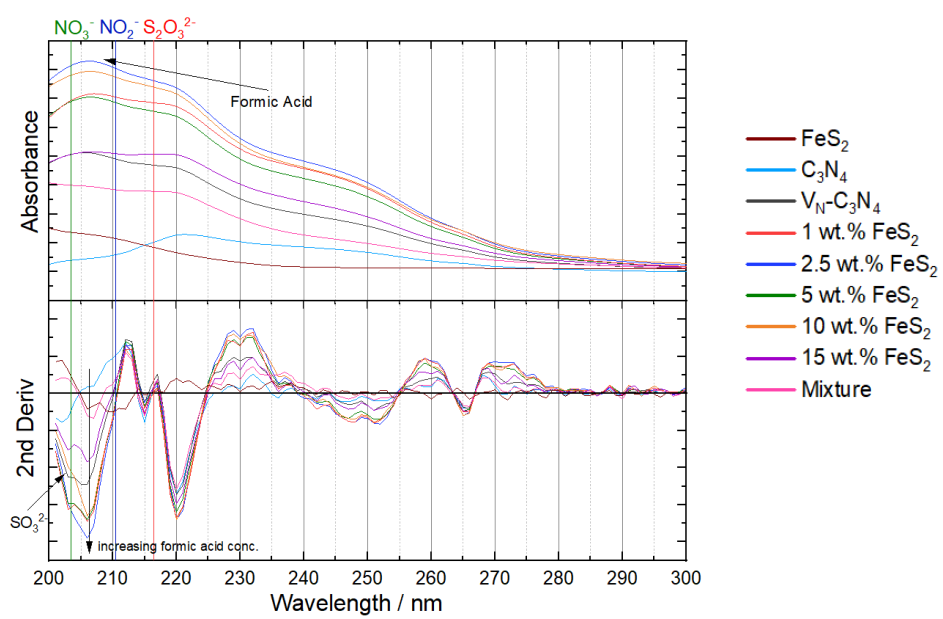
Figure S23 2nd derivative of the UV spectra of the NRR solution.
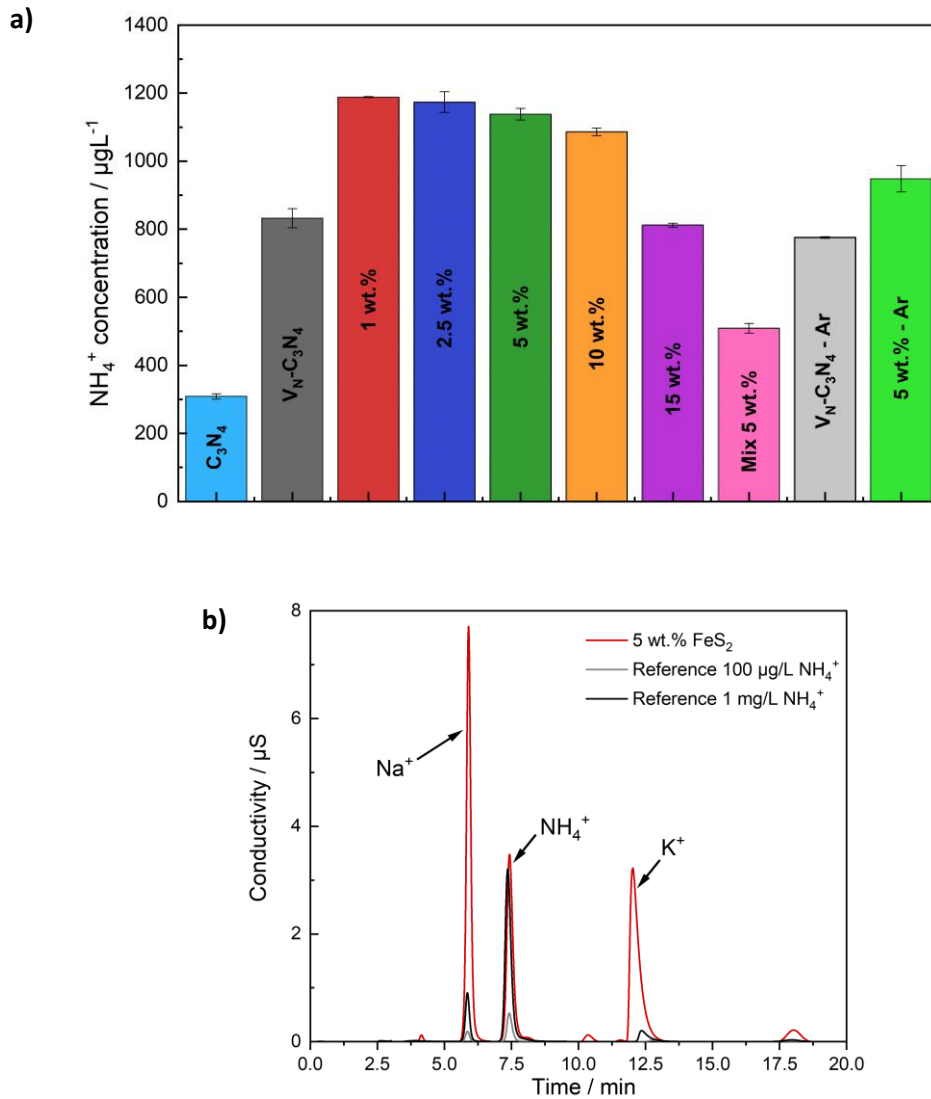
Figure S24 Ammonia concentrations determined with ion chromatography (a), and an exemplary chromatographic trace for the composite containing 5 wt.% of FeS$_2$ (b). Sodium impurities were found in all samples, as well as the calibration standards and are likely contaminations the glass vessels. Additionally, potassium residues were detected.
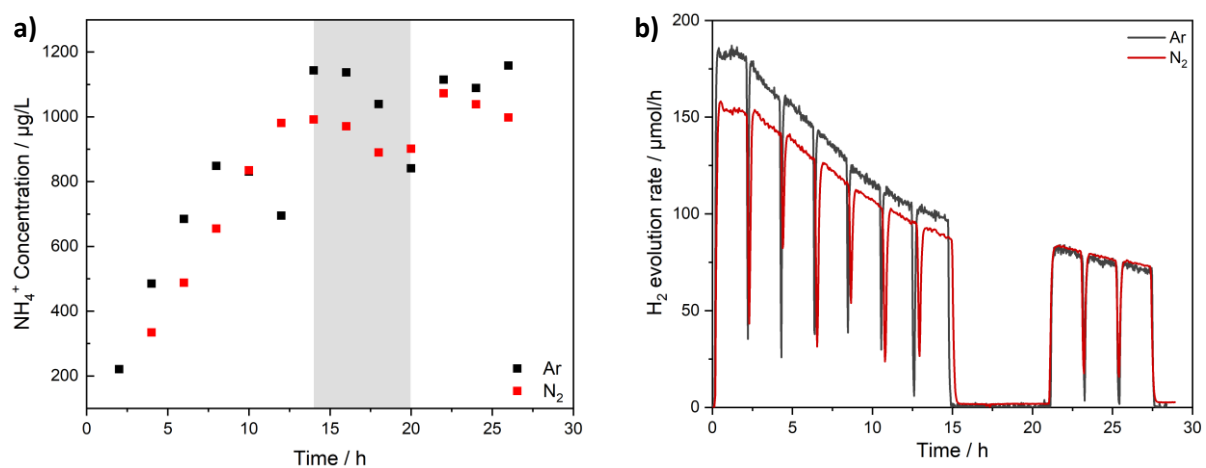
Figure S25 Ammonia concentration development during the longtime measurement in nitrogen and argon atmosphere, respectively and corresponding hydrogen evolution.

Table S8 Accumulated ammonia determined in the acid traps.

	Accumulated ammonia (12 % hypochlorite solution) /µg
C_3N_4	0.848 ± 0.041
V_N-C_3N_4	1.648 ± 0.001
V_N-C_3N_4 - Ar	3.675 ± 0.101
FeS_2	
1 wt.% FeS_2	3.480 ± 0.004
2.5 wt.% FeS_2	3.022 ± 0.053
5 wt.% FeS_2	3.193 ± 0.007
10 wt.% FeS_2	2.080 ± 0.014
15 wt.% FeS_2	2.294 ± 0.004
5 wt.% FeS_2 - Ar	6.552 ± 0.055
Mix – 5 wt.% FeS_2	0.941 ± 0.039
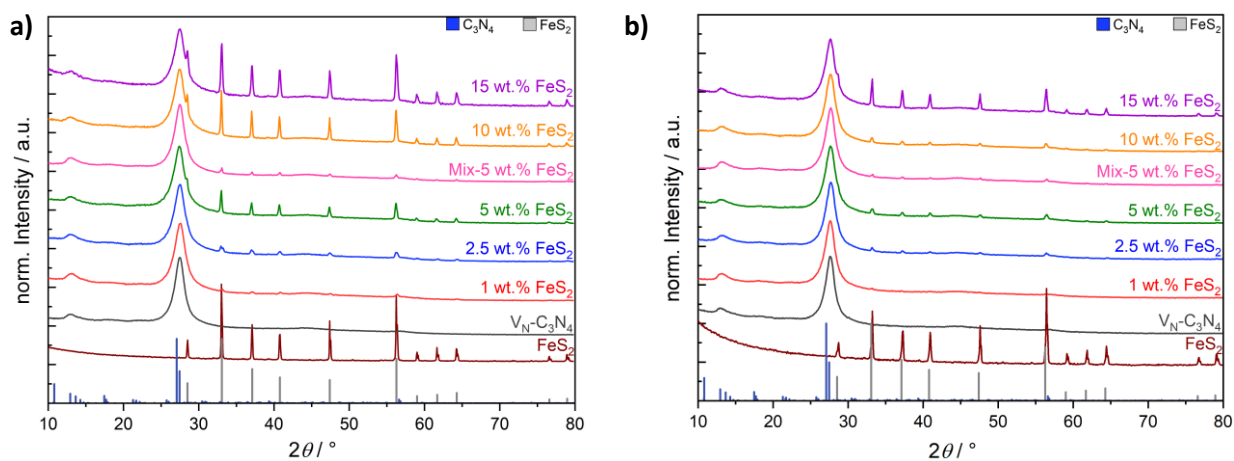
Figure S26 PXRD patterns for the composites before (a) and after (b) photocatalytic experiments, showing a reduction in the relative intensity of the reflections for FeS_2 but otherwise retained composition.
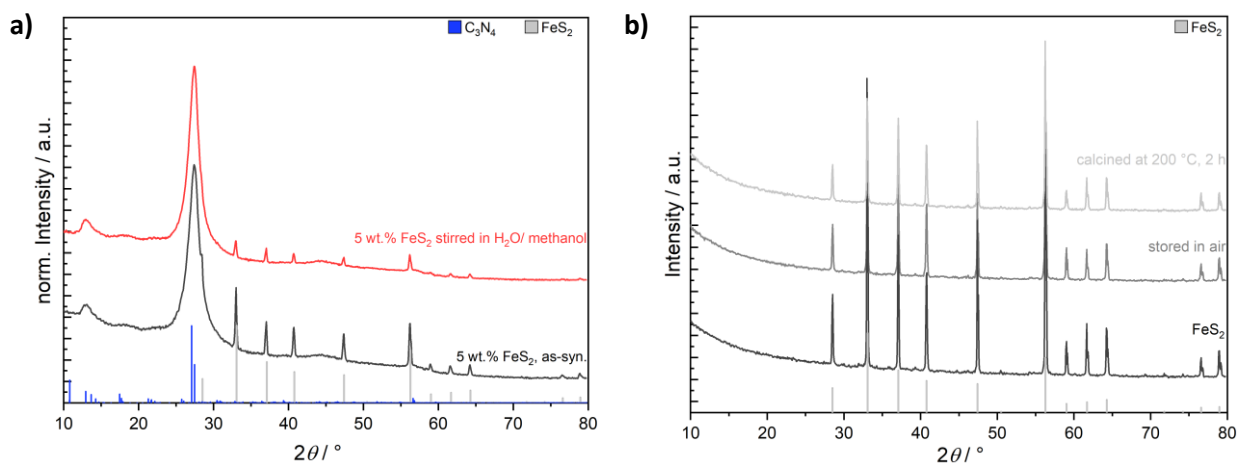
Figure S27 XRD patterns indicating the removal of FeS_2 in the composite after dispersion in water/ methanol mixtures (a) and the effect of storage in air and calcination at 200 °C on the structure of FeS_2 (b).
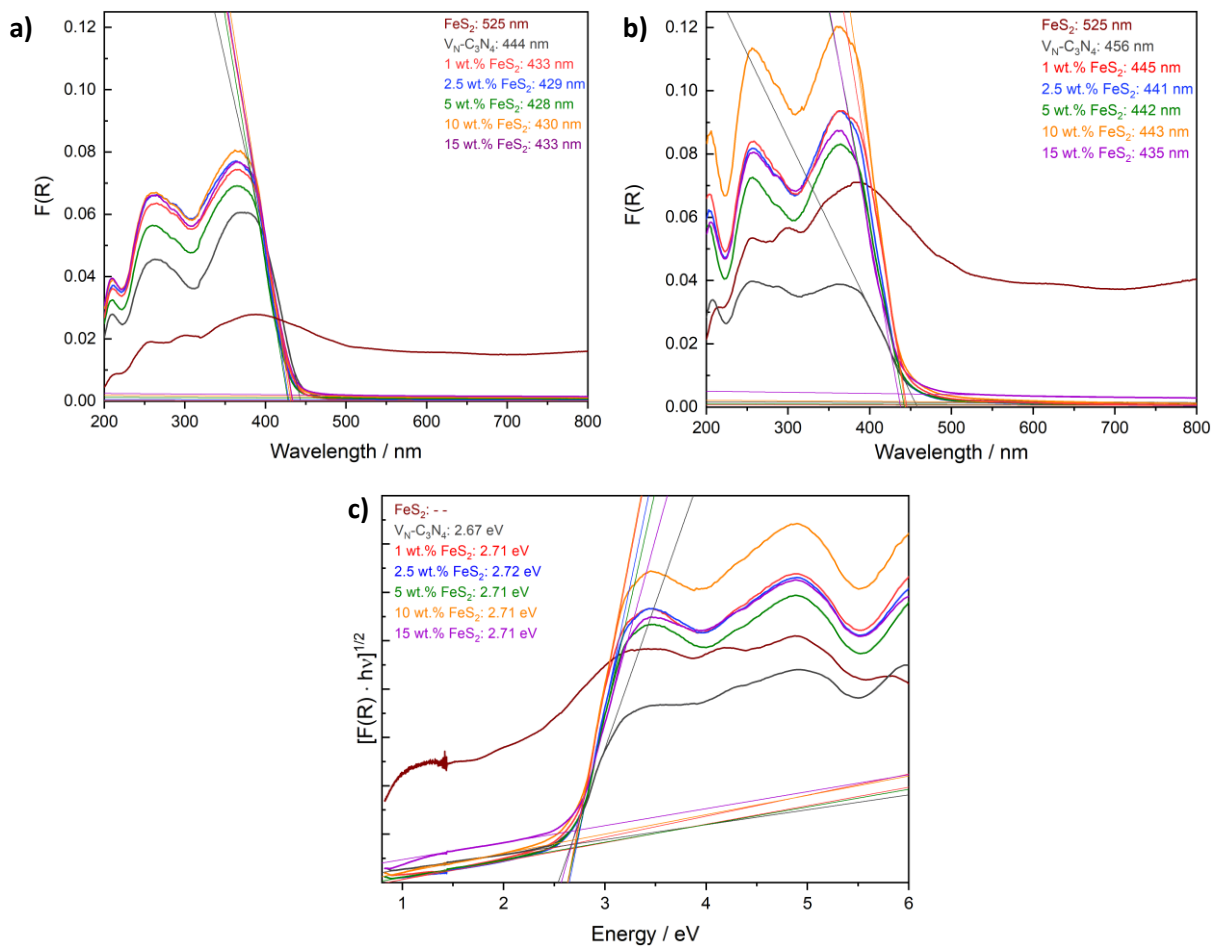
Figure S28 Kubelka-Munk plots of the composites before (a) and after the photocatalysis (b) showing increased UV-light absorption, and corresponding indirect Tauc plots after the photocatalytic ammonia generation (c).
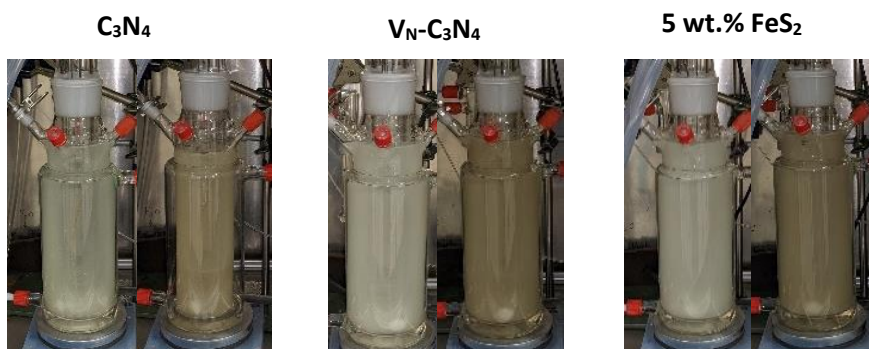
Figure S29 Color change of the photocatalysts over the course of the NRR.
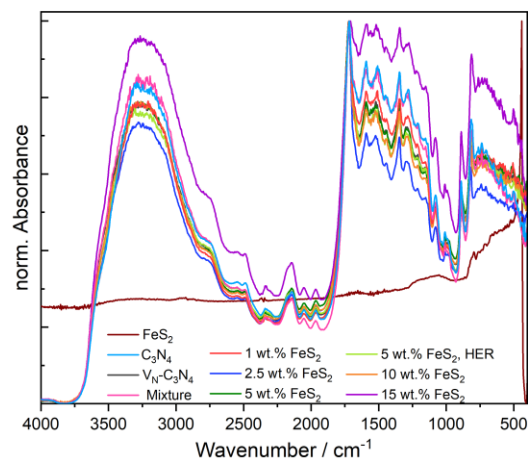
Figure S30 DRIFT spectra of the composites after the photocatalytic experiments.
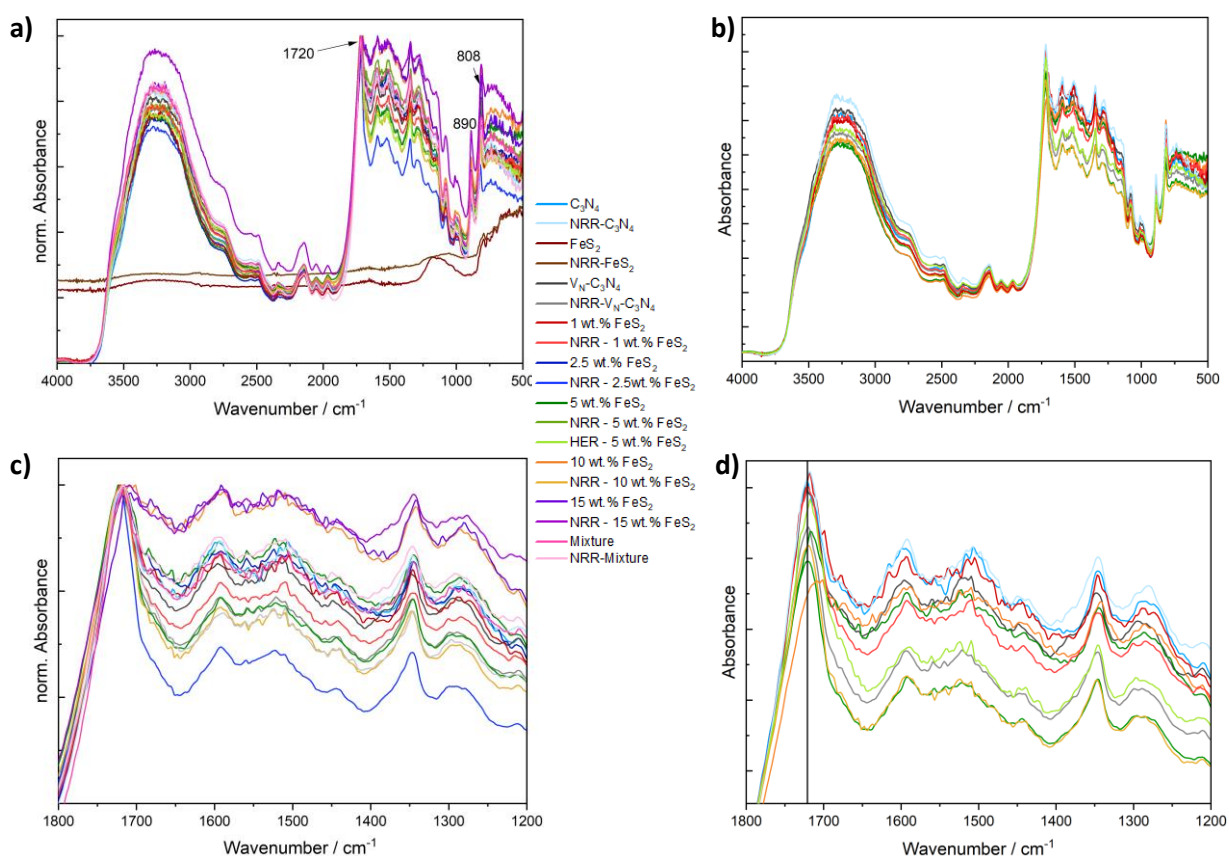
Figure S31 DRIFT spectra of the composite before and after the photocatalytic experiments. The spectra are shown normalized (a and c) and for exemplary composites without normalization (b and d). An excerpt for the C-N vibrational range of the aromatic system is shown at the bottom. The intensity for the vibration at 1720 cm^{-1} is slightly reduced, but not as much, as the other C-N vibrations of the heptazine units, as elucidated by normalization. It is additionally shifted back towards higher wavenumbers, indicating an increase in the energy of the system.
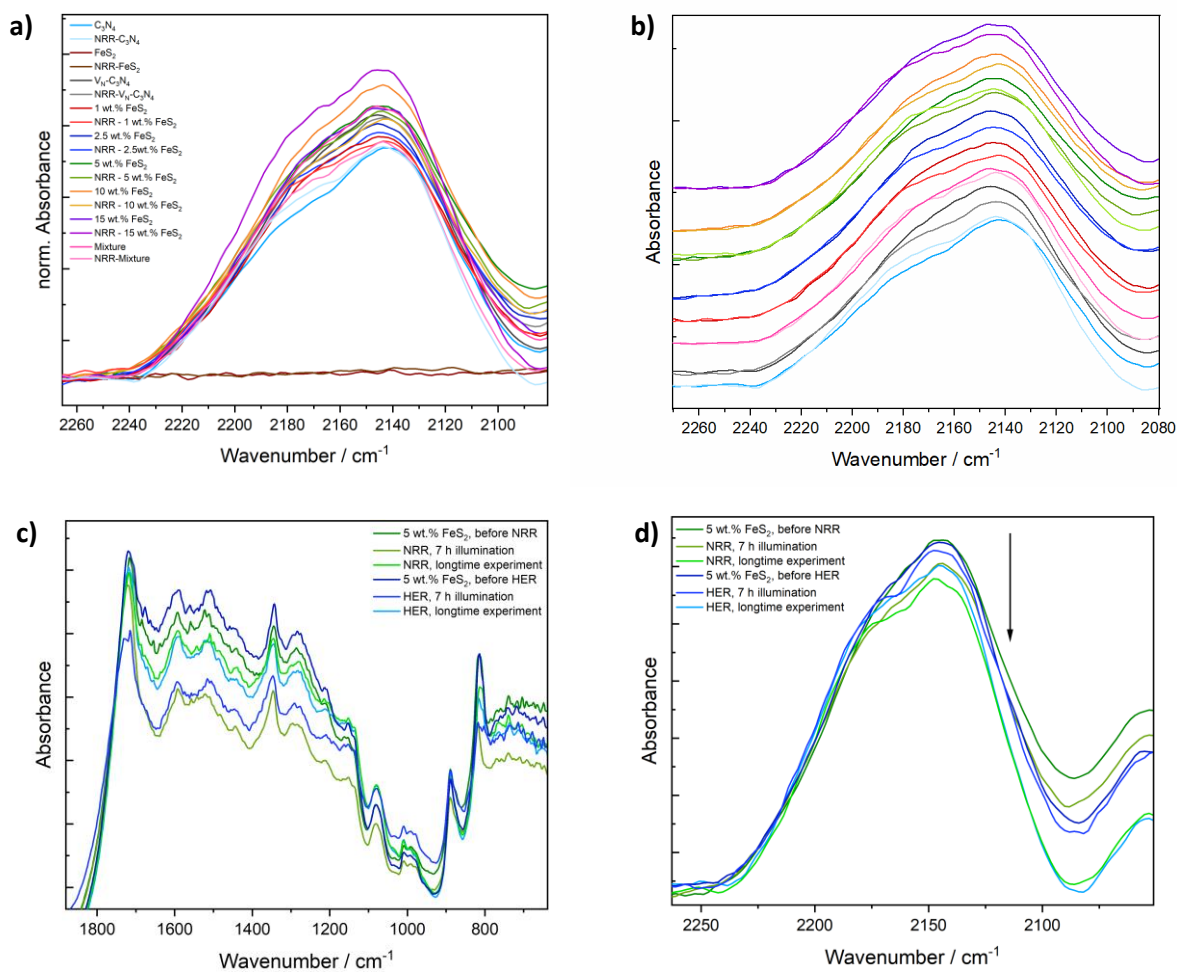
Figure S32 Structural evolution of the heptazine framework and cyano groups after the photocatalytic NRR as observed in DRIFT measurements (a and b) and for the longtime experiments (c and d).
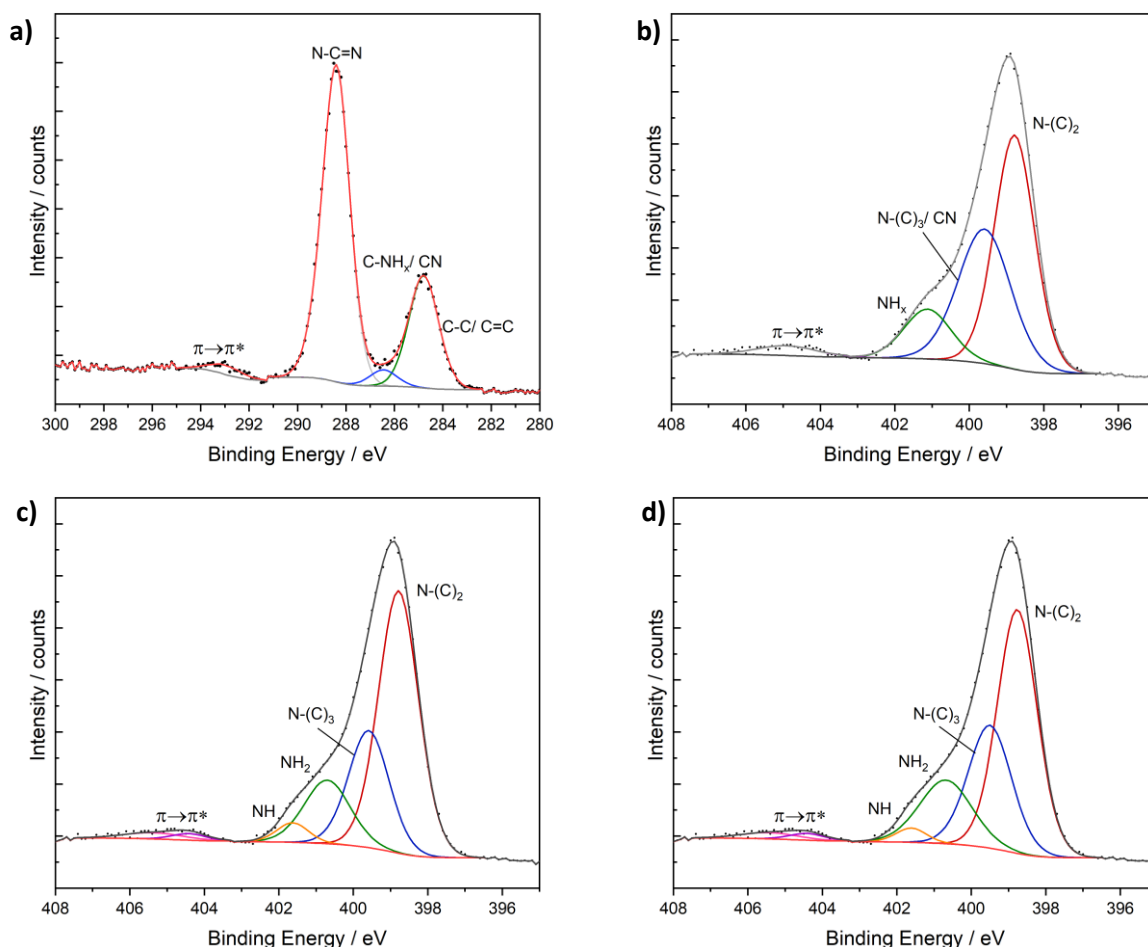
Figure S33 Photoelectron spectra for the composite (5 wt.% FeS$_2$) after the NRR. C 1s spectrum (a), N 1s spectrum fitted, treating the amino group signals as one (b), N 1s spectrum using the parameters for the fit of the composite, that was based on a maintained NH/NH$_2$ ratio as starting conditions (removing the constraints for the fit) (c), N1s spectrum, using the parameters for the fit of the composite with retained NH/N-(C)$_3$ ratio as starting conditions (removing the constraints for the fit itself) (d).

Table S8 Binding energy and ratio for carbon and nitrogen species in a composite before and after NRR.

		-NH	-NH$_2$	N-(C)$_3$	N-(C)$_2$	$\pi \rightarrow \pi*$	N-(C)$_2$/N-(C)$_3$	N-(C)$_2$/NH
5 wt.% before NRR	Binding energy / eV	401.6	400.5	399.4	398.8			
	Amount / at.%	5.1	17.5	27.8	49.7		1.79	9.75
5 wt.% After NRR (d)	Binding energy / eV	401.6	400.7	399.5	398.8	404.4, 405.4		
	Amount / at.%	2.3	17.7	28.3	51.7		1.83	22.4
after NRR (c)	Binding energy / eV	401.6	400.7	399.6	398.8	404.4; 405.3		
	Amount / at.%	3.3	15.6	25.3	55.9		2.21	16.9

		C-C	N-C=N	C-NH$_x$; CN	$\pi \rightarrow \pi*$	$\pi \rightarrow \pi*$	CN/N-C=N	CN/C-C
5 wt.% before NRR	Binding energy / eV	284.8	288.5	286.5	293.1	295.6		284.8
	Amount / at.%	11.3	84.4	4.3			0.051	11.3
5 wt.% after NRR	Binding energy / eV	284.8	288.4	286.4	293.0			
	Amount / at.%	27.0	69.4	3.6			0.052	0.13

The N 1*s* spectrum was fitted using the parameters for the N 1*s* spectrum of the composite before NRR as starting parameters (***Figure S10***, ***Table S6***). Constraints were removed for the fitting, since no information about relative ratio relations and possible shifts were available.
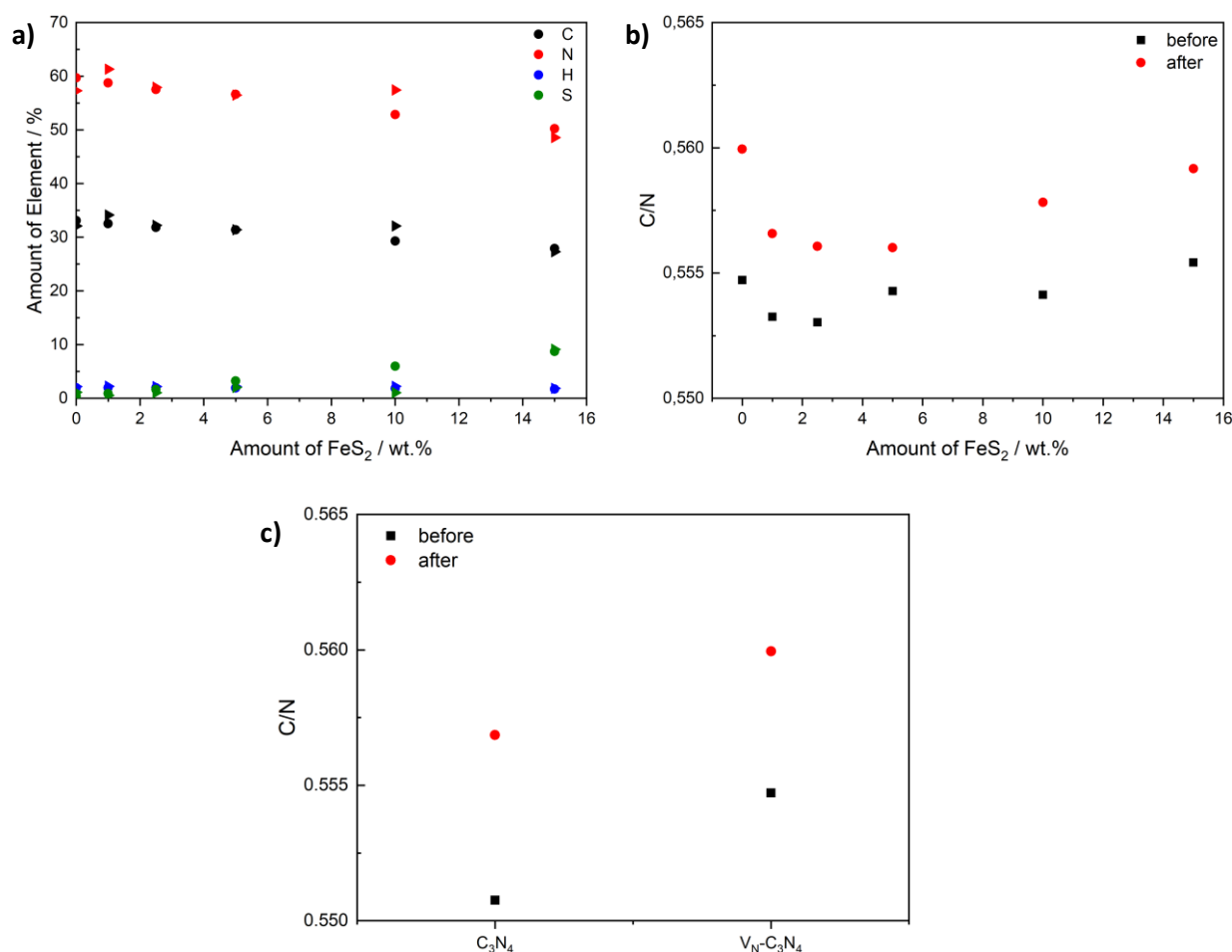
Figure S34 Elemental Analysis for CHNS for the composites before (circle) and after (triangle) the photocatalytic experiment (a). For better accuracy, the analysis was performed at least twice and the results averaged. C/N ratios for the different composites before and after photocatalytic NRR (b). The change in the C/N ratio upon KOH treatment is illustrated in (c).

Determination of the fraction of extracted nitrogen:

The degraded fraction of V_N-C_3N_4 might roughly be estimated from the C/N ratio obtained from elemental analysis. However, this is based on small portions of the catalyst and thus not very accurate, as already shown by the deviation of the ratio from the ideal value of 0.75. The C/N ratio in V_N-C_3N_4 itself changed by approx. 0.005, which equals to 0.9 %.

If the difference is calculated as:

$$\Delta\frac{C}{N} = \frac{3}{4-x} - \frac{3}{4} = 0.005 \quad \rightarrow \quad x = 0.02649$$

This equal to a change in the N-fraction of 0.66 %. The nitrogen content for V_N-CN (200 mg total) is 121.74 mg (based on a composition of C/N=0.75). This would equal to a nitrogen extraction of 0.00662*121.74 mg = 0.806 mg, which is larger than the generated amounts of ammonia determined with IC, but can still show, that large amounts of nitrogen are extracted from the framework and that the ammonia is thus probably mainly generated from the nitrogen of the C_3N_4 framework.

If the C/N ratio of 0.55471, as obtained from EA, is taken as a starting ratio, a rough composition of $C_3N_{5.408}$ can be estimated. Following the same calculation as illustrated above, a change in the N-fraction of 0.93 % is obtained, resulting in a nitrogen extraction of 1.27 mg.

The calculation was performed for CN-CN and not for the composites, as a decreased C/N ratio before the reaction (as compared to VN-CN) illustrates some uncertainties in the exact ratio for the composites, likely due to strong interactions with the iron.

If the calculation is performed backwards, *it est* estimating the extracted nitrogen fraction based on the generated amount of ammonia (IC results), one arrives at an extracted fraction of 0.32 % for V_N-CN if a C/N ratio of 0.75 is considered, or 0.29 % based on the ratio obtained from EA. For the composite containing 1 wt.% of FeS2, values of 0.59 % or 0.53 % of extracted nitrogen are calculated. These values are smaller than those obtained above, illustrating, how large amounts of nitrogen are extracted from the framework. This is a good indication, that the ammonia is generated from nitrogen in the framework.
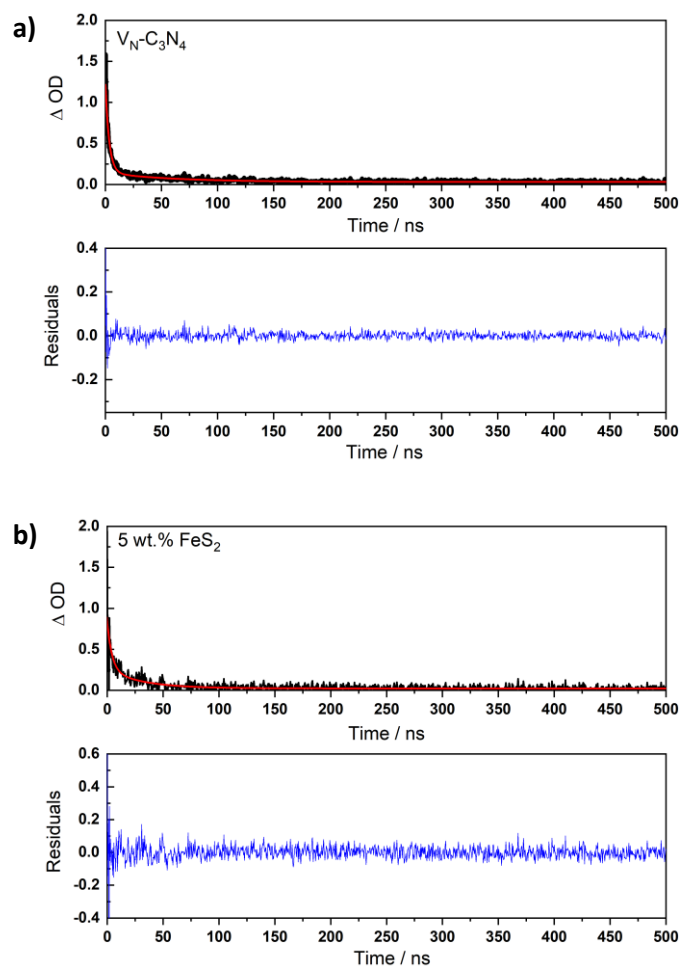
Figure S35 ns-TAS decay kinetics at 800 nm and corresponding exponential fit for V_N-C_3N_4 (a) and the composite with 5 wt.% of FeS_2 (b).
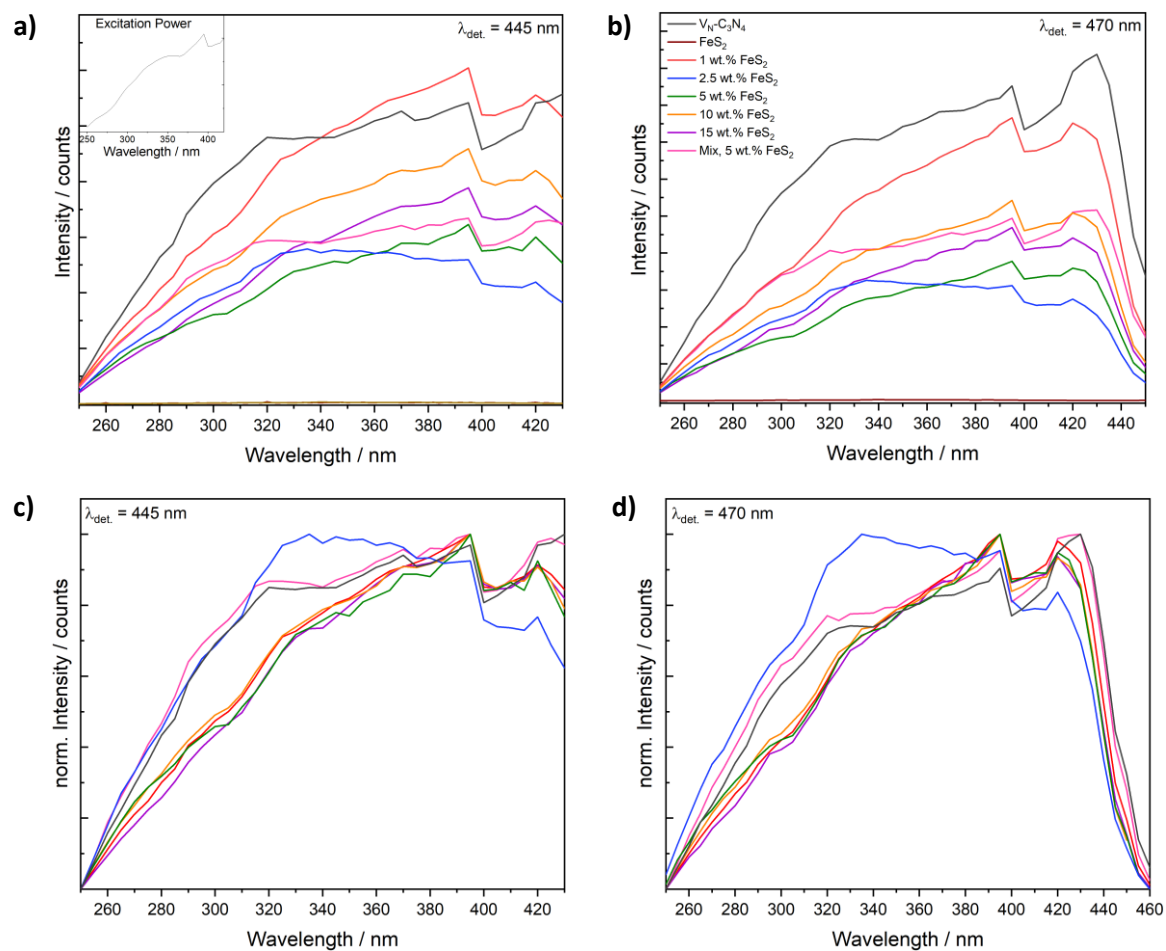
Figure S36 Excitation spectra for the composites at detection wavelengths of 445 nm (shoulder to the left of the emission spectra) (a and c) and 470 nm (main emission peak) (b and d). The dip at 400 nm is not a feature belonging to the sample, as it is also apparent in the curve for the excitation power (insert). The spectra are depicted with absolute intensity (top) and again with normalized intensity (bottom).
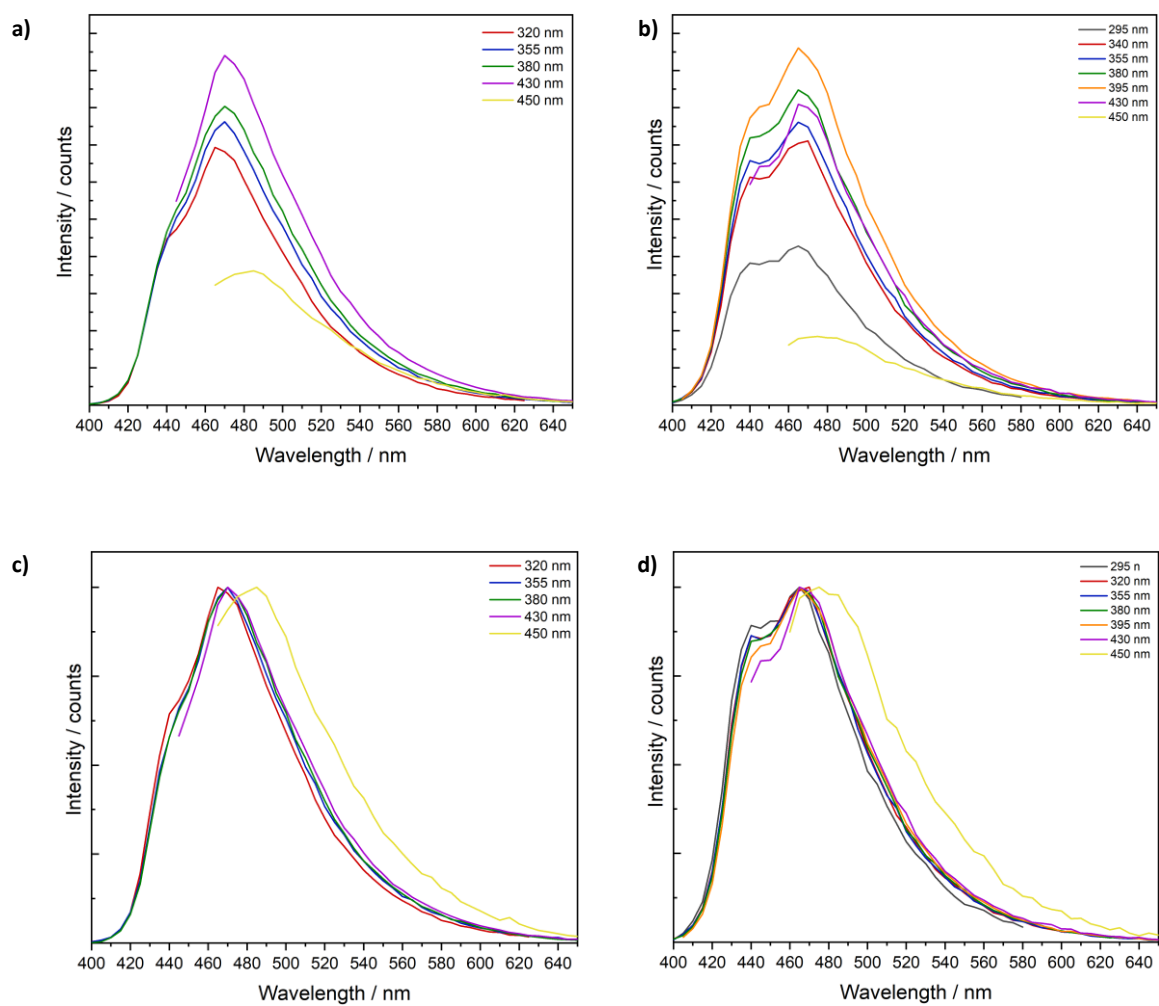
Figure S37 Emission spectra for V_N-C_3N_4 (a) and the composite containing 1 wt.% of FeS_2 (b) with excitation at different wavelengths. Normalized spectra are shown in (c) and (d).
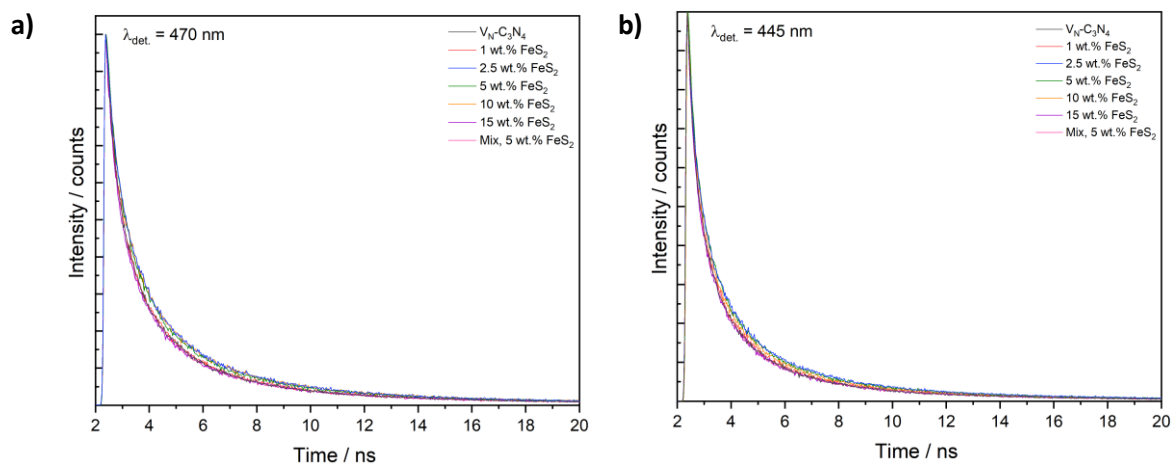
Figure S38 Exponential decay of emission at 470 nm (a) and 445 nm (b), measured with single photon counting after laser excitation at 355 nm.
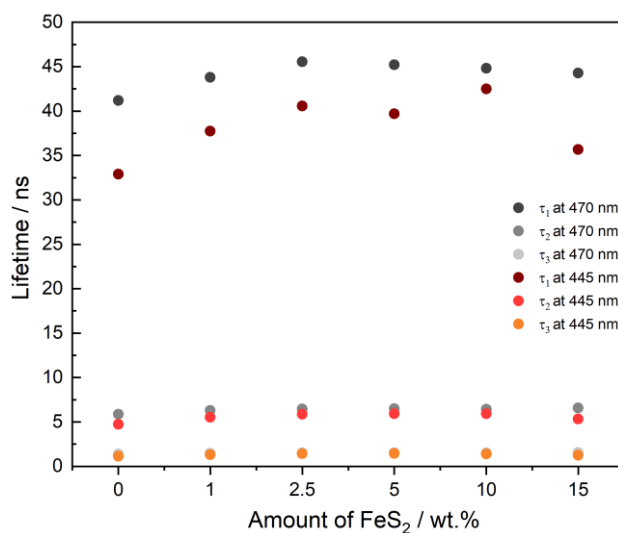
Figure S39 Fluorescent lifetimes for C_3N_4, V_N-C_3N_4 and thereof derived composites.

Table S9 Fluorescent lifetimes in ns for C_3N_4, V_N-C_3N_4 and thereof derived composites.

	τ_1', 470 nm	τ_2', 470 nm	τ_3', 470 nm	τ_1, 445 nm	τ_2, 445 nm	τ_3, 445 nm
V_N-C_3N_4	41.2	5.86	1.39	32.9	4.74	1.13
1 % FeS$_2$	43.8	6.30	1.48	37.7	5.52	1.32
2.5 % FeS$_2$	45.6	6.45	1.53	40.6	5.88	1.42
5 % FeS$_2$	45.2	6.50	1.53	39.7	5.93	1.44
10 % FeS$_2$	44.8	6.44	1.53	42.5	5.92	1.38
15 % FeS$_2$	44.3	6.58	1.55	35.7	5.34	1.26
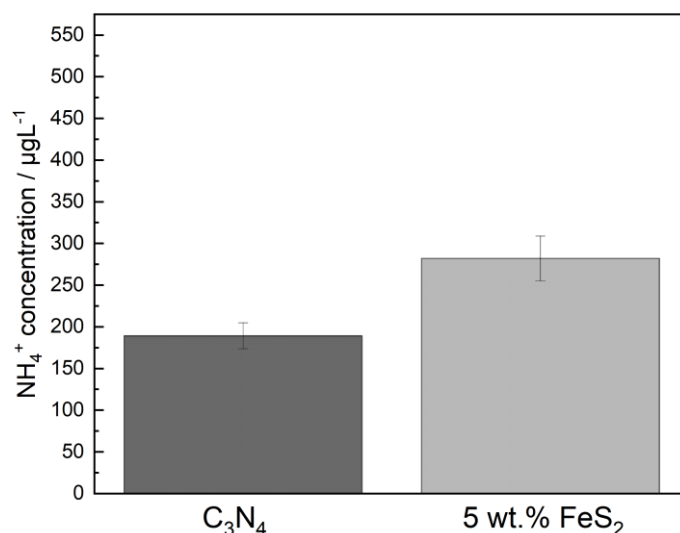
Figure S40 Ammonia concentrations determined for NRR with bulk (not KOH-treated) C_3N_4 and a thereof derived composite with 5 wt.% of FeS_2. Here, the composite formation only results in a lower improvement of the activity compared to V_N-C_3N_4. Concentrations determined with ion chromatography are 309 µg/L NH_4^+ for C_3N_4 and 442 µg/L NH_4^+ for the composite, respectively.
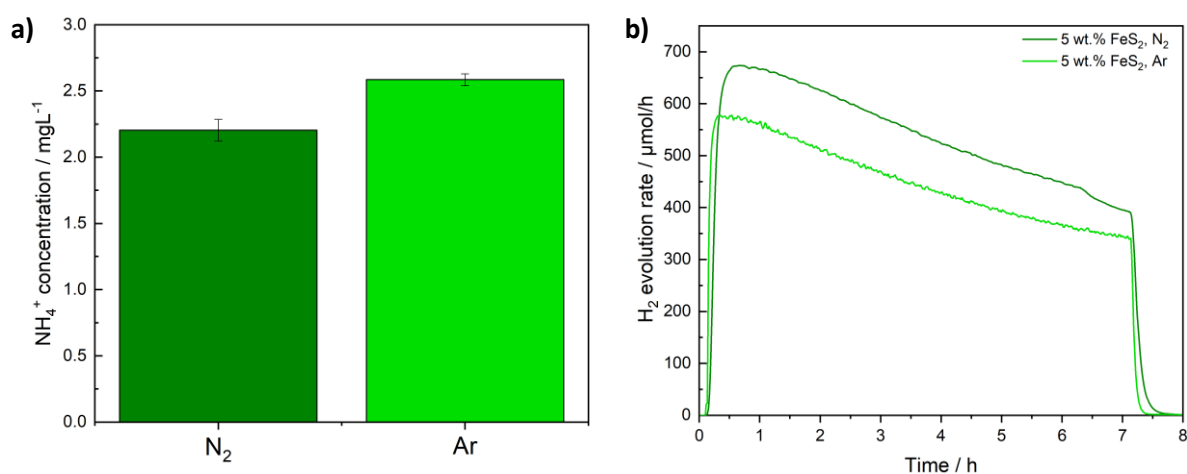
Figure S41 Generated ammonia concentrations in 100 % of methanol as a solvent (a) and corresponding hydrogen evolution (b). The amount of ammonia generated is larger in both nitrogen and argon atmosphere, due to the better hole scavenging ability of pure methanol compared to an aqueous solution. Ammonia concentrations were determined with IC.

9 List of Scientific Contributions

9.1 Peer-Reviewed Publications

- **J. Zander**, M. Weiss, R. Marschall, „Fast and Facile Microwave Synthesis of Cubic $CuFe_2O_4$ Nanoparticles for Electrochemical CO_2 Reduction", *Adv. Energy Sustain. Res.* **2023**, *4*, 2200184; DOI: 10.1002/aesr.202200184

- **J. Zander**, J. Timm, M. Weiss, R. Marschall, „ Light-Induced Ammonia Generation over Defective Carbon Nitride Modified with Pyrite", *Adv. Energy Mater*. **2022**, *12*, 2202403; DOI: 10.1002/aenm.202202403

- **J. Zander**, R. Marschall, "Ni_2FeS_4 as highly efficient earth-abundant co-catalyst in photocatalytic hydrogen evolution", *J. Mater. Chem. A* **2023***, DOI: 10.1039/D3TA02439C

Publications that are not included in this thesis:

- **J. Zander**, J. Wölfel, M. Weiss, Y. Jiang, N. Cheng, S. Zhang, R. Marschall, "Medium- and high-entropy spinel ferrite nanoparticles via low-temperature synthesis for the oxygen evolution reaction", *Adv. Funct. Mater.* **2023**, 2310179, DOI: 10.1002/adfm.202310179

- D. Ziegenbalg, **J. Zander**, R. Marschall, „Photocatalytic Nitrogen Reduction: Challenging Materials with Reaction Engineering", *ChemPhotoChem* **2021**, *5*, 792–807; DOI: 10.1002/cptc.202100084

- C. Simon, **J. Zander**, T. Kottakkat, M. Weiss, J. Timm, C. Roth, R. Marschall, „Fast Microwave Synthesis of Phase-Pure Ni_2FeS_4 Thiospinel Nanosheets for Application in Electrochemical CO_2 Reduction", *ACS Appl. Energy Mater.* **2021**, *4*, 8702–8708, DOI: 10.1021/acsaem.1c01341

- R. Fertig, T. Irrgang, F. Freitag, **J. Zander**, R. Kempe, „Manganese-Catalyzed and Base-Switchable Synthesis of Amines or Imines *via* Borrowing Hydrogen or Dehydrogenative Condensation", *ACS Catalysis* **2018**, *8*, 8525-8530, DOI: 10.1021/acscatal.8b02530

9.3 Contributions to Conferences

- **Oral** contribution to the 241st ECS Meeting 2022 in Vancouver, Canada, 29.05.2022 – 02.06.2022:
  J. Zander, R. Marschall, "Novel Iron-Based Cocatalysts for Photocatalytic Water Splitting and Nitrogen Reduction"

- **Poster** contribution to the 23rd International Conference on Photochemical Conversion and Storage of Solar Energy (IPS) 2022 in Lausanne, Switzerland, 02.08.2022 – 05.08.2022: **J. Zander**, J. Timm, M. Weiss, R. Marschall, "Activity Enhancement of Carbon Nitride by Modification with Pyrite for Photocatalytic Ammonia Generation"

- **Poster** contribution to the 21st Conference on Inorganic Chemistry of the GDCh (Gesellschaft Deutscher Chemiker) divisions of Inorganic Chemistry and Solid-State Chemistry & Materials Research 2022 in Marburg, Germany, 26.09.2022 – 28.09.2022: **J. Zander**, J. Timm, M. Weiss, R. Marschall, "Activity Enhancement of Carbon Nitride for Photocatalytic Ammonia Generation by Modification with Pyrite"

- **Poster** contribution to the 3rd Conference of the GDCh Division of Chemistry and Energy 2023 in Pfinztal, Germany, 24.05.2023 – 25.05.2023: **J. Zander**, J. Timm, M. Weiss, R. Marschall, "Light-Induced Ammonia Generation over Defective Carbon Nitride Modified with Pyrite"

10 Abbreviations & Symbols

10.1 Abbreviations

A	acceptor
AC	alternating current
ad.	adsorbed
AM	air mass
approx.	approximately
AQE	apparent quantum efficiency
AQY	apparent quantum yield
as-syn	as-synthesised
ASTM	American Society for Testing and Materials
ATP	adenosine triphosphate
at.%	atomic percent
a.u.	arbitrary units
BET	Brunauer-Emmett-Teller
BG	band gap
CB	conduction band
CF	crystal field
CFSE	crystal field stabilisation energy
CN	carbon nitride
CO$_2$RR	CO_2 reduction reaction
COD	Crystallography Open Database
CV	cyclic voltammetry
D	donor
DC	direct current
DFT	density functional theory
DLS	dynamic light scattering
DRIFT	diffuse reflectance infrared Fourier transformed
DSC	differential scanning calorimetry
EA	elemental analysis
ECSA	electrochemical active surface area
EDX	energy dispersive X-ray (spectroscopy)
EG	ethylene glycol
_e.g._	_exempli gratia_ (for example)
EIS	electrochemical impedance spectroscopy
eq.	equation
_et al._	_et alii_ (and others)
FE	Faradaic efficiency
FTO	fluorine doped tin oxide
FWHM	full width half maximum
GC	gas chromatography
GDP	gross domestic product

HER	hydrogen evolution reaction
HOMO	highest occupied molecular orbital
HS	high spin
IC	ion chromatography
ICDD	International Centre for Diffraction Data
i.e.	*id est* (that is)
iR	internal resistance
IR	infrared
ISCT	inter-sublattice charge transfer
IUPAC	International Union of Pure and Applied Chemistry
IVCT	intervalent charge transfer
LDH	layered double hydroxide
LMCT	ligand to metal charge transfer
LMO	$LiMn_2O_4$
LSPR	localised surface plasmon resonance
LUMO	lowest unoccupied molecular orbital
MS	mass spectrometry
NAP	near ambient pressure
NASA	National Aeronautics and Space Administration
NCEI	National Center for Environmental Informations
NHE	normal hydrogen electrode
NIR	near infrared
NOAA	National Oceanic and Atmospheric Administration
norm.	normalised
NREL	National Renewable Energy Laboratory
NRR	nitrogen reduction reaction
OER	oxygen evolution reaction
O_h	octahedra
OD	optical density
OWS	overall water splitting
Ox	oxidation
PEC	photoelectrochemistry
PHI	poly(heptazine)imide
PL	photoluminescence
PTI	poly(triazine)imide
PZC	point of zero charge
PODAAC	Physical Oceanography Distributed Active Archive Center
QE	quantum efficiency
QY	quantum yield
RCP	representative concentration pathways
Red	reduction
RHE	reversible hydrogen electrode
SB	Schottky barrier
SC	semiconductor
SEM	scanning electron microscopy
SMARTS2	Simple Model of the Atmospheric Radiative Transfer of Sunshine

STH		solar to hydrogen efficiency
T_d		tetrahedra
TAS		transient absorption spectroscopy
TCSPC		time correlated single photon counting
TEG		triethylene glycol
TEM		transmission electron microscopy
TG/ TGA		thermogravimetry/ thermogravimetric analysis
TOF		turnover frequency
US		United States
UV		ultra violet
VB		valence band
vis		visible
vs		versus
wt.%		weight percent
XAS		X-ray absorption
XRD/ PXRD		X-ray diffraction/ powder X-ray diffraction
XPS		X-ray photoelectron spectroscopy

10.2 List of Symbols

Symbol	Unit	Description
a	Å	lattice parameter
A	m^2	area
α		charge transfer coefficient
C	F	capacitance
χ^2		goodness of fit (Rietveld)
d	m	diameter
e	C	charge of an electron
E	eV	energy
E_{BG}	eV	band gap energy
E_F	eV	Fermi level
e^-		electron
ϵ		vacuum permittivity
ϵ_0	$F\ m^{-1}$	relative permittiviy
F	$C\ mol^{-1}$	Faraday constant
$F(R)$	a.u.	Kubelka-Munk function
G	$kJ\ mol^{-1}$	Gibbs free energy
η	V	overpotential
h	J s	Planck constant
h^+		hole
hkl		Miller indices

j	A cm^{-1}	current density
k		wave vector
λ	nm	wavelength
λ		degree of inversion
N_d	m^{-3}	donor density
p	Pa	pressure
ϕ	V	potential
q_p		photon flux
r	m	radius
R	J mol^{-1} K^{-1}	universal gas constant
R		reflectance
R_{exp}	%	expected R-factor
R_{wp}	%	weighted R-factor
S	nm^{-1}	Scattering vector
t	s	time
T	K	temperature
τ		lifetime
Θ	°	diffraction angle (XRD)
V	m^{-3}	volume
V_N		nitrogen vacancy
V_O		oxygen vacancy
ξ		dielectric field/ photonic efficiency
Z_I	Ω	impedance (imaginary part)
Z_R	Ω	impedance (real part)

11 Eidesstaatliche Versicherung und Erklärungen

(§ 9 Satz 2 Nr. 3 PromO BayNAT)

Hiermit versichere ich eidesstattlich, dass ich die Arbeit selbstständig verfasst und keine anderen als die von mir angegebenen Quellen und Hilfsmittel benutzt habe (vgl. Art. 64 Abs. 1Satz 6 BayHSchG).

(§ 9 Satz 2 Nr. 3 PromO BayNAT)

Hiermit erkläre ich, dass ich die Dissertation nicht bereits zur Erlangung eines akademischen Grades eingereicht habe und dass ich nicht bereits diese oder eine gleichartige Doktorprüfung endgültig nicht bestanden habe.

(§ 9 Satz 2 Nr. 4 PromO BayNAT)

Hiermit erkläre ich, dass ich Hilfe von gewerblichen Promotionsberatern bzw. -vermittlern oder ähnlichen Dienstleistern weder bisher in Anspruch genommen habe noch künftig in Anspruch nehmen werde.

(§ 9 Satz 2 Nr. 7 PromO BayNAT)

Hiermit erkläre ich mein Einverständnis, dass die elektronische Fassung der Dissertation unter Wahrung meiner Urheberrechte und des Datenschutzes einer gesonderten Überprüfung unterzogen werden kann.

(§ 9 Satz 2 Nr. 8 PromO BayNAT)

Hiermit erkläre ich mein Einverständnis, dass bei Verdacht wissenschaftlichen Fehlverhaltens Ermittlungen durch universitätsinterne Organe der wissenschaftlichen Selbstkontrolle stattfinden können.

_____	_____
Ort, Datum	Judith Zander